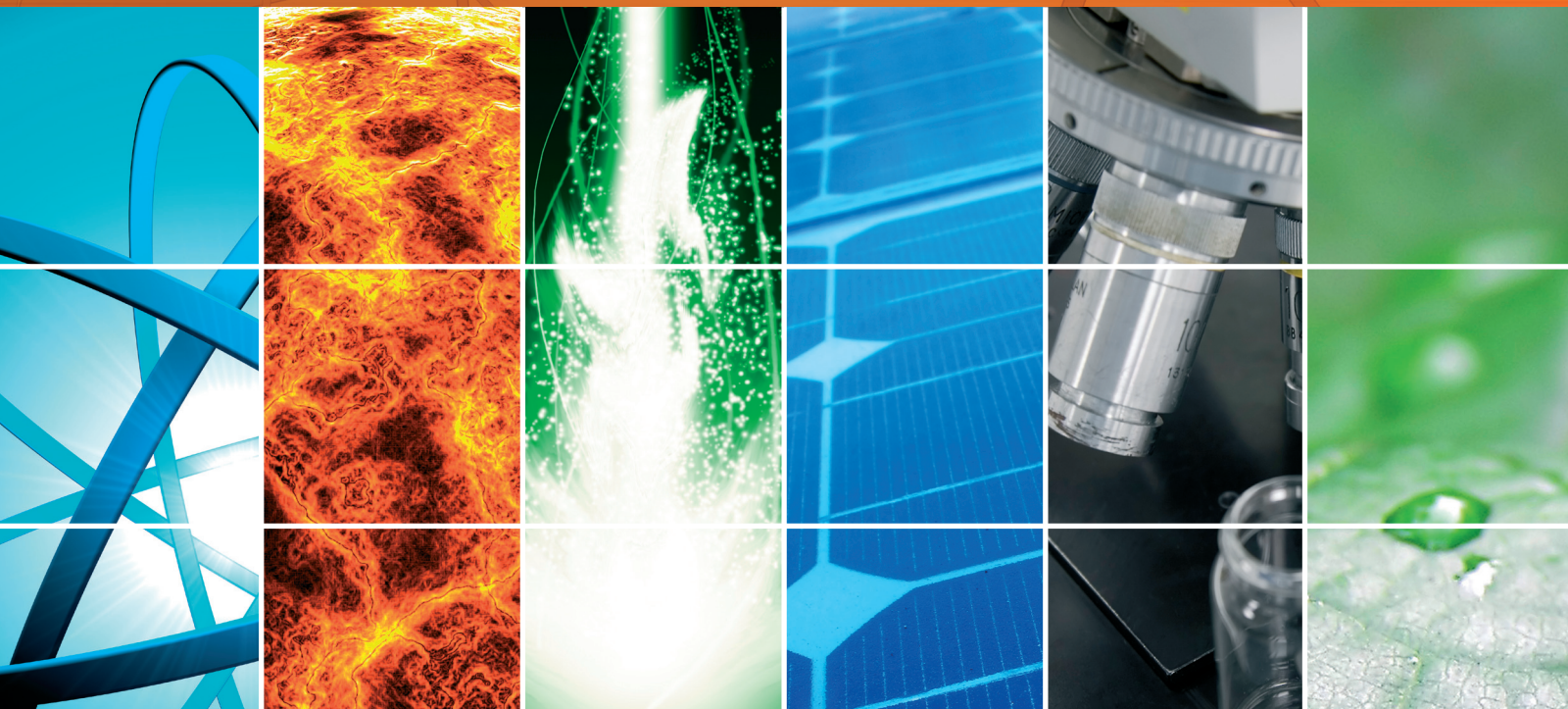


# Solar Energy and Clean Energy: Trends and Developments 2014

Guest Editors: Ching-Song Jwo, Ho Chang, Chao-Rong Chen, Yen-Lin Chen, and Mohammad Yusri Hassan





---

# **Solar Energy and Clean Energy: Trends and Developments 2014**

International Journal of Photoenergy

---

**Solar Energy and Clean Energy:  
Trends and Developments 2014**

Guest Editors: Ching-Song Jwo, Ho Chang, Chao-Rong Chen,  
Yen-Lin Chen, and Mohammad Yusri Hassan



---

Copyright © 2015 Hindawi Publishing Corporation. All rights reserved.

This is a special issue published in "International Journal of Photoenergy." All articles are open access articles distributed under the Creative Commons Attribution License, which permits unrestricted use, distribution, and reproduction in any medium, provided the original work is properly cited.

## Editorial Board

- M. S. A. Abdel-Mottaleb, Egypt  
Xavier Allonas, France  
Nicolas Alonso-Vante, France  
Wayne A. Anderson, USA  
Yanhui Ao, China  
Raja S. Ashraf, UK  
V. Augugliaro, Italy  
Detlef W. Bahnemann, Germany  
I. R. Bellobono, Italy  
Raghu N. Bhattacharya, USA  
Pramod H. Borse, India  
Alessio Bosio, Italy  
Stephan Buecheler, Switzerland  
Gion Calzaferri, Switzerland  
C. Chen, China  
Sung Oh Cho, Republic of Korea  
V. Cimrová, Czech Republic  
Juan M. Coronado, Spain  
Ying Dai, China  
D. D. Dionysiou, USA  
Pingwu Du, China  
M. M. El-Nahass, Egypt  
Polycarpos Falaras, Greece  
Chris Ferekides, USA  
Paolo Fornasiero, Italy  
Hermenegildo García, Spain  
Germà Garcia-Belmonte, Spain  
E. I. Garcia-Lopez, Italy  
Beverley Glass, Australia  
M. A. Gondal, Saudi Arabia  
Jr-Hau He, Taiwan  
Shinya Higashimoto, Japan  
Cheuk-Lam Ho, Hong Kong  
Wing-Kei Ho, Hong Kong  
Fuqiang Huang, China  
Adel A. Ismail, Egypt  
Chun-Sheng Jiang, USA  
Misook Kang, Republic of Korea  
Shahed Khan, USA  
Sun-Jae Kim, Republic of Korea  
Jong Hak Kim, Republic of Korea  
Sungjee Kim, Republic of Korea  
Cooper H. Langford, Canada  
Tae-Woo Lee, Republic of Korea  
Lecheng Lei, China  
Xinjun Li, China  
Zhaosheng Li, China  
Yuexiang Li, China  
Stefan Lis, Poland  
Vittorio Loddo, Italy  
Gongxuan Lu, China  
Dongge Ma, China  
N. M. Mahmoodi, Iran  
Nai Ki Mak, Hong Kong  
Rajaram S. Mane, India  
D. Mantzavinos, Greece  
Ugo Mazzucato, Italy  
Sheng Meng, China  
Jacek Miller, Poland  
Claudio Minero, Italy  
Antoni Morawski, Poland  
Franca Morazzoni, Italy  
F. Morlet-Savary, France  
M. Muneer, India  
Kun Na, Republic of Korea  
Ebinazar B. Namdas, Australia  
Maria Neves, Portugal  
Tebello Nyokong, South Africa  
Kei Ohkubo, Japan  
Haridas Pal, India  
Leonidas Palilis, Greece  
Leonardo Palmisano, Italy  
Ravindra K. Pandey, USA  
H. Park, Republic of Korea  
Pierre Pichat, France  
Gianluca Li Puma, UK  
Tijana Rajh, USA  
Peter Robertson, UK  
Avigdor Scherz, Israel  
Elena Selli, Italy  
Ganesh D. Sharma, India  
Jinn Kong Sheu, Taiwan  
Panagiotis Smirniotis, USA  
Zofia Stasicka, Poland  
Elias Stathatos, Greece  
J. Subbiah, Australia  
M. Swaminathan, India  
Kazuhiro Takanabe, Saudi Arabia  
Mohamad-Ali Tehfe, Canada  
K. R. Justin Thomas, India  
Yang Tian, China  
Nikolai V. Tkachenko, Finland  
Ahmad Umar, Saudi Arabia  
Thomas Unold, Germany  
Veronica Vaida, USA  
Roel van De Krol, Germany  
Mark van Der Auweraer, Belgium  
Rienk Van Grondelle, Netherlands  
Wilfried Van Sark, Netherlands  
Sheng Wang, China  
Xuxu Wang, China  
Mingkui Wang, China  
Ezequiel Wolcan, Argentina  
Man Shing Wong, Hong Kong  
David Worrall, UK  
Jeffrey C. S. Wu, Taiwan  
Yanfa Yan, USA  
Jiannian Yao, China  
Minjoong Yoon, Republic of Korea  
Jiangbo Yu, USA  
Hongtao Yu, USA  
Ying Yu, China  
Klaas Zachariasse, Germany  
Juan Antonio Zapien, Hong Kong  
Tianyou Zhai, China  
Lizhi Zhang, China  
Guijiang Zhou, China  
Yong Zhou, China  
Rui Zhu, China

# Contents

**Solar Energy and Clean Energy: Trends and Developments 2014**, Ching-Song Jwo, Ho Chang, Chao-Rong Chen, Yen-Lin Chen, and Mohammad Yusri Hassan  
Volume 2015, Article ID 109861, 4 pages

**The Application Study in Solar Energy Technology for Highway Service Area: A Case Study of West Lushan Highway Low-Carbon Service Area in China**, Xiaochun Qin, Yi Shen, and Shegang Shao  
Volume 2015, Article ID 703603, 8 pages

**An Innovative Application of a Solar Storage Wall Combined with the Low-Temperature Organic Rankine Cycle**, Tzu-Chen Hung, Duen-Sheng Lee, and Jaw-Ren Lin  
Volume 2014, Article ID 239137, 12 pages

**Bridging Photonics and Optoelectronics Curriculum for the Solar Photovoltaic and LED Industries**, Yu-Shan Su and Han-Chao Chang  
Volume 2014, Article ID 146810, 12 pages

**Crystalline Silicon Solar Cells with Thin Silicon Passivation Film Deposited prior to Phosphorous Diffusion**, Ching-Tao Li, Fangchi Hsieh, Shi Yan, Cuifeng Wan, Yakun Liu, Jing Chen, and Likarn Wang  
Volume 2014, Article ID 491475, 8 pages

**Improving Light Extraction of Organic Light-Emitting Devices by Attaching Nanostructures with Self-Assembled Photonic Crystal Patterns**, Kai-Yu Peng and Da-Hua Wei  
Volume 2014, Article ID 936049, 9 pages

**Photoirradiation Caused Controllable Wettability Switching of Sputtered Highly Aligned *c*-Axis-Oriented Zinc Oxide Columnar Films**, P. W. Chi, C. W. Su, B. H. Jhuo, and D. H. Wei  
Volume 2014, Article ID 765209, 10 pages

**Effect of Electrodeposition Potential on Composition of  $\text{CuIn}_{1-x}\text{Ga}_x\text{Se}_2$  Absorber Layer for Solar Cell by One-Step Electrodeposition**, Rui-Wei You, Kar-Kit Lew, and Yen-Pei Fu  
Volume 2014, Article ID 478428, 8 pages

**Fabrication of Antireflection Nanodiamond Particle Film by the Spin Coating Deposition Technique**, Chii-Ruey Lin, Hong-Ming Chang, Minh-Khoa BenDao, Hsiu Hsien Chiang, and Wei-En Chen  
Volume 2014, Article ID 517878, 6 pages

**Development of High-Performance UV Detector Using Nanocrystalline Diamond Thin Film**, C. R. Lin, D. H. Wei, M. K. BenDao, W. E. Chen, and T. Y. Liu  
Volume 2014, Article ID 492152, 8 pages

**On-Road Driver Monitoring System Based on a Solar-Powered In-Vehicle Embedded Platform**, Yen-Lin Chen, Chao-Wei Yu, Zi-Jie Chien, Chin-Hsuan Liu, and Hsin-Han Chiang  
Volume 2014, Article ID 309578, 12 pages

**Structure-Property Relationship of New Organic Sensitizers Based on Multicarbazole Derivatives for Dye-Sensitized Solar Cells**, Hyo Jeong Jo, Jung Eun Nam, Dae-Hwan Kim, Hyojeong Kim, and Jin-Kyu Kang  
Volume 2014, Article ID 872617, 7 pages

**A Novel Hybrid Model for Short-Term Forecasting in PV Power Generation**, Yuan-Kang Wu, Chao-Rong Chen, and Hasimah Abdul Rahman  
Volume 2014, Article ID 569249, 9 pages

**Constructing Employability Indicators for Enhancing the Effectiveness of Engineering Education for the Solar Industry**, Chin-Guo Kuo, Chi-Cheng Chang, and Chun-Cheng Huang  
Volume 2014, Article ID 491353, 11 pages

**ITO-Free Semitransparent Organic Solar Cells Based on Silver Thin Film Electrodes**, Zhizhe Wang, Chunfu Zhang, Dazheng Chen, Shi Tang, Jincheng Zhang, Li Sun, Ting Heng, and Yue Hao  
Volume 2014, Article ID 209206, 7 pages

**Block Textured a-Si:H Solar Cell**, Seung Jae Moon, Chang Min Keum, Ju-Yeon Kim, Jin Kuk Kim, and Byung Seong Bae  
Volume 2014, Article ID 972828, 6 pages

**Experimental Investigation on Thermoelectric Chiller Driven by Solar Cell**, Yen-Lin Chen, Zi-Jie Chien, Wen-Shing Lee, Ching-Song Jwo, and Kun-Ching Cho  
Volume 2014, Article ID 102510, 8 pages

**Cost-Effectiveness Analysis of a PVGS on the Electrical Power Supply of a Small Island**, Cheng-Ting Hsu, Roman Korimara, and Tsun-Jen Cheng  
Volume 2014, Article ID 264802, 9 pages

**The Effects of Annealing Parameters on the Crystallization and Morphology of Cu(In,Ga)Se<sub>2</sub> Absorber Layers Prepared by Annealing Stacked Metallic Precursors**, Chia-Ho Huang and Dong-Cherng Wen  
Volume 2014, Article ID 568648, 8 pages

**Theoretical Insight into Organic Dyes Incorporating Triphenylamine-Based Donors and Binary  $\pi$ -Conjugated Bridges for Dye-Sensitized Solar Cells**, Shuxian Wei, Xiaoqing Lu, Xiaofan Shi, Zhigang Deng, Yang Shao, Lianming Zhao, Wenyue Guo, and Chi-Man Lawrence Wu  
Volume 2014, Article ID 280196, 9 pages

**Fabrication of a Miniature Zinc Aluminum Oxide Nanowire Array Gas Sensor and Application for Environmental Monitoring**, Chin-Guo Kuo, Chi-Wu Huang, Jung-Hsuan Chen, and Yueh-Han Liu  
Volume 2014, Article ID 515268, 7 pages

**Characterization of the Organic Thin Film Solar Cells with Active Layers of PTB7/PC<sub>71</sub>BM Prepared by Using Solvent Mixtures with Different Additives**, Masakazu Ito, Kumar Palanisamy, Abhirami Kumar, Vijay Srinivasan Murugesan, Paik-Kyun Shin, Norio Tsuda, Jun Yamada, and Shizuyasu Ochiai  
Volume 2014, Article ID 694541, 8 pages

**Competing in the Global LED Industry: The Case of Taiwan**, Yu-Shan Su  
Volume 2014, Article ID 735983, 11 pages

## Contents

**Prepared and Characteristics of ZnO:YAG/Silicon Nanostructure Diodes Prepared by Ultrasonic Spraying**, Chih-Hung Hsu, Lung-Chien Chen, and Jia-Ren Wu  
Volume 2014, Article ID 128235, 6 pages

**Performance Evaluation of a Small Scale Modular Solar Trigeration System**, Handong Wang  
Volume 2014, Article ID 964021, 9 pages

**Improved Performance for Dye-Sensitized Solar Cells Using a Compact TiO<sub>2</sub> Layer Grown by Sputtering**, Hung-Chih Chang, Ming-Jenq Twu, Chun-Yao Hsu, Ray-Quen Hsu, and Chin-Guo Kuo  
Volume 2014, Article ID 380120, 8 pages

**The Photocatalytic Activity and Compact Layer Characteristics of TiO<sub>2</sub> Films Prepared Using Radio Frequency Magnetron Sputtering**, H. C. Chang, H. H. Huang, C. Y. Wu, R. Q. Hsu, and C. Y. Hsu  
Volume 2014, Article ID 786165, 8 pages

**Analyzing Thermal Module Developments and Trends in High-Power LED**, Jung-Chang Wang  
Volume 2014, Article ID 120452, 11 pages

**Investigation of Elastic Energy on Single Crystal GaN Nanobeams with Different Span**, Shang-Chao Hung, Cheng-Fu Yang, and Yi-Cheng Hsu  
Volume 2014, Article ID 917360, 6 pages

**Fabrication of a Zinc Aluminum Oxide Nanowire Array Photoelectrode for a Solar Cell Using a High Vacuum Die Casting Technique**, Chin-Guo Kuo, Jung-Hsuan Chen, and Yueh-Han Liu  
Volume 2014, Article ID 302075, 5 pages

**Effects of Hydrogen Plasma on the Electrical Properties of F-Doped ZnO Thin Films and p-i-n  $\alpha$ -Si:H Thin Film Solar Cells**, Fang-Hsing Wang, Shang-Chao Hung, Cheng-Fu Yang, and Yen-Hsien Lee  
Volume 2014, Article ID 425057, 7 pages

**Enhanced Particle Swarm Optimization-Based Feeder Reconfiguration Considering Uncertain Large Photovoltaic Powers and Demands**, Ying-Yi Hong, Faa-Jeng Lin, and Fu-Yuan Hsu  
Volume 2014, Article ID 704839, 10 pages

**Building Professional Competencies Indices in the Solar Energy Industry for the Engineering Education Curriculum**, Chin-Guo Kuo and Chi-Cheng Chang  
Volume 2014, Article ID 963291, 6 pages

**Growth of Anodic Aluminum Oxide Templates and the Application in Fabrication of the BiSbTe-Based Thermoelectric Nanowires**, Chin-Guo Kuo, Yuan-Tai Hsieh, Cheng-Fu Yang, Ching-Ho Huang, and Chia-Ying Yen  
Volume 2014, Article ID 978184, 7 pages

## Editorial

# Solar Energy and Clean Energy: Trends and Developments 2014

**Ching-Song Jwo,<sup>1</sup> Ho Chang,<sup>2</sup> Chao-Rong Chen,<sup>3</sup>  
Yen-Lin Chen,<sup>4</sup> and Mohammad Yusri Hassan<sup>5</sup>**

<sup>1</sup>*Emission Reduction & Energy Conservation Center, National Taipei University of Technology,  
No. 1, Section 3, Chung-Hsiao E. Road, Taipei 10608, Taiwan*

<sup>2</sup>*Graduate Institute of Manufacturing Technology, National Taipei University of Technology,  
No. 1, Section 3, Chung-Hsiao E. Road, Taipei 10608, Taiwan*

<sup>3</sup>*Department of Electrical Engineering, National Taipei University of Technology,  
No. 1, Section 3, Chung-Hsiao E. Road, Taipei 10608, Taiwan*

<sup>4</sup>*Department of Computer Science and Information Engineering, National Taipei University of Technology,  
No. 1, Section 3, Chung-Hsiao E. Road, Taipei 10608, Taiwan*

<sup>5</sup>*Centre of Electrical Energy Systems (CEES), Faculty of Electrical Engineering, Universiti Teknologi Malaysia,  
81310 Johor Bahru, Johor, Malaysia*

Correspondence should be addressed to Ching-Song Jwo; [frankjwo@ntut.edu.tw](mailto:frankjwo@ntut.edu.tw)

Received 1 December 2014; Accepted 1 December 2014

Copyright © 2015 Ching-Song Jwo et al. This is an open access article distributed under the Creative Commons Attribution License, which permits unrestricted use, distribution, and reproduction in any medium, provided the original work is properly cited.

Solar energy and other clean energy are emerging and growing rapidly in the globe nowadays. Solar energy with less carbon emission is renewable and clean energy for our living environment. Solar energy can be converted to electricity in photovoltaic (PV) devices, solar cells, or solar thermal/electric power plants.

It is a current trend that solar energy becomes the important renewable energy. This special issue addresses the role of the development of solar energy. The themes include dye-sensitized solar cells (DSSCs), organic solar cells (OSCs), copper indium gallium diselenide (CIGS), zinc, crystalline silicon solar cells, light-emitting diode (LED), semiconductor sensors, photovoltaic generation system (PVGS), solar cell applications, solar cell, and LED development trend. From 60 submissions, 33 papers are published in this special issue. Each paper was reviewed by at least two reviewers and revised according to review comments.

*Dye-Sensitized Solar Cells (DSSCs).* The design of light-absorbent sensitizers with sustainable and environment-friendly material is one of the key issues for the future

development of dye-sensitized solar cells (DSSCs). In this work, a series of organic sensitizers incorporating alkoxy-substituted triphenylamine (tpa) donors and binary  $\pi$ -conjugated bridges were investigated using density functional theory (DFT) and time-dependent DFT (TD-DFT). Molecular geometry, electronic structure, and optical absorption spectra are analyzed in the gas phase, chloroform, and dimethylformamide (DMF) solutions. In S. Wei et al.'s paper, the authors show that properly choosing the heteroaromatic atoms and/or adding one more alkoxy-substituted tpa group can finely adjust the molecular orbital energy. In H. J. Jo et al.'s paper, a new multicarbazole based organic dye (C2A1, C2S1A1) with a twisted structure was designed and synthesized, and the corresponding dye (C1A1) without the twisted structure was synthesized for comparison. They were successfully applied in dyesensitized solar cells (DSSCs). The results showed that the nonplanar structure of C2A1 and C2S1A1 can efficiently retard the dye aggregation and charge recombination. TiO<sub>2</sub> compact layers are used in dye-sensitized solar cells (DSSCs) to prevent charge recombination between the electrolyte and the transparent conductive

substrate (indium tin oxide, ITO; fluorine-doped tin oxide, FTO). In H. C. Chang et al.'s paper, the authors presented that thin TiO<sub>2</sub> compact layers are deposited onto ITO/glass by means of radio frequency (rf) magnetron sputtering, using deposition parameters that ensure greater photocatalytic activity and increased DSSC conversion efficiency. The photoinduced decomposition of methylene blue (MB) and the photoinduced hydrophilicity of the TiO<sub>2</sub> thin films are also investigated. In H.-C. Chang et al.'s paper, the authors presented that a series of compact TiO<sub>2</sub> layers are prepared using radio frequency (rf) reactive magnetron sputtering. The films are characterized using X-ray diffraction (XRD), atomic force microscopy (AFM), scanning electron microscopy (SEM), and UV-Vis spectroscopy. The results show that when the A<sub>r</sub>/O<sub>2</sub>/N<sub>2</sub> flow rates are 36:18:9, the photoinduced decomposition of methylene blue and photoinduced hydrophilicity are enhanced. After annealing at 450°C in an atmosphere ambient for 30 min, the compact TiO<sub>2</sub> layers exhibit higher optical transmittance.

*Organic Solar Cells (OSCs).* In Z. Wang et al.'s paper, the authors investigated ITO-free semitransparent organic solar cells (OSCs) based on MoO<sub>3</sub>/Ag anodes with poly(3-hexylthiophene) and [6,6]-phenyl-C61-butyric acid methyl ester films as the active layer. In M. Ito et al.'s paper, the authors presented that organic thin film solar cells (OTFSCs) were fabricated with blended active layers of poly[[4,8-bis[(2-ethylhexyl)oxy]benzo[1,2-b:4,5-b']dithiophene-2,6-diyl][3-fluoro-2-[(2-ethylhexyl)carbonyl]thieno[3,4-b]thiophenediyl]] (PTB7)/[6,6]-phenyl-C71-butyric (PC71BM). The performances of active layers are prepared in chlorobenzene (CB) with different additives of 1-chloronaphthalene (CN) and 1,8-Diiodooctane (DIO) by a wet process with spin coating technique.

*Copper Indium Gallium Diselenide (CIGS).* In C.-H. Huang and D.-C. Wen's paper, the authors presented a dense chalcopyrite CIGS film with a thickness of about 1.5-1.6 μm, with large grains (~1.2 μm) and no cracking or peeling is obtained after selenizing at a temperature of 550°C, an Ar pressure of 300 Torr, a heating rate of 60°C/min, and a soaking time of 20 min. By adequate design of the stacked precursor and controlling the annealing parameters, single-stage annealing of the solid Se-coated In/Cu-Ga bilayer precursor is simplified for the fabrication of fully crystallized chalcopyrite CIGS absorber layers with good crystallization and large grains. CIGS polycrystalline thin films were successfully fabricated by one-step cathodic electrodeposition on Mo-coated glass. In R.-W. You et al.'s paper, the authors applied a galvanometry mode with three-electrode potentiostatic systems to produce a constant concentration electroplating solution, which were composed of CuCl<sub>2</sub>, InCl<sub>3</sub>, GaCl<sub>3</sub>, and SeO<sub>2</sub>. Then these as-electrodeposited films were annealed in argon atmosphere and characterized by X-ray diffraction. The results revealed that annealing treatment significantly improved the crystallinity of electrodeposited films and formed CIGS chalcopyrite structure, but at low applied deposition voltage (-950 mV versus SCE) there appeared second phase.

*Zinc.* Zinc aluminum alloy nanowire was fabricated by the vacuum die casting. Zinc aluminum alloy was melted, injected into nanomold under a hydraulic pressure, and solidified as nanowire shape. In C.-G. Kuo et al.'s paper, the authors presented that zinc aluminum oxide nanowire array was produced using the thermal oxidation method and designed for the photoelectrode application. 1.5 wt% zinc fluoride (ZnF<sub>2</sub>) was mixed with zinc oxide powder to form the F-doped ZnO (FZO) composition. In F.-H. Wang et al.'s paper, the authors show that using H<sub>2</sub>-plasma-treated and HCl-etched FZO thin films as transparent electrodes would improve the efficiency of the fabricated thin film solar cells. In P. W. Chi et al.'s paper, the authors presented the microstructure morphology and UV photoirradiation coupling effects of the c-axis-oriented zinc oxide (ZnO) columnar films. Highly aligned c-axis-oriented films have been deposited onto glass substrates at room temperature by radio-frequency (RF) magnetron sputtering without introducing any oxygen source under different sputtering powers ranging from 50 to 150 W.

*Crystalline Silicon Solar Cells.* In C.-T. Li et al.'s paper, the authors presented demonstration of the performance improvement of p-type single-crystalline silicon (sc-Si) solar cells resulting from front surface passivation by a thin amorphous silicon (a-Si) film deposited prior to phosphorus diffusion. The conversion efficiency was improved for the sample with a-Si film of ~5 nm thickness deposited on the front surface prior to high-temperature phosphorus diffusion, with respect to the samples with a-Si film deposited on the front surface after phosphorus diffusion. For the textured solar cell, the surface was much rougher than that of the plain glass, which also contributes to the improvement of the efficiency. In S. J. Moon et al.'s paper, the authors presented block shaped light trapping structure for the first time by wet etching of the glass substrate, which enables the high efficiency thin film solar cell with the aid of the good step coverage deposition. Nanocrystalline diamond (NCD) films are promising materials for widespread applications due to their outstanding characteristics of chemical, physical, and highly smooth surface. In C. R. Lin et al.'s paper, the authors presented that the electrical property and photoconductivity of the fabricated devices were tested for UV detection application. It was found that the NCD films possessed high sp<sup>3</sup> fraction of 68.6%, low surface roughness of 9.6 nm, and good hydrophobicity, as deposited under working pressure of 40 Torr. Also, the NCD/Au structure annealed at 500°C exhibited a good ohmic contact characteristic, high detection efficiency, and fast response to UV irradiation in air ambient.

*Light-Emitting Diode (LED).* In J.-C. Wang's paper, the authors used thermal performance experiments with the illumination-analysis method and window program (vapour chamber thermal module, VCTM V1.0) to investigate and analyze the high-power LED (Hi-LED) lighting thermal module, in order to achieve the best solution of the fin parameters under the natural convection. The computing core of the VCTM program employs the theoretical thermal resistance analytical approach with iterative convergence stated in this study to obtain a numerical solution. Results showed that the

best geometry of thermal module is 4.4 mm fin thickness, 9.4 mm fin pitch, and 37 mm fin height with the LED junction temperature of 58.8°C. In K.-Y. Peng and D.-H. Wei's paper, the authors presented a single-monolayered hexagonal self-assembled photonic crystal (PC) pattern fabricated onto polyethylene terephthalate (PET) films by using simple nanosphere lithography (NSL) method which has been demonstrated in this research work. The patterned nanostructures acted as a scattering medium to extract the trapped photons from substrate mode of optical-electronic device for improving the overall external quantum efficiency of the organic light-emitting diodes (OLEDs).

**Semiconductor Sensors.** The potentiostatic deposition and pulse electrodeposition (PED) processes were used to deposit the  $(\text{Bi,Sb})_{2-x}\text{Te}_{3+x}$ -based materials. Field-emission scanning electron microscope and energy dispersive spectrometers were used to analyze the compositions of the deposited  $(\text{Bi,Sb})_{2-x}\text{Te}_{3+x}$ -based materials. In C.-G. Kuo et al.'s paper "Growth of Anodic Aluminum Oxide Templates and the Application in Fabrication of the BiSbTe-Based Thermoelectric Nanowires," the authors found that optimal deposition parameter of the PED process the AAO nanotube arrays were used as the templates to deposit the  $(\text{Bi,Sb})_{2-x}\text{Te}_{3+x}$ -based thermoelectric nanowires.

In C.-G. Kuo et al.'s paper "Fabrication of a Miniature Zinc Aluminum Oxide Nanowire Array Gas Sensor and Application for Environmental Monitoring," the authors presented that a miniature n-type semiconductor gas sensor was fabricated successfully using zinc aluminum oxide nanowire array and applied to sense oxygen. The present study provided a novel method to produce zinc aluminum alloy nanowire 80 nm in diameter by the vacuum die casting technique and then obtain zinc aluminum oxide nanowire array using the thermal oxidation technique. In S.-C. Hung et al.'s paper, the authors presented a novel technique which can more efficiently fabricate different spans of nanobeams on the same substrate. It requires less time to prepare specimen and further shortens the process of aligning, clamping, and testing. Also, the authors probe into the elastic deformation properties of clamped freestanding GaN nanobeams with different spans.

In C.-H. Hsu et al.'s paper, the authors presented white light source. An yttrium aluminum garnet (YAG) phosphor incorporated zinc oxide (ZnO) ( $\text{ZnO}:\text{YAG}$ ) film is deposited on a silicon substrate by ultrasonic spray pyrolysis to form a nanostructure diode. A nanoflower consisting of a hexagonal nanopetal is formed on the surfaces of the silicon substrate. A white broad band at the room temperature photoluminescence ranging from 420 to 650 nm for the  $\text{ZnO}:\text{YAG}$ /silicon nanostructure diode was observed. Diamond-based antireflective (AR) coatings were fabricated using a spin coating of diamond suspension at room temperature as nucleation enhancement procedure and microwave plasma enhanced chemical vapour deposition. Various working pressures were used to investigate their effect on the optical characterization of the as-deposited diamond films. Scanning electron microscopy (SEM) and atomic force microscopy (AFM) were employed to analyze

the surface properties of the diamond films. Raman spectra and transmission electron microscopy (TEM) also were used for analysis of the microstructure of the films. In C.-R. Lin et al.'s paper, the authors showed that working pressure had a significant effect on thickness, surface roughness, and wettability of the as-deposited diamond films.

**Photovoltaic Generation System (PVGS).** A large PV array (several MW) may incur several operation problems, for example, low power quality and reverse power. In Y.-Y. Hong et al.'s paper, the authors presented a method to reconfigure the distribution feeders in order to prevent the injection of reverse power into a substation connected to the transmission level. Moreover, a two-stage algorithm is developed, in which the uncertain bus loads and PV powers are clustered by fuzzy-c-means to gain representative scenarios; optimal reconfiguration is then achieved by a novel mean-variance-based particle swarm optimization. In Y.-K. Wu et al.'s paper, an experimental database of solar power output, solar irradiance, air, and module temperature data has been utilized. It includes data from the Green Energy Office Building in Malaysia, the Taichung Thermal Plant of Taipower, and National Penghu University. Based on the historical PV power and weather data provided in the experiment, all factors that influence photovoltaic-generated energy are discussed. Moreover, five types of forecasting modules were developed and utilized to predict the one-hour-ahead PV output. They include the ARIMA, SVM, ANN, ANFIS, and the combination models using GA algorithm. The maximum allowable photovoltaic generation system (PVGS) installation capacity is obtained by executing load flow analysis without violating the voltage magnitude and voltage variation ratio limits. However, the estimated power generation of PVGS is applied to know its impact on the power system according to the hourly solar irradiation and temperature. In C.-T. Hsu et al.'s paper, the authors presented that the cost-benefit analysis of payback years (PBY) and net present value (NPV) method is derived considering the cash flow from utilities annual fuel and loss saving, the operation and maintenance (O&M) cost, and the capital investment cost. The power network in Kiribati (PUB DNST) is selected for study in C.-T. Hsu et al.'s paper.

**Solar Cell Applications.** In Y.-L. Chen et al.'s paper "On-Road Driver Monitoring System Based on a Solar-Powered In-Vehicle Embedded Platform," the authors presented an on-road driver monitoring system, which is implemented on a stand-alone in-vehicle embedded system and driven by effective solar cells. The driver monitoring function is performed by an efficient eye detection technique. Through the driver's eye movements captured from the camera, the attention states of the driver can be determined and any fatigue states can be avoided. This driver monitoring technique is implemented on a low-power embedded in-vehicle platform. In Y.-L. Chen et al.'s paper "Experimental Investigation on Thermoelectric Chiller Driven by Solar Cell," the authors presented experimental explorations on cooling performance of thermoelectric chillers being driven by solar cells, as well as comparison results to the performance being driven by fixed

direct current. Solar energy is clear and limitless and can be collected by solar cells. In T.-C. Hung et al.'s paper, the authors presented that the study is to collect energy on the waste heat from air produced by solar ventilation systems. This heat used for electricity generation by an organic Rankine cycle (ORC) system was implemented. The advantages of this method include the use of existing building's wall, and it also provides the region of energy scarcity for reference. In X. Qin et al.'s paper, the authors took West Lushan highway low-carbon service area in Jiangxi Province of China as the case study, and the advantages, technical principles, and application methods of solar energy technology for highway service area including solar photoelectric technology and solar water heating technology were discussed based on the analysis of characteristics of highway low-carbon service area. In H. Wang's paper, the authors presented a novel modular system combining cooling, heating, and power generation (CCHP). This modular CCHP system can simultaneously provide 10 kW electricity,  $-15\sim 5^{\circ}\text{C}$  coolant, and  $60^{\circ}\text{C}$  hot water to meet the requirements of cooling, heating, and electricity in a general family or other fields.

*Solar Cell and LED Development Trend.* In C.-G. Kuo and C.-C. Chang's paper "Building Professional Competencies Indices in the Solar Energy Industry for the Engineering Education Curriculum," the authors presented professional competency indices and their subindices as needed by the solar energy industry, to establish a basis for development of the engineering education curriculum. The methodologies adopted by the study are literature analysis, expert advisories, and focus groups. In C.-G. Kuo et al.'s paper "Constructing Employability Indicators for Enhancing the Effectiveness of Engineering Education for the Solar Industry," the authors presented a set of employability indicators that capture the competency requirements and performance expectations that solar energy enterprises have of their employees. In the qualitative component of the study, 12 administrators and 32 engineers in the industry were interviewed, and meetings with focus groups were conducted to formulate a questionnaire for a survey of Taiwanese solar energy companies for the confirmation and prioritisation of the employability indicators. In Y.-S. Su and H.-C. Chang's paper "Bridging Photonics and Optoelectronics Curriculum for the Solar Photovoltaic and LED Industries," the authors presented the study and collected the current 103 course programs from all optoelectronics-related departments in 36 Taiwanese colleges and universities and sorted these curriculums by three domains of education objectives theory. This theoretical framework was verified on the basis of samples from 150 Taiwanese industrial experts and 354 optoelectronics-related undergraduates and postgraduates.

In Y.-S. Su's paper "Competing in the Global LED Industry: The Case of Taiwan," the author found that Taiwanese LED companies specialize and achieve an optimal efficiency by vertically disintegrating across the upstream, midstream, and downstream sectors in the value chains. Taiwanese LED companies create economies of scale and economies of scope through a complete industrial value chain.

These papers represent an exciting, insightful observation into the state-of-the-art as well as emerging future topics in this important interdisciplinary field. We hope that this special issue would attract a major attention of the peers.

### Acknowledgments

The authors would like to express their appreciation to all the authors and reviewers.

*Ching-Song Jwo  
Ho Chang  
Chao-Rong Chen  
Yen-Lin Chen  
Mohammad Yusri Hassan*

## Research Article

# The Application Study in Solar Energy Technology for Highway Service Area: A Case Study of West Lushan Highway Low-Carbon Service Area in China

Xiaochun Qin,<sup>1,2</sup> Yi Shen,<sup>1</sup> and Shegang Shao<sup>1</sup>

<sup>1</sup>Research Institute of Highway, Ministry of Transport, Beijing 100088, China

<sup>2</sup>Tsinghua University, Beijing 10084, China

Correspondence should be addressed to Xiaochun Qin; 110843281@qq.com

Received 16 May 2014; Revised 14 August 2014; Accepted 19 August 2014

Academic Editor: Yen-Lin Chen

Copyright © 2015 Xiaochun Qin et al. This is an open access article distributed under the Creative Commons Attribution License, which permits unrestricted use, distribution, and reproduction in any medium, provided the original work is properly cited.

A lot of research works have been made concerning highway service area or solar technology and acquired great achievements. However, unfortunately, few works have been made combining the two topics together of highway service areas and solar energy saving to make a systemic research on solar technology application for highway service area. In this paper, taking West Lushan highway low-carbon service area in Jiangxi Province of China as the case study, the advantages, technical principles, and application methods of solar energy technology for highway service area including solar photoelectric technology and solar water heating technology were discussed based on the analysis of characteristics of highway low-carbon service area; the system types, operation mode, and installing tilt angle of the two kinds of solar systems suitable for highway service areas were confirmed. It was proved that the reduction of the cost by electricity savings of solar system was huge. Taking the investment of the solar systems into account, the payback period of solar photoelectric systems and solar water heating systems was calculated. The economic effect of the solar systems in West Lushan highway service area during the effective operation periods was also calculated and proved very considerable.

## 1. Introduction

As the renewable and clean energy, solar energy will not cause environmental pollution that is produced by traditional energy like coal, oil, and other fossil fuels during the using process. Development and utilization of green energy are one of the most important energy saving measures. During the past 30 years, many developed industrial countries and some developing countries have attached great importance to the development of solar technology and solar technology has been widely promoted and used in residential areas. The pace of research and application of solar energy in Europe is also very fast and the use of solar heat is more extensive, involving power generation, domestic hot water, heating, local heating water, and so forth. More than 90% of the solar heat is used for residential areas in the EU [1].

China began to use solar energy early in the 1970s, achieving good results in the beacon lights. In the 1990s, solar

photovoltaic technology began to be used in road lighting and signals and solar water heating system entered the rural residential areas under the support of China government by the late 20th century. In the 21st century, solar photovoltaic technology has been greatly promoted by the growing attention of government and the improvement of solar cell production technology, meanwhile solar energy applications field also expanded gradually.

Nowadays, solar technology is gradually extended to highway traffic field with the introduction of new traffic lighting devices like solar traffic lights, solar orientation lights, solar street lamps, and so forth. However, few solar energy technologies have been used in highway service area in China. As the basic infrastructure serving for vehicles and passengers, the overall function of highway service area determines the quality and efficiency and the economic benefits of the service. Because of the far location away from urban areas, generally highway service areas have

few external energy sources to use, while also consuming more energy. It is relatively closed and independent system. The closeness and independence of highway service area determines its dependence and pressure on resources and environment. The application of solar technology in the construction of highway service area could not only alleviate the scarcity of resources, reduce energy consumption, and improve efficiency of resource and energy, but also reduce environmental pollution, maintain ecological balance, improve highway operational efficiency, and optimize the service quality.

The extensive researches on highway service area began aboard in the early 1990s. American Association of State Highway and Transportation (AASHTO) published the third edition of "expressway service construction guide" in 2001, which stressed the application of green building technology from the aspects of domestic sewage, garbage, and so forth. The studies in the field of highway service facilities in Japan defined the planning layout, architectural forms, design principles, and so on comprehensively, clearly, and in detail. According to "Japan Highway Design Manual" of 1980 version, the design essentials of service rest facilities were defined. The technical standards and design methods of highway new rest facilities are made in "Japanese highway design essentials" in 1991 from more comprehensive aspects. The researches on highway service area were launched relatively late in China. The function, size, and technical requirements of service facilities were simply regulated in "Technical Standards of Highway Construction (JT/G B01-2003)" [2], without involving the energy saving technology. Hui and Liu [3] analyzed the space size and parking capacity of highway rest facilities according to the field survey data and theoretical calculations for Shenda Highway service area in Northeast China. Luo [4] made a study in the function, location, spacing control, and architectural design requirements of highway service. Wu [5] proposed the biological disposal method of highway service area sewerage for vegetation watering and toilet flushing. Yang [6] discussed the economic effects of biological contact oxidation treatment technology using highway service area sewage disposal. It could be seen that the researches on highway service area in China focused mainly on the layout and scale of the facilities, the operation way, water supply and sewage treatment, and so forth but few on energy saving technology.

In the meanwhile, many researches were made on the economic effect assessment of solar technology. Maria and Marano [7] discussed the economic analysis methods of solar photovoltaic systems under different climatic conditions and pointed out that the economic analysis methods were related to local policy as well as technical level and climatic conditions. Schröder and Reddemann [8] made an analysis in the economic influence of hot water consumption and energy efficiency on solar collectors in different months and climatic conditions in terms of the German federal government's economic conditions. Zilla and Abraham [9] proved that the economic effects became better with the increase of useful life period, fuel prices, and market demand based on the establishment of a model for the economic practicability of solar hot water systems and also concluded that

the effect of series solar collectors is better than that of parallel collectors. Hawlader et al. [10] made the economic evaluation for solar heating water system by using different variables and concluded that the designed collector area is 1000 m<sup>2</sup> for best payback period and internal rate of return. Yi [11] made an analysis in the energy consumption constitution and energy saving way for residential building. It can be seen that solar technology brings very considerable economic benefits as well as reducing environmental pollution.

In summary, a lot of research works have been made related to the two fields of highway service area and solar technology and acquired great achievement. However, unfortunately, few works were made combining the two topics together of highway services and solar energy saving to make a systemic research on solar technology in green highway service area due to the design and construction of the service mainly undertaken by the transport authorities, coupled with the faraway location of the service and its subordinate position in the highway system. In this context, it is quite necessary and urgent for launching the research on solar technology and economic effects of highway service area to promote low-carbon highway service area development and guide solar engineering practice.

## 2. Objectives

The main objectives of this paper were as follows:

- (1) confirming the applicability and advantages of solar technology for highway service;
- (2) choosing the suitable type and the best tilt angle of solar photovoltaic system for highway service area based on the location and local climate conditions;
- (3) choosing the suitable operation type of solar water heating system, suitable type, and the best installing angle of collectors for highway service area;
- (4) calculating the economic effects and environmental effects of solar technologies on highway service area.

## 3. Methods

*3.1. The General Situation of Low-Carbon Highway Service Area.* In recent years, with the development of green transportation ideas in China the concept of low-carbon highway service area has been proposed and people are increasingly concerned about the comfort and green level of the service area. Low-carbon highway services generally refer to the services which integrate various measures throughout the entire life cycle of planning, designing, construction, operation, and management to maximize saving resources, protect environment, reduce pollution, and provide people with a safe, healthy, comfortable, and efficient highway service area based on the principle of the virtuous circle of ecosystem in design conception and construction practice. Some highway service areas have begun to employ different energy saving technologies to try establishing low-carbon service areas in China. Green building and clean energy technologies have



FIGURE 1: The aerial view of Lushan highway service area.

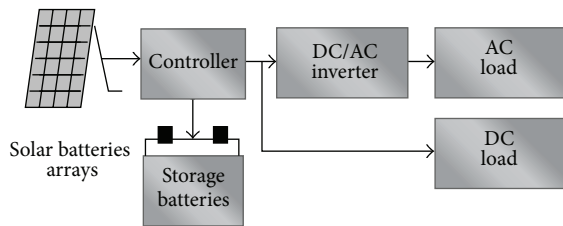


FIGURE 2: The diagrammatic sketch of solar photoelectric technology.

been used in a small number of service areas and achieved good effects [12].

In this paper, utilization technologies and methods of solar photoelectric and water heating technology for highway service area were analyzed according to the natural geographical and climatic conditions of West Lushan scenic area, which would achieve effective operational cost reductions and good energy saving effects.

West Lushan highway is located in northern Lushan Scenic Area in Jiangxi Province of China, with the extremely rich and natural landscape resources along and it is the highway with the highest environmental protection requirements in Jiangxi as seen in Figure 1. The location of West Lushan highway service area is in the southern region and has rich solar energy resources with  $4494.35 \text{ MJ/m}^2$  (horizontal) annual radiation and 1700.7 sunshine hours. In the construction of West Lushan service area, solar energy technologies are fully made in use in order to maximize energy savings and environment protection.

### 3.2. Solar Photoelectric Technology for Highway Service Area

**3.2.1. Technical Principles and Constitution.** Solar photoelectric technology is based on the photoelectric effect, through the using of solar cells to convert solar energy directly into electricity, as shown in Figure 2. There are two main types of solar photovoltaic systems: independent photovoltaic power generation and grid-connected photovoltaic power generation.

Photovoltaic power generation system consists of three major components of solar panels, controller, and inverter. Solar panel is the core part of the system and its role is to convert solar radiation to electrical energy stored in batteries or generated. Solar controller is to control the working status of the entire system and make an overcharge or overdischarge protection for battery [13]. The role of the inverter is to

convert DC (direct current) solar power into AC (alternating current) power, directly transmitting 12 VDC, 24 VDC, and 48 VDC solar energy to provide 220 VAC electrical power [14].

#### 3.2.2. Advantages of Solar Photovoltaic (PV) System for Highway Service Area. They are as follows

- (1) small size, light weight, and small occupational space like building integrated photovoltaic (BIPV);
- (2) long useful life period: the life of PV systems can reach 20 to 50 years;
- (3) zero pollution emissions: PV consumes no fuel with no noise and no pollution to the service area;
- (4) power generation without water: PV systems can be applied for highway service area in the uninhabited areas.

**3.2.3. The Selection of Solar Photovoltaic System Type for Highway Service Area.** Highway service area is usually to use independent photovoltaic systems, with the appropriate choice of voltage levels and the number of phases in accordance with electricity requirements, as shown in Table 1 [15].

**3.2.4. The Determination of the Tilt Angle of Solar Photovoltaic Systems for Highway Service Area.** In the photovoltaic system, the solar radiation received by PV arrays differs according to its tilt angle. For a fixed PV array, if the designed inclined plane is not rational, there may be a waste of more solar modules to meet the power or causes of the unreasonable capacity of battery, which makes the cost of the entire system higher. For determining the best angle of PV arrays, the nature of the load, local weather, and geographical conditions should be taken into account. There are three kinds of load of PV systems including balanced, seasonal, and temporary load. Balanced load refers to the daily electricity for production and life. Air conditioning is the seasonal load and temporary load is generally for the unexpected emergency electrical events. In general, the tilt angle of PV system is determined by application amount of the balanced load and the specific load condition should also be considered. The basic principle is to reach the best tilt angle, reduce the instability of the solar radiation throughout the year, and make the solar radiation amount more evenly for the entire year received by inclined planes.

Research [15] has showed that the designed installing tilt angle of photovoltaic panels equals the local latitude  $\pm 15^\circ$ . Considering the average amount of electricity use throughout the year, the tilt angle = local latitude; considering the amount of electricity use in summer months (April to September), the tilt angle = local latitude  $- 15^\circ$ ; considering the amount of electricity use in winter months (October to March), the tilt angle = local latitude  $+ 15^\circ$ . And the specific azimuth and tilt angle should be considered together for the actual situation of the buildings in service areas.

TABLE 1: Design and selection of solar photovoltaic system.

System type	Type of current	Whether it has the energy storage device	Application scope
Stand-alone photovoltaic system	Direct current (DC)	Yes	Remote areas with no power, DC power load equipment, and high power continuity requirements for power supply
		No	Remote areas with no power, DC power load equipment, and no continuity requirements for power supply
	Alternating current (AC)	Yes	Remote areas with no power, AC power load equipment, and high power continuity requirements for power supply
		No	Remote areas with no power, AC power load equipment, and no continuity requirements for power supply

### 3.3. Solar Water Heating Technology for Highway Service Area

**3.3.1. Technical Principles and Characteristics.** Solar heating water system is the system converting solar radiation into thermal energy to heat water and delivering to each user and typically includes a solar collector, heat storage, circulation pumps, pipe connections, brackets, and other components. The system constitutional diagram is shown in Figure 3.

There are three types of solar water heating system including natural circulation systems, DC systems, and forced circulation system. According to the presence or absence of heat exchanger, solar water heating systems are divided into two types of direct and indirect systems. According to hot water providing range, solar water heating systems are divided into three types of centralized heating water systems, centralized-decentralized heating water systems and decentralized water heating systems.

**3.3.2. The Selection of Solar Water Heating Systems for Service.** Separation system is preferred from architectural aesthetic considerations; indirect system is preferred from water sanitation considerations; from water and energy saving considerations, the insulation measures must be taken into account according to the different forms of buildings.

Solar heating water system operation mode generally is determined by the user basic conditions, the relative needs of the user, the installation location of collector and storage tank, and other factors [16]. The recommended mode is shown in Table 2. The type of collector is based on the operation time of solar heating water system, the minimum temperature, and other factors.

By the comparison of flat plate collector and evacuated tubular collector, it can be seen that the economical efficiency, operation environment, useful life period, and stability of evacuated tube collector are all better than those of flat plate solar collector. Therefore all-glass evacuated tube collector is preferred for highway service. Solar water heating system should be installed in residential buildings, shower room, kitchen, and other building roofs or exterior for providing hot water for the service areas. The area of solar collector

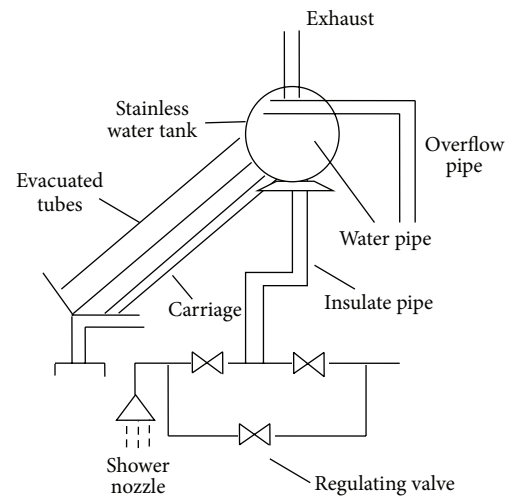


FIGURE 3: The constitutional diagram of solar heating water system.

should also be designed based on the demand of hot water. When collector is installed on the roof, the designed tilt angle of collector is based on local solar elevation angle and the general criterion for the optimum tilt angle of solar collector is the local latitude plus 10 degrees [16].

## 4. Results

### 4.1. The Application of Solar Photovoltaic Technology for Highway Service Area

**4.1.1. Location and System Selection.** The solar photovoltaic systems in West Lushan service were installed on the North-east logistics building floor roof terrace, with the capacity of 20.24 kWp, medium-sized photovoltaic systems. In terms of the natural and geographical conditions and the demand for electricity of West Lushan service area, the independent DC with energy storage device solar photovoltaic power generation system was chosen as seen in Figures 5 and 6.

TABLE 2: The comparison of recommended operating mode of solar heating water system for highway service area.

Operating conditions	Operating mode		
	Natural circulation	Direct circulation	Forced circulation
Instability water pressure	Available	Unavailable (1)	Available
Insufficient power supply	Available	Unavailable (2)	Unavailable (3)
Instant hot water	Unavailable	Available	Unavailable
The relative installation location of collector and storage tank			
High collector	Unavailable	Available	Available
High storage tank	Available	Available	Available
Operating temperature			
Above 0°C	Available	Available	Available
Below 0°C	Available with antifreezing measures		

(1) Available with thermostat control pump.

(2) Available with thermostatic valve.

(3) Available with DC pump under photoelectric cell.



FIGURE 4: The solar panels of solar photovoltaic systems in West Lushan highway service area.



FIGURE 5: The solar controller of solar photovoltaic systems in West Lushan highway service area.

*4.1.2. The Determination of Solar Panel Type and Installing Angle.* The model of solar panel was S-220D (230 Wp), a total of 88 with a 220 V, 100 A solar controller as well as a 220 VDC/220 VAC 5 kVA separate inverter, which could meet the power supply for 3 consecutive rainy days as shown in Figure 4.

Considering the average amount of electricity use throughout the year, the tilt angle equalled the local latitude. The local latitude of West Lushan was 28.67 degrees, so the tilt angle was set as 28 degrees.

#### 4.2. The Application of Solar Water Heating Technology for Highway Service Area

*4.2.1. Selection of System Type and Installing Angle.* Solar water heating systems were installed in the buildings of West Lushan highway service area for hand washing, showers, and other hot water needs like Lushan West Visitor Centre, dining lounge, logistics building, service stations, and maintenance station.

The direct system was chosen and the control mode was set with three modes of constant temperature control, difference temperature control, and timing control by freedom



FIGURE 6: Solar photovoltaic power generation storage batteries of solar photovoltaic systems in West Lushan highway service area.

choice. The operation mode was forced circulation and the collector type was evacuated tubular collector based on the comparison analysis of flat plate collector and evacuated tubular collector for highway service area, as illustrated in Table 3.

According to the local solar elevation angle, the tilt angle of solar collector was the local latitude plus 10 degrees, which was 38 degrees.

TABLE 3: The comparison of flat plate collector and evacuated tubular collector for highway service area.

Features	Flat plate solar collector	Evacuated tubular solar collector
System efficiency	About 50% (summer) About 20% (winter)	About 50% (summer) About 40% (winter)
Useful life period	5 years	15 years
Operation temperature	Above 0°C	Above -40°C
Manufacturing cost	Low	Low
Key component efficiency	Fast heat absorption and fast heat release	Fast heat absorption and slow heat release
Efficiency in wet or rainy day	Low	High

TABLE 4: List of installed solar collectors in West Lushan highway service area.

Installation location	Visitor centre	Dining lounge	Logistics building	Service station	Maintenance station	Total
Number of collectors	64	24	48	24	1	161
Size (each piece)	15 × Φ47 × 1500 mm					
Collecting area (m <sup>2</sup> )	120	45	90	45	1.875	301.875

4.2.2. *The Solar Collector Installation Condition.* The solar collector installation condition in West Lushan highway service area was shown in Table 4.

#### 4.3. Economic Effects Analysis of Solar Energy Technology in West Lushan Highway Low-Carbon Service

4.3.1. *The Power Generation Capacity of Solar Photovoltaic System.* We can get the power generation capacity of solar photovoltaic system in West Lushan highway low-carbon service according to the following formula [17]:

$$G_{pv} = A_c \cdot J_r \cdot T \cdot n_b \cdot n_s, \quad (1)$$

where  $A_c$  is the effective area of photovoltaic cells m<sup>2</sup>,  $J_r$  is the solar radiation intensity under the best tilt angle per year kw/m<sup>2</sup>,  $T$  is the effective hours of sunshine per year h,  $n_b$  is the component efficiency, and  $n_s$  is the system efficiency.

The parameters of solar water photovoltaic system in West Lushan service were as follows: the effective area of photovoltaic cells was about 140 m<sup>2</sup> in terms of the capacity of 20.24 kWp; the solar radiation intensity per year under the best tilt angle 28 degrees in West Lushan district was 1330 kw/m<sup>2</sup>; The effective hours of sunshine per year was 1700.7; the component efficiency of silicon battery was generally set 15%; and the system efficiency was generally set 75%.

So the power generation capacity of solar photovoltaic system per year in West Lushan highway low-carbon service was 35625.41 kW·h.

4.3.2. *Energy Saving Capacity of Solar Water Heating System.* The total collecting area of solar water heating system in

West Lushan highway service area was 301.875 m<sup>2</sup>, which was calculated in terms of the following formula:

$$\Delta Q_{\text{save}} = A_c \cdot J_t \cdot (1 - \eta_c) \cdot \eta_{cd}, \quad (2)$$

where  $A_c$  is the solar collecting area of direct system m<sup>2</sup>,  $J_t$  is the solar radiation of collecting surface per year MJ/m<sup>2</sup>,  $\eta_c$  is the heat loss of pipeline and water tank,  $\eta_{cd}$  is the thermal efficiency in full daytime of solar collector %, and  $d$  is the number of days.

The parameters of solar water heating system in West Lushan service were as follows: the total solar collecting area in the service  $A_c$  was 301.875 m<sup>2</sup>, solar radiation per year  $J_t$  was 4494.35 MJ/m<sup>2</sup>, set  $\eta_c$  was 0.1, and set  $\eta_{cd}$  was 0.5.

So the amount of saving energy of solar water heating system in West Lushan service per year was 610530 MJ.

If the energy was generated by electricity heating, the consuming electricity was determined in terms of the following formula:

$$G = \frac{\Delta Q_{\text{save}}}{n_d q_0}, \quad (3)$$

where  $n_d$  is the efficiency of electricity heating and  $q_0$  is the calorific value of electricity kJ/kW·h.

Generally,  $n_d$  is 0.9 and  $q_0$  is 3595 kJ/kW·h.

So the electricity saving by the energy saving of solar water heating system per year is 188697.26 kW·h.

4.3.3. *Economic Profit of Solar Energy Technology in West Lushan Highway Low-Carbon Service.* Taking the investment of the solar water heating systems into account, the payback period of the investment of solar system was calculated according to the following formula:

$$T = \frac{y}{n_0}, \quad (4)$$

where  $Y$  is the investment of the system and  $n_0$  is the cost saving of the system.

According to the current electricity price of 0.60 RMB/kW·h in Jiangxi Province, the reduction of the cost by electricity savings of solar photovoltaic system in West Lushan highway service area was 21.38 thousand RMB per year. The cost of solar photovoltaic system per square meter was around 1300 RMB, so the total investment of solar photovoltaic system was 182 thousand RMB. Therefore, the payback period of the investment of solar photovoltaic system was 8.5 years. As we know the useful life period of solar photovoltaic system was at least 25 years, so economic profits of solar photovoltaic system were relatively high.

Taking 25 years as the effective operation period, the economic profit of the solar photovoltaic system in West Lushan highway service area would reach 352.5 thousand RMB.

The reduction of the cost by electricity savings of solar water heating system in West Lushan highway service area was 113.22 thousand RMB according to the current electricity price of 0.60 RMB/kW·h in Jiangxi Province. Because one piece of solar evacuated tubular collector was about 4000 RMB, the total investment of 161 pieces of solar evacuated tubular collector was 644 thousand RMB. Therefore, the payback period of the investment of solar water heating system was 5.69 years. As we know the useful life period of solar photovoltaic system was at least 15 years, so economic profits of solar photovoltaic system were very high.

Taking 15 years as the operation period, the economic profit of the solar photovoltaic system in West Lushan highway service area would reach 1.05 million RMB.

*4.4. Environmental Benefits Analysis of Solar Energy Technology in West Lushan Highway Low-Carbon Service.* The statistics from National Development and Reform Commission of China reveals that every saving of 1 kWh electricity equaled the consumption of 0.4 kg standard coal and also equaled a decrease of standard coal combustion producing 0.997 kg carbon dioxide (CO<sub>2</sub>), 0.03 kg sulfur dioxide (SO<sub>2</sub>), 0.015 kg nitrogen oxides (NO<sub>x</sub>), 0.272 kg smoke, and other pollutants.

The energy saving of the solar technology in West Lushan highway service area equaled the reduction of 89.73 tons standard coal, also 233.65 tons CO<sub>2</sub>, 6.73 tons SO<sub>2</sub>, 3.36 tons NO<sub>x</sub>, and 61.02 tons smoke. It could be seen that the solar technology of West Lushan highway service area would make great contributions to the reduction of environment pollution.

## 5. Conclusion

(1) The closeness and independence of highway service area determined its dependence and pressure on resources and environment. The application of solar technology for highway service area could not only reduce energy consumption and improve energy efficiency, but also reduce air pollution and protect ecological environment.

(2) Solar photovoltaic (PV) system was quite suitable for highway service area based on its advantages of small size

and occupational room, long useful life period, zero pollution emissions, and generation of power without water.

(3) Based on the comparison analysis of solar photovoltaic systems and the natural and geographical conditions of West Lushan in Jiangxi Province, independent photovoltaic system with energy storage device was chosen for West Lushan highway service. And considering the average amount of electricity use throughout the year, the tilt angle of solar panel equalled the local latitude, set as 28 degrees according to the local latitude of West Lushan of 28.67 degrees.

(4) It was proved that evacuated tubular collector and the operation mode of forced circulation were preferred for West Lushan highway service area by the comparison analysis. The selection of designed tilt angle of collector was based on local solar elevation angle and the tilt angle of solar collector in West Lushan highway service area was the local latitude plus 10 degrees, which was 38 degrees.

(5) The power generation capacity of solar photovoltaic system per year in West Lushan highway low-carbon service was 35625.41 kW·h by calculation analysis. The reduction of the cost by electricity savings of solar photovoltaic system in West Lushan highway service area was 21.38 thousand RMB per year according to the current electricity price of 0.60 RMB/kW·h in Jiangxi Province.

Taking the investment of the solar water heating systems into account, the payback period of the investment of solar photovoltaic system was 8.5 years.

Taking 25 years as the effective operation period, the economic benefits of the solar photovoltaic system in West Lushan highway service area would reach 352.5 thousand RMB.

(6) The electricity saving by the saving energy of solar water heating system per year was 188697.26 kW·h. The reduction of the cost by electricity savings of solar water heating system in West Lushan highway service area was 113.22 thousand RMB per year.

Taking the investment into account, the payback period of the investment of solar water heating system was 5.69 years.

Taking 15 years as the operation period, the economic effect of the solar photovoltaic system in West Lushan highway service area would reach 1.05 million RMB.

(7) The energy saving of the solar technology in West Lushan highway service area equalled the reduction of 89.73 tons standard coal, also 233.65 tons CO<sub>2</sub>, 6.73 tons SO<sub>2</sub>, 3.36 tons NO<sub>x</sub>, and 61.02 tons smoke. It could be seen that the solar technology of West Lushan highway service area would make great contributions to the reduction of environment pollution.

## Conflict of Interests

The authors declare that there is no conflict of interests regarding the publication of this paper.

## Acknowledgments

The research work was supported by National Natural Science Foundation of China under Grant no. 51108216. The authors

are very grateful for the helpful comments and criticisms of the anonymous reviewers.

## References

- [1] C. Shi, "The application of solar central heating systems in residential community of European cities," *Solar*, vol. 4, pp. 18–20, 2003.
- [2] "Profession standard of People's Republic of China," Technical Standards of Highway Construction JT/G B01, 2003.
- [3] G. Hui and L. Liu, "The planning of Parking capacity and land size of rest facilities," *Northeast Highway*, 2006.
- [4] H. Luo, *Study in Design of Highway Service*, Northwest Highway, 2010.
- [5] R. Wu, "Case Study of wastewater treatment ecological technology for highway service," *Environmental Science and Technology*, vol. 11, pp. 96–98, 2007.
- [6] W. Yang, *Study in wastewater biological contact oxidation treatment technology for highway service [M.S. thesis]*, Chang'an University, 2006.
- [7] A. D. Maria and D. Marano, "Tech-economic analysis of solar photovoltaic system," *International Energy Journal*, no. 5, pp. 47–68, 2004.
- [8] M. Schröder and B. Reddemann, "Three different criteria to evaluate the economics of solar water heating systems," *Solar Energy*, vol. 29, no. 6, pp. 549–555, 1982.
- [9] S.-S. Zilla and M. Abraham, "Simulation of a solar energy system for heating water," *Computers and Industrial Engineering*, vol. 8, pp. 1073–1084, 2004.
- [10] M. N. A. Hawlader, K. C. Ng, T. T. Chandratilleke, D. Sharma, and H. L. Kelvin Koay, "Economic evaluation of a solar water heating system," *Energy Conversion and Management*, vol. 27, no. 2, pp. 197–204, 1987.
- [11] J. Yi, *Energy Saving*, Beijing China Architecture & Building Press, Beijing, China, 2006.
- [12] Ministry of Housing and Urban-Rural Development of the People's Republic of China. *GBT 50378-2006 Green Building Assessment Standard*. Beijing China Architecture & Building Press, 2006.
- [13] M.-S. Hsu and F.-J. Lin, "The developing strategy of green energy industry cluster A case study of the solar photoelectric industry in Taiwan," *Procedia—Social and Behavioral Sciences*, vol. 40, pp. 165–173, 2012.
- [14] V. V. Tyagi, N. A. A. Rahim, and J. A. L. Selvaraj, "Progress in solar PV technology: research and achievement," *Renewable and Sustainable Energy Reviews*, vol. 20, pp. 443–461, 2013.
- [15] C. L. Benson and C. L. Magee, "On improvement rates for renewable energy technologies solar PV, wind turbines, capacitors," *Renewable Energy*, vol. 68, pp. 745–751, 2014.
- [16] Ministry of Housing and Urban-Rural Development of the People's Republic of China, *GBT 50378-2006 Civil Architecture Soar Water Heating System Application Standard*, Architecture & Building Press, Beijing, China, 2005.
- [17] J. Wang, *Study on the economic evaluation of solar water heating system for building in Wuhan [Master's, thesis]*, Wuhang University, Wuhan, China, 2012.

## Research Article

# An Innovative Application of a Solar Storage Wall Combined with the Low-Temperature Organic Rankine Cycle

Tzu-Chen Hung,<sup>1</sup> Duen-Sheng Lee,<sup>2</sup> and Jaw-Ren Lin<sup>3</sup>

<sup>1</sup> Department of Mechanical Engineering, National Taipei University of Technology, Taipei 10608, Taiwan

<sup>2</sup> Graduate Institute of Mechanical and Electrical Engineering, National Taipei University of Technology, Taipei 10608, Taiwan

<sup>3</sup> Department of Mechanical Engineering, Taoyuan Innovation Institute of Technology, Zhongli 32091, Taiwan

Correspondence should be addressed to Tzu-Chen Hung; [tchung@ntut.edu.tw](mailto:tchung@ntut.edu.tw)

Received 9 June 2014; Accepted 25 July 2014; Published 7 September 2014

Academic Editor: Chao-Rong Chen

Copyright © 2014 Tzu-Chen Hung et al. This is an open access article distributed under the Creative Commons Attribution License, which permits unrestricted use, distribution, and reproduction in any medium, provided the original work is properly cited.

The objective of this study is to collect energy on the waste heat from air produced by solar ventilation systems. This heat used for electricity generation by an organic Rankine cycle (ORC) system was implemented. The advantages of this method include the use of existing building's wall, and it also provides the region of energy scarcity for reference. This is also an innovative method, and the results will contribute to the efforts made toward improving the design of solar ventilation in the field of solar thermal engineering. In addition, ORC system would help generate electricity and build a low-carbon building. This study considered several critical parameters such as length of the airflow channel, intensity of solar radiation, pattern of the absorber plate, stagnant air layer, and operating conditions. The simulation results show that the highest outlet temperature and heat collecting efficiency of solar ventilation system are about 120°C and 60%, respectively. The measured ORC efficiency of the system was 6.2%. The proposed method is feasible for the waste heat from air produced by ventilation systems.

## 1. Introduction

The development of the economy and society on a global scale has been accompanied by energy crises and environment pollution, which have become two major problems worldwide. Therefore, the application of renewable energies (solar energy, wind energy, and geothermal energy) in electricity generation is becoming increasingly crucial. In addition, power generation in which the organic Rankine cycle (ORC) is used to recover low-grade energy sources has attracted considerable attention. In recent years, Hung et al. [1, 2] have extensively studied the development and applications of ORC electrical generating systems.

Among these sources, geothermal and solar energy are typically used in converting low-grade heat into power and in other applications [3–8]. Wang et al. [3, 6] designed a low-temperature solar Rankine system. Both evacuated solar collectors and the flat-plate solar collectors are used in this experimental system. Hettiarachchi et al. [4] presented a cost-effective optimal design criterion for organic Rankine power

cycles using low-temperature geothermal heat sources. Karel-las et al. [7] reported that a heat recovery system could be used to increase the efficiency of the cement plant and, thus, contributes to the emissions reduction when using a typical cement production procedure. Wang et al. [8] investigated the performance of a low-temperature solar Rankine cycle system using working fluid R245fa. The experimental results indicated that the highest heat-collecting efficiency of a flat-plate collector is approximately 50%. Hung [9] investigated a maximum work output from various combinations of thermodynamic cycles from a viewpoint of the cycle systems. The study shows that the series-type triple cycle exhibits no significant difference as compared with the combined cycle. Hung et al. [10] analyzed parametrically and compared the efficiencies of ORCs using cryogenics such as benzene, ammonia, R11, R12, R134a, and R113 as working fluids.

According to the statistical data, air conditioning takes about 40% of electricity demand for building. Therefore, natural ventilation has received considerable attention because it reduces heat gain and induces natural cooling or heating

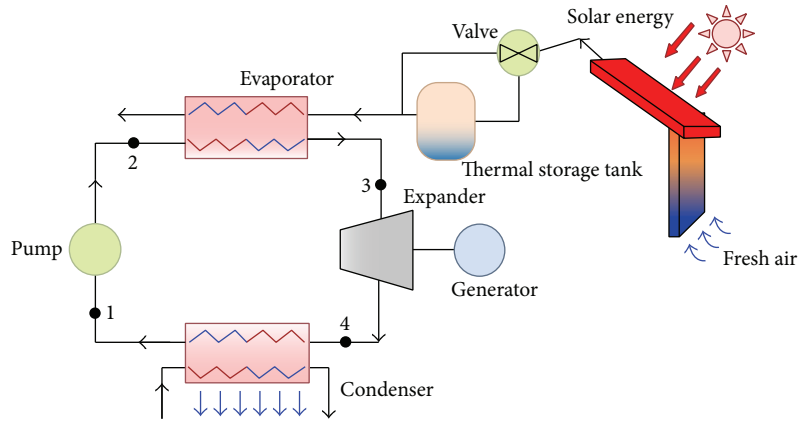


FIGURE 1: Schematic diagram of the ventilation in building combined with ORC system.

in both commercial and residential buildings and provides potential benefits regarding operational costs, energy requirements, and carbon dioxide emission.

The objective of this study is to collect the waste heat from air produced by ventilation systems. The waste heat was used for electricity generation in which an ORC system was implemented, as shown in Figure 1. This method also served the purpose of combining the waste heat produced by ventilation system with an ORC system to facilitate the creation of a reasonable indoor environment characterized by human thermal comfort, energy efficiency, and environmental friendliness and to construct a low-carbon building. The advantages of this method include the use of existing building's wall, and it also provides the region of energy scarcity for reference. This is an innovative method, and the results will contribute to the efforts made toward improving the design of solar ventilation in the field of solar thermal engineering. Thus far, relatively little research in this area has been conducted.

A wide variety of natural ventilation systems are presented in the literatures. Solar wind towers [11], Trombe walls [12], and solar chimneys [13] are examples. Zhai et al. [14] proposed that active solar systems can be used to enhance the ventilation performance of solar chimneys. The main configurations and integrated renewable energy systems based on solar chimneys were investigated. El-Sawi et al. [15] investigated the chevron pattern of fold structure produced using a recently developed continuous folding technique. Arce et al. [16] experimentally investigated the thermal performance of a solar chimney for natural ventilation. The experimental model was implemented under full-scale and real meteorological conditions, to compare the experimental results with simulation results. Yadav and Bhagoria [17] presented a detailed review of the literature that involves the application of CFD in the design of solar air heaters. The solar chimney concept used for improving the natural ventilation of rooms was analytically and numerically studied [18]. The present study considered several geometrical parameters such as chimney inlet size and width, which are considered to have a significant effect on space ventilation. CFD modelling techniques were used to assess the effects of

inclination angle, double glazing, and low-emissivity finishes on the induced ventilation rate [19]. Hu et al. [20] investigated a simple-structure mechanical ventilation solar air collector (MV-SAC) with internal baffles. A numerical model was developed in the present study to predict solar air collector internal flow and heat transfer characteristics. Tian and Zhao [21] and Alkilani et al. [22] reported that various types of thermal energy storage systems are also reviewed and discussed, including sensible heat storage, latent heat storage, chemical storage, and cascaded storage.

In this study, we applied experiments and CFD to solve problem of solar storage wall combined with the organic Rankine cycle. The fluid flow and heat transfer of this solar storage wall were analyzed numerically, and the results were validated based on the experimental data. Subsequently the parameters, such as the thickness of the air gap, the operating conditions, and height of flow, that clearly influence collector efficiency were analyzed. These results provide a reference for the future design and optimization of solar storage wall.

## 2. Experimental Analysis

In this section, we present the details of the experiments and performance analysis conducted in this study.

**2.1. Solar Simulator.** Factors such as time, season, and weather cause the experimental results to become unstable. Therefore, we constructed a solar simulator that can provide stable energy on an absorber plate, as shown in Figure 2(a). The spectral range of the solar simulator was visible light, the wavelength of which 500–600 nm, and the distributed heat flux was between 780 and 820 W/m<sup>2</sup>, as shown in Figure 2(c). The measured results indicate that the variation in the maximal heat flux at various locations was less than 50 W/m<sup>2</sup> and that the solar simulator produced uniform heat flux.

**2.2. Experimental Setup.** The collector module consisted of glass, an absorber plate, an airflow channel, a stagnant air layer, insulation, and an aluminum collector frame used to

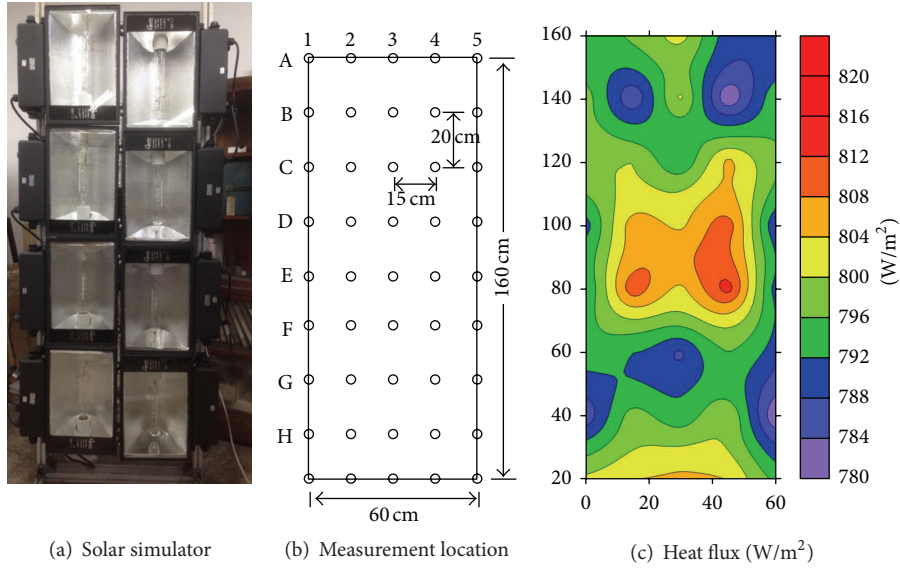


FIGURE 2: Distribution of heat flux on glazing for solar simulator.

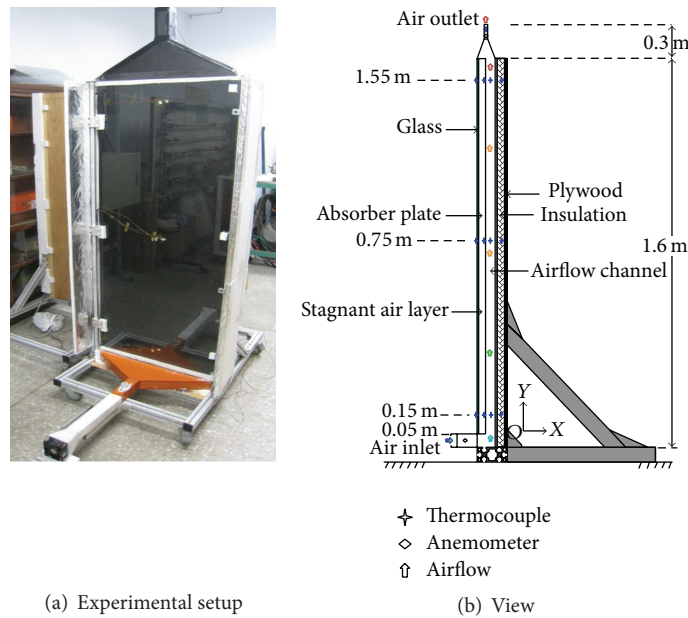


FIGURE 3: Schematic diagram of the experimental setup and view of the solar chimney.

install the components, as shown in Figure 3(a). The absorber plate was 1.6 m high, 0.6 m wide, and 0.08 m thick; the stagnant air layer was 0.18 m deep; and the glass cover was 0.004 m thick. To collect sufficient solar radiation, the surface of the absorber plate was painted black. The purpose of using a glass cover and a stagnant air layer was to decrease convection heat losses from the absorber plate. The surface of the aluminum collector frame was insulated to achieve minimal heat loss. The insulation was protected using a fiberglass wool envelope.

The air inlet to the chimney was located at the bottom of solar storage wall and the air outlet was located at the top.

Inlet airflow was collimated by employing a laminated array to provide the velocity component in the  $x$ -direction only. The inlet and outlet cross-section were maintained equal and constant ( $A_{in} = A_{out} = 0.002 \text{ m}^2$ ) to reduce the pressure loss in the inlet and outlet areas. Before conducting the performance tests, both the thermocouples and flow meters used were calibrated to ensure accurate measurements. The collectors, based on their respective settings, were tested for leaks under the operating pressure.

2.3. *Instrumentation.* The variables measured in this experiment included the inlet and outlet air temperature, ambient

temperature, and the solar radiation and mass flow rate of the air. The collector was instrumented with three T-type thermocouples ( $H = 0.15, 0.75,$  and  $1.55$  m) for measuring the temperatures in each component. The airflow rate was calculated using the measured air velocity and the known duct area. The data acquisition system consisted of a data logger, which was connected to a personal computer through an RS232 serial port. The locations of each sensor are shown in Figure 3(b).

**2.4. Performance Analysis.** The useful energy gained using the solar ventilation system can be expressed as [23]

$$Q_u = \dot{m}C_p (T_{\text{out}} - T_{\text{in}}), \quad (1)$$

and the following heat balance equation expresses the thermal performance of a collector under steady-state conditions:

$$Q_u = AF_R [I(\tau\alpha)_c - U_L (T_i - T_{\text{amb}})], \quad (2)$$

where  $F_R$  is the collector heat removal factor and  $U_L$  is the top loss coefficient, which is dependent on temperature and wind speed. A measure of collector performance is collector efficiency, defined as the ratio of useful heat gain over any time period to the incident solar radiation over the same period. Thus, the efficiency equation is written as follows:

$$\eta_c = \frac{Q_u}{IA}. \quad (3)$$

From (1) and (3), the collector efficiency can be expressed as follows:

$$\eta_c = \dot{m}C_p \frac{(T_{\text{out}} - T_{\text{in}})}{IA}. \quad (4)$$

The general test procedure involves determining  $Q_u$  using (1) and measuring  $I$ ,  $T_i$ , and  $T_{\text{amb}}$  by operating the collector under nearly steady-state conditions in test facilities.

### 3. Numerical Analysis

In this study, commercial CFD code ANSYS FLUENT [24] software was used as to perform the numerical calculations. CFD is a simulation tool that uses powerful computer and applied mathematics to model fluid-flow situations to predict heat.

**3.1. Governing Equation.** In the ventilation system, the study used rectangle pipe flow, and the hydraulic diameter,  $D_h = 4A/P$ , was calculated by four times the ratio of the cross-section flow area divided by the wetted perimeter,  $P$ , of the pipe. The Reynolds number,  $Re = \rho v D_h / \mu$ , was greater than 2300. Therefore, the standard  $k$ - $\varepsilon$  equation was adopted in the chimney region. The flow phenomenon that occurs in a ventilation channel is governed by the continuity, momentum, and energy equations involved in the steady-state regime which can be written as follows [17].

Continuity equation:

$$\frac{\partial}{\partial x_i} (\rho u_i) = 0. \quad (5)$$

Momentum equation:

$$\begin{aligned} \frac{\partial}{\partial x_i} (\rho u_i u_j) = & -\frac{\partial P}{\partial x_i} + \frac{\partial}{\partial x_j} \left[ \mu \left( \frac{\partial u_i}{\partial x_j} + \frac{\partial u_j}{\partial x_i} \right) \right] \\ & + \frac{\partial}{\partial x_j} \left( -\overline{\rho u_i' u_j'} \right). \end{aligned} \quad (6)$$

Energy equation:

$$\frac{\partial}{\partial x_i} (\rho u_i T) = \frac{\partial}{\partial x_j} \left[ (\Gamma + \Gamma_t) \frac{\partial T}{\partial x_j} \right], \quad (7)$$

$$\Gamma = \frac{\mu}{Pr}, \quad \Gamma_t = \frac{\mu_t}{Pr_t}, \quad (8)$$

where  $\Gamma$ ,  $\Gamma_t$ , and  $Pr$  are the molecular thermal diffusivity, turbulent thermal diffusivity, and Prandtl number, respectively.  $\mu_t$  in (8) is the turbulent viscosity.

The discrete ordinates (DO) model was chosen for conducting the simulation of radiation heat transfer. This was achieved by coupling radiative transfer equation (RTE) and the convective energy equation [25]. Solar ray tracing was used to calculate radiation effects produced by the sun's rays that irradiate the computational domain. The solar load model's ray tracing algorithm was used to predict the direct illumination energy source that results from incident solar radiation.

**3.2. Geometric Modeling and Meshing.** The complete geometry of the system is divided into three sections: the entrance, test, and exit sections. The 3D domain used for CFD analysis was set up to have a height of 1.9 m, width of 0.6 m, and a depth of 0.04 m. The depth of the stagnant air layer and airflow is 0.18 m and 0.02 m, respectively. To reduce the burden of computational time and memory space on the computer, the system under consideration was assumed to have a symmetric plane.

The 3D computational domain of the solar ventilation system was created and meshed according to its actual size by using Gambit [26] software. A uniform mesh comprising extremely fine mesh near the wall was used to resolve the laminar sublayer as shown in Figure 4. The nearest grid point to the wall was carefully adjusted to place it in the linear region and thereby ensure that the nondimensional wall distance  $y^+$  was less than 3.0. The total grid number was determined to be 1,525,068 cells after the grid independence was investigated.

**3.3. Boundary Conditions and Material Properties.** Uniform air velocity was introduced at the inlet while a constant pressure was applied at the outlet. The system under consideration was assumed to have a symmetric plane. In addition, the collector frame was assumed to be adiabatic. The heat loss from the back plate and the glass to the surroundings was considered, and no-slip boundary condition was assigned to the walls in contact with the fluid in the model.

The properties of the working fluid (air), absorber plate (aluminum), and glass material were assumed to remain constant. The glass and absorber plate were homogeneous and

TABLE 1: Thermophysical properties of working fluid (air) and absorber plate (aluminum) for computational analysis.

Properties	Working fluid (air)	Absorber plate (aluminum)	Glass
Density, $\rho$ (kg/m <sup>3</sup> )	Incompressible ideal gas	2719	2500
Specific heat, $C_p$ (J/kg-K)	1006.43	871	750
Viscosity, $\mu$ (N/m <sup>2</sup> )	$1.7894 \times 10^{-5}$	—	—
Thermal conductivity, $k$ (W/m-K)	0.0242	202.4	1.4
Absorptivity, $\alpha$	—	0.9	0.12
Emissivity, $\varepsilon$	—	0.4	0.9

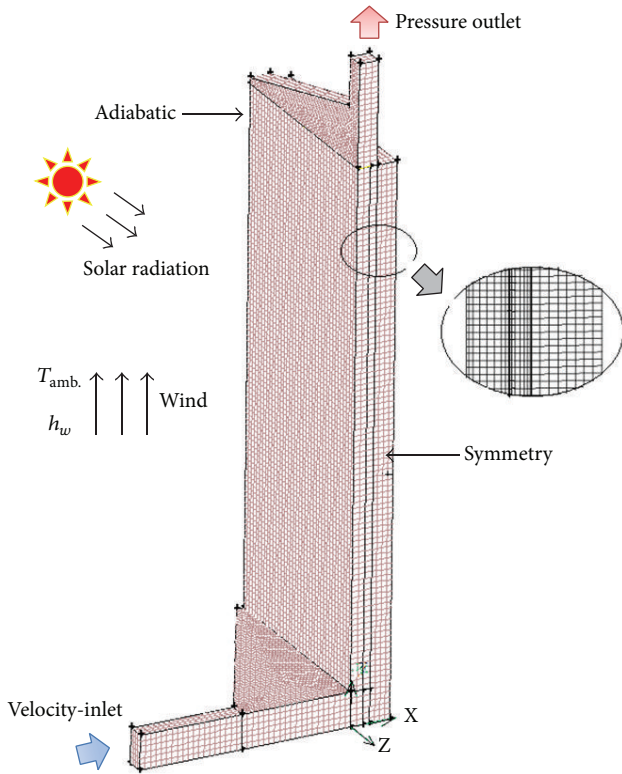


FIGURE 4: Computational model and boundary conditions.

isotropic. The thermal conductivity of the frame, absorber plate, and glass was temperature independent. The thermophysical properties of the working fluid, glass, and absorber plate are listed in Table 1. Because the flow velocity in the ventilation system and the decrease in pressure were relatively small, the air was considered as incompressible fluid, and the density was assumed to be approximately that of ideal gas, considering the thermal expansion effect.

After establishing all the relevant settings, ANSYS FLUENT performed the calculation in an iterative manner until a sufficient tolerance, defined by the user, was achieved. The convergence criterion of  $10^{-6}$  represents the residuals in the continuity equation;  $10^{-3}$  for the residuals of the velocity components and  $10^{-6}$  for the residuals of the energy were assumed.

**3.4. Validation of the Computation Fluid Dynamics Results.** We investigated the feasibility of solar ventilation in natural convection and compared the measured and calculated results. The results of solar simulator show that the uniform heat flux can be assumed as  $800 \text{ W/m}^2$ . The heat transfer coefficient of the wind and temperature of ambience were assumed to be  $20 \text{ W/m}^2\text{-K}$  and  $30^\circ\text{C}$ , respectively. The error of the temperature between the CFD and experimental results is given by

$$\zeta = \frac{|T_{\text{CFD}} - T_{\text{Exp.}}|}{T_{\text{Exp.}} - T_{\text{amb.}}} \times 100\%. \quad (9)$$

Figure 5 shows the air temperature comparison between measured and calculated results under free convection. It shows that the deviation of the solutions obtained using CFD simulations was generally within the acceptable range, in which the inlet air velocity is  $0.45 \text{ m/s}$ . This proves that CFD is an effective tool for predicting the behavior and performance of a ventilation system. The flow field and temperature distribution in the computational domain are shown in Figure 6. The computed temperature variation behavior was clearly within reasonable accuracy. The simulation results also indicated that the temperature of the air increased as the airflow height increased.

In this study, the maximal temperature and mass flow rate were determined using various lengths of airflow under ideal conditions for the proposed system. Figure 7 shows the temperature and mass flow rate for various lengths of airflow under ideal conditions. It is clearly seen that the disparity of temperature between the ideal (Figure 5) and actual measurements (Figure 7) was approximately  $40^\circ\text{C}$ . The main reason is that actual measurements have energy loss. The analysis results for the parameters that clearly influence collector efficiency, such as the thickness of the air gap, the operating conditions, and height of flow, are presented and considered to be references for the future design and optimization of solar ventilation systems which are provided in the following section.

## 4. Results and Discussion

The accuracy of the calculated numerical results was accepted. Therefore, the experiment and simulation were applied to obtain optimal geometric design. CFD provides numerical advantages over experiment-based approaches,

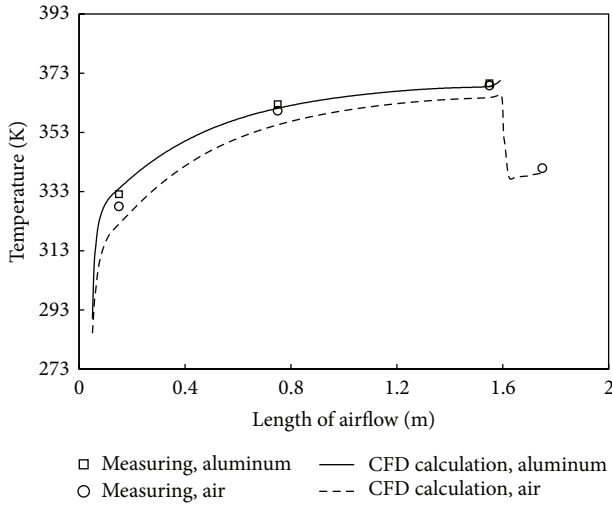


FIGURE 5: Air temperature comparison between measured and calculated results under free convection.

such as the substantial reduction in human labor and work time and the costs of materials. This study investigated the influence of various lengths of airflow, operating conditions of the inlet, the energy of heat flux, the type of absorber used for achieving efficiency, and the width of the air layer.

**4.1. Natural Convection and Forced Convection.** According to the results described in Section 3.4, the performance of waste heat recovery was not significant because of the low mass flow rate of the system. Therefore, the potential enhancement of mass flow rate was investigated by changing the velocity of the air inlet. A fan was installed at the air inlet to facilitate heat circulation. The following velocities at the air inlet were used, that is, 1, 1.5, 2, 3, 4, 5, and 6 m/s. Figure 8 shows the effect of the mass flow rate on the outlet temperature and on the efficiency of the ventilation system, which were measured experimentally. The outlet temperature clearly decreased as the mass flow rate increased, and the efficiency increased at a decreasing rate. The results clearly indicate that forced convection is more efficient than natural convection.

The measurement results and CFD simulation, in which forced convection ( $V_{in} = 2$  m/s) was used, are shown in Figure 9. The results obtained using the CFD approach were similar to the experimental results, indicating that CFD can be used for predicting the behavior and performance of a ventilation system in which forced convection is involved. The results indicate that exit temperature decreased because the temperature of the airflow channel was not uniform at the same elevation, as shown in Figure 10.

The longer the residence time in the airflow channel, the smaller the temperature difference between the aluminum and the air. Thus, the heat transferred to the air via the aluminum is reduced. If the air does not very smoothly flow in and out through the flow channel, it may cause a high percentage of heat returned to the environment by way of thermal radiation.

**4.2. Actual Test of Natural Convection.** The experimental study was conducted on the Penghu Islands. The Penghu Island of Taiwan was located at  $23^{\circ}28'17''$  latitude north and  $119^{\circ}30'45''$  longitude west. Figure 11 shows a photo of the solar ventilation system. The angle and length of airflow were  $15^{\circ}$  and 4 m for solar ventilation system, respectively. The time step for data collection was set as 1 min. The maximal glass, absorber plate, airflow channel, and plywood temperature were obtained at a height of 1.55 m, as shown in Figure 3(b). Figure 12(a) shows that the maximal temperature values were obtained approximately at noon. It is obvious that the overall changing trend with time of the temperature follows that of the solar radiation. At about 11:15, the solar radiation was blanked. However, the temperature will not be affected immediately, because the system still provides energy. The results also indicated that the air temperature difference between the exit and the inlet was approximately  $50^{\circ}\text{C}$ . The velocity of the ambience and the air of airflow channel is shown in Figure 12(b). The velocity of ambience was greater than that of airflow channel.

**4.3. Length of the Airflow Channel.** Regarding heat transfer, a large absorber area may result in a substantial increase in temperature during solar ventilation. Therefore, potential enhancement of heat removal was investigated by the changing length of airflow and solar radiation, and  $v_{in}$  was assumed to be 2 m/s. Five airflow channel lengths were used for heat transfer analysis: 0.8, 1.6, 2.4, 3.2, and 4.0 m. Figure 13(a) shows the effect of the airflow length and solar radiation on the outlet temperature by CFD simulation. Clearly, the outlet temperature increased when the airflow length increased. However, the change was not obvious when the height exceeded approximately 3.5 m. Therefore, an optimal length of approximately 3.5–4 m can be selected.

Furthermore, the intensity of solar radiation depends on the orientation of the solar ventilation system, the day of the year, and the hour of the day, among other working conditions. Therefore, this study investigated the effect of solar radiation, and the results are shown in Figure 13(a). The outlet temperature was increased by approximately 4% when the solar radiation increased as  $200\text{ W/m}^2$ . Figure 13(b) shows the effect of the airflow length and solar radiation on the efficiency by CFD simulation. It shows that the efficiency in energy collection decreased when the airflow length increased.

**4.4. Pattern of the Absorber Plate.** The convective heat transfer rate in the airflow channel can be augmented by increasing the heat transfer surface area and increasing the turbulence inside the channel. This study investigated the effect of various types of absorber plates which are inexpensive and common. Figure 14 shows that three independent sets of experiments were conducted to investigate the performance of both the flat and rectangular tubes; the cross-section was  $6 \times 2$  and  $10 \times 1$  cm, respectively.

Figure 15(a) shows the difference between inlet air temperature of the solar ventilation and outlet air temperature of the solar ventilation for various patterns of the absorber plate.

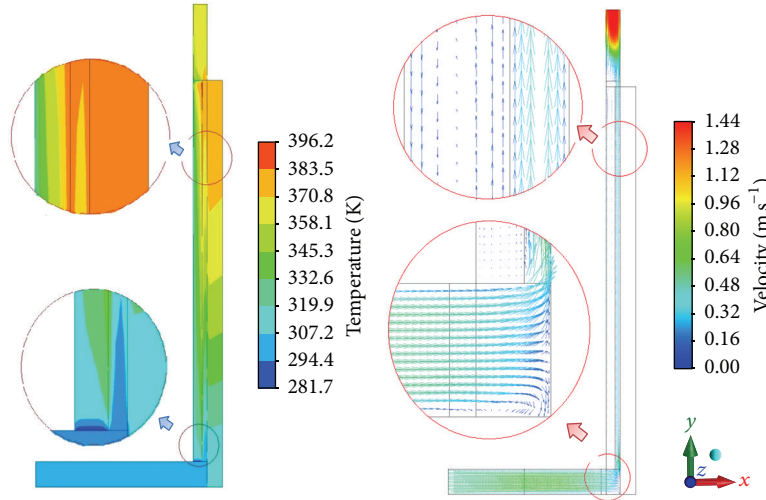


FIGURE 6: The flow field and temperature distribution in the computational domain.

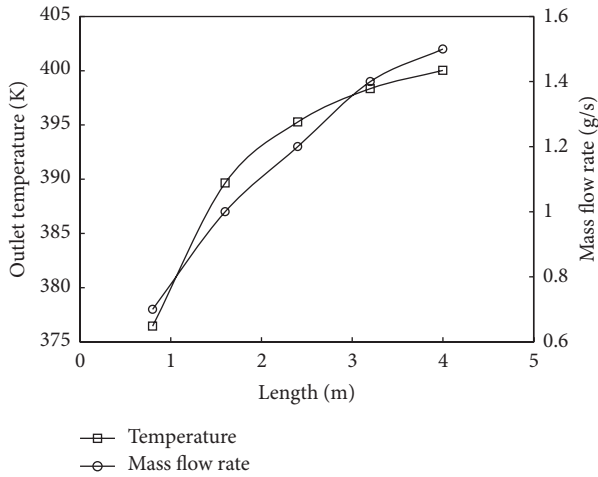


FIGURE 7: The maximum temperature and mass flow rate with various lengths of airflow.

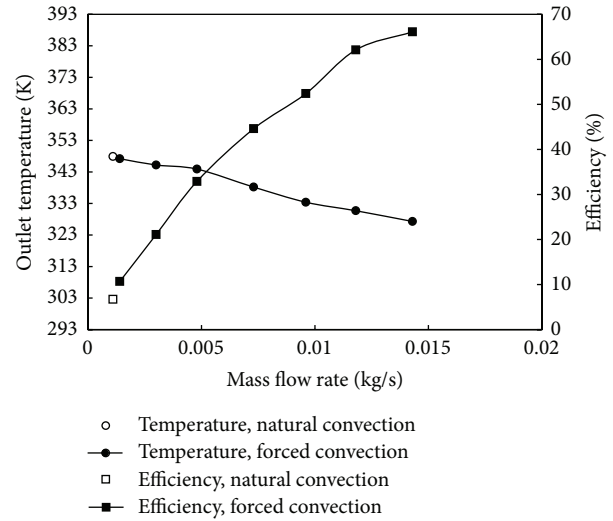


FIGURE 8: Outlet temperature and efficiency of the collector versus mass flow rate at  $T_i = T_{amb.} = 20^\circ\text{C}$ .

It shows that the temperature produced in Case I was clearly higher than that in Cases II and III. The main reason for this result is that the heat transfer surface area was increased, for the temperature difference of Case III exceeds Case II when the mass flow rate is higher than about 0.008 kg/s. The main reason is that the material is different between Cases II and III. The effect of material is more significant than that of heat transfer surface. The efficiency for three types of collectors is shown in Figure 15(b). The efficiency of three various absorber plates increased when the mass flow rate increased. It also shows that Case I absorber plate was more efficient than those used in Cases II and III. The optimal design and control range of the solar thermal collector were approximately 2-3 m/s for effective ORC waste heat recovery.

**4.5. Stagnant Air Layer and Operating Conditions.** Heat loss occurs in the air space between the glazing and absorber plate

through convection and conduction back the atmosphere. To reduce the heat loss of the absorber plate, the influence of various widths of the stagnant air layer and the associated heat transfer coefficient of wind on thermal performance was investigated. Five air layer widths were used in the CFD simulation: 0.3, 0.8, 1.8, 2.8, and 3.8 cm. The heat transfer coefficients were 10, 20, and 30  $\text{W/m}^2\text{-K}$ , respectively.

The various air layer widths and wind velocity are shown in Figure 16. The change in loss heat was not obvious when the heat transfer coefficient of wind was lower than approximately 20  $\text{W/m}^2\text{-K}$ . In addition, the heat loss of the absorber plate was not obvious when the air layer width was higher than that of 2 m. The main reason for these results is that the effective buoyancy force driven by the air density difference between the glass and absorber plate airflow channel was disrupted when the width of the air layer was too thin.

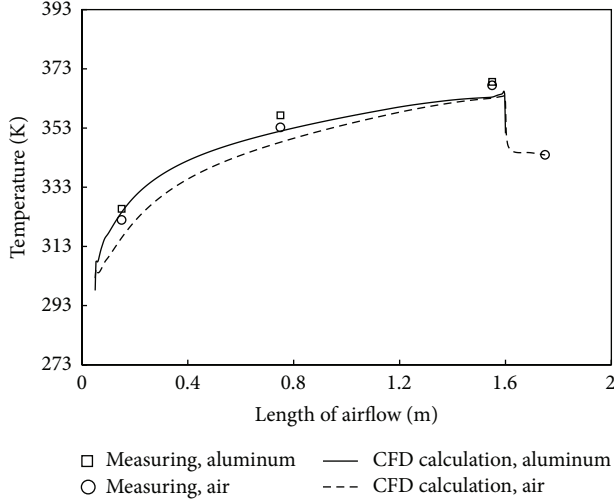


FIGURE 9: Temperature comparison between measurement and CFD calculation at  $v_{in} = 2$  m/s.

The overall effects of the width and heat transfer coefficient of wind on the outlet temperature were not obvious and exhibited 3% variation.

**4.6. Economic Assessment of ORC Combined with the Solar Storage Wall.** In this section, we investigated the economic assessment for solar storage wall combined with the organic Rankine cycle, as shown in Figure 1. Figure 17 illustrates the thermodynamic process described above. A theoretical Rankine cycle consists of the following processes:

- 1  $\rightarrow$  2: compression (working fluid feed pump);
- 2  $\rightarrow$  3: heat supply (solar ventilation system);
- 3  $\rightarrow$  4: expansion (expander);
- 4  $\rightarrow$  5: heat rejection (condenser).

At the same time, the process 3  $\rightarrow$  4a which appeared in Figure 17 is the ideal isentropic expansion process. Although this process cannot be reached during real operation, it is an evaluation criterion of the real expansion process. For the Rankine cycle system utilizing R245fa, the efficiency of the ORC is written as follows:

$$\eta_R = \frac{w_{34} + w_{12}}{q_{23}}, \quad (10)$$

where  $w_{34}$  is the power output obtained from the expander,  $w_{12}$  is power consumed by the feed pump, and  $q_{23}$  is the heat quantity absorbed by R245fa from solar collector. The power generation efficiency of the system is written as follows:

$$\eta_{sys} = \eta_c \times \eta_R. \quad (11)$$

From above, result indicates that the highest outlet temperature and efficiency of air collected were approximately 100°C and 60% (with 4 m length of air channel and absorber plate of Case I). In this study, heat exchanger's performance was assumed as 80%, and the temperature of hot water

TABLE 2: Energy and outputs of the experimental cycle.

Properties	Working fluid (air)
Area of collector, m <sup>2</sup>	48 (8 m $\times$ 6 m)
Solar radiation, kW/m <sup>2</sup>	0.80
Efficiency of collector, $\eta_c$	60%
Energy, kWh/day (8 hours/day)	184.3
Efficiency of Rankine cycle, $\eta_R$	6.2%
Power generated, kWh/day	11.43

was approximately 80°C. Figure 17 shows the schematic  $T$ - $S$  diagram of the low-temperature Rankine cycle system, and the efficiency of ORC was 6.2%. The assessment for ORC combined with the solar storage wall is shown in Table 2. For this study, the area of collector for building was assumed to have a width of 6 m and height of 8 m. The result indicates that the effective system efficiency for thermal to power is about 3.7% with the power generation of about 11.43 kWh per day. If the future wall structure can be modified with appropriate design, its cost is expected to be lower than current type. The proposed method is feasible for the solar heat collected by air ventilation systems, and the heat was used for electricity generation in a system incorporated with ORC.

## 5. Conclusions

An innovative application of ORC systems combined with solar ventilation was investigated and an experimental prototype was designed, constructed, and tested in this study. Experiments and CFD simulations were used to investigate the performance of the proposed solar ventilation system. The results are summarized as follows.

- (1) The deviation of the solutions obtained using CFD simulations was generally within the acceptable range, which proves that CFD is a qualified tool for predicting the behavior and performance of a ventilation system.
- (2) The thermal performance and outlet temperature of air, when a slight forced convection was supplemented, were superior to those produced when a pure natural convection was considered.
- (3) An optimal configuration of a solar ventilation system has a stagnant air layer of 2 cm, an air channel length of 4 m, and an absorber plate of Case I, and the optimal range of air inlet for thermal performance of a collector is approximately 2-3 m/s.
- (4) The proposed method is feasible for the solar heat collected by air ventilation systems, and the heat was used for electricity generation in a system incorporated with ORC.

## Highlights

- (i) Numerical and experimental methodologies are treated.

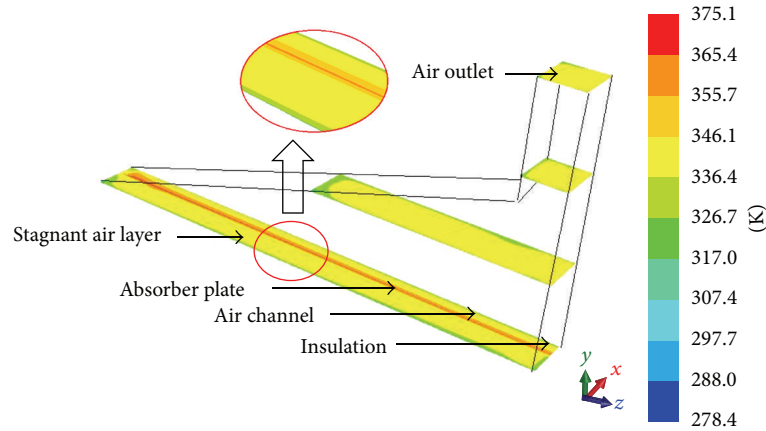


FIGURE 10: The temperature distribution in the exit section of solar ventilation.



FIGURE 11: Photo of the solar chimney.

- (ii) An innovative concept of combining the waste heat of ventilation with ORC system is introduced.
- (iii) Various types of solar ventilation system are discussed.

## Nomenclature

$A$ : Area ( $\text{m}^2$ )  
 $C_p$ : Specific heat ( $\text{J/kg}\cdot\text{K}$ )  
 $D_h$ : Hydraulic diameter of duct (m)  
 $F_R$ : Collector heat removal factor  
 $H$ : Height of absorber plate (m)  
 $h$ : Enthalpy ( $\text{kJ/kg}\cdot\text{K}$ ), heat transfer coefficient ( $\text{W/m}^2\cdot\text{K}$ )  
 $I$ : Intensity of solar radiation ( $\text{W/m}^2$ )  
 $k$ : Thermal conductivity ( $\text{W/m}^2\cdot\text{K}$ )  
 $\text{Pr}$ : Prandtl number  
 $\dot{m}$ : Mass flow rate ( $\text{kg/s}$ )  
 $P$ : Wetted perimeter  
 $Q_u$ : Useful energy gain (W)  
 $T$ : Temperature (K)  
 $U_L$ : Top loss coefficient  
 $v$ : Velocity (m/s)  
 $w$ : Power (kW).

## Greek Symbols

$\alpha$ : Absorptivity  
 $(\tau\alpha)_e$ : Effective transmittance-absorptance product  
 $\rho$ : Density of material  
 $\varepsilon$ : Emissivity  
 $\mu$ : Viscosity  
 $\mu_t$ : Turbulent viscosity  
 $\Gamma$ : Molecular thermal diffusivity  
 $\Gamma_t$ : Turbulent thermal diffusivity  
 $\eta$ : Thermal efficiency  
 $\eta_c$ : Collection efficiency of the solar collector  
 $\eta_R$ : Rankine cycle efficiency  
 $\eta_s$ : Overall efficiency of the system  
 $\Delta$ : Different  
 $\xi$ : Error of temperature.

## Subscript

$\text{amb.}$ : Ambient  
 $c$ : Solar ventilation  
 $\text{in}$ : Inlet  
 $\text{out}$ : Outlet  
 $R$ : Rankine cycle  
 $w$ : Wind  
 $t$ : Turbulent.

## Conflict of Interests

The authors declare that there is no conflict of interests regarding the publication of this paper.

## Acknowledgment

This research work has been supported by the National Science Council, Taiwan, under Grant of Contract nos. NSC 103-3113-P-007-002 and NSC 101-2221-E-027-039.

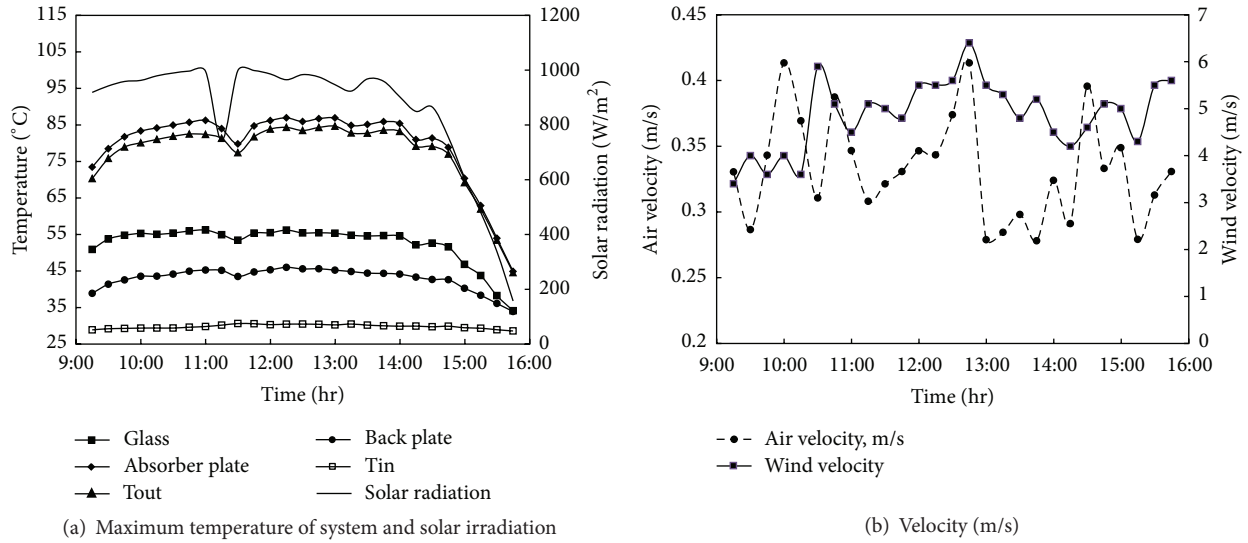


FIGURE 12: Surface temperature variation at different location and weather condition (September 18, 2013).

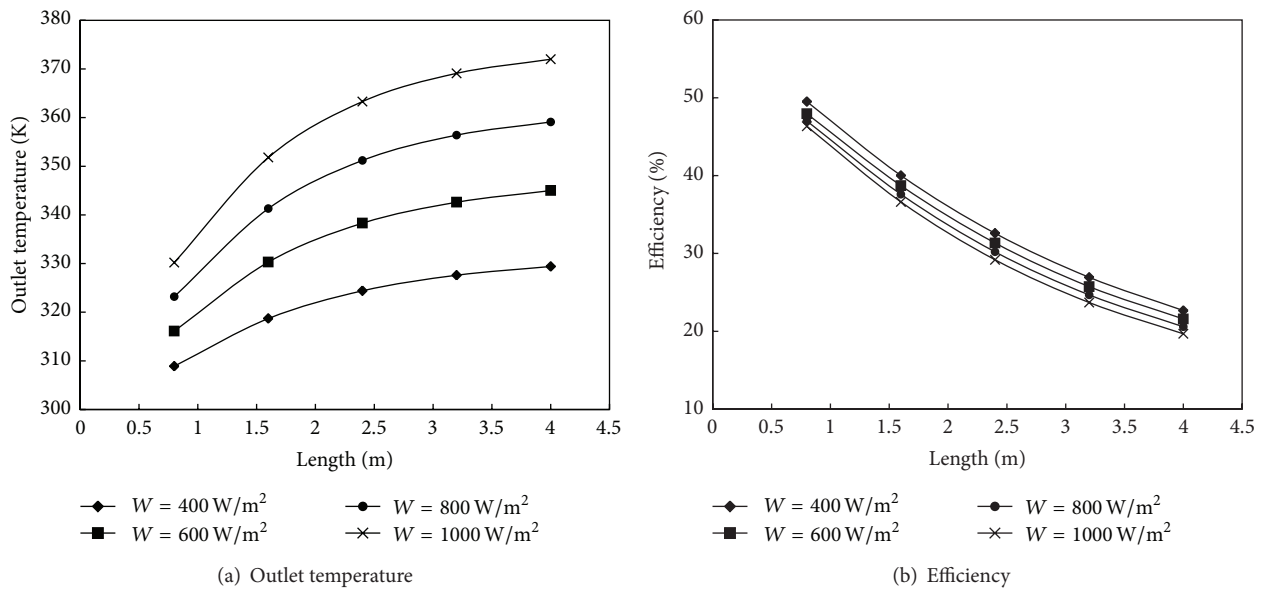


FIGURE 13: Effect of the lengths of airflow channel and solar heat flux by CFD simulation at  $\dot{m} = 0.003 \text{ kg/s}$ ,  $T_{\text{amb.}} = 293 \text{ K}$ .

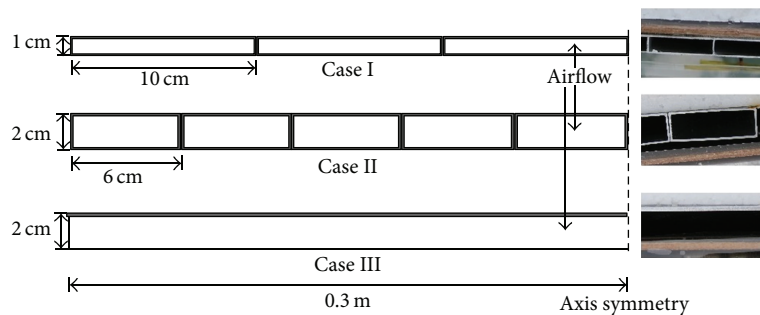


FIGURE 14: Three types of absorber plate in the solar ventilation.

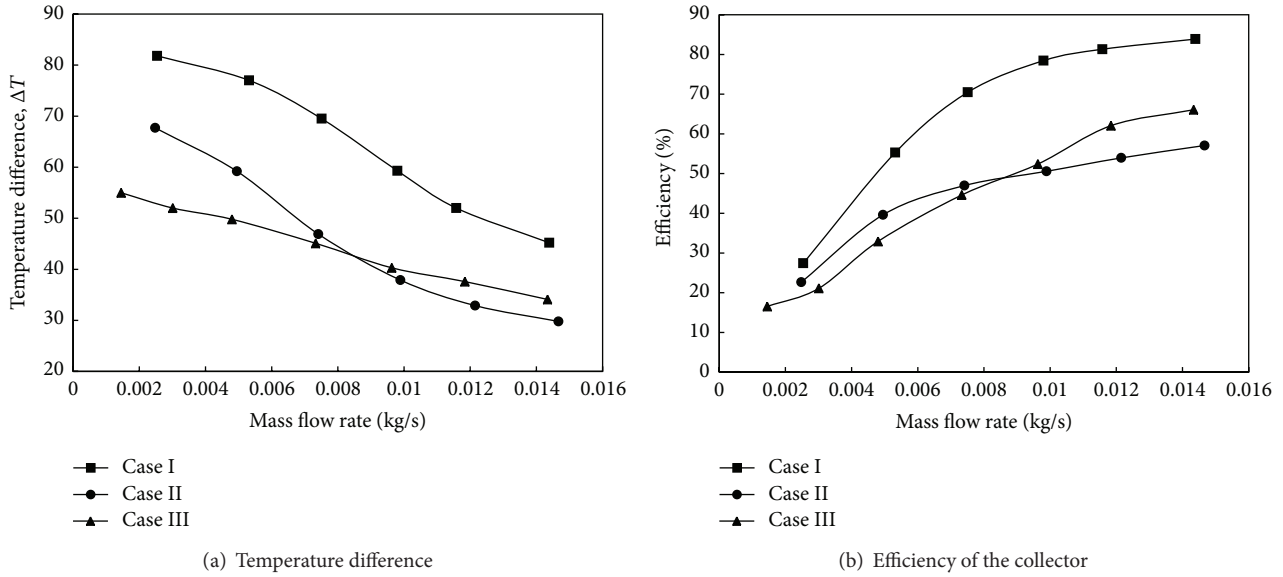


FIGURE 15: Temperature difference and efficiency of the collector versus mass flow rate for various absorber plates by experiment measurement.

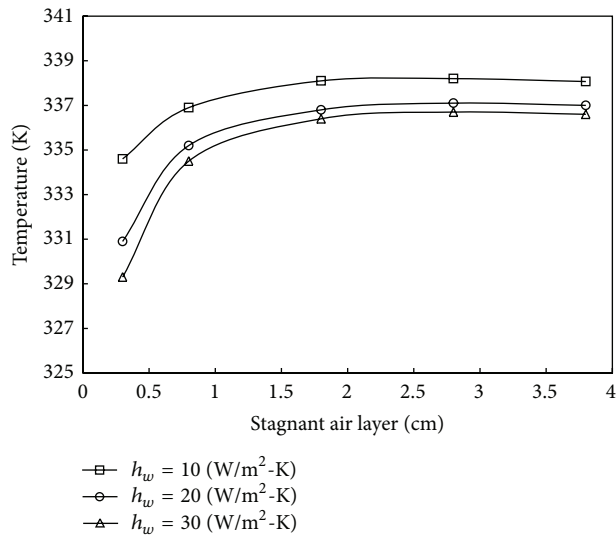


FIGURE 16: The outlet temperature for various widths of air layer and heat transfer coefficient of wind by CFD simulation.

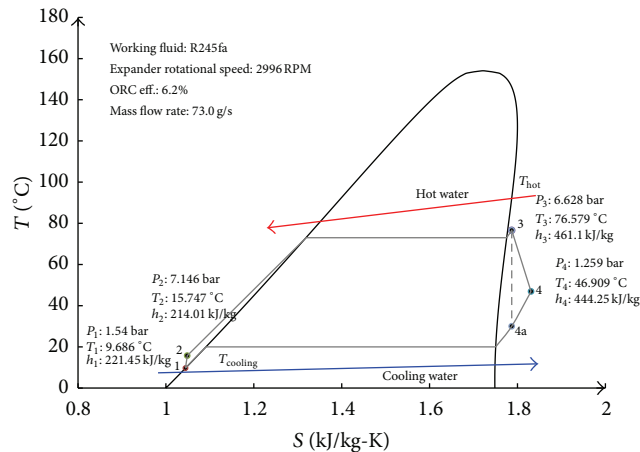


FIGURE 17: Schematic  $T$ - $S$  diagram of the low-temperature Rankine cycle system.

## References

- [1] T.-C. Hung, "Waste heat recovery of organic Rankine cycle using dry fluids," *Energy Conversion and Management*, vol. 42, no. 5, pp. 539–553, 2001.
- [2] T. C. Hung, S. K. Wang, C. H. Kuo, B. S. Pei, and K. F. Tsai, "A study of organic working fluids on system efficiency of an ORC using low-grade energy sources," *Energy*, vol. 35, no. 3, pp. 1403–1411, 2010.
- [3] X. D. Wang, L. Zhao, J. L. Wang, W. Z. Zhang, X. Z. Zhao, and W. Wu, "Performance evaluation of a low-temperature solar Rankine cycle system utilizing R245fa," *Solar Energy*, vol. 84, no. 3, pp. 353–364, 2010.
- [4] H. D. M. Hettiarachchi, M. Golubovic, W. M. Worek, and Y. Ikegami, "Optimum design criteria for an organic rankine cycle using low-temperature geothermal heat sources," *Energy*, vol. 32, no. 9, pp. 1698–1706, 2007.
- [5] T. Guo, H. X. Wang, and S. J. Zhang, "Fluids and parameters optimization for a novel cogeneration system driven by low-temperature geothermal sources," *Energy*, vol. 36, no. 5, pp. 2639–2649, 2011.
- [6] M. Wang, J. Wang, Y. Zhao, P. Zhao, and Y. Dai, "Thermodynamic analysis and optimization of a solar-driven regenerative organic Rankine cycle (ORC) based on flat-plate solar collectors," *Applied Thermal Engineering*, vol. 50, no. 1, pp. 816–825, 2013.
- [7] S. Karellas, A.-D. Leontaritis, G. Panousis, E. Bellos, and E. Kakaras, "Energetic and exergetic analysis of waste heat recovery systems in the cement industry," *Energy*, vol. 58, pp. 147–156, 2013.
- [8] X. D. Wang, L. Zhao, and J. L. Wang, "Experimental investigation on the low-temperature solar Rankine cycle system using R245fa," *Energy Conversion and Management*, vol. 52, no. 2, pp. 946–952, 2011.
- [9] T. C. Hung, "Triple cycle: a conceptual arrangement of multiple cycle toward optimal energy conversion," *Journal of Engineering for Gas Turbines and Power*, vol. 124, no. 2, pp. 429–436, 2002.
- [10] T. C. Hung, T. Y. Shai, and S. K. Wang, "A review of organic rankine cycles (ORCs) for the recovery of low-grade waste heat," *Energy*, vol. 22, no. 7, pp. 661–667, 1997.
- [11] B. R. Hughes, J. K. Calautit, and S. A. Ghani, "The development of commercial wind towers for natural ventilation: a review," *Applied Energy*, vol. 92, pp. 606–627, 2012.
- [12] O. Saadatian, K. Sopian, C. H. Lim, N. Asim, and M. Y. Sulaiman, "Trombe walls: a review of opportunities and challenges in research and development," *Renewable and Sustainable Energy Reviews*, vol. 16, no. 8, pp. 6340–6351, 2012.
- [13] R. Khanal and C. Lei, "Solar chimney: a passive strategy for natural ventilation," *Energy and Buildings*, vol. 43, no. 8, pp. 1811–1819, 2011.
- [14] X. Q. Zhai, Z. P. Song, and R. Z. Wang, "A review for the applications of solar chimneys in buildings," *Renewable & Sustainable Energy Reviews*, vol. 15, no. 8, pp. 3757–3767, 2011.
- [15] A. M. El-Sawi, A. S. Wafi, M. Y. Younan, E. A. Elsayed, and B. B. Basily, "Application of folded sheet metal in flat bed solar air collectors," *Applied Thermal Engineering*, vol. 30, no. 8-9, pp. 864–871, 2010.
- [16] J. Arce, M. J. Jiménez, J. D. Guzmán, M. R. Heras, G. Alvarez, and J. Xamán, "Experimental study for natural ventilation on a solar chimney," *Renewable Energy*, vol. 34, no. 12, pp. 2928–2934, 2009.
- [17] A. S. Yadav and J. L. Bhagoria, "Heat transfer and fluid flow analysis of solar air heater: a review of CFD approach," *Renewable and Sustainable Energy Reviews*, vol. 23, pp. 60–79, 2013.
- [18] R. Bassiouny and N. S. A. Koura, "An analytical and numerical study of solar chimney use for room natural ventilation," *Energy and Buildings*, vol. 40, no. 5, pp. 865–873, 2008.
- [19] D. J. Harris and N. Helwig, "Solar chimney and building ventilation," *Applied Energy*, vol. 84, no. 2, pp. 135–146, 2007.
- [20] J. J. Hu, X. S. Sun, J. L. Xu, and Z. X. Li, "Numerical analysis of mechanical ventilation solar air collector with internal baffles," *Energy and Buildings*, vol. 62, pp. 230–238, 2013.
- [21] Y. Tian and C. Y. Zhao, "A review of solar collectors and thermal energy storage in solar thermal applications," *Applied Energy*, vol. 104, pp. 538–553, 2013.
- [22] M. M. Alkilani, K. Sopian, M. A. Alghoul, M. Sohif, and M. H. Ruslan, "Review of solar air collectors with thermal storage units," *Renewable and Sustainable Energy Reviews*, vol. 15, no. 3, pp. 1476–1490, 2011.
- [23] J. A. Duffie and W. A. Beckman, *Solar Engineering of Thermal Processes*, John Wiley & Sons, New York, NY, USA, 4th edition, 2013.
- [24] ANSYS Inc, *FLUENT V12 User's Guide*, 2009.
- [25] D.-S. Lee, M.-L. Liu, T.-C. Hung, C.-H. Tsai, and Y.-T. Chen, "Optimal structural analysis with associated passive heat removal for AP1000 shield building," *Applied Thermal Engineering*, vol. 50, no. 1, pp. 207–216, 2013.
- [26] *GAMBIT Users Guide Version 2.4.*, FLUENT Incorporated, Lebanon, NH, USA, 2006.

## Research Article

# Bridging Photonics and Optoelectronics Curriculum for the Solar Photovoltaic and LED Industries

Yu-Shan Su<sup>1</sup> and Han-Chao Chang<sup>2</sup>

<sup>1</sup> Department of Industrial Education, National Taiwan Normal University, Taipei 106, Taiwan

<sup>2</sup> Instrument Technology Research Center, National Applied Research Laboratories, Hsinchu 300, Taiwan

Correspondence should be addressed to Han-Chao Chang; roman@narlabs.org.tw

Received 22 May 2014; Revised 11 August 2014; Accepted 12 August 2014; Published 28 August 2014

Academic Editor: Chao-Rong Chen

Copyright © 2014 Y.-S. Su and H.-C. Chang. This is an open access article distributed under the Creative Commons Attribution License, which permits unrestricted use, distribution, and reproduction in any medium, provided the original work is properly cited.

The gap between learning courses and practical demands has existed in Taiwanese solar photovoltaic and LED industries; therefore, this study attempts to analyze the existing curriculum design of universities. This study collected the current 103 course programs from all optoelectronics-related departments in Taiwanese 36 colleges and universities and sorted these curriculums by three domains of education objectives theory. This theoretical framework was verified on the basis of samples from 150 Taiwanese industrial experts and 354 optoelectronics-related undergraduates and postgraduates. We found that the levels of correlation among the independent variables including cognitive, affective, and skill-based domains and the dependent variable employability are all positively related to each other. We also found the currently curriculum design in Taiwanese universities rarely fit into theory of education objectives from the results of multiple regression analysis. Industrial and student's group also have few consistent ideas on courses within the curriculum. Finally in order to bridge the gap between learning and practical application, the study provides an idea on curriculum design and suggests that curriculum review should be executed by industrial experts to confirm the courses related to the employability.

## 1. Introduction

Climate change and energy shortage is one of the world's greatest challenges of the 21st century. Most countries treat renewable energy and energy conservation as the infrastructures for their sustainable development of the environment. Furthermore, the top priority of their national technology is the enhancements of low-carbon energy. In recent years, Taiwan has also followed this trend, investing plenty of assets into the solar photovoltaic and LED industries and constantly expanding production capacity. The integration of whole supply chains has matured.

However, like other export-oriented industries the cost of production, product yield, and employees' professional ability still affect the development of these two industries. The most common complaint from many local CEO's and managers is the insufficient professional ability of both the undergraduates and postgraduates from the universities, and that this is the primary reason for lagging behind the United States and Germany [1, 2].

Therefore, this study used the educational theory framework from Bloom and his colleagues to examine the existing curriculum design from undergraduate and postgraduate programs. Hoping the defects of the current curriculum design could be discovered. Next, the study attempted to formulate a better course program that will lead industrial requirements and photoelectric department's curriculum [3–6].

## 2. Literature Review

The theory of education objectives has been established by Bloom since 1956 [7]. Cognitive domain was the initial concept he devoted. Educational objectives are the goals set by educational establishments, which concentrates on people's studies. He emphasizes that, within the contents of the curriculum of courses, lecturers have to achieve their teaching mission and students have to realize the learning goals synchronously. The checkpoints or exams

include knowledge, skills, and abilities or attitudes after completing the assigned course [8]. After few years, affective and skill-based domain were came up by Krathwohl and Bloom [9]. Therefore, cognitive, affective, and skill-based (also called psychomotor) are three domains in their theory. The following is a summary of the three domains within education theory and education objectives.

(i) *Cognitive Domain*

*Objective Scope.* Encompasses memory, thinking, recognition, application, and so forth about people, events, and things.

*Objective Hierarchy.* Krathwohl and Bloom [9] divide the cognitive domain into “basic knowledge memory” division and “intelligence and skills” division [7]. Basic knowledge memory refers to the memory of various forms of information, where such information tends to have a standard answer. However, “intelligence and skills” division emphasizes thinking abilities of criticalness, introspection, and problem-solving.

In addition, the major hierarchies in the cognitive domain are divided into six levels, the sequential order is remember, understand, apply, analyze, evaluate, and create [10].

- (1) Remember: to remember a host of information in the teaching process, it often requires the learner to memorize the important information from the content of the textbook.
- (2) Comprehension: this determines the meaning of the teaching information, including verbal, written, and graphic.
- (3) Application: to apply the learned knowledge in a new scenario.
- (4) Analysis: to analyze the elements that make up knowledge or information, bringing a clearer hierarchy correlation.
- (5) Evaluation: to render a value judgment based on specific standards.
- (6) Synthesis: to streamline all elements in one to form innovative or comprehensive works.

(ii) *Affective Domain*

*Objective Scope.* Encompasses attitude, emotion, and appreciation of the teaching objectives, beliefs, and the like.

*Objective Hierarchy.* The affective is a form of mental state or emotional tendency, together with positive and negative reactions. Therefore, the affective domain is mostly abstract in expression of the means of educational objectives. Krathwohl and Bloom [9] divided affective domain into five levels, where the classification is a continuous and spiral structure. The lower levels indicate simplistic, tangible, and unique behaviors. The higher levels contain the more common, abstract, and generalized behaviors. The meanings of the five levels are described as follows [11].

- (1) Receiving: to show concern for specific matters or activities.

- (2) Responding: to react to matters by a form of participation.
- (3) Valuing: to express approval or opposition to specific matters through positive or negative attitudes.
- (4) Organizing: the ability to organize and determine importance when faced with multiple values that require judgment.
- (5) Characterizing: the students handle the matter based on the values they have learned and also internalize the behavior into their personal characteristics.

(iii) *Skill-Based Domain*

*Objective Scope.* It focuses on the visible movements or behaviors.

*Objective Hierarchy.* Krathwohl [11] had not designed the objective hierarchy for the skill-based domain in 1969. However many scholars proposed an objective hierarchy. For example, since 1966, Simpson did divide the skill-based domain into seven levels including perception, set, guided response, mechanism, complex over-response, adaptation, and origination [12, 13]. Later on 2000, Anderson et al. [10] issued a revision of Bloom’s taxonomy of educational objectives and included the skill-based domain in this book.

In addition, the Taiwanese scholars [14] collected literature and experts’ opinions; they thought that “employability” is an effective ability to join work matters. They also found that the interpretation model formulated effectively interprets the relationship between solar enterprises’ expectations and students’ employability. Furthermore, some scholars emphasized that employability has to combine knowledge, skills, and attitudes together and then assist people to learn or work continually [1, 15, 16]. This study sorts the characteristics from literature into Table 1.

### 3. Methodology

Based on the above, the following research framework (Figure 1) is proposed and the causal relationship between each domain of educational objectives theory and employability is hypothesized. The theory of education objectives of Bloom and Krathwohl [7, 10, 11], which includes cognitive, affective, and skill-based domains, is employed in the current study as independent variables. Employability [10, 14, 15] is used as a dependent variable.

*3.1. Research Design and Methodology.* This study collected the current 103 course programs from all optoelectronics-related departments in Taiwanese 36 colleges and universities and asked about the level of importance related to employability for respondents. Based on the course content and program goal, this study sorted these curriculums by three domains of education objectives theory [7, 10, 11]. Multiple linear regression analysis was employed to test the capability of each course program to predict employability. It is worth noting that some courses have one more property and cross domains simultaneously, and some names of course are approximate.

TABLE 1: Three dimensions of employability.

Knowledge	Skill	Attitude	
The use of mathematical logic	Work independently	Physical and mental traits	Frustration tolerance
Language expression	Use of technology	Adapt to the changes	Interpersonal social skills
Cultural learning	Solve the problem	Emotional management	Teamwork
Obtain and use of information	Creativity and critical thinking	Responsibility	Communication and coordination
Know and understand multiculturalism	Decision	Active learning	Respect and mutual trust
		Career planning	Participation in public affairs

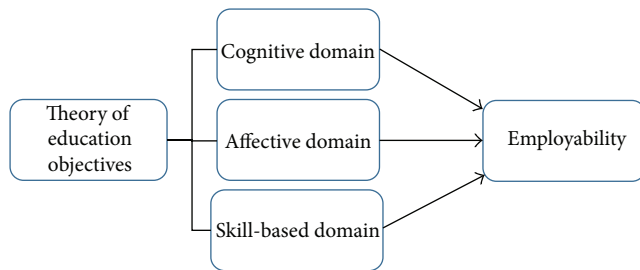


FIGURE 1: Framework of study.

The study initially implemented the expert interview method [17] and invited professionals from universities, Taiwan's solar optoelectronics industry, and the LED industry. By relying on expert interviews (November 2013, 10 experts), the study was able to sort the trends and human resource planning along with the demands of the solar optoelectronics and LED industry for the future. Most of the experts thought the disparity between university course programs and career demand is a wide gap. Experts emphasized prototype production, patent application [18], foreign language, and oral expressiveness as the foundations for employability; however the weighing of pure academy courses is too much on common curriculum design.

Next, a cross-sectional, descriptive, and inferential research study design was used in the current study. Purposive sampling techniques were employed, focusing on Taiwanese solar optoelectronics and LED industries. The contacts (including telephone numbers and email addresses) were obtained from respective firms' websites, as well as through personal relationships. Following initial contact and agreement, the questionnaire was sent via email. Frequent follow-up calls were made after one week if the questionnaire was not returned. Inclusion criteria included (1) college/university students; (2) industry operators. Each participant supplied written consent after being fully informed of the study and completed the self-administered questionnaire at his or her convenience.

To assess content validity, three experts from expert interviewing completed and scored the first draft of the questionnaire. A 5-point Likert scale was used for this process (1 = strongly unacceptable (delete), 2 = unacceptable (significantly revise), 3 = acceptable (partial amendment

needed), 4 = acceptable (detail needs amending), and 5 = acceptable (no amendment)). All questions obtained scores of 4 or 5 after amendments were made, leading us to consider the questionnaire possessed acceptable content validity.

A total of 371 questionnaires were distributed to college/university students at optoelectronics-related departments, and 354 were retrieved (95.4%); after removing 16 nonvalid questionnaires, 338 were available for analysis (Table 2). The schools were represented from all over Taiwan Island, including National Taiwan University (Taipei), National Taiwan Normal University (Taipei), Ming Chuan University (Taipei), Yuan Ze University (ChungLi), Chung Hwa University (HsinChu), and Nan Tai University of Technology (Tainan). Meanwhile, 163 questionnaires were distributed to industry senior staff and 150 were returned (92.0%) from the LED, solar optoelectronics, and general industries (Table 3). The total number of questionnaires returned was 504.

## 4. Research Findings

The study divided the sample data into two segments, comprised of the college/university students and the industry operators. The tools and methods of statistical analysis used included sample demographic data, reliability analysis, product-moment correlation analysis, and multiple regression analysis and performed with SPSS 20.0.

**4.1. Reliability Analysis.** A Cronbach's  $\alpha$  value was used to measure reliability and inner consistency within the same dimension. According to Anastasi [19] and McKinley et al. [20], a value between 0.7 and 0.98 can be judged as having high reliability, while a value under 0.6 is unacceptable for exploratory research. In this study, the scores were in the range of 0.939 to 0.961 (Table 4) for the universities sample and 0.884 to 0.976 (Table 5) for the industries sample.

**4.2. Product-Moment Correlation Analysis.** Coefficient of correlation was used to express the correlation direction and level of two variables. 0.6 to 1.00 are highly correlated; 0.40 to .59 are intermediately correlated; and under 0.40 is low correlation. The study adopted product-moment correlation  $r$  to analyze the level of correlation of two variables belonging to the same tendency scale or equal measurement scale.

TABLE 2: Demographic data from universities respondents.

Variable	Scale	Number	%
Gender	Male	257	76%
	Female	81	24%
University	National	124	36.7%
	Private	214	63.3%
School	Normal University	234	69.2%
	University of Science and Technology	92	27.2%
	University of Education	12	3.6%
Grade	Freshman	5	1.5%
	Sophomore	119	35.2%
	Junior	156	46.2%
	Senior	47	12.1%
	Postpone	17	5%
Department	Electrical engineering	217	64.2%
	Dep. of Chemical and Materials Engineering	6	1.8%
	Dep. of Electro-Optical Science and Technology	108	32%
	Dep. of Environmental Engineering	1	0.3%
	Other	6	1.8%

TABLE 3: Demographic data from industries respondents.

Variable	Scale	Number	%
Gender	Male	134	89.3%
	Female	16	1.7%
Age	25–35	75	50%
	36–45	48	32%
	46–55	22	14.7%
	Older then 56	5	3.3%
Job title	Person in charge	3	2%
	Department Manager	16	10.7%
	Other	131	87.3%
Type of company	Small- and medium-sized enterprises (less than capital 8,000 ten thousand)	57	38%
	Large enterprises (more than capital 8,000 ten thousand)	93	62%
Industry	Solar photovoltaic	85	56.7%
	LED/lighting	11	7.3%
	Other related	54	36%

TABLE 4: Reliability analysis—universities sample.

Dimensions	Number	Cronbach's $\alpha$	Mean
Cognitive	43	.955	3.89
Affective	25	.961	3.845
Skill-based	26	.956	3.836
Employability	15	.939	4.224
Overall reliability	119	.982	3.907

TABLE 5: Reliability analysis—industry sample.

Dimensions	Number	Cronbach's $\alpha$	Mean
Cognitive	43	.947	4.541
Affective	25	.930	4.500
Skill-based	26	.884	4.483
Employability	15	.925	4.450
Overall reliability	119	.976	4.505

In the college/university segment (Table 6), the levels of correlation among the four domains of cognitive, affective, skill-based, and employability are all positively associated

with each other. The level of correlation shows intermediate and high correlation. Cognitive is highly correlated to

TABLE 6: Correlation analysis—universities sample.

Dimensions	Mean	s.d.	Cognitive	Affective	Skill-based	Employability
Cognitive	3.89	.473	1			
Affective	3.84	.530	<b>.817</b>	1		
Skill-based	3.84	.623	<b>.709</b>	<b>.760</b>	1	
Employability	4.22	.581	<b>.481</b>	<b>.501</b>	<b>.466</b>	1

TABLE 7: Correlation analysis—industry sample.

Dimensions	Mean	s.d.	Cognitive	Affective	Skill-based	Employability
Cognitive	4.555	.4581	1			
Affective	4.5	.4435	<b>.937</b>	1		
Skill-based	4.483	.4274	<b>.884</b>	<b>.896</b>	1	
Employability	4.449	.5316	<b>.522</b>	<b>.513</b>	<b>.482</b>	1

ffective (0.817) and the skill-based (0.709) domain individually. This variable also shows intermediate correlation to employability (0.481). Affective is highly correlated to skill-based (0.760) and intermediate correlation to employability (0.501). The skill-based domain also shows intermediate correlation to employability (0.466). The findings indicate a certain level of correlations among the four domains. Namely, the hypothesis of this study, the causal relationship between educational goal of curriculum and employability, was supported in the university segment.

In the industry segment (Table 7), the levels of correlation among the four domains of cognitive, skill-based, affective, and employability are also positively associated to each other with highly significant correlation. Cognitive is highly correlated to affective (0.937) and the skill-based (0.884) domain individually. This variable also shows intermediate correlation to employability (0.522). Affective is highly correlated to skill-based (0.896) and intermediately correlated to employability (0.513). The skilled-based domain also shows intermediate correlation to employability (0.482). The findings indicate a certain level of correlations among the four domains. Namely, the hypothesis of this study, the causal relationship between educational goal of curriculum and employability, was supported in the industry segment.

## 5. Multiple Regression Analysis

Multiple regression was employed to account for (predict) the variance in an interval dependent based on linear combinations of interval, dichotomous, or dummy independent variables. Multiple regression can establish that a set of IVs explains a proportion of the variance in a DV at a significant level (through a significance test of  $R^2$ ) and can establish the relative predictive importance of independent variables by comparing beta weights [21].

The multiple regression equation takes the form  $y = b_1X_1 + b_2X_2 + \dots + b_nX_n + \epsilon$ . The  $b$ 's are the regression coefficients, representing the amount the dependent variable  $y$  changes when the corresponding independent variable changes by 1 unit. The  $\epsilon$  is the constant (so called "residual"), where the regression line intercepts the  $y$ -axis, representing

the amount the dependent  $y$  will be when all the independent variables are zero. The standardized versions of the  $b$  coefficients are the beta weights, and the ratio of the beta coefficients is the ratio of the relative predictive power of the independent variables. Associated with multiple regressions is  $R^2$ , the multiple correlations, which is the percentage of the variance in the dependent variable, explained collectively by all of the independent variables.

Multiple linear regression attempts to model the relationship between two or more explanatory variables and a response variable by fitting a linear equation into observed data [21, 22]. The estimates ( $b$  coefficients,  $F$  test, and adjusted  $R^2$ ) can be used to construct a prediction equation and generate predicted scores of a variable for further analysis. The  $P$  value in regression analysis decided whether the correct or causal relationship was established. Generally, the value of (.05) is an accepted point to reject the null hypothesis. It can say with a 95% probability of being correct that the variable is having some effect, assuming the model is specified correctly with a  $P$  value of 5%; namely, the lower the  $P$  value in the result of regression analysis, the higher the correction of assuming the model [22].

*5.1. Multiple Regression Analysis on Various Curriculum Domains to Employability.* First, the demographic data, such as gender, university type, school, grade, and department, were employed from the university segment as independent variables, while employability was set as a dependent variable. Results (see Table 8) indicate that the demographic data accounted for 7.8% of the variance in employability ( $R^2 = 0.072$ ,  $F = 5.143$ ,  $P < 0.001$ ). Evaluation of the regression coefficients indicates that gender ( $b = 0.185$ ,  $P < 0.005$ ), university type ( $b = 0.273$ ,  $P < 0.001$ ), school ( $b = -0.234$ ,  $P < 0.01$ ), and department ( $b = -0.100$ ,  $P < 0.1$ ) were the statistically significant components of model 1. However, the grade of university sample showed no significance for mode 1.

Second, the demographic data and cognitive domain from education objectives theory were employed from the university segment as independent variables, while employability was set as a dependent variable. Results (see Table 8)

TABLE 8: Multiple regression analysis—three-domain curriculum on employability (university sample).

Variable	Employability			
	$\beta$ estimate (standard error)			
Gender	<b>.185 (.072)*</b>	<b>.167 (.061)**</b>	<b>.167 (.061)**</b>	<b>.180 (.063)*</b>
University type	<b>.273 (.074)***</b>	.041 (.066)	.044 (.066)	.083 (.067)
School studying	<b>-.234 (.073)**</b>	<b>-.260 (.062)***</b>	<b>-.262 (.062)***</b>	<b>-.261 (.064)***</b>
Grade	.011 (.042)	.003 (.035)	-.001 (.035)	.006 (.036)
Department	<b>-.100 (.036)+</b>	<b>-.108 (.031)***</b>	<b>-.115 (.030)***</b>	<b>-.128 (.031)***</b>
Cognitive		<b>.269 (.100)+</b>	<b>.274 (.096)+</b>	<b>.125 (.067)+</b>
Affective			<b>.317 (.097)**</b>	<b>.352 (.087)***</b>
Skill-based				<b>.629 (.060)***</b>
$R^2$	.072	.342	.335	.302
Adjusted $R^2$	.058	.326	.321	.290
$F$	<b>5.143***</b>	<b>21.404***</b>	<b>23.788***</b>	<b>23.909***</b>

Note: + $P < 0.100$ , \* $P < 0.050$ , \*\* $P < 0.010$ , and \*\*\* $P < 0.001$ .

indicate that the cognitive domain accounted for 34.2% of the variance in employability ( $R^2 = 0.342$ ,  $F = 21.404$ ,  $P < 0.001$ ). Evaluation of the regression coefficients indicates that gender ( $b = 0.167$ ,  $P < 0.01$ ), school ( $b = -0.260$ ,  $P < 0.001$ ), department ( $b = -0.109$ ,  $P < 0.001$ ), and cognitive ( $b = 0.269$ ,  $P < 0.1$ ) were the statistically significant components of model 2. However, the university type and grade from the university sample showed no significance for mode 2.

Third, the demographic data and cognitive and affective domain from education objectives theory were employed from the university segment as independent variables, while employability was set as a dependent variable. Results (see Table 8) indicate that the affective domain accounted for 33.5% of the variance in employability ( $R^2 = 0.335$ ,  $F = 23.788$ ,  $P < 0.001$ ). Evaluation of the regression coefficients indicate that gender ( $b = 0.167$ ,  $P < 0.01$ ), school ( $b = -0.262$ ,  $P < 0.001$ ), department ( $b = -0.115$ ,  $P < 0.001$ ), cognitive ( $b = 0.274$ ,  $P < 0.1$ ), and affective ( $b = 0.317$ ,  $P < 0.01$ ) were the statistically significant components of model 3. However, the university type and grade from university sample showed no significance for mode 3.

Fourth, the demographic data and three domains from education objectives theory were employed from the university segment as independent variables, while employability was set as a dependent variable. Results (see Table 8) indicate that the skill-based accounted for 30.2% of the variance in employability ( $R^2 = 0.302$ ,  $F = 23.7909$ ,  $P < 0.001$ ). Evaluation of the regression coefficients indicates that gender ( $b = 0.180$ ,  $P < 0.05$ ), school ( $b = -0.261$ ,  $P < 0.001$ ), department ( $b = -0.128$ ,  $P < 0.001$ ), cognitive ( $b = 0.125$ ,  $P < 0.1$ ), affective ( $b = 0.352$ ,  $P < 0.001$ ), and skill-based ( $b = 0.629$ ,  $P < 0.001$ ) were the statistically significant components of model 4. However, the university type and grade from university sample still showed no significance for mode 4.

Therefore, the hypothesis, the causal relationship between each domain of educational objectives theory and employability were supported by the results of multiple regression analysis from the university segment. In the manifestation of

the coefficients, gender, university type, school, and department from the demographic data was associated with the variable employability.

In addition, the demographic data, such as gender, age, business type, and industry type were employed from the industry segment as independent variables, while employability was set as a dependent variable. Results (see Table 9) indicate that the demographic data accounted for 5.7% of the variance in employability ( $R^2 = 0.056$ ,  $F = 1.739$ ). Evaluation of the regression coefficients indicate that business type ( $b = -0.231$ ,  $P < 0.05$ ) and industry type ( $b = 0.059$ ,  $P < 0.05$ ) were the statistically significant components of model 1. However, gender, age, and title from industry sample show no significance for mode 1.

Second, the demographic data and cognitive domain from education objectives theory were employed from the industry segment as independent variables, while employability was set as a dependent variable. Results (see Table 9) indicate that the cognitive domain accounted for 32.3% of the variance in employability ( $R^2 = 0.323$ ,  $F = 11.351$ ,  $P < 0.001$ ). Evaluation of the regression coefficients indicates that business type ( $b = -0.170$ ,  $P < 0.1$ ), industry type ( $b = 0.06$ ,  $P < 0.01$ ), and cognitive ( $b = 0.630$ ,  $P < 0.001$ ) were the statistically significant components of model 2. However, gender, age, and title from the industry sample showed no significance for mode 2.

Third, the demographic data and cognitive and affective domain from education objectives theory were employed from the industry segment as independent variables, while employability was set as a dependent variable. Results (see Table 9) indicate that the affective domain accounted for 32.4% of the variance in employability ( $R^2 = 0.324$ ,  $F = 9.722$ ,  $P < 0.001$ ). Evaluation of the regression coefficients indicate that business type ( $b = -0.174$ ,  $P < 0.1$ ), industry type ( $b = 0.058$ ,  $P < 0.05$ ), and cognitive ( $b = 0.506$ ,  $P < 0.05$ ) were the statistically significant components of model 3. However, gender, age, title, and affective domain from the industry sample showed no significance for mode 3.

TABLE 9: Multiple regression analysis—three-domain curriculum on employability (industry sample).

Variable	Employability			
	$\beta$ estimate (standard error)			
Gender	-.030 (.143)	.084 (.122)	.072 (.125)	.071 (.126)
Age	.009 (.057)	.069 (.050)	.070 (.050)	.070 (.050)
Title	-.076 (.090)	-.003 (.077)	.000 (.077)	.000 (.080)
Business type	-.231 (.107)*	-.170 (.092) <sup>+</sup>	-.174 (.092) <sup>+</sup>	-.174 (.093) <sup>+</sup>
Industry type	.059 (.026)*	.060 (.022)**	.058 (.023)*	.058 (.023)*
Cognitive		.630 (.084)***	.506 (.246)*	.505 (.261) <sup>+</sup>
Affective			.133 (.249)	.132 (.271)
Skill-based				.003 (.211)
$R^2$	.057	.323	.324	.324
Adjusted $R^2$	.024	.294	.291	.286
$F$	1.739	11.351***	9.722***	8.447***

Note: <sup>+</sup> $P < 0.100$ , \* $P < 0.050$ , \*\* $P < 0.010$ , and \*\*\* $P < 0.001$ .

Fourth, the demographic data and three domains from education objectives theory were employed from the industry segment as independent variables, while employability was set as a dependent variable. Results (see Table 9) indicate that skill-based accounted for 32.4% of the variance in employability ( $R^2 = 0.324$ ,  $F = 8.447$ ,  $P < 0.001$ ). Evaluation of the regression coefficients indicates that business type ( $b = -0.174$ ,  $P < 0.1$ ), industry ( $b = 0.058$ ,  $P < 0.05$ ), and cognitive ( $b = 0.505$ ,  $P < 0.1$ ) were the statistically significant components of model 4. However, gender, age, title, affective, and skill-based from the industry sample still showed no significance for mode 4.

Therefore, the hypothesis, the causal relationship between cognitive domain and employability, is supported by the results of multiple regression analysis from the industry university segment. Both the affective and skill-based domain of educational objectives theory have no association with employability in this study. In the manifestation of the coefficients, the business type and industry type from the demographic data were associated with the variable employability.

**5.2. Multiple Regression Analysis on Courses with Cognitive Domain to Employability.** Results (see Table 10) show that the course program in cognitive domain accounted for 70.4% of the variance in employability ( $R^2 = 0.704$ ,  $F = 6.721$ ,  $P < 0.001$ ), with a significant interpretability from the university segment. Evaluation of the regression coefficients indicates that there were only 13 courses, LED Engineering Introduction ( $b = 0.128$ ,  $P < 0.05$ ), Solar Energy System Application Introduction ( $b = 0.162$ ,  $P < 0.01$ ), Semiconductor Memory ( $b = -0.097$ ,  $P < 0.05$ ), Optoelectronics Engineering Introduction ( $b = -0.108$ ,  $P < 0.05$ ), Optoelectronics Technology Introduction ( $b = 0.135$ ,  $P < 0.05$ ), Energy Engineering Introduction ( $b = -0.167$ ,  $P < 0.05$ ), New Energy Introduction ( $b = 0.113$ ,  $P < 0.05$ ), Electromagnetic Optics ( $b = 0.243$ ,  $P < 0.001$ ), Electronics ( $b = 0.146$ ,  $P < 0.01$ ), Physics of Semiconductor Devices ( $b = 0.201$ ,  $P < 0.001$ ), Semiconductor Sense Devices ( $b = 0.111$ ,  $P < 0.1$ ), Polymer Material and Devices ( $b = -0.135$ ,  $P < 0.1$ ),

and Calculated Optoelectronic Devices ( $b = 0.018$ ,  $P < 0.05$ ) that were statistically significant components of the model.

Results (see Table 11) show that the course program in cognitive domain accounted for 61.5% of the variance in employability ( $R^2 = 0.615$ ,  $F = 3.937$ ,  $P < 0.001$ ), with a significant interpretability from the industry segment. Evaluation of the regression coefficients indicate that there were only 8 courses, Solar Energy System Application Introduction ( $b = 0.225$ ,  $P < 0.05$ ), Semiconductor Memory ( $b = -0.451$ ,  $P < 0.05$ ), Optoelectronics Technology Introduction ( $b = 0.230$ ,  $P < 0.1$ ), Recent Optoelectronics ( $b = 0.222$ ,  $P < 0.1$ ), Lighting Engineering Introduction ( $b = 0.426$ ,  $P < 0.05$ ), Optoelectronics Introduction ( $b = 0.321$ ,  $P < 0.05$ ), Material of Organic Optic ( $b = -0.399$ ,  $P < 0.1$ ), and Subject of Optoelectronic Engineering ( $b = 0.825$ ,  $P < 0.05$ ) that were statistically significant components of the model. Thus, industry and students group have a consistent idea on 3 courses within the course program in cognitive domain.

**5.3. Multiple Regression Analysis on Skill-Based Domain Course to Employability.** Results (see Table 12) show that the course program in skilled-based domain accounted for 69.3% of the variance in employability ( $R^2 = 0.693$ ,  $F = 7.97$ ,  $P < 0.001$ ), with a significant interpretability from the university segment. Evaluation of the regression coefficients indicate that there were only 10 courses within 35 courses, Design of Solar Power and Lighting ( $b = 0.120$ ,  $P < 0.05$ ), Optoelectronic Nanometer Structure ( $b = 0.135$ ,  $P < 0.05$ ), Optoelectronic Circuit Application ( $b = 0.154$ ,  $P < 0.1$ ), Solar Energy Technical ( $b = -0.092$ ,  $P < 0.1$ ), Process of Semiconductor Devices ( $b = -0.152$ ,  $P < 0.1$ ), Optoelectronic Storage Technical ( $b = 0.135$ ,  $P < 0.01$ ), Semiconductor Circuit Package ( $b = 0.151$ ,  $P < 0.01$ ), Optoelectronic Testing ( $b = -0.055$ ,  $P < 0.05$ ), Optoelectronic Interference ( $b = 0.015$ ,  $P < 0.05$ ), and Light-Spot Testing ( $b = 0.002$ ,  $P < 0.01$ ) that were statistically significant components of the model.

Results (see Table 13) show that the course program in skilled-based domain accounted for 59.6% of the variance

TABLE 10: Multiple regression analysis—cognitive domain curriculum on employability (university sample).

Program name	Employability $\beta$ estimate (standard error)
LED Engineering Introduction	<b>.128 (.051)*</b>
LED Lighting Application Introduction	-.070 (.051)
Solar Power System Introduction	<b>.162 (.056)**</b>
Battery of Solar Power Introduction	-.120 (.073)
Theory of semiconductor luminous	.027 (.055)
Semiconductor Memory	<b>-.097 (.048)*</b>
FPD Introduction	.017 (.055)
Optoelectronics Engineering Introduction	<b>-.108 (.048)*</b>
Optoelectronics Technical Introduction	.039 (.055)
Optoelectronics Technology Introduction	<b>.135 (.054)*</b>
Energy Engineering Introduction	<b>-.167 (.052)*</b>
Theory of Optoelectronics Instrument	-.059 (.055)
Recent Optoelectronics Introduction	.061 (.055)
Fourier Optics Introduction	-.070 (.053)
New Energy Introduction	<b>.113 (.046)*</b>
Lighting Engineering Introduction	-.033 (.052)
Optoelectronics	-.037 (.051)
Wave Optic	.013 (.049)
Semiconductor Laser	.082 (.062)
Semiconductor Optic	.069 (.061)
Electromagnetics Optic	<b>.243 (.058)***</b>
Optoelectronics System	.045 (.055)
Optoelectronics Introduction	.074 (.050)
Innovation of Optoelectronics	.025 (.048)
Geometrical Optic	-.017 (.046)
Electronics	<b>.146 (.045)**</b>
Electric Circuitry	-.071 (.045)
Physics of Semiconductor Devices	<b>.201 (.053)***</b>
Semiconductor Light Emitting Devices	-.034 (.056)
Semiconductor Sense Devices	<b>.111 (.062)<sup>+</sup></b>
Optoelectronics Devices	-.061 (.061)
Optoelectronic Materials	-.002 (.045)
Optoelectronic Materials and Physical	.027 (.045)
Semiconductor Optic and optical fiber	.012 (.054)
Advanced Optoelectronic Materials	.049 (.059)
Organic Optic and Semiconductor	-.043 (.053)
Material of Organic Optic	-.025 (.052)
Energy Material	.017 (.051)
Polymer Material and Devices	<b>-.136 (.048)<sup>+</sup></b>
High frequency Semiconductor Devices	-.057 (.047)
Subject of Optoelectronic Engineering	.159 (.053)
Subject of Electrical Engineering	-.042 (.045)
Calculate of Optoelectronic Devices	<b>.018 (.052)*</b>
$R^2$	.704
Adjusted $R^2$	.496
$F$	<b>6.721***</b>

Note: <sup>+</sup> $P < 0.100$ , \* $P < 0.050$ , \*\* $P < 0.010$ , and \*\*\* $P < 0.001$ .

TABLE 11: Multiple regression analysis—cognitive domain curriculum on employability (industry sample).

Course name	Employment $\beta$ estimate (standard error)
LED Engineering Introduction	-.100 (.173)
LED Lighting Application Introduction	-.038 (.161)
Solar Power System Introduction	<b>.225 (.096)*</b>
Battery of Solar Power Introduction	.034 (.100)
Theory of semiconductor luminous	.102 (.112)
Semiconductor Memory	<b>-.451 (.150)*</b>
FPD Introduction	.068 (.127)
Optoelectronics Engineering Introduction	.005 (.062)
Optoelectronics Technical Introduction	<b>.230 (.121)<sup>+</sup></b>
Optoelectronics Technology Introduction	.172 (.120)
Energy Engineering Introduction	.015 (.131)
Theory of Optoelectronics Instrument	-.413 (.359)
Recent Optoelectronics Introduction	<b>.222 (.127)<sup>+</sup></b>
Fourier Optics Introduction	.014 (.106)
New Energy Introduction	-.090 (.129)
Lighting Engineering Introduction	<b>.426 (.125)**</b>
Optoelectronics	-.095 (.155)
Wave Optic	-.031 (.121)
Semiconductor Laser	-.028 (.128)
Semiconductor Optic	-.160 (.113)
Electromagnetics Optic	.131 (.142)
Optoelectronics System	-.114 (.097)
Optoelectronics Introduction	<b>.321 (.139)*</b>
Innovation of Optoelectronics	-.168 (.400)
Geometrical Optic	-.009 (.260)
Electronics	-.022 (.180)
Electric Circuitry	-.053 (.115)
Physics of Semiconductor Devices	.005 (.116)
Semiconductor Light Emitting Devices	.132 (.386)
Semiconductor Sense Devices	-.245 (.357)
Optoelectronics Devices	.154 (.243)
Optoelectronic Materials	-.059 (.159)
Optoelectronic Materials and Physical	.035 (.248)
Semiconductor Optic and optical fiber	.223 (.163)
Advanced Optoelectronic Materials	.016 (.240)
Organic Optic and Semiconductor	-.117 (.365)
Material of Organic Optic	<b>-.399 (.220)<sup>+</sup></b>
Energy Material	.197 (.328)
Polymer Material and Devices	-.036 (.160)
High frequency Semiconductor Devices	.030 (.181)
Subject of Optoelectronic Engineering	<b>.825 (.344)*</b>
Subject of Electrical Engineering	-.095 (.300)
Calculate of Optoelectronic Devices	-.057 (.104)
$R^2$	.615
Adjusted $R^2$	.459
$F$	<b>3.937***</b>

Note: <sup>+</sup> $P < 0.100$ , \* $P < 0.050$ , \*\* $P < 0.010$ , and \*\*\* $P < 0.001$ .

TABLE 12: Multiple regression analysis—skill-based curriculum on employability (university sample).

Course name	Employment $\beta$ estimate (standard error)
Design of LED Driving Circuit	.042 (.053)
Design of Solar power and Lighting	<b>.120 (.050)*</b>
Semiconductor Sensor	.002 (.057)
Design of Optoelectronic Devices	.001 (.056)
Optoelectronic Nanometer Structure	<b>.135 (.061)*</b>
Optoelectronic Circuit Application	<b>.154 (.054)<sup>+</sup></b>
Design of Optoelectronic Film	.050 (.055)
Design of Lighting and Optoelectronic	.021 (.050)
Solar Optoelectronic Technical	.057 (.045)
Solar Energy Technical	<b>-.092 (.050)<sup>+</sup></b>
Process of Semiconductor Devices	<b>-.152 (.054)<sup>+</sup></b>
Semiconductor Package Testing and Practice	-.009 (.057)
Semiconductor Design Control	.084 (.056)
Semiconductor Wafer Science and Technical	.028 (.057)
Semiconductor Lighting Application	.026 (.057)
Optoelectronic Interaction Technical	-.078 (.060)
Optoelectronic Sense Technical	.000 (.061)
Optoelectronic Storage Technical	<b>.135 (.052)**</b>
Computer aide Optoelectronic System Analysis	-.060 (.056)
Semiconductor Circuit Package	<b>-.151 (.057)**</b>
Semiconductor Circuit Process	.157 (.056)
Film Engineering	-.006 (.057)
Semiconductor Testing	-.056 (.050)
Semiconductor and MEMS Testing	.019 (.056)
Optoelectronic Engineering Testing	.054 (.051)
Optoelectronic Devices and Testing	-.032 (.057)
Optoelectronic Testing	<b>-.055 (.056)*</b>
Optoelectronic Translate and Driving	-.128 (.050)
Optoelectronic Interference	<b>.015 (.055)*</b>
Optoelectronic Testing	.097 (.048)
Light-Spot Testing	<b>.002 (.050)**</b>
Advanced photonics Testing	.151 (.059)
Introduction to Optics Testing	-.019 (.047)
Optomechatronic Integration Engineering	.074 (.049)
Electronic Practice	.050 (.040)
$R^2$	.693
Adjusted $R^2$	.480
$F$	<b>7.97***</b>

Note: <sup>+</sup> $P < 0.100$ , \* $P < 0.050$ , \*\* $P < 0.010$ , and \*\*\* $P < 0.001$ .

in employability ( $R^2 = 0.596$ ,  $F = 4.813$ ,  $P < 0.001$ ), with a significant interpretability from the industry segment. Evaluation of the regression coefficients indicates that there were only 13 courses within 35 courses, Semiconductor Sensor ( $b = 0.439$ ,  $P < 0.1$ ), Design of Optoelectronic Devices ( $b = 0.175$ ,  $P < 0.1$ ), Optoelectronic Nanometer

TABLE 13: Multiple regression analysis—skilled-based domain curriculum on employability (industry sample).

Course name	Employment $\beta$ estimate (standard error)
Design of LED Driving Circuit	-.077 (.088)
Design of Solar power and Lighting	.167 (.129)
Semiconductor Sensor	<b>.439 (.261)<sup>+</sup></b>
Design of Optoelectronic Devices	<b>.175 (.100)<sup>+</sup></b>
Optoelectronic Nanometer Structure	<b>-.837 (.444)<sup>+</sup></b>
Optoelectronic Circuit Application	-.104 (.133)
Design of Optoelectronic Film	.178 (.291)
Design of Lighting and Optoelectronic	-.101 (.111)
Solar Optoelectronic Technical	.201 (.204)
Solar Energy Technical	<b>.156 (.082)<sup>+</sup></b>
Process of Semiconductor Devices	<b>.195 (.104)<sup>+</sup></b>
Semiconductor Package Testing and Practice	-.083 (.088)
Semiconductor Design Control	-.032 (.058)
Semiconductor Wafer Science and Technical	<b>-.132 (.074)<sup>+</sup></b>
Semiconductor Lighting Application	-.078 (.130)
Optoelectronic Interaction Technical	-.075 (.255)
Optoelectronic Sense Technical	-.700 (.392)
Optoelectronic Storage Technical	-.053 (.087)
Computer aide Optoelectronic System Analysis	<b>.159 (.083)<sup>+</sup></b>
Semiconductor Circuit Package	<b>-.157 (.084)<sup>+</sup></b>
Semiconductor Circuit Process	-.034 (.113)
Film Engineering	-.090 (.107)
Semiconductor Testing	-.129 (.100)
Semiconductor and MEMS Testing	<b>.133 (.065)<sup>+</sup></b>
Optoelectronic Engineering Testing	.067 (.065)
Optoelectronic Devices and Testing	.194 (.243)
Optoelectronic Testing	<b>-.148 (.077)<sup>+</sup></b>
Optoelectronic Translate and Driving	-.049 (.073)
Optoelectronic Interference	<b>.190 (.059)**</b>
Optoelectronic Testing	.225 (.302)
Light-Spot Testing	.034 (.115)
Advanced photonics Testing	<b>1.040 (.485)*</b>
Introduction to Optics Testing	.008 (.084)
Optomechatronic Integration Engineering	-.236 (.303)
Electronic Practice	<b>.215 (.118)<sup>+</sup></b>
$R^2$	.596
Adjusted $R^2$	.472
$F$	<b>4.813***</b>

Note: <sup>+</sup> $P < 0.100$ , \* $P < 0.050$ , \*\* $P < 0.010$ , and \*\*\* $P < 0.001$ .

Structure ( $b = -0.837$ ,  $P < 0.1$ ), Solar Energy Technical ( $b = 0.156$ ,  $P < 0.1$ ), Semiconductor Wafer Science and Technical ( $b = -0.132$ ,  $P < 0.1$ ), Computer Aide Optoelectronic System Analysis ( $b = 0.159$ ,  $P < 0.01$ ), Semiconductor Circuit Package ( $b = -0.157$ ,  $P < 0.1$ ), Semiconductor and MEMS Testing ( $b = 0.133$ ,  $P < 0.1$ ), Optoelectronic

TABLE 14: Multiple regression analysis—affective domain curriculum on employability (university sample).

Course name	Employment $\beta$ estimate (standard error)
Industrial Safety	-.074 (.040) <sup>+</sup>
Semiconductor Industrial Japanese	-.077 (.034) <sup>*</sup>
Semiconductor Industrial English	.053 (.032)
Energy Saving	-.115 (.051) <sup>*</sup>
Communication and Co-ordination; Teamwork	-.045 (.047)
Environment Protection	.032 (.040)
Industrial sustainable development	.097 (.043) <sup>*</sup>
Optoelectronic and Energy Industry	.022 (.049)
Optoelectronic and Industry	.184 (.045) <sup>***</sup>
Tread of Optoelectronic Development	.005 (.052)
Analysis Industrial and Competition	.078 (.050)
Production and Operation Management	.052 (.048)
Marketing Management	.192 (.044) <sup>***</sup>
Knowledge Management	-.029 (.052)
Financial Management	.112 (.059)
High-Tech Marketing Management	-.156 (.057) <sup>**</sup>
Project Management	.124 (.058) <sup>*</sup>
New Energy System and Management	-.066 (.050)
Forensic and Safety Management	-.110 (.053) <sup>*</sup>
Low-Carbon Energy Technology	.039 (.057) <sup>+</sup>
Technology Forecasting and Evaluation	-.094 (.053) <sup>+</sup>
Technology Law and IP Protection	.162 (.046) <sup>*</sup>
Energy Cost Analysis	.141 (.059) <sup>*</sup>
Intellectual Property Rights	-.008 (.057)
The Standard of Green Purchasing	.002 (.049)
$R^2$	.700
Adjusted $R^2$	.491
$F$	11.52 <sup>***</sup>

Note: <sup>+</sup> $P < 0.100$ , <sup>\*</sup> $P < 0.050$ , <sup>\*\*</sup> $P < 0.010$ , and <sup>\*\*\*</sup> $P < 0.001$ .

Testing ( $b = -0.148$ ,  $P < 0.1$ ), Optoelectronic Interference ( $b = 0.190$ ,  $P < 0.01$ ), Advanced Photonics Testing ( $b = 1.04$ ,  $P < 0.05$ ), and Electronic Practice ( $b = 0.215$ ,  $P < 0.1$ ) that were statistically significant components of the model. Thus, industry and students group have a consistent idea on 7 courses within the course program in skilled-based domain.

**5.4. Multiple Regression Analysis on Affective Domain Course to Employability.** Results (see Table 14) show that the course program in affective domain accounted for 70.0% of the variance in employability ( $R^2 = 0.700$ ,  $F = 11.52$ ,  $P < 0.001$ ), with a significant interpretability from the university segment. Evaluation of the regression coefficients indicate that there were 14 courses within 26 courses including Optoelectronic and Industry ( $b = 0.184$ ,  $P < 0.001$ ) and Marketing Management ( $b = 0.192$ ,  $P < 0.001$ ) that were

TABLE 15: Multiple regression analysis—affective domain curriculum on employability (industry sample).

Course name	Employment $\beta$ estimate (standard error)
Industrial Safety	-.018 (.087)
Semiconductor Industrial Japanese	-.213 (.072) <sup>*</sup>
Semiconductor Industrial English	-.031 (.096)
Energy Saving	.019 (.073)
Communication and Co-ordination; Teamwork	.117 (.092)
Environment Protection	.011 (.059)
Industrial sustainable development	.424 (.126) <sup>*</sup>
Optoelectronic and Energy Industry	-.109 (.072)
Optoelectronic and Industry	-.319 (.128) <sup>*</sup>
The Tread of Optoelectronic Development	.245 (.085) <sup>**</sup>
The Analysis Industrial and Competition	.240 (.106) <sup>*</sup>
Production and Operation Management	.030 (.062)
Marketing Management	-.111 (.130)
Knowledge Management	-.114 (.095)
Financial Management	.075 (.103)
High-Tech Marketing Management	.056 (.061)
Project Management	-.042 (.063)
New Energy System and Management	.081 (.051)
Forensic and Safety Management	.112 (.045) <sup>*</sup>
Low-Carbon Energy Technology	-.008 (.096)
Technology Forecasting and Evaluation	-.030 (.071)
Technology Law and IP Protection	.113 (.065) <sup>+</sup>
Energy Cost Analysis	.017 (.079)
Intellectual Property Rights	-.053 (.075)
The Standard of Green Purchasing	.061 (.085)
$R^2$	.524
Adjusted $R^2$	.424
$F$	5.214 <sup>**</sup>

Note: <sup>+</sup> $P < 0.100$ , <sup>\*</sup> $P < 0.050$ , <sup>\*\*</sup> $P < 0.010$ , and <sup>\*\*\*</sup> $P < 0.001$ .

statistically significant components of the model. Results (see Table 15) show that the course program in affective domain accounted for 52.4% of the variance in employability ( $R^2 = 0.524$ ,  $F = 5.214$ ,  $P < 0.01$ ), with a significant interpretability from the industry segment. Evaluation of the regression coefficients indicate that there were only 7 courses within 26 courses including Tread of Optoelectronic Development ( $b = 0.245$ ,  $P < 0.01$ ) and Technology Law and IP Protection ( $b = 0.113$ ,  $P < 0.1$ ) that were statistically significant components of the model. In addition, industry and students group have a consistent idea on 5 courses within the course program in this domain. There are Semiconductor Industrial Japanese, Industrial Sustainable Development, Optoelectronic and Industry, Forensic and Safety Management, and Technology Law and IP Protection. This finding is also consistent with experts' suggestions while

proceeding the expert interview method; patent application and foreign language are the foundations for employability.

From the results of multiple regression analysis, this study found the currently curriculum design in Taiwanese universities rarely fit into theory of education objectives of Bloom and Krathwohl [7, 10, 11], which includes cognitive, affective, and skill-based domains. Industry and students group also have few consistent ideas on courses within the course program. Therefore, the study attempted to provide an idea on curriculum design for the optoelectronics department according to the statistical results in order to bridge the gap between learning and practical application. First when professors design curriculum, the theory of education objectives of Bloom and Krathwohl should be followed in either domain. Second, if it is possible, expert interview method or expert review should be processed on that curriculum to make sure the courses related to the employability are instructional.

## 6. Conclusion

The study's findings can be used as critical indicators in developing optoelectronics-related school/department curriculum for colleges and universities. By relying on industry operators from the solar optoelectronics and LED industries in selecting a curriculum that caters to what the industries need, one is able to recommend to universities how to develop better curriculum planning. Finer curriculum planning at universities aligns the students' school curriculum to better meet the needs of industry, helping to shorten the industry's developmental training period. It also bridges the student to being able to directly tackle the workplace in the future. Only when a consensus on curriculum planning is reached between industry and the academic sector can the content of the teaching curriculum be bridged with industry needs, thus helping to bridge the gap between learning and practical application.

## Conflict of Interests

The authors declare that there is no conflict of interests regarding the publication of this paper.

## Acknowledgment

The authors are grateful for the research support from the Ministry of Science and Technology of Taiwan, under Grant nos. NSC 101-3113S-003-014- and MOST 103-3114-Y-076-28.

## References

- [1] A. Duff, J. Ferguson, and K. Gilmore, "Issues concerning the employment and employability of disabled people in UK accounting firms: an analysis of the views of human resource managers as employment gatekeepers," *British Accounting Review*, vol. 39, no. 1, pp. 15–38, 2007.
- [2] A. H. Shamsuddin, A. Hunger, and A. Mughtar, "Over 10 years of cooperation between Universiti Kebangsaan Malaysia and University of Duisburg-Essen, Germany case study of the development of a fruitful partnership," *Procedia—Social and Behavioral Sciences*, vol. 102, pp. 11–20, 2013.
- [3] A. Azapagica, S. Perdan, and D. Shallcross, "How much do engineering students know about sustainable development? The findings of an international survey and possible implications for the engineering curriculum," *European Journal of Engineering Education*, vol. 30, no. 1, pp. 1–19, 2005.
- [4] C. J. Desha and K. C. Hargroves, "Surveying the state of higher education in energy efficiency, in Australian engineering curriculum," *Journal of Cleaner Production*, vol. 18, no. 7, pp. 652–658, 2010.
- [5] A. G. K. Abdullah, S. H. Keat, A. Ismail, M. H. Abdullah, and M. Purba, "Mismatch between higher education and employment in Malaysian electronic industry: an analysis of the acquired and required competencies," *International Journal of Engineering Education*, vol. 28, no. 5, pp. 1232–1242, 2012.
- [6] H. Baytiyeh, "Disparity between college preparation and career demands for graduating engineers," *International Journal of Engineering Education*, vol. 28, no. 5, pp. 1221–1231, 2012.
- [7] B. Bloom, *Taxonomy of Educational Objectives The Classification of Educational Goals; Handbook I: Cognitive Domain*, David McKay, New York, NY, USA, 1956.
- [8] K. R. Koedinger, A. T. Corbett, and C. Perfetti, "The knowledge-learning-instruction framework: bridging the science-practice chasm to enhance robust student learning," *Cognitive Science*, vol. 36, no. 5, pp. 757–798, 2012.
- [9] D. R. Krathwohl and B. Bloom, *Taxonomy of Educational Objectives: The Classification of Educational Goals. Handbook II: The Affective Domain*, David McKay, New York, NY, USA, 1969.
- [10] L. W. Anderson, D. R. Krathwohl, and P. W. Airasian, *A Taxonomy for Learning, Teaching, and Assessing: A Revision of Bloom's Taxonomy of Educational Objectives*, Addison Wesley Longman, New York, NY, USA, Complete edition, 2000.
- [11] D. R. Krathwohl, "The taxonomy of educational objectives—its use in curriculum Building," in *Defining Educational Objectives*, C. M. Lindvall, Ed., University of Pittsburgh Press, Pittsburgh, Pa, USA, 1964.
- [12] E. J. Simpson, *The Classification of Education Objectives: Psychomotor Domain*, US Department of Health, University of Illinois, 1966.
- [13] C.-S. Koong, T.-I. Tang, C.-C. Wu, H.-T. Li, and C.-C. Tseng, "An investigation into effectiveness of different reflective learning strategies for learning operational software," *Computers & Education*, vol. 72, pp. 167–186, 2014.
- [14] C.-G. Kuo, C.-C. Chang, and C.-C. Huang, "Constructing employability indicators for enhancing the effectiveness of engineering education for the solar industry," *International Journal of Photoenergy*, vol. 2014, Article ID 491353, 11 pages, 2014.
- [15] T. Lucas, E. Barkho, C. Rudolph, L. Zhdanova, M. Fakhouri, and L. Thompson, "Political affiliation, collective self-esteem and perceived employability of immigrants: inducing national identity polarizes host-nation employers," *International Journal of Intercultural Relations*, vol. 39, pp. 136–151, 2014.
- [16] B. Rienties, N. Brouwer, and S. Lygo-Baker, "The effects of online professional development on higher education teachers' beliefs and intentions towards learning facilitation and technology," *Teaching and Teacher Education*, vol. 29, no. 1, pp. 122–131, 2013.
- [17] C. Boyce and P. Neale, *Conducting In-Depth Interviews: A Guide for Designing and Conducting In-Depth Interviews for Evaluation Input*, Pathfinder, Watertown, Mass, USA, 2006.

- [18] C. Huang, H. Chang, and S. Henderson, "Knowledge transfer barriers between research and development and marketing groups within Taiwanese small-and medium-sized enterprise high-technology new product development teams," *Human Factors and Ergonomics In Manufacturing*, vol. 18, no. 6, pp. 621–657, 2008.
- [19] A. Anastasi, *Psychological Testing*, Prentice Hall, Upper Saddle River, NJ, USA, 6th edition, 1988.
- [20] R. K. McKinley, T. Manku-Scott, A. M. Hastings, D. P. French, and R. Baker, "Reliability and validity of a new measure of patient satisfaction with out of hours primary medical care in the United Kingdom: development of a patient questionnaire," *British Medical Journal*, vol. 314, no. 7075, pp. 193–198, 1997.
- [21] J. Cohen, P. Cohen, S. G. West, and L. S. Aiken, *Applied Multiple Regression/Correlation Analysis for the Behavioral Sciences*, Routledge, New York, NY, USA, 3rd edition, 2013.
- [22] E. T. Lee and J. W. Wang, *Statistical Methods for Survival Data Analysis*, John Wiley & Sons, New York, NY, USA, 4th edition, 2013.

## Research Article

# Crystalline Silicon Solar Cells with Thin Silicon Passivation Film Deposited prior to Phosphorous Diffusion

Ching-Tao Li,<sup>1</sup> Fangchi Hsieh,<sup>2</sup> Shi Yan,<sup>2</sup> Cuifeng Wan,<sup>2</sup> Yakun Liu,<sup>2</sup>  
Jing Chen,<sup>2</sup> and Likarn Wang<sup>1</sup>

<sup>1</sup> Institute of Photonics Technologies, National Tsing Hua University, Hsinchu 30013, Taiwan

<sup>2</sup> Jiangsu Aide Solar Energy Technology Co., Ltd., Xuzhou 221121, China

Correspondence should be addressed to Likarn Wang; [lkwang@ee.nthu.edu.tw](mailto:lkwang@ee.nthu.edu.tw)

Received 25 May 2014; Revised 9 July 2014; Accepted 14 July 2014; Published 10 August 2014

Academic Editor: Chao-Rong Chen

Copyright © 2014 Ching-Tao Li et al. This is an open access article distributed under the Creative Commons Attribution License, which permits unrestricted use, distribution, and reproduction in any medium, provided the original work is properly cited.

We demonstrate the performance improvement of p-type single-crystalline silicon (sc-Si) solar cells resulting from front surface passivation by a thin amorphous silicon (a-Si) film deposited prior to phosphorus diffusion. The conversion efficiency was improved for the sample with an a-Si film of ~5 nm thickness deposited on the front surface prior to high-temperature phosphorus diffusion, with respect to the samples with an a-Si film deposited on the front surface after phosphorus diffusion. The improvement in conversion efficiency is 0.4% absolute with respect to a-Si film passivated cells, that is, the cells with an a-Si film deposited on the front surface after phosphorus diffusion. The new technique provided a 0.5% improvement in conversion efficiency compared to the cells without a-Si passivation. Such performance improvements result from reduced surface recombination as well as lowered contact resistance, the latter of which induces a high fill factor of the solar cell.

## 1. Introduction

Because of long-term stability and relatively high light-to-electricity conversion, crystalline silicon (c-Si) solar cells have dominated the photovoltaic market for quite a while. Commercially, p-type silicon substrates are used as a common photovoltaic (PV) material and occupy a large majority of the PV market sales. Today, many research groups are focusing on various techniques for producing high efficiency p-type c-Si solar cells, while paying attention to the issue of cost reduction commensurate with a mass-production process. With this aim, many techniques for manufacturing silicon solar cells have been developed, including selective emitter solar cells [1–3], buried contact solar cells [4], surface passivated solar cells [5–8], back-side contact solar cells [9, 10], and heterojunction with intrinsic thin layer (HIT) solar cells [11–14].

In the PV industry, front surface passivation is quite an important technique and has been applied to improve silicon solar cells for a long time. A thermal oxide layer

has been considered a good candidate material for reducing surface dangling bonds [15], while amorphous silicon nitride with hydrogen, that is, SiN<sub>x</sub>:H, has proven a good surface passivating counterpart [16, 17]. Hydrogen-rich amorphous silicon (a-Si:H), on the other hand, has been a well-known surface passivating material [5–8]. In the latter application, a-Si:H passivates the front surface of a phosphorus diffused silicon solar cell mainly owing to the annihilation of surface dangling bonds by hydrogen atoms originally residing in the a-Si:H layer. Even without hydrogen-passivation effect as stated above, a polysilicon film deposited at 620°C upon the surfaces of a phosphorus diffused silicon wafer in an LPCVD chamber proved to increase the open-circuit voltage ( $V_{oc}$ ). From a lifetime test, the polysilicon film was believed to passivate the surface of the solar cell [18]. This LPCVD technique proved to improve the conversion efficiency by ~0.3% absolute with respect to conventional cells.

In this study, we present a different technique in which a thin a-Si film is deposited onto a p-type substrate prior to the phosphorus diffusion process and later turns into a

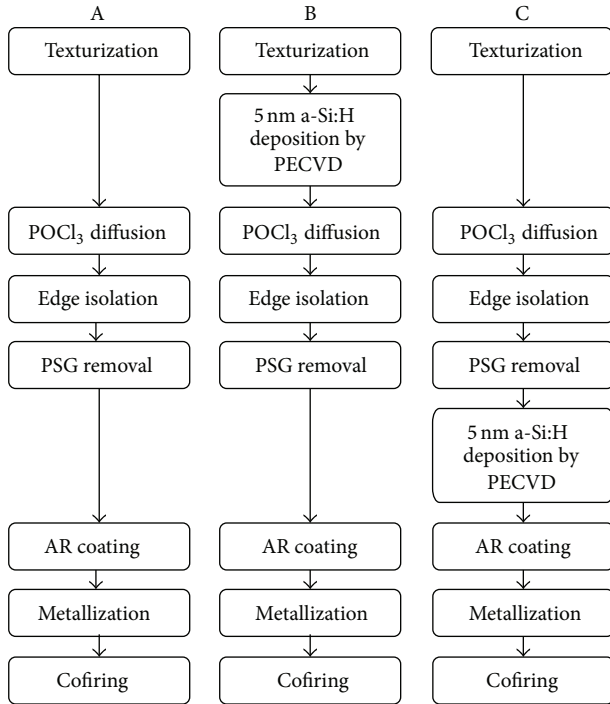


FIGURE 1: Process flow diagram for three groups of solar cells fabricated in this study. A, B, and C denote, respectively, the main fabrication steps for the three different groups.

polysilicon film after the phosphorus diffusion process. The polysilicon exhibits a peak dopant concentration, inducing a lower contact resistance and henceforth a higher fill factor.

In section two, three groups of solar cell samples are introduced for comparison. Group A refers to reference cells following a standard industrial production sequence and group B represents the polysilicon passivated solar cells obtained by the new technique, while group C consists of a-Si passivated solar cells with an a-Si film deposited after the phosphorus diffusion. The performances of the three groups of solar cells are compared in section three. A discussion is also given. Then section four concludes this paper.

## 2. Sample Preparation

We have used three groups of solar-grade p-type silicon wafers in this study for fabrication of solar cells following a standard process. The fabrication was performed mostly in a mass-production line situated at Aide Solar, a cell manufacturer in China. For all experiments in the fabrication, the silicon substrates were (100)-oriented sc-Si p-type Czochralski (Cz) wafers with resistivity in the range 1–3  $\Omega$ -cm and with an average thickness of  $\sim 190 \mu\text{m}$ . The solar wafers were pseudosquare and had a dimension of  $156 \times 156 \text{ mm}^2$ .

Figure 1 shows the three processes for the solar cell fabrication without showing the wafer cleaning procedures though. The wafers were divided into three groups. Group A followed fabrication steps of a standard manufacturing

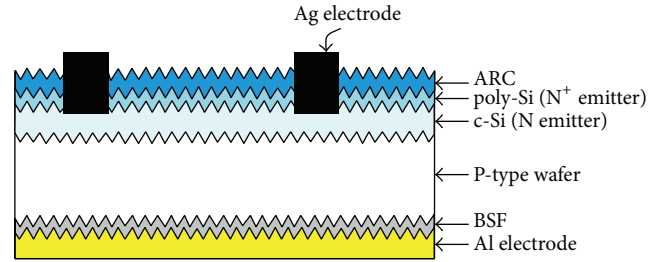


FIGURE 2: Cross-sectional sketch of the solar cell in group B.

process that starts with a basic cleaning, followed by texturization,  $\text{POCl}_3$  diffusion, edge isolation, phosphorus glass removal, deposition of antireflection coating (ARC), metallization on both sides, and then cofiring. These procedures are described in more detail as follows. In the first step, these wafers were cleaned and then dipped in an alkaline solution with IPA additive to form a pyramid-like surface on both sides. After being cleaned and dried, the wafers were placed back to back in pair on a quartz boat and loaded into a high-temperature phosphorus diffusion furnace with  $\text{POCl}_3$  as a source to form an emitter with a sheet resistance of  $\sim 70 \Omega/\text{square}$  on the front side. Edge isolation was performed by plasma etching to ensure that the front-side emitter was electrically isolated from the back side. The phosphorous glass (PSG) was afterwards removed by a diluted HF solution. A  $\text{SiN}_x$  film of  $\sim 82 \text{ nm}$  thickness used as an antireflection coating (ARC) on the front surface of the cell was deposited at  $450^\circ\text{C}$  by plasma enhanced chemical vapor deposition (PECVD) system, followed by screen printing of aluminum paste (plus silver busbar paste) on the back surface and silver paste on the front surface in a 3-busbar H-shaped grid pattern. Finally, the two-side printed contacts were cofired in a belt furnace.

Wafers in group B followed the same process as that for group A except that the wafers were deposited to form an a-Si:H film of  $\sim 5 \text{ nm}$  (4.8 nm, more correctly) thickness on the front surface prior to the phosphorus diffusion. The a-Si:H film was deposited by PECVD at  $285^\circ\text{C}$ . This step was conducted at the CNMSN (Center for Nanotechnology, Material Science and Microsystems) located at National Tsing Hua University. This step is a key requirement in optimizing the performance of solar cells in this study. Thereafter, wafers in groups B followed the steps of a standard process as stated for group A, that is,  $\text{POCl}_3$  diffusion, edge isolation, deposition of ARC, metallization on both sides, and cofiring. A cross-sectional sketch of the device of this group is shown in Figure 2.

Wafers in groups C also followed the same process as that for group A except that a  $\sim 5 \text{ nm}$  a-Si:H film was deposited on front sides of these wafers after PSG removal. Deposition of the a-Si:H films was done by PECVD at CNMSN. The difference between groups C and B resides in the order of the a-Si deposition process in the fabrication sequence. For a-Si:H passivated solar cells, process C is a common method to form surface passivation layer. Wafers in groups A were considered as a reference, while wafers in both groups of A

TABLE 1: Electrical characteristics of solar cell parameters measured under the standard test condition (25°C, AM 1.5 G). The average and best efficiencies obtained in the measurement are shown for each group of solar cells. Series resistances and shunt resistances for the best cell and the average are also shown.

		$V_{oc}$ (V)	$J_{sc}$ (mA/cm <sup>2</sup> )	F.F. (%)	$E_{ff}$ (%)	$R_s$ ( $\Omega$ )	$R_{sh}$ ( $\Omega$ )
(A) Standard cell	Average	0.623	36.19	77.55	18.01 $\pm$ 0.063	0.0056	40.23
	Best	0.625	36.26	77.70	18.07	0.0051	41.11
(B) Solar cell with poly-Si film	Average	0.630	36.46	79.15	18.51 $\pm$ 0.082	0.0038	54.13
	Best	0.631	36.57	79.24	18.61	0.0035	56.76
(C) Solar cell with a-Si film	Average	0.629	36.32	77.79	18.11 $\pm$ 0.125	0.0045	43.20
	Best	0.631	36.37	78.32	18.29	0.0041	44.65

and C were compared with group B in this study. Note that wafers of groups A and B were diffused at the same time in the same quartz boat, with almost an identical sheet resistance of 70~80  $\Omega$ /square formed. Wafers of group C were diffused earlier in the same production line, having a sheet resistance in the range of 70~80  $\Omega$ /square.

### 3. Results and Discussion

**3.1. Conversion Efficiency Improvement.** The conversion efficiencies of the solar cells were measured with a solar simulator and an IV test equipment under the standard test condition of AM 1.5 G illumination (100 mW/cm<sup>2</sup>) at 25°C. Table 1 presents the average and best experimental data of  $V_{oc}$ ,  $J_{sc}$ , and F.F. and conversion efficiency ( $E_{ff}$ ) for solar cells of groups A, B, and C, respectively. There, values for the series resistance  $R_s$  and the shunt resistance  $R_{sh}$  are also shown. The solar cells in groups A, B, and C are, respectively, standard solar cells, the solar cells with poly-Si films, and the solar cells with a-Si films. Each group contains 15 samples. Note that the poly-Si of group-B cells was formed in the high-temperature diffusion process by crystallization of the a-Si film that was deposited prior to the diffusion and that the a-Si films of group-C cells were deposited onto the wafers after the diffusion process. On average,  $V_{oc}$  of the standard solar cells (i.e., the reference cells) is 0.623 V,  $J_{sc}$  is 36.19 mA/cm<sup>2</sup>, and F.F. is 77.55%, and the efficiency is 18.01% (with the standard deviation  $\delta = 0.063\%$ ). The solar cells with poly-Si films have an average efficiency of 18.51% (with  $\delta = 0.082\%$ ) while the solar cells with a-Si films have an average efficiency of 18.11% (with  $\delta = 0.125\%$ ). The best cell of group B has  $V_{oc} = 0.631$  V and  $J_{sc} = 36.57$  mA/cm<sup>2</sup> and a fill factor of 79.24% and an efficiency of 18.61%. Notably, this test cell has an efficiency improvement over the standard cell by 0.54% (absolute) and over the cell on group C by 0.32% (absolute).

**3.2. Crystallization.** In order to observe the crystallization property of silicon films deposited by PECVD followed by a high-temperature diffusion process, we deposited silicon films with a thickness of 133 nm on two quartz substrates. Then, only one of them was loaded into a high-temperature furnace at 833°C. Figure 3 shows the Raman spectra of silicon films with and without going through a high-temperature process, respectively. A broad transverse optic (TO) peak around 480 cm<sup>-1</sup> in the Raman spectrum of the silicon film

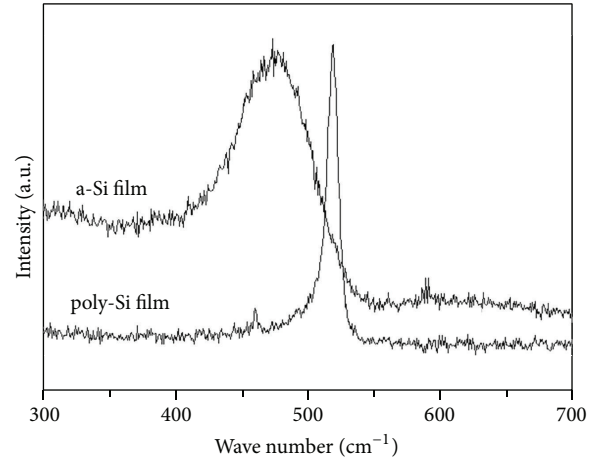


FIGURE 3: Raman spectra of silicon films with and without going through a high-temperature process, respectively.

deposited by PECVD at 285°C without going through a high-temperature process, corresponding to amorphous silicon phase, is observed [19, 20]. The sharp TO peak around 520 cm<sup>-1</sup> was obtained in the Raman spectrum of the silicon film deposited by PECVD at 285°C and subsequently going through a high-temperature process. The sharp TO peak around 520 cm<sup>-1</sup> corresponds to a crystalline phase with a grain size larger than 10 nm [20, 21]. This result makes us believe that a high-temperature diffusion process rendered the original a-Si film crystallized to form a poly-Si film on the substrate. This was also confirmed by the work in high-temperature diffusion process [22].

In order to verify the thickness uniformity of the silicon films, we used two polished (100) sc-Si substrates and deposited silicon films with a thickness of ~5 nm on the two substrates. One of them was loaded into a high-temperature diffusion furnace with POCl<sub>3</sub> as a doping source at 833°C followed by phosphorous glass (PSG) removal. The two samples were measured by transmission electron microscopy (TEM). Figure 4 shows the TEM cross-sectional images for the films at the a-Si/sc-Si and poly-Si/sc-Si interfaces, respectively. The figure shows the thickness uniformity of both silicon films. As shown by the TEM cross-sectional images in Figure 4, the thickness of the poly-Si film formed by a high-temperature

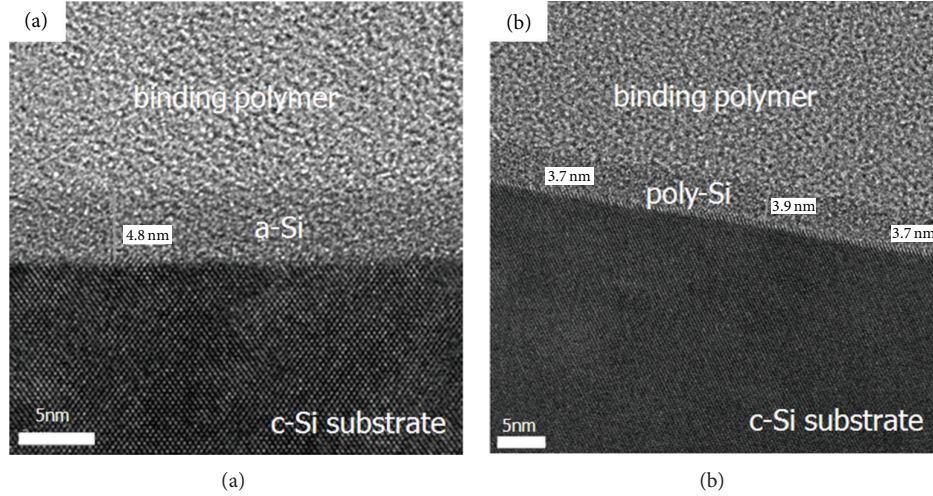


FIGURE 4: Cross-sectional TEM images of (a) the a-Si film deposited by PECVD and (b) the poly-Si film formed by crystallization of a-Si after going through a high-temperature diffusion process.

diffusion process was reduced from 4.8 nm to  $3.8 \pm 0.1$  nm owing to the PSG removal for this sample.

**3.3. Open-Circuit Voltage Improvement.** Open-circuit voltage is inversely related to the saturation current  $J_o$  in accordance with [23]

$$V_{oc} = \frac{kT}{q} \ln \left[ 1 + \frac{J_{sc}}{J_o} \right]. \quad (1)$$

Theoretically,  $J_o$  can be expressed in a simplified formula as

$$\begin{aligned} J_o &= J_{ob} + J_{oc} \\ &= \frac{qn_i^2 D_n}{N_A L_n} \\ &\quad \times \left[ \frac{S_n \cosh(W_P/L_N) + (D_n/L_n) \sinh(W_P/L_N)}{(D_n/L_n) \cosh(W_P/L_N) + S_n \sinh(W_P/L_N)} \right] \\ &\quad + \frac{qn_i^2 D_p}{N_D L_p} \\ &\quad \times \left[ \frac{S_p \cosh(W_N/L_P) + (D_p/L_p) \sinh(W_N/L_P)}{(D_p/L_p) \cosh(W_N/L_P) + S_n \sinh(W_N/L_P)} \right], \end{aligned} \quad (2)$$

where  $J_o$  is total saturation current density,  $J_{ob}$  and  $J_{oc}$  are the p-base and n-emitter contribution to the reverse saturation current density,  $(D_n, L_n)$  and  $(D_p, L_p)$  are the diffusivity and diffusion length of the minority carriers in the base and emitter, respectively,  $W_P$  and  $W_N$  are the base and emitter widths beyond the junction edges, and  $S_n$  and  $S_p$  are the surface recombination velocities, respectively, at the front side of the emitter and at the back side of the base [23]. Because all three groups of wafers considered here can be assumed to have the same amount of bulk defects and the same junction width, the transport behaviors of their minority carriers differ as a result of different surface conditions.

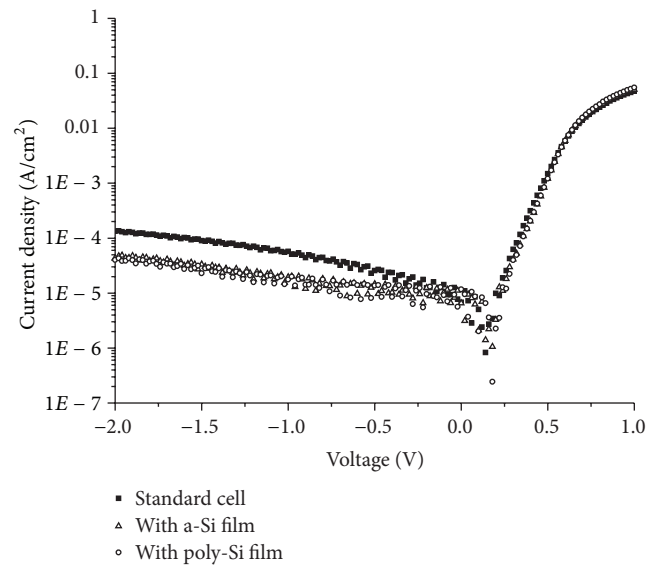


FIGURE 5: Comparison of dark log  $I$ - $V$  plots of the standard cell (■), solar cell with an a-Si film (△), and solar cell with a poly-Si film (○).

From (2), a better surface passivation and henceforth a lower front surface recombination velocity  $S_n$  reduce  $J_o$ .

We measured the dark current-voltage characteristics of the three aforementioned groups of solar cells, obtaining the results in Figure 5. It can be seen that a lower saturation current density  $J_o$  is induced by surface passivation through either a-Si or poly-silicon, with respect to the case of the standard sample (i.e., the sample without silicon film deposited). This is an important evidence for the reduced surface defect density by using the a-Si or poly-Si film. Therefore, in our study we can verify that the surface recombination can be reduced by forming a poly-Si film or an a-Si film [5, 18]. It is apparent from (1) that the major benefit of reduced front surface recombination is the increase in open-circuit voltage

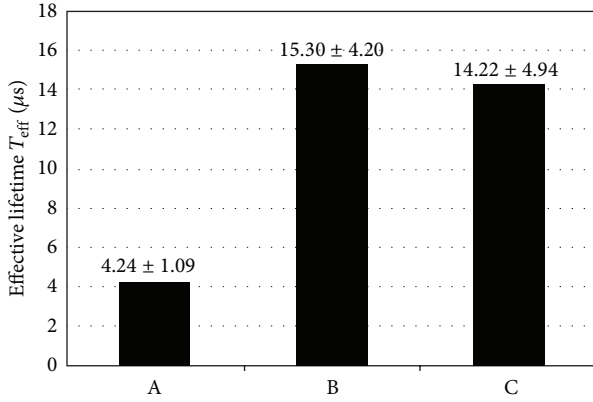


FIGURE 6: Average effective lifetimes measured for sample (A) without silicon films deposited, sample (B) with  $\sim 4$  nm poly-silicon films, and sample (C) with  $\sim 5$  nm a-Si films.

$V_{\text{oc}}$  which results from reduction of the saturation current  $J_0$ . This is confirmed by higher  $V_{\text{oc}}$  for cells of groups B and C than for cells of group A in Table 1.

Surface passivation effect can also be pinpointed by carrier lifetime measurement of the samples. Figure 6 shows the effective lifetimes of the samples in groups A, B, and C measured by the microwave photoconductivity decay technique (with the machine SEMILAB WT-2000). The three groups were all diffused samples without ARC deposition. Note that the samples in group A are samples without a-Si film; those in group B are samples with an about 4 nm poly-Si film and those in group C are samples with an about 5 nm a-Si film. An average effective lifetime was obtained from 16-point data measured for each sample, with each group including 15 samples. The effective lifetimes were 4.24, 15.30, and 14.22  $\mu\text{s}$ , respectively, for groups A, B, and C. The standard deviations for the three groups A, B, and C were, respectively, 1.09, 4.20, and 4.94  $\mu\text{s}$ . According to the Shockley-Read-Hall theory, the surface recombination rate is proportional to the density of the surface states. Because the bulk lifetimes of these samples used in the study were about the same, the increase in effective lifetime as measured was attributed to a reduction in surface recombination velocity [24].

In this study, we used silicon films with a  $\sim 5$  nm thickness for surface passivation. The thickness of silicon films needs to be limited to avoid absorption of light by the silicon film in the UV-blue range [25, 26]. We believe that the a-Si and poly-Si films with a  $\sim 5$  nm thickness are beneficial to the conversion efficiency for the following additional reasons. First, a thinner silicon film avoids the hindrance of electron transport which results from unsaturated bonds, grain boundaries, and other defects which act as recombination centers. Secondly, hydrogen atoms in the silicon nitride AR coating can more easily move across a thinner silicon film toward the Si film/c-Si interface and accordingly passivate the interfacial defects.

To further clarify the passivation effect, the internal quantum efficiency (IQE) was measured and shown in Figure 7 as a function of the optical wavelength ranging from 300 to 1100 nm for the three groups of solar cells. The spectral

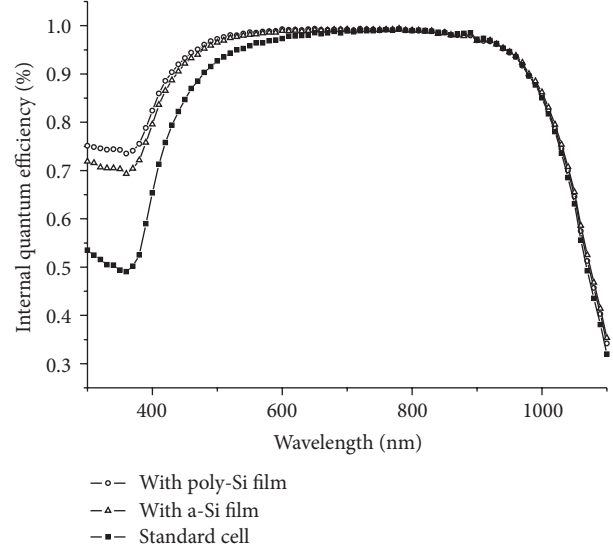


FIGURE 7: Internal quantum efficiency for a standard solar cell ( $\blacksquare$ ), a solar cell with  $\sim 4$  nm poly-silicon film ( $\circ$ ), and a solar cell with  $\sim 5$  nm amorphous-silicon film ( $\triangle$ ).

responses for the three groups of solar cells are an indication of surface passivation by a-Si and poly-Si films. As shown, there is a major difference in IQE at wavelengths of 300~600 nm between the film passivated cells and the standard cells, indicating an improvement in short-wavelength IQE by the poly-Si film with respect to the standard cells. Passivation by a-Si film can be also observed at the shorter wavelengths. And this has been reflected by the dark  $I$ - $V$  characteristics shown in Figure 5 as well as the lifetime data shown in Figure 6. In summary, the surface passivation by both silicon films results in an improved performance in IQE as well as in open-circuit voltage.

**3.4. Fill Factor Improvement.** The diffusion profiles in the emitters of the standard cell, the cell with  $\sim 5$  nm amorphous-silicon film, and the cell with  $\sim 4$  nm poly-silicon film were analyzed by spreading resistance profile (SRP) technique. These samples were diffused in the same diffusion furnace. Figure 8 indicates that junction depths of all the cell samples were around  $0.4 \mu\text{m}$ . The sample with a-Si film and the standard solar cell sample have an identical phosphorus concentration profile because the a-Si film was deposited on the as-diffused sample (see the dotted and the dashed curves). However, there exists a narrow peak on the concentration profile of the poly-Si film deposited sample. Such a peak was formed by the low activation energy of the phosphorus impurities in a-Si. This can be explained as follows. Diffusion of phosphorus at a high temperature in a-Si was carried out by migration through a large number of vacancies in a-Si in a high-temperature environment [27]. The activation energy of the phosphorus diffusion in a-Si is lower than that in sc-Si. Thus, in the process of  $\text{POCl}_3$  diffusion after a-Si deposition, more phosphorus atoms diffuse into the a-Si film than into the sc-Si substrate, leading to a higher phosphorus

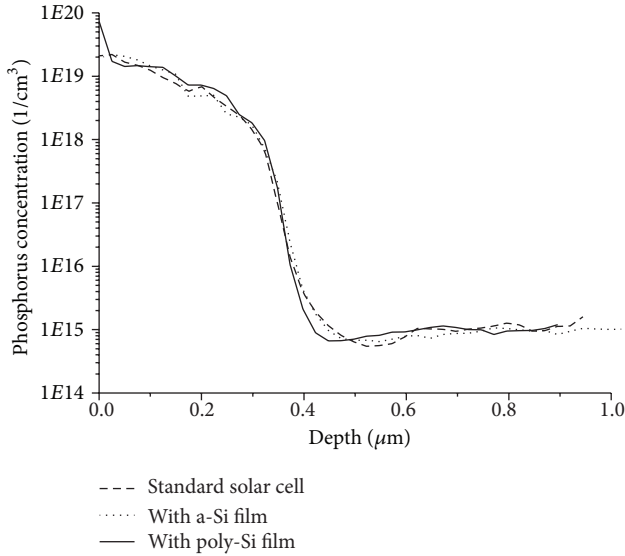


FIGURE 8: Spreading resistance profiles of phosphorus concentration in the emitter of a standard cell (---), a cell with ~5 nm amorphous-silicon film (···), and a cell with ~4 nm poly-silicon film (—).

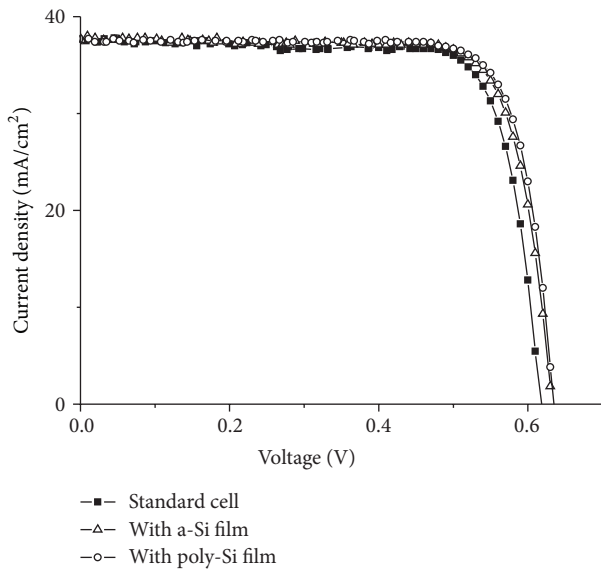


FIGURE 9:  $I$ - $V$  plots of a standard cell (■), a cell with poly-Si film (○), and a cell with a-Si film (Δ) obtained under the standard test condition.

concentration in the a-Si film (which was later transformed into a poly-Si film during the high-temperature process) than in the sc-Si region. The high phosphorus concentration in the poly-silicon film forms a low-contact resistance and therefore enhances the fill factor.

Figure 9 shows the measured  $I$ - $V$  curves for the three different solar cells under the standard test condition. Obviously, the solar cells with a poly-silicon film and with an a-Si film outperform the standard solar cell. It appears that surface passivation by poly-silicon film and a-Si film reduces the surface defects and thus improves  $V_{oc}$ . The solar cells with

polysilicon film presented the best efficiency among the three different solar cells. It is not only because the reduced surface recombination in solar cell with a polysilicon film improves  $V_{oc}$ , but also because the low-contact resistance improves the FF. The latter is evident from the data shown in Table 1.

It should be noted that the ARC (which is a silicon nitride film) is supposed to be a passivation layer as well. However, the ARC was deposited at the temperature of 450°C, making a large part of hydrogen atoms diffuse out and henceforth weakening the passivation effect. To date, some cell manufacturers have lowered the ARC deposition temperature to 400°C with a view to enhancing the passivation effect. The passivation effect resulting from the hydrogen atoms that reside in the ARC and are supposed to fix the dangling bonds at the surface of the silicon wafer is still limited. We have measured the lifetimes of diffused wafers with and without an ARC and found that the increase in lifetime with an ARC is only incremental. Therefore, it may be considered that the passivation results mostly from the thin silicon film, especially the poly-Si film.

The a-Si:H film deposited after phosphorous diffusion contributes many hydrogen atoms for fixing the dangling bonds and thereof upgrades the lifetime, as indicated in Figure 6 for the case without ARC. On the other hand, the poly-Si film for the case of group B cells is found to improve the lifetime without the hydrogen atoms for passivation. However, such passivation is believed to come from the heavily doped poly-Si layer as mentioned in Section 3.4. The heavy doping in such a layer induces a strong field, rejecting photogenerated holes and henceforth reducing the electron/hole recombination at the surface. And because the poly-Si film is so thin that there is not much photogenerated carriers in there, optical response at short wavelengths is not weakened. It is noted that the passivation from a-Si film for the case of group C cells remains at the ARC deposition temperature, 450°C, although the a-Si loses some of its hydrogen atoms at such a temperature.

#### 4. Conclusions

We have presented a new approach to increase the open-circuit voltage ( $V_{oc}$ ), the fill-factor (FF), and henceforth the conversion efficiencies of the solar cells by depositing an a-Si film prior to the standard diffusion process. The conversion efficiency was improved by 0.5% absolute with respect to the standard solar cell, in the case that the  $POCl_3$  diffusion process was treated after the deposition of a-Si film on the front side of a solar cell. The improvement in conversion efficiency was 0.4% absolute with respect to the cells with a-Si deposition after the  $POCl_3$  diffusion process. Raman spectra of the silicon film with a high-temperature diffusion process indicate that an a-Si film became a poly-Si film. Dark  $I$ - $V$  characteristics and the effective lifetimes of three groups of samples (i.e., standard solar cells, the solar cells with a-Si films, and the solar cells with poly-silicon films) demonstrate the surface passivation effect induced by the poly-silicon film on the surface of solar cell. The measurements indicate that the decrease of surface defect density and the reduction of

recombination rate can be achieved by a poly-silicon film. The spectral responses of internal quantum efficiency in the short wavelength range also shows the improvement due to reduced surface recombination rates on the front surface of the cell. Spreading resistance profile of the poly-Si deposited solar cells can explain the increase in the fill factor of the solar cell. Therefore, the high-temperature  $\text{POCl}_3$  diffusion process after the deposition of an a-Si film on the front sides of a silicon solar cell proves to be an effective means in obtaining performance-improved silicon solar cells.

## Conflict of Interests

The authors declare that there is no conflict of interests regarding the publication of this paper.

## Acknowledgments

The authors would like to thank the Jiangsu Aide Solar, Energy Tech. Co., Ltd., Xuzhou, China, National Tsing Hua University, Hsinchu, Taiwan, and the Grant 103-3113-E-007-003 from MOST, Taiwan, for financially supporting this research.

## References

- [1] A. Dastgheib-Shirazi, H. Haverkamp, B. Raabe, F. Book, and G. Hahn, "Selective emitter for industrial solar cell production: a wet chemical approach using a single side diffusion process," in *Proceedings of the 23rd European Photovoltaic Solar Energy Conference and Exhibition (Euro-PVSEC '08)*, pp. 1197–1199, 2008.
- [2] F. Book, B. Raabe, and G. Hahn, "Two diffusion step selective emitter: comparison of mask opening by laser or etching paste," in *Proceedings of the 23rd Euro-PVSEC*, pp. 1546–1549, 2008.
- [3] R. Monna, N. Enjalbert, Y. Veschetti, M. Lozac'h, and M. Pirot, "17.8% efficiency obtained on c-Si solar cells using a selective emitter industrial type process," in *Proceedings of the 23rd European Photovoltaic Solar Energy Conference and Exhibition (Euro-PVSEC '08)*, pp. 1733–1736, 2008.
- [4] S. R. Wenham, C. B. Honsberg, S. Edmiston et al., "Simplified buried contact solar cell process," in *Proceedings of the 1996 25th IEEE Photovoltaic Specialists Conference*, pp. 389–392, May 1996.
- [5] S. Olibet, E. Vallat-Sauvain, and C. Ballif, "Model for a-Si:H/c-Si interface recombination based on the amphoteric nature of silicon dangling bonds," *Physical Review B*, vol. 76, no. 3, Article ID 035326, 2007.
- [6] S. de Wolf, S. Olibet, and C. Ballif, "Stretched-exponential a-Si:H/c-Si interface recombination decay," *Applied Physics Letters*, vol. 93, no. 3, Article ID 032101, 2008.
- [7] T. F. Schulze, H. N. Beushausen, C. Leendertz, A. Dobrich, B. Rech, and L. Korte, "Interplay of amorphous silicon disorder and hydrogen content with interface defects in amorphous/crystalline silicon heterojunctions," *Applied Physics Letters*, vol. 96, no. 25, Article ID 252102, 2010.
- [8] J. Damon-Lacoste, L. Fesquet, S. Olibet, and C. Ballif, "Ultra-high quality surface passivation of crystalline silicon wafers in large area parallel plate reactor at 40 MHz," *Thin Solid Films*, vol. 517, no. 23, pp. 6401–6404, 2009.
- [9] E. Schneiderlöchner, R. Preu, R. Ldemann, and S. W. Glunz, "Laser-fired rear contacts for crystalline silicon solar cells," *Research and Applications*, vol. 10, no. 1, pp. 29–34, 2002.
- [10] R. Woehl, J. Krause, F. Granek, and D. Biro, "19.7% efficient all-screen-printed back-contact back-junction silicon solar cell with aluminum-alloyed emitter," *IEEE Electron Device Letters*, vol. 32, no. 3, pp. 345–347, 2011.
- [11] M. Tanaka, S. Okamoto, S. Tsuge, and S. Kiyama, "Development of HIT solar cells with more than 21% conversion efficiency and commercialization of highest performance HIT modules," in *Proceedings of the 3rd World Conference on Photovoltaic Energy Conversion*, vol. 1, pp. 955–958, May 2003.
- [12] E. Maruyama, A. Terakawa, M. Taguchi et al., "Sanyo's challenges to the development of high-efficiency HIT solar cells and the expansion of HIT business," in *Proceedings of the IEEE 4th World Conference on Photovoltaic Energy Conversion (WCPEC '06)*, pp. 1455–1460, May 2006.
- [13] L. Zhao, H. L. Li, C. L. Zhou, H. W. Diao, and W. J. Wang, "Optimized resistivity of p-type Si substrate for HIT solar cell with Al back surface field by computer simulation," *Solar Energy*, vol. 83, no. 6, pp. 812–816, 2009.
- [14] V. A. Dao, J. Heo, H. Choi et al., "Simulation and study of the influence of the buffer intrinsic layer, back-surface field, densities of interface defects, resistivity of p-type silicon substrate and transparent conductive oxide on heterojunction with intrinsic thin-layer (HIT) solar cell," *Solar Energy*, vol. 84, no. 5, pp. 777–783, 2010.
- [15] A. W. Stephens, A. G. Aberle, and M. A. Green, "Surface recombination velocity measurements at the silicon-silicon dioxide interface by microwave-detected photoconductance decay," *Journal of Applied Physics*, vol. 76, no. 1, pp. 363–370, 1994.
- [16] M. J. Kerr and A. Cuevas, "Very low bulk and surface recombination in oxidized silicon wafers," *Semiconductor Science and Technology*, vol. 17, no. 1, pp. 35–38, 2002.
- [17] H. F. W. Dekkers, S. de Wolf, G. Agostinelli, F. Duerinckx, and G. Beaucarne, "Requirements of PECVD  $\text{SiN}_x$ :H layers for bulk passivation of mc-Si," *Solar Energy Materials and Solar Cells*, vol. 90, no. 18–19, pp. 3244–3250, 2006.
- [18] C. T. Li, F. C. Hsieh, and L. K. Wang, "Performance improvement of p-type silicon solar cells with thin silicon films deposited by low pressure chemical vapor deposition method," *Solar Energy*, vol. 88, pp. 104–109, 2013.
- [19] M. Z. Lai, P. S. Lee, and A. Agarwal, "Thermal effects on LPCVD amorphous silicon," *Thin Solid Films*, vol. 504, no. 1–2, pp. 145–148, 2006.
- [20] D. Beeman, R. Tsu, and M. F. Thorpe, "Structural information from the Raman spectrum of amorphous silicon," *Physical Review B*, vol. 32, no. 2, pp. 874–878, 1985.
- [21] S. Y. Lien, B. R. Wu, J. C. Liu, and D. S. Wu, "Fabrication and characteristics of n-Si/c-Si/p-Si heterojunction solar cells using hot-wire CVD," *Thin Solid Films*, vol. 516, no. 5, pp. 747–750, 2008.
- [22] H. Kim, J. Choi, and J. Lee, "Effects of silicon-hydrogen bond characteristics on the crystallization of hydrogenated amorphous silicon films prepared by plasma enhanced chemical vapor deposition," *Journal of Vacuum Science and Technology A*, vol. 17, no. 6, pp. 3240–3245, 1999.
- [23] A. Rohatgi and P. Rai-Choudhury, "Design, fabrication, and analysis of 17–18-percent efficient surface-passivated silicon solar cells," *IEEE Transactions on Electron Devices*, vol. 31, no. 5, pp. 576–601, 1984.

- [24] T. Mueller, S. Schwertheim, M. Scherff, and W. R. Fahrner, "High quality passivation for heterojunction solar cells by hydrogenated amorphous silicon suboxide films," *Applied Physics Letters*, vol. 92, no. 3, Article ID 033504, 2008.
- [25] P. P. Altermatt, H. Plagwitz, R. Bock et al., "The surface recombination velocity at boron-doped emitters comparison between various passivation techniques," in *Proceedings of the 21st European Photovoltaic Solar Energy Conference*, pp. 647–650, 2006.
- [26] H. Fujiwara and M. Kondo, "Effects of a-Si:H layer thicknesses on the performance of a-Si:H/c-Si heterojunction solar cells," *Journal of Applied Physics*, vol. 101, no. 5, Article ID 054516, 2007.
- [27] A. F. Khokhlov, V. A. Panteleev, E. V. Dobrokhotov, G. A. Maksimov, and V. A. Sidorov, "Phosphorus Diffusion in Amorphous Silicon," *Physica Status Solidi (A) Applied Research*, vol. 81, no. 1, pp. K15–K18, 1984.

## Research Article

# Improving Light Extraction of Organic Light-Emitting Devices by Attaching Nanostructures with Self-Assembled Photonic Crystal Patterns

**Kai-Yu Peng and Da-Hua Wei**

*Graduate Institute of Manufacturing Technology and Department of Mechanical Engineering,  
National Taipei University of Technology (TAIPEI TECH), Taipei 10608, Taiwan*

Correspondence should be addressed to Da-Hua Wei; [dhwei@ntut.edu.tw](mailto:dhwei@ntut.edu.tw)

Received 7 April 2014; Revised 23 June 2014; Accepted 28 June 2014; Published 20 July 2014

Academic Editor: Ching-Song Jwo

Copyright © 2014 K.-Y. Peng and D.-H. Wei. This is an open access article distributed under the Creative Commons Attribution License, which permits unrestricted use, distribution, and reproduction in any medium, provided the original work is properly cited.

A single-monolayered hexagonal self-assembled photonic crystal (PC) pattern fabricated onto polyethylene terephthalate (PET) films by using simple nanosphere lithography (NSL) method has been demonstrated in this research work. The patterned nanostructures acted as a scattering medium to extract the trapped photons from substrate mode of optical-electronic device for improving the overall external quantum efficiency of the organic light-emitting diodes (OLEDs). With an optimum latex concentration, the distribution of self-assembled polystyrene (PS) nanosphere patterns on PET films can be easily controlled by adjusting the rotation speed of spin-coater. After attaching the PS nanosphere array brightness enhancement film (BEF) sheet as a photonic crystal pattern onto the device, the luminous intensity of OLEDs in the normal viewing direction is 161% higher than the one without any BEF attachment. The electroluminescent (EL) spectrum of OLEDs with PS patterned BEF attachment also showed minor color offset and superior color stabilization characteristics, and thus it possessed the potential applications in all kinds of display technology and solid-state optical-electronic devices.

## 1. Introduction

Organic light-emitting diode is one of the optical-electronic devices for the various applications not only in general illumination but also for consumer displays due to the probable advantages of excellent EL performances, good flexibility, light weight, better durability, low power consumption, and convenient fabrication. Therefore, the OLEDs seem to be one of the potential candidates for the next-generation emissive display technology [1–5]. However, many research articles have reported that almost 70–80% of the photons generated inside the organic layers is confined in the OLEDs caused by three major factors: (1) the total internal reflection (TIR) occurred at the glass/air interface and organic layers/substrate (substrate and waveguiding mode); (2) the reflection loss is due to the refractive index mismatch between interfaces (Fresnel loss); (3) the emitted light is lost due to absorption and plasmonic dissipation of the metal electrode

(absorption and SP mode) [6–9]. For the reduction of the waveguiding mode of the organic layers, various methods such as introducing textured surface, inserting low-index materials, and fabricating patterned nanostructures into the device have been proposed [10–13]. But the light extracted from organic layers still suffers from the light confinement of the device substrate. Using light-coupling structures onto the surface of device can help extract light suffering from the TIR at glass substrate/air interface, thus increasing the total external quantum efficiency (EQE) [14, 15]. Many researches have proposed different ways to extract the trapped light in the substrate mode, including rough or textured substrate surface, microlens array (MLA) film, diffusive particles, and silica colloidal gel [14–16]. It is worth mentioning that, due to the limitation of the standard photolithography technique, the used microlens with diameters near the wavelength of the emitted light from the OLEDs cannot be made. In the presented work, we introduced a facile and effective

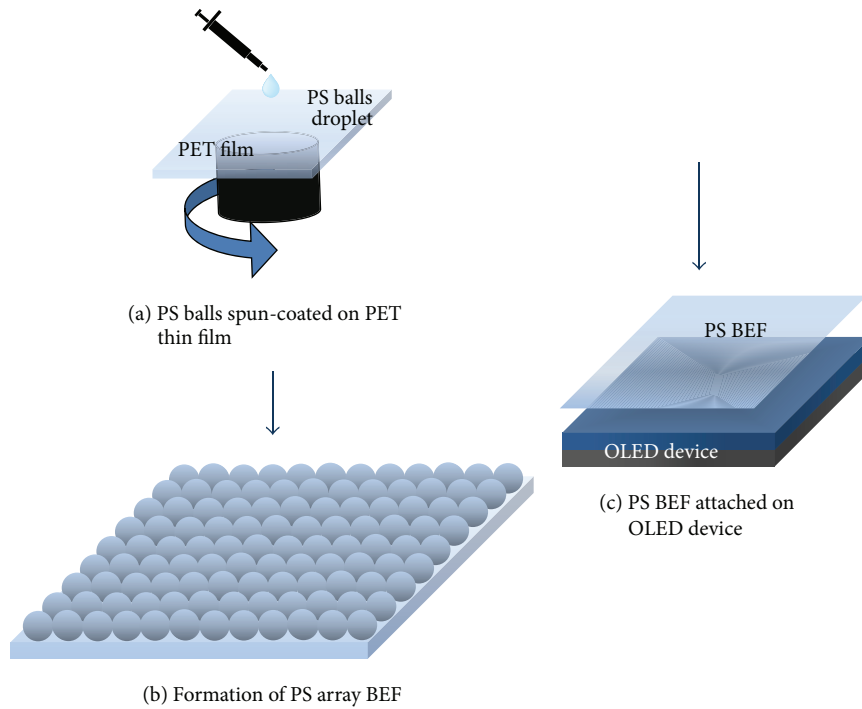


FIGURE 1: The schematic diagrams of (a) the fabrication procedures for (b) the preparation of single-monolayered self-assembled polystyrenes (PS) arrays, and then (c) the brightness enhancement film (BEF) and its application attached onto organic light-emitting diodes (OLEDs) devices.

fabrication method named as nanosphere lithography for the production of periodic particle array surfaces with nanometer-scale features. NSL was firstly reported by the research work of Hultheen and Van Duyne [17] and has been widely employed in the area of two- and three-dimensional (2D and 3D) micro/nanostructures patterning, such as quantum dots, nanowires, nanomesh, antireflection structure (ARS), and 3D inverse-opal photonic crystals [18–23]. Compared to those traditional sophisticated lithographic methods, NSL has shown a great many advantages that include a simple nanofabrication technique, an inexpensive route for the patterning of long-range periodic nanostructure arrays in a large scale area, and high throughput. Methods for the deposition of PS nanosphere solution onto desired substrates include electrophoretic deposition, electrochemical deposition, Langmuir-Blodgett- (L-B-) like technique, drop-coating, and spin-coating which we utilized spin-coating in our present research work [24–28].

Here, we demonstrated an unsophisticated way to effectively extract the trapped photons in the glass substrate to the outer media by attaching the PS nanosphere patterned brightness enhancement film (BEF) onto the OLEDs surface. Owing to the large increase of light extraction from trapped photons, the total luminous intensity enhancement for the device with a single-monolayered nanospheres arrangement patterned film attachment in the normal direction shows a great improvement of 161% when compared to the traditional indium tin oxide (ITO) based OLEDs without any BEF sheet attachment. The OLEDs attached with PS patterned BEF also possessed potential application in flat panel consumer

display technology due to the minor color offset and good color stabilization properties in different viewing angles [29].

## 2. Experimental Procedure

Figure 1 shows the schematic diagrams of the fabrication process for the preparation of a single-monolayered PS array BEF and its application in OLED devices. At first, the methanol solution mixing with a surfactant Triton X-100 (400:1 in volume) is prepared to dilute the purchased PS beads. Then the surfactant-free nanometer-scale polystyrenes with latex colloids (Bangs Laboratories Inc., ~10 wt% in water, PS mean diameters: ranging from 200 to 800 nm) were further diluted by the above-mentioned methanol solution in ultrasonic bath. Those as-prepared diluted PS nanospheres with latex solution were spun-coated onto clean PET substrates by the spin-coater as shown in Figure 1(a). The distribution of a single-monolayered self-assembled PS nanosphere arrays can be easily controlled by adjusting the rotation speed of spin-coater as shown in Figure 1(b). The period of the hexagonal patterns is determined by the initial diameter of PS beads and attaching the PS nanosphere array BEF sheet as a photonic crystal pattern onto the OLED device as shown in Figure 1(c). The product information and experimental details for the PS nanospheres with the periodicity ranging from 200 to 800 nm are listed in Table 1.

The commonly used techniques for fabricating the OLEDs are separated into two major types, including dry and wet-chemical processes. The wet-chemical process includes

TABLE 1: The product information and experimental details are for the PS nanosphere with different periodicities.

Diameter of PS balls (nm)	Product number	Content of solid PS in stock solution (%)	Solution proportion (methanol : PS latex)	Concentration of PS beads in prepared solution (%)	Spin speed (rpm)
200	PS02N	10.0	2 : 1	3.33	2000
300		10.0	1 : 1.5	6.00	1400
400		9.7	1 : 1.5	5.82	1100
500	PS03N	10.1	1 : 2	6.73	800
600		10.5	1 : 2	7.00	600
700		9.9	1 : 2	6.60	500
800		10.1	1 : 2	6.73	400

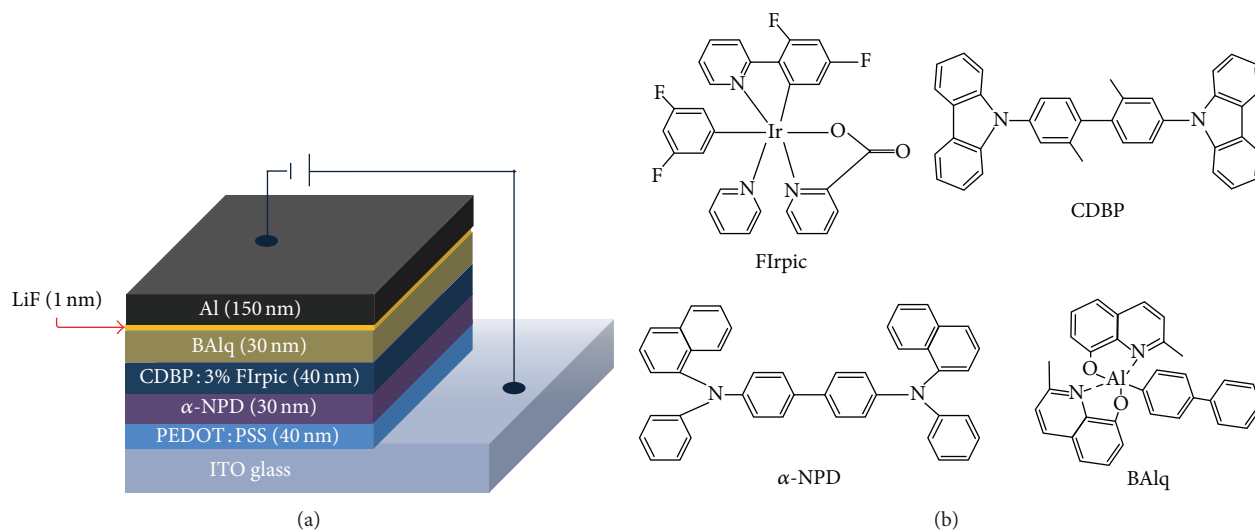


FIGURE 2: (a) The diagram is for the OLEDs device structure, and (b) the chemical structures of the molecules employed in the presented research work.

the spin-coating and inkjet-printing methods, which is suitable for the fabrication of the polymer OLEDs [30, 31]. However, the dry process (vacuum evaporation deposition) applied in our work is mainly used to fabricate the small molecule OLEDs [15]. In the parts of the blue phosphorescent OLED fabrication process, the FIrpic-based light-emitting diode was made onto an ITO coated glass substrate (ITO film thickness: 200 nm, sheet resistance:  $10 \Omega/\square$ ). Prior to the organic layers evaporation process, the ITO glass was thoroughly cleaned with acetone, isopropyl alcohol, ethanol, and deionized water in sequence and then treated with an UV-ozone cleaner. The multilayers structure for the OLEDs is depicted in Figure 2(a). The 40 nm thick poly(3,4-ethylenedioxythiophene) : poly(4-styrenesulfonate) (PEDOT : PSS) thin films were spun onto the ITO coated glass to reduce the possibility of electrical shorts. The organic layers were continuously deposited onto the substrates in an ultrahigh vacuum (around  $5 \times 10^{-6}$  torr) by thermal evaporation deposition system. The hole-transporting layer (*N,N'*-diphenyl-*N,N'*-bis(1-naphthyl)-(1,1'-biphenyl)-4,4'-diamine,  $\alpha$ -NPD), blue emissive layer (CDBP : 3% FIrpic), electron-transporting,

and hole-blocking layer (aluminum (III) bis(2-methyl-8-quinolinolato)-4-phenylphenolate, BAQ) were sequentially evaporated onto the substrates. Then LiF and thick Al were set as the opaque cathode for the OLED device. The detailed device structure is composed of ITO (200 nm)/PEDOT : PSS (40 nm)/ $\alpha$ -NPD (30 nm)/CDBP : 3% FIrpic (40 nm)/BAQ (40 nm)/LiF (1 nm)/Al (150 nm). Figure 2(b) shows the molecule structures of  $\alpha$ -NPD, CDBP, FIrpic, and BAQ, respectively. The surface morphology was observed by field emission scanning electron microscope (FESEM, Hitachi S-4800). In order to prepare the SEM specimens, the dilute PS nanosphere latex was spun-coated on the flat PET film thus forming a single-layered close-packed PS array at first. Then the as-prepared samples were put into a vacuum sputtering system to deposit 5 nm Au film. The conductivity of those samples is increased and the point discharge effect would be decreased. Finally, those above-mentioned SEM samples were cut into two pieces for the preparation of the SEM cross-sectional analysis. The EL spectrum, current-voltage characteristics, and luminance for optical-electronic devices were examined by a measuring system consisting of

TABLE 2: The distribution results for the self-assembled PS nanosphere patterns at different spin speed conditions.

Diameter of PS balls (nm)	Concentration (methanol : PS latex)	Spin speed (rpm)	Corresponding image	Results
400	1:2	2000	Figure 3(a)	Random arranged PS patterns with obvious defects
400	1:2	500	Figure 3(b)	Single- or multilayered PS balls stacking
400	1:2	1100	Figures 3(c) and 3(d)	Single-layered and close-packed PS patterns

a spectrophotometer (Minolta CS-1000) connecting with a computer and a power supply unit (Keithley model 2400) to drive the OLEDs. The angular dependence of the EL intensity was measured by putting the OLEDs device vertically on the center of the rotation stage.

### 3. Results and Discussion

In the typical spin-coating process, the PS balls followed the lowest energy level rule of self-assembly and rearranged onto any kinds of the substrates freely till the solution was dried. Following the lowest energy level rule of self-assembly, a single-monolayered hexagonal closed-packed structure with uniform distribution is formed onto the PET films after few minutes. The period of this hexagonal pattern was determined by the diameter values of PS nanospheres. Since the assembly process occurs during the drying step, two parameters including the colloid latex concentration and rotation speed of spin-coater both play a main role in achieving the monolayer hexagonal and closed-packed PS patterns over the large areas. With a specified latex concentration, the distribution of PS nanosphere patterns on PET films can be easily controlled by simply adjusting the rotation speed. Figures 3(a)–3(c) show the SEM images for 400 nm PS nanospheres spun-coated at different rotation speed conditions after the self-assembly process. The rapid evaporation and stronger centrifugal force occurred at a spin speed of 2000 rpm resulting in the obvious empty space between nanoparticle islands because there is not enough time for those PS nanospheres rearranging into well-ordered 2D islands as shown in Figure 3(a). On the other hand, if the spin speed was reduced to a lower value such as 500 rpm, the slow evaporation rate and weak centrifugal force would lead the consequence into randomly distributed single- or multilayered PS balls stacking as shown in Figure 3(b). Figure 3(c) shows that a single-monolayered close-packed PS pattern formed onto PET sheet in a large area can be achieved by tuning the rotation speed of spin-coater to a proper value, such as 1100 rpm for 400 nm PS nanospheres in the presented work. Figure 3(d) shows the enlarged SEM image of a single-layered close-packed 400 nm period PS nanosphere patterns enlarged from Figure 3(c), and the inset image is the corresponding cross-sectional morphology. Figure 3 also shows the SEM images for (e) 200 and (f) 800 nm PS nanosphere arrays spun-coated at rotation speed of 2000 and 400 rpm,

respectively. The distribution results for self-assembled PS nanosphere patterns with 400 nm periodicity at different spin speed parameters are summarized and listed in Table 2.

The emission peak for the used OLED device in the presented work is located at the wavelength of 466 nm and with a subpeak at 497 nm as shown in Figure 4(a), which agreed with the work reported by Tokito et al. [32]. The turn-on voltage and the saturated current efficiency of the OLED device at the current density of 10 mA/cm<sup>2</sup> are 8.7 V and 7.0 cd/A, respectively, as shown in Figure 4(b).

The schematic diagram as depicted in Figure 5(a) illustrated that most of the emitted light generated from the organic layer was confined in the device because of the waveguiding effect and substrate mode. In general, less than one-third of the generated photons can escape from emitting devices in typical OLEDs. One-third of these photons are guided in the glass substrate and the others are trapped in the organic layers. The photons trapped in the glass substrate can be further coupled out when applying a patterned BEF sheet attached onto OLEDs as shown in Figure 5(a). Using the coupling equation can help to understand the coupling of light in the optical-electronic device. The diffraction angle ( $\theta_b$ ) for the light trapped in the substrate is calculated by

$$\frac{2\pi}{\lambda_0} n_b \sin \theta_b \pm m \frac{2\pi}{\Lambda} = k_{\text{glass}} = \frac{2\pi}{\lambda_0} n_b, \quad (1)$$

where  $m = 1$  (the diffraction order),  $k_{\text{glass}}$  is the propagation constant in the glass,  $n_b = 1.52$  for a typical BK7 glass,  $\lambda_0 = 466$  nm, and  $\Lambda = 400$  nm (the periodicity of the PS nanospheres) in this case.  $\theta_b$  is 13.6° smaller than the refraction angle in the air ( $\theta = 20.9^\circ$ , calculated by Snell's law) demonstrating the trapped photons can escape from glass to air. The insets in Figure 5(b) show the optical images of OLEDs with and without 2D PS nanosphere patterned film attachment. It reveals that the overall luminous intensity of OLED device with 2D PS photonic crystal patterned film attachment is higher than the referenced device. The PS patterned film acted as a BEF to help in extracting trapped photons in the glass/air interface to the outside. The luminous enhancement of OLED devices attached with 2D photonic crystal patterned films of various nanosphere diameters (from 200 to 800 nm) is also shown in Figure 5(b). It can be seen that the luminous enhancement is increased with the decrease of the PS nanosphere diameter values for

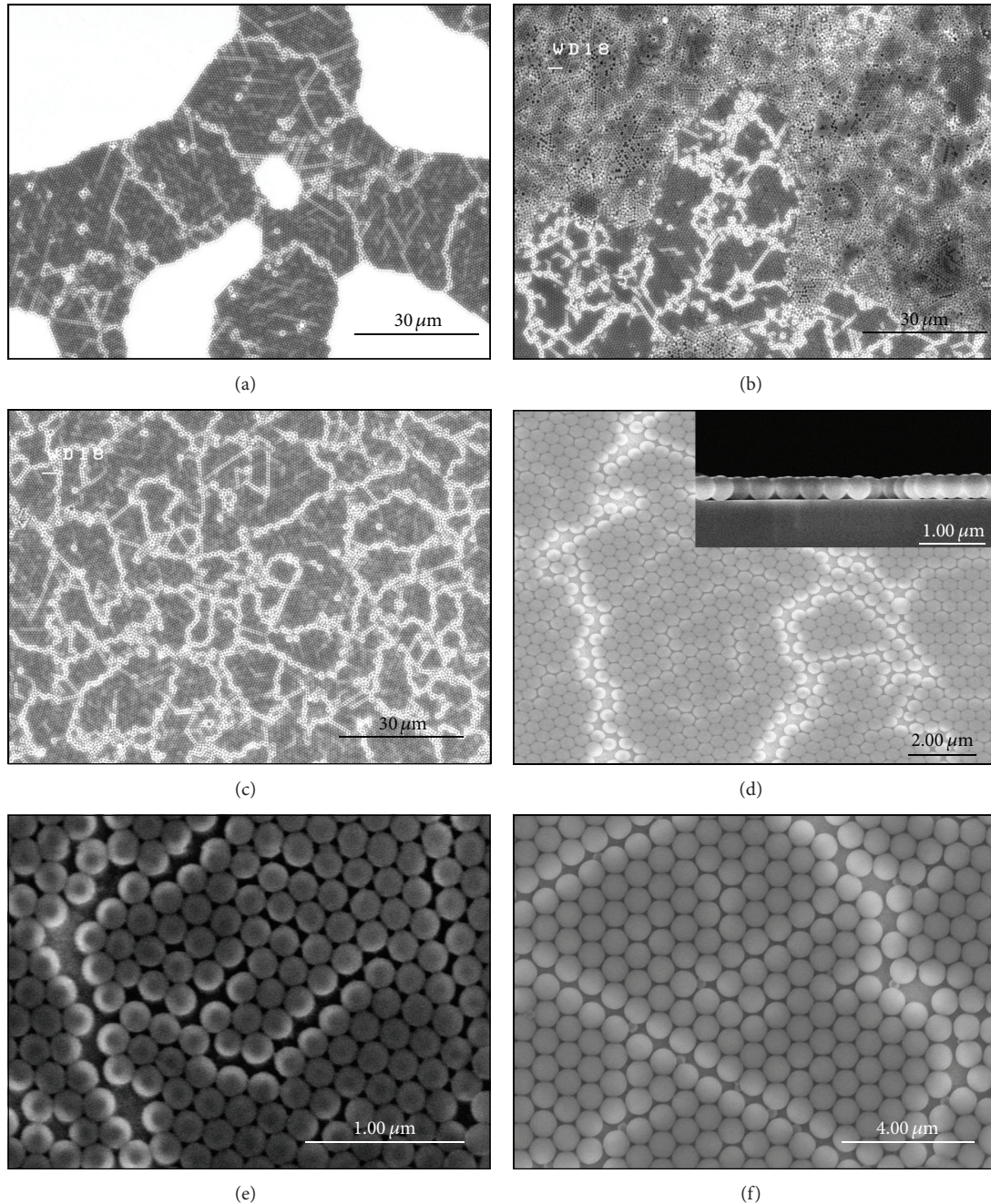


FIGURE 3: SEM images are for the 400 nm period PS nanospheres distribution at spin speed of (a) 2000 rpm, (b) 500 rpm, and (c) 1100 rpm, respectively. (d) The enlarged SEM image is from (c) for a single-monolayered nanosphere array patterns with hexagonal close-packed uniform distribution and the inset image is the corresponding cross-sectional morphology. SEM images are for PS nanospheres arrays with (e) 200 and (f) 800 nm periodicity at spin speed of 2000 and 400 rpm, respectively.

the photonic crystal patterns with the periodicity of 400–800 nm. According to the diffraction term ( $2\pi/\Lambda$ ) as shown in the grating coupling equation, the PS balls with 400 nm diameter (e.g.,  $\Lambda = 400$  nm) show the greatest luminous enhancement efficiency and the total luminous enhancement for the device with applying PS nanosphere arrangement patterned film attachment shows a great improvement of 61% when compared to the traditional ITO-OLEDs without any

BEF attachment owing to the large increase of light extraction from trapped photons. The luminance enhancement factor then drops as the PS diameters in the range between 200 and 300 nm. The results can be concluded into two reasons: (1) the scattering effect of the PS ball pattern is decreased because the diameter values of the PS are smaller than the wavelength of visible light; (2) the diffraction term ( $2\pi/\Lambda$ ) is increasing as the PS diameters decrease; therefore,

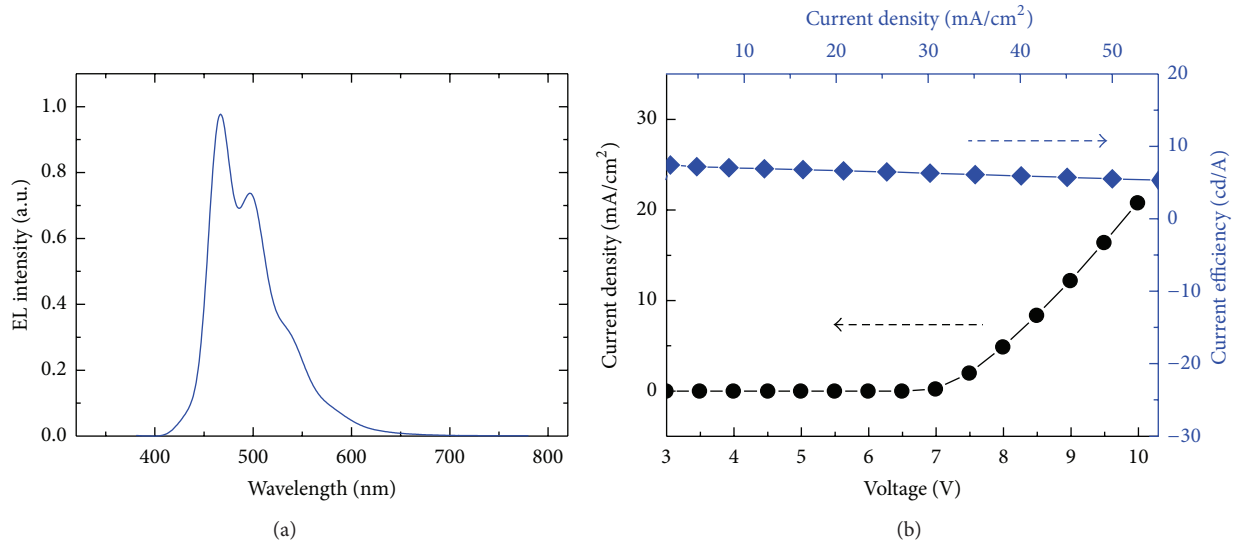


FIGURE 4: (a) EL spectrum of the OLED device. (b)  $J$ - $V$  characteristic and current efficiency versus current density of the OLED device.

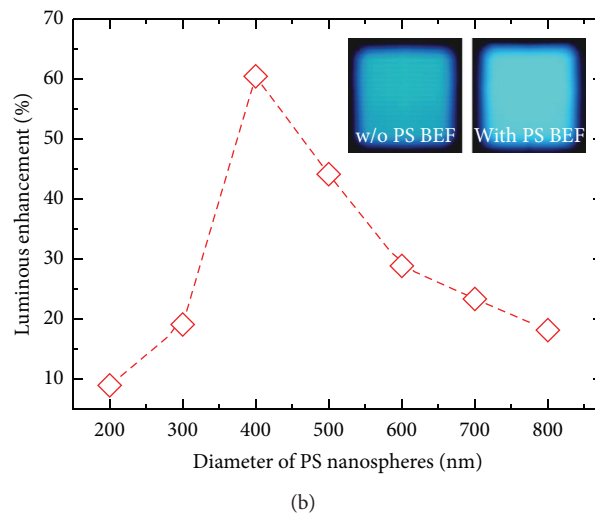
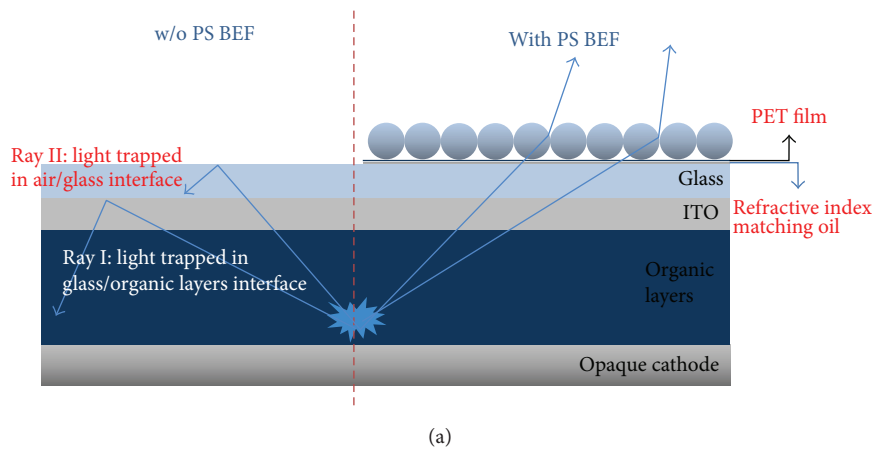


FIGURE 5: (a) Light extraction of trapped photons in glass substrate and organic layer of bottom emission OLED and (b) luminous enhancement of OLED devices attached with 2D photonic crystal pattern structures of various nanosphere diameters ranging from 200 to 800 nm.

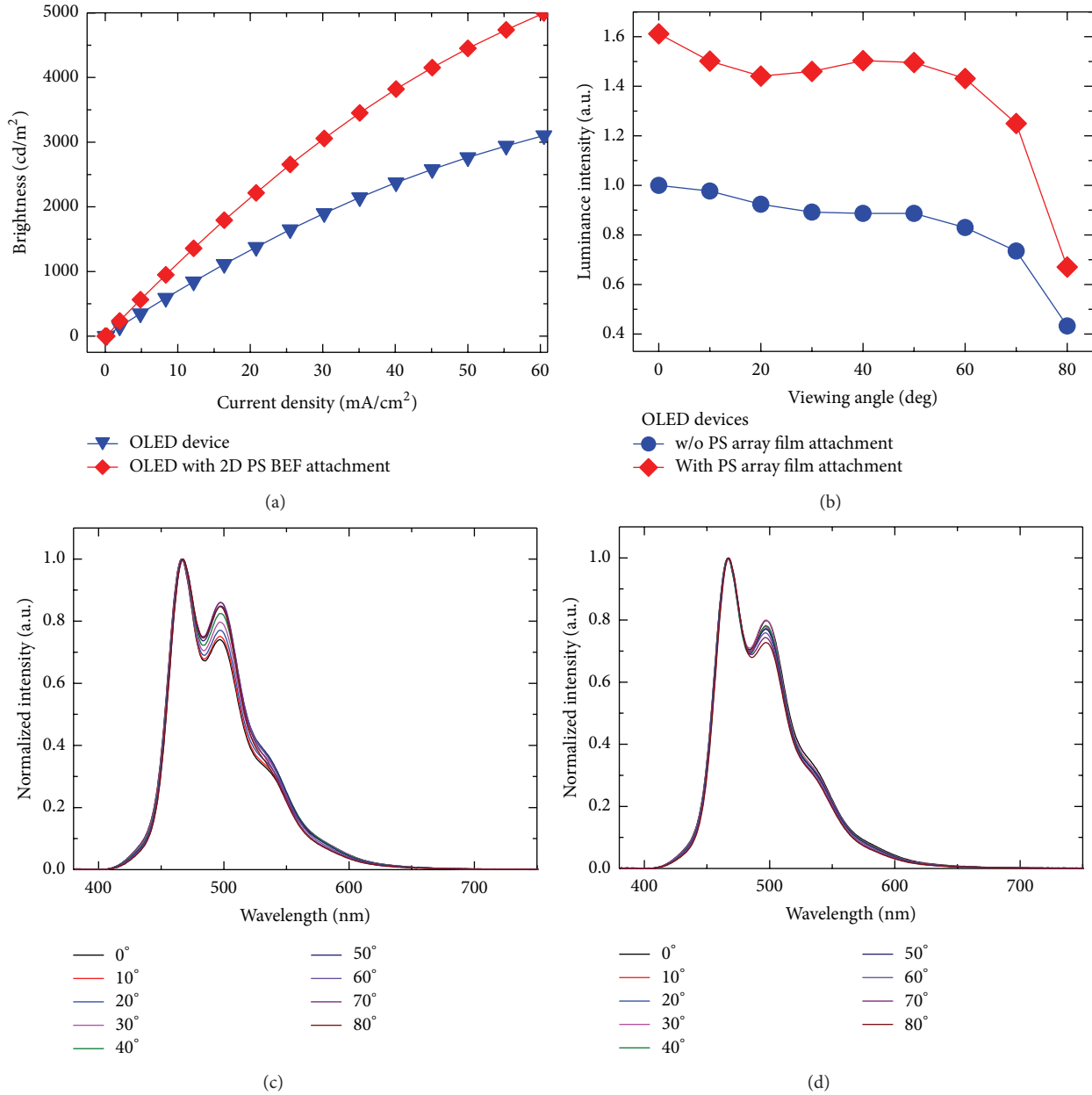


FIGURE 6: (a) Luminance versus current density and (b) the luminous intensity as a function of viewing angle for the OLED device with and without PS patterned BEF attachment. The EL spectrum for the OLED device (c) without and (d) with attaching 2D PS array patterned films (diameter: 400 nm).

the calculated diffraction angle would be negative, hence lowering the scattering effect caused by the PS nanosphere patterns.

We further measured the emission light at different viewing angle (VA) to confirm the light extraction enhancement efficiency. Figure 6(a) shows the luminance values for the OLEDs with and without PS nanosphere patterned BEF sheet attachment under  $30 \text{ mA/cm}^2$  operating current density in normal viewing angle that are about  $3050$  and  $1900 \text{ cd/m}^2$ , respectively. The brightness improvement is about 60.5%, which is in good agreement with the result of luminous

enhancement for 400 nm PS patterned BEF sheet attaching onto OLEDs as shown in Figure 5(b). The luminance intensity of device as a function of viewing angle with a constant current injection ( $60 \text{ mA/cm}^2$ ) is shown in Figure 6(b). The luminance intensity of device without PS patterned BEF attachment drops as the viewing angle increases. When we applied a patterned BEF sheet onto OLEDs, the angular emission pattern was broadened and the luminance intensity was also increased. Figure 6(c) shows the normalized EL spectrum for OLEDs without attaching PS patterned BEF sheet. The normalized intensity in the wavelength of 497 nm

was changed from 0.741 ( $VA = 0^\circ$ ) to 0.849 ( $VA = 50^\circ$ ). It revealed an obvious color offset property in the wavelength of 497 nm at different viewing direction. But the color offset phenomenon can be minimized after applying the PS patterned BEF as shown in Figure 6(d). The normalized intensity was slightly shifted from 0.799 ( $VA = 0^\circ$ ) to 0.771 ( $VA = 50^\circ$ ). The reason for the minor color offset of the OLEDs attached with PS BEF sheet is attributed to the omnidirectional light harvesting enhancement, which is consistent with the result as shown in Figure 6(b). The emission spectrum also shows that there is almost no wavelength shift when utilizing such a PS patterned BEF attachment, which performs excellent color stabilization characteristics. The results can be confirmed by the Commission Internationale de L'Éclairage coordinates (CIE 1931) and the corresponding CIE coordinates calculated from the EL spectrum for OLEDs without and with PS patterned BEF attachment are (0.1635, 0.2798) and (0.1619, 0.2776), respectively.

#### 4. Conclusions

In summary, using an external patterned BEF sheet to efficiently improve the total OLED's luminous efficiency has been successfully demonstrated by a facile NSL technique in the presented research work. With a specified latex concentration, the distribution of PS arrays on PET films can be easily controlled by only adjusting the rotation speed of spin-coater. The luminous intensity of OLEDs with attaching PS patterned sheet in the normal viewing direction is 161% higher than the one without any BEF attachment. The presented experimental results indicated that the trapped photons are further coupled out from the substrate mode, thus increasing the light extraction efficiency. The EL spectrum of OLEDs with PS patterned BEF attachment shows minor color offset and outstanding color stabilization property that possess potential future applications in all kinds of optical-electronic display devices and solid-state lighting technology.

#### Conflict of Interests

The authors declare that there is no conflict of interests regarding the publication of this paper.

#### Acknowledgment

The authors acknowledge financial support of the main research projects of the National Science Council of Taiwan under Grant nos. NSC 101-2221-E-027-042 and NSC 101-2622-E-027-003-CC2, respectively.

#### References

- [1] Y. Luo, L. Wang, Y. Ding, L. Li, and J. Shi, "High light-extracting efficiency for OLED directly fabricated on double-side nanotextured silica substrate," *Optics Letters*, vol. 38, no. 14, pp. 2394–2396, 2013.
- [2] J. Huang, G. Li, E. Wu, Q. Xu, and Y. Yang, "Achieving high-efficiency polymer white-light-emitting devices," *Advanced Materials*, vol. 18, no. 1, pp. 114–117, 2006.
- [3] C. W. Tang and S. A. Vanslyke, "Organic electroluminescent diodes," *Applied Physics Letters*, vol. 51, no. 12, pp. 913–915, 1987.
- [4] S. R. Forrest, D. D. C. Bradley, and M. E. Thompson, "Measuring the efficiency of organic light-emitting devices," *Advanced Materials*, vol. 15, no. 13, pp. 1043–1048, 2003.
- [5] B. Niesen and B. P. Rand, "Thin film metal nanocluster light-emitting devices," *Advanced Materials*, vol. 26, no. 9, pp. 1446–1449, 2014.
- [6] J. B. Kim, J. H. Lee, C. K. Moon, S. Y. Kim, and J. J. Kim, "Highly enhanced light extraction from surface plasmonic loss minimized organic light-emitting diodes," *Advanced Materials*, vol. 25, no. 26, pp. 3571–3577, 2013.
- [7] S. Nowy, B. C. Krummacher, J. Frischeisen, N. A. Reinke, and W. Brütting, "Light extraction and optical loss mechanisms in organic light-emitting diodes: Influence of the emitter quantum efficiency," *Journal of Applied Physics*, vol. 104, no. 12, Article ID 123109, 2008.
- [8] R. Meerheim, M. Furno, S. Hofmann, B. Lüssem, and K. Leo, "Quantification of energy loss mechanisms in organic light-emitting diodes," *Applied Physics Letters*, vol. 97, no. 25, Article ID 253305, 2010.
- [9] S. Y. Kim and J. J. Kim, "Outcoupling efficiency of organic light emitting diodes and the effect of ITO thickness," *Organic Electronics: Physics, Materials, Applications*, vol. 11, no. 6, pp. 1010–1015, 2010.
- [10] I. Schnitzer, E. Yablonovitch, C. Caneau, T. J. Gmitter, and A. Scherer, "30% external quantum efficiency from surface textured, thin-film light-emitting diodes," *Applied Physics Letters*, vol. 63, no. 16, pp. 2174–2176, 1993.
- [11] M. Sloatsky and S. R. Forrest, "Enhancing waveguided light extraction in organic LEDs using an ultra-low-index grid," *Optics Letters*, vol. 35, no. 7, pp. 1052–1054, 2010.
- [12] D. H. Wei, W. H. Liao, and K. Y. Peng, "Light guide of au nanostructures for color-filterless optoelectronic display devices," *Journal of Nanoscience and Nanotechnology*, vol. 12, no. 2, pp. 1341–1343, 2012.
- [13] Y. Sun and S. R. Forrest, "Enhanced light out-coupling of organic light-emitting devices using embedded low-index grids," *Nature Photonics*, vol. 2, no. 8, pp. 483–487, 2008.
- [14] S. Möller and S. R. Forrest, "Improved light out-coupling in organic light emitting diodes employing ordered microlens arrays," *Journal of Applied Physics*, vol. 91, no. 5, pp. 3324–3327, 2002.
- [15] Y. H. Ho, K. Y. Chen, K. Y. Peng, M. C. Tsai, W. C. Tian, and P. K. Wei, "Enhanced light out-coupling of organic light-emitting diode using metallic nanomesh electrodes and microlens array," *Optics Express*, vol. 21, no. 7, pp. 8535–8543, 2013.
- [16] T. Tsutsui, M. Yahiro, H. Yokogawa, K. Kawano, and M. Yokoyama, "Doubling coupling-out efficiency in organic light-emitting devices using a thin silica aerogel layer," *Advanced Materials*, vol. 13, no. 15, pp. 1149–1152, 2001.
- [17] J. C. Hulthen and R. P. Van Duyn, "Nanosphere lithography: a materials general fabrication process for periodic particle array surfaces," *Journal of Vacuum Science & Technology A*, vol. 13, no. 3, pp. 1553–1558, 1995.
- [18] Y. H. Ho, K. Y. Chen, S. W. Liu, Y. T. Chang, D. W. Huang, and P. K. Wei, "Transparent and conductive metallic electrodes fabricated by using nanosphere lithography," *Organic Electronics*, vol. 12, no. 6, pp. 961–965, 2011.

- [19] A. Kosiorek, W. Kandulski, H. Glaczynska, and M. Giersig, "Fabrication of nanoscale rings, dots, and rods by combining shadow nanosphere lithography and annealed polystyrene nanosphere masks," *Small*, vol. 1, no. 4, pp. 439–444, 2005.
- [20] S. Ji, J. Park, and H. Lim, "Improved antireflection properties of moth eye mimicking nanopillars on transparent glass: flat antireflection and color tuning," *Nanoscale*, vol. 4, no. 15, pp. 4603–4610, 2012.
- [21] C. Li, G. Hong, and L. Qi, "Nanosphere lithography at the gas/liquid interface: a general approach toward free-standing high-quality nanonets," *Chemistry of Materials*, vol. 22, no. 2, pp. 476–481, 2010.
- [22] S. B. Kim, W. W. Lee, J. Yi, W. I. Park, J. S. Kim, and W. T. Nichols, "Simple, large-scale patterning of hydrophobic ZnO nanorod arrays," *ACS Applied Materials and Interfaces*, vol. 4, no. 8, pp. 3910–3915, 2012.
- [23] J. J. Dong, X. W. Zhang, Z. G. Yin et al., "Controllable growth of highly ordered ZnO nanorod arrays via inverted self-assembled monolayer template," *ACS Applied Materials and Interfaces*, vol. 3, no. 11, pp. 4388–4395, 2011.
- [24] A. Winkleman, B. D. Gates, L. S. McCarty, and G. M. Whitesides, "Directed self-assembly of spherical particles on patterned electrodes by an applied electric field," *Advanced Materials*, vol. 17, no. 12, pp. 1507–1511, 2005.
- [25] J. Aizenberg, P. V. Braun, and P. Wiltzius, "Patterned colloidal deposition controlled by electrostatic and capillary forces," *Physical Review Letters*, vol. 84, no. 13, article 2997, 2000.
- [26] N. D. Denkov, O. D. Velev, P. A. Kralchevsky, I. B. Ivanov, H. Yoshimura, and K. Nagayama, "Mechanism of formation of two-dimensional crystals from latex particles on substrates," *Langmuir*, vol. 8, no. 12, pp. 3183–3190, 1992.
- [27] A. S. Dimitrov and K. Nagayama, "Continuous convective assembling of fine particles into two-dimensional arrays on solid surfaces," *Langmuir*, vol. 12, no. 5, pp. 1303–1311, 1996.
- [28] D. Wang and H. Möhwald, "Rapid fabrication of binary colloidal crystals by stepwise spin-coating," *Advanced Materials*, vol. 16, no. 3, pp. 244–247, 2004.
- [29] L. Wang, Y. Jiang, J. Luo et al., "Highly efficient and color-stable deep-blue organic light-emitting diodes based on a solution-processible dendrimer," *Advanced Materials*, vol. 21, no. 47, pp. 4854–4858, 2009.
- [30] T. R. Hebner, C. C. Wu, D. Marcy, M. H. Lu, and J. C. Sturm, "Ink-jet printing of doped polymers for organic light emitting devices," *Applied Physics Letters*, vol. 72, no. 5, pp. 519–521, 1998.
- [31] J. P. J. Markham, S.-C. Lo, S. W. Magennis, P. L. Burn, and I. D. W. Samuel, "High-efficiency green phosphorescence from spin-coated single-layer dendrimer light-emitting diodes," *Applied Physics Letters*, vol. 80, no. 15, pp. 2645–2647, 2002.
- [32] S. Tokito, T. Iijima, Y. Suzuri, H. Kita, T. Tsuzuki, and F. Sato, "Confinement of triplet energy on phosphorescent molecules for highly-efficient organic blue-light-emitting devices," *Applied Physics Letters*, vol. 83, no. 3, pp. 569–571, 2003.

## Research Article

# Photoirradiation Caused Controllable Wettability Switching of Sputtered Highly Aligned *c*-Axis-Oriented Zinc Oxide Columnar Films

P. W. Chi, C. W. Su, B. H. Jhuo, and D. H. Wei

*Institute of Manufacturing Technology and Department of Mechanical Engineering, National Taipei University of Technology (TAIPEI TECH), Taipei 10608, Taiwan*

Correspondence should be addressed to D. H. Wei; [dhwei@ntut.edu.tw](mailto:dhwei@ntut.edu.tw)

Received 3 May 2014; Accepted 11 June 2014; Published 20 July 2014

Academic Editor: Ho Chang

Copyright © 2014 P. W. Chi et al. This is an open access article distributed under the Creative Commons Attribution License, which permits unrestricted use, distribution, and reproduction in any medium, provided the original work is properly cited.

This study presents the microstructure morphology and UV photoirradiation coupling effects of the *c*-axis-oriented zinc oxide (ZnO) columnar films. Highly aligned *c*-axis-oriented films have been deposited onto glass substrates at room temperature by radio-frequency (RF) magnetron sputtering without introducing any oxygen source under different sputtering powers ranging from 50 to 150 W. Self-assembled ZnO columnar structures that were successfully obtained belong to wurtzite structure, and the corresponding columnar structures and crystalline orientation were confirmed by the FE-SEM and XRD, respectively. All the ZnO columnar films exhibit good transparency with a visible light averaged transmittance over 82%. According to water contact angle (CA) measurement, ZnO columnar films exhibit hydrophobic behavior. After exposing to photoirradiation under ultraviolet (UV) environment, all the ZnO samples showed remarkable transition from hydrophobic to superhydrophilic surfaces and could return to their original hydrophobicity after being placed in the dark. It is demonstrated that the controllable wettability of ZnO columnar films under changing between the UV photoirradiation and dark storage is due to the surface charges accumulation and discharging processes. As a result, this study could provide important applications for many fields such as ZnO-based hybrid sensors/solar cells functional devices with photoirradiation disinfection surfaces accompanied with reversible wettability switches.

## 1. Introduction

Self-cleaning is a special mechanism of surface property; it relates with the chemical composition and surface morphology. It has been focused for many potential applications, such as environmental cleanup [1, 2] and optoelectronic devices [3–5]. The photocatalytic behavior, in which the coating reacts with daylight to decompose dirt and hydrophilic action, in which water spreads on the surface, cleans up the dirt without any traces of water. Therefore, those two actions have quite important roles in self-cleaning effect [6–10]. Solar energy represents a probable renewable energy that includes visible and ultraviolet regions which is an important factor of driving photocatalytic process due to its high efficiency, low cost, and stability. However, oxide-based hybrid self-cleaning nanodevices have deeply potential of all renewable energies [11, 12].

The lotus leaves demonstrate high water contact angle, as high as  $160^\circ$  due to their particular surface nanoscale structures [13–17]. Thus, the surface roughness plays an important role in wettability of bulk solid materials, and the hydrophobic materials are usually prepared by modifying surface with low surface energy for forming nanostructures. The multifunctional ZnO compound with the lowest surface free energy of the most densely packed (0002) planes in the wurtzite structure can easily form nanoscale products, which is also a good choice for self-cleaning coating.

The control of wettability transition for several special materials from hydrophilic to hydrophobic could via optical, mechanical, and chemical modifications [18–23]. Recently, several metal oxide semiconductors such as  $\text{TiO}_2$ ,  $\text{V}_2\text{O}_5$ , and ZnO have been widely explored and controlled with exhibiting switchable wettability from hydrophilic to hydrophobic via different external factors such as pH value, exposure to

light-induced irradiation, electric field, and heat treatment and then stored in different environment processes. Among them, the light irradiation is especially attractive because of its flexible on- and off-switching, remote control, and other advantages for potential industrial applications. This special property has attracted much focused attention due to its great advantages in applications such as self-cleaning device, antifogging glass, smart window, and construction materials just only controlled by reversible-switching wettability [24, 25].

ZnO and TiO<sub>2</sub> are general materials for photocatalysts among the above metal oxides; both of them react under ultraviolet (UV) light due to their large band gaps of 3.37 and 3.2 eV [26, 27], respectively, and their wettability could be modified significantly by irradiation with UV light [28, 29]. Among these two materials, ZnO can easily form nanostructure. There are many reports about a reversible light-controlled hydrophobic/hydrophilic process for ZnO-based thin film and nanostructures [30–32]. ZnO has direct wide band gap (3.37 eV) and high exciton binding energy (60 meV) and is optically transparent for visible light. It is therefore an expected material for many novel applications such as piezoelectric transducers, transparent thin film transistors, chemical gas sensors or biosensors [33–35], solar cells, and UV detectors [36–38]. According to the above functionalities, ZnO can provide a hydrophobic surface, which may be transformed into hydrophilic surface by UV irradiation, which coexists with intrinsic semiconductor properties and a particular surface morphology [39–44]. As for the surface chemical property of ZnO compound, the tunable and reversible wettability was explained to be the competition results between desorption and adsorption of organic chains and hydroxyl groups rearrangement on the material surface. However, the ZnO nanostructures have highly developed surface properties and are expected to exhibit more advanced controllable wettability including a quickly hydrophilic/hydrophobic switch with tunable contact angles. There are many kinds of shapes, sizes and arrangements of ZnO nanostructures, including nanorods, nanopillars, nanowires, nanoneedles, and nanobelts. Many current scientific articles have been reported on different nanostructures, which were generally used to enhance the wetting effects on ZnO films, and some of them obtained the superhydrophobic surface.

In this research work, we investigated the self-cleaning properties of highly *c*-axis-oriented ZnO thin films, deposited at room temperature by radio-frequency (RF) sputtering system. The surface morphology and grain size were controlled by varying sputtering power conditions. The transparency for all highly *c*-axis-oriented ZnO thin films ranging from 50 to 150 W was also measured. The surface wettability of ZnO thin films was examined by water contact angle measurements. The switchable wettability was investigated by changing the conditions of UV photoirradiation exposure and dark room storage. This research work not only extends the scope of potential applications for *c*-axis-oriented ZnO columnar films, but also provides a profound understanding of UV modulated wettability of ZnO (0002) columnar films.

## 2. Experimental Procedures

A radio-frequency (RF) magnetron sputtering system was employed to deposit the ZnO thin films onto D263T glass substrates, and all the substrates were placed parallel to the ZnO ceramic target. ZnO target is composed of 99.99% purely pressed ZnO powder, and the size is of 0.075 m diameter and 0.006 m thickness. All the substrates were rinsed in deionized water, ultrasonically cleaned in ethanol and acetone to remove organic contamination, then dried in hot air before they load into the vacuum chamber. The sputtering chamber was pumped down to a base pressure of  $3 \times 10^{-7}$  torr. Argon was filled into sputtering chamber sequentially with the low working pressure of  $5 \times 10^{-3}$  torr. The ZnO thin films were deposited with different RF powers in the range of 50, 75, 100, and 150 W at a fixed deposition time of 30 mins. The crystalline structure of ZnO thin films was characterized by X-ray diffraction (XRD, PANalytical X'Pert PRO MRD) with Cu K<sub>α</sub> radiation ( $\lambda = 1.54 \text{ \AA}$ ) in the range of  $2\theta = 20\text{--}60^\circ$ . The surface morphology of ZnO thin films was observed by field emission scanning electron microscopy (FE-SEM, JEOL JSM-6500F). The surface topography and roughness values of ZnO thin films were further analyzed by the atomic force microscope (AFM, DI NS3a). The optical transmittance was recorded by using a UV-Vis-NIR spectrophotometer (MPI100-ME). The wettability of ZnO thin films was estimated from the contact angle  $\theta$  of water droplets onto each ZnO sample surface (Pentad FTA 125). After completing the UV photoirradiation, the water contact angle was measured on the irradiated surface by using a water droplet ( $\sim 3 \mu\text{L}$ ) and with a digital camera to record the droplet photos. The UV photoirradiation onto ZnO thin films was conducted by 1520 mW/cm<sup>2</sup> mercury arc lamp (HAMAMATSU-Deuterium L2D2) with a wavelength of 365 nm, and all the ZnO samples were stored in air ambient after UV photoirradiation.

## 3. Results and Discussion

**3.1. Crystalline Structure and Corresponding Preferred Orientation.** Figure 1 shows the X-ray diffraction patterns for the ZnO thin films deposited onto glass substrates with different RF powers ranging from 50 to 150 W at a fixed deposition time of 30 mins, respectively. The XRD patterns show that all the samples exhibit only a strong peak located at  $2\theta = 34.5^\circ$ , which corresponds to the ZnO (0002) plane (JCPDS Card: 361451), indicating that highly aligned *c*-axis-oriented ZnO film possesses a hexagonal wurtzite structure. The intensity of (0002) diffraction peak increased with increasing RF power, which is due to the increase of total film thickness and improvement of film crystallinity with increasing RF power. It can be understood that when the *c*-axis-oriented ZnO films have greater film thickness, the diffraction intensity raised from the (0002) plane will be stronger. The similar phenomenon of the effect of deposition power on ZnO polycrystalline thin films was reported elsewhere [45, 46]. The strong signal intensity of the (0002) diffraction peak from the (0002) plane is due to the lowest surface energy of the (0002) basal plane in ZnO phase, leading to a preferred

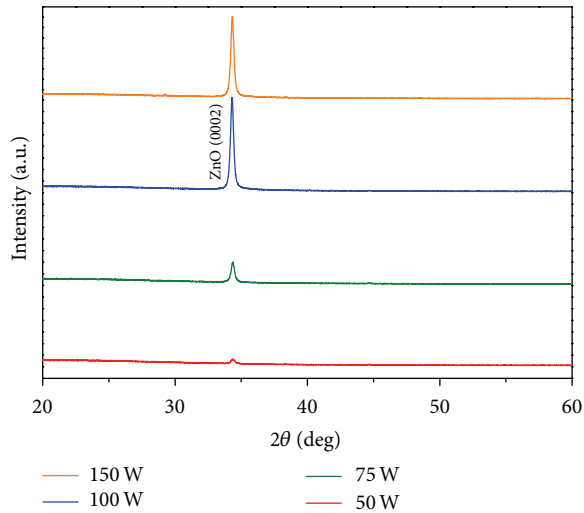


FIGURE 1: XRD patterns for the ZnO thin films deposited onto glass substrates at room temperature with RF deposition powers in the range of 50, 75, 100, and 150 W at a fixed deposition time of 30 mins, respectively.

orientation perpendicular to (0001) plane. Therefore the ZnO films have been successfully deposited onto glass substrates at room temperature, and the crystalline quality degree of  $c$ -axis orientation could be controlled under optimum growth conditions.

**3.2. Top View and Cross-Sectional View Microstructures and Corresponding Wettability Images.** The top view SEM images for the ZnO thin films deposited onto glass substrates at room temperature with different RF powers ranged from 50 to 150 W as shown in Figures 2(a)–2(d). Figures 2(a)–2(d) show two different types of grain structures denoted by nanograin and submicrograin cases. The different grain structure was caused by different RF powers during the deposition process. The nanograin structure of ZnO thin films can be observed at lower RF powers (50 and 75 W) as shown in Figures 2(a)–2(b). On the other hand, the submicrograin could be observed at higher deposition power of 150 W as shown in Figure 2(d). When the deposition power is 100 W, the mixed nanograin and submicrograin structures of ZnO phases coexist in the microstructure as shown in Figure 2(c). Above results could be attributed to high plasma energy bombardment in which, leading to the grain transformation, the microstructure of the ZnO thin films could be controlled by the deposition power. It can be understood that, with increasing deposition power, the nanograins with multiple domains coalesce and connect to each other to conjoin into a big grain as shown in Figure 2(d). It also can be observed that apertures, which can trap air inside, present onto the surface of ZnO thin films.

The corresponding images for surface water contact angle measurement are shown in Figures 2(e)–2(h), respectively. The surface water contact angle (CA,  $\theta$ ) values are 71.3°, 90.6°, 91.8°, and 71.6° for each ZnO sample deposited at 50, 75, 100, and 150 W, respectively. The ZnO samples show hydrophilic wetting at the depositing power of 50 W, which is due to

the fact that smooth surface and smaller grain size get fewer apertures that cannot provide the trapping of air as shown in Figure 2(e). While increasing depositing power up to 100 W, the nanograin structure surface shows hydrophobic behavior, which is because large grain size and more apertures provide more trapping of air that reduces the contact area between water and smooth surface as shown in Figure 2(g). The small contact angle is observed from Figure 2(h), which is due to grain transformation from nanograin to submicrograin. This transformation caused the CA to decrease which was due to the less apertures formed at the depositing power of 150 W [47], and the contact angle ( $\theta$ ) was denoted as the interface angle measured between the liquid and solid surface.

The thickness values as a function of the ZnO thin films deposited onto glass substrates at room temperature with different RF powers ranged from 50 to 150 W and are shown in Figure 3(a). Figures 3(b) and 3(c) are the cross-sectional micrographs of the ZnO thin films deposited at RF powers of 50 and 150 W, respectively. The measured thickness values for ZnO thin films by cross-sectional SEM images were 65, 104, 301, and 337 nm which corresponded to the deposition powers of 50, 75, 100, and 150 W, respectively. The thickness of ZnO thin films deposited onto glass substrates is increased with increasing the RF power. Figures 3(b) and 3(c) showed the highly textured ZnO films perpendicular to (0001) plane. Typical self-assembled columnar structure of the ZnO films perpendicular to the glass substrate and with a hillock surface morphology was observed. Figures 3(b) and 3(c) also confirmed that thickness value of the ZnO films at the deposition power of 50 W was about 65 nm and at the deposition power of 150 W was 337 nm, respectively.

Shown in Figures 4(a)–4(h) are the three-dimensional (3D) and the corresponded two-dimensional (2D) AFM micrographs ( $1\ \mu\text{m} \times 1\ \mu\text{m}$ ). The surface topography images in either 2D or 3D images show the surface roughness of ZnO thin films increased with increasing the deposition power. The average surface roughness values (root mean square, RMS) of the ZnO thin films increase with increasing the deposition power. The average RMS values are 1.7 nm, 1.6 nm, 3.3 nm, and 5.6 nm for each ZnO sample deposited at 50, 75, 100, and 150 W, respectively. Above results indicated that the high  $c$ -axis orientation ZnO (0002) thin films could provide the nanoscale surface roughness to demonstrate aperture formation which can trap the air. This kind of ZnO nanostructures could also provide nanometer-scale smoothness topography for suitable subsequent deposition of any top-electrode material onto its surface to function as a potential future sensing nanodevice [37].

Figures 5(a)–5(c) are the schematic diagram illustrations of the different types, showing the state of water droplet onto various surfaces of the ZnO thin films. Figure 5(a) is the smooth surface structure with hydrophilic wetting property for the ZnO thin films deposited at the lower powers of 50 and 75 W, respectively, which is denoted as nanograin type. When the deposition power of the ZnO thin films is increased to 100 W, the grain growth begins to form apertures that could provide the trapped air, which is denoted by a mixed nanograin and submicrograin type as shown in Figure 5(b). At the highest deposition power of 150 W for the ZnO thin

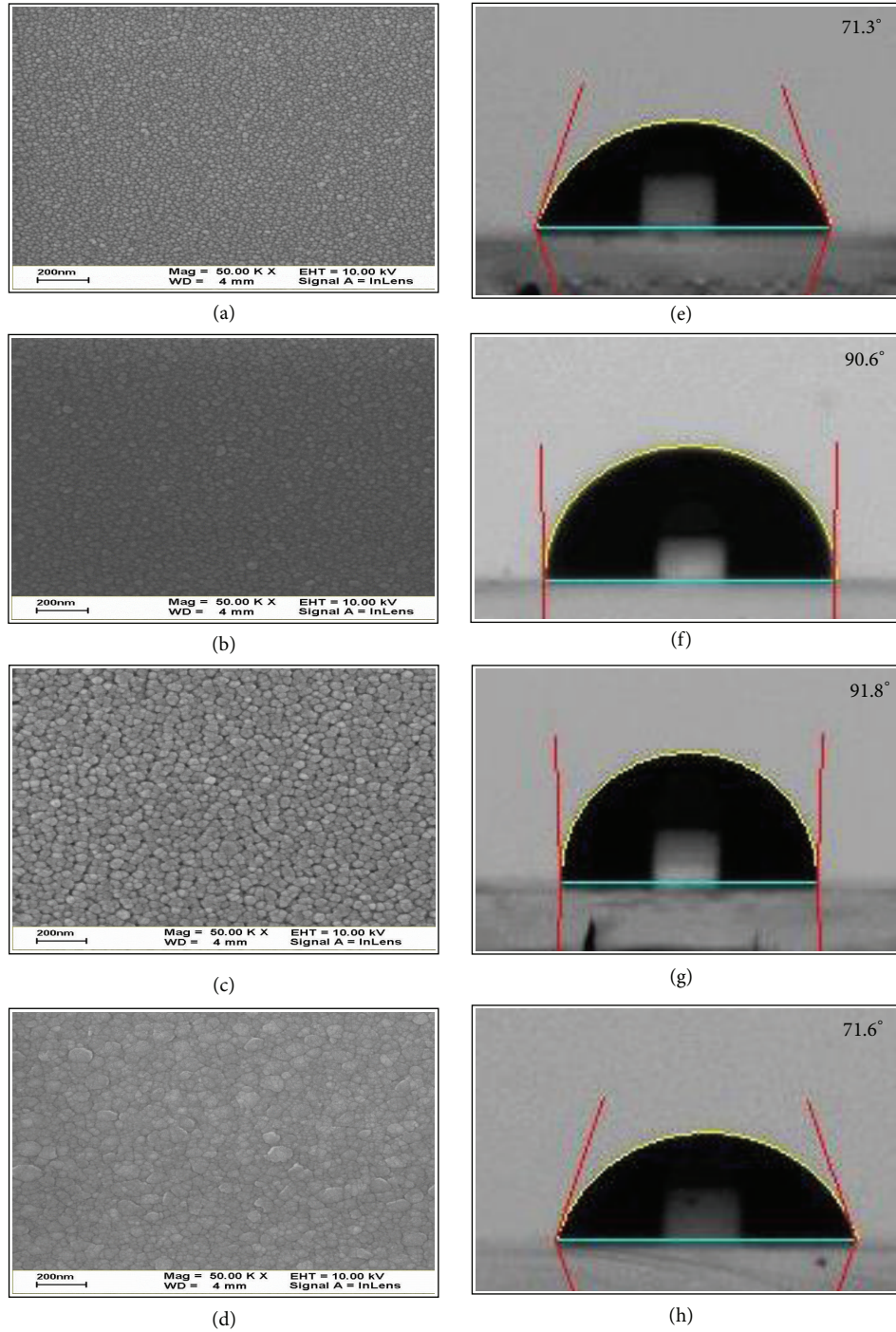


FIGURE 2: Top view SEM images for the ZnO thin films with deposition powers of (a) 50, (b) 75, (c) 100, and (d) 150 W, respectively. The contact angle images for different ZnO thin films corresponded to the right side denoted by (e), (f), (g), and (h), respectively.

films, the formation of submicrograin microstructure gives more opportunity for the water droplet to contact with the surface area of the ZnO thin films, which is denoted by submicrograin type as shown in Figure 5(c).

In order to understand the wetting behavior of the ZnO thin films, we consider the typical Cassie-Baxter's (CB) equation that can be explained in this research work [48].

In the typical CB equation, the drops are suspended onto a hydrophobic surface with air trapped underneath as an incomplete filling and the equilibrium contact angle (CA,  $\theta$ ) of a drop onto a nanostructure film can be described as

$$\cos \theta' = f_1 \cos \theta + f_2, \quad (1)$$

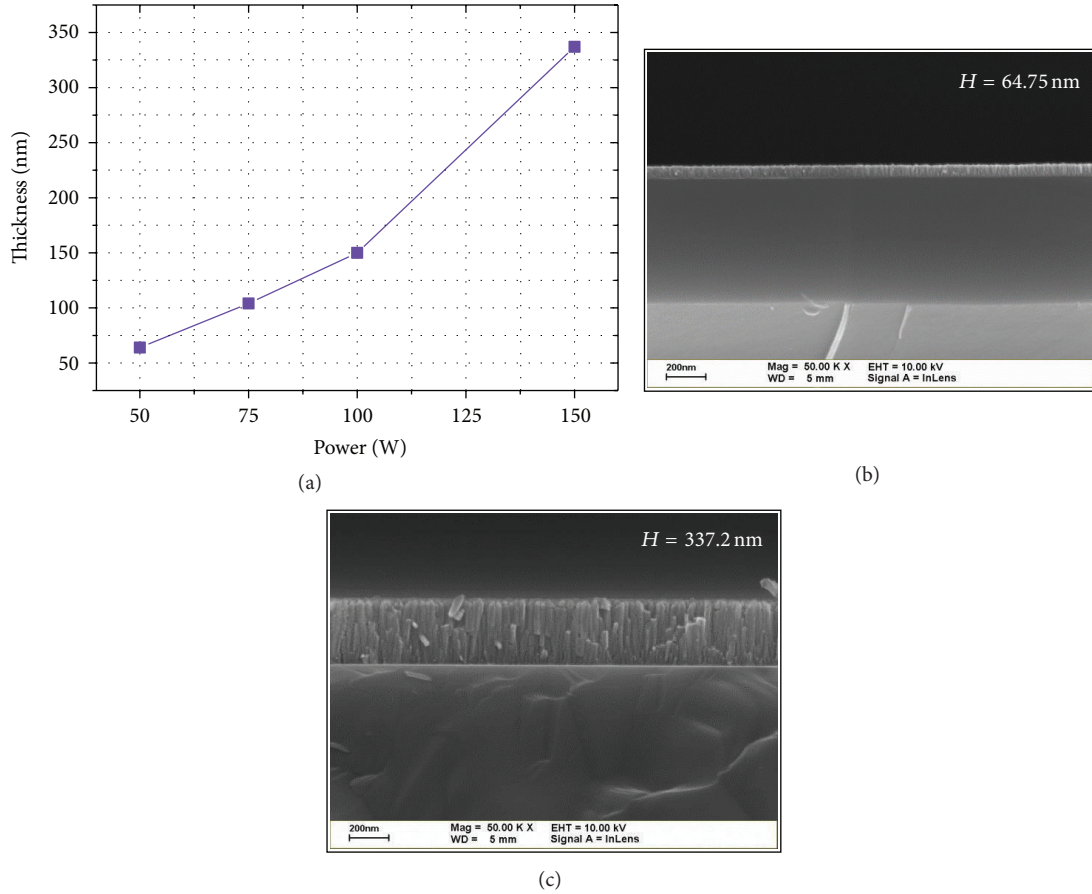


FIGURE 3: (a) The thickness values as a function of the ZnO thin films with different RF powers ranged from 50 to 150 W. (b) and (c) are the cross-sectional micrographs for the ZnO thin films deposited at the RF powers of 50 and 150 W, respectively.

where  $f_1$  and  $f_2$  are the area fractions of liquid-solid interface and liquid-air interface, respectively. As for  $f_1 + f_2 = 1$ , (1) can be converted to

$$\cos \theta' = f_1 (\cos \theta + 1) - 1, \quad (2)$$

where  $\theta$  is a constant that represents the CA on a smooth surface and  $\theta'$  is the CA on a rough surface. Based on (2), it can be understood that  $\theta'$  increases with decreasing the area fraction of liquid-solid interface ( $f_1$ ), and the surface fraction will make a significant contribution to CA. It is demonstrated that surface hydrophobicity improves when there is more air trapped between the liquid and solid surface exhibiting a larger CA as schematically shown in Figure 5(b). Therefore, more air is trapped between the water droplet and the surface of ZnO thin films. The CA of ZnO thin films will be much larger due to the fact that it prevents complete wetting of the surface. We have also explored the morphology and grain size effect on the controllable wettability of highly  $c$ -axis-oriented ZnO (0002) thin films, and the proposed mechanism was used to explain the related phenomena.

**3.3. Optical Transmittance Measurement.** Figure 6 shows the transparency of the ZnO thin films deposited onto glass substrates at room temperature with different RF powers ranging

from 50 to 150 W. The oscillating property of spectrum is due to the formation of uniform and smooth surface for ZnO thin films, and it can be indicated to lead less light scattering [49]. As a result, all the highly  $c$ -axis-oriented ZnO columnar films deposited at room temperature with RF powers of 50, 75, 100, and 150 W have good transparency and exhibit a visible light-averaged transmittance over 82%. For the functional oxide-based coatings of self-disinfection glass or smart window combined with the hybrid devices such as sensors and solar cells, this high transmittance plays an important role in the particular industrial products application.

**3.4. Surface Wettability Switching for Self-Disinfection Caused by UV Photoirradiation.** According to the above results, the highly  $c$ -axis-oriented ZnO columnar film deposited at RF power of 100 W shows the best hydrophobicity. In order to change the wettability transition of the ZnO thin films, which was deposited onto glass substrate at RF power of 100 W at first, and then it was put under an ultraviolet (UV) light of wavelength 365 nm, which could provide larger photon energy than the intrinsic band gap (3.37 eV) of the ZnO phase. The relationship between the UV photoirradiation times varied from 1 to 60 mins and water contact angle (CA) for the ZnO thin films deposited at 100 W as shown in

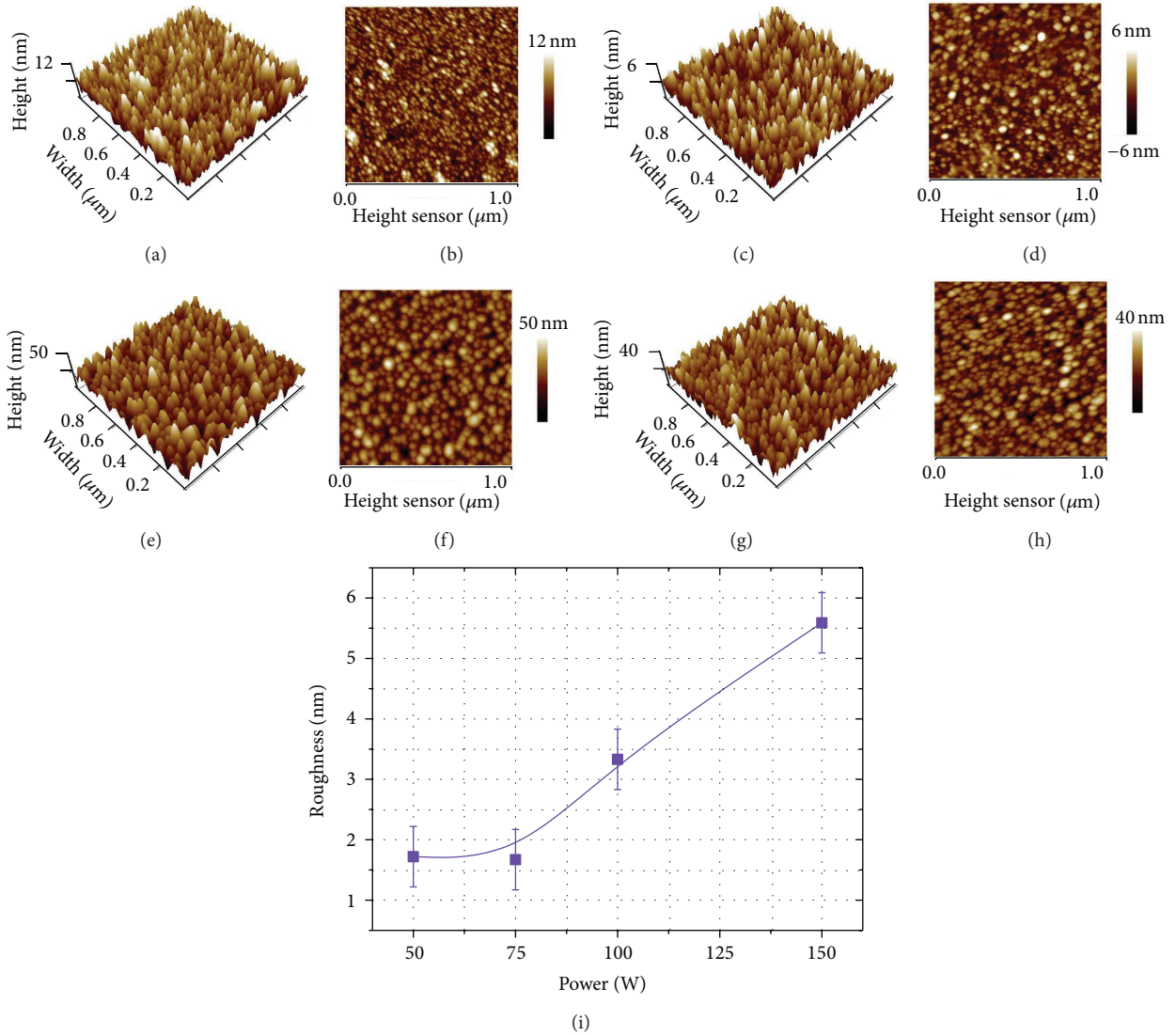
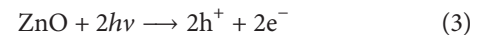


FIGURE 4: Atomic force microscope (AFM) 3D images for the ZnO thin films with different RF powers of (a) 50, (c) 75, (e) 100, and (g) 150 W; (b), (d), (f), and (h) are the corresponding 2D surface images for (a), (c), (e), and (g) forms, respectively. The scanning size of all domain images was fixed at  $1 \times 1 \mu\text{m}^2$ . (i) The surface roughness values as a function of the ZnO thin films with different deposition powers ranged from 50 to 150 W.

Figure 7. Inset showed the corresponding water CA images accompanied with the measured values for the ZnO (0002) columnar film. The ZnO sample deposited at RF power of 100 W was repeatedly measured after being stored in the dark for one day for reversing the initial wettability state. The CA values of ZnO columnar film decreased significantly with increasing the UV photoirradiation time, and the surface wettability was switched from hydrophobic to hydrophilic state. The CA value of ZnO columnar film deposited at RF power of 100 W changed from  $91.8^\circ$  to  $14.1^\circ$  after 60 mins of UV irradiation. The rapid decrease of CA value of ZnO phase can be attributed to the photocatalytic behavior caused by the accumulation of positive surface charges by photoelectron emission. The switching of wettability transition can also be explained by the following mechanism: via UV

photoirradiation by photon energy, higher than or equal to the band gap of ZnO phase, the electrons ( $e^-$ ) in the valence band are excited to the conduction band. At the same time, the same number of holes ( $h^+$ ) generated in valence band.



Some of the holes react with lattice oxygen ( $\text{O}^{2-}$ ) or surface oxygen atoms to form surface oxygen vacancies  $\text{O}^{1-}$ , while some of the electrons react with lattice metal ions ( $\text{Zn}^{2+}$ ) to form  $\text{Zn}^{2+}$  defective sites, as listed in the following equations:



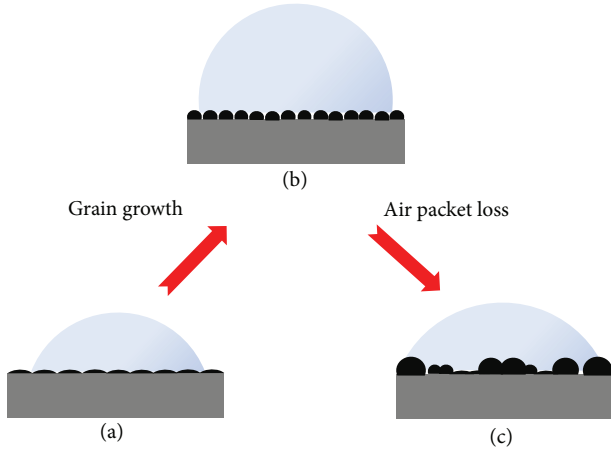


FIGURE 5: Schematic diagrams illustrating the ZnO films with different scales of grain size induced by different deposition powers: (a) nanograin (50 and 75 W), (b) mixed nanograin and submicrograin (100 W), and (c) submicrograin (150 W) types, respectively.

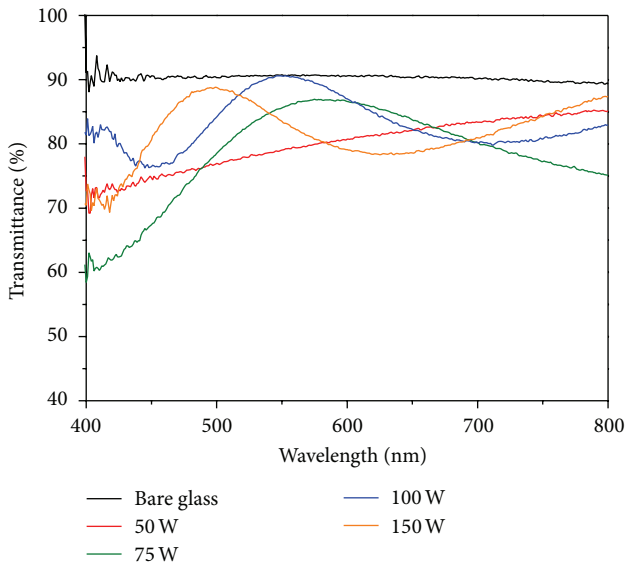
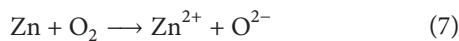


FIGURE 6: Optical transmittance spectra for the pure-bare glass substrate and ZnO thin films with different RF powers ranged from 50 to 150 W, respectively.



The water molecules and oxygen may compete with each other to dissociatively be absorbed on the defective sites. The surface trapped electrons ( $\text{Zn}^{+}$ ) tend to react with oxygen molecules adsorbed on the surface as follows:



At the same time, the water molecules may act in concert with oxygen vacancy sites ( $\text{V}_\text{O}$ ), which cause the dissociative adsorption of the water molecules onto the ZnO film

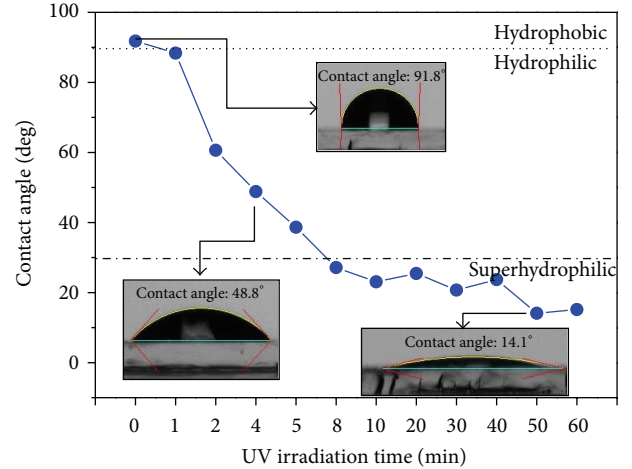


FIGURE 7: Time dependence of water contact angles (CAs) for the ZnO thin films deposited at 100 W under ultraviolet (UV) photoirradiation with the light wavelength of 365 nm. Inset showed the corresponding water CA images accompanied with the measured values of the ZnO (0002) columnar films.

surface. The defective sites are kinetically more favorable for hydrophilic hydroxyl groups ( $\text{OH}^{-}$ ) adsorption than oxygen adsorption. In general, the oxygen adsorption is favorable in thermodynamic behavior; therefore, when the UV light irradiated ZnO film was moved to dark conditions, the oxygen atoms could gradually replace the hydroxyl groups which made the surface come back to its initial state (without UV photoirradiation) and return its original hydrophobicity. This behavior provides a foundation for photoresponse and the fraction structure enhances CA value. So the UV photoirradiation can modify the chemical and physical surface states of the ZnO columnar film, in turn switching its wettability. This is helpful in the research field focused on controllable switching behavior from superhydrophilicity (contact angle  $\text{CA} < 15^{\circ}$ ) to hydrophobicity that can be used in many potential devices such as biosensors, microfluidic tools, intelligent membranes, and the encapsulation of biocompatibility/bioinertness *in vivo* biodevices [50–52].

The relationship between the time of storing in the dark varied from 10 to 600 mins and water CA values for the ZnO thin films deposited at 100 W as shown in Figure 8. Inset showed the corresponding water CA images accompanied with the measured values for the ZnO (0002) columnar film. The recovery time for the ZnO columnar film stored in the dark took about 10 hours to reach the initial/original water contact angle. The recovery behavior of the initial wettability is due to the surface discharging from the ZnO (0002) columnar film. The recovery behavior of hydrophobic surface from the ZnO columnar film is due to the replacement of adsorbed hydroxyl groups with oxygen molecules onto ZnO columnar film surface. After adsorbing hydroxyl groups under UV photoirradiation, the ZnO surface turns back to an unstable surface state. When the oxygen adsorption is preferred and strongly bonded on defective sites, the adsorbed hydroxyl groups on the defective sites could replace

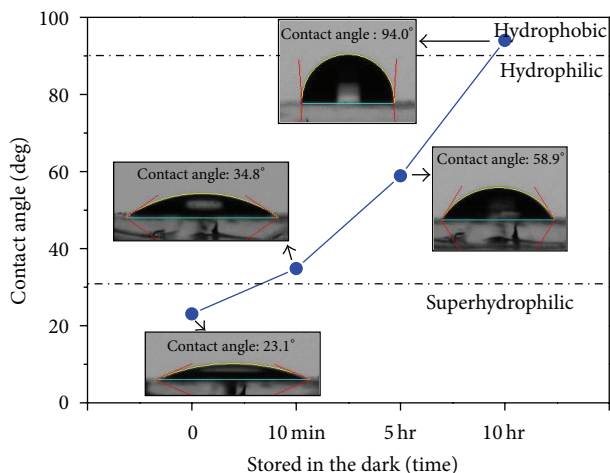


FIGURE 8: Stored in dark time dependence of water CAs for the ZnO thin films deposited at 100 W under UV photoirradiation. Inset showed the corresponding water CA images accompanied with the measured values of the ZnO (0002) columnar films.

oxygen molecules within the ZnO film stored in the dark environment. Above results demonstrate that the surface charge is strongly influenced by the UV photoirradiation.

#### 4. Conclusions

Highly *c*-axis-oriented ZnO (0002) columnar films have been successfully deposited onto glass substrates at room temperature by radio-frequency magnetron sputtering system. All the ZnO columnar films exhibited good crystallinity and had good visible-averaged transparency (over 82%), and all the ZnO films showed hydrophobic behavior. The wettability of the ZnO columnar film could be switched from hydrophobic ( $\sim 92^\circ$ ) to superhydrophilic ( $\sim 14^\circ$ ) during the UV photoirradiation process. The rapid transition of contact angle (CA) value for ZnO columnar film can be attributed to the photocatalytic behavior caused by the accumulation of positive surface charges via photoelectron emission. A simple method is presented here for controlling the CA value and switching wettability of ZnO phase only by the RF deposition power and inducing UV light photoirradiation, respectively.

#### Conflict of Interests

The authors declare that there is no conflict of interests regarding the publication of this paper.

#### Acknowledgment

The authors acknowledge financial support of the main research projects of the National Science Council of China under Grant nos. NSC 101-2622-E-027-003-CC2 and NSC 101-2221-E-027-042.

#### References

- [1] D. H. W. Li, J. C. Lam, C. C. S. Lau, and T. W. Huan, "Lighting and energy performance of solar film coating in air-conditioned cellular offices," *Renewable Energy*, vol. 29, no. 6, pp. 921–937, 2004.
- [2] Q. B. Ma, Z. Z. Ye, H. P. He et al., "Highly infrared reflective behavior of transparent conductive ZnO:Ga films synthesized by dc reactive magnetron sputtering," *ChemPhysChem*, vol. 9, no. 4, pp. 529–532, 2008.
- [3] Z. Y. Huang, M. Chen, S. R. Pan, and D. H. Chen, "Effect of surface microstructure and wettability on plasma protein adsorption to ZnO thin films prepared at different RF powers," *Biomedical Materials*, vol. 5, no. 5, Article ID 54116, 2010.
- [4] H. C. Barshilia, N. Selvakumar, N. Pillai, L. M. Devi, and K. S. Rajam, "Wettability of ZnO: a comparison of reactively sputtered; thermally oxidized and vacuum annealed coatings," *Applied Surface Science*, vol. 257, no. 9, pp. 4410–4417, 2011.
- [5] H. Li, M. Zheng, S. Liu, L. Ma, C. Zhu, and Z. Xiong, "Reversible surface wettability transition between superhydrophobicity and superhydrophilicity on hierarchical micro/nanostructure ZnO mesh films," *Surface and Coatings Technology*, vol. 224, pp. 88–92, 2013.
- [6] K. Guan, "Relationship between photocatalytic activity, hydrophilicity and self-cleaning effect of TiO<sub>2</sub>/SiO<sub>2</sub> films," *Surface and Coatings Technology*, vol. 191, no. 2-3, pp. 155–160, 2005.
- [7] X. Feng and L. Jiang, "Design and creation of superwetting/antiwetting surfaces," *Advanced Materials*, vol. 18, no. 23, pp. 3063–3078, 2006.
- [8] S. Wang, Y.-L. Song, and L. Jiang, "Photoresponsive surfaces with controllable wettability," *Journal of Photochemistry and Photobiology C: Photochemistry Reviews*, vol. 8, no. 1, pp. 18–29, 2007.
- [9] N. Katsonis, M. Lubomska, M. M. Pollard, B. L. Feringa, and P. Rudolf, "Synthetic light-activated molecular switches and motors on surfaces," *Progress in Surface Science*, vol. 82, no. 7-8, pp. 407–434, 2007.
- [10] G. Kenanakis, E. Stratakis, K. Vlachou, D. Vernardou, E. Koudoumas, and N. Katsarakis, "Light-induced reversible hydrophilicity of ZnO structures grown by aqueous chemical growth," *Applied Surface Science*, vol. 254, no. 18, pp. 5695–5699, 2008.
- [11] M. N. Chong, B. Jin, C. W. K. Chow, and C. Saint, "Recent developments in photocatalytic water treatment technology: a review," *Water Research*, vol. 44, no. 10, pp. 2997–3027, 2010.
- [12] Y. C. Lan, Y. L. Lu, and Z. F. Ren, "Mini review on photocatalysis of titanium dioxide nanoparticles and their solar applications," *Nano Energy*, vol. 2, pp. 1031–1045, 2013.
- [13] R. Rosario, D. Gust, A. A. Garcia et al., "Lotus effect amplifies light-induced contact angle switching," *Journal of Physical Chemistry B*, vol. 108, no. 34, pp. 12640–12642, 2004.
- [14] T. L. Sun, L. Feng, X. F. Gao, and L. Jiang, "Bioinspired surfaces with special wettability," *Accounts of Chemical Research*, vol. 38, no. 8, pp. 644–652, 2005.
- [15] P. H. Yang, K. Wang, Z. W. Liang et al., "Enhanced wettability performance of ultrathin ZnO nanotubes by coupling morphology and size effects," *Nanoscale*, vol. 4, no. 18, pp. 5755–5760, 2012.
- [16] E. Pakdel, W. A. Daoud, and X. G. Wang, "Self-cleaning and superhydrophilic wool by TiO<sub>2</sub>/SiO<sub>2</sub> nanocomposite," *Applied Surface Science*, vol. 275, pp. 397–402, 2013.

- [17] K. Midtdal and B. P. Jelle, "Self-cleaning glazing products: a state-of-the-art review and future research pathways," *Solar Energy Materials and Solar Cells*, vol. 109, pp. 126–141, 2013.
- [18] Y. B. Kwon, B. M. Weon, K. H. Won, J. H. Je, Y. Hwu, and G. Margaritondo, "X-ray-induced changes in wettability," *Langmuir*, vol. 25, no. 4, pp. 1927–1929, 2009.
- [19] L. Q. Tang, B. Zhou, Y. M. Tian, F. Sun, Y. L. Li, and Z. C. Wang, "Synthesis and surface hydrophobic functionalization of ZnO nanocrystals via a facile one-step solution method," *Chemical Engineering Journal*, vol. 139, no. 3, pp. 642–648, 2008.
- [20] P. Suresh Kumar, J. Sundaramurthy, D. Mangalaraj, D. Nataraj, D. Rajarathnam, and M. P. Srinivasan, "Enhanced superhydrophobic and switching behavior of ZnO nanostructured surfaces prepared by simple solution—immersion successive ionic layer adsorption and reaction process," *Journal of Colloid and Interface Science*, vol. 363, no. 1, pp. 51–58, 2011.
- [21] X. M. Hou, L. X. Wang, F. Zhou, and L. Q. Li, "Fabrication of ZnO submicrorod films with water repellency by surface etching and hydrophobic modification," *Thin Solid Films*, vol. 519, no. 22, pp. 7813–7816, 2011.
- [22] P. S. Kumar, J. Sundaramurthy, X. Zhang, D. Mangalaraj, V. Thavasi, and S. Ramakrishna, "Superhydrophobic and antireflecting behavior of densely packed and size controlled ZnO nanorods," *Journal of Alloys and Compounds*, vol. 553, pp. 375–382, 2013.
- [23] S. Anitha, B. Brabu, D. John Thiruvadigal, C. Gopalakrishnan, and T. S. Natarajan, "Optical, bactericidal and water repellent properties of electrospun nano-composite membranes of cellulose acetate and ZnO," *Carbohydrate Polymers*, vol. 97, no. 2, pp. 856–863, 2013.
- [24] X. Du and J.-H. He, "Structurally colored surfaces with antireflective, self-cleaning, and antifogging properties," *Journal of Colloid and Interface Science*, vol. 381, no. 1, pp. 189–197, 2012.
- [25] G. Yakovlev, G. Pervushin, I. Maeva et al., "Modification of Construction Materials with Multi-Walled Carbon Nanotubes," *Procedia Engineering*, vol. 57, pp. 407–413, 2013.
- [26] L. Gao, X. G. Li, H. Hu, G. J. Li, H. W. Liu, and Y. Yu, "TiO<sub>2</sub> mesoporous microspheres with nanorod structure: facile synthesis and superior electrochemical performance," *Electrochimica Acta*, vol. 120, pp. 231–239, 2014.
- [27] J. Godnjavec, J. Zabret, B. Znoj, S. Skale, N. Veronovski, and P. Venturini, "Investigation of surface modification of rutile TiO<sub>2</sub> nanoparticles with SiO<sub>2</sub>/Al<sub>2</sub>O<sub>3</sub> on the properties of polyacrylic composite coating," *Progress in Organic Coatings*, vol. 77, no. 1, pp. 47–52, 2014.
- [28] V. Iliev, D. Tomova, S. Rakovsky, A. Eliyas, and G. L. Puma, "Enhancement of photocatalytic oxidation of oxalic acid by gold modified WO<sub>3</sub>/TiO<sub>2</sub> photocatalysts under UV and visible light irradiation," *Journal of Molecular Catalysis A: Chemical*, vol. 327, no. 1–2, pp. 51–57, 2010.
- [29] C. Song, P. Chen, C. Y. Wang, and L. Y. Zhu, "Photodegradation of perfluorooctanoic acid by synthesized TiO<sub>2</sub>-MWCNT composites under 365 nm UV irradiation," *Chemosphere*, vol. 86, no. 8, pp. 853–859, 2012.
- [30] V. R. Shinde, C. D. Lokhande, R. S. Mane, and S. Han, "Hydrophobic and textured ZnO films deposited by chemical bath deposition: annealing effect," *Applied Surface Science*, vol. 245, no. 1–4, pp. 407–413, 2005.
- [31] P. S. Kumar, A. D. Raj, D. Mangalaraj, and D. Nataraj, "Hydrophobic ZnO nanostructured thin films on glass substrate by simple successive ionic layer adsorption and reaction (SILAR) method," *Thin Solid Films*, vol. 518, no. 24, pp. e183–e186, 2010.
- [32] Y. Z. Yang, C. X. Wang, H. D. Li, and Q. Lin, "Ultrahydrophobicity of ZnO modified CVD diamond films," *Applied Surface Science*, vol. 270, pp. 260–266, 2013.
- [33] J. J. Hassan, M. A. Mahdi, C. W. Chin, H. Abu-Hassan, and Z. Hassan, "A high-sensitivity room-temperature hydrogen gas sensor based on oblique and vertical ZnO nanorod arrays," *Sensors and Actuators B: Chemical*, vol. 176, pp. 360–367, 2013.
- [34] C. L. Hsu, K. C. Chen, T. Y. Tsai, and T. J. Hsueh, "Fabrication of gas sensor based on p-type ZnO nanoparticles and n-type ZnO nanowires," *Sensors and Actuators B Chemical*, vol. 182, pp. 190–196, 2013.
- [35] V. A. Minh, L. A. Tuan, T. Q. Huy, V. N. Hung, and N. V. Quy, "Enhanced NH<sub>3</sub> gas sensing properties of a QCM sensor by increasing the length of vertically orientated ZnO nanorods," *Applied Surface Science*, vol. 265, pp. 458–464, 2013.
- [36] Y. N. He, W. Zhang, S. C. Zhang, X. Kang, W. B. Peng, and Y. L. Xu, "Study of the photoconductive ZnO UV detector based on the electrically floated nanowire array," *Sensors and Actuators A: Physical*, vol. 181, pp. 6–12, 2012.
- [37] C. H. Chao, M. Y. Chen, C. R. Lin, Y. C. Yu, Y. D. Yao, and D. H. Wei, "Postannealing effect at various gas ambients on ohmic contacts of Pt/ZnO nanobilayers toward ultraviolet photodetectors," *International Journal of Photoenergy*, vol. 2013, Article ID 372869, 9 pages, 2013.
- [38] N. K. Hassan and M. R. Hashim, "Flake-like ZnO nanostructures density for improved absorption using electrochemical deposition in UV detection," *Journal of Alloys and Compounds*, vol. 577, pp. 491–497, 2013.
- [39] L. J. Wang and G. J. Exarhos, "Persistent conductivity in post-growth doped ZnO films following pulsed UV laser irradiation," *Thin Solid Films*, vol. 519, no. 5, pp. 1495–1500, 2010.
- [40] V. Eskizeybek, F. Sari, H. Gülce, A. Gülce, and A. Avci, "Preparation of the new polyaniline/ZnO nanocomposite and its photocatalytic activity for degradation of methylene blue and malachite green dyes under UV and natural sun lights irradiations," *Applied Catalysis B: Environmental*, vol. 119–120, pp. 197–206, 2012.
- [41] X. J. Liu, L. K. Pan, Q. F. Zhao et al., "UV-assisted photocatalytic synthesis of ZnO-reduced graphene oxide composites with enhanced photocatalytic activity in reduction of Cr(VI)," *Chemical Engineering Journal*, vol. 183, pp. 238–243, 2012.
- [42] P. Pradhan, J. C. Alonso, and M. Bizarro, "Photocatalytic performance of ZnO: Al films under different light sources," *International Journal of Photoenergy*, vol. 2012, Article ID 780462, 7 pages, 2012.
- [43] X. L. Zhang, K. S. Hui, and K. N. Hui, "High photo-responsivity ZnO UV detectors fabricated by RF reactive sputtering," *Materials Research Bulletin*, vol. 48, no. 2, pp. 305–309, 2013.
- [44] Y. H. Mun, S. H. Park, S. Y. An, C. M. Lee, and H. W. Kim, "NO<sub>2</sub> gas sensing properties of Au-functionalized porous ZnO nanosheets enhanced by UV irradiation," *Ceramics International*, vol. 39, pp. 8615–8622, 2013.
- [45] R. G. Zhang, B. Y. Wang, and L. Wei, "Influence of RF power on the structure of ZnS thin films grown by sulfurizing RF sputter deposited ZnO," *Materials Chemistry and Physics*, vol. 112, no. 2, pp. 557–561, 2008.
- [46] X. H. Yu, J. Ma, F. Ji et al., "Effects of sputtering power on the properties of ZnO:Ga films deposited by r.f. magnetron-sputtering at low temperature," *Journal of Crystal Growth*, vol. 274, no. 3–4, pp. 474–479, 2005.

- [47] J. Han and W. Gao, "Surface wettability of nanostructured Zinc oxide films," *Journal of Electronic Materials*, vol. 38, no. 4, pp. 601–608, 2009.
- [48] D. Wu, Q. D. Chen, H. Xia et al., "A facile approach for artificial biomimetic surfaces with both superhydrophobicity and iridescence," *Soft Matter*, vol. 6, no. 2, pp. 263–267, 2010.
- [49] A. Nakajima, K. Hashimoto, T. Watanabe, K. Takai, G. Yamauchi, and A. Fujishima, "Transparent superhydrophobic thin films with self-cleaning properties," *Langmuir*, vol. 16, no. 17, pp. 7044–7047, 2000.
- [50] Y. Liu, Z. Lin, W. Lin, K. S. Moon, and C. P. Wong, "Reversible superhydrophobic-superhydrophilic transition of ZnO nanorod/epoxy composite films," *ACS Applied Materials and Interfaces*, vol. 4, no. 8, pp. 3959–3964, 2012.
- [51] C. Mondal, M. Ganguly, A. K. Sinha, J. Pal, and T. Pal, "Fabrication of a ZnO nanocolumnar thin film on a glass slide and its reversible switching from a superhydrophobic to a superhydrophilic state," *RSC Advances*, vol. 3, no. 17, pp. 5937–5944, 2013.
- [52] W. H. Liao, C. R. Lin, D. H. Wei et al., "Concurrent improvement in biocompatibility and bioinertness of diamond-like carbon films with nitrogen doping," *Journal of Biomedical Materials Research A*, vol. 100, no. 11, pp. 3151–3156, 2012.

## Research Article

# Effect of Electrodeposition Potential on Composition of $\text{CuIn}_{1-x}\text{Ga}_x\text{Se}_2$ Absorber Layer for Solar Cell by One-Step Electrodeposition

Rui-Wei You,<sup>1</sup> Kar-Kit Lew,<sup>1</sup> and Yen-Pei Fu<sup>1,2</sup>

<sup>1</sup> Department of Materials Science and Engineering, National Dong Hwa University, Shoufeng, Hualien 97401, Taiwan

<sup>2</sup> Nanotechnology Research Center, National Dong Hwa University, Shoufeng, Hualien 97401, Taiwan

Correspondence should be addressed to Yen-Pei Fu; [d887503@alumni.nthu.edu.tw](mailto:d887503@alumni.nthu.edu.tw)

Received 3 March 2014; Revised 6 June 2014; Accepted 10 June 2014; Published 14 July 2014

Academic Editor: Ho Chang

Copyright © 2014 Rui-Wei You et al. This is an open access article distributed under the Creative Commons Attribution License, which permits unrestricted use, distribution, and reproduction in any medium, provided the original work is properly cited.

CIGS polycrystalline thin films were successfully fabricated by one-step cathodic electrodeposition on Mo-coated glass. In this study, we applied a galvanometry mode with three-electrode potentiostatic systems to produce a constant concentration electroplating solution, which were composed of  $\text{CuCl}_2$ ,  $\text{InCl}_3$ ,  $\text{GaCl}_3$ , and  $\text{SeO}_2$ . Then these as-electrodeposited films were annealed in argon atmosphere and characterized by X-ray diffraction. The results revealed that annealing treatment significantly improved the crystallinity of electrodeposited films and formed CIGS chalcopyrite structure, but at low applied deposition voltage ( $-950$  mV versus SCE) there appeared second phase. The cross-section morphology revealed that applied voltage at  $-1350$  mV versus SCE has uniform deposition, and higher applied voltage made grain more unobvious. The deposition rate and current density are proportional to deposition potential, and hydrogen was generated apparently when applying potential beyond  $-1750$  mV versus SCE. It was found that the CIGS compound did not match exact stoichiometry of  $\text{Cu}:\text{In}:\text{Ga}:\text{Se} = 1:x:(1-x):2$ . This result suggests the possibility of controlling the property of thin films by varying the applied potential during electrodeposition.

## 1. Introduction

$\text{CuInSe}_2$  (CIS) and  $\text{Cu}(\text{In}, \text{Ga})\text{Se}_2$  (CIGS) to be candidate materials as absorber material for the thin film photovoltaic device are popular because of high optical absorption and direct band gap. We present that the optimum band gap for solar cell is 1.45 eV. But  $E_g$  of  $\text{CuInSe}_2$  film is near 1.02 eV at room temperature, not exactly located within the best operation area. CIGS cells offer a tunable direct band gap by adjusting the ratio of In to Ga to maximize the absorption of the solar spectrum. To add Ga with appropriate concentration to CIS material could form  $\text{CuIn}_x\text{Ga}_{1-x}\text{Se}_2$  and adjust the band gap ranges from 1.02 eV (pure  $\text{CuInSe}_2$ ) to 1.68 eV (pure  $\text{CuGaSe}_2$ ) [1]. This property could be utilized to fabricate multijunction devices for increasing efficiency. Taking CIGS film as an absorber can apparently cause efficiencies of up to 19.5% on a laboratory scale. CIGS cells also have the highest

absorption coefficient of any thin film ( $\alpha > 10^5 \text{ cm}^{-1}$ ), which allows for greater than 99% of the incoming photons to be absorbed within the first micron of the material. Cost would be down because of low material requirement. It is estimated that the theoretical efficiency could reach 25% to 30%. After mass production the cost would probably be about US\$0.03/W. In sum, a CIGS modules device will have great competition potential for solar energy in the future.

There are different techniques to prepare the CIGS absorber layer including both physical and chemical methods. The main concern for CIGS solar cell is to develop a low-cost and large-scale production technology. It is desirable technically to form the concerned thin film by a simple, safe, and inexpensive procedure. Many researches have reported the fabrication of CIGS by different approaches [2–16]. Xu et al. reported that applying a novel single source

three-stage evaporation process to fabricate CIGS thin film solar cells with a power conversion efficiency of 10.6%. This technique enables the deposition of CIGS thin films using a conventional one-source-at-a-time evaporator and device quality films are formed in situ without selenization [3]. Chen et al. reported one-step fabrication of the chalcopyrite CIGS absorber layer without excess Se supply during/after deposition or postselenization treatments with an efficiency of 10.14% by using pulse DC sputtering route [9]. Later, Chen et al. discussed the characteristics of one-step sputtered CIGS films including compositional, structural, optical, morphological, and electrical properties. For the device fabrication, the authors claimed that Mo back contacts dominated the growth behavior of CIGS films deposited at high temperature [10]. Duchatelet et al. presented new advances on an atmospheric-based deposition process for  $\text{Cu(In, Ga)Se}_2$  with an efficiency of 12.4%. The electrodeposition consisted of a Cu-In-Ga mixed oxide/hydroxide layer from an aqueous solution at room temperature, followed by a thermochemical reduction and selenization. This process enables the one-step codeposition of the three elements, from a simple aqueous electrolyte containing nitrate ions as oxygen precursor, with fast growing rates and precise control of composition [11]. Wang et al. reported a novel approach for the fabrication of chalcopyrite  $\text{CuIn}_x\text{Ga}_{1-x}\text{Se}_2$  thin film solar cells by inkjet printing with a power conversion efficiency of 5.04%. The authors claimed that inkjet printing in atmospheric environment offers an opportunity for the direct patterning of absorber materials at large scale. Moreover, inkjet printing increases the raw material utilization ratio compared to more wasteful vacuum-based deposition techniques [12]. The techniques for the deposition of the CIGS layer can be either vacuum or solution-based methods [13–15]. Although the cell efficiencies obtained from CIGS layer fabricated by the vacuum methods were higher, the cheap and convenient solution-based approaches still attract a lot of research interest as a potential alternative [16].

Among various solution-based methods, electrodeposition is a potentially suitable preparation method for obtaining the low-cost CIGS layer. One-step electrodeposition, especially, has the most various advantages for high throughput and large-area fabrication, because of its low processing cost, the fact that there is no vacuum system needed, its high deposition speed, the fact that there is no use of toxic gases, its low operation temperature, and its simple operation steps. The whole process involves electrodeposition of precursor films of Cu-In-Ga-Se alloy and subsequent recrystallization by thermal annealing at high temperature. The most important part is to optimize deposition parameters and conditions to offer the prospect of achieving stoichiometry. The main emphasis and purpose of this paper focused on details of one-step electrodeposition process. It took depositions' potentials to be process parameters. The goal of this work was to study the effect of the different deposition conditions and treatments used on the structural and morphological properties of CIGS in order to find out the trend of obtaining high quality precursor layers. Grain growth during annealing was observed. The mechanism of film growth

TABLE 1: Bath composition that used to prepare precursor CIGS thin films by electrodeposition. All chemicals were dissolved in a solution of pH 2 with DI water.

	Bath composition (mM)				LiCl
	$\text{Cu}^{2+}$	$\text{In}^{3+}$	$\text{Ga}^{3+}$	$\text{Se}^{4+}$	
Fixed	12	3.75	6.81	10.8	250

and influence of hydrogen generated at cathode are also discussed.

## 2. Experimental Details

**2.1. Thin Film Preparation.** One-step electrodeposition was carried out potentiostatically in an aqueous solution containing  $\text{CuCl}_2$ ,  $\text{InCl}_3$ ,  $\text{GaCl}_3$ ,  $\text{SeO}_2$ , and  $\text{LiCl}$ ; the concentration of each electrolyte is shown in Table 1. No stirring was employed during deposition in first cases; then follow-up cases are under stirring with the velocity using a magnetic bar to improve the uniformity of the deposited sample during deposition (to protect the sample from a bubble generated under the electrolyte solution). The solution temperature was under room temperature without heating and recirculation. Diluted HCl was added drop by drop to adjust the pH of the solution to be between 1.9 and 2.0. It used a classical three-electrode potential static device with platinum (Pt) coated titanium gauze as an auxiliary electrode. Saturated calomel electrode (SCE) is to be a reference for measurement of the local potential of the cathode. The working electrode was a  $1\text{-}\mu\text{m}$  thick Mo film on a glass substrate (with active deposition area of  $1.0\text{ cm}^2$ ) deposited by DC sputtering on soda-lime glass. Ultrasonic cleaner cleaned the specimens with deionized water and acetone. Then they were dried in flowing air. The electrodeposition was controlled using an EG&G Mod. 263 Potentiostat/Galvanostat. To minimize the experimental error, electrodeposition was conducted under the same conditions (concentration of the electrolyte, pH of solution, supporting electrolyte, sample size, and magnetic stirring), except for applied bias. The applied potential was varied from  $-1950\text{ mV}$  to  $-950\text{ mV}$  versus SCE [17]. During electrodeposition the current variation was recorded. After electrodeposition precursor thin films were annealed in a tube furnace for 1 hour in Ar atmosphere at  $400^\circ\text{C}$  to form CIGS without oxidation and to improve their crystalline properties.

**2.2. Thin Film Characterization.** The specimens are characterized X-ray diffraction (XRD) by X-ray Diffractometer Rigaku using  $\text{Cu K}\alpha$  radiation ( $\lambda = 1.54\text{ \AA}$ ) to confirm the formation and crystallization of the quaternary compound. The data obtained by XRD was compared with JCPDS file cards in order to determine the phases of the films. The field emission scanning electron microscopy (FESEM) images were used to demonstrate the surface morphology. EDX was done to define compound stoichiometry. The roughness of sample surfaces was detected by atomic force microscopy (AFM).

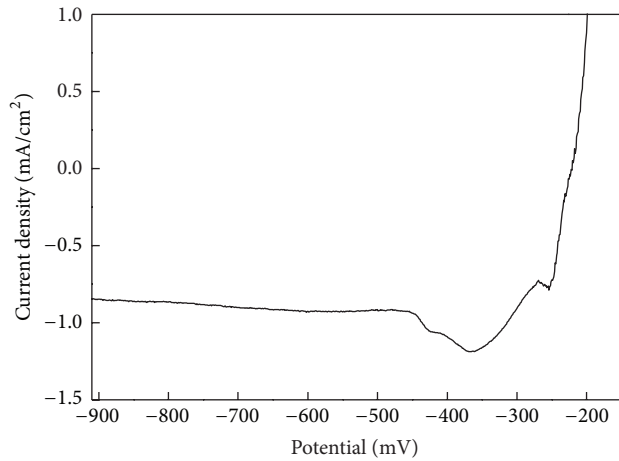


FIGURE 1: Polarization curve was conducted to determine the reduction potentials of each element (scan rate = 1 mV/s).

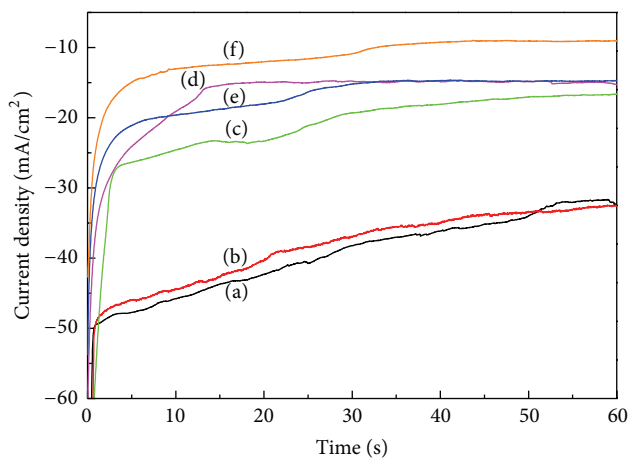
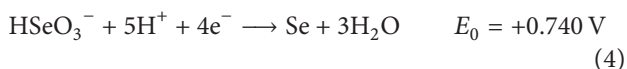
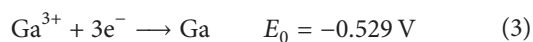
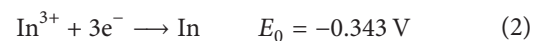
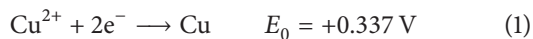


FIGURE 2:  $I$ - $T$  curve of thin films under different potentials (a)  $-1950$  mV, (b)  $-1750$  mV, (c)  $-1550$  mV, (d)  $-1350$  mV, (e)  $-1150$  mV, and (f)  $-950$  mV.

### 3. Results and Discussion

The anions of  $\text{Cu}^{2+}$ ,  $\text{In}^{3+}$ ,  $\text{Ga}^{2+}$ , and  $\text{HSeO}_3^-$  are believed to exist in the solution. There are reduction reactions which are shown as follows [18, 19]. The optimum reduction potentials of each element listed after chemical formula are standard reduction potentials:



Polarization curve was conducted as in Figure 1. The deviation of these reaction potentials from the theoretically expected values was caused by various factors, such as the

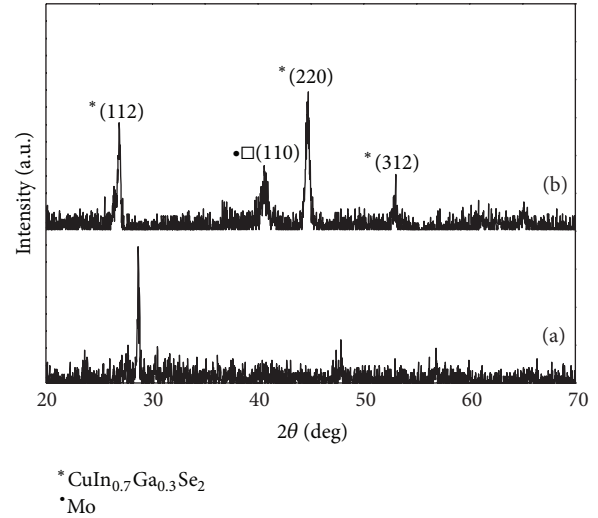


FIGURE 3: XRD pattern of thin film deposited under potentials  $-1350$  mV versus SCE for (a) as-annealing and (b) annealing under Ar atmosphere.

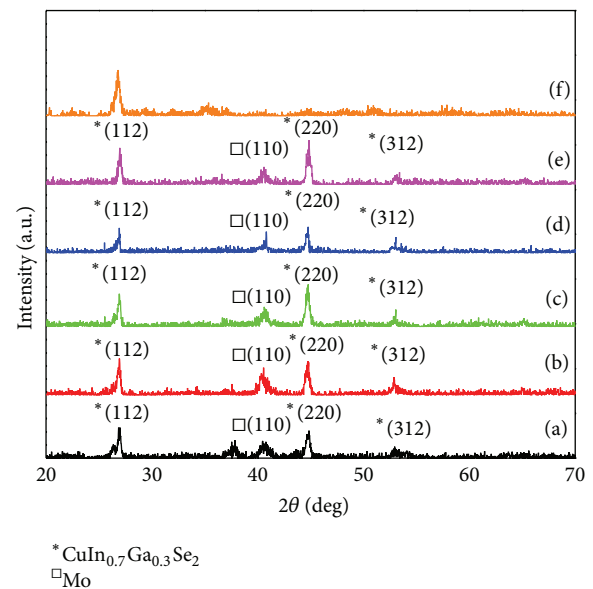


FIGURE 4: XRD pattern of thin films deposited under potentials (a)  $-950$  mV, (b)  $-1150$  mV, (c)  $-1350$  mV, (d)  $-1550$  mV, (e)  $-1750$  mV, and (f)  $-1950$  mV.

concentration of the electrolyte, pH of the solution, used substrate size, supporting electrolyte, and the absence or presence of magnetic stirring [20–23]. Based on theory and [17], the most applicable potential to codeposit these four components should be located between  $-950$  mV versus SCE and  $-1950$  mV versus SCE.

After a round of experiments without stirring, it was found that at higher bias (over  $-1750$  mV versus SCE) a great deal of hydrogen was produced in 10 seconds. Figure 2 shows the  $i$ - $t$  curves under different potentials. The current density of low bias (below  $-1350$  mV versus SCE) would tend

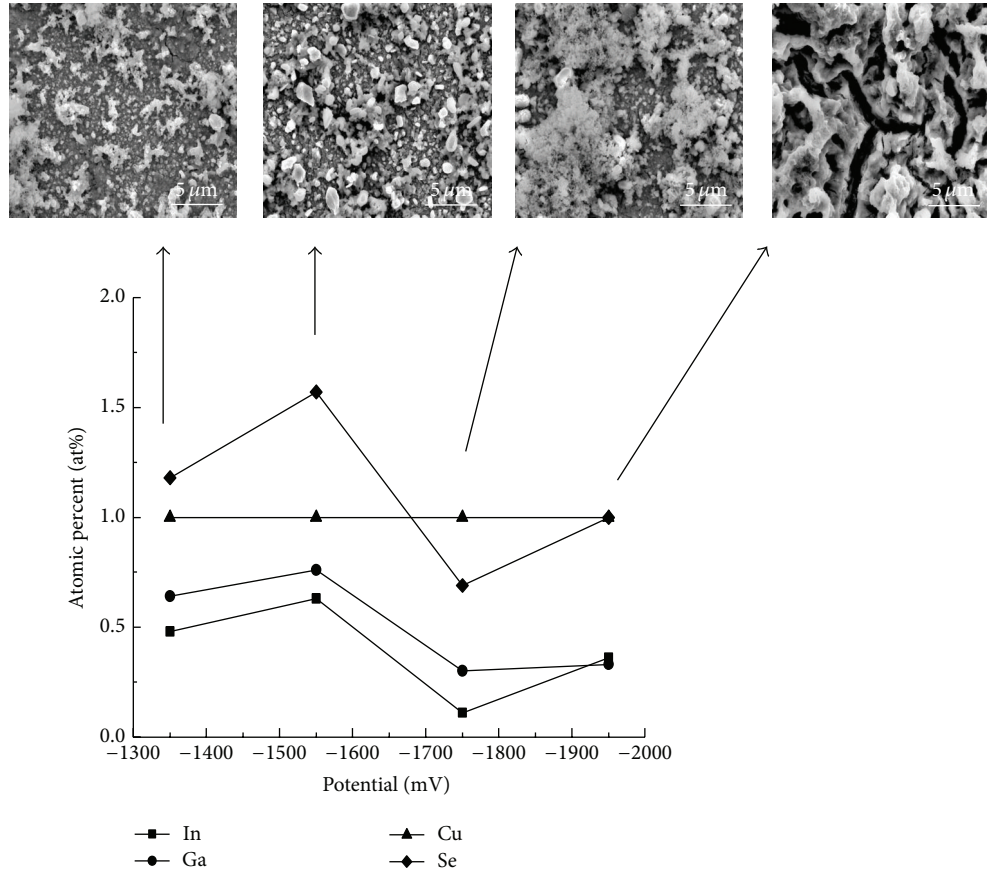


FIGURE 5: EDS results of CIGS thin films deposited under different potential (normalized to Cu = 1) and its relative surface morphology.

to stabilize and made *i-t* curves horizontal, but for high ones the values of current density were raised with time. Observing the surface after experiments, some areas had no film deposition because of seethe or bubbles adherence. And when presented in aqueous deposition baths, In and Ga deposition efficiencies are limited by  $H^+$  reduction, which cause composition inhomogeneity and pinholes in the film and hence limit the cell efficiencies [18]. To eliminate the effect of hydrogen generation, thereafter electrodeposition was performed by stirring with a magnetic bar.

Figure 3 shows the representative XRD pattern for stoichiometry CIGS samples, annealed and as-annealed, prepared at  $-1350$  mV versus SCE. In the as-deposited sample, pattern just showed a peak at  $2\theta = 28.7^\circ$  and the preferred formation of compound is not formed. Furthermore, the uniformity of the thin film is not good without magnetic stirring being used in the deposition procedure. After annealing the sample ( $400^\circ\text{C}$ , 1 hours, Ar ambient), the quaternary compound, CIGS, is dominantly formed to be chalcopyrite structure in the deposited film. Sharp peaks at  $2\theta = 26.9^\circ$ ,  $44.7^\circ$ , and  $53.0^\circ$  corresponding to the diffraction of the (112), (220), and (312) planes were formed. The  $2\theta$  value for (112) plane changed from  $28.7^\circ$  to  $26.9^\circ$ . The phenomenon could be due to the facts that the residual stress would exist in the thin film during electrodeposition processes. The residual stress might lead to lattice anisotropic deformation. The diffraction

peak shifted from high to low degree indicated that the lattice spaces increased after annealing. Furthermore, it suggested that the residual stress may be responsible for tensile stress. Figure 4 presents XRD patterns of the samples and thus heat treated after electrodeposition by different deposition potentials. Formation of the main phase of chalcopyrite structure is observed in all samples except  $-1950$  mV one, which had only one preferred orientation at  $2\theta = 26.9^\circ$ . However, in cases of potentials  $-950$  mV and  $-1150$  mV, there appeared another peak at  $2\theta = 37.5^\circ$ . But the peak disappeared when applied potential was beyond  $-1350$  mV. It suggested that would have been a secondary phase at lower electrodeposition bias. The peak of secondary phase corresponded to (203) plane of Cu-In alloyed film that annealed to be crystallized to provide the  $C_{11}In_9$  phase (stable up to  $320^\circ\text{C}$ ) [18]. The small positive shift in  $2\theta$  value of (112) peak indicated the incorporation of Ga and In sites and hence a decrease in lattice parameter [24].

Figure 5 shows the EDX compositional analysis data, which are normalized to Cu = 1, of the precursor films prepared by electrodeposition at different potentials and corresponded morphologies of top view by SEM. It notes that samples at which  $-950$  mV and  $-1150$  mV were applied are excluded because they did not detect Ga element in thin film. Surface morphology revealed a dendrite surface affected by the electrolyte concentration and duration of deposition which is due to limited ion concentration [18].

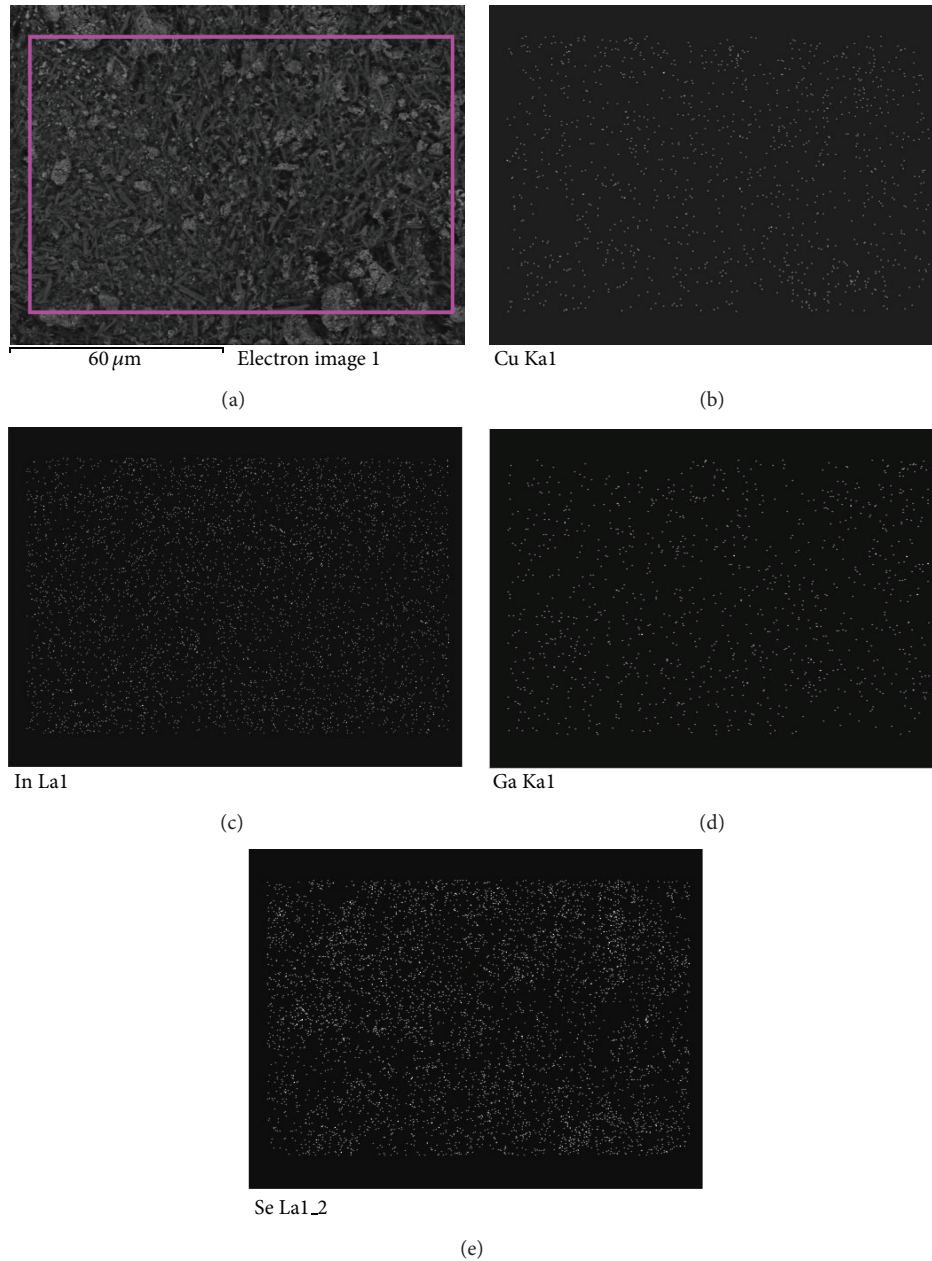


FIGURE 6: (a) SEM image and corresponding compositional mapping of (b) Cu, (c) In, (d) Ga, and (e) Se of the CIGS film prepared at  $-1350$  mV via electrodeposition.

When electrodeposition process begins, a compact thin film comprising metal elements is formed on the substrate. Based on our group's previous experimental results, it showed that the electrochemical kinetic behavior of the CIGS thin film is strongly influenced by the structure of the electrical double layer existing between the substrate and the electrolyte with different concentrations of  $\text{Ga}^{3+}$ . With an increase in the electrodeposition time, the kinetic behavior of this electrodeposition system was gradually dominated by the diffusion process rather than the charge-transfer process [25]. In this study, we also observed similar kinetic behavior. With time increasing, the diffusion-controlled reaction gradually dominated the mechanism of the electrodeposition of CIGS layers.

The limitation of the electrolyte concentration reaches the substrate, which ions consumed and deposited CIGS. Then, the dendrite structure appeared on the surface [26]. From the SEM images, it could be observed that when more potential was applied, the dendrite size decreased and surface porosity increased. This indicated that the number of nucleation sites in the case of lower deposition potentials is less than that of the higher one. It means that the coalescence of the elements occurs in fewer nucleated sites. Compositional analysis showed that stoichiometry of specimen prepared at  $-1550$  mV was the closest to ratio with  $\text{Cu} : \text{In} : \text{Ga} : \text{Se} = 1 : (1 - x) : x : 2$ . It seems the applied potential and compound stoichiometry are independent, and composition of In, Ga, and Se had

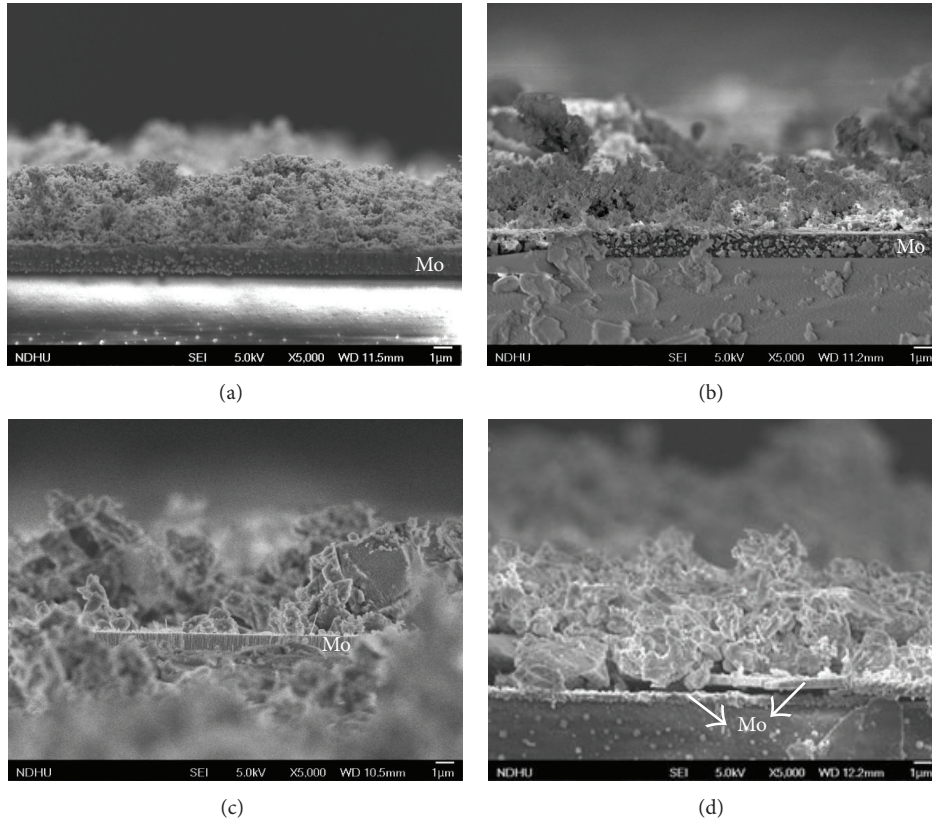


FIGURE 7: FE-SEM morphology cross-section of thin films deposition at potentials (a)  $-1350$  mV, (b)  $-1550$  mV, (c)  $-1750$  mV, and (d)  $-1950$  mV versus SCE.

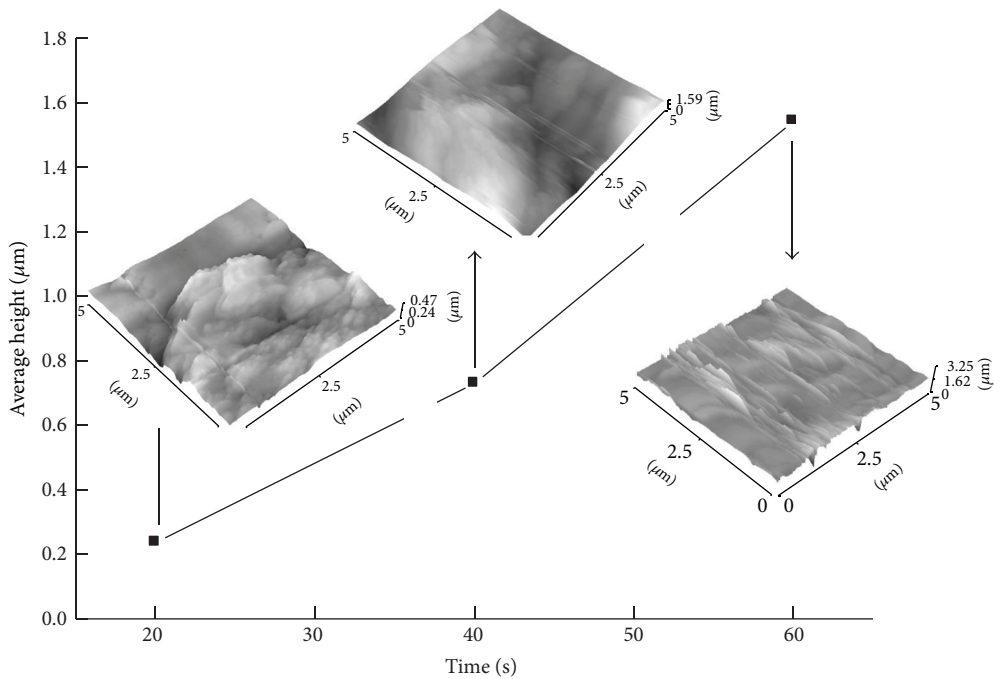


FIGURE 8: Average height measure by AFM for thin films deposited under potential  $-1350$  mV with different time and its relative surface morphology of AFM image.

TABLE 2: Roughness measured by AFM for CIGS thin films prepared at electrodeposition potential of  $-1350$  mV.

Electrodeposition time (s)	20	40	60
Roughness average (Ra)	0.0483	0.2516	0.1906
Roughness root mean square (RMS)	0.0606	0.2960	0.2601
Average height maximum	0.2354	0.7289	1.5423
Height maximum	0.4706	1.5879	3.2496

Unit:  $\mu\text{m}$ .

same trend with potential when normalized to  $\text{Cu} = 1$ . To investigate the elemental distribution of CIGS film prepared at  $-1350$  mV via electrodeposition, it was examined by SEM equipped with EDX. The compositional mapping of Cu, In, Ga, and Se exhibited uniform distribution of each element as shown in Figure 6, indicating that no second phases existed on the surface of film.

Figure 7 shows the morphology of the cross-section. As mentioned in the last paragraph, the deposition is limited by the electrolyte concentration that reaches the substrate. At lower applied potential, the metal ions in the bath were consumed slower and diffused more sufficiently than with higher applied potential conduction. Deposit film prepared at  $-1350$  mV was uniform and orderly. The bottom part of  $-1550$  mV cross-section is dense and compact, but with deposition time increasing, the follow-up deposit would become less smooth because of the effect of point discharge and diffusion. Even at  $-1750$  mV and  $-1950$  mV samples, some areas of Mo substrate were rarely deposited and some areas had masses of deposition. Table 2 shows the roughness compared with different deposition time measured by AFM. The roughness root mean square (RMS) and roughness average (Ra) values varied significantly between 20 seconds and 40 seconds; after 40 seconds the roughness varied slightly. It suggested that a large number of atoms did not generate and deposit on substrate surface at initial stage (from 0 to 20 seconds). When certain area of substrate surface had covered the early deposits, it would get advantages to enhance mass transfer process progress with short diffusion distance and high electrical potential gradients. Then the surface would become coarse in this stage (after 40 seconds). Figure 8 shows images and plots of the surface average height. The AFM was used to study the nucleation and development of roughness of the growth of CIGS film. The curve indicated that the roughness increased with deposition time. It was the evidence to explain the surface of thin film deposition influenced by point discharge and diffusion. At first, metal ions at cathode vicinity were depleted in the beginning, but ions cannot supply deposition on time completely. Some areas that had deposits would get advantages, such as short distance for diffusion and high electrical potential gradients due to high charge density. These effects enhanced mass transfer process progress at these knobby parts; then the surface would not worsen uniformly with time. To avoid this behavior, deposition potential, operation time, and stirring should be considered as control parameters. The theoretical

thickness of the electrodeposited CIGS layer is determined by the following relationship [27]:  $d = (j \cdot Mt) / (n \cdot F \cdot p)$ , where  $j$  is the current density ( $\text{mA}/\text{cm}^2$ ),  $M$  is the molecular weight of CIGS (for  $\text{CuIn}_{0.5}\text{Ga}_{0.5}\text{Se}_2$  is 315.18 g),  $t$  is the time for which the current is passed,  $p$  is the density of CIGS,  $F$  is the Faraday constant (96500 C), and  $n$  is the number of electrons transferred. Based on this equation, one could evaluate the deposited thickness of the CIGS material which was controlled.

## 4. Conclusions

One-step cathodic electrodeposition of CIGS thin films has been prepared, and the XRD patterns show that annealing treatment improved the crystallization of electrodeposited films and formed CIGS chalcopyrite structure, and at low applied deposition voltage (below  $-1150$  mV versus SCE) there appeared the second phase of Cu-In alloys. The morphology of cross-section displayed that applied voltage at  $-1350$  mV versus SCE has uniform deposition. Ga element could not be detected by EDX when deposition potential is below  $-1150$  mV versus SCE. It was found that the compound did not match exact stoichiometry of  $\text{Cu}:\text{In}:\text{Ga}:\text{Se} = 1 : x : (1 - x) : 2$ . Varying the applied potentials during electrodeposition could control the properties and compounds of CIGS thin film, but the effect was restricted. It should therefore be operated in coordination with electrolyte concentration adjustment in solution to achieve a more ideal composition.

## Conflict of Interests

The authors declare that there is no conflict of interests regarding the publication of this paper.

## Acknowledgments

The authors would like to thank the National Science Council of Taiwan for financially supporting this research under Contract no. NSC 99-2113-M-259-003 and Nanotechnology Research Center, National Dong Hwa University, for FE-SEM morphology measurements.

## References

- [1] J. E. Jaffe and A. Zunger, "Theory of the band-gap anomaly in  $\text{ABC}_2$  chalcopyrite semiconductors," *Physical Review B*, vol. 29, no. 4, pp. 1882–1906, 1984.
- [2] R. N. Bhattacharya, "CIGS-based solar Cells prepared from electrodeposited stacked Cu/In/Ga Layers," *Solar Energy Materials and Solar Cells*, vol. 113, pp. 96–99, 2013.
- [3] C. Xu, H. Zhang, J. Parry, S. Perera, G. Long, and H. Zeng, "A single source three-stage evaporation approach to CIGS absorber layer for thin film solar cells," *Solar Energy Materials and Solar Cells*, vol. 117, pp. 357–362, 2013.
- [4] N. D. Sang, P. H. Quang, L. T. Tu, and D. T. B. Hop, "Effect of electrodeposition potential on composition and morphology of CIGS absorber thin film," *Bulletin of Materials Science*, vol. 36, no. 4, pp. 735–741, 2013.

- [5] S. Nakamura and A. Yamamoto, "Electrodeposited  $\text{CuInS}_2$ -based thin-film solar cells," *Solar Energy Materials and Solar Cells*, vol. 75, no. 1-2, pp. 81–86, 2003.
- [6] A. M. Martínez, L. G. Arriaga, A. M. Fernández, and U. Cano, "Band edges determination of  $\text{CuInS}_2$  thin films prepared by electrodeposition," *Materials Chemistry and Physics*, vol. 88, no. 2-3, pp. 417–420, 2004.
- [7] A. M. Fernandez and R. N. Bhattacharya, "Electrodeposition of  $\text{CuIn}_{1-x}\text{Ga}_x\text{Se}_2$  precursor films: optimization of film composition and morphology," *Thin Solid Films*, vol. 474, pp. 10–13, 2005.
- [8] S. Taunier, J. Sixx-Kurdi, P. P. Grand et al., " $\text{Cu}(\text{In,Ga})(\text{S,Se})_2$  solar cells and modules by electrodeposition," *Thin Solid Films*, vol. 480–481, pp. 526–531, 2005.
- [9] C. H. Chen, W. C. Shih, C. Y. Chien, C. H. Hsu, Y. H. Wu, and C. H. Lai, "A promising sputtering route for one-step fabrication of chalcopyrite phase  $\text{Cu}(\text{In,Ga})\text{Se}_2$  absorbers without extra Se supply," *Solar Energy Materials and Solar Cells*, vol. 103, pp. 25–29, 2012.
- [10] C. Chen, T. Lin, C. Hsu, S. Wei, and C. Lai, "Comprehensive characterization of Cu-rich  $\text{Cu}(\text{In,Ga})\text{Se}_2$  absorbers prepared by one-step sputtering process," *Thin Solid Films*, vol. 535, no. 1, pp. 122–126, 2013.
- [11] A. Duchatelet, T. Sidali, N. Loones, G. Savidand, E. Chassaing, and D. Lincot, "12.4% Efficient  $\text{Cu}(\text{In,Ga})\text{Se}_2$  solar cell prepared from one step electrodeposited Cu-In-Ga oxide precursor layer," *Solar Energy Materials and Solar Cells*, vol. 119, pp. 241–245, 2013.
- [12] W. Wang, Y. W. Su, and C. H. Chang, "Inkjet printed chalcopyrite  $\text{CuIn}_x\text{Ga}_{1-x}\text{Se}_2$  thin film solar cells," *Solar Energy Materials & Solar Cells*, vol. 95, no. 9, pp. 2616–2620, 2011.
- [13] A. E. Delahoy, L. Chen, M. Akhtar, B. Sang, and S. Guo, "New technologies for CIGS photovoltaics," *Solar Energy*, vol. 77, no. 6, pp. 785–793, 2004.
- [14] M. Kaelin, D. Rudmann, and A. N. Tiwari, "Low cost processing of CIGS thin film solar cells," *Solar Energy*, vol. 77, no. 6, pp. 749–756, 2004.
- [15] M. Venkatachalam, M. D. Kannan, N. Muthukumarasamy et al., "Investigations on electron beam evaporated  $\text{Cu}(\text{In}_{0.85}\text{Ga}_{0.15})\text{Se}_2$  thin film solar cells," *Solar Energy*, vol. 83, no. 9, pp. 1652–1655, 2009.
- [16] V. S. Saji, I. H. Choi, and C. W. Lee, "Progress in electrodeposited absorber layer for  $\text{CuIn}_{(1-x)}\text{Ga}_x\text{Se}_2$  (CIGS) solar cells," *Solar Energy*, vol. 85, no. 11, pp. 2666–2678, 2011.
- [17] T. Yukawa, K. Kuwabara, and K. Koumoto, "Electrodeposition of  $\text{CuInS}_2$  from aqueous solution (II) electrodeposition of  $\text{CuInS}_2$  film," *Thin Solid Films*, vol. 286, no. 1-2, pp. 151–153, 1996.
- [18] M. Paunovic and M. Schlesinger, *Fundamentals of Electrochemical Deposition*, Wiley-Interscience, Hoboken, NJ, USA, 1998.
- [19] R. Caballero, C. Guillén, M. T. Gutiérrez, and C. A. Kaufmann, " $\text{CuIn}_{1-x}\text{Ga}_x\text{Se}_2$ -based thin-film solar cells by the selenization of sequentially evaporated metallic layers," *Progress in Photovoltaics: Research and Applications*, vol. 14, no. 2, pp. 145–153, 2006.
- [20] M. E. Calixto, P. J. Sebastian, R. N. Bhattacharya, and R. Noufi, "Compositional and optoelectronic properties of CIS and CIGS thin films formed by electrodeposition," *Solar Energy Materials and Solar Cells*, vol. 59, no. 1, pp. 75–84, 1999.
- [21] F. Chraïbi, M. Fahoume, A. Ennaoui, and J. L. Delplancke, "Influence of citrate ions as complexing agent for electrodeposition of  $\text{CuInSe}_2$  thin films," *Physica Status Solidi (A) Applied Research*, vol. 186, no. 3, pp. 373–381, 2001.
- [22] M. C. F. Oliveira, M. Azevedo, and A. Cunha, "A voltammetric study of the electrodeposition of  $\text{CuInSe}_2$  in a citrate electrolyte," *Thin Solid Films*, vol. 405, pp. 129–134, 2002.
- [23] R. N. Bhattacharya, W. Batchelor, H. Wiesner et al., "14.1%  $\text{CuIn}_{1-x}\text{Ga}_x\text{Se}_2$ -based photovoltaic cells from electrodeposited precursors," *Journal of the Electrochemical Society*, vol. 145, no. 10, pp. 3435–3440, 1998.
- [24] S. M. Babu, A. Ennaoui, and M. C. Lux-Steiner, "Composition and growth procedure-dependent properties of electrodeposited  $\text{CuInSe}_2$  thin films," *Journal of Crystal Growth*, vol. 275, no. 1-2, pp. e1241–e1246, 2005.
- [25] Y. P. Fu, R. W. You, and K. K. Lew, "Electrochemical properties of solid-liquid interface of  $\text{CuIn}_{1-x}\text{Ga}_x\text{Se}_2$  prepared by electrodeposition with various gallium concentrations," *Journal of the Electrochemical Society*, vol. 156, no. 9, pp. E133–E138, 2009.
- [26] S. H. Kang, Y. Kim, D. Choi, and Y. Sung, "Characterization of electrodeposited  $\text{CuInSe}_2$  (CIS) film," *Electrochimica Acta*, vol. 51, no. 21, pp. 4433–4438, 2006.
- [27] A. Parrettam, M. L. Addonizio, A. Agati et al., "Influence of morphology and structure of Cu/In alloys on the properties of  $\text{CuInSe}_2$ ," *Japanese Journal of Applied Physics*, vol. 32, pp. 80–83, 1993.

## Research Article

# Fabrication of Antireflection Nanodiamond Particle Film by the Spin Coating Deposition Technique

Chii-Ruey Lin,<sup>1,2,3</sup> Hong-Ming Chang,<sup>2,3</sup> Minh-Khoa BenDao,<sup>2,3</sup>  
Hsiu Hsien Chiang,<sup>2,3</sup> and Wei-En Chen<sup>2,3</sup>

<sup>1</sup> Department of Mechanical Engineering and Institute of Manufacturing Technology, National Taipei University of Technology, Taipei 106, Taiwan

<sup>2</sup> Graduate Institute of Mechanical and Electrical Engineering, National Taipei University of Technology, Taipei 106, Taiwan

<sup>3</sup> Institute of Mechatronic Engineering, National Taipei University of Technology, Taipei 106, Taiwan

Correspondence should be addressed to Chii-Ruey Lin; [chanyu.2@hotmail.com](mailto:chanyu.2@hotmail.com)

Received 6 May 2014; Revised 23 May 2014; Accepted 23 May 2014; Published 14 July 2014

Academic Editor: Ching-Song Jwo

Copyright © 2014 Chii-Ruey Lin et al. This is an open access article distributed under the Creative Commons Attribution License, which permits unrestricted use, distribution, and reproduction in any medium, provided the original work is properly cited.

Diamond-based antireflective (AR) coatings were fabricated using a spin coating of diamond suspension at room temperature as nucleation enhancement procedure and microwave plasma enhanced chemical vapour deposition. Various working pressures were used to investigate their effect on the optical characterization of the as-deposited diamond films. Scanning electron microscopy (SEM) and atomic force microscopy (AFM) were employed to analyze the surface properties of the diamond films. Raman spectra and transmission electron microscopy (TEM) also were used for analysis of the microstructure of the films. The results showed that working pressure had a significant effect on thickness, surface roughness, and wettability of the as-deposited diamond films. Deposited under 35 Torr or working pressure, the film possessed a low surface roughness of 13.8 nm and fine diamond grain sizes of 35 nm. Reflectance measurements of the films also were carried out using UV-Vis spectrometer and revealed a low reflectance value of the diamond films. The achievement demonstrated feasibility of the proposed spin-coating procedure for large scale production and thus opens up a prospect application of diamond film as an AR coating in industrial optoelectronic device.

## 1. Introduction

In last decades, prosperous achievements in material processing technologies as well as semiconductor engineering have opened up a prospect of optoelectronic devices in many fields such as solar energy, photo detectors, measurement, medical, and so forth [1–5]. Many efforts have been devoted aiming at the performance and reliability of the devices in harsh working conditions. Since the operation of these device is mainly based on optoelectronic conversion, the optical characteristics are vital to the fate of the devices, leading to the demand in high transmittance absorption layers on various wavelength ranges. Besides the improvement in optical transparency, antireflective (AR) coatings are also used in most of the aforementioned optical devices to eliminate light reflection and inhomogeneities on the surface of the absorption layers. Till now, AR coatings structured by

various transparent layers with distinctive optical refractive indices are one of the most popular and have attained much attention owing to their high reflective performance on even infrared wavelength range of few micrometers [6–8]. These coatings usually consist of commonly fluoride layers with low refractive indices and other high refractive indices layers. It should be noticed here that those fluoride materials lack good mechanical and chemical properties which can be seriously affected by severe environment, resulting in requirement of protective layers, thus increasing manufacturing cost as well as performance of the whole optical system.

Diamonds are promising candidates for AR coating materials owing to their excellent properties including high hardness, high thermal conductivity, optical transparency, and high refractive index [9–13]. Few techniques have been developing to deposit diamond films on various substrate materials such as physical vapor deposition (PVD), chemical

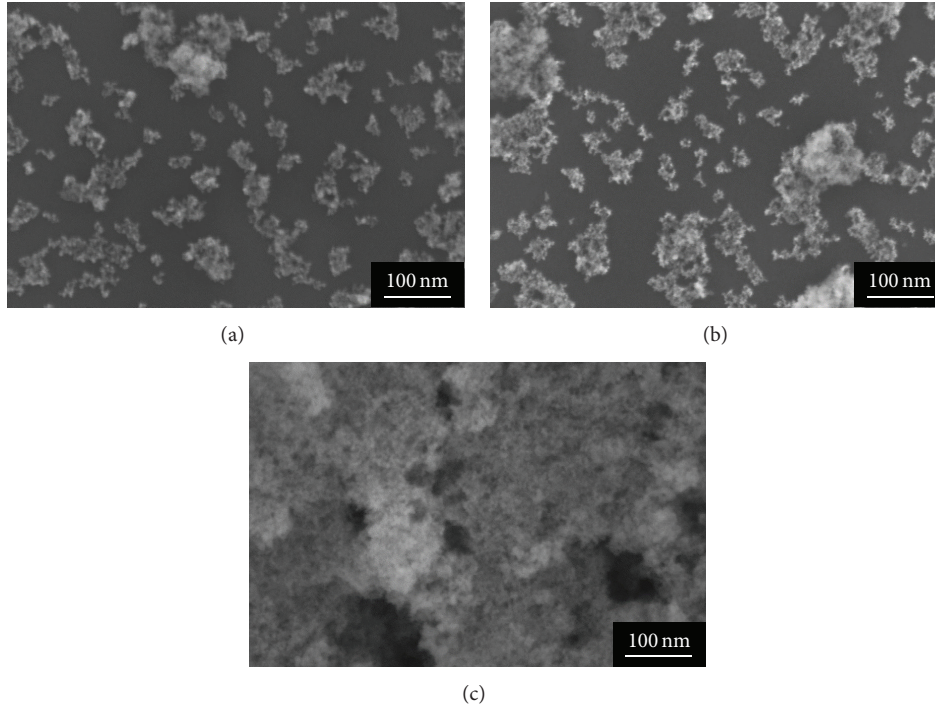


FIGURE 1: Morphology of the as-prepared diamond layers on D263T glass substrate using spin coating with different parameters.

vapor deposition (CVD), and sol-gel methods [14–16]. In this study, we demonstrate a method to fabricate diamond-based AR coatings using a spin coating process of nanodiamond particles (NDPs) suspension on optical glass. This method is inexpensive, environmental friendly, and relatively easy to conduct and thus has the feasibility for large scale production.

This study aimed to deposit antireflection NPs thin films on quartz substrates at various working conditions to identify the properties of the NPs films. The corresponding microstructure and mechanical and optical properties of NDPs films were investigated by scanning electron microscope (SEM), atomic force microscopy (AFM), contact angle goniometry, and optical analysis measurements, respectively.

## 2. Experimental

Diamond suspension was prepared using NDPs, having 5–10 nm in size, dispersed in methanol solution ( $\text{CH}_3\text{OH}$ , Sigma Aldrich). Various concentrations of the suspension were used as 0.1, 0.3, and 0.5 wt%. In order to improve the purity of pristine particles, an acid treatment procedure was employed using a mixture of nitrite, sulfuric acid, and hydrogen peroxide. The details of the purification process were reported in our previous works [2]. The treated NDPs were then rinsed in DI water, followed by a recovery step with centrifugation equipment, and finally evaporated at room temperature.

The diamond suspensions were prepared dispersion of purified NDPs in methanol solution for 2 hours with ultrasonication enhancement. Spin coating was then employed

TABLE 1: The spin coating parameters of NDPs films for each factor and level as defined by the Taguchi experiment design.

Parameters	Sample 1	Sample 2	Sample 3
Spin speed (rpm)	2500	3500	5500
Spin time (sec.)	30	30	30
Heat treatment ( $^{\circ}\text{C}$ )	300	300	300
Concentration (wt%)	0.1	0.3	0.5

to disperse NDPs onto quartz substrate. The substrate was purchased from Mustec Corp., having high luminous transmittance and refractive index of 1.45. In this study, spin coating procedures were carried out at room temperature, with parameters shown in Table 1. The nucleated substrates were used for preparation of diamond films in microwave plasma enhanced vapour deposition (MPECVD) process. In all our experiments, the plasma during the diamond growth was induced by a microwave power of 900 W and in mixture of methane and hydrogen as the precursor gases whose concentration ratio was 5%  $\text{CH}_4$ :95%  $\text{H}_2$ . The working pressure was varied from 40 Torr to 100 Torr (40, 55, 70, 85, and 100 Torr).

Optical emission spectrometry (OES, B&WTEK BTC112E) was utilized to on-line monitor the produced carbon radicals in plasma under various deposition pressures. The assessment of the as-deposited diamond films was carried out using field emission scanning electron microscope (FESEM, LEO 1530), atomic force microscope (Digital instrument D3100), and transmission electron microscope (TEM, JEOL JEM-2100F). The bonding structure of the films was

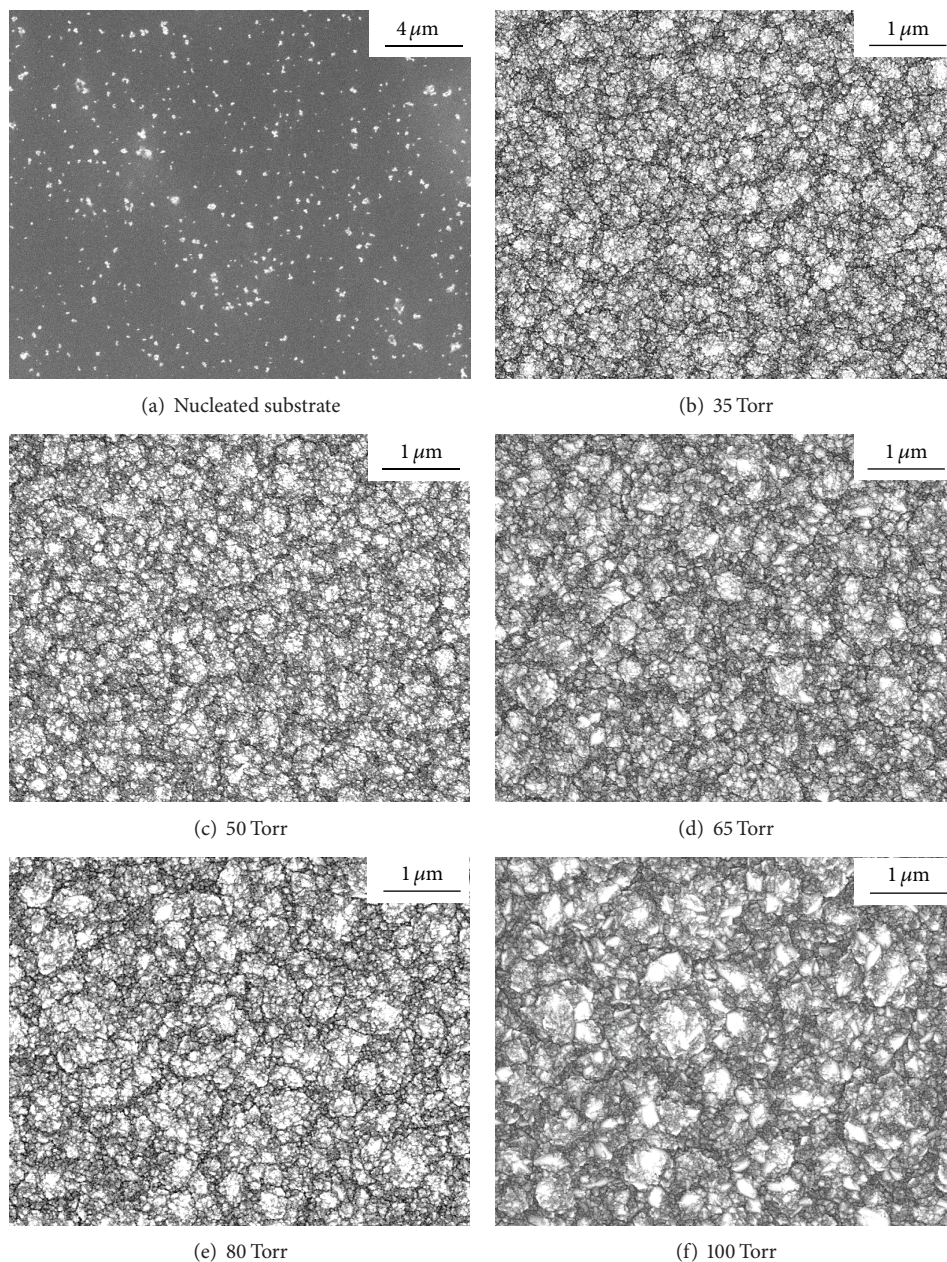


FIGURE 2: SEM images of (a) quartz substrate spin coated with NDPs and diamond films grown at various working pressures: (b) 35 Torr, (c) 50 Torr, (d) 65 Torr, (e) 80 Torr, and (f) 100 Torr, respectively.

also characterized by X-ray photoelectron spectroscopy (XPS) and Raman spectrophotometer (Ar laser, wavelength of 325 nm).

### 3. Results and Discussion

Figure 1 shows the morphology from the plan view of the surface of the as-prepared NDPs layers for samples 1, 2, and 3. The quartz substrates were coated under various parameters such as spin speed, spin time, heat treatment, and concentration wt%. The results demonstrated that sample 2 (Figure 1(b)) possessed a relatively high diamond nucleation density for further CVD diamond film deposition.

The morphology of the as-deposited diamond films was analyzed by SEM. Figure 2(a) represents the quartz substrate after spin coating procedure with 0.3 wt% solution of the NDPs. The homogeneous distribution of the NDPs on the substrate exhibited a good dispersion of the prepared diamond suspension. It is reported that the diamond growth in the  $\text{CH}_4 : \text{H}_2$  plasma was found to be induced by both methyl radicals and  $\text{C}_2$  species. Since the nucleations via  $\text{C}_2$  dimer species are not allowed by nondiamond substrates such as quartz, the existence of the spin coated diamond particles on the substrate surface can enhance the diamond growth. Figures 2(b)–2(e) show the evolution of surface morphology of the diamond films grown by MPECVD with various

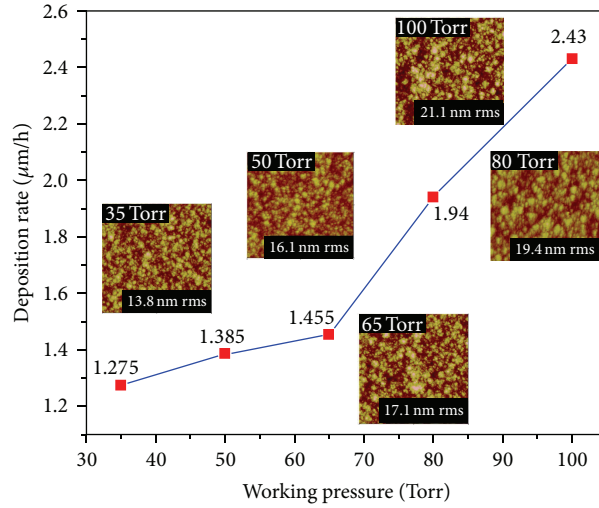


FIGURE 3: The dependence of deposition rate and surface roughness of the as-prepared diamond films on the working pressure.

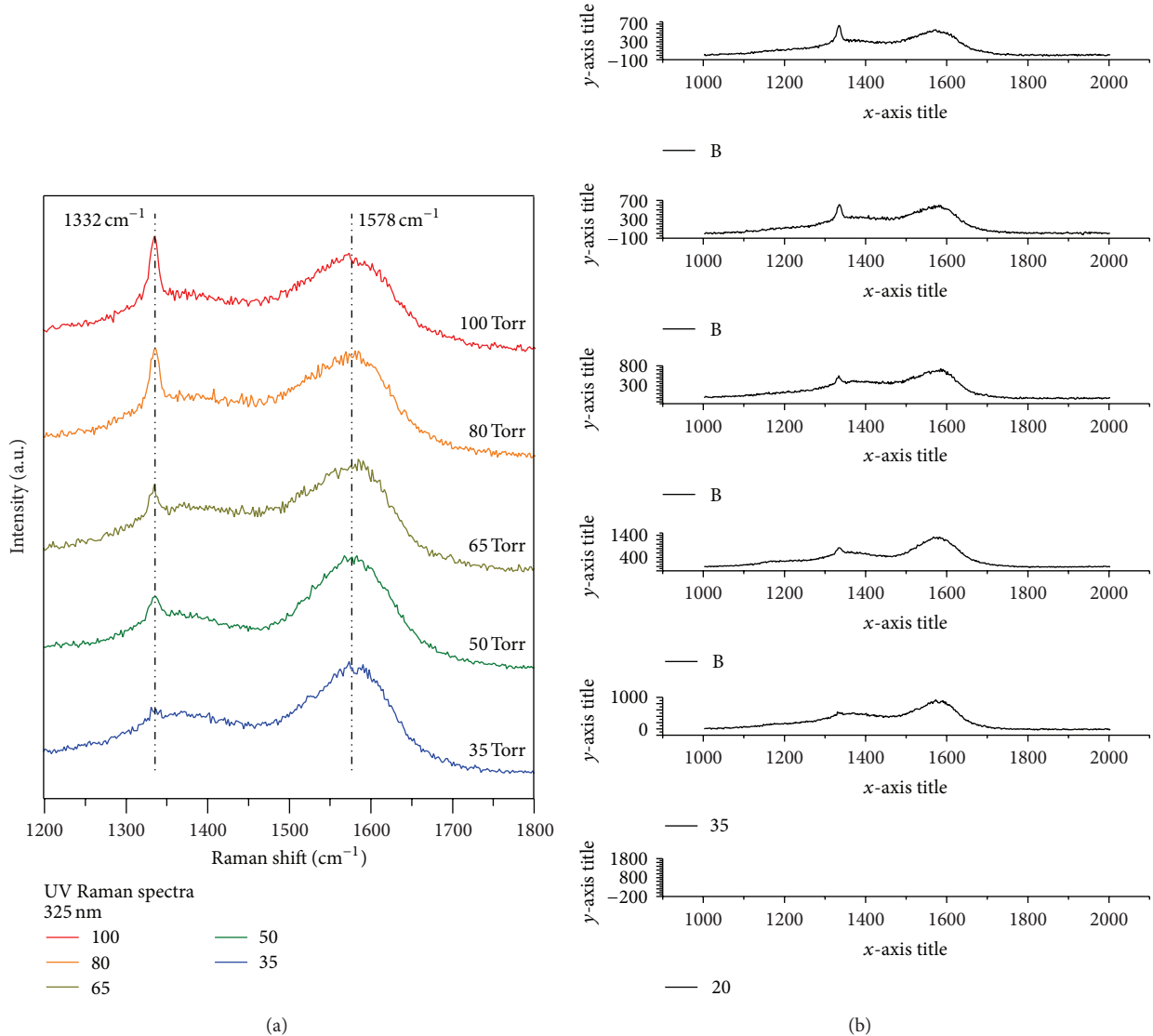


FIGURE 4: The Raman spectra of the as-prepared diamond films deposited under working pressure ranged from 35 Torr to 100 Torr.

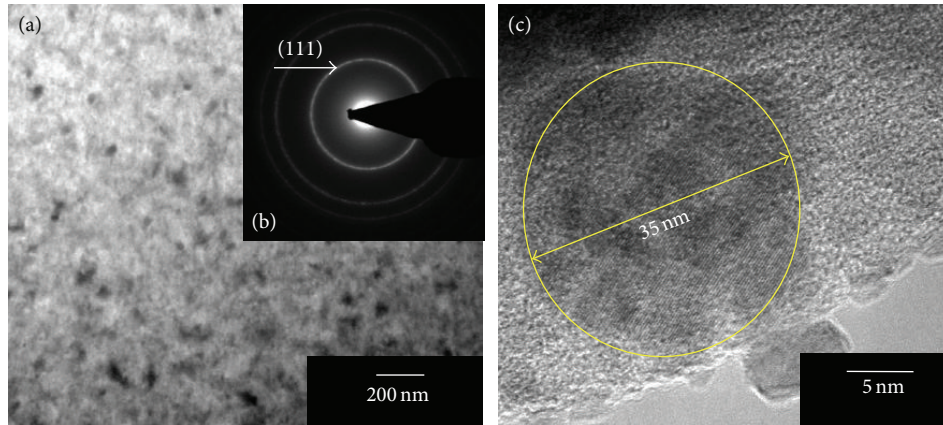


FIGURE 5: (a), (b), and (c) Bright field TEM image, corresponding SAED pattern, and high resolution TEM images for diamond films deposited at 35 Torr of working pressure.

working pressures. Diamond films grown at 35 Torr exhibited a smooth morphology with very fine grains less than 50 nm in size and without any apparent pinholes. The surface morphology of the diamond films deposited at 100 Torr, as shown in Figure 2(f), reveals relatively large grain cluster having size of 100 nm and above.

The effects of working pressure on the deposition rate and surface roughness of the as-prepared films are demonstrated in Figure 3. As the deposition pressure increases from 35 to 100 Torr, the average deposition rate which was calculated based on cross-section SEM images owing to the increase in produced carbon precursors and surface roughness was increased from 1.275 to 2.43 m/h and from 13.8 to 21.1 nm, respectively. These confirm the aforementioned trends on the change of clustered degree and grain size of the diamond films.

The Raman spectra of the diamond films deposited under various working pressures are shown in Figure 4. Depositing under 35 Torr, the diamond peak at  $1332\text{ cm}^{-1}$  ( $\text{sp}^3$ -bonded carbon phase) of the films is weak and seems to be overlapped by the disordered band (D band,  $\text{sp}^2$ -bonded carbon phase) at around  $1350^{-1}$ , exhibiting the nanometered size of diamond crystallite size. This overlap can be confirmed through Raman spectra analysis conducted with visible wavelength (514 nm). With the increasing of the deposition pressure, the characteristic peak of diamond gradually sharpens and increases in intensity indicate the increasing of diamond crystallite size. Moreover, the relative ratio in intensity between the diamond peak and the G band ( $\text{sp}^2$ -bonded carbon phase) at  $1579\text{ cm}^{-1}$  reveals the decrease in content of the grain boundary in the films.

Figure 4(a) shows the plan view TEM image of the diamond films deposited with working pressure of 35 Torr, which demonstrates that the films consisted of diamond grain with nanometered size dispersed in the amorphous carbon matrix. As shown in Figure 4(b), the corresponding SAED pattern of the diamond films with sharp rings diffraction patterns revealed that the diamond grain possessed high crystallinity, Figure 5.

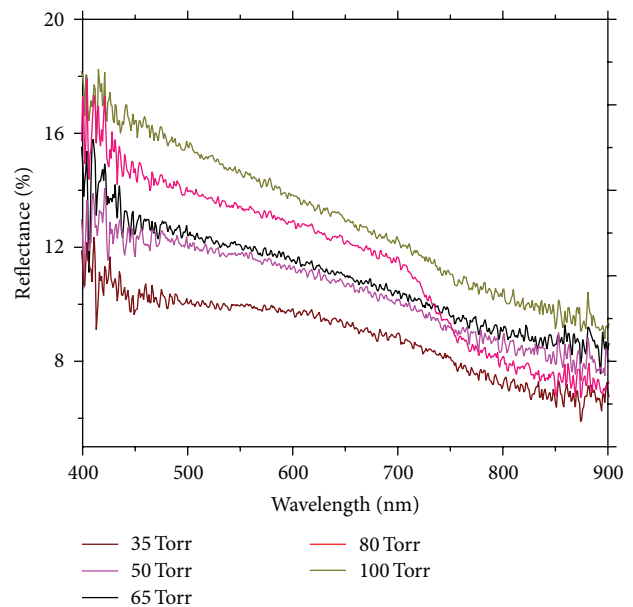


FIGURE 6: Reflection of the diamond films deposited under working pressure ranged from 35 Torr to 100 Torr.

Figure 6 shows the reflection of the fabricated diamond-based AR coating on quartz substrate under various deposition pressures. All the reflection analyses were conducted by a UV/vis spectrophotometer. The result revealed that diamond film deposited under 25 Torr possessed quite low reflectance of 10% and below in visible wavelength range which is feasible for further antireflective applications in solar cell devices. Depositing under higher working pressure, both grain sizes and surface roughness of the films significantly increased, thus increasing the reflectance.

#### 4. Conclusions

In this study, diamond-based antireflection coating was fabricated using spin coating and microwave plasma enhanced

chemical vapour deposition. It was shown that spin coating of 0.3 wt% of NDPs suspension ensured a high nucleation density and low surface roughness for CVD diamond growth. Diamond films deposited under 35 Torr of working pressure were found to have low surface roughness and the lowest reflectance of 10% and below at visible wavelength range. The above results demonstrate that the proposed fabrication procedures are feasible for large scale production, thus opening up a prospect application of diamond-based AR coating in optoelectronic device.

### Conflict of Interests

The authors declare that there is no conflict of interests regarding the publication of this paper.

### Acknowledgment

This work was financially supported by the main research projects of the National Science Council of Republic of China under Grant nos. NSC 103-2622-E-027-005-CC2 and NSC 102-2221-E-027-040-MY2.

### References

- [1] C. C. Chou and S. H. Lee, "Rheological behavior and tribological performance of a nanodiamond-dispersed lubricant," *Journal of Materials Processing Technology*, vol. 201, no. 1-3, pp. 542-547, 2008.
- [2] C.-R. Lin, D.-H. Wei, M.-K. BenDao, H.-M. Chang, W.-E. Chen, and J.-A. Lee, "Effects of surface modification of nanodiamond particles for nucleation enhancement during its film growth by microwave plasma jet chemical vapour deposition technique," *Advances in Materials Science and Engineering*, vol. 2014, Article ID 937159, 5 pages, 2014.
- [3] W. H. Liao, C. R. Lin, and D. H. Wei, "Effect of CH<sub>4</sub> on the growth behavior, structure, and transparent properties of ultrananocrystalline diamond films synthesized by focused microwave Ar/CH<sub>4</sub>/H<sub>2</sub> jets," *Applied Surface Science*, vol. 27, pp. 324-330, 2013.
- [4] C. Lu, S. B. Tian, C. Z. Gu, and J. J. Li, "Grain boundary effect on the superconducting transition of microcrystalline boron-doped diamond films," *Diamond and Related Materials*, vol. 20, no. 2, pp. 217-220, 2011.
- [5] H. Li, D. Sang, S. Cheng et al., "Epitaxial growth of ZnO nanorods on diamond and negative differential resistance of n-ZnO nanorod/p-diamond heterojunction," *Applied Surface Science*, vol. 280, pp. 201-206, 2013.
- [6] Y. Pan, L. Hang, Z. Wu, and Y. Yin, "Design and fabrication of ultra broadband infrared antireflection hard coatings on ZnSe in the range from 2 to 16 μm," *Infrared Physics and Technology*, vol. 52, no. 5, pp. 193-195, 2009.
- [7] G. G. Bhatt, A. L. Patel, M. S. Desai, and C. J. Panchal, "Laser induced damage studies on Al<sub>2</sub>O<sub>3</sub>, SiO<sub>2</sub>, and MgF<sub>2</sub> thin films for anti-reflection coating application in high power laser diode," *Journal of Nano & Electronic Physics*, vol. 5, Article ID 02016, 2013.
- [8] W. Glaubitt and P. Löbmann, "Antireflective coatings prepared by sol-gel processing: principles and applications," *Journal of the European Ceramic Society*, vol. 32, no. 11, pp. 2995-2999, 2012.
- [9] A. G. Kutsay, N. V. Gontar, S. N. Novikov et al., "Diamond-like carbon films in multilayered interference coatings for IR optical elements," *Diamond & Related Materials*, vol. 10, pp. 1846-1849, 2001.
- [10] H. Krüger, A. Hertwig, U. Beck, and E. Kemnitz, "Low temperature sol-gel metal oxide and fluoride layer stacks for optical applications," *Thin Solid Films*, vol. 518, no. 21, pp. 6080-6086, 2010.
- [11] C. R. Lin, H. M. Chang, and C. K. Chang, "Fabrication of high transparency diamond-like carbon film coating on D263T glass at room temperature as an antireflection layer," *International Journal of Photoenergy*, vol. 2013, Article ID 612163, 8 pages, 2013.
- [12] C.-R. Lin, D.-H. Wei, M.-K. BenDao, W.-E. Chen, and T.-Y. Liu, "Development of high-performance UV detector using nanocrystalline diamond thin film," *International Journal of Photoenergy*, vol. 2014, Article ID 452192, 2014, In press.
- [13] C. W. Padgett, O. Shenderova, and D. W. Brenner, "Thermal conductivity of diamond nanorods: molecular simulation and scaling relations," *Nano Letters*, vol. 6, no. 8, pp. 1827-1831, 2006.
- [14] Y. Lifshitz, C. H. Lee, Y. Wu, W. J. Zhang, I. Bello, and S. T. Lee, "Role of nucleation in nanodiamond film growth," *Applied Physics Letters*, vol. 88, Article ID 243114, 2006.
- [15] T. Makino, H. Kato, S. Ri, S. Yamasaki, and H. Okushi, "Homoepitaxial diamond  $p-n^+$  junction with low specific on-resistance and ideal built-in potential," *Diamond and Related Materials*, vol. 17, no. 4-5, pp. 782-785, 2008.
- [16] K. Hanada, K. Matsuzaki, and T. Sano, "Nanocrystalline diamond films fabricated by sol-gel technique," *Surface Science*, vol. 601, no. 18, pp. 4502-4505, 2007.

## Research Article

# Development of High-Performance UV Detector Using Nanocrystalline Diamond Thin Film

C. R. Lin,<sup>1,2</sup> D. H. Wei,<sup>1,2</sup> M. K. BenDao,<sup>1,2</sup> W. E. Chen,<sup>1,2</sup> and T. Y. Liu<sup>1,2</sup>

<sup>1</sup> Department of Mechanical Engineering and Institute of Manufacturing Technology, National Taipei University of Technology, Taipei 106, Taiwan

<sup>2</sup> Institute of Mechatronic Engineering, National Taipei University of Technology, Taipei 106, Taiwan

Correspondence should be addressed to C. R. Lin; [crlin@ntut.edu.tw](mailto:crlin@ntut.edu.tw)

Received 11 April 2014; Accepted 19 May 2014; Published 13 July 2014

Academic Editor: Yen-Lin Chen

Copyright © 2014 C. R. Lin et al. This is an open access article distributed under the Creative Commons Attribution License, which permits unrestricted use, distribution, and reproduction in any medium, provided the original work is properly cited.

Nanocrystalline diamond (NCD) films are promising materials for wide-spread applications due to their outstanding characteristics of chemical, physical, and highly smooth surface. Our present work aimed at the fabrication of high performance diamond-based UV detector. NCD films were prepared by microwave plasma enhanced chemical vapor deposition process, and then Au interdigital electrodes were deposited onto the surface of the as-grown NCD film by sputtering technique. Annealing procedures were conducted at various temperatures to obtain Ohmic contact of NCD/Au structure. The surface morphology, microstructure, and wettability of the NCD films were analyzed by scanning electron microscopy, atomic force microscopy, Raman spectroscopy, X-ray photoelectron spectroscopy, transmission electron microscopy, and water contact angle measurement, respectively. The electrical property and photoconductivity of the fabricated devices were tested for UV detection application. It was found that the NCD films possessed high  $sp^3$  fraction of 68.6%, low surface roughness of 9.6 nm, and good hydrophobicity, as deposited under working pressure of 40 Torr. Also, the NCD/Au structure annealed at 500°C exhibited a good Ohmic contact characteristic, high detection efficiency, and fast response to UV irradiation in air ambient. The proposed study indeed demonstrates prospective applications of NCD films in UV detector, photocatalyst, solar cell, and so on.

## 1. Introduction

Along with the development of electronics engineering and nanotechnologies, ultraviolet (UV) sensors have attained increasing attention in which their applications have flourished over the past decade, including energy, defense, space-to-space communications, medical treatment, food processing, and water treatment. Till now, several wide-band-gap materials like GaN, Si, AlN, and ZnO compounds have been investigated for the uses in UV sensors [1–4]. Aiming at the aforementioned practical applications, however, many researches have been devoted to achieve highly efficient and highly stable operations of the device in harsh environment, leading to the quest for good performance materials and functional structures [5–7].

Among the semiconductor materials, diamonds possess unrivalled characteristics such as good hardness, wear resistivity, high thermal conductivity, high optical transparency,

and chemical inertness [8–12]. As nanoscale structures, nanodiamonds are considered to possess a wide band-gap (~5.5 eV) and large breakdown electric field (~10 MV/cm), resulting in low leakage current [13]. To date, the synthesis techniques of nanodiamond materials have been developed for decades [14–17]. Owing to the above advantages, nanodiamond materials are indeed a promising candidate for UV detection applications. The diamond-based devices with homojunction (including p-n, p-i-m, or p-i-n types), however, seem to be challenged by inadequate dopant concentration in diamond growth processes and a required low resistivity doping layer which tends to exclude voltage loss and Joule heat [18]. In addition, orientation-selective growth of doped diamond films is usually needed for the production of these devices [19, 20], resulting in a high cost and thus hindering the feasibility of their applications. Therefore, we present here the fabrication of nanocrystalline

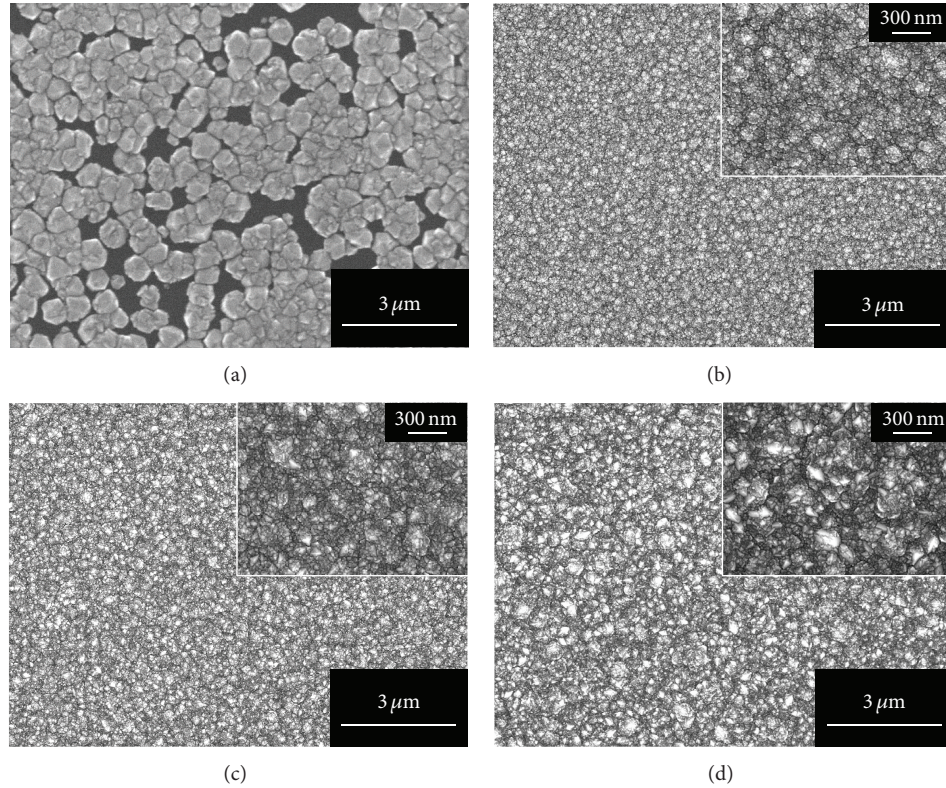


FIGURE 1: SEM images for the diamond films grown at various working pressures under (a) 20 Torr, (b) 40 Torr, (c) 60 Torr, and (d) 80 Torr, respectively.

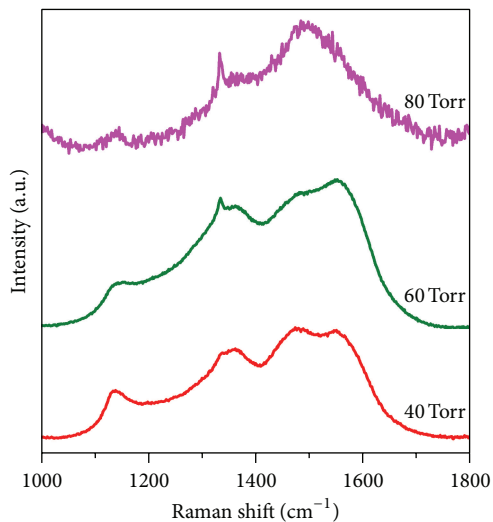


FIGURE 2: Raman spectra for the diamond films grown at various working pressures under 40 Torr, 60 Torr, and 80 Torr, respectively.

diamond (NCD) thin film based UV detectors using metal-semiconductor-metal structure, aiming at higher production rate and higher quality of the films deposition for improving the efficiency and repeatability/reproducibility of the devices. It is of importance to note here that though a postannealing procedure is found to be necessary for good junctions of

metal electrodes and diamond films, the profound effect of that procedure on the characteristics of the diamond films as well as the whole device is not understood well yet.

So far, the growth of NCD films on foreign substrates is usually performed by chemical vapor deposition (CVD) equipment using  $H_2/CH_4$  or  $Ar/H_2/CH_4$  gas mixtures [15, 21]. The microwave plasma enhanced chemical vapor deposition (MPECVD) technique is well-known to increase the plasma density and secondary nucleation rate during the diamond growth process and, consequently, ensures high deposition rate and high density of the as-grown diamond films. In the present work, NCD thin films were grown onto silicon substrates by the MPECVD equipment at fixed  $H_2/CH_4$  concentration ratio and under various working pressures. Subsequently, Au interdigital electrodes (IDE) were coated onto the as-prepared NCD films using nanolithography and sputtering techniques, followed by annealing procedures in vacuum ambient at various temperatures in order to obtain an Ohmic contact for further photodetector investigations. The as-constructed NCD-based UV detector was characterized through either photoresponse or repeatability tests.

## 2. Experimental Procedures

In this work, the fabrication procedures of diamond-based UV sensor were divided into two stages. In the first stage, the polished single crystal Si wafer (n-type) with (1 0 0) crystalline orientation and  $15 \times 15 \times 1$  mm size was used

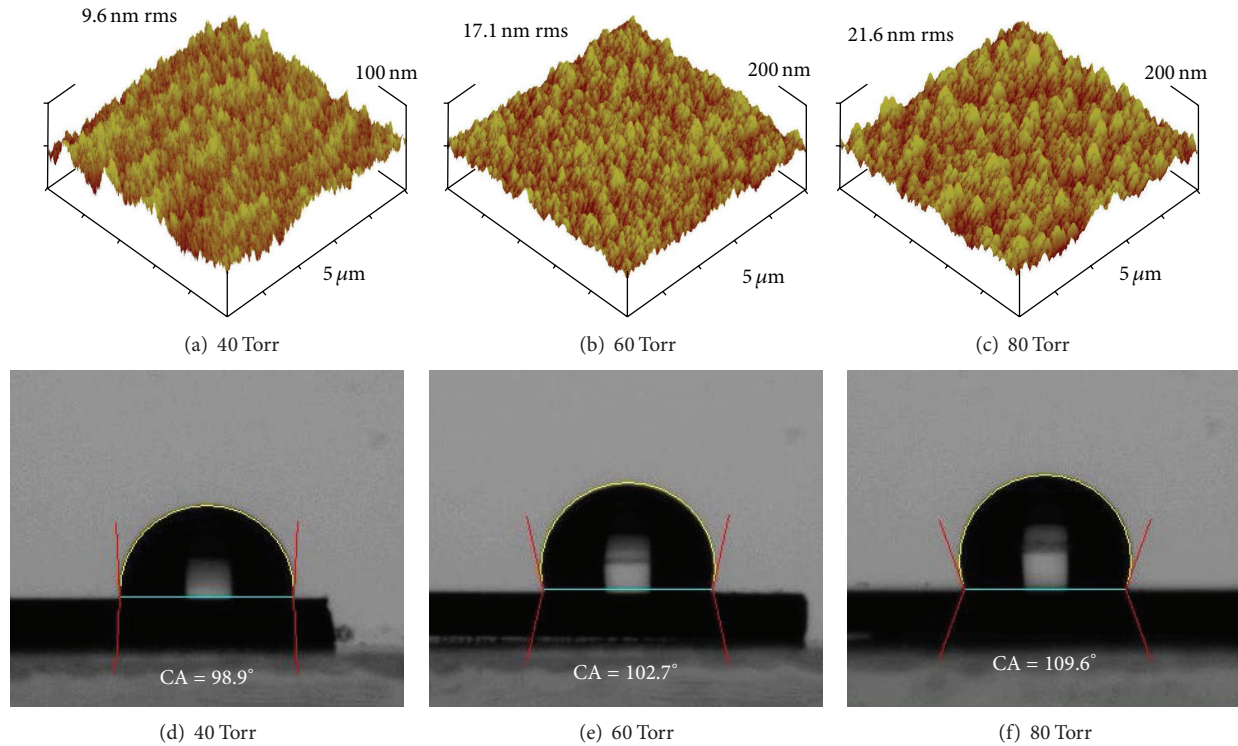


FIGURE 3: The surface roughness and contact angle values with water for the diamond films grown under various working pressures of 40, 60, and 80 Torr, respectively.

as substrate for NCD deposition. The Si substrates were successively cleaned in methanol and acetone solutions for 10 min, respectively, and then were dried by nitrogen. Prior to the CVD growth process, the substrates were nucleated for 15 min in a suspension of ultradispersed diamond nanoparticles having size of 5 nm in ethanol, followed by a thorough rinse in double distilled water. The plasma was induced under microwave power of 700 W without external heating source,  $\text{CH}_4/\text{H}_2$  gas concentration ratio of 8%, and gas flow rate of 800 sccm (standard cubic centimeter per minute). The total pressures were controlled at 20, 40, 60, and 80 Torr, respectively. The deposition time in all of experiments was 2 h. During the CVD deposition process, the plasma condition was *in situ* monitored using an optical electron spectroscopy (OES). The characteristics of the prepared diamond films were analyzed by field emission scanning electron microscopy (FE-SEM, Libra-200 FE), high resolution transmission electron microscopy (HR-TEM, Philips Tecnai F30), atomic force microscopy (AFM, Veeco Nanoscope 3100), Raman spectroscopy (Renishaw, inVia), and X-ray photoelectron spectroscopy (XPS).

In the second stage, the nanomask was patterned onto surface of the as-prepared diamond films by a nanolithography procedure with positive photoresistor. Au was then deposited onto the as-patterned diamond films at room temperature employing sputtering equipment [22]. Detailed sputtering parameters were as follows: RF power of 50 W, working pressure of 3 mTorr, Ar flow rate of 20 sccm, and

processing time of 8 min, respectively. The remaining photoresistor was thoroughly removed by rinsing in acetone for 15 min. Finally, in order to obtain the Ohmic contact for UV detector applications, the diamond/Au structured films were thermally treated in vacuum ambient for 8 min at various temperatures ( $300^\circ\text{C}\sim 500^\circ\text{C}$ ) using rapid thermal annealing (RTA) equipment. The properties of Au interdigitated electrode pattern with thickness of  $\sim 80$  nm on NCD film will be discussed in following parts. All performance tests of the fabricated diamond-based UV detectors were conducted in measurement system equipped with a mercury arc lamp ( $26\text{ mW}/\text{cm}^2$  of power, 365 nm of wavelength) and Keithley 2400 as UV light source and nanoamperometer, respectively.

### 3. Results and Discussion

Figure 1 shows the surface morphologies for the diamond films grown on Si substrate at microwave power of 700 W,  $\text{CH}_4/\text{H}_2$  concentration ratio of 8%, and deposition pressures of 20, 40, 60, and 80 Torr, respectively. For the diamond films grown under 20 Torr, SEM image reveals a discontinuous morphology of the as-grown diamond film which consists of discrete grains with island-like shape as shown in Figure 1(a). Figures 1(b)–1(d) indicate that the increase of working pressure drastically changed the morphology of diamond films and resulted in the aggregation of diamond grains. As shown in Figure 1(b), the film grown under 40 Torr

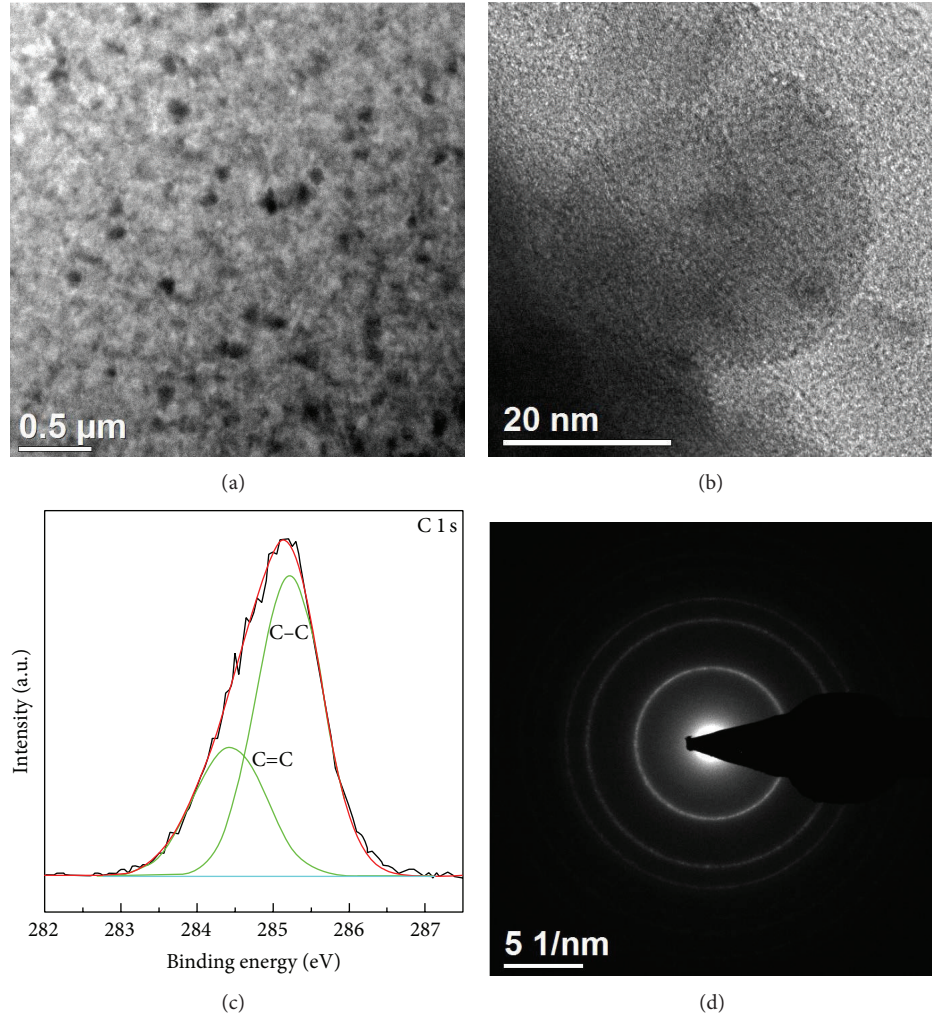


FIGURE 4: (a) Bright field TEM, (b) HR-TEM, and (c) XPS spectra for the diamond film grown at 40 Torr and (d) the corresponding SAED pattern, respectively.

possesses highly uniform diamond grains having size smaller than 50 nm with cauliflower-like shape. This suggests a good performance of our prior pretreatment procedure which has benefit in high diamond nucleation density on the surface of Si substrate the surface of the bare Si substrates. Higher deposition pressure is found to cause the nonuniformity in diamond grains size observed from the formation of cluster aggregation, obviously leading to a higher surface roughness of the as-grown films. As shown in Figure 1(d), the surface morphology of the film grown at 80 Torr reveals relatively large grain cluster having submicron scale size (~100–200 nm). The formation of the larger grain cluster with gradual increase in deposition pressure can be interpreted through the emission of  $H_{\alpha}$  and the formation of diamond growth species in the gas phase. At a fixed  $CH_4/H_2$  concentration ratio, the plasma density increases as a function of the deposition pressure because of the shortening in mean free path of radicals owing to the shortening in mean free path of radicals, and thus induces a higher concentration

of  $H_{\alpha}$  emission. In plasma CVD diamond growth, the  $H_{\alpha}$  species have twofold benefits. First, the  $H_{\alpha}$  reacts with the carbon gaseous precursors in plasma surrounding and then produces  $CH_x$  species and  $C_2$  dimers for the growth of  $sp^3$  cluster and secondary nucleation [22]. Second, the  $H_{\alpha}$  species induce the hydrogen-etching of the produced nondiamond phase which mainly consisted in grain boundaries and lead to the formation of larger grain size. This also can be observed through the appearance of the small sized diamond grains around the big cluster as shown in the inset of Figure 1(d). In addition, the higher plasma density can significantly increase the plasma temperature as well as the kinetic energy of the radicals in the gas phase, eventually enhancing the deposition rate and leading to the formation of the grain cluster in the diamond films. Therefore, the low deposition pressure may cause insufficiency of diamond growth species as well as slow growth rate, inducing discontinuous film morphology as shown in Figure 1(a). It should be noted here, however, that the exact alteration in grain size of the as-prepared diamond

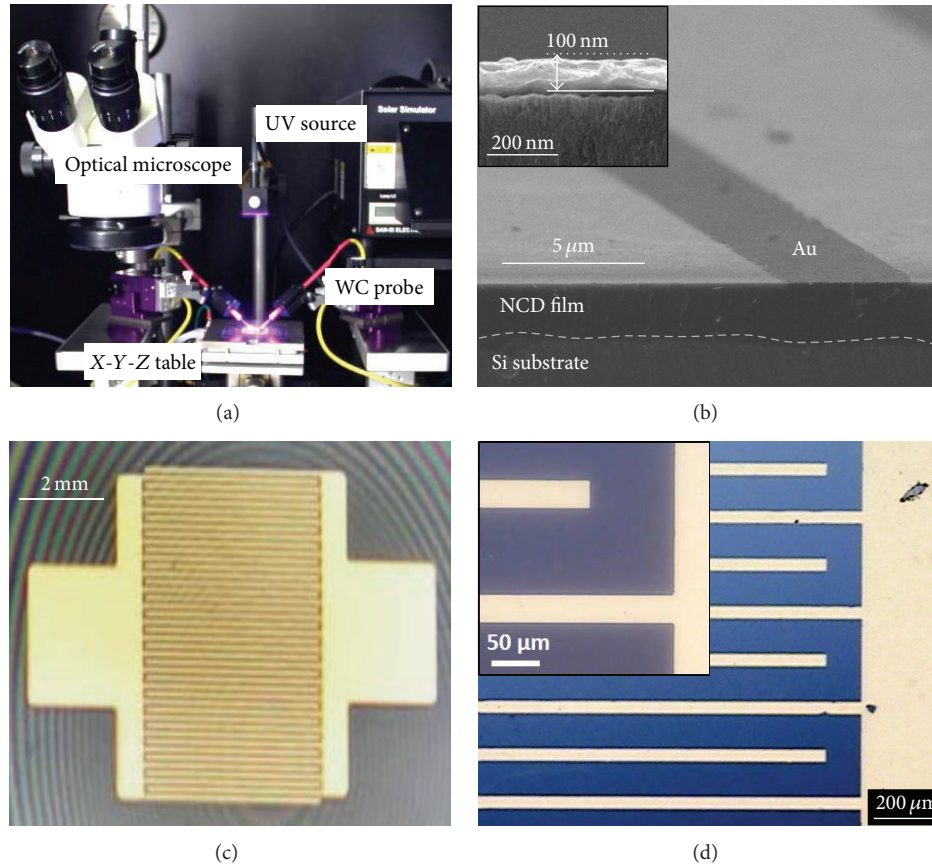


FIGURE 5: (a) Photovoltaic measurement system, (b) SEM images of the fabricated NCD/Au films, and (c), (d) captured photo and OM images of IDE electrodes on the surface of the NCD film grown at a working pressure of 40 Torr.

films cannot be definitely investigated by SEM technique due to the limitation in resolution; therefore, further investigation in the nanostructure is discussed below.

The Raman spectra for the diamond films grown under working pressures of 40, 60, and 80 Torr are shown in Figure 2. The spectra for all samples show the typical characteristic peak of NCD films. Under 40 Torr, the diamond peak at  $1332\text{ cm}^{-1}$  ( $\text{sp}^3$ -bonded carbon phase) is weak and seems to be overlapped by the disordered band (D band,  $\text{sp}^2$ -bonded carbon phase) at around  $1350^{-1}$ , indicating a high fraction of grain boundaries of the films with nanometered size of diamond crystallite size. As the working pressure increased, the position of G-band at  $\sim 1580\text{ cm}^{-1}$  shifted to the lower Raman shift side demonstrate the increase of disordering in  $\text{sp}^2$  structure. This can be explained as result of the aforementioned hydrogen-etching. Also, the characteristic peak of diamond gradually sharpens and increases in intensity, indicating the increase of diamond crystallite size. The increase of plasma temperature as a function of working pressure can be investigated through the peaks of C–H bonds (at  $\sim 1140\text{ cm}^{-1}$ ) in the grain boundaries and the surface of as-grown NCD films. The relation of plasma temperature and the hydrogen incorporation in diamond films which forms C–H bonds has been reported previously [15].

Figure 3 shows the surface roughness and contact angle values with water for the as-grown diamond films under various working pressures of 40, 60, and 80 Torr, respectively. AFM image for the NCD film grown at 40 Torr exhibits a high smooth surface morphology with very low surface roughness of 9.6 nm (root-mean-square, rms) as shown in Figure 3(a). This smooth surface morphology of the as-deposited NCD film indeed improve NCD/Au junction for the further constructed UV detectors. As the deposition pressure increased from 40 to 80 Torr, the surface roughness was increased to 21.6 nm ( $5\text{ }\mu\text{m} \times 5\text{ }\mu\text{m}$  of scanned area). These results are in good agreement with our shown SEM images and prove the trends in the change of clustered degree and grain size of the diamond films. The hydrophobic property for the grown NCD films on Si substrate was investigated by contact angle measurements as shown in Figures 3(d)–3(f). It can be determined that all the as-prepared films possess highly hydrophobic surface, in which the contact angles with water are  $95^\circ$  above. In addition, further increase in deposition pressure is found to improve the wettability. This can be explained by considering surface energy and the microstructure of the films. The larger diamond grain and higher surface roughness of NCD films are caused by the higher working pressure, which not only can robustly

enhance the hydrophobic property but also can increase the internal stress of the films, as the typical characteristics of  $sp^3$  phase structure. The observed hydrophobic NCD films also confirm their prospect in further applications such as protective layer, bioengineering, and solar cell.

The details in nanostructures for the NCD films grown under the working pressure of 40 Torr were investigated by TEM and XPS as shown in Figure 4. Plan-view TEM image shows that the diamond films consisted of nanosized nanocrystallite, which uniformly disperse in disorder phase matrix as shown in Figure 4(a). High-resolution TEM reveals the obtained diamond grain possesses 30 nm in crystallite size with round shape in geometry as shown in Figure 4(b). The above data exhibit both our ideal prior diamond nucleation enhancement stage and high plasma density which significantly assist the secondary nucleation during diamond growth. The crystalline structure of the NCD film can be studied by the selected area electron diffraction (SAED) pattern as shown in Figure 4(d), indicating that the films have good polycrystalline structure. Figure 4(c) shows the C-1s peak of XPS spectra of the NCD film grown at working pressure of 40 Torr. Owing to overlap phenomena of the peaks of  $sp^2$  and  $sp^3$  bonds (at binding energy of 284.5 eV and 285.3 eV, resp.), the spectra were curve-fitted using the Gaussian method in the literature [23]. It is calculated that the film consists of a high  $sp^3$  phase fraction of 68.6%.

Figure 5 shows the photos of the patterned Au IDE electrodes on the surface of the NCD films grown at a working pressure of 40 Torr. SEM image shows that Au films were successfully deposited onto the NCD films, having thickness of 100 nm as shown in the inset of Figure 5(b). The fabricated Au electrodes have finger-pattern with 30  $\mu\text{m}$  in width and 150  $\mu\text{m}$  in interspacing. Figures 5(c)-5(d) show the captured photo and optical microscope image for the NCD/Au structure films after RTA procedure in vacuum at 500°C for 8 min. It is observed that the high annealing temperature has no effect on the surface morphologies of the structure films.

The electric characteristics of the as-constructed NCD-based UV detector were investigated by  $I$ - $V$  curve measurement as shown in Figure 6. All the measurements were conducted at room temperature with bias voltage ranging from  $-5$  V to 5 V. The originated NCD/Au structure exhibits a poor junction characteristic with unstable resistance. Annealed at 300°C and 400°C, the measured  $I$ - $V$  curves of the device also show a nonlinear behavior. Interestingly, the sheet resistances of annealed NCD/Au structure seemed to be higher than the original one. We suggest that this can be elucidated by further studies in the formation of carbide structure and Au : H bonds during the annealing process. From the  $I$ - $V$  curves of the device annealed at 500°C, the observed linear characteristics indicate that a high-quality Ohmic contact has been obtained at the junction area of NCD and Au with relatively low Ohmic resistance. However, it is not unreasonable to notice here that the thermal treatment may lead to graphitization or disorderization of  $sp^3$  structure which hampers the photovoltaic efficiency of the NCD as absorbance layer. Our above data indeed propose a fabrication technique for obtaining a good

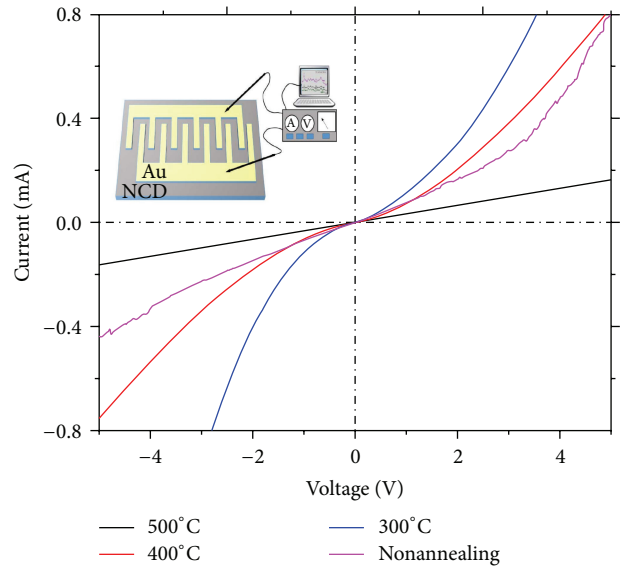


FIGURE 6:  $I$ - $V$  characteristics of the as-fabricated NCD/Au structures for UV photodetector device.

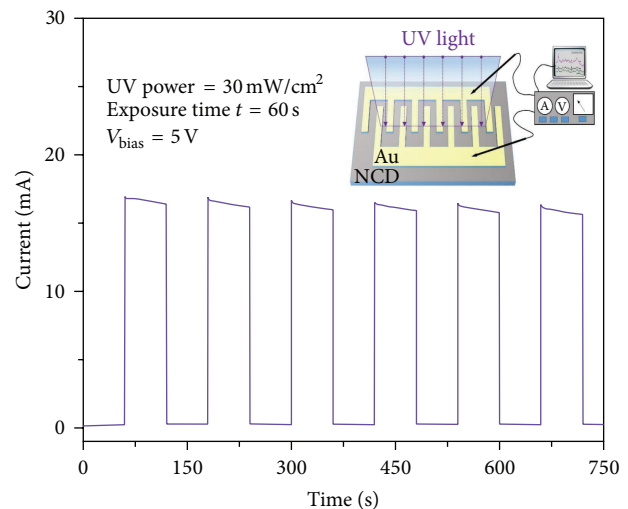


FIGURE 7: Photocurrent as a function of time measured by switching on and off UV irradiation on the as-fabricated NCD/Au UV detector.

performance of Ohmic junction of NCD and metal electrodes which is feasible for not only UV photodetectors but also future applications in solar cell industry.

The photoresponse efficiency of the as-constructed UV detector was investigated in dark currents and photocurrents measured from its repeatability/reproducibility tests using repeatedly turning UV light on and off. All the tests were carried out at room temperature and 5 V of bias voltage, as shown in Figure 7. It is found that the detector has quite a low and stable dark current of  $\sim 0.2$  mA, even for long measuring time of 60 s. This indicates a low resistance of the whole UV detector and thus eliminate thermal stress in NCD/Au junction which caused by Joule heat. As irradiated

by UV light, the current increased sharply and endured during exposure time of 60 s. It can be seen that the response and decay corresponding to the turning on and off of the UV irradiation are fast, in which the rise and decay time were 0.8 s and 1.2 s, respectively. The measured results also showed a significant deference of the dark currents and photocurrents as two orders of magnitude. Indeed, the photoresponse and stable operation of the device prove the feasibility in UV sensor applications.

#### 4. Conclusion

In conclusion, a complete fabrication method of nano-diamond-based UV detector device with high performance is proposed. The NCD films grown at a working pressure of 40 Torr exhibited high  $sp^3$  fraction, low surface roughness, and good hydrophobicity. The Au electrodes deposited onto surface of NCD film show Ohmic contact characteristics after 8 min of rapid thermal annealing procedure at 500°C in vacuum ambient. The fabricated diamond photodetector achieves high detection efficiency and fast response to UV irradiation in air ambient. The proposed method is indeed cost effective and feasible to large scale production. In addition, this method also can be applied to other photovoltaic-based applications such as solar cell, photocatalyst, and X-ray detection.

#### Conflict of Interests

The authors declare that there is no conflict of interests regarding the publication of this paper.

#### Acknowledgment

This work was financially supported by the main research projects of the National Science Council of Republic of China under Grant nos. NSC 103-2622-E-027-005-CC2 and NSC 101-2622-E-027-003-CC2, respectively.

#### References

- [1] D. T. Phan and G. S. Chung, "Characteristics of SAW UV sensors based on a ZnO/Si structure using third harmonic mode," *Current Applied Physics*, vol. 12, no. 1, pp. 210–213, 2012.
- [2] A. Baltakesmez, S. Tekmen, P. Ko, S. Tuzemen, K. Meral, and Y. Onganer, "UV-visible detector and LED based n-ZnO/p-Si heterojunction formed by electrodeposition," *AIP Advances*, vol. 3, no. 3, Article ID 032125, 2013.
- [3] K. Bayat, Y. Vygranenko, A. Sazonov, and M. Farrokh-Baroughi, "Design, fabrication and characterization of an a-Si:H-based UV detector for sunburn applications," *Semiconductor Science and Technology*, vol. 21, no. 12, pp. 1699–1702, 2006.
- [4] M. L. Tu, Y. K. Su, S. J. Chang, and R. W. Chuang, "GaN UV photodetector by using transparency antimony-doped tin oxide electrode," *Journal of Crystal Growth*, vol. 298, pp. 744–747, 2007.
- [5] Y. Li, F. D. Valle, M. Simonnet, I. Yamada, and J. Delaunay, "High-performance UV detector made of ultra-long ZnO bridging nanowires," *Nanotechnology*, vol. 20, no. 4, Article ID 045501, 2009.
- [6] Y. Iwakaji, M. Kanasugi, O. Maida, and T. Ito, "Characterization of diamond ultraviolet detectors fabricated with high-quality single-crystalline chemical vapor deposition films," *Applied Physics Letters*, vol. 94, no. 22, Article ID 223511, 2009.
- [7] G. Hellings, J. John, A. Lorenz, P. Malinowski, and R. Mertens, "AlGaN schottky diodes for detector applications in the UV wavelength range," *IEEE Transactions on Electron Devices*, vol. 56, no. 11, pp. 2833–2839, 2009.
- [8] C. W. Padgett, O. Shenderova, and D. W. Brenner, "Thermal conductivity of diamond nanorods: molecular simulation and scaling relations," *Nano Letters*, vol. 6, no. 8, pp. 1827–1831, 2006.
- [9] W. H. Liao, C. R. Lin, and D. H. Wei, "Effect of CH<sub>4</sub> concentration on the growth behavior, structure, and transparent properties of ultrananocrystalline diamond films synthesized by focused microwave Ar/CH<sub>4</sub>/H<sub>2</sub> plasma jets," *Applied Surface Science*, vol. 270, pp. 324–330, 2013.
- [10] C. Lu, S. B. Tian, C. Z. Gu, and J. J. Li, "Grain boundary effect on the superconducting transition of microcrystalline boron-doped diamond films," *Diamond and Related Materials*, vol. 20, no. 2, pp. 217–220, 2011.
- [11] A. Qureshi, W. P. Kang, J. L. Davidson, and Y. Gurbuz, "Review on carbon-derived, solid-state, micro and nano sensors for electrochemical sensing applications," *Diamond and Related Materials*, vol. 18, no. 12, pp. 1401–1420, 2009.
- [12] W. Gajewski, P. Achatz, O. A. Williams et al., "Electronic and optical properties of boron-doped nanocrystalline diamond films," *Physical Review B—Condensed Matter and Materials Physics*, vol. 79, no. 4, Article ID 045206, 2009.
- [13] C. Pietzka, A. Denisenko, L. A. Kibler, J. Scharpf, Y. Men, and E. Kohn, "Surface modification of single-crystal boron-doped diamond electrodes for low background current," *Diamond and Related Materials*, vol. 18, no. 5–8, pp. 816–819, 2009.
- [14] C. Lin, W. Liao, D. Wei, J. Tsai, C. Chang, and W. Fang, "Formation of ultrananocrystalline diamond films with nitrogen addition," *Diamond and Related Materials*, vol. 20, no. 3, pp. 380–384, 2011.
- [15] Y. Lifshitz, C. H. Lee, Y. Wu, W. J. Zhang, I. Bello, and S. T. Lee, "Role of nucleation in nanodiamond film growth," *Applied Physics Letters*, vol. 88, no. 24, Article ID 243114, 2006.
- [16] Y. Morita, T. Takimoto, H. Yamanaka et al., "A facile and scalable process for size-controllable separation of nanodiamond particles as small as 4 nm," *Small*, vol. 4, no. 12, pp. 2154–2157, 2008.
- [17] J. Zhao, L. Wu, and J. Zhi, "Non-enzymatic glucose detection using as-prepared boron-doped diamond thin-film electrodes," *Analyst*, vol. 134, no. 4, pp. 794–799, 2009.
- [18] T. Makino, H. Kato, S. Ri, S. Yamasaki, and H. Okushi, "Homoepitaxial diamond  $p-n^+$  junction with low specific on-resistance and ideal built-in potential," *Diamond and Related Materials*, vol. 17, no. 4–5, pp. 782–785, 2008.
- [19] T. Making, H. Kato, M. Ogura et al., "Strong excitonic emission from (001)-oriented diamond  $P-N$  junction," *Japanese Journal of Applied Physics*, vol. 44, part 2, no. 37–41, pp. L1190–L1192, 2005.
- [20] H. Okushi, H. Watanabe, S. Ri, S. Yamanaka, and D. Takeuchi, "Device-grade homoepitaxial diamond film growth," *Journal of Crystal Growth*, vol. 237–239, no. 1–4, pp. 1269–1276, 2002.
- [21] R. N. Tiwari, J. N. Tiwari, L. Chang, and M. Yoshimura, "Enhanced nucleation and growth of diamond film on Si by CVD using a chemical precursor," *The Journal of Physical Chemistry C*, vol. 115, no. 32, pp. 16063–16073, 2011.

- [22] K. Teii and T. Ikeda, "Effect of enhanced  $C_2$  growth chemistry on nanodiamond film deposition," *Applied Physics Letters*, vol. 90, no. 11, Article ID 111504, 2007.
- [23] C. Lin, H. Chang, and C. Chang, "Fabrication of high transparency diamond-like carbon film coating on D263T glass at room temperature as an antireflection layer," *International Journal of Photoenergy*, vol. 2013, Article ID 612163, 8 pages, 2013.

## Research Article

# On-Road Driver Monitoring System Based on a Solar-Powered In-Vehicle Embedded Platform

Yen-Lin Chen,<sup>1</sup> Chao-Wei Yu,<sup>1</sup> Zi-Jie Chien,<sup>2</sup> Chin-Hsuan Liu,<sup>1</sup> and Hsin-Han Chiang<sup>3</sup>

<sup>1</sup> Department of Computer Science and Information Engineering, National Taipei University of Technology, Taipei 10608, Taiwan

<sup>2</sup> Department of Energy and Refrigerating Air-Conditioning Engineering, National Taipei University of Technology, Taipei 10608, Taiwan

<sup>3</sup> Department of Electrical Engineering, Fu Jen Catholic University, New Taipei City 24205, Taiwan

Correspondence should be addressed to Hsin-Han Chiang; [hsinhan@ee.fju.edu.tw](mailto:hsinhan@ee.fju.edu.tw)

Received 16 May 2014; Accepted 16 June 2014; Published 3 July 2014

Academic Editor: Ching-Song Jwo

Copyright © 2014 Yen-Lin Chen et al. This is an open access article distributed under the Creative Commons Attribution License, which permits unrestricted use, distribution, and reproduction in any medium, provided the original work is properly cited.

This study presents an on-road driver monitoring system, which is implemented on a stand-alone in-vehicle embedded system and driven by effective solar cells. The driver monitoring function is performed by an efficient eye detection technique. Through the driver's eye movements captured from the camera, the attention states of the driver can be determined and any fatigue states can be avoided. This driver monitoring technique is implemented on a low-power embedded in-vehicle platform. Besides, this study also proposed monitoring machinery that can detect the brightness around the car to effectively determine whether this in-vehicle system is driven by the solar cells or by the vehicle battery. On sunny days, the in-vehicle system can be powered by solar cell in places without the vehicle battery. While in the evenings or on rainy days, the ambient solar brightness is insufficient, and the system is powered by the vehicle battery. The proposed system was tested under the conditions that the solar irradiance is 10 to 113 W/m<sup>2</sup> and solar energy and brightness at 10 to 170. From the testing results, when the outside solar radiation is high, the brightness of the inside of the car is increased, and the eye detection accuracy can also increase as well. Therefore, this solar powered driver monitoring system can be efficiently applied to electric cars to save energy consumption and promote the driving safety.

## 1. Introduction

The economic development has caused large amount of energy to be consumed, and largely consumption of petrochemical inventories, resulting in the energy crisis. To reduce the petrochemical energy consumption on vehicles, the electric cars arise. In order to achieve higher endurance driving, we should care about the car battery power. The in-vehicle instruments in the electric cars also consume electric energy and may reduce the energy for car driving. Moreover, there are many traffic accidents which occur due to the inattentive and fatigued driving. Thus, an effective monitoring system for drivers' attention states is also very important for the development of electric cars. Therefore, the solar energy can be adopted to drive the in-vehicle embedded computing platform to conduct the driver monitoring functions, and both the electric energy consumption and the driving safety can be effectively achieved.

Photovoltaic (PV) technology is one of the most important renewable sources of energy generation. Since the first recognition in 1839 [1], there have been many research works on the performance of PV. However, efficiency improvement and cost reduction of PV technology still need many efforts. The solar cells based on crystalline silicon (c-Si) are known as materials in first generation solar cell [2]. From the points of view on the cost, performance, and processibility, the applications of new advanced materials such as amorphous silicon (a-Si), cadmium telluride (CdTe), and copper indium gallium diselenide (CIGS) are achieved in the second and third generations of solar cells. Typical conversion efficiencies of first generation technologies are currently 15% to 20%, whereas those of second generation technologies are currently 7% to 15% [3].

Photovoltaic system can be categorized as stand-alone photovoltaic system and grid-connected photovoltaic system [4]. The stand-alone systems do not supply power to the grid.

Such systems may vary widely in size and applications, such as consumer electronics and remote buildings. Chien et al. [5] have presented the experimental investigations on absorption refrigerators driven by solar cells. The system was tested by the varying solar irradiance ranged from 550 to 700 W/m<sup>2</sup> as solar energy and 500 mL ambient temperature water as cooling load. After 160 minutes, this refrigerator can maintain the temperature at 5 to 8°C. Huang et al. [6] presented a solar LED street lighting system using constant-power and dimming control. The test results showed that the power of 18 W and 100 W LED luminaires can be controlled accurately with error at 2–5%.

To achieve the monitoring functions of drivers' fatigue state, the human body features and actions should be efficiently analyzed. Human body feature sensing and detection have currently played important roles in many application areas, such as human surveillance and human-computer interaction applications [7–9]. In recent research studies, many human action detection techniques aiming at detecting different human body parts have been developed for human-computer interaction applications, such as the whole human motions [10–12], the faces, and the eye gazes [13–23]. Among the above-mentioned human body parts, the faces and eye gazes play the most important roles in interpreting and understanding a person's attentions, intentions, and needs in human communications and interactions, especially for driver state monitoring. In this sense, tracking of faces and eye gazes provide necessary information to obtain the car driver's attentive states.

Moreover, the computational power and flexibility of in-vehicle embedded systems have recently increased significantly because of the development of system-on-chip technologies and the advanced computing power of newly released portable devices. Thus, performing real-time vision-based eye detection and tracking in driver assistance and monitoring applications has become feasible on modern embedded platforms for driver assistance systems. This paper presents an on-road driver monitoring system that uses solar-cell powered in-vehicle embedded platform. The on-road driver monitoring system could detect driver's mental state and determine which system is driven by battery or by solar cell by brightness of environment. The system could be driven by solar cell on sunny day which could save finite battery capacity in vehicle.

This study presents an on-road driver monitoring system, which is implemented on an in-vehicle embedded system and driven by solar cells. The driver monitoring function is performed by an efficient eye detection technique. Through the driver's eye movements captured from the camera, the attentive states of the driver can be determined and any fatigue states can be avoided. This driver monitoring technique is implemented on a low-power embedded in-vehicle platform. Besides, this study also proposed monitoring machinery that can detect the brightness around the car to effectively determine whether this in-vehicle system is driven by the solar cells or by vehicle batteries. On sunny days, the in-vehicle system can be powered by solar cell in places without the vehicle battery. While in the evenings or on rainy days,

the ambient solar brightness is insufficient, and the system is powered by the vehicle battery. From the experimental results, the proposed solar powered driver monitoring system demonstrates its efficiency in energy savings and driving safety for electric cars.

## 2. Brightness Detection and Power Source Determination

In the proposed system, we adopt a camera, pyranometer, and powermeter to obtain information of the solar irradiance and power generation efficiency of solar cells via analytical results of the images captured outside the car. First, the RGB (red, green, and blue) color model of the captured image sequences of the road environments will be adopted to compute the brightness value, denoted as  $V$ . Then, the brightness ( $V$ ) value can be adopted to determine the ambient brightness conditions with respect to the strengths of the solar irradiance. The range of  $V$  value is ranged from 0 to 255. The brightness value can be computed as follows:

$$V = \max \{R, G, B\}. \quad (1)$$

Equation (1) indicates the  $V$  value is the maximum of the color values of  $R$ ,  $G$ , and  $B$ . We can use the brightness value as the threshold to determine the strengths of the solar irradiance. In this way, when the  $V$  value is lower than the threshold, system will conduct two operations: (1) changing the power source from the solar cell to the vehicle battery; (2) turning on the infrared light sources to more accurately detect the fatigue state of the driver. When the  $V$  value is higher than the threshold, the system will then conduct two operations: (1) changing the power source from the battery to solar cells; (2) turning off the infrared light sources, because the ambient lighting condition is sufficient for detecting the driver's states. In the proposed system, the threshold of the brightness is experimentally determined as 130, as depicted in Figure 14.

## 3. Driver Monitoring by Eye Detection Methods

To monitor the driver's attentive states, their eyesight is important information. This study presents a classification-based approach to detect and analyze the drivers' eyes to determine their attention states. A fast face and eye detection process based on boost classification approach is presented to detect and locate the regions of faces and eyes in the image sequences captured via a video camera. In this detection process, we improve and optimize the boost classification method to provide necessary computational efficiency for embedded and portable devices.

*3.1. Classification-Based Methods.* Here each weak classifier stage is performed by selecting a combinative set of features being computed based on the integral images, which reflects integrals over the subregions contained in the region, as depicted in Figure 1. The features utilized in the proposed

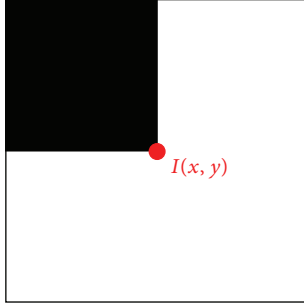


FIGURE 1: The integral image.

TABLE 1: The scaling factors of the resolutions used by the image pyramids [21].

Level	Width	Height	Scale factor
0	640	480	1
1	320	240	2
2	160	120	4
3	128	96	5
4	80	60	8
5	64	48	10
6	40	30	16
7	32	24	20

system are a variety of Haar-like features [24], which are reminiscent of Haar wavelets and reflect the human visual responses, such as linear, center-surround, and diagonal directional responses, as shown in Figure 2.

In this sense, a boosted cascade of strong classifiers can be constructed where each stage is a strong classifier having a suitable threshold  $\theta$  for determining whether the input image comprises target objects, as shown in Figure 3. Each stage classifier is trained and performed by analyzing a combination of features obtained from the integral image, and thus detecting most target objects while screening out a certain portion of noninterested objects that might be accepted by previous classifier stages.

**3.2. Face Detection.** Having the boosting classification techniques, the faces in the grabbed image sequences can be detected and located via the trained boosted cascade detectors. The proposed system adopts  $24 \times 24$  pixel resolution for face training patterns.

Because the proposed system is designed mainly for the interactive user interface applications, the distances between the camera and the face are mostly within 25 cm to 60 cm. Therefore, to computationally effectively perform the real-time face detection by the cascade detectors, the proposed system adopts the scaling factors of the resolutions for the image pyramids [21] on the face images, as depicted in Table 1. The proposed system adopts the scale factors of 2–7 on the face images to perform fast multiscale detection via the boosted cascade detectors.

For the purpose of running the system under different environments with varying ambient lighting conditions, the

histogram equalization is applied on the scaled face images to obtain uniform gray level distributions, as shown in Figure 4. Accordingly, the boosted cascade detectors are applied on the histogram equalized images to detect faces using the Haar-like features, as depicted in Figure 5.

As a result, after the faces in images are detected, their positions and sizes are recorded for further face and eye detection processes. Based on the positions and sizes of the current detected faces, the searching area for detecting the faces in the subsequent image frames is performed in the areas with the two times of the widths and heights of the current detected faces, and thus the computational costs of the face detection can be effectively saved in the following image frames.

**3.3. Eye Detection.** Having the face positions, the eyes can be effectively detected based on the interesting regions specified by the facial areas. Besides, to save the computational costs for performing real-time detection process of the boosting classification techniques, the face detection process on the whole image is only performed in the situation that the eyes have not been detected in the previous frame. Otherwise, if the face or eyes have already been detected in the previous frame, the proposed system will perform the eye detection process within the adaptive regions of interest (ROIs) according to the locations and areas of the face and eyes detected in previous frames.

In this way, the proposed system adopts two types of regions of interest for eye detection for the two situations: the face has been detected and the eyes have been detected in the previous frames [20]. In the first situation, the face has just been detected in the previous frame as depicted in Figure 6, and the ROIs for detecting the left eye and the right eye are determined as follows.

The ROI starting position  $(X_{ROI_L}, Y_{ROI_L})$  for detecting the left eye is obtained by

$$(X_{ROI_L}, Y_{ROI_L}) = \left( X_{face} + \frac{2}{5}W_{face}, Y_{face} + \frac{1}{5}H_{face} \right). \quad (2)$$

The ROI starting position  $(X_{ROI_R}, Y_{ROI_R})$  for detecting the right eye is determined by

$$(X_{ROI_R}, Y_{ROI_R}) = \left( X_{face}, Y_{face} + \frac{1}{5}H_{face} \right), \quad (3)$$

where  $X_{face}$  and  $Y_{face}$  denote the  $x$  and  $y$  coordinate of the top-left position of the detected face region, respectively;  $W_{face}$  and  $H_{face}$  represent the width and height of the detected face region, respectively.

Here the width  $W_{ROI}$  and height  $H_{ROI}$  of the eye detection ROIs are computed by

$$W_{ROI} = \frac{3}{5}W_{face}, \quad H_{ROI} = \frac{1}{3}H_{face}. \quad (4)$$

In the second situation, the eyes have already been detected in some previous frames, and then the eyes in the subsequent frames can be searched and detected based on their regions in previous frames.

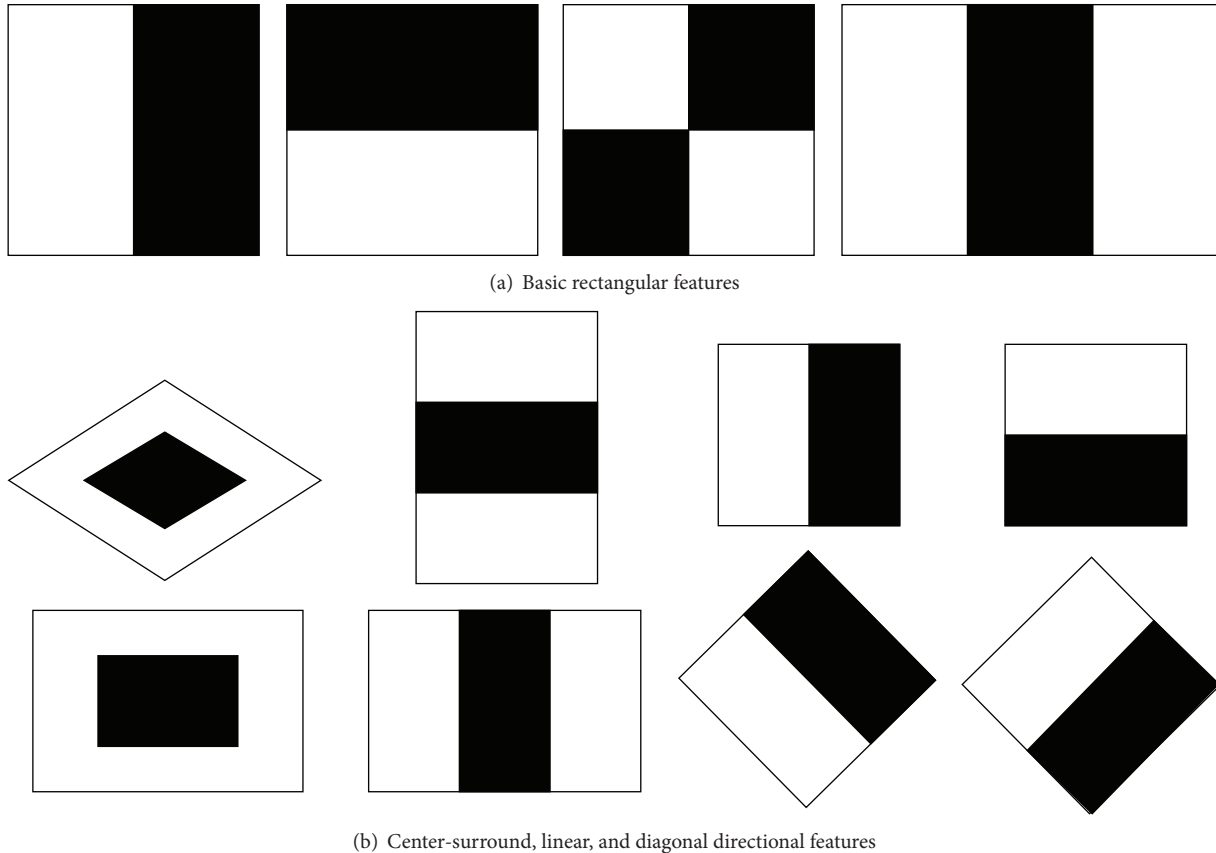


FIGURE 2: The Haar-like feature prototypes.

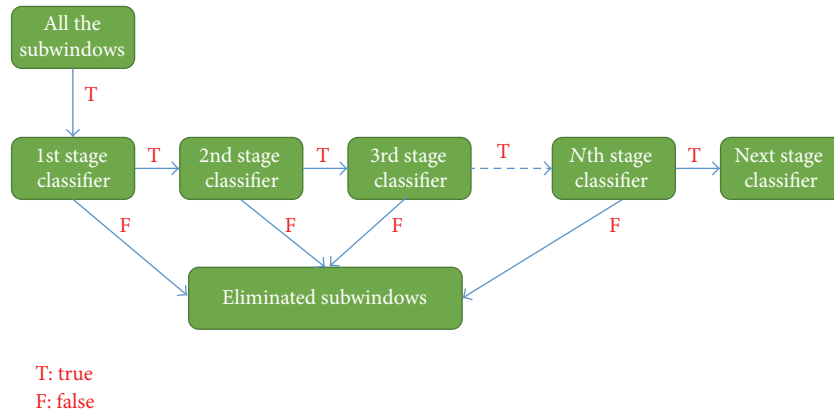


FIGURE 3: The cascaded classifier.

Based on the detected eye region that includes the eye and the eyebrow and the displacement of the users' eyes, the ROIs for detecting left and right eyes in the current frames can be determined by extending the detected eye regions by two times of their corresponding widths and heights. As illustrated in Figure 7, the red rectangular regions are the ROIs for detecting left and right eyes in the current frames, while the green rectangular regions are the detected eye regions in the previous frames.

Accordingly, the boosting classifier is applied on the eye ROIs based on the above-mentioned two types of ROIs to obtain the left and right eye regions in the image sequences. Having the eyes' regions, the proposed system then extracts the eyeballs and eyelids for further determining of the user-interactions. To computationally effectively obtain the positions of the eyeballs, the central regions of detected eye regions, which mostly contain the eyeballs of interest, are firstly extracted and transformed to gray-intensity images.

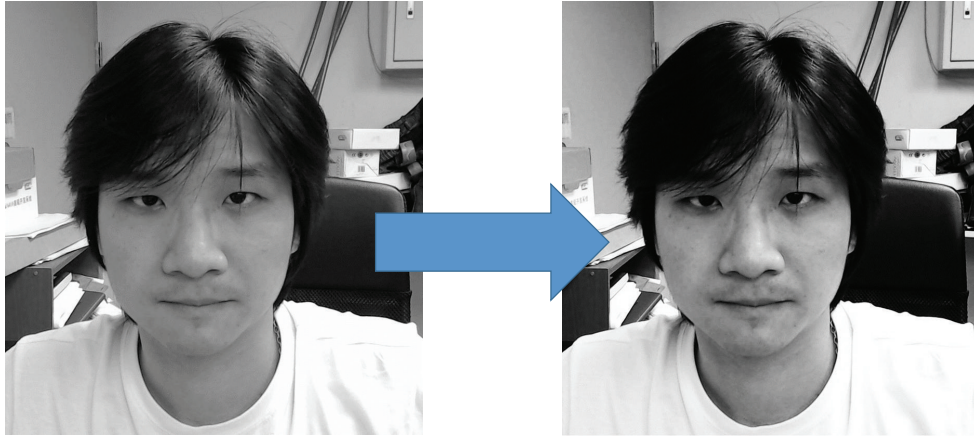


FIGURE 4: The histogram equalized facial images.



FIGURE 5: The example of applying the boosted cascade detectors with the Haar-like features on images.

Then, to extract the eyeball blob pixels from other uninteresting object pixels of different illumination features under various ambient lighting conditions, an effective automatic thresholding technique is needed to adaptively segment the salient eyeball blob pixels of interest. Using the properties of discriminant analysis, our previous research presents an effective automatic multilevel thresholding technique for image segmentation [25]. The pixel regions of eyeball blobs can be appropriately extracted from other uninteresting objects contained in the detected eye regions. Then, to locate the eyeball blobs from the extracted bright object plane, a connected-component extraction process [26] is performed on the pixel regions of eyeball blobs to label and locate the connected components of the eyeball blobs. Locating the connected components reveals the meaningful features of the position, area, and pattern associated with each eyeball blob. Figure 8 illustrates the extraction process of the eyeball regions in the detected left and right eye regions. As depicted in Figure 9, after performing the automatic thresholding and connected-component extraction processes on the eyeball regions, the eyeball blobs and their features are obtained for further user interactive applications.

**3.4. Blinking Eyelid Detection.** In addition to detecting normal eye movements, the eye blinking events can also be adopted as the determination for fatigue detection of the drivers. To detect blinking events, we need to detect the blinking eyelids following the recent detected eyes in previous frames. Having the detected eye regions of the last previous frames, the blinking eyelids in the current frames can be determined by referring to the precious regions of the eyeball blobs. Based on the blinking eye detection approach presented in [27], this study presents a simplified and improved method to detect the blinking eyelids. The blinking eyelid detection process is illustrated in Figure 10. Firstly, the automatic thresholding process is applied on the possible eyelid regions, which are obtained by referring to the previously detected eye regions, to obtain the binary pixel regions. Then, the eyelid detection process starts by vertically scanning the first occurring black object pixels along with the coordinates at  $1/4$ ,  $1/2$ ,  $3/4$  widths of the eye regions. We can obtain three turning points A, B, C, which reflect the features of the eyelids, as depicted in Figure 10. Accordingly, the slopes of the feature lines  $\overline{AB}$  and  $\overline{BC}$  are computed, and if the slope of  $\overline{AB} > 0$  and the slope of  $\overline{BC} \leq 0$ , then we can determine that it is a blinking eyelid.

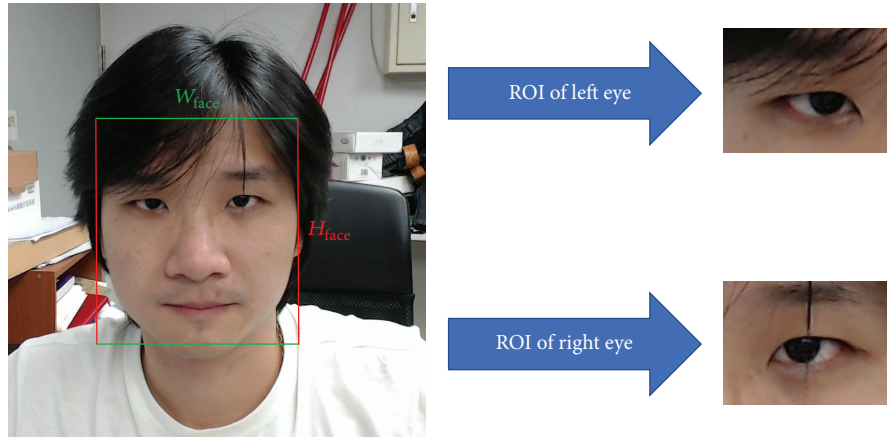


FIGURE 6: Illustration of the ROIs for detecting left and right eyes based on the detected face region [20].

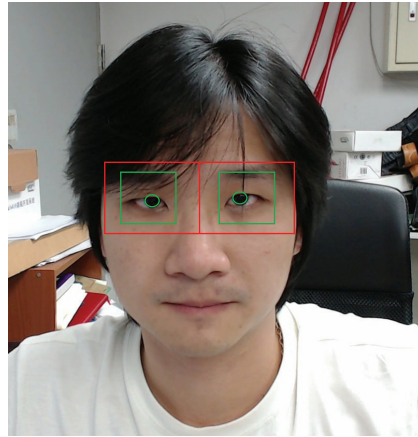


FIGURE 7: Illustration of the ROIs for detecting left and right eyes based on the detected eye regions.

#### 4. The Experimental Setup

The architecture of the proposed solar-powered on-road driver monitoring system is shown in Figure 11. In the study, we use a multicore embedded development platform to perform the tasks of image capturing, eye detection and monitoring of driver, and brightness detection for power source switching. In order to promote the computational performance of the proposed system, we assign the computing tasks as shown in Figure 12. In this computing architecture, one CPU core focuses on monitoring the driver's state by detecting the eye states from the camera's video streams, while the other core is used for detecting ambient brightness and selecting the suitable power sources. Figure 13 gives an overview of the experimental car, and the hardware specifications of the proposed system are depicted in Table 2.

The software architecture of our proposed solar-powered driver monitoring system consists of two parts. The first part includes the face and eye detection module based on the classification-based methods. This software module will detect the driver's face and then will detect eye position and movements based on face locations. The second part

is the brightness detection module. This module analyzes the ambient brightness around the vehicle and determines the system to be powered by solar cells or vehicle batteries. When the ambient brightness is sufficiently high, the driver monitoring system is powered by the solar cells; otherwise, when the ambient brightness is insufficient, the system will switch to being powered by vehicle batteries. The software architecture is depicted in Figure 14.

#### 5. Results and Discussion

This section presents the results of the proposed solar-powered driver monitoring system. The face and eye detection, fatigue detection, and the brightness detection with power source switching techniques are implemented on a TI OMAP4430 dual-core embedded platform. This platform consists of dual Cortex A9 ARM-based general-purpose processor with a 1.0 GHz operational speed and 1 GB of DDR2 memory for executing the software modules. In this study, we used one CPU core focusing on monitoring the driver's state by detecting the eye states from the RGB color model of camera's video streams, while the other core is used for

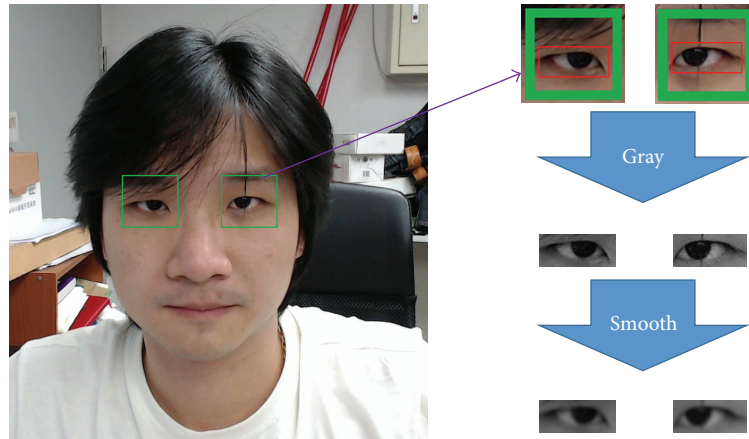


FIGURE 8: Illustration of extracting the eyeball regions in the detected eye regions.



FIGURE 9: The located eyeballs of the left and right eyes.

detecting ambient brightness and selecting the suitable power sources. In this way, the computational performance of the proposed system can be effectively promoted. By releasing the source code project associated with the software modules, the proposed techniques can be conveniently distributed and migrated onto different hardware platforms (such as different embedded platforms) with various operating systems (such as Linux, Android, and Windows Mobile). Thus, the application developers can easily implement and design many customized driver monitoring systems under different hardware and software environments.

Since the ambient brightness will affect the eye detection rate of the driver monitor system. Therefore, this study evaluates the relations of the ambient brightness with the eye detection accuracy rates, as can be seen from Figure 15. When the brightness is more than 60, the eye detection accuracy rate can be greater than 90%. Therefore, if the ambient brightness is insufficient, the proposed system will automatically activate the infrared lights to promote the eye detection performance to ensure the high detection rate for monitoring the driver's fatigue states.

In our experimental platform, the power of the solar cell is 20 W, but it can only support about 18% of its power. However,

the power consumption of the proposed embedded platform requires about 18 W of power. Thus, this study uses six solar cells connected in parallel to supply the proposed system. As shown in Figure 16, when the solar irradiance achieves more than  $52 \text{ W/m}^2$ , the total power supply of the solar cells can be greater than 18 W, which is sufficient for the proposed driver monitor system. In this condition, the brightness becomes higher than 130, as solar irradiance is about  $52 \text{ W/m}^2$ , and the eye detection accuracy rate can also reach higher than 90%, as depicted in Figure 15. It is shown that eye detection system can achieve the accuracy rate of above 90% with brightness value higher than 130, and the solar irradiance in this situation can achieve above  $52 \text{ W/m}^2$ .

Therefore, this study will select 130 as the brightness threshold to determine whether the system is driven by solar cells or batteries. When the brightness is higher than 130, the system will switch to being powered by the solar cells; otherwise, the system is driven by vehicle batteries.

The frame rate of the vision system is approximately 30 frames per second, and the resolution of each frame of the RGB color model of captured image sequences is 640 pixels by 480 pixels per frame. An experimental set of several driving videos captured in various illumination conditions

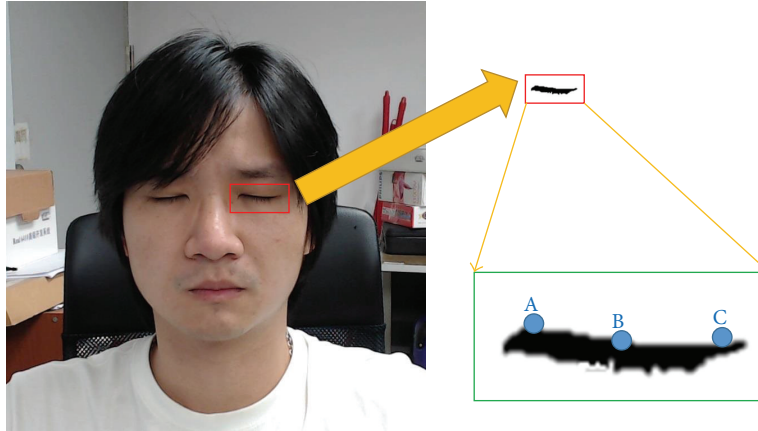


FIGURE 10: Illustration of blinking eyelid detection for fatigue monitoring.

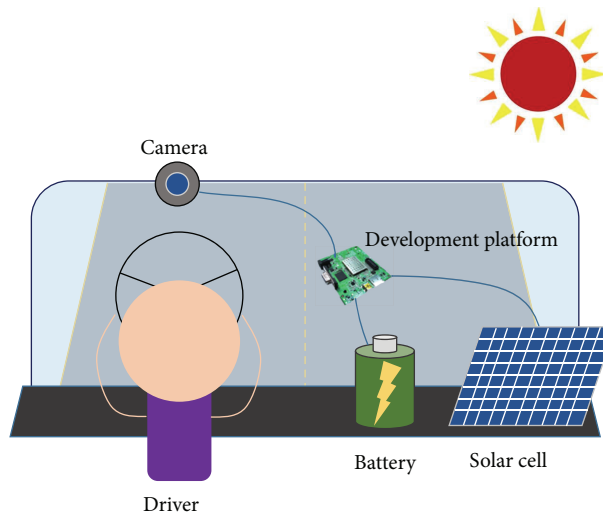


FIGURE 11: System architecture.

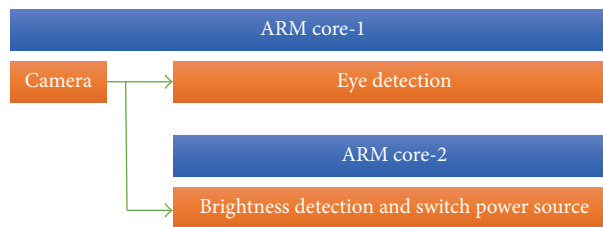


FIGURE 12: Task dispatches of the proposed system on the multicore platform.



FIGURE 13: Overview of the experimental car.

TABLE 2: Specification of driver monitor system.

(a)		(b)	
Solar cell		Camera	
Maximum power	20 W	Category	Webcam
Output tolerance	$\pm 5\%$	Connection type	USB
Maximum power voltage	17.6 V	USB protocol	USB 2.0
Maximum power current	1.14 A	USB VID_PID	082D
Open circuit voltage	21.6 V	UVC support	Yes
Short circuit current	1.39 A	Frame rate (max)	480p@30fps
Maximum system voltage	1000 V		
Dimension ( $L * W * D$ )	552 * 352 * 25 mm		

(b)	
TI OMAP4430 embedded platform	
ARM CPU	ARM Cortex-A9
Memory	1 GB
Size ( $L \times W$ )	85 mm $\times$ 70 mm
Operating system	Android 4.0.1
Power voltage	5 V
Power current	3.6 A
Input power	18 W

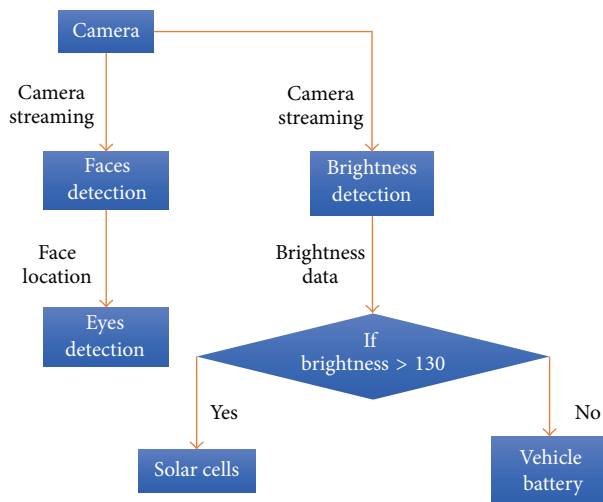


FIGURE 14: Software architecture.

and application environments was adopted to evaluate the system's face and eye detection for intelligent driver monitor applications. Figure 17 shows the results of faces and eyes detection and fatigue state identification. The yellow region of Figure 17 is the eyes location and the green region is representing the left-eye and right-eye. The red region of Figure 17 depicts the fact that fatigue state has been detected. Figure 18 demonstrates results of the proposed system in different face angles and illumination conditions.

The proposed system was tested under the conditions that the solar irradiance is 10 to 113  $W/m^2$  and solar energy and brightness at 10 to 170. From the testing results, when the outside solar radiation is high, the brightness of the inside of

the car is increased, and the eye detection accuracy can also increase as well.

## 6. Conclusions

This study has presented an on-road driver monitoring system, which is implemented on a stand-alone in-vehicle embedded system and powered by effective solar cells. An efficient eye detection technique is developed to monitor the driver's fatigue states. This driver monitoring technique is implemented on a low-power embedded in-vehicle platform. To efficiently switch the appropriate power sources, this study also proposed monitoring machinery that can detect the brightness around the car to effectively determine whether the system is driven by the solar cells or by the vehicle battery. On sunny days, the in-vehicle system can be powered by solar cell in places without the vehicle battery. While in the evenings or on rainy days, the ambient solar brightness is insufficient, the system is powered by the vehicle battery. The proposed eye detection system can achieve the accuracy rate of above 90% with the brightness value higher than 130, and the solar irradiance in this situation can achieve above 52  $W/m^2$ .

The proposed system has been tested under the conditions that the solar irradiance is 10 to 113  $W/m^2$  and solar energy and brightness at 10 to 170. From the experimental results, when the outside solar radiation is high, the brightness of the inside of the car is increased, and the eye detection accuracy can also increase as well. Therefore, this solar powered driver monitoring system can be efficiently applied on electric cars to save energy consumption and promote the driving safety.

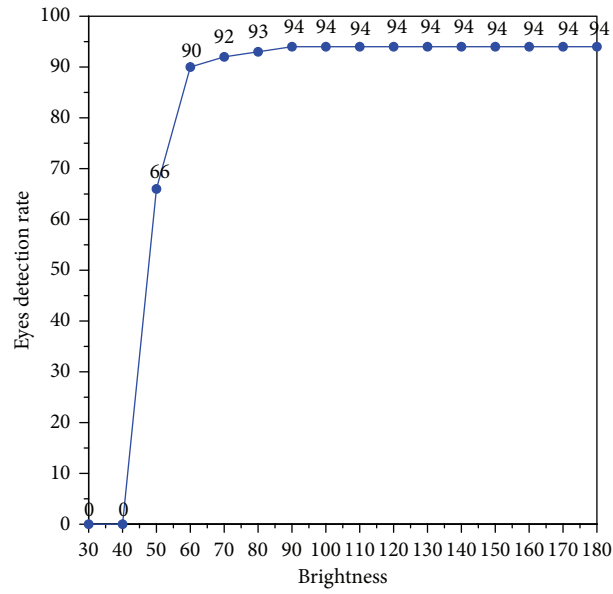


FIGURE 15: The relationship between detection rate and brightness.

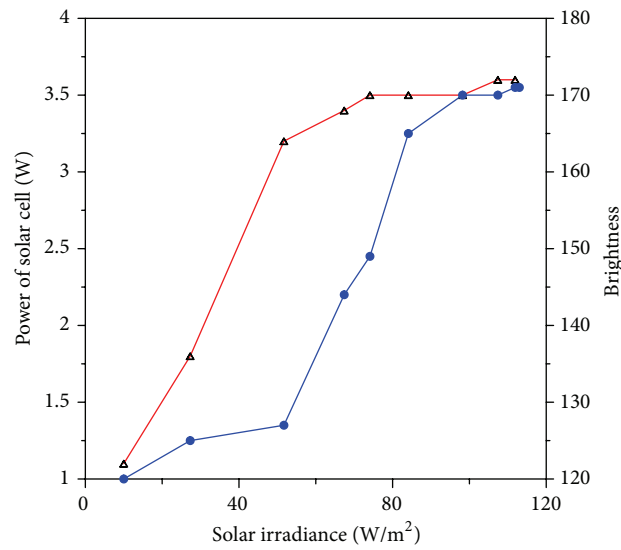


FIGURE 16: Solar irradiance, brightness with power of solar cell analysis.

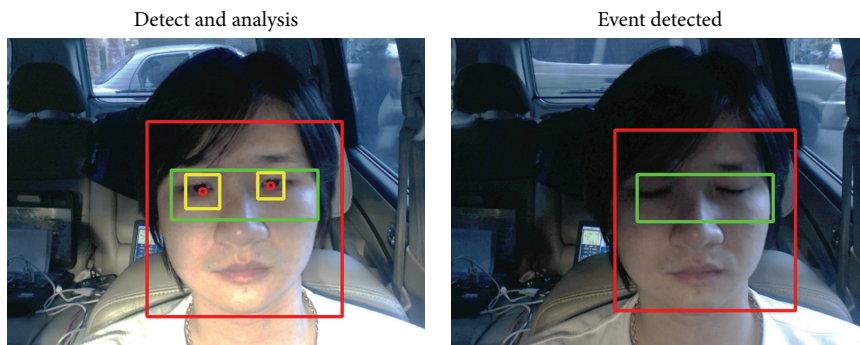


FIGURE 17: The result of faces and eyes detection and fatigue detection.

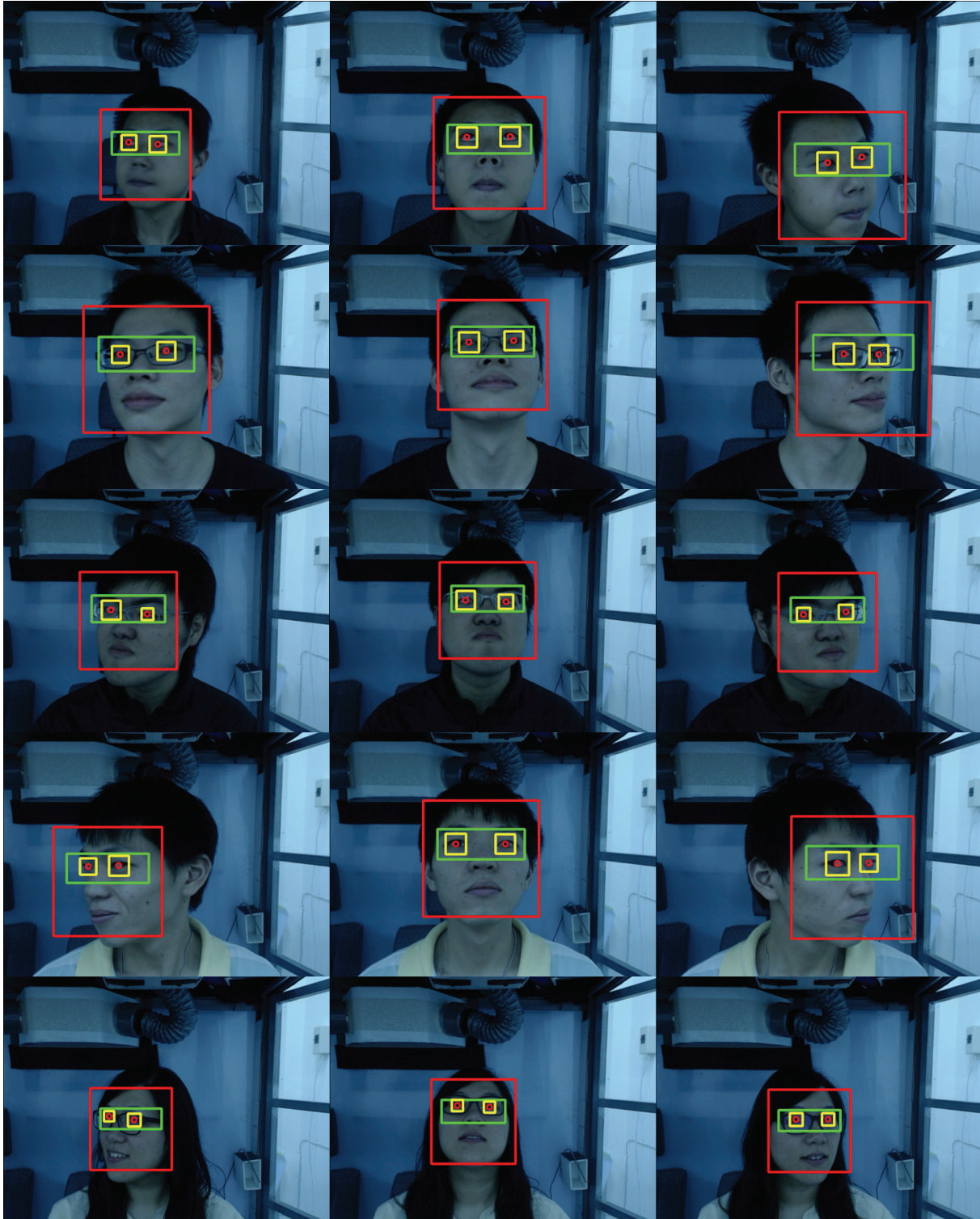


FIGURE 18: The result of evaluate the proposed system capability in different angles.

### Conflict of Interests

None of the authors of the present work have direct or indirect financial relation that might lead to conflict of interests of any kind for any of the authors.

### Acknowledgment

This project is financially sponsored by the National Science Council under Grants nos. NSC-102-2219-E-027-006 and NSC-102-2622-E-027-027-CC2.

## References

- [1] D. Yang and H. Yin, "Energy conversion efficiency of a novel hybrid solar system for photovoltaic, thermoelectric, and heat utilization," *IEEE Transactions on Energy Conversion*, vol. 26, no. 2, pp. 662–670, 2011.
- [2] A. Gaur and G. N. Tiwari, "Performance of photovoltaic modules of different solar cells," *Journal of Solar Energy*, vol. 2013, Article ID 734581, 13 pages, 2013.
- [3] G. van de Kaa, J. Rezaei, L. Kamp, and A. de Winter, "Photovoltaic technology selection: a fuzzy MCDM approach," *Renewable and Sustainable Energy Reviews*, vol. 32, pp. 662–670, 2014.
- [4] G. K. Singh, "Solar power generation by PV (photovoltaic) technology: a review," *Energy*, vol. 53, pp. 1–13, 2013.
- [5] Z. J. Chien, H. P. Cho, C. S. Jwo, C. C. Chien, S. L. Chen, and Y. L. Chen, "Experimental investigation on an absorption refrigerator driven by solar cells," *International Journal of Photoenergy*, vol. 2013, Article ID 490124, 6 pages, 2013.
- [6] B. Huang, C. Chen, P. Hsu, W. Tseng, and M. Wu, "Direct battery-driven solar LED lighting using constant-power control," *Solar Energy*, vol. 86, no. 11, pp. 3250–3259, 2012.
- [7] M. Turk, "Computer vision in the interface," *Communications of the ACM*, vol. 47, no. 1, pp. 61–67, 2004.
- [8] T. B. Moeslund, A. Hilton, and V. Krüger, "A survey of advances in vision-based human motion capture and analysis," *Computer Vision and Image Understanding*, vol. 104, no. 2-3, pp. 90–126, 2006.
- [9] I. Haritaoglu, D. Harwood, and L. S. Davis, "W4: real-time surveillance of people and their activities," *IEEE Transactions on Pattern Analysis and Machine Intelligence*, vol. 22, no. 8, pp. 809–830, 2000.
- [10] N. Dalal and B. Triggs, "Histograms of oriented gradients for human detection," in *Proceedings of the IEEE Computer Society Conference on Computer Vision and Pattern Recognition (CVPR '05)*, vol. 1, pp. 886–893, June 2005.
- [11] H. Fujiyoshi and A. J. Lipton, "Real-time human motion analysis by image skeletonization," in *Proceedings of the 4th IEEE Workshop on Applications of Computer Vision (WACV '98)*, pp. 15–21, Princeton, NJ, USA, October 1998.
- [12] P. Viola, M. J. Jones, and D. Snow, "Detecting pedestrians using patterns of motion and appearance," *International Journal of Computer Vision*, vol. 63, no. 2, pp. 153–161, 2005.
- [13] T. Ishikawa, S. Baker, I. Matthews, and T. Kanade, "Passive driver gaze tracking with active appearance models," in *Proceedings of the 11th World Congress on Intelligent Transportation Systems*, pp. 1–18, October 2004.
- [14] R. Herpers and G. Sommer, "An attentive processing strategy for the analysis of facial features," in *Face Recognition: From Theory to Applications*, pp. 457–468, Springer, 1998.
- [15] R.-L. Hsu, M. Abdel-Mottaleb, and A. K. Jain, "Face detection in color images," *IEEE Transactions on Pattern Analysis and Machine Intelligence*, vol. 24, no. 5, pp. 696–706, 2002.
- [16] Z. Li and S. Kim, "A modification of Otsu's method for detecting eye positions," in *Proceedings of the 3rd International Congress on Image and Signal Processing (CISP '10)*, vol. 5, pp. 2454–2457, IEEE, Yantai, China, October 2010.
- [17] D. W. Hansen and A. E. C. Pece, "Eye tracking in the wild," *Computer Vision and Image Understanding*, vol. 98, no. 1, pp. 155–181, 2005.
- [18] A. L. Yuille, P. W. Hallinan, and D. S. Cohen, "Feature extraction from faces using deformable templates," *International Journal of Computer Vision*, vol. 8, no. 2, pp. 99–111, 1992.
- [19] Y. Nara, J. Yang, and Y. Suematsu, "Face detection using the shape of face with both color and edge," in *Proceeding of the IEEE Conference on Cybernetics and Intelligent Systems*, vol. 1, pp. 147–152, December 2004.
- [20] A. Królak and P. Strumiłło, "Eye-blink controlled human-computer interface for the disabled," in *Human-Computer Systems Interaction*, vol. 60 of *Advances in Intelligent and Soft Computing*, pp. 123–133, 2009.
- [21] J. J. Magee, M. R. Scott, B. N. Waber, and M. Betke, "EyeKeys: a real-time vision interface based on gaze detection from a low-grade video camera," in *Computer Vision and Pattern Recognition Workshop*, vol. 10, p. 159, 2004.
- [22] C.-Y. Ho, *Applying Connected Component Labeling in Real-Time Eye Tracking*, National Taipei University of Technology, Taipei, Taiwan, 2010.
- [23] M. Gopi Krishna and A. Srinivasulu, "Face detection system on AdaBoost algorithm using Haar classifiers," *International Journal of Modern Engineering Research*, vol. 2, no. 5, pp. 3556–3560, 2012.
- [24] P. Viola and M. J. Jones, "Robust real-time face detection," *International Journal of Computer Vision*, vol. 57, no. 2, pp. 137–154, 2004.
- [25] B. F. Wu, Y. L. Chen, and C. C. Chiu, "A discriminant analysis based recursive automatic thresholding approach for image segmentation," *IEICE Transactions on Electronics*, no. 8, pp. 1716–1723, 2005.
- [26] K. Suzuki, I. Horiba, and N. Sugie, "Linear-time connected-component labeling based on sequential local operations," *Computer Vision and Image Understanding*, vol. 89, no. 1, pp. 1–23, 2003.
- [27] C.-Y. Ho, *Applying connected component labeling in real-time eye tracking [M.S. thesis]*, National Taipei University of Technology, Taipei, Taiwan, 2010.

## Research Article

# Structure-Property Relationship of New Organic Sensitizers Based on Multicarbazole Derivatives for Dye-Sensitized Solar Cells

Hyo Jeong Jo, Jung Eun Nam, Dae-Hwan Kim, Hyojeong Kim, and Jin-Kyu Kang

Daegu Gyeongbuk Institute of Science and Technology, 50-1 Sang-ri, Hyeonpung-myeon, Dalseong-gun, Daegu 711-873, Republic of Korea

Correspondence should be addressed to Jin-Kyu Kang; [apollon@dgist.ac.kr](mailto:apollon@dgist.ac.kr)

Received 10 April 2014; Accepted 13 June 2014; Published 30 June 2014

Academic Editor: Ching-Song Jwo

Copyright © 2014 Hyo Jeong Jo et al. This is an open access article distributed under the Creative Commons Attribution License, which permits unrestricted use, distribution, and reproduction in any medium, provided the original work is properly cited.

A new multicarbazole based organic dye (**C2A1**, **C2S1A1**) with a twisted structure was designed and synthesized, and the corresponding dye (**C1A1**) without the twisted structure was synthesized for comparison. They were successfully applied in dye-sensitized solar cells (DSSCs). The results showed that the nonplanar structure of **C2A1** and **C2S1A1** can efficiently retard the dye aggregation and charge recombination. The organic dye (**C2S1A1**) with thiophene units also exhibited a higher molar extinction coefficient and red-shifted absorption, which leads to an improved light harvesting efficiency. The **C2S1A1**-sensitized solar cell produced a solar-to-electricity conversion efficiency of 5.1%, high open circuit voltage ( $V_{oc}$ ) of 0.69 V, and short-circuit photocurrent density of  $10.83 \text{ mA cm}^{-2}$  under AM 1.5 irradiation ( $100 \text{ mW cm}^{-2}$ ) conditions.

## 1. Introduction

Since the first successful fabrication of sandwich type solar cells by O'Regan and Grätzel in 1991 [1], the dye-sensitized solar cells (DSSCs) have received significant attention in both the academic and industrial fields, owing to their efficiency, high adaptability, economic feasibility, and relatively less environmental issues compared with the traditional Si-based solar cells. A DSSC consists of three main components: a photoanode, an electrolyte, and a sensitizer. Among these components, the sensitizer plays the important role of capturing the photons and generating the electrons, which are injected into the conduction band of the semiconductor (e.g.,  $\text{TiO}_2$ ). Significant research efforts have been made to develop efficient sensitizers to enhance the efficiency of DSSCs. Among dyes used as sensitizers, the sensitization of nanocrystalline  $\text{TiO}_2$  solar cells with Ru-complex photosensitizers (e.g., N3 and N719) has been intensively studied. As a result, power conversion efficiencies (PCEs) higher than 11% under AM 1.5 irradiation have been achieved [2–4]. However, metal-free organic sensitizers have shown PCEs between 6% and 10% [5–9] under the same conditions. Nevertheless, organic

dyes possess many advantages, such as high molar extinction coefficients ( $\epsilon$ ), ease of customized molecular design for the desired photophysical and photochemical properties, cost effectiveness without the need for transition metals, and in some cases being environmentally friendly. However, one drawback of organic dyes is that the electron lifetimes ( $\tau_e$ ) of the DSSCs with organic dyes were shorter than with a Ru dye. This is due to the charge recombination between the injected electrons in the  $\text{TiO}_2$  electrode and  $\text{I}_3^-$  ion in the liquid electrolyte and the aggregation of the dyes on  $\text{TiO}_2$  ( $\pi$ - $\pi$  stacking). Usually, charge recombination can be decreased by introducing alkyl side chains into the dye molecule backbones [10, 11], and dye aggregation can be restrained via molecular design that changes the molecular structure from planar to nonplanar or twisted [12–14]. Hence, careful design of dyes containing a twisted structure is a preferred strategy for the development of high performance DSSCs [15–17]. The attachment of a carbazole unit to the conjugated polymer backbone can efficiently depress  $\pi$ -stacking of the polymers in the solid state [18–21], and such a unit has been introduced to the dye molecules used in the DSSCs.

In this study, a new multicarbazole based organic dye (**C2A1** and **C2SIA1**) with a twisted structure was designed and synthesized, and the corresponding dye (**CIA1**) without the twisted structure was synthesized for comparison. The results showed that nonplanar molecular structures prevented charge recombination and dye aggregation. Furthermore, the organic dye (**C2SIA1**) with thiophene units exhibited a higher  $\epsilon$  value and red-shifted absorption band because of the improved electron extraction paths from the extension of  $\pi$ -conjugation. All the aforementioned factors contributed to an improved light harvesting ability. To verify the strategy, the photovoltaic performances of the DSSCs containing the dyes were compared using their current-voltage ( $I$ - $V$ ) curves, monochromatic photon-to-current efficiencies, and impedance spectroscopy (EIS) analysis, which were used to study the interfacial electron transfer process, light harvesting efficiency for photons of particular wavelengths, and estimate  $\tau_e$ , respectively.

## 2. Materials and Methods

**2.1. Instrumental Analysis.** Structural analysis was performed using the  $^1\text{H}$  NMR spectra recorded on a Bruker Avance NMR 400 spectrometer in  $\text{CDCl}_3$  and  $\text{DMSO}-d_6$ . UV/Vis spectra were recorded using a CARY5000 UV/Vis/NIR spectrophotometer. The redox properties were examined by cyclic voltammetry (CV, model: IviumStat). The electrolyte solution of 0.1 M tetrabutylammonium hexafluorophosphate ( $\text{TBAPF}_6$ ) was prepared in freshly dried dimethylformamide ( $\text{CHCl}_3$ ) solution. The  $\text{Ag}/\text{AgCl}$  and platinum wire (0.5 mm in diameter) electrodes were used as the reference and counter electrodes, respectively.

**2.2. Synthesis.** All the starting materials and solvents were commercially available and were purchased from Aldrich, TCI, and Alfa Aesar. They were used without further purification. The synthetic procedure of **CIA1**, **C2A2**, and **C2SIA1** is illustrated in Scheme 1.

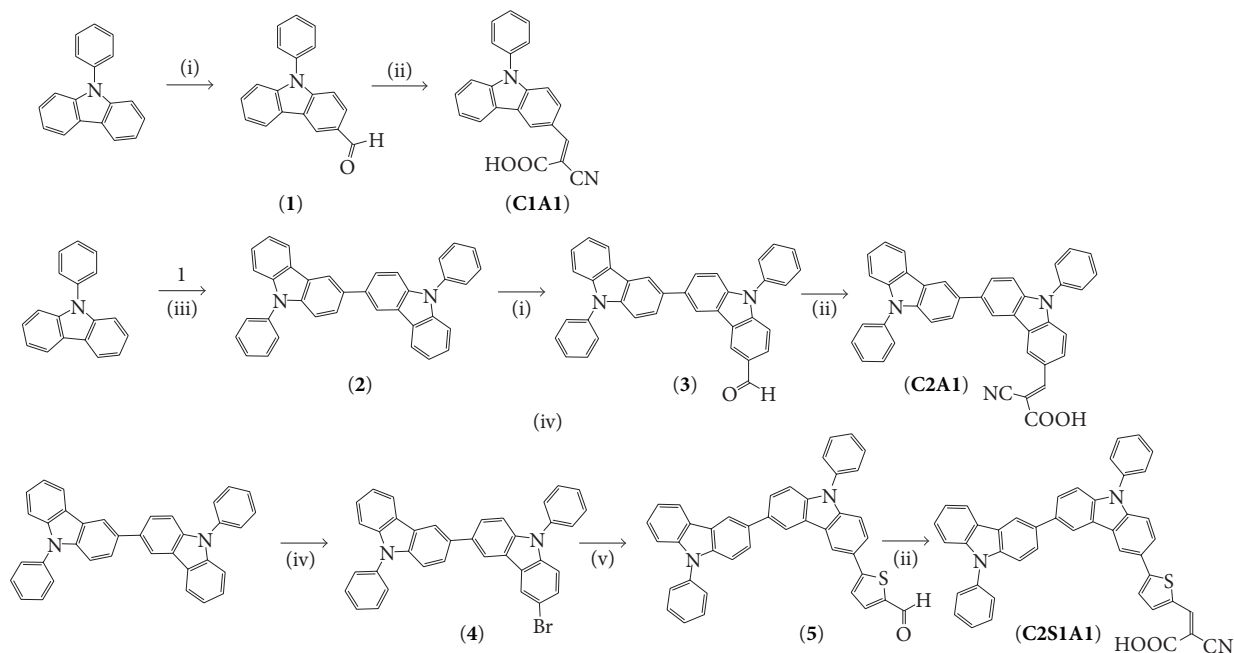
**2.2.1. Synthesis of 9-Phenyl-9H-carbazole-3-carbaldehyde (1).** 9-Phenyl-9H-carbazole (1 g, 8.2 mmol) was dissolved in  $\text{CHCl}_3$  (in 20 mL) and DMF (1 g, 1.23 mmol). Phosphorus oxychloride ( $\text{POCl}_3$ , 1.9 g, 1.23 mmol) was carefully added through a dropping funnel, while the reaction temperature was maintained below  $0^\circ\text{C}$ . After the complete addition of  $\text{POCl}_3$ , the reaction solution turned red color and was stirred under reflux for 8 h. The solution was then poured into water, following which it was neutralized using a sodium hydroxide ( $\text{NaOH}$ ) solution and extracted using methylene chloride ( $\text{CH}_2\text{Cl}_2$ ). The formed precipitate was filtered, dried over magnesium sulfate ( $\text{MgSO}_4$ ), and purified using column chromatography on a silica gel with ethyl acetate/hexane as the eluent (1:3, v/v). The product was obtained as a pale yellow powder. Yield: (1.3 g, 58.5%). mp  $^1\text{H}$  NMR (400 MHz,  $\text{CDCl}_3$ ):  $\delta$  10.1 (s, 1H), 8.14 (s, 1H), 7.67–7.63 (m, 3H), 7.38–7.34 (m, 5H), 6.99–5.86 (m, 3H).

**2.2.2. Synthesis of 2-Cyano-3-(9-phenyl-9H-carbazol-3-yl)-acrylic Acid (CIA1).** 9-Phenyl-9H-carbazole-3-carbaldehyde (**1**) (1 g, 3.68 mmol), 2-cyanoacetic acid (0.4 g, 0.48 mmol), and a catalytic amount of piperidine in acetonitrile ( $\text{CH}_3\text{CN}$ , 30 mL) were mixed and heated under reflux for 4 h. After the solution was cooled to room temperature, it was poured into ice water. The precipitate was filtered, washed with distilled water, and dried under vacuum. The product was obtained as a yellow powder. Yield: (0.5 g, 40.3%).  $^1\text{H}$  NMR (400 MHz,  $\text{DMSO}-d_6$ ):  $\delta$  8.23 (s, 1H), 8.15–8.13 (m, 4H), 7.71–7.68 (m, 3H), 7.01–6.98 (m, 3H). GC-MS: Calcd. for  $\text{C}_{22}\text{H}_{14}\text{N}_2\text{O}_2$   $m/z$ : 338.36; found  $m/z$ : 338.11 $[\text{M}+\text{H}]^+$ ; anal. calcd. for C: 78.09; N: 8.28; H: 4.17; found, C: 79.1; N: 8.16; H: 4.84%.

**2.2.3. Synthesis of 9,9'-Diphenyl-9H,9'H-[3,3']bicarbazolyl (2).** 9-Phenyl-9H-carbazole (5 g, 20.5 mmol) was dissolved in 50 mL  $\text{CHCl}_3$ , and iron (III) chloride (15 g, 90 mmol) was added through a dropping funnel at room temperature. After  $\text{CHCl}_3$  was removed under vacuum, the reaction mixture was poured into methanol ( $\text{CH}_3\text{OH}$ ), and the obtained yellow solid was filtered. The organic phase was washed with ammonia ( $\text{NH}_3$ ), water, and  $\text{CH}_3\text{OH}$ . The product was obtained as a yellow powder. Yield: (4.3 g, 90%).  $^1\text{H}$  NMR (400 MHz,  $\text{CDCl}_3$ ):  $\delta$  8.44 (d, 2H), 8.23–8.21 (d, 2H), 7.78 (dd, 2H), 7.61–7.53 (m, 8H), 7.50–7.43 (m, 8H), 7.30 (m, 2H).

**2.2.4. Synthesis of 9,9'-Diphenyl-9H,9'H-[3,3']bicarbazolyl-6-carbaldehyde (3).** 9,9'-Diphenyl-9H,9'H-[3,3']bicarbazolyl (**2**) (2 g, 4.12 mmol) was dissolved in  $\text{CHCl}_3$  (in 20 mL) and DMF (0.4 g, 5 mmol), and  $\text{POCl}_3$  (0.75 g, 5 mmol) was carefully added through a dropping funnel, while the reaction temperature was maintained below  $0^\circ\text{C}$ . After the complete addition of  $\text{POCl}_3$ , the reaction solution turned red color and was stirred under reflux for 8 h. The mixture was then poured into water. The solution was neutralized using  $\text{NaOH}$  solution and extracted using  $\text{CH}_2\text{Cl}_2$ . The formed precipitate was filtered, dried over  $\text{MgSO}_4$ , and purified using column chromatography on a silica gel with ethyl acetate/hexane as the eluent (1:1, v/v). The product was obtained as a yellow powder. Yield: (1.3 g, 61.9%).  $^1\text{H}$  NMR (400 MHz,  $\text{CDCl}_3$ ):  $\delta$  9.98 (s, 1H), 8.14 (s, 1H), 7.75–7.67 (m, 8H), 7.59–7.5 (m, 8H), 7.35 (m, 5H).

**2.2.5. Synthesis of 2-Cyano-3-(9,9'-diphenyl-9H,9'H-[3,3']bicarbazolyl-6-yl)-acrylic Acid (C2A1).** 9,9'-Diphenyl-9H,9'H-[3,3']bicarbazolyl-6-carbaldehyde (**3**) (0.8 g, 1.56 mmol), 2-cyanoacetic acid (0.15 g, 1.71 mmol), and a catalytic amount of piperidine in  $\text{CH}_3\text{CN}$  (15 mL) were mixed and heated under reflux for 8 h. After the solution was cooled to room temperature, the mixture was poured into ice water. The precipitate was filtered, washed with distilled water, and dried under vacuum. The product was obtained as a dark yellow powder. Yield: (0.4 g, 44.4%).  $^1\text{H}$  NMR (400 MHz,  $\text{DMSO}-d_6$ ):  $\delta$  8.25 (s, 1H), 8.15–8.14 (dd, 4H), 7.84–7.82 (dd, 4H), 7.80–7.78 (m, 4H), 7.61 (d, 4H), 7.40–7.38 (m, 6H). HR-MS (MARDI): Calcd. for  $\text{C}_{40}\text{H}_{25}\text{N}_3\text{O}_2$   $m/z$ : 579.19; found  $m/z$ : 579  $[\text{M}+\text{H}]^+$ ; anal. calcd. for C: 82.88; N: 7.25; H: 4.35; found, C: 83.64; N: 7.10; H: 4.48%.



SCHEME 1: Synthetic procedure of organic dyes. (i) DMF, POCl<sub>3</sub>, and 1,2-dichloroethane, reflux; (ii) cyanoacetic acid, piperidine, and CH<sub>3</sub>CN, reflux; (iii) FeCl<sub>3</sub>, CHCl<sub>3</sub>, and RT; (iv) Br<sub>2</sub> and AcOH; and (v) DME, H<sub>2</sub>O, K<sub>2</sub>CO<sub>3</sub>, and 5-formyl-2-thienylboronic acid, reflux.

**2.2.6. Synthesis of 6-Bromo-9,9'-diphenyl-9H,9'H-[3,3']bicarbazolyl (4).** Bromine (0.7 g, 4.47 mmol) was slowly added to a solution of 9,9'-diphenyl-9H,9'H-[3,3']bicarbazolyl (1.97 g, 4.1 mmol) and acetic acid (10 mL) using a syringe. After stirring the mixture at room temperature for 12 h, the reaction was terminated by adding dilute aqueous NaOH (0.1 M). The reaction mixture was extracted using CH<sub>2</sub>Cl<sub>2</sub> and water. The organic layer was separated and dried over anhydrous MgSO<sub>4</sub>. The crude product was purified by recrystallization using CH<sub>2</sub>Cl<sub>2</sub> and CH<sub>3</sub>OH. The product was obtained as a red solid. Yield: (1.7 g, 74%). <sup>1</sup>H NMR (300 MHz, CDCl<sub>3</sub>): δ 8.38–8.34 (d, 2H), 7.78–7.76 (m, 4H), 7.65–7.63 (m, 6H), 7.58–7.56 (d, 4H), 7.52–7.47 (m, 4H), 7.31 (m, 3H).

**2.2.7. Synthesis of 5-(9,9'-Diphenyl-9H,9'H-[3,3']bicarbazolyl-6-yl)-thiophene-2-carbaldehyde (5).** 6-Bromo-9,9'-diphenyl-9H,9'H-[3,3']bicarbazolyl (4) (1 g, 1.77 mmol) was dissolved in dimethyl ether (DME, 50 mL), water (in 25 mL), potassium carbonate (K<sub>2</sub>CO<sub>3</sub>, 0.6 g, 4.42 mmol), and tetrakis(triphenylphosphine)palladium(0) (Pd(PPh<sub>3</sub>)<sub>4</sub>, 0.2 g, 0.18 mmol), and the solution was mixed and heated overnight under reflux. The reaction mixture was poured into water and then extracted using CH<sub>2</sub>Cl<sub>2</sub> and water. The organic phase was washed with brine and dried over MgSO<sub>4</sub>. The solvent was removed, and the product was purified using column chromatography on a silica gel with CHCl<sub>3</sub>/hexane as the eluent (1:3, v/v). The product was obtained as a yellow powder. Yield: (0.53 g, 50.4%). <sup>1</sup>H NMR (300 MHz, CDCl<sub>3</sub>): δ 9.61 (s, 1H), δ 8.35–8.32 (d, 4H), 8.15–8.13 (m, 4H), 7.75–7.72 (d, 2H), 7.54–7.49 (m, 6H), 7.49–7.47 (m, 6H), 7.40–7.36 (m, 3H).

**2.2.8. Synthesis of 2-Cyano-3-[5-(9,9'-diphenyl-9H,9'H-[3,3']bicarbazolyl-6-yl)-thiophen-2-yl]-acrylic Acid (C2AISI).** 5-(9,9'-Diphenyl-9H,9'H-[3,3']bicarbazolyl-6-yl)-thiophene-2-carbaldehyde (5) (0.5 g, 0.84 mmol), 2-cyanoacetic acid (0.085 g, 1.0 mmol), and a catalytic amount of piperidine in CH<sub>3</sub>CN (30 mL) were mixed and heated under reflux for 4 h. After the solution was cooled to room temperature, the mixture was poured into ice water. The precipitate was filtered, washed with distilled water, and dried under vacuum. The product was obtained as an orange powder. Yield: (0.28 g, 50.3%). <sup>1</sup>H NMR (400 MHz, DMSO-*d*<sub>6</sub>): δ 8.45 (s, 1H), 8.38–8.35 (d, 2H), 8.23–8.21 (m, 3H), 8.19–8.16 (m, 4H), 7.71–7.69 (d, 2H), 7.56–7.51 (m, 6H), 7.49–7.47 (m, 6H), 7.40–7.36 (m, 3H). HR-MS (MARDI): Calcd. for C<sub>44</sub>H<sub>27</sub>N<sub>3</sub>O<sub>2</sub>S *m/z*: 661.18; found *m/z*: 661.2 [M+H]<sup>+</sup>; anal. calcd. for C: 79.86; N: 6.35; S: 4.85; H: 4.11; found, C: 80.15; N: 5.98; S: 4.26; H: 4.97%.

**2.3. Fabrication and Characterization of DSSCs.** The TiO<sub>2</sub> paste was coated on a pre-cleaned glass substrate containing fluorine doped tin oxide (FTO, TEC8, Pilkington, 8 Ωcm<sup>-2</sup>, thickness: 2.3 mm) using the doctor-blade coating method and sintered at 500°C for 1 h. The other TiO<sub>2</sub> paste was recoated over the sintered layer using TiO<sub>2</sub> particles (approximately 400 nm) as the scattering layer, and the glass substrate was sintered again at 500°C for 1 h. The prepared TiO<sub>2</sub> film was dipped in an aqueous solution of 0.04 M titanium tetrachloride (TiCl<sub>4</sub>) at 70°C for 30 min. For dye adsorption, the annealed TiO<sub>2</sub> electrodes were immersed in the dye solution (0.3 mM of dye in ethanol) at room temperature for 24 h. The dye-adsorbed TiO<sub>2</sub> electrode and platinum counter electrode were assembled using a 60 μm thick Surlyn (Dupont, 1702)

TABLE 1: Electrochemical parameters of organic dyes.

Dye	$\epsilon_{\max}^a / M^{-1} \text{ cm}^{-1}$	$\lambda_{\max}^a / \text{nm (Sol)}$	$E_{0-0}^b (\text{eV}) (\text{abs})$	$E_{\text{ox}}^c (\text{V vs. NHE})$	$E_{\text{ox}} - E_{0-0}^d (\text{V vs. NHE})$	HOMO (eV)	LUMO (eV)
<b>C1A1</b>	15260	392	2.64	0.84	-1.8	-5.23	-2.59
<b>C2A2</b>	22815	417	2.5	0.68	-1.82	-5.07	-2.57
<b>C2S1A1</b>	26191	442	2.28	0.5	-1.78	-4.89	-2.61

<sup>a</sup>Maximum absorption and extinction coefficient at maximum absorption of dyes in chloroform solution. <sup>b</sup> $E_{0-0}$  (band gap) was determined from intersection of absorption and emission spectra in chloroform solution. <sup>c</sup>Oxidation potential ( $E_{\text{HOMO}}$ ) of dye was measured using cyclic voltammogram in chloroform solution. <sup>d</sup> $E_{\text{HOMO}} - E_{0-0} = E_{\text{LUMO}}$ .

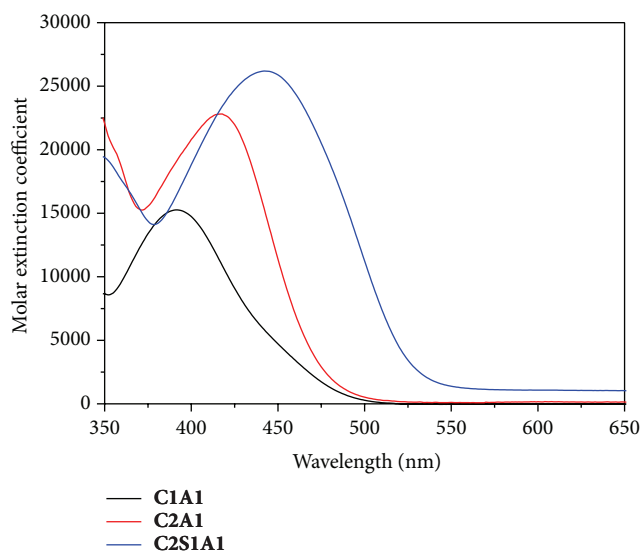


FIGURE 1: Absorption spectra for organic dyes in chloroform solution.

as the bonding agent. The liquid electrolyte was introduced through a prepunctured hole on the counter electrode. The electrolyte comprised 3-propyl-1-methyl-imidazolium iodide (PMII, 1 M), lithium iodide (LiI, 0.2 M), iodide ( $I_2$ , 0.05 M), and *tert*-butylpyridine (TBP, 0.5 M) in  $\text{CH}_3\text{CN}$ /valeronitrile (85:15). The active areas of the dye-adsorbed  $\text{TiO}_2$  films were estimated using a digital microscope camera with image analysis software (Moticam 1000).

The photovoltaic  $I$ - $V$  characteristics of the prepared DSSCs were measured under 1 sunlight intensity ( $100 \text{ mW cm}^{-2}$ , AM 1.5), which was verified using a standard Si-solar cell (Keithley 2400, ORIEL, Newport, PV Measurement Inc.). The monochromatic incident photon-to-current efficiencies (IPCEs) were plotted as a function of the wavelength of light by using an IPCE measurement system (PEC-S20, Peccell Technologies, Inc.).

### 3. Results and Discussion

**3.1. Electronic Absorption Properties of Organic Dyes.** The UV/Vis absorption spectra of the organic dyes in  $\text{CHCl}_3$  are shown in Figure 1 and the corresponding data are summarized in Table 1. The absorption band at 390–450 nm can be attributed to the intramolecular charge transfer (ICT) between the donor and acceptor. The absorption maxima of

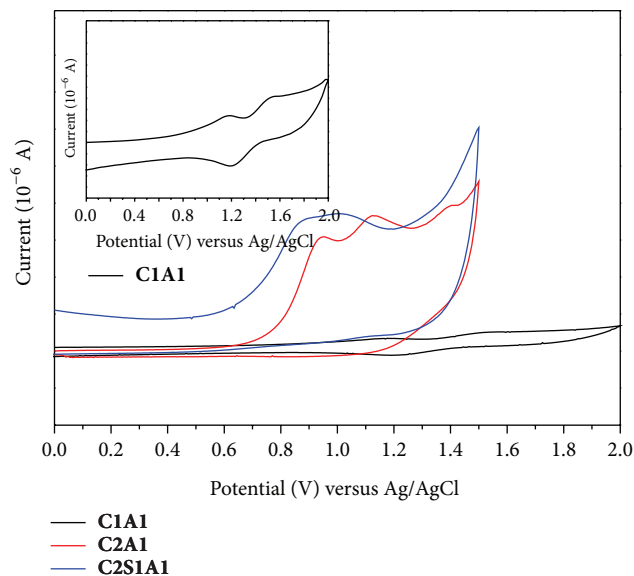


FIGURE 2: The cyclic voltammetric curves of the dyes in chloroform containing 0.1 M  $\text{TBAPF}_6$  as supporting electrolyte at a scan rate of  $50 \text{ mV s}^{-1}$ .

the charge-transfer band in  $\text{CHCl}_3$  are at 392, 417, and 442 nm for **C1A1**, **C2A1**, and **C2S1A1**, respectively. Compared to the **C1A1** dye, the **C2A1** and **C2S1A1** dyes exhibited red-shifted absorption at 25 nm and 50 nm, respectively. This shows that the added carbazole units are beneficial to extend the light absorption and to increase the electron donating ability in comparison to a single carbazole unit (**C1A1**). The  $\epsilon$  values of the organic dyes are larger than that of the N719 dye, which indicates that these dyes have good light harvesting ability.

The electrochemical behavior of the organic dyes was measured by CV, as shown in Figure 2. The detailed data are listed in Table 1. The highest occupied molecular orbital (HOMO) levels of these dyes were 0.84 V, 0.68 V, and 0.5 V for **C1A1**, **C2A1**, and **C2S1A1** versus normal hydrogen electrode (NHE), respectively. The obtained values are more positive than the  $I_3^-/I^-$  redox potential value (0.4 V versus NHE). This indicates that the oxidized dyes formed after the electron injection into the conduction band of  $\text{TiO}_2$  could accept electrons from the electrolyte thermodynamically. They could also accept electrons from the LUMO levels that are more negative than the  $\text{TiO}_2$  conduction band. This indicates that the electrons from the excited LUMO level can be easily injected onto the photoelectrode and that the oxidized dyes may be regenerated using the  $I_3^-/I^-$  redox couple.

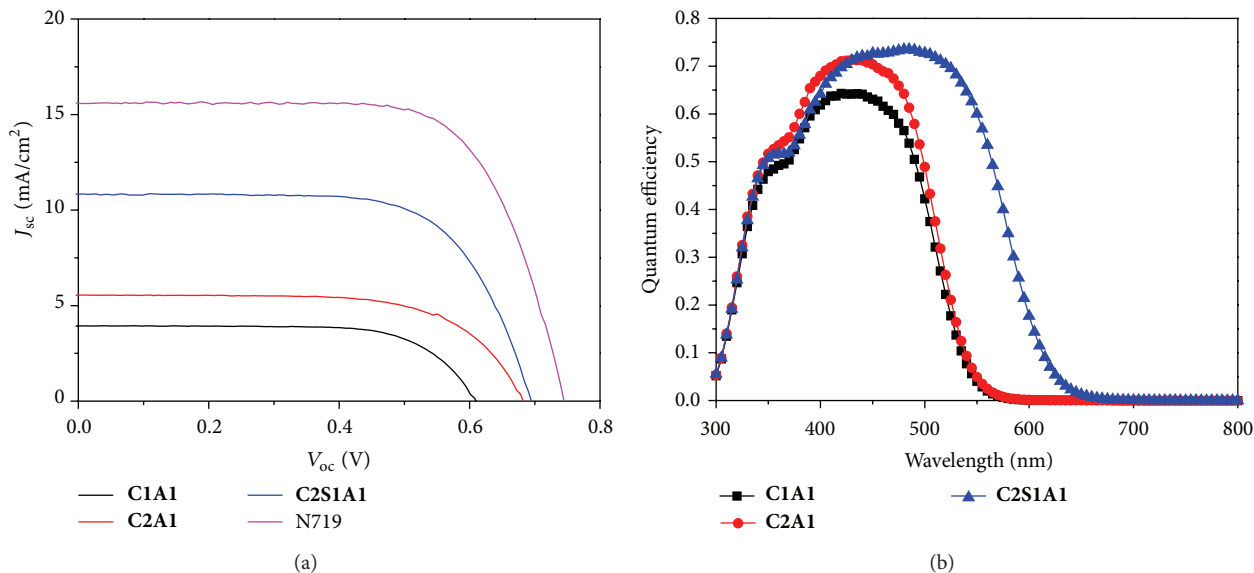


FIGURE 3: (a) Current density-voltage characteristics of dye-sensitized solar cells containing organic dyes under illumination using simulated solar light (AM 1.5,  $100 \text{ mW cm}^{-2}$ ). (b) Incident photon-to-current efficiency curves for dye-sensitized solar cells containing organic dyes.

**3.2. Photovoltaic Measurements.** The photovoltaic performances of the DSSCs based on organic dyes were compared using the variation of flow current with the bias voltage, IPCE, impedance, and electron lifetime analysis. Figure 3(a) shows the  $I$ - $V$  curves of the DSSCs with the different organic dyes, as summarized in Table 2.

Under the standard global AM 1.5 solar irradiation, the cells based on **C2A1S1** and **C2A1** dyes containing two carbazole units exhibited higher efficiency compared to those based on the **CIA1** dye. The short-circuit current density ( $J_{sc}$ ), open circuit voltage ( $V_{oc}$ ), and overall yield ( $\eta$ ) of the three dyes are in the order of **C2SIA1** > **C2A1** > **CIA1**. This is due to the improved light absorption ability by the added carbazole units and the existence of twisted structures, which resulted in an increased current density and inhibited dye aggregation and charge recombination [22]. The higher efficiency of the **C2SIA1** dye can be explained by the increased electron donating ability and  $\epsilon$  values due to the introduction of thiophene. The thiophene unit in the **C2SIA1** dye may have caused strong  $\pi$ - $\pi$  interactions that could be attributed to the light harvesting efficiency.

In order to rationalize these observations, the spectra of the monochromatic IPCE of the DSSCs based on the organic dyes are shown in Figure 3(b). The carbazole-based sensitizers efficiently converted visible light to photocurrent across the higher energy region over the wavelength range of 350–550 nm. A maximum IPCE of 74% was realized at 480 nm for the **C2SIA1** dye, while the **C2A1** and **CIA1** dyes exhibited a maximum IPCE of 69% and 63% at 440 nm, respectively. This is probably due to the fact that the **C2SIA1** dye has a much broader absorption spectrum whose contributions are expected to enhance the photogenerated current values.

In addition, EIS was employed to study the electron recombination in the DSSCs. The EIS measurement is shown

TABLE 2: Photovoltaic performance of dye-sensitized solar cells<sup>a</sup>.

Dye <sup>b</sup>	$J_{sc}/\text{mA cm}^{-2}$	$V_{oc}/\text{V}$	FF (%)	$\eta/\%$
<b>CIA1</b>	3.939	0.608	69.84	1.67
<b>C2A1</b>	5.548	0.681	66.04	2.5
<b>C2SIA1</b>	10.83	0.69	67.68	5.1
N719	15.58	0.745	69.66	8.09

<sup>a</sup>Photovoltaic performance under AM1.5 irradiation of dye-sensitized solar cells containing organic dyes based on 3-propyl-1-methyl-imidazolium iodide (1 M), lithium iodide (0.2 M), iodide (0.05 M), and *tert*-butylpyridine (0.5 M) in acetonitrile/valeronitrile (85 : 15). <sup>b</sup>Dye bath: chloroform solution ( $3 \times 10^{-4}$  M).

in Figure 4, and the data is listed in Table 3. The  $R_s$  and  $R_{rec}$  represent the series resistance and charge-transfer resistance at the dye/ $\text{TiO}_2$ /electrolyte interface, respectively, and  $R_{CE}$  represents the resistance at the counter electrode. The values of  $R_s$  and  $R_{CE}$  (the first semicircle in the Nyquist plot) were almost the same for the three dyes because of the same electrode material and same electrolyte used. The  $R_{rec}$  was determined by the middle semicircle in the Nyquist plot. From the EIS measurements, the  $\tau_e$ , which expresses the electron recombination between the electrolyte and  $\text{TiO}_2$ , was calculated following a literature procedure [23]. The  $R_{rec}$  for the dyes **CIA1**, **C2A1**, and **C2SIA1** was 36.65, 19.71, and 13.84  $\Omega$ , respectively. Under illumination, the smaller  $R_{rec}$  values indicated fast charge generation and transport. The calculated  $\tau_e$  of **CIA1**, **C2A1**, and **C2SIA1** was 2.36, 3.52, and 4.7 ms, respectively. Among the dyes, the **C2SIA1**-based cell had a longer  $\tau_e$ , which led to a lower rate of charge recombination and thus improved  $V_{oc}$ . Therefore, the **C2SIA1** dye provided a much faster electron transport and prolonged  $\tau_e$ . The improved values of  $J_{sc}$  and  $V_{oc}$  of the DSSCs with the **C2SIA1** dye can be mainly attributed to the improved light harvesting efficiency.

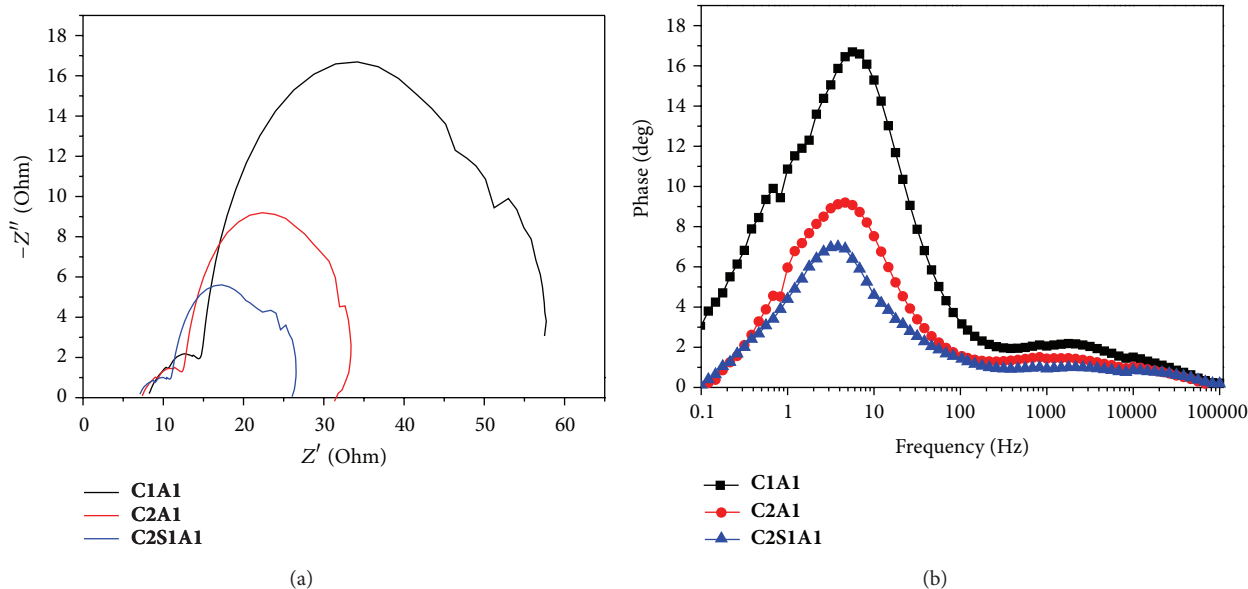


FIGURE 4: (a) Measured dye-sensitized solar cell impedance spectrum at forward bias condition under illumination. (b) Bode-phase plots for the dye-sensitized solar cells.

TABLE 3: Performances of mercurochrome and organic dye based dye-sensitized solar cells and electron transport properties of their photoanodes as determined by impedance analysis. Cell areas are  $0.24 \text{ cm}^2$ .

Dyes	$R_1$ ( $\Omega$ ) <sup>a</sup>	$R_2$ ( $\Omega$ ) <sup>b</sup>	$R_3$ ( $\Omega$ ) <sup>c</sup>	$\tau_e$ <sup>d</sup> (ms)
C1A1	8.29	6.32	36.65	2.4
C2A1	7.41	5.1	19.71	3.5
C2SIA1	6.97	3.99	13.84	4.7

<sup>a</sup> $R_1$  is fluorine doped tin oxide interface resistance. <sup>b</sup> $R_2$  is due to resistance at interface between counter electrode and electrolyte. <sup>c</sup> $R_3$  possibly originated from backward charge transfer from  $\text{TiO}_2$  to electrolyte and electron conduction in porous  $\text{TiO}_2$  film. <sup>d</sup> $\tau$  is lifetime of an electron in dye-sensitized solar cells.

## 4. Conclusions

In this study, a new multicarbazole based organic dye (C2A1 and C2SIA1) with a twisted structure was designed and synthesized, and the corresponding dye (CIA1) without twisted structure was synthesized for comparison. The addition of carbazole units to the organic dyes is an effective method to adjust and control the photochemical and electrochemical properties of the dyes, which determine the charge recombination and overall energy conversion efficiency. The C2SIA1 dye exhibited the highest PCE of 5.1% with a  $V_{oc}$  of 0.69 V and short-circuit photocurrent density of  $10.83 \text{ mA cm}^{-2}$ . The increased electron donating ability of the C2SIA1 molecule provided higher  $\epsilon$  values and a much broader absorption spectrum.

## Conflict of Interests

The authors declare that there is no conflict of interests regarding the publication of this paper.

## Acknowledgment

This work was supported by the DGIST R&D Programs of the Ministry of Science, ICT and Future Planning of Korea (13-BD-05).

## References

- [1] B. O'Regan and M. Grätzel, "A low-cost, high-efficiency solar cell based on dye-sensitized colloidal  $\text{TiO}_2$  films," *Nature*, vol. 353, pp. 737–740, 1991.
- [2] M. K. Nazeeruddin, S. M. Zakeeruddin, R. Humphry-Baker et al., "Acid-base equilibria of (2,2'-bipyridyl-4,4'-dicarboxylic acid)ruthenium(II) complexes and the effect of protonation on charge-transfer sensitization of nanocrystalline titania," *Inorganic Chemistry*, vol. 38, no. 26, pp. 6298–6305, 1999.
- [3] M. K. Nazeeruddin, F. de Angelis, S. Fantacci et al., "Combined experimental and DFT-TDDFT computational study of photoelectrochemical cell ruthenium sensitizers," *Journal of the American Chemical Society*, vol. 127, no. 48, pp. 16835–16847, 2005.
- [4] M. J. Grätzel, "Dye-sensitized solar cells," *Journal of Photochemistry and Photobiology C: Photochemistry Reviews*, vol. 4, no. 2, pp. 145–153, 2003.
- [5] T. Horiuchi, H. Miura, K. Sumioka, and S. Uchida, "High efficiency of dye-sensitized solar cells based on metal-free indoline dyes," *Journal of the American Chemical Society*, vol. 126, no. 39, pp. 12218–12219, 2004.
- [6] Z. Wang, Y. Cui, K. Hara, Y. Dan-Oh, C. Kasada, and A. Shinpo, "A high-light-harvesting-efficiency coumarin dye for stable dye-sensitized solar cells," *Advanced Materials*, vol. 19, no. 8, pp. 1138–1141, 2007.
- [7] K. Hara, T. Sato, R. Katoh et al., "Molecular design of coumarin dyes for efficient dye-sensitized solar cells," *The Journal of Physical Chemistry B*, vol. 107, no. 2, pp. 597–606, 2003.

- [8] S. Hwang, J. H. Lee, C. Park et al., "A highly efficient organic sensitizer for dye-sensitized solar cells," *Chemical Communications*, no. 46, pp. 4887–4889, 2007.
- [9] S. S. Park, Y. S. Won, Y. C. Choi, and J. H. Kim, "Molecular design of organic dyes with double electron acceptor for dye-sensitized solar cell," *Energy & Fuels*, vol. 23, no. 7, pp. 3732–3736, 2009.
- [10] J. E. Kroeze, N. Hirata, S. Koops et al., "Alkyl chain barriers for kinetic optimization in dye-sensitized solar cells," *Journal of the American Chemical Society*, vol. 128, pp. 16376–16383, 2006.
- [11] J. He, W. Wu, J. Hua et al., "Bithiazole-bridged dyes for dye-sensitized solar cells with high open circuit voltage performance," *Journal of Materials Chemistry*, vol. 21, pp. 6054–6062, 2011.
- [12] L. Y. Lin, C. H. Tsai, K. T. Wong et al., "Organic dyes containing coplanar diphenyl-substituted dithienosilole core for efficient dye-sensitized solar cells," *The Journal of Organic Chemistry*, vol. 75, no. 14, pp. 4778–4785, 2010.
- [13] N. Cho, H. Choi, D. Kim et al., "Novel organic sensitizers containing a bulky spirobifluorene unit for solar cell," *Tetrahedron*, vol. 65, no. 31, pp. 6236–6243, 2009.
- [14] D. Heredia, J. Natera, M. Gervaldo et al., "Spirobifluorene-bridged donor/acceptor dye for organic dye-sensitized solar cells," *Organic Letters*, vol. 12, no. 1, pp. 12–15, 2010.
- [15] Y. Liang, B. Peng, J. Liang, Z. Tao, and J. Chen, "Triphenylamine-based dyes bearing functionalized 3,4-propylenedioxythiophene linkers with enhanced performance for dye-sensitized solar cells," *Organic Letters*, vol. 12, no. 6, pp. 1204–1207, 2010.
- [16] X. Zhang, Z. Wang, Y. Cui, N. Koumura, A. Furube, and K. Hara, "Organic sensitizers based on hexylthiophene-functionalized indolo[3, 2-b]carbazole for efficient dye-sensitized solar cells," *Journal of Physical Chemistry C*, vol. 113, no. 30, pp. 13409–13415, 2009.
- [17] J. I. Nishida, T. Masuko, Y. Cui et al., "Molecular design of organic dye toward retardation of charge recombination at semiconductor/dye/electrolyte interface: introduction of twisted  $\pi$ -linker," *Journal of Physical Chemistry C*, vol. 114, no. 41, pp. 17920–17925, 2010.
- [18] E. M. Barea, C. Zafer, B. Gultekin et al., "Quantification of the effects of recombination and injection in the performance of dye-sensitized solar cells based on N-substituted carbazole dyes," *Journal of Physical Chemistry C*, vol. 114, no. 46, pp. 19840–19848, 2010.
- [19] Z. J. Ning, Q. Zhang, W. J. Wu, H. C. Pei, B. Liu, and H. J. Tian, "Starburst triarylamine based dyes for efficient dye-sensitized solar cells," *The Journal of Organic Chemistry*, vol. 73, pp. 3791–3797, 2008.
- [20] D. Kim, J. K. Lee, S. O. Kang, and J. Ko, "Molecular engineering of organic dyes containing N-aryl carbazole moiety for solar cell," *Tetrahedron*, vol. 63, no. 9, pp. 1913–1922, 2007.
- [21] N. Koumura, Z. S. Wang, S. Mori, M. Miyashita, E. Suzuki, and K. Hara, "Alkyl-functionalized organic dyes for efficient molecular photovoltaics," *Journal of the American Chemical Society*, vol. 128, no. 44, pp. 14256–14257, 2006.
- [22] H. Lai, J. Hong, P. Liu, C. Yuan, Y. Li, and Q. Fang, "Multi-carbazole derivatives: New dyes for highly efficient dye-sensitized solar cells," *RSC Advances*, vol. 2, no. 6, pp. 2427–2432, 2012.
- [23] L. C. Zou and C. Hunt, "Characterization of the conduction mechanisms in adsorbed electrolyte layers on electronic boards using AC impedance," *Journal of the Electrochemical Society*, vol. 156, no. 1, pp. C8–C15, 2009.

## Research Article

# A Novel Hybrid Model for Short-Term Forecasting in PV Power Generation

Yuan-Kang Wu,<sup>1</sup> Chao-Rong Chen,<sup>2</sup> and Hasimah Abdul Rahman<sup>3</sup>

<sup>1</sup> Department of Electrical Engineering, National Chung-Cheng University, 168 University Road, Minhsiung, Chiayi 62102, Taiwan

<sup>2</sup> Department of Electrical Engineering, National Taipei University of Technology, Section 3, Chung-hsiao E. Road, Taipei 10608, Taiwan

<sup>3</sup> Centre of Electrical Energy Systems, Universiti Teknologi Malaysia (UTM), 81310 Johor Bahru, Malaysia

Correspondence should be addressed to Yuan-Kang Wu; [allenwu@ccu.edu.tw](mailto:allenwu@ccu.edu.tw)

Received 3 April 2014; Accepted 13 June 2014; Published 30 June 2014

Academic Editor: Ching-Song Jwo

Copyright © 2014 Yuan-Kang Wu et al. This is an open access article distributed under the Creative Commons Attribution License, which permits unrestricted use, distribution, and reproduction in any medium, provided the original work is properly cited.

The increasing use of solar power as a source of electricity has led to increased interest in forecasting its power output over short-time horizons. Short-term forecasts are needed for operational planning, switching sources, programming backup, reserve usage, and peak load matching. However, the output of a photovoltaic (PV) system is influenced by irradiation, cloud cover, and other weather conditions. These factors make it difficult to conduct short-term PV output forecasting. In this paper, an experimental database of solar power output, solar irradiance, air, and module temperature data has been utilized. It includes data from the Green Energy Office Building in Malaysia, the Taichung Thermal Plant of Taipower, and National Penghu University. Based on the historical PV power and weather data provided in the experiment, all factors that influence photovoltaic-generated energy are discussed. Moreover, five types of forecasting modules were developed and utilized to predict the one-hour-ahead PV output. They include the ARIMA, SVM, ANN, ANFIS, and the combination models using GA algorithm. Forecasting results show the high precision and efficiency of this combination model. Therefore, the proposed model is suitable for ensuring the stable operation of a photovoltaic generation system.

## 1. Introduction

Taiwan generally imports more than 97% of its energy; 88% of all energy is generated by burning fossil fuels. Additionally, Taiwan's power grid is mainly a centralized power grid, which can cause insufficient peak power supply and lacks diversified energy sources and distributed peak-load auxiliary power. Growing domestic and foreign environmental awareness has made the development of clean power increasingly important. Wind and solar energy are the most common natural energies. In metropolitan areas with weak winds, solar energy has become the dominant renewable energy. Notably, many developed countries have invested heavily in R&D and provided incentives that promote the use and development of photovoltaic (PV) systems. During 2000–2013, the compound growth rate of the global solar cell market reached 35.5%, indicating that the PV industry is growing rapidly. However, due to the fact that solar irradiance and climate factors can influence solar power output, variation

in power generation capacity may be a nonsteady random process. Additionally, the types and installation locations of PV panels by users and utilized in local power generation systems may vary markedly. Hence, PV panels may impact a power system once integrated into the power grid. To reduce the uncertainty associated with PV power generation capacity and to incorporate energy storage systems into power systems, analyzing and predicting PV power output have become essential.

Many factors, such as the sun's elevation angle, atmospheric conditions, hours of sunshine, and the season, affect solar irradiance. This results in significant randomness in solar power generation. As meteorology has progressed, many studies of solar irradiance have applied several models, such as the clear-sky solar irradiance model [1], for example, the American Society of Heating, Refrigerating and Air-Conditioning Engineers (ASHRAE) energy model, the semi-sinusoidal model, and the Collares-Pereira and Rabl model. These models do not consider variations in surface

solar irradiance due to complex weather and environmental effects, typically resulting in large differences between calculation results and actual values. Additionally, although huge databases of weather forecasts exist, determining surface solar irradiance accurately and predicting power output accurately are difficult tasks. Therefore, one must consider using artificial intelligence and statistical theory to make short-term predictions about the amount of power generated by PV systems.

Among the many solar energy-related studies, the prediction of solar irradiance remains a basis for most predictions of PV power generation [2–7]. Many solar irradiance forecasting models have been developed. These models can be divided into two main groups: statistical models and NWP models. Statistical models are based upon the analysis of historical data. They include time-series models, satellite data based models, sky images based models, ANN models, and wavelet analysis based models. NWP models are based on the reproduction of physical phenomenon. From the practical point of view, different data sources and forecasting techniques vary significantly with the time scope of forecasting. Generally, statistical models are typically used for the short-term forecasting, that is, from few minutes to hours. NWP models results tend to have large error for the very short horizons. However, the longer-term forecasts will depend much more heavily on the NWP models. Additionally, cloud imagery and a hybrid model can improve the results of forecasting when solar irradiance presents a strong variability like in many of insular territories.

In Taiwan, a Weather Research and Forecasting (WRF) based data assimilation system was implemented to configure the operational numerical weather prediction system (NWP) at Central Weather Bureau (CWB) of Taiwan. The NWP system consists of the Advanced Research WRF dynamical core model and the three-dimensional variational data assimilation (3DVAR) system. The triple nested model domains were centered over Taiwan Island with horizontal resolution of 45-, 15-, and 5-km and 45 levels in the vertical. The outermost domain covered most of the Asian and west Pacific area in order to better describe the evolution of the subtropical high over the Pacific Ocean and avoid the dilution from the lateral boundary problem due to the Tibetan Plateau. The operational NWP system was running 4 times a day and provided hourly output up to 84-hr forecast length. The short wave radiation parameterization chosen is based on the Goddard shortwave radiation scheme, which is two-stream multiband scheme that accounts for both diffuse and direct solar radiation. This scheme provides the downward short wave radiation flux as used in this study. A standard Monin-Obukhov similarity theory was applied in the model surface layer to interpolate the wind field at 10-m AGL.

In recent years, several research works have discussed direct prediction of PV power output [8–17]. These studies mainly used various neural network-based prediction techniques [8–10], time-series analysis [11], and hybrid forecasting models [14–17]. Various hybrid models for the PV power forecasting have become more popular. For instance, reference [14] proposed a power forecasting system that combines three forecasting modules: two numerical weather prediction

models (one global and one at mesoscale) and an artificial intelligence based model. Reference [15] proposed a two-stage method where first the clear-sky model approach is used to normalize the solar power and then adaptive linear time-series models are applied for prediction. Reference [17] combines two well-known methods: the seasonal autoregressive integrated moving average method (SARIMA) and the support vector machines method (SVMs) to predict the short-term PV power. The aim of those hybrid models for PV power forecasting is to benefit from the advantages of each model and obtain globally optimal forecasting performance. For instance, several statistical and AI-based methods are utilized to determine the optimum weight between online measurements and meteorological forecasts. An accurate measurement can significantly improve the accuracy of PV power generation predictions.

There are several differences between renewable energy forecasting and load forecasting. The load forecasting is highly dependent on the historical data because load curve is periodical and seasonal. However, most of renewable energy output is not periodical; therefore, the input valuables of the PV forecasting module need not only historical PV measurement data but weather-related variables, such as solar irradiance and temperature.

The main objective of this study is to propose a novel hybrid model for PV power forecasting. The proposed model combines the ARIMA, SVM, ANN, and ANFIS methods with GA algorithm. The detail about the hybrid forecasting model is illustrated in the following sections.

## 2. System Monitoring and Database

In this study, PV power generation systems at three different locations were considered as our case studies for 1-hour-ahead prediction of PV output; the locations of PV systems are Malaysia's Green Energy Office (GEO) Building, Taiwan's Taichung Thermal Power Plant, and an academic building at the National Penghu University (NPU). Although the environment in which each building is located differs slightly, monitoring records for these locations are similar, including power generation data, atmospheric temperature, solar irradiance, and module temperature. Table 1 lists the characteristics and related parameters for these three PV systems.

By the end of 2013, the total installed capacity of PV systems in Taiwan is up to 333.4 MW. To encourage solar PV installations in Taiwan, drive economic growth, and facilitate the development of the solar PV industry, the Bureau of Energy, Ministry of Economic Affairs (BOE, MOEA), has launched the "Million Solar Rooftop Program." The target of installed capacity of the PV systems is 6200 MW by 2030 in Taiwan.

In view of abundant agriculture residue, sunshine, and rainfall, the most significant sources of renewable energy in Malaysia are biomass, solar, and small-hydropower. Currently, the installed capacity of renewable energy in Malaysia stands at less than 1% (55 MW) of total power generation capacity, including 1.5 MW of cumulative grid-connected PV installations. Nevertheless, renewable energy is expected to grow with the implementation of an FiT scheme, in which

TABLE 1: PV database utilized in this study.

Data sources	Installed capacity	Sampling data	Measurement item	Total number of data
PTM Green Energy Office (GEO) Building Pusat Tenaga Malaysia	45.36 kWp	Average values for 15-minute	(i) PV generation (ii) Atmospheric temperature (iii) Solar irradiance ( $W/m^2$ ) (iv) PV module temperature	9009
Taichung Thermal Power Plant	72 kWp	Average values for 60-minute	(i) PV generation (ii) Atmospheric temperature (iii) Solar irradiance ( $W/m^2$ ) (iv) PV module temperature	6830
An academic building at the National Penghu University (NPU)	70 kWp	Average values for 10-minute	(i) PV generation (ii) Atmospheric temperature (iii) Solar irradiance ( $W/m^2$ ) (iv) PV module temperature	17280

individuals can sell the power generated to utility companies such as TNB and Sabah Electricity Sendirian Berhad (SESB) at a fixed premium rate for specific period.

Although daily PV output power varies, by observing time-series characteristics, a regular daily pattern can be identified. If two similar days with similar solar irradiance and cloud distribution are compared, the patterns of power output on those two days should be very similar. However, due to dramatic variations in cloud cover and the difficulty in making accurate predictions, the actual curve of PV power generation is a fundamental waveform with random fluctuations. For instance, the PV system power output curve of Malaysia's GEO Building has large fluctuations, mainly because data are sampled at 15-minute intervals (Figure 1). Short-term variations in the amount of solar irradiance and cloud cover also produce different daily fluctuations in its power curve. Figure 2 shows time-series data of PV power generation by the Taichung Thermal Power Plant for one week in July using a three-dimensional (3-D) graphic representation. This daily variation curve has a fundamental curved waveform with some increasing and decreasing random fluctuations. Figure 3 compares PV power generation curves of the Taichung Thermal Power Plant in summer and winter. The power output in summer (solid line) is markedly higher than that in winter (dashed line); however, dramatic fluctuations within a pattern occur in both summer and winter. Additionally, variation in power output during roughly 13-14 hours of sunshine generally corresponds to the variation in solar irradiance (Figure 3). However, when a day suddenly changes from a sunny day into a rainy day or from a very cloudy day into a partially cloudy day, irradiance changes dramatically, resulting in an inaccurate prediction of power output. Therefore, using hourly weather forecast information, such as sunny day, cloudy day, rainy day, and average cloud cover, as input variables for a prediction model can increase its prediction accuracy for sudden changes in day type.

### 3. Determination on Input Variables for the PV Power Forecasting Model

Generally, sufficiently accurate solar irradiance data can be input into a formula to derive predicted output power.

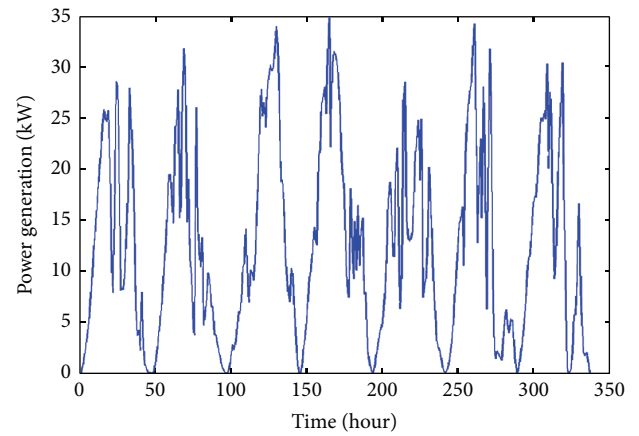


FIGURE 1: Photovoltaic power generation recorded at PTM Green Energy Office (GEO) Building in Malaysia.

Predicting power output from renewable energies is closely related to weather forecast predictions. To predict the amount of solar irradiance or power generated, various environmental factors, such as solar irradiance, cloud cover, atmospheric pressure, and temperature, along with the conversion efficiency of PV panels, installation angles, dust on a PV panel, and other random factors must be considered. All these factors affect PV system output. Hence, in choosing input variables for a prediction model, one should consider deterministic factors strongly correlated with power generation. Additionally, time-series data for PV power generation are strongly autocorrelated and therefore these historical data should be the input data of the forecasting model. An accurate prediction of PV power generation must be accompanied by a stable and detailed monitoring system to record all related information that may aid in solar energy prediction. Many large renewable energy systems with a large number of weather stations and highly stable monitoring systems exist worldwide. This infrastructure is very important to predicting PV power output.

One must choose model input variables carefully, as they are essential to accurate predictions and include weather data that can affect PV power output. However, these detailed

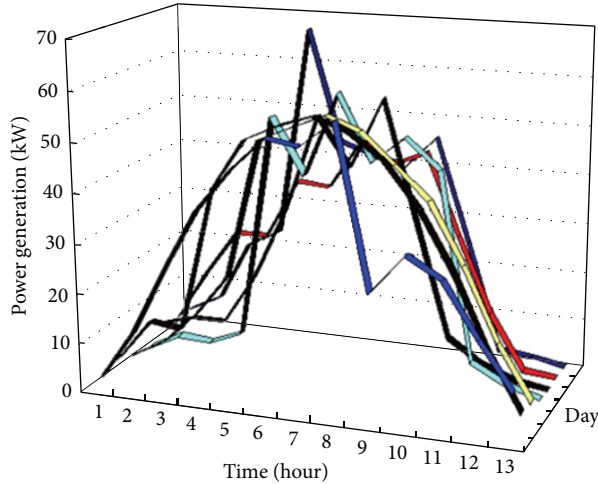


FIGURE 2: Photovoltaic power generation recorded at Taichung Thermal Power Plant in Taiwan.

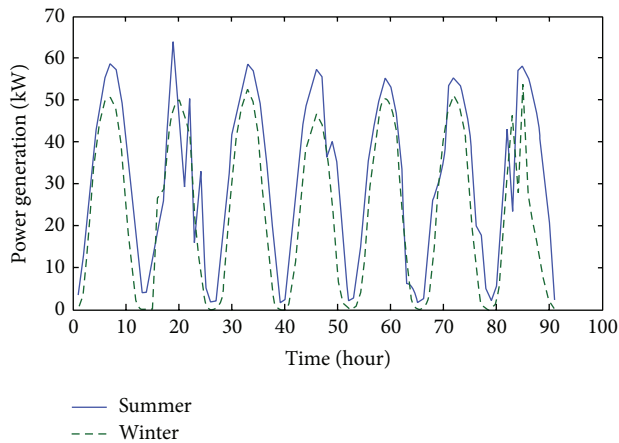


FIGURE 3: PV power generation curves at Taichung Thermal Power Plant in different seasons.

data are not recorded by existing systems that monitor atmospheric data for various PV power generation systems. For small-capacity PV systems in small areas, typical data collected are limited to solar irradiance, power output, atmospheric temperature, and module temperature [18]. Notably, most systems cannot monitor cloud cover accurately. Additionally, typical meteorological centers usually predict hourly average cloud cover inaccurately, such that predicting PV power output accurately becomes extremely difficult. In this study, correlation analysis of measured data for the selected PV systems was applied to the three PV systems to identify variables that are strongly correlated with PV power output. Figure 4 shows the correlation analysis of power output with respect to module temperature of the Malaysian PV system. Analytical results indicate that these two variables, power output and module temperature, are strongly and positively correlated.

Figure 5 shows correlation analysis of power output with respect to solar irradiance for the Malaysian PV system. Although some data deviate slightly from the straight line

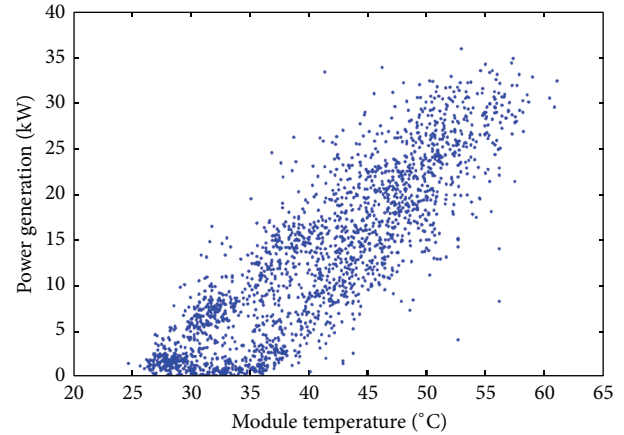


FIGURE 4: Correlation analysis of power output with respect to module temperature at the PTM Green Energy Office (GEO).

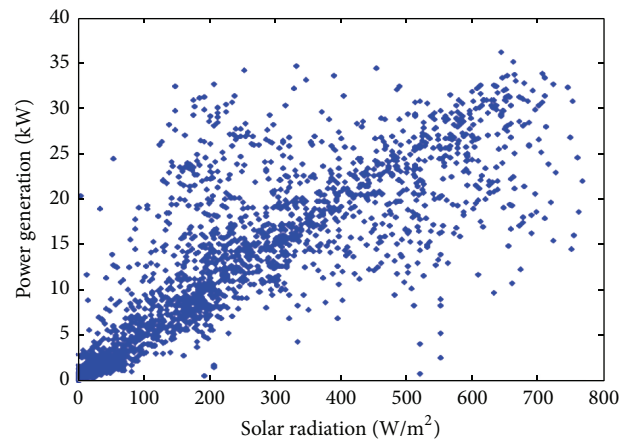


FIGURE 5: Correlation analysis of power output with respect to solar irradiance at the PTM Green Energy Office (GEO).

with a correlation coefficient of 1, the overall trend indicates that these two variables remain strongly correlated.

In this study, correlation coefficients of power output with respect to the other three external variables for these three PV systems are calculated (Table 2). Hourly power output and hourly solar irradiance produce the strongest correlations, and hourly power output has an extremely weak correlation with hourly atmospheric temperature. Power generation module temperature is also strongly correlated with power output. However, module temperature should not be utilized as an external variable for a prediction model because it is unpredictable and weakly correlated with atmospheric temperature. Furthermore, solar irradiance can be estimated using a physical model with appropriate correction. Therefore, solar irradiance in this study is used as an external variable in the prediction model for PV power output. Further, the time-series data of power output are autocorrelated. Table 2 shows correlation coefficients of independent variables for the three PV systems. Table 2 also lists the first three correlation coefficients of independent variables. This study calculates correlation statistics for the

TABLE 2: Comparative analysis on correlation coefficients between PV generation and external variables.

Data sources	External variables			Independent variable		
	Solar irradiance	Module temperature	Atmospheric temperature	$P(t-1)$	$P(t-2)$	$P(t-3)$
PTM Green Energy Office (GEO) Building Pusat Tenaga Malaysia	0.817	0.75	0.13	0.714	0.399	0.044
Taichung Thermal Power Plant	0.978	0.68	0.05	0.786	0.538	0.213
An academic building at the National Penghu University (NPU)	0.840	0.85	0.18	0.864	0.598	0.279

Note:  $P(t-1)$  means one-hour-ahead PV power output.

first three entries and autocorrelations for the first 4–40 entries. Calculation results demonstrate that historical data with high correlation coefficients are data from the previous entry and the previous and next entries of the previous two cycles. These correlation analyses will be a very important reference when choosing input variables to construct any prospective model.

#### 4. Description of the Proposed PV Power Forecasting System

This work utilizes four statistical and artificial intelligence methods, including the autoregressive integrated moving average (ARIMA) model, least-squares support vector machines (LS-SVMs) model, artificial neural network (ANN), and adaptive neurofuzzy inference systems (ANFISs). Furthermore, a novel two-stage model combining these models with the GA is applied to predict short-term wind power.

Several approaches exist for time-series modeling. In an ARIMA model, the future value of a variable is assumed a linear function of several past observations and random errors. An ARIMA model has three iterative steps for model identification, parameter estimation, and diagnostic. The autocorrelation function (ACF) and the partial ACF (PACF) of sample data are utilized as basic tools to identify the best order of the ARIMA model; this involves selecting the most appropriate lags for the AR and MA parts, as well as determining whether a variable requires first differencing to induce stationarity. Once a tentative model is specified, estimation of model parameters is straightforward, usually involving the use of a least-squares estimation process. The last step in model building is diagnostic assessment of model adequacy. This three-step model construction process is typically repeated several times until a satisfactory model is finally selected. This selected model can then be utilized for prediction purposes. Compared to other forecasting techniques, the ARIMA time-series model does not require the meteorological forecast of solar irradiance that is often complicated. Due to its simplicity, the ARIMA model has been widely discussed as a statistical model for forecasting power output from a PV system. An ARIMA model is a single-variable time-series model; the basic description of the ARIMA model is illustrated by the following equation:

$$\phi_p(B) \Phi(B^s) \nabla^d \nabla_s^D Y_t = \theta_q(B) \Theta(B^s) a_t, \quad (1)$$

where  $\phi_p$ ,  $\Phi$ ;  $\theta_q$ ,  $\Theta$  are autoregressive and seasonal-moving average parameters of the ARIMA model,  $\nabla^d$  and  $\nabla_s^D$  are trend and seasonal difference equations, and  $B$  is a backshift operator that defines  $Y(t-1) = BY(t)$ . By the difference equations and both ACF and PACF plots, the significant historical data in certain time lags were chosen as input variables.

The ANN techniques have been used widely to solve forecasting problems. An ANN is a mathematical tool originally based on the way the human brain processes information. An ANN, which may be considered a multivariate, nonlinear, and nonparametric method, should be able to model complex nonlinear relationships much better than conventional linear models. In this work, the multilayer feed-forward back-propagation network is used as the training algorithm because it has been the most frequently used method for training networks of PV power forecasts; furthermore, a Levenberg-Marquardt approach is applied to train the ANN model. The accuracy of ANN solutions relies heavily on chosen input variables. Many methods for identification of ANN input variables have been developed. Most utilized correlation analysis is accompanied by heuristics and an operator's experience. In this work, significant exogenous variables and actual measured historical data have been utilized as input for the ANN model.

Fuzzy systems and neural networks are complementary tools when building intelligent systems; however, fuzzy systems lack the ability to learn and cannot adjust themselves. Merging a neural network with a fuzzy system into an integrated system would be a promising approach for building wind prediction models. The ANFIS system, a fuzzy inference system based on the Sugeno model, incorporates the self-learning ability of an ANN with the linguistic expression function of fuzzy inference, whose membership functions and fuzzy rules are acquired from a large lot of existing data instead of by experience or intuition. The classical network structure is a five-layer feed-forward neural network, which includes a fuzzification layer, rule layer, normalization layer, defuzzification layer, and a single summation neuron. In this work, the Gaussian function is the membership function.

A support vector machine (SVM) is a machine learning algorithm based on statistical learning theory and the principle of structural risk minimization. Various SVM technologies have been applied successfully for such purposes as pattern recognition, nonlinear regression estimation, and

time-series forecasting. The least-squares support vector machines LS-SVM is an extension of the standard SVM. Let  $(x_i, y_i)$  be independent data pairs with each  $x_i \in \mathfrak{R}^n$  denoting a vector belonging to an input space and let each  $y_i \in \mathfrak{R}$  be its corresponding target value in an output space, where  $i = 1, 2, \dots, N$ , and  $N$  is the number of data pairs. In a SVM, data are nonlinearly mapped from the input space to a high dimensional feature space using  $\phi(x)$ . The forecasting function can be introduced as  $f(x) = w \cdot \phi(x) + b$ , where  $w$  is the connection weight vector and  $b$  is bias. The optimization problem for the standard SVM is represented as

$$\begin{aligned} \text{Minimize} \quad & \frac{1}{2} w^T w + \gamma \sum_{i=1}^N \zeta_i \\ \text{Subject to} \quad & y_i [w^T \phi(x_i) + b] \geq 1 - \zeta_i, \quad \zeta_i \geq 0, \end{aligned} \quad (2)$$

where  $\zeta_i$  is a slack variable and  $\gamma$  is a positive real constant for determining penalties for forecasting errors. The above formula can be modified for the LS-SVM; the final LS-SVM model can be represented as

$$f(x) = \sum_{i=1}^N (\alpha_i - \alpha_i^*) \cdot \kappa(x_i, x) + b, \quad (3)$$

where  $\alpha_i$  and  $\alpha_i^*$  are Lagrange multipliers. The Kernel function, which is an inner product of two  $\phi(x)$  functions, is incorporated into computations. This work uses the radial basis function (RBF) kernel.

Each single prediction model has advantages and disadvantages. For instance, some prediction models have a better response capability for rapid changes in a waveform, while other models may be better at capturing steady-state periodical variations. A novel hybrid model combining these prediction models is proposed in this work. It includes a two-stage forecasting process: in the first stage, the PV power is predicted individually by four models; then the forecasting results become the inputs of the second-stage model. In the second stage, the objective of the proposed second-stage hybrid forecasting model is to assign the weight coefficient for each first-stage individual model and form the final hybrid model. In this work, weight coefficients are acquired using an adaptive GA. This weighted-variable hybrid forecasting model consisting of  $m$  prediction models can be denoted as follows:

$$f_c = \alpha_1 \cdot f_1 + \alpha_2 \cdot f_2 + \dots + \alpha_n \cdot f_n, \quad (4)$$

where  $\alpha_1 + \alpha_2 + \dots + \alpha_n = 1$  and  $n$  is the number of forecasting models. In this work,  $n = 4$ , indicating that four first-stage forecasting models are used, that is, the ARIMA, ANN, ANFIS, and SVM models.

The GA in this work, which is based on natural selection, is a parallel, stochastic, and adaptive search algorithm. The GA simultaneously optimizes the entire populations of designs, among which initial populations can be produced randomly. New populations are produced by such operations as selection, crossover, and mutation based on the fitness of the object function, which controls the survival of different

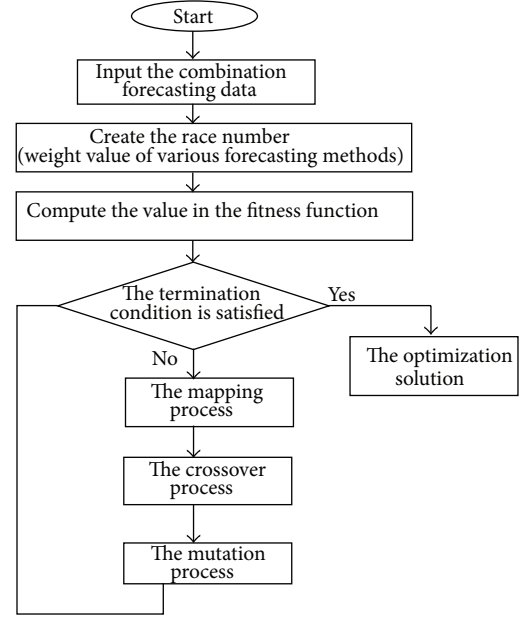


FIGURE 6: Flowchart of the proposed hybrid GA-based model.

samples in offspring and continuously improves the object's property in the next generation to generate the best results. Figure 6 shows the flowchart of the proposed hybrid GA-based model. Additionally, the complete model block diagram is shown in Figure 7.

Actually, there are many methods to construct the combinational forecasting model. For example, the immune algorithm (IA) can also be utilized, which mimics a basic immune system defending against bacteria, viruses, and other disease-related organisms. Additionally, the coding structure for an IA is similar to that of a GA but adds the diversity and affinity calculation strategy. In this paper, the GA was utilized to combine the first-stage forecasting models because it is routinely used to generate useful solutions to optimization and search problems, including the forecasting works.

## 5. Forecasting Results and Discussions

In this study, five prediction models, including four individual models and one combination model, are used for a 1-hour-ahead prediction of power output by the three PV systems. Among these models, the ARIMA model uses a single input variable, in which the autocorrelation coefficient of time-series data is used to identify important historical lead times; the ANN prediction model uses two input variables, including PV power output with high correlation coefficients and the anticipated value of hourly solar irradiance; the LS-SVM and ANFIS prediction models use the previous entry of PV power output and the current entry of predicted solar irradiance. Although the LS-SVM and ANFIS models can use additional input variables, estimation and prediction time for model parameters will increase. Thus, this study mainly uses two input variables to reduce the time required for a prediction. The proposed hybrid prediction model, which is based on the genetic algorithm, uses evolutionary theory to

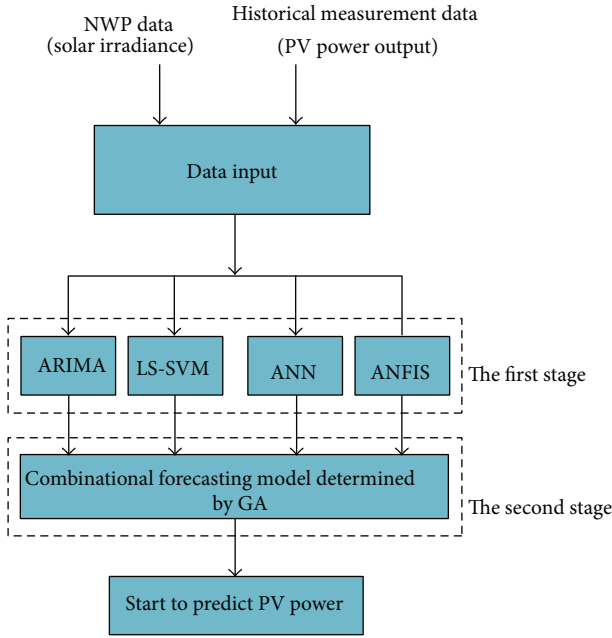


FIGURE 7: The complete model block diagram for the proposed forecasting model.

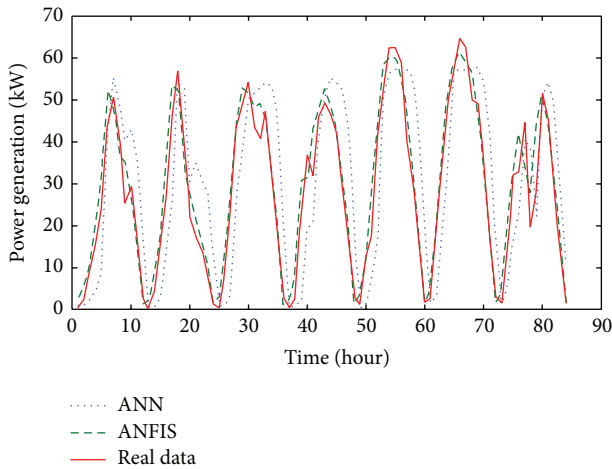


FIGURE 8: Forecasting results for PV power at NPU by using ANN and ANFIS.

estimate the weight of each single prediction model in the hybrid model; these weights are then used to predict PV power output during the next hour.

Figures 8, 9, and 10 present prediction results by applying each prediction model to the PV system installed at NPU. Due to the length limitation for this paper, only the predicted power within a certain week in a predicted month is shown. In this case, the ANFIS and LS-SVM predictions are the most accurate, and predicted curves fit the actual power output curve well. However, some peaks and turning points for the PV output are not predicted accurately. The ARIMA model generates a relatively less accurate prediction. Particularly, when the profile of the daily PV curve varies markedly, fitting the curve with a linear mathematical function is very difficult. According to anticipated prediction results, the

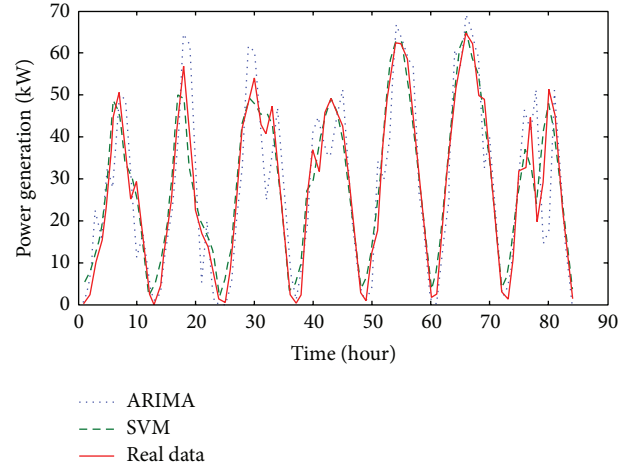


FIGURE 9: Forecasting results for PV power at NPU by using ARIMA and SVM.

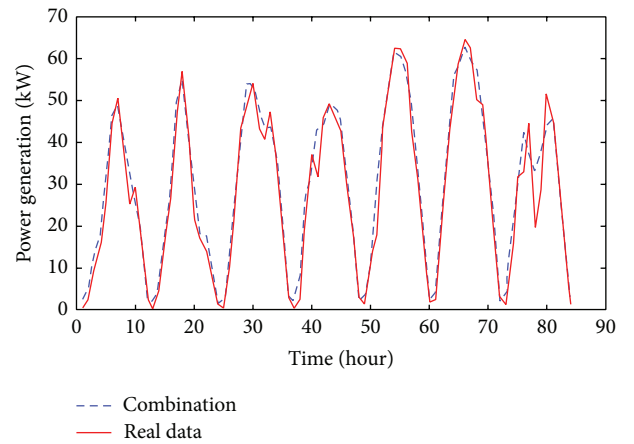


FIGURE 10: Forecasting results for PV power at NPU by using the hybrid combination model.

prediction PV power time series obtained by the ARIMA model normally follows the time sequence profile from the previous cycle. Therefore, values from the previous cycle or even the previous two cycles are used as input variables for this model, such that prediction results can exhibit a memory effect from previous cycles. Figure 10 shows prediction results by the hybrid model using the genetic algorithm. The time-series data correspond to actual data; however, some inconsistencies fail to generate a very accurate result.

The performance of the proposed forecasting model must be evaluated. There are several evaluation criteria for PV forecasting models, such as mean absolute error (MAE), root mean square error (RMSE), and others. In this work, the normalized root mean square error (NRMSE) was utilized because it can provide the comparative analysis for different PV installed-capacity cases. It is defined as follows:

$$NRMSE = 100 \cdot \sqrt{\frac{1}{N} \sum_{i=1}^N \left( \frac{P_a^i - P_f^i}{P_{install}} \right)^2} \% \quad (5)$$

TABLE 3: Comparative analysis on PV power forecasting errors by using different methods.

PV data sources	PTM Green Energy Office (GEO) (%)	Taichung Thermal Power Plant (%)	An academic building at the National Penghu University (NPU) (%)
Forecasting model			
ARIMA	9.52	16.49	13.48
LS-SVM	6.42	4.78	12.03
ANN	7.78	4.75	16.77
ANFIS	7.93	6.82	12.32
Hybrid model	5.64	3.43	6.57

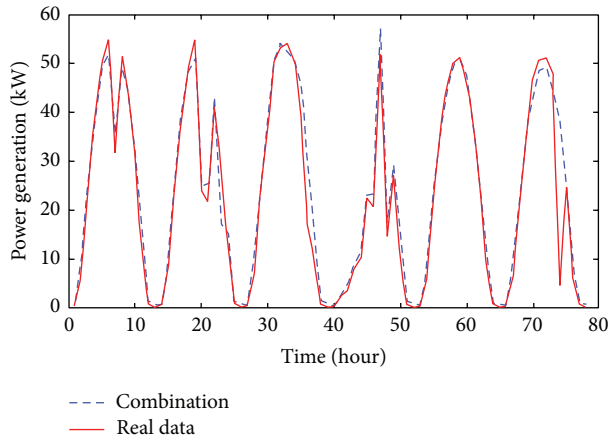


FIGURE 11: Forecasting results for PV power at Taichung Thermal Power Plant by using the hybrid combination model.

where  $P_{\text{install}}$ ,  $P_a$ ,  $P_f$  indicate PV installed capacity, actual PV power output, and PV power forecasting value, respectively, and  $N$  is the total number of samples. Table 3 summarized the forecasting results at three PV systems by using different forecasting models. It is obvious that the proposed hybrid model is superior to other traditional statistical or artificial intelligent methods because its forecasting error is the minimum.

Figure 11 shows the prediction of hourly power output by the PV system at the Taichung Thermal Power Plant. This figure presents the predicted value, which is compared with actual data, and the analyzed time series was taken only for a certain week in the predicted month. Although the actual profile of time-series data of PV power output varied greatly due to varying weather conditions, applying the relatively more accurate hybrid prediction model still provides a much more accurate 1-hour-ahead prediction of power output.

## 6. Conclusions

As the construction scale and capacity of the PV power systems continue expanding, PV power prediction techniques can reduce the effect of randomness on PV power output. In this study, five prediction models were applied for short-term prediction of power output by three PV systems, and actual predictions have been performed for these PV systems

in Taiwan and Malaysia. In terms of input variables used by prediction models, the correlation analyses of related external variables have been carried out and historical power output data and solar irradiance intensities are used as input variables by the prediction models. Analytical results demonstrate that the hybrid prediction model generates the most accurate predictions in most cases; however, it still needs additional and accurate data to monitor the prediction process for large variations in time-series data of PV power output. Specifically, the classification of any daily prediction with respect to the weather forecast data should be performed first. These data are used to predict weather patterns for that day. The amount of cloud cover is also an input variable for the PV prediction model. However, this requires long-term and precise observational records, and an obvious, individual exception sample should be excluded prior to analysis. Furthermore, for yearly prediction models, date and time should also be considered as input variables.

## Conflict of Interests

The authors declare that there is no conflict of interests regarding the publication of this paper.

## Acknowledgments

This work was partially supported by National Science of Council (NSC) of Taiwan under Grant no. NSC 102-2221-E-194-032.

## References

- [1] S. A. Al-Sanea, M. F. Zedan, and S. A. Al-Ajlan, "Adjustment factors for the ASHRAE clear-sky model based on solar-radiation measurements in Riyadh," *Applied Energy*, vol. 79, no. 2, pp. 215–237, 2004.
- [2] M. Diagne, M. David, P. Lauret, J. Boland, and N. Schmutz, "Review of solar irradiance forecasting methods and a proposition for small-scale insular grids," *Renewable and Sustainable Energy Reviews*, vol. 27, pp. 65–76, 2013.
- [3] J. Cao and X. Lin, "Study of hourly and daily solar irradiation forecast using diagonal recurrent wavelet neural networks," *Energy Conversion and Management*, vol. 49, no. 6, pp. 1396–1406, 2008.
- [4] M. Chaabene and M. Ben Ammar, "Neuro-fuzzy dynamic model with Kalman filter to forecast irradiance and temperature

- for solar energy systems,” *Renewable Energy*, vol. 33, no. 7, pp. 1435–1443, 2008.
- [5] G. Reikard, “Predicting solar radiation at high resolutions: a comparison of time series forecasts,” *Solar Energy*, vol. 83, no. 3, pp. 342–349, 2009.
- [6] H. Ohtake, K. Shimose, J. G. D. S. Fonseca Jr., T. Takashima, T. Oozeki, and Y. Yamada, “Accuracy of the solar irradiance forecasts of the Japan Meteorological Agency mesoscale model for the Kanto region, Japan,” *Solar Energy*, vol. 98, pp. 138–152, 2013.
- [7] A. Mellit and A. M. Pavan, “A 24-h forecast of solar irradiance using artificial neural network: application for performance prediction of a grid-connected PV plant at Trieste, Italy,” *Solar Energy*, vol. 84, no. 5, pp. 807–821, 2010.
- [8] A. Mellit, S. Sađlam, and S. A. Kalogirou, “Artificial neural network-based model for estimating the produced power of a photovoltaic module,” *Renewable Energy*, vol. 60, pp. 71–78, 2013.
- [9] C. Chen, S. Duan, T. Cai, and B. Liu, “Online 24-h solar power forecasting based on weather type classification using artificial neural network,” *Solar Energy*, vol. 85, no. 11, pp. 2856–2870, 2011.
- [10] V. L. Brano, G. Ciulla, and M. D. Falco, “Artificial neural networks to predict the power output of a PV panel,” *International Journal of Photoenergy*, vol. 2014, Article ID 193083, 12 pages, 2014.
- [11] Y. Li, Y. Su, and L. Shu, “An ARMAX model for forecasting the power output of a grid connected photovoltaic system,” *Renewable Energy*, vol. 66, pp. 78–89, 2014.
- [12] V. P. A. Lonij, A. E. Brooks, A. D. Cronin, M. Leuthold, and K. Koch, “Intra-hour forecasts of solar power production using measurements from a network of irradiance sensors,” *Solar Energy*, vol. 97, pp. 58–66, 2013.
- [13] C. Chupong and B. Plangklang, “Forecasting power output of PV grid connected system in Thailand without using solar radiation measurement,” *Energy Procedia*, vol. 9, pp. 230–237, 2011.
- [14] L. A. Fernandez-Jimenez, A. Muñoz-Jimenez, A. Falces et al., “Short-term power forecasting system for photovoltaic plants,” *Renewable Energy*, vol. 44, pp. 311–317, 2012.
- [15] P. Bacher, H. Madsen, and H. A. Nielsen, “Online short-term solar power forecasting,” *Solar Energy*, vol. 83, no. 10, pp. 1772–1783, 2009.
- [16] S. K. H. Chow, E. W. M. Lee, and D. H. W. Li, “Short-term prediction of photovoltaic energy generation by intelligent approach,” *Energy and Buildings*, vol. 55, pp. 660–667, 2012.
- [17] M. Bouzardoum, A. Mellit, and A. Massi Pavan, “A hybrid model (SARIMASVM) for short-term power forecasting of a small-scale grid-connected photovoltaic plant,” *Solar Energy*, vol. 98, pp. 226–235, 2013.
- [18] G. Ciulla, V. lo Brano, and E. Moreci, “Forecasting the cell temperature of PV modules with an adaptive system,” *International Journal of Photoenergy*, vol. 2013, Article ID 192854, 10 pages, 2013.

## Research Article

# Constructing Employability Indicators for Enhancing the Effectiveness of Engineering Education for the Solar Industry

Chin-Guo Kuo,<sup>1</sup> Chi-Cheng Chang,<sup>2</sup> and Chun-Cheng Huang<sup>3</sup>

<sup>1</sup> Department of Industrial Education, National Taiwan Normal University, No. 162, Sec. 1, Ho-Ping East Road, Taipei 106, Taiwan

<sup>2</sup> Department of Information Management, Lunghwa University of Science and Technology, No. 300, Sec. 1, Wanshou Road, Guishan, Taoyuan County 333, Taiwan

<sup>3</sup> Taipei Municipal Nangang Vocational High School, No. 29, Xingzhong Road, Taipei 115, Taiwan

Correspondence should be addressed to Chi-Cheng Chang; [chig@mail.lhu.edu.tw](mailto:chig@mail.lhu.edu.tw)

Received 10 April 2014; Accepted 8 May 2014; Published 30 June 2014

Academic Editor: Ho Chang

Copyright © 2014 Chin-Guo Kuo et al. This is an open access article distributed under the Creative Commons Attribution License, which permits unrestricted use, distribution, and reproduction in any medium, provided the original work is properly cited.

The aim of this research is to establish a set of employability indicators that capture the competency requirements and performance expectations that solar energy enterprises have of their employees. In the qualitative component of the study, 12 administrators and 32 engineers in the industry were interviewed, and meetings with focus groups were conducted to formulate a questionnaire for a survey of Taiwanese solar energy companies for the confirmation and prioritisation of the employability indicators. On the basis of the results of the quantitative component, an interpretational model relating competence, job performance, working attitude, and employability for solar corporation recruitment and training purposes as well as for school curricular development was developed. The interpretation model formulated effectively interprets the relationship between solar enterprises' expectations and students' employability. The research contributes a framework for the selection and cultivation of talent, as well as providing a basis for fundamental development of the solar engineering curriculum.

## 1. Introduction

The study of employability is a field of complex nature about which questions are often raised, questions for which there is not at all times a clear and definitive answer [1]. As pointed out by many researchers, employability is closely related to the competence and performance possibilities demonstrated by individuals [2–4]. Its ultimate measure is the contribution to the performance of an enterprise by the employee where the said performance is the output or production results of the enterprise. When the employee commands the competence required by the enterprise then it can be expected that the employee will demonstrate the performance anticipated by the enterprise [5]. Such competence can be broken down into four types: core competence, professional competency, management competence, and general competence [6]. In addition, the common core competences needed by staff of all departments of an enterprise could include customer orientation, teamwork cooperation, profession orientation, active

aggressiveness, and performance orientation [4]. Obviously, the competence and performance requirements that enterprises bring to the attention of their employees have made employability an issue of concern for all solar enterprises and every employee.

As pointed out in competence-based theory, the important features of solar industry employability are the emphasis on advancing competence by individuals and, in particular, a focus on the advancement of competence in long-term self-career development embarked upon by engineers. Therefore, this research aims to answer the following questions: what job performance skills are graduates of universities of technology from solar energy-related departments required to demonstrate by employers and how should these skills be reflected in major student employability indicators? The major contribution of these indicators in the solar industry would be for the selection of talent in recruitment and as a reference for the internal cultivation of talent and for on-the-job training, while in engineering education, they would

provide a basis for the planning and design of the solar energy curriculum, enhancing university students' employability [5, 7].

Accordingly, the research focused on what is required for students who have been employed in the solar industry to sustain long-term employment there, translating these job performance requirements of the workplace via qualitative research methods into employability indicators [8, 9], as well as confirming the applicability of the employability indicators through a qualitative survey and analysis [10]. Thus the purpose of the research was to establish a set of employability indicators for students contemplating employment in the solar industry after graduation from universities of technology. The aim was that the indicators would represent the performance that solar industry enterprises expected students to demonstrate in their future job positions in ways that made the demands of such jobs painfully obvious. From which starting point, the research desired to establish a competence and performance interpretation model for the selection of talent by enterprise recruiters and for reference by internal solar enterprise talent cultivation planners. With these goals, the role of and implications for curricular planning in engineering education take on clearer shape. The research's primary contribution to theory is the establishing of an interpretation model for the relationship between competence, job performance, working attitudes, and employability, by means of the establishment of employability indicators in the solar industry.

## 2. Employability

Employability is generally recognised as the ability of a student to successfully apply for employment after graduation in a smooth way, to maintain their long-term prospects for similarly acquired positions and to develop their job careers favourably over the remainder of their working lives [11]. Cox and King [12] consider employability to signify a person's possession of the ability to acquire skills for the implementation of required jobs, indicating that employability does not necessarily mean a person could start working immediately without further training. Employability can be deemed to be a special feature of a person's capability for work and the desire to maintain his or her attractiveness in the labour market [13]. Hillage and Pollard [14] assume "employability" to mean that the individual could self-sufficiently realise his or her potential for employment in the labour market and continue to demonstrate self-sufficiency in his or her work position even when there are limited job resources. Pool and Sewell [15] believe that employability could be understood as its embodiment in an individual who possesses a set of skills, knowledge, and ability to develop satisfactorily and successfully in the employment market. Rothwell and Arnold [2] deem from the point of view of an individual's employment and career development that employability is concerned with long-term career development in professional fields, even to the point of inclusion of the capability to shift into different professions [16]. In this view, the essence of employability can even be seen as the capability of an individual to shift into another profession for employment

after the employment market of the individual's professional field is saturated. Hence, employability also emphasises the possession of a good profession spill-over effect. On the basis of these definitions, this paper defines employability in the domain of the solar industry as the embodiment in an individual of the capability to maintain the ongoing acquisition of knowledge, skills, and positive attitudes and to properly translate learning experiences into such forms, so as to maintain demonstrations of the performances expected by enterprises on being employed. Persons with high employability potential can learn fast when they are asked to execute a task demanded by a job, and they can transform personal knowledge and skills into the expected job performance according to the job scenario's requirements of the solar industry.

*2.1. Diverse Point of View of Employability.* Three different aspects, input, process, and result, afford different views on employability, contributing to the direction of research.

- (i) The input point of view, which sets out from the point of view of structuralism to explore the composition of employability, based on competence-based theory, considers that an individual must possess good competence to be able to demonstrate high performance on the job. Such researchers as Hafeez and Essmail [17], Peng [18], and Rae [1] demonstrate this point of view.

Research results based on competence-based performance theory are emerging [19]. Robbins [20] assumes that performance measurement based on competence could include individual job output, behaviour, and personal characteristics (including the exhibition of attitudes, self-confidence, independence, cooperation, experience, and others related to superb job performance). Competence-based theory has done well explaining the reference criteria adopted by modern enterprises for recruitment, so graduates need to possess the competences required by the employment market.

- (ii) The process point of view, which emphasizes a high level of association between school curricula and the employment market, considers it necessary to reflect enterprise experts' expectations of students in curricular design and learning activities. School subjects should maintain focus on the changes in practical needs [21]. Rae [1] believes that the students' experience of learning core subjects should be associated with enterprises and employability.
- (iii) The result point of view, which takes the point of view of behaviourism and follows resource-based theory exploring the demonstration of employability, translates performance standards required by the working world into the job performances expected by enterprises, by, for example, the empirical investigation of resource-driven performance conducted by Fernandes et al. [22].

Resource-based theory considers the three elements, company-critical resources, capabilities and competencies to be associated concepts [23], where capabilities and competencies are considered to be interchangeable [24]. The term capabilities was considered by the Ljungquist [25] study to have two meanings, one was the ability of a work team to utilize resources needed in execution of a certain task or activity; the other was an individual's tacit knowledge and organizational memory, which could be incorporated and applied to job coordination. As pointed out in resource-based theory, enterprises expect graduates who are devoted to the workplace to demonstrate good ability in integrative planning and the disposal of available resources. Therefore this research took its direction from the result point of view on employability and emphasized job performance standards to be decided according to the enterprise workplace's surroundings, coupled with experts' judgment, developing the requirements for students' employability in solar enterprises.

**2.2. Employability Indicators.** Employability indicators from the performance point of view naturally put emphasis on job performance. So-called job performance can be defined as the pursuance of special action by a person with the ability to maintain and conform to the condition, policy, and procedure given by the organizational environment to effectively accomplish the job demands [26]. "Job" is considered to be a certain special appointment in the achievement of a certain task, while the task is a description of the activity content of a certain job for an employee [27]. The performance of an employee can include the two categories of job behaviour and activity and job result [28]. The former applies to the job process itself and is assessed mainly by measuring the activity engaged in and the behaviour demonstrated on the job by the employee, while the latter assesses the degree of accomplishment by the employee of a predetermined target. As pointed out by SPSP [29], job performance needs to emphasize ACT, which means the following:

- A: employees' effective and timely completion of a job activity;
- C: employees' competence to do a good job;
- T: their possession of tools and techniques.

In respect of employability indicators, Table 1 summarizes related studies.

In summary of the above, the logical process for the establishment of draft employability indicators in this research following the performance point of view is

- (1) to define the performance point of view of employability;
- (2) to obtain "diverse points of view on employability;"
- (3) to fold in the path of research from the "result point of view."

For (1), we took the point of view of Ljungquist [25], SPSP [29], Chang [5, 30], and Kuo and Sheen [31] and decided performance-point-of-view employability to be on-the-job

integrated planning, evaluation and judgment, working efficiency, working quality, working spirit, monitoring control, and working attitude.

Based on the needs of the research, the operational definitions for each indicator are as shown in Table 2.

### 3. Methodology

The study adopted field interviews and meetings with focus groups as its qualitative methods, while a questionnaire survey provided data for its quantitative methods.

**3.1. Field Interviews.** The field interviews were conducted with 12 administrators (see Table 3) from solar enterprises throughout Taiwan and with 32 of the top-10%, high-performing workers. All interviews were completed within a 5-month period. The interview form used in this study followed Dessler's methods [32] for the collection of duties for graduates' first employment in solar enterprises, where the STAR specific behavioural events included (1) situation: the circumstance surrounding an incident; (2) task: the target generated in response to the demands of the situation; (3) action: the behaviour exhibited by the person in charge; and (4) result: the outcome of the action. The Behavioural Event Interview (BEI) method was applied in translating the behavioural events into the questionnaire items.

Key points in the STAR-specific behavioural event interview included the listing of each STAR item with emphasis on the response a good performance worker should exhibit for each supposed demonstrative behavioural feature, the degree of improvement through training, the possibility to make up a performance insufficiency via recruiting new employees, the capacity standard (certificate requirement) needed by individuals, and the suggestion for measures when the individual's competence is inadequate to demonstrate the anticipated performance (see Tables 4 and 5).

**3.2. Focus Group Method.** A group was formed of 12 experts, amongst whom were a manpower resources consultant and specialists from industry and academia. Focus group meetings were held with the participation of the consultant, general manager, marketing plan manager, manpower resources department staff representatives, department heads, managers, scholars, and high-performing workers. In the process of the group's repeated discussion, the draft questionnaire that originally contained 110 questions was modified and combined to formulate the final questionnaire with 37 questions. The structure of the questionnaire is shown in Table 6.

**3.3. Survey Research.** Through analysis by the experts of the focus group, the draft questionnaire was tested for its reliability and overall validity. Cronbach's  $\alpha$  coefficient was used to examine the internal consistency of responses from pretest receivers. The content validity of the test was assessed through the confirmation of the employability indicators by the focus group and systematic examination of the questionnaire content to determine whether the questionnaire did fully reflect the practical behaviours represented by the

TABLE 1: Related studies of students' employability in engineering education.

Experts/institution	Employability indicators
Tsai et al. [28]	Work attitude and job performance are closely related.
Kagaari [33]	Application of skills, responsibilities, challenges, creativity, originality, safety, career development, adaptation to status quo, technical knowledge at work, and so forth.
MOE [34]	The most needed to enhance employability: foreign language ability, job searching and self-promoting capacity, innovation capability, and leadership capacity.
NTNU [35]	Core employability: working attitude and cooperation capacity favourable for employment, occupational career planning capacity and aggressive learning to advance, possession of professional knowledge, and ability to apply them at work.
Peng [18]	(i) Employability is constructed from three elements: capacity, attitude, and confidence. (ii) Detailed indicators: presentation and communication skills, teamwork cooperation, mother tongue language capability, stability or stress resistance, professional knowledge and techniques, basic computer application skills, the ability to explore and solve problems confronted at work, good working attitudes, strong willingness to continue with studies, high degree of plasticity, professional ethics and morality, optimism in facing career development prospects, active dedication to current job, leadership capacity, innovation capacity, the capacity to apply theory to actual work, professional certificates or related capacities, knowledge of the relevant industrial environment and its development status, foreign language capacity, full understanding and planning for self-career development, and possession of job searching and self-promoting capacity.
NTNU [35]	A 2005 follow-up survey of university graduates after one year of employment found insufficiencies in employability and concluded the causes to be lack of leadership capacity, innovation capacity, the capacity to apply theory to actual work, professional certificates or related capacities, knowledge of the relevant industrial environment and its development status, foreign language capacity, full understanding and planning for self-career development, and possession of job searching and self-promoting capacity.
Jaffer et al. [36]	Efficiency and quality are the challenges of industry for advanced education.
Kuo et al. [37]	Four common dynamic capabilities in response to external demands: "market-oriented sensitivity," "the ability to absorb knowledge," "social-networking capability," and "the integrative ability to communicate and negotiate." Three special dynamic capabilities required by business practices: "the capability to identify what drives market growth," "the capability to develop a good sense of market-entry timing," and "the capability to alter/create customers' needs."
Chang [30]	Market-oriented sensitivity, the ability to absorb knowledge, social-networking capability, and the integrative ability to communicate and negotiate are the dynamic capabilities required of IT entrepreneurs.

employability indicators. Afterwards, Bartlett's sphericity test was applied to confirm whether each aspect was near normal multivariate, and the KMO (Kaiser-Meyer-Olkin) measure of sampling adequacy was adopted for the factor validity test to determine whether factor analysis was appropriate or not. Finally, the major step of content analysis was performed, conducting oblique rotation for maximum variance of the factors revealed by the factor analysis with the intent of assessing the validity of the construction of the questionnaire and the order of importance of the employability indicators.

Random sampling of small and medium solar enterprises in the Taiwan area for the addressing of a survey with the internet version of the questionnaire was the method adopted for data collection. After removing repeated mailings of the questionnaire returned, a total of 501 valid returns were received representing a response rate of 50.1%. The purpose of analysing the data was to understand whether the employability indicators established by the research could receive popular recognition from the solar energy industry.

The application of the above mentioned research methods followed the logical procedure listed below, with a research result being associated with each of the different stages:

- (i) literature analysis: to obtain key points for field interviews;
- (ii) focus group meetings I: to confirm key points for field interviews via experts' points of view;
- (iii) behavioural events interview method: to obtain the draft employability indicators from the performance point of view;
- (iv) focus group meetings II: to confirm the draft employability indicators and the draft questionnaire;
- (v) implementation of survey and data analysis. Following this procedure, several meetings were held during Stage II of the focus group process due to diverging opinions from experts on the significance of the employability indicators. It was considered that

TABLE 2: The definition of employability indicators in the solar industry.

Indicators	Operational definitions
Integrated planning	To do project planning and implementation with the ability to consider the project’s marketability, executability, and effectiveness, so as to further integrate resources in generating the maximum value for the company and customers.
Evaluation and judgment	To execute difficult work with the ability to conduct prior assessments and find the best work procedures, methods and possible supporting resources within the company.
Working efficiency	To execute work with the capacity for self-adjustment, active acquisition of new knowledge and techniques, goal-oriented work, advanced completion according to quality requirements, finding problems, and finding the right person to do the thing right.
Working quality	To ensure that quality is the priority for the completion of work content, with the ability to fully control each factor in a workflow, with self-inspection exhibiting a high level of quality of work results.
Working spirit	To accept challenging work targets, focus attention, make good use of strategies, manage resources, and finish job tasks on time.
Monitoring control	To observe cost control and work progress control, put emphasis on process monitoring and control, eliminate potential interfering factors, and present satisfactory work results to supervisors.
Working attitude	To be proactive, active, and aggressive without the need for others to urge or remind, have great ambition and willingness to take on jobs and help colleagues actively, have good relationships with people stemming from a positive attitude towards others, and exhibit work results surpassing supervisors’ expectations.

TABLE 3: Taiwanese solar product manufacturers sampled and interviewed in this study.

Manufacturers’ positions in the supply chain	Chief products	Number of companies sampled	Percentage (%)	Number of companies interviewed (%)
Upper-stream firms	Silica materials, silicon wafer materials	17	13.93	3 (25%)
Mid-stream firms		<b>47</b>	<b>38.51</b>	4 (33.33%)
	Solar cells	15	12.30	
	Solar cell modules	18	14.73	
	Thin-film solar cell modules	9	7.38	
	Dye-sensitized solar cells	3	2.46	
	Concentrator solar cell modules	2	1.64	
Lower-stream firms		<b>58</b>	<b>47.56</b>	5 (41.67%)
	Solar photovoltaic system	39	31.98	
	Solar photovoltaic converters	10	8.20	
	Sales channels/suppliers of solar photovoltaic products	9	7.38	
Total		122	100	12 (100%)

Source: [37, 38].

TABLE 4: Structure of field interviews with administrators and good performance engineers (form I).

Employability indicators	Behavioural feature	Weighted demonstration (%)	Difficulty	Importance	Frequency	Improvement via training	Improvement via recruiting	Certificate requirement	Competence deficiency handling
Situation									
Task									
Action									
Result									

TABLE 5: Structure of field interviews with administrators and good performance engineers (form II).

Employability indicators	Behavioural feature	Weighted demonstration (%)	Difficulty	Importance	Frequency	Improvement via training	Improvement via recruiting	Certificate requirement	Competence deficiency handling
Integrated planning									
Evaluation and judgment									
Working efficiency									
Working quality									
Working spirit									
Monitoring control									
Working attitude									

TABLE 6: Structure of the employability survey questionnaire.

Construct	Number of questions for behavioural event
Integrated planning	4
Evaluation and judgment	4
Working efficiency	8
Working quality	4
Working spirit	6
Monitoring control	5
Working attitude	6

such large differences existed in the direct performance requirements of solar enterprises in manufacturing and services that it was not appropriate to directly translate the direct performance indicators for employees into requirements for students' employability. Therefore, the direct performance requirements for field interviews were transformed to become indirect requirements so that they could represent enterprises' expectations for performance as they affected employability.

### 4. Results and Discussion

4.1. Working Attitudes, Competence, Job Performance, and Employability Form an Interactional Model. The research used competence-based theory to explore performance standards expected to be demonstrated through field interviews with solar industry representatives in order to formulate seven employability indicators that included working attitude, working efficiency, integrated planning, working spirit, evaluation and judgment, monitoring control, and working

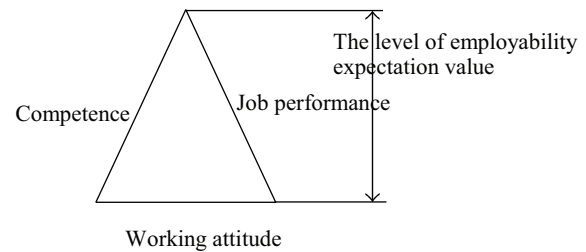


FIGURE 1: Standard competence, job performance, and working attitude.

quality. A triangle shaped interpretation model can be used to summarize the research results. This triangle model is jointly constructed by competence, job performance, and working attitude, where the combination of the mutually dependent competence and job performance determines the expected value of students' employability in the industry. The concept is shown in Figure 1. From the results of field interviews, it was seen that "working attitude" establishes a basis upon which an employee can fully express his or her competence and demonstrate the "job performance" expected by the company. Employability demonstrates consistency between the level of an individual's "competence" and "job performance;" these two also contribute to high employability, in the form of the individual's long-term value for the company. The implications include the following (as in Figure 2).

- (i) Working attitude and competence and job performance together form an interactional model. The height of the triangle signifies employability in the long term for the individual in the enterprise.
- (ii) Variation in employability is based on working attitude, and working attitude determines the level demonstrated in competence and job performance in the enterprise.

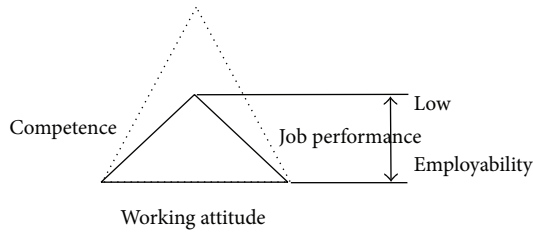


FIGURE 2: Work attitude determines the level of competence and job performance.

- (iii) There is interdependence between competence and job performance, where engineers who possess competence can demonstrate the expected job performance in the enterprise.
- (iv) As a result of problems in the enterprise's internal organizational behaviour, employees with high competence might not necessarily demonstrate high job performance. However, the possession of a superior working attitude may compensate for such a condition.
- (v) Working attitude determines the level of competence and job performance. The possession of an aggressive working attitude and active learning competence can help increase job performance. When an individual's job performance is not as expected, good working attitude could enable the individual to pursue a higher job performance and to improve his/her value for long-term employment by the enterprise.

**4.2. The Contribution of Competence Was Augmented and the Performance Requirement Was Diminished.** From a cross-comparison of field interview results it was seen that even if the interviewed objectives were screened in advance, the interviewees still exhibited for some of the work items exaggerated opinions of the competencies required. Conversely, they also exhibited for some of the enterprises' job performance requirements weakened expectations. Possible reasons for this may include the following.

- (i) Enterprises are generally likely to consider students who are the first to be employed as the ones who are more likely to execute their jobs with the assistance of senior supervisors.
- (ii) Enterprises usually consider students' possession of professional certificates as merely establishing the minimum level needed to enter the workplace, with on-the-job training (OJT) more or less still being needed for students to properly qualify for the job.
- (iii) The phenomenon of exaggerated expressions, if not truly heightened beliefs, in the requirements of competence could be explained from the expectation theory angle of Chang [5]. The interviewed persons might expect their opinions to be respected by their administrators and thus affect the company's salary adjustment policy.

**4.3. The Questionnaire Had Good Reliability and Validity.** In the qualitative study, reliability of the questionnaire overall, as measured by Cronbach's  $\alpha$ , reached a value of 0.927, indicating that reliability was excellent. The maximum KMO value was 0.838 while the validity of all factors reached a medium (KMO > 0.7) level, indicating the questionnaire data was stable. Meanwhile, the Bartlett value of 869.15 ( $P < 0.01$ ) also indicated each dimension of the data to be near normal multivariate and suitable for further factor analysis.

Principal component analysis was adopted for the factor analysis, and Promax with Kaiser normalization was performed. For the employability index eigenvalues >0.7 were chosen, with factor loadings >0.6. The standard for extracted factors was that they should contain at least two items for assessment. The reason for selecting eigenvalues >0.7 was to ensure that the goodness-of-fit of the factor model reached an acceptable level and the adoption of the Kaiser method and Scree test to find solutions was feasible. In order to ensure the integrity of the factors, a Scree test was conducted to decide on the number of factors. The analysis results extracted 18 items and 7 factors with the interpretation capability reaching 80.35% as listed in Table 7.

The purpose of factor analysis was to examine the construct validity of the questionnaire and to form the basis for judging the order of importance of the employability indicators. The application of factor analysis allowed extraction of common factors between the variables, leaving a less complicated data structure in the end. Through the finding of common factors, the conceptual structure of employability can be said to be confirmed. The factor analysis results showed the questionnaire itself to be of good validity, and the ranking of each employability indicator by eigenvalue, in order of importance from high to low, was integrated planning, working spirit, monitoring control, working attitude, evaluation and judgment, working efficiency, and working quality.

**4.4. Description of Statistical Analysis.** The valid returns consisted of responses from 338 males (67.5%), the majority, and 163 females, while the age distribution was 26–30 (57.5%), 21–25 (21.25%), and 31–35 (16.25%). Technical duties were the most represented (71.8%) among the duties surveyed, as listed in Table 8, while seniority from 3 years to less than 5 years (41.0%) was most common, as listed in Table 9. Averages and standard deviations for different categories are shown in the Table 10.

Observation of the individual average of each employability indicator shows the three items: working spirit, evaluation and judgment, and working quality to be significantly higher. It is possible that as a result of the fact that a large majority of the survey respondents had technical duties as their responsibility, these three items were particularly emphasized.

**4.5. The Radar Chart Indicates the Level of Employability Required by Enterprises for Students of Solar Technology.** The purpose of the radar chart is to help understand whether the questionnaire survey results indicate that enterprises regard a score of 60 percent for university students' employability

TABLE 7: Employability indicators factor analysis.

Number of questions	Integrated planning	Working spirit	Monitoring control	Working attitude	Evaluation and judgment	Working efficiency	Working quality
A2	<b>0.94</b>						
A1	<b>0.93</b>						
A3	<b>0.86</b>						
A4	<b>0.79</b>						
A26		<b>0.83</b>					
A25		<b>0.83</b>					
A27		<b>0.71</b>					
A14			<b>0.87</b>				
A28			<b>0.86</b>				
A36				<b>0.92</b>			
A35				<b>0.89</b>			
A8					<b>0.87</b>		
A7					<b>0.86</b>		
A24						<b>0.81</b>	
A12						<b>0.76</b>	
A15						<b>0.72</b>	
A20							<b>0.94</b>
A33							<b>0.65</b>
Eigenvalue	7.95	1.93	1.21	0.95	0.90	0.78	0.75
Descriptive variation	44.19%	10.71%	6.70%	5.29%	4.99%	4.33%	4.14%
Accumulative descriptive variation value	44.19%	54.90%	61.60%	66.89%	71.88%	76.21%	80.35%

Factor extraction: principal component analysis.  
Rotation method: Promax with Kaiser normalization.

TABLE 8: Distribution of respondent duties  $N = 501$ .

Valid	%	Accumulated %
Sales duties	5.1	5.1
Technical duties	71.8	76.9
Management duties	5.1	82.1
Administrative duties	7.7	89.7
Others	10.3	100.0
Total	100.0	

TABLE 9: Distribution of respondent seniority  $N = 501$ .

Valid	%	Accumulated %
less than 1 year	5.1	5.1
1 year to less than 3 years	20.5	25.6
3 years to less than 5 years	41.0	66.7
5 years to less than 10 years	23.1	89.7
over 10 years	10.3	100.0
Total	100.0	

as a generally acceptable level. The degree of employability expected by solar enterprises, as measured by the responses to the indicator questions in the survey, were plotted according to the average for each indicator to form the radar chart as shown in Figure 3. Assuming that the weighted value for each factor is the same and taking level 5 from the questionnaire scale as the highest and 1 as the lowest, then a triangle can be formed between any two factors. The ratio method was applied to calculate the area of the included angle between the two factors ( $\Delta$ ) with the equation  $\Delta = (1/2)ab \sin \theta$ , where  $a, b$  represent the 2 arm lengths (e.g., for the  $\Delta 1$  area calculation where  $a = 3.26, b = 3.84$ ) [11]. Hence, the level of employability is  $\sum \Delta_i = 92.20$  in comparison to the ideal value  $\sum \Delta = 150$  (i.e., the two arms  $a = 5$  and  $b = 5$ ) and so a value of 61.47% after being expressed as a percentage. This indicates that the individual enterprise workers who took the survey considered a score of about 60 to be an acceptable level for the employability that students of solar technology should be required to demonstrate.

As indicated by the radar chart analysis of each employability indicator, the averages obtained from the survey on

TABLE 10: Averages and standard deviations of job performance indicators.

Category	Indicator	Individual average	Individual standard deviation	Average	Standard deviation
Employability indicators from performance point of view	Integrated planning	3.26	0.93	3.60	0.57
	Working spirit	3.70	0.70		
	Monitoring control	3.54	0.67		
	Working attitude	3.60	0.84		
	Evaluation and judgment	3.84	0.69		
	Working efficiency	3.68	0.61		
	Working quality	3.79	0.68		

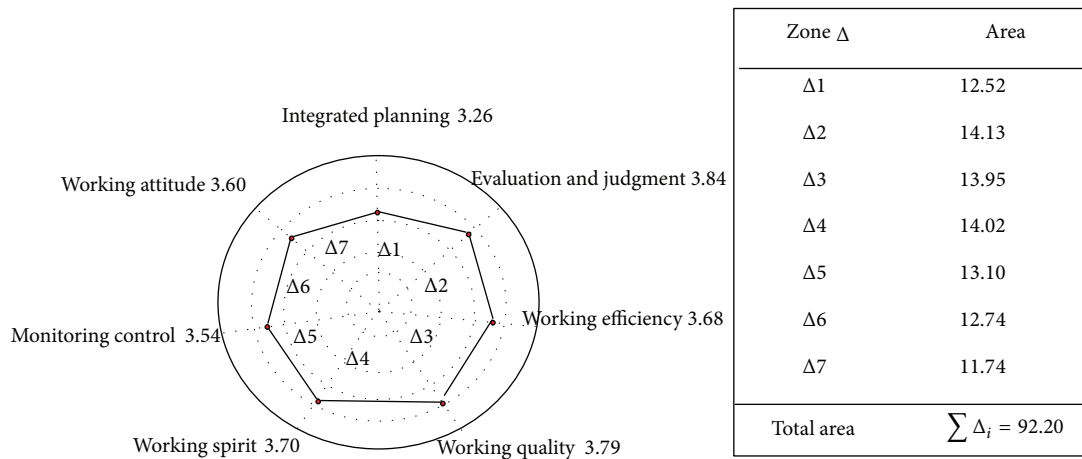


FIGURE 3: Area of employability expected by individual workers to be demonstrated.

the Likert scale were all over the level of 3 (e.g., 3.26 for integrated planning). However, from conversions of the radar chart areas, we see that the industry responders did not hold very high levels of expectation for students' performance. This implies that enterprises require students' employability at only the minimum level and emphasize the formation of employees' competence and working attitudes after their entry into the workforce.

### 5. Conclusions

The procedure this study followed to obtain its seven employability indicators was to take the concept of key performance indicators (KPI) and infer an application to the employability of students of universities of technology. The research process was essentially competence-based and as such was meant to achieve the goal of estimating competence from performance. The interpretation model, relating competence, job performance, working attitude, and employability, allows for effective interpretations of the relationship between enterprises' expectations and students' employability. In addition, the fact that the development of the employability indicators came from the results of field interviews signifies that there is

a correspondence between the employability indicators and the short life cycle of Taiwanese solar industry products and the special requirement of the fierce market competition. Meanwhile, each indicator is also appropriate as the basis for curricular planning in solar technology departments of universities in the Taiwan area. In other words, when students possess the employability items named in this research then they shall hopefully be more encouraged to brave the challenge of the ever stricter requirements for long-term employment in the industry.

As for an immediate practical application, enterprises can use the employability indicators to develop an "Employability Assessment Form" that meets the requirement by individual enterprises for the most objective method of recruiting new employees possible. The employability indicators can be further used for planning enterprise-internal training courses to enhance workers' employability in the long term.

Performance assessment can be quite difficult for the industry, which is made up of product manufacturing, service, and technical service businesses whose knowledge requirements and business activities can vary largely. As a result of the depth and broadness of this variation, therefore, each company may expect students to perform differently.

A limitation of this research is that it only explored “job performance” in terms of its direct relationship with work.

The natural follow-up to this study and the development of the framework are curricular design based on the employability indicators. The seven employability indicators obtained from this research allow the matching of job positions in the solar industry suitable for recent graduates with the planning of courses that keep curriculum enhancement in mind as well as employability. The curriculum could include both the formal curriculum and informal curriculum. The formal curriculum should have a definite goal structure, including employment targeted curriculum, practical training in solar enterprises, and industrial and academic-type optional courses, while the informal curriculum can be based on industrial and academic activities, such as topical lectures, field visits to enterprises, and workplace experiencing. The curriculum should be reviewed periodically by experts invited directly from industry in order to ensure that the design of the curriculum corresponds to the requirements described in the employability indicators.

### Conflict of Interests

The authors declare that there is no conflict of interests regarding the publication of this paper.

### References

- [1] D. Rae, “Connecting enterprise and graduate employability: challenges to the higher education culture and curriculum?” *Education and Training*, vol. 49, no. 8-9, pp. 605–619, 2007.
- [2] A. Rothwell and J. Arnold, “Self-perceived employability: development and validation of a scale,” *Personnel Review*, vol. 36, no. 1, pp. 23–41, 2007.
- [3] A. Shahin and M. A. Mahbod, “Prioritization of key performance indicators: an integration of analytical hierarchy process and goal setting,” *International Journal of Productivity and Performance Management*, vol. 56, no. 3, pp. 226–240, 2007.
- [4] C. C. Chang, “Fuzzy assessment of core competence for human resources in a representative technological organization,” *NTU Management Review*, vol. 18, no. 2, pp. 105–132, 2008.
- [5] C. C. Chang, “Obtaining IT competencies for curricular development using Q-technique,” *International Journal of Academic Research in Business and Social Sciences*, vol. 4, no. 3, pp. 60–74, 2014.
- [6] D. Lei and J. W. Slocum, “Global strategy, competence-building and strategic alliances,” *California Management Review*, vol. 35, no. 1, pp. 81–97, 1992.
- [7] C. G. Kuo and C. C. Chang, “Building professional competencies indices in the solar energy industry for the engineering education curriculum,” *International Journal of Photoenergy*, vol. 2014, Article ID 963291, 6 pages, 2014.
- [8] C. G. Kuo, C. Y. Hsu, S. S. Wang, and D. C. Wen, “Photocatalytic characteristics of TiO<sub>2</sub> films deposited by magnetron sputtering on polycarbonate at room temperature,” *Applied Surface Science*, vol. 258, no. 18, pp. 6952–6957, 2012.
- [9] C. G. Kuo, C. F. Yang, L. R. Hwang, and J. S. Huang, “Effects of titanium oxide nanotube arrays with different lengths on the characteristics of dye-sensitized solar cells,” *International Journal of Photoenergy*, vol. 2013, Article ID 650973, 6 pages, 2013.
- [10] C. C. Chang, “Building an approach to evaluate capabilities development,” *Pensee Journal*, vol. 76, no. 1, pp. 167–179, 2014.
- [11] C. C. Chang, “Improving employment services management using IPA technique,” *Expert Systems with Applications*, vol. 40, no. 17, pp. 6948–6954, 2013.
- [12] S. Cox and D. King, “Skill sets: an approach to embed employability in course design,” *Education and Training*, vol. 48, no. 4, pp. 262–274, 2006.
- [13] J. Sanders and A. De Grip, “Training, task flexibility and the employability of low-skilled workers,” *International Journal of Manpower*, vol. 25, no. 1, pp. 73–140, 2004.
- [14] J. Hillage and E. Pollard, “Employability: developing a framework for policy analysis,” Research Report RR85, Institute for Employment Studies, DfEE, Brighton, UK, 1998.
- [15] L. D. Pool and P. Sewell, “The key to employability: developing a practical model of graduate employability,” *Education and Training*, vol. 49, no. 4, pp. 277–289, 2007.
- [16] R. Z. Wang, “The new evaluative indicator for university—employability,” 2008, <http://epaper.heeact.edu.tw/archive/2008/09/01/723.aspx>.
- [17] K. Hafeez and E. A. Essmail, “Evaluating organization core competence and associated personal competencies using analytical hierarchy process,” *Management Research News*, vol. 30, no. 8, pp. 530–547, 2007.
- [18] S. M. Peng, “A year after graduating from university survey report,” 2008, [http://www.cher.ntnu.edu.tw/wp-content/uploads/file/report/report\\_94\\_pba.pdf](http://www.cher.ntnu.edu.tw/wp-content/uploads/file/report/report_94_pba.pdf).
- [19] D. D. Dubois, “Competence-based performance improvement: a strategy for organizational change,” 2007, <http://www.knowledge.hut.fi/projects/itss/referDubois.pdf>.
- [20] S. P. Robbins, *Essentials of Organizational Behavior*, Prentice Hall, New Jersey, NJ, USA, 6th edition, 2000.
- [21] F. J. Landy and J. M. Conte, *Work in the 21st Century*, McGraw-Hill Companies, New York, NY, USA, 2004.
- [22] B. H. R. Fernandes, J. F. Mills, and M. T. L. Fleury, “Resources that drive performance: an empirical investigation,” *International Journal of Productivity and Performance Management*, vol. 54, no. 5-6, pp. 340–354, 2005.
- [23] G. Hamel and C. K. Prahalad, “Corporate imagination and expeditionary marketing,” *Harvard Business Review*, vol. 69, no. 4, pp. 81–92, 1991.
- [24] Y. E. Spanos and G. Prastacos, “Understanding organizational capabilities: towards a conceptual framework,” *Journal of Knowledge Management*, vol. 8, no. 3, pp. 31–43, 2004.
- [25] U. Ljungquist, “Core competency beyond identification: presentation of a model,” *Management Decision*, vol. 45, no. 3, pp. 393–402, 2007.
- [26] D. Boyatzis, *The Competence Manager: A Model for Effective Performance*, John Wiley & Son, New York, NY, USA, 1982.
- [27] R. A. Noe, *Employee Training and Development*, McGraw-Hill/Irwin, Singapore, 3rd edition, 2005.
- [28] M. C. Tsai, Q. S. Zheng, and J. H. Lee, “A study on the competence and job performance of the Mainland China direct employees-In case of Taiwanese enterprises of component parts of monitors,” *Business Review*, vol. 10, no. 1, pp. 53–74, 2005.
- [29] Success Performance Solutions, “Success performance solutions-Hire competence with confidence,” 2009, <http://www.super-solutions.com/criteriaone.sap>.

- [30] C. C. Chang, "Exploring IT entrepreneurs' dynamic capabilities using Q-technique," *Industrial Management and Data Systems*, vol. 112, no. 8, pp. 1201–1216, 2012.
- [31] C. G. Kuo and B. J. Sheen, "Seaweed chlorophyll on the light-electron efficiency of DSSC," *Journal of the Chinese Chemical Society*, vol. 58, no. 2, pp. 186–190, 2011.
- [32] G. Dessler, *Human Resource Management*, Prentice Hall, New York, NY, USA, 11th edition, 2007.
- [33] J. R. K. Kagaari, "Evaluation of the effects of vocational choice and practical training on students' employability," *Journal of European Industrial Training*, vol. 31, no. 6, pp. 449–471, 2007.
- [34] Ministry of Education, "Constructing a mechanism of supply chain and integration for high level talents-grasping the flow of university graduates," 2009, [http://www.edu.tw/high/news.aspx?news\\_sn=2513](http://www.edu.tw/high/news.aspx?news_sn=2513).
- [35] National Taiwan Normal University, "Integrated higher education database system in Taiwan," 2009, <http://www.cher.ntnu.edu.tw/sindex.php>.
- [36] S. Jaffer, D. N'gambi, and L. Czerniewicz, "The role of ICTs in higher education in South Africa: one strategy for addressing teaching and learning challenges," *International Journal of Education and Development Using Information and Communication Technology*, vol. 3, no. 4, pp. 131–142, 2007.
- [37] C. G. Kuo, C. F. Yang, M. J. Kao et al., "An analysis and research on the transmission ratio of dye sensitized solar cell photoelectrodes by using different etching process," *International Journal of Photoenergy*, vol. 2013, Article ID 151973, 8 pages, 2013.
- [38] IDBMEA, "Industrial Development Bureau, Ministry of Economic Affairs," 2013, <http://www.moeaidb.gov.tw/external/view/tw/inquery/index.html>.

## Research Article

# ITO-Free Semitransparent Organic Solar Cells Based on Silver Thin Film Electrodes

**Zhizhe Wang, Chunfu Zhang, Dazheng Chen, Shi Tang, Jincheng Zhang, Li Sun, Ting Heng, and Yue Hao**

*State Key Discipline Laboratory of Wide Band Gap Semiconductor Technology, School Of Microelectronics, Xidian University, 2 South Taibai Road, Xi'an 710071, China*

Correspondence should be addressed to Chunfu Zhang; cfzhang@xidian.edu.cn and Yue Hao; yhao@xidian.edu.cn

Received 11 April 2014; Revised 9 June 2014; Accepted 11 June 2014; Published 30 June 2014

Academic Editor: Chao-Rong Chen

Copyright © 2014 Zhizhe Wang et al. This is an open access article distributed under the Creative Commons Attribution License, which permits unrestricted use, distribution, and reproduction in any medium, provided the original work is properly cited.

ITO-free semitransparent organic solar cells (OSCs) based on  $\text{MoO}_3/\text{Ag}$  anodes with poly(3-hexylthiophene) and [6,6]-phenyl-C61-butyric acid methyl ester films as the active layer are investigated in this work. To obtain the optimal transparent ( $\text{MoO}_3/\text{Ag}$  anode, ITO-free reference OSCs are firstly fabricated. The power conversion efficiency (PCE) of 2.71% is obtained for OSCs based on the optimal  $\text{MoO}_3$  (2 nm)/Ag (9 nm) anode, comparable to that of ITO-based reference OSCs (PCE of 2.85%). Then based on  $\text{MoO}_3$  (2 nm)/Ag (9 nm) anode, ITO-free semitransparent OSCs with different thickness combination of Ca and Ag as the cathodes are investigated. It is observed from our results that OSCs with Ca (15 nm)/Ag (15 nm) cathode have the optimal transparency. Meanwhile, the PCE of 1.79% and 0.67% is obtained for illumination from the anode and cathode side, respectively, comparable to that of similar ITO-based semitransparent OSCs (PCE of 1.59% and 0.75% for illumination from the anode and cathode side, resp.) (Sol. Energy Mater. Sol. Cells, 95, pp. 877–880, 2011). The transparency and PCE of ITO-free semitransparent OSCs can be further improved by introducing a light couple layer. The developed method is compatible with various substrates, which is instructive for further research of ITO-free semitransparent OSCs.

## 1. Introduction

Due to the advantage of low cost, light weight, simple process, flexibility, and possibility of roll-to-roll mass production [1–5], organic solar cells (OSCs) have become a highly attractive research topic over the past decade. With the development of the research, obvious progress has been made. Recently, even OSCs with certified power conversion efficiency (PCE) above 10% have been reported [6], which has approached the requirement of commercialization.

However, there are still some bottlenecks for commercialization of OSCs. One awkward drawback is that most organic materials can cover only a fraction of the solar spectrum, and inefficient light harvest results in the low photocurrent [7]. One efficient way to enhance broad spectral absorption of OSCs is the realization of organic tandem solar cells based on complementary thin absorber materials. As we all know, the semitransparent electrode [8, 9] or recombination contact used to connect two subcells is of vital importance in the fabrication of tandem solar cells.

Meanwhile, semitransparent OSCs make sense from the aspect of application. For example, these semitransparent OSCs can be employed as the windows of our houses and cars, providing electric power without occupying living space. Thus, various semitransparent electrodes for OSCs have been developed in recent years [10–12]. It should be noted that good transparency and high PCE are required simultaneously for the application of semitransparent OSCs.

Another bottleneck for commercialization of OSCs stems from the commonly used transparent anode in the fabrication of OSCs—indium tin oxide (ITO) sputtered on glass. Although ITO has excellent properties in optical transparency and electrical conductivity, it is unsuitable for cheap roll-to-roll fabrication of OSCs, which relies on the flexible electrodes with low cost. For example, the scarce indium source and stringent process conditions (usually sputter) result in high cost for ITO electrode [13]. Meanwhile, both the brittleness of ITO electrode and high temperature condition in the fabrication of ITO make it unsuitable for the roll-to-roll mass production of OSCs [14]. Thus, more and

more attention has been focused on alternative transparent conductive electrodes. Indium-free transparent conducting oxides (such as Ga-doped ZnO (GZO) and Al-doped ZnO (AZO)) [15–17], poly(3,4-ethylenedioxythiophene):poly(styrenesulfonate) (PEDOT:PSS) [18, 19], Ag nanowires [14, 20], graphene [13], and carbon nanotubes [21] are used as the alternative of ITO electrode. However, although GZO or AZO has a lower cost than ITO, the fabrication of these electrodes still needs sputter. Although the PEDOT:PSS electrode can be easily fabricated by solution method, the resistivity of this electrode is still a little too high [22, 23]. Since the surfaces of Ag nanowire, graphene, and carbon nanotube electrodes are usually rough, charge injection into or extraction from active layer has been restricted [13, 14, 24]. In addition, complex film processing of these electrodes also makes them inappropriate for application in large-scale OSCs [13, 14, 24].

On the contrary, a smooth metal thin film (e.g., Ag) can be easily fabricated by thermal evaporation, compatible with the mass production process. Moreover, due to their intrinsic flexibility and high conductivity [24], metal thin film electrodes are suitable for the flexible substrates in roll-to-roll mass production of OSCs. Thus, more and more attention is attracted to this topic. Various transparent metal thin film electrodes (such as Au [25], Ag [26], Cu [27], Cu/Ni [28], and MoO<sub>3</sub>/Au/MoO<sub>3</sub> [24]) are reported and employed in the fabrication of OSCs.

However, in the previous work, semitransparent OSCs are usually fabricated on ITO electrodes. Here, we have reported ITO-free semitransparent OSCs based on Ag thin film anodes. The ITO-free semitransparent OSC has combined the advantages of ITO-free OSCs and semitransparent OSCs, solving two bottlenecks discussed above for commercialization of OSCs simultaneously. At first, ITO-free reference OSCs based on (MoO<sub>3</sub>)/Ag anodes are fabricated, with poly(3-hexylthiophene) (P3HT) and [6,6]-phenyl-C61-butyric acid methyl ester (PCBM) films as the active layer. The optimal anode, MoO<sub>3</sub> (2 nm)/Ag (9 nm) anode, is obtained. The PCE of 2.71% is achieved for corresponding OSCs (also the highest PCE among all the ITO-free reference OSCs), comparable to that of ITO-based reference OSCs (PCE of 2.85%). Then based on this MoO<sub>3</sub> (2 nm)/Ag (9 nm) anode, ITO-free semitransparent OSCs with different thickness combination of Ca and Ag as the cathodes are fabricated. It is observed from our results that OSCs with Ca (15 nm)/Ag (15 nm) cathode have the optimal transparency. Meanwhile, the PCE of 1.79% (illuminated from the anode side) and 0.67% (illuminated from the cathode side) is obtained for the corresponding device, comparable to that of similar ITO-based semitransparent OSCs (PCE of 1.59% and 0.75% for illumination from the anode and cathode side, resp.) [10, 11]. The result is instructive for further research of ITO-free semitransparent OSCs.

## 2. Experimental Details

**2.1. Material and Substrate Preparation.** P3HT was purchased from Rieke Metals Inc., PCBM was purchased from Nano-C Inc., and 1,2-dichlorobenzene and MoO<sub>3</sub> were provided

from Aldrich Inc. All the materials were used without any further purification. P3HT and PCBM were dissolved in 1,2-dichlorobenzene with a concentration of 20 mg/mL, respectively. They were mixed in a weight ratio of 1:0.8 and stirred at room temperature for 2 h before use. Glass substrates were cleaned sequentially with detergent (Decon 90, UK), deionized water, acetone, and ethanol in an ultrasonic bath for about 15 min.

**2.2. Electrode Deposition and Characterization.** Cleaned glass substrates were dried with a nitrogen (N<sub>2</sub>) flow and then transferred into a custom-made multichamber ultrahigh vacuum evaporation system. The (MoO<sub>3</sub>)/Ag electrodes were deposited on glass by thermal evaporation at a vacuum pressure  $<5 \times 10^{-4}$  Pa, with a evaporation rate of 0.02 and 0.1 nm/s for MoO<sub>3</sub> and Ag, respectively. The substrates during deposition were at room temperature. The thicknesses and evaporation rates of MoO<sub>3</sub>, Ag, Al, and Ca were estimated in situ with a calibrated quartz crystal monitor.

The spectral transmission and reflectance were recorded by using an UV-VIS-NIR spectrophotometer (Lambda 950, Perkin Elmer). Since transmission was measured relative to air, the reflection of the glass substrate was included. The sheet resistances of the samples were measured by using a four-point probe setup. The transmission electron microscope (TEM) cross-sectional image was taken by a FEI Tecnai G2 F20 S-Twin transmission electron microscope.

**2.3. Device Fabrication and Measurement.** After the electrode deposition, a 10 nm thick MoO<sub>3</sub> layer was first thermally evaporated onto the substrates as the hole transport layer with high work function. Then P3HT:PCBM solution was spin-coated onto the samples at 1000 rpm for 60 s in a N<sub>2</sub> glove box attached to the vacuum system, followed by annealing at 150°C for 10 min. Finally, Ca and Ag with different thicknesses were further deposited on top of the active layer as the cathode through a metal shadow mask to finish the ITO-free semitransparent OSCs, resulting in an active solar cell area of 6 mm<sup>2</sup>. ITO-free and ITO-based reference OSCs were fabricated in nearly the same procedure except that they were postannealed after the deposition of the 70 nm thick Al cathode. Device geometry of ITO-free reference or ITO-free semitransparent OSCs is illustrated in Figure 1(a). TEM cross-sectional image of corresponding ITO-free semitransparent OSCs is shown in Figure 1(b). The current density-voltage (*J*-*V*) characteristics were measured with a source measurement unit 2400 SMU (Keithley, USA) and simulated AM 1.5 G sun light (San-Ei Electric) in air without any device encapsulation. The illumination intensity was kept at 100 mW/cm<sup>2</sup> through using a Si standard solar cell calibrated by the National Renewable Energy Laboratory (NREL).

## 3. Results and Discussion

To fabricate ITO-free semitransparent OSCs, ITO-free reference OSCs with Al cathode were firstly investigated so that we can obtain the optimal transparent Ag thin film anode.

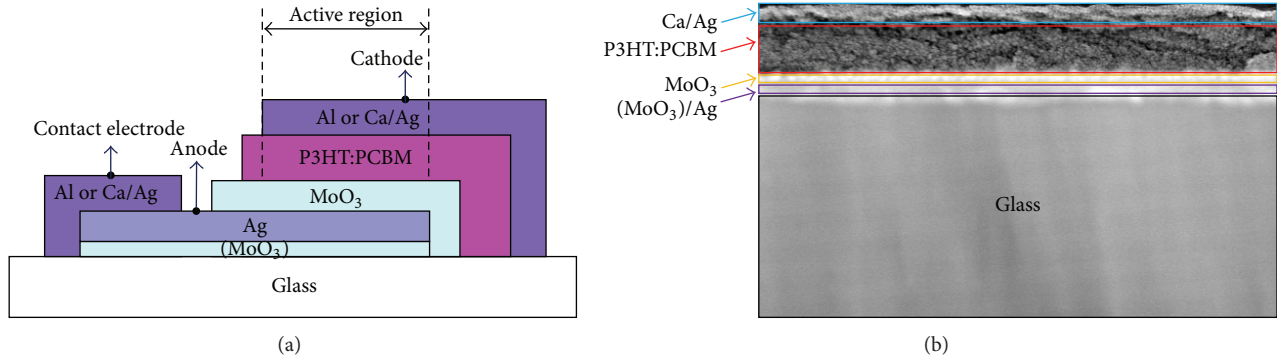


FIGURE 1: (a) Device geometry of ITO-free reference or ITO-free semitransparent OSCs based on  $(\text{MoO}_3)/\text{Ag}$  anodes and (b) TEM cross-sectional image of ITO-free semitransparent OSCs.

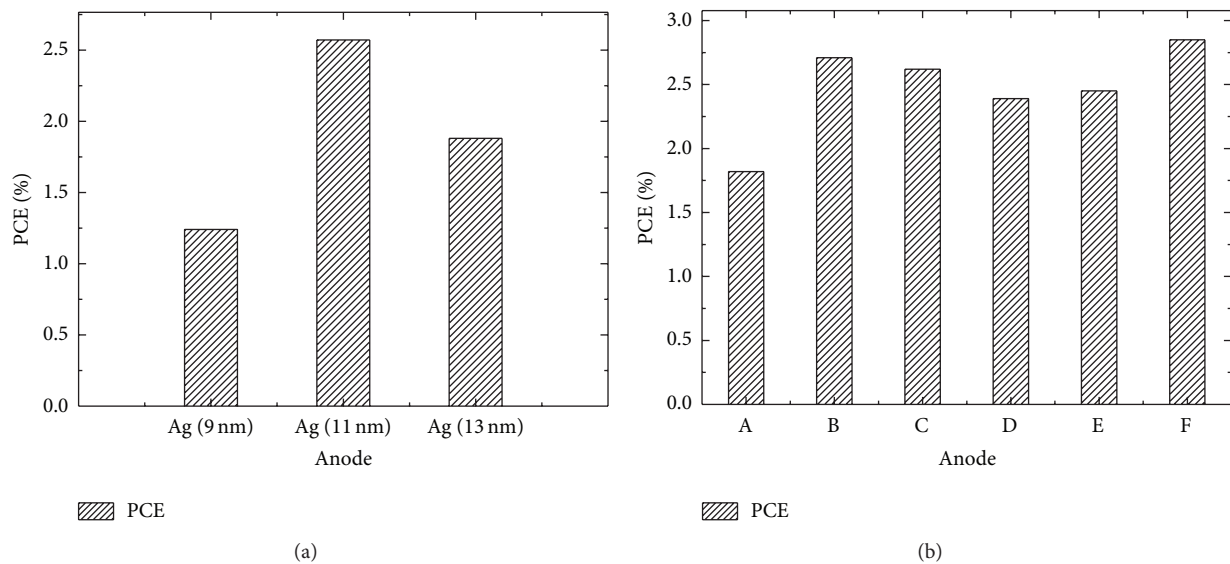


FIGURE 2: The PCE of ITO-free reference OSCs fabricated on the (a) Ag or (b)  $\text{MoO}_3/\text{Ag}$  anodes. For comparison, the PCE of the ITO-based reference OSC is also shown in (b). The characters A, B, C, D, E, and F on the X axis of (b) indicate  $\text{MoO}_3$  (2 nm)/Ag (7 nm),  $\text{MoO}_3$  (2 nm)/Ag (9 nm),  $\text{MoO}_3$  (2 nm)/Ag (11 nm),  $\text{MoO}_3$  (10 nm)/Ag (9 nm),  $\text{MoO}_3$  (10 nm)/Ag (11 nm), and ITO anode, respectively.

As we all know, the thermally evaporated Ag layer prefers Volmer-Weber growth, which starts from isolated island [29]. Thus, Ag atoms agglomerate to form isolated clusters at first when Ag is thermally evaporated on glass substrates. It can cause surface plasmon resonances with light in the visible range which significantly reduces the film transparency [30]. With the increase of the Ag film thickness, the percolation threshold of Ag is reached, which is defined as equivalent thickness where isolated metal islands start to connect and form a continuous layer [31]. If the thickness of Ag layer is over this transition point, the transparency is decreased with an increased conductivity. Thus the best performance of OSCs based on Ag thin film anode is generally achieved close to the percolation threshold, indicating the best trade-off between increasing conductivity and decreasing transparency.

The PCE of ITO-free reference OSCs fabricated on the Ag or  $\text{MoO}_3/\text{Ag}$  anodes is illustrated in Figures 2(a) and 2(b),

respectively. For comparison, the PCE of the ITO-based reference OSC is also shown in Figure 2(b). As shown in Figure 2(a), the PCE of 2.57% is obtained for OSCs based on Ag (11 nm) anode, the best performance among the devices fabricated on pure Ag anodes. It may suggest that the percolation threshold of Ag in our case is approximately 11 nm. Then a  $\text{MoO}_3$  interlayer between the Ag layer and glass substrate is introduced. Since a closed  $\text{MoO}_3$  layer is formed with the approximate thickness of 4 nm [32], two different thicknesses of  $\text{MoO}_3$  (2 nm or 10 nm) are chosen here. It can be observed from Figure 2 that the introduction of the  $\text{MoO}_3$  interlayer can improve the performance of OSCs effectively, particularly when the thickness of  $\text{MoO}_3$  is 2 nm. The PCE of OSCs based on  $\text{MoO}_3$  (2 nm)/Ag (9 nm) anode is even enhanced to 2.71% (also the highest PCE among all the ITO-free reference OSCs), comparable to that of ITO-based reference OSCs (PCE of 2.85%). Improvement in the performance of the Ag thin film electrode can be attributed

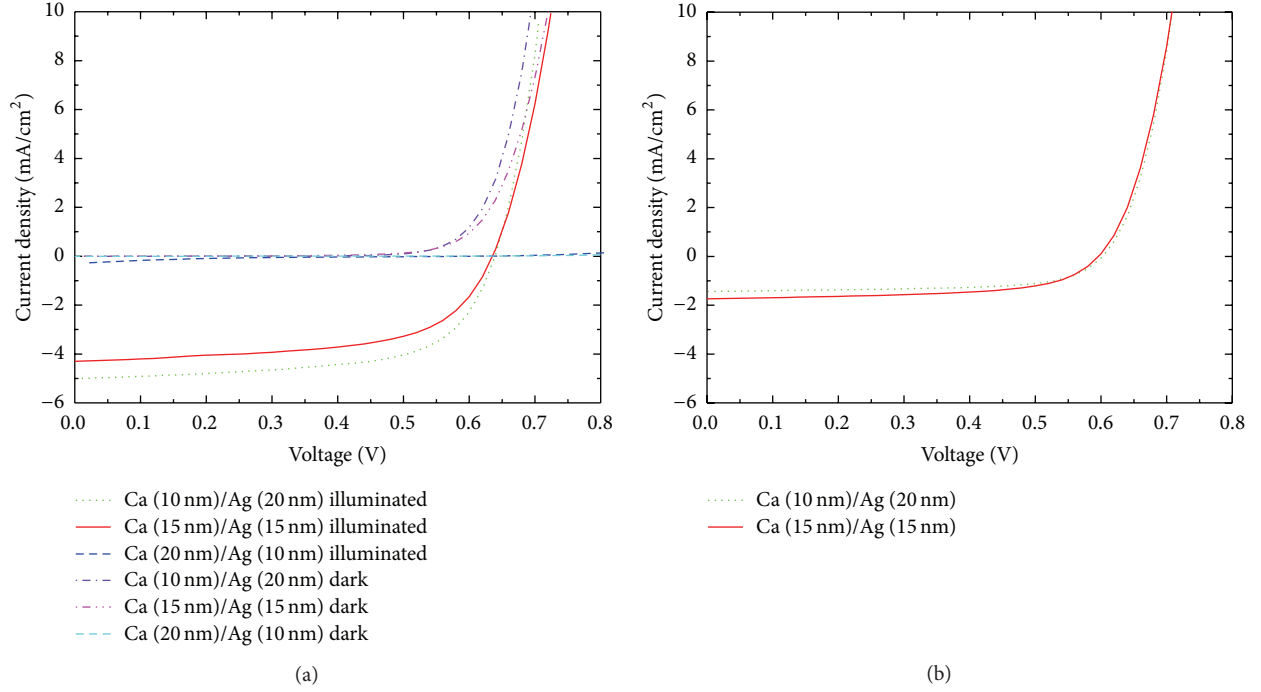


FIGURE 3:  $J$ - $V$  characteristics of devices  $\text{MoO}_3$  (2 nm)/Ag (9 nm)/ $\text{MoO}_3$  (10 nm)/P3HT:PCBM/Ca/Ag with different thickness combination of Ca and Ag as the cathodes when illuminated from the (a) anode side and (b) cathode side. Corresponding dark  $J$ - $V$  curves are also shown in (a) for comparison.

TABLE 1: Photovoltaic performance parameters of ITO-free semitransparent OSCs with different thickness combination of Ca and Ag as the cathodes illuminated from the anode (bottom) and cathode (top) side.

Ca (nm)	Ag (nm)	Illumination	$V_{OC}$ (V)	$J_{SC}$ (mA/cm <sup>2</sup> )	FF (%)	PCE (%)	$R_S$ ( $\Omega$ /cm <sup>2</sup> )	$R_{sh}$ (k $\Omega$ /cm <sup>2</sup> )
10	20	Bottom	0.64	5.03	62.4	2.01	1.2	1.08
10	20	Top	0.60	1.44	64.6	0.56	1.3	5.07
15	15	Bottom	0.64	4.70	59.5	1.79	2.1	1.12
15	15	Top	0.60	1.90	59.3	0.67	1.7	2.31
20	10	Bottom	0.62	0.31	10.1	0.02	/	/
20	10	Top	/	/	/	/	/	/

to decreased percolation threshold of Ag by introducing a  $\text{MoO}_3$  interlayer (especially when the  $\text{MoO}_3$  layer is thin).  $\text{MoO}_3$  works as a surfactant here to modify the surface of Ag film. When the thickness of  $\text{MoO}_3$  is 2 nm, the unclosed layer may create preferred nucleation sites on the glass substrate to enhance the lateral growth of Ag film and decrease Ag threshold. The detailed discussion and analysis can be seen in our previous work [33].

Based on this optimal  $\text{MoO}_3$  (2 nm)/Ag (9 nm) anode, ITO-free semitransparent OSCs are fabricated with different thickness combination of Ca and Ag as the cathodes.  $J$ - $V$  characteristics of corresponding OSCs illuminated from the anode or cathode side are shown in Figures 3(a) and 3(b), respectively. Dark  $J$ - $V$  curves are also shown in Figure 3(a) for comparison. The corresponding photovoltaic parameters have been summarized in Table 1. As shown in Figure 3(a) and Table 1, the best performance is obtained for OSCs with

Ca (10 nm)/Ag (20 nm) cathode when illuminated from the anode side, with an open-circuit voltage ( $V_{OC}$ ) of 0.64 V, a short-circuit current density ( $J_{SC}$ ) of 5.03 mA/cm<sup>2</sup>, a fill factor (FF) of 62.4%, and a PCE of 2.01%. However, when illuminated from the cathode side, a higher  $J_{SC}$  of 1.90 mA/cm<sup>2</sup> and a higher PCE of 0.67% are obtained for OSCs based on Ca (15 nm)/Ag (15 nm) cathode, compared with that of devices with Ca (10 nm)/Ag (20 nm) cathode. Moreover, a very low  $J_{SC}$  of 0.31 mA/cm<sup>2</sup> is obtained for OSCs with Ca (20 nm)/Ag (10 nm) cathode when illuminated from the anode side.

In order to better understand the effect of different cathodes on the device performance, the cathode-only samples of Ca (10 nm)/Ag (20 nm), Ca (15 nm)/Ag (15 nm), and Ca (20 nm)/Ag (10 nm) are fabricated on glass substrates through the same procedure as the device production and characterized. The wavelength-dependent transmittance and reflectance spectra of these samples are shown in Figure 4.

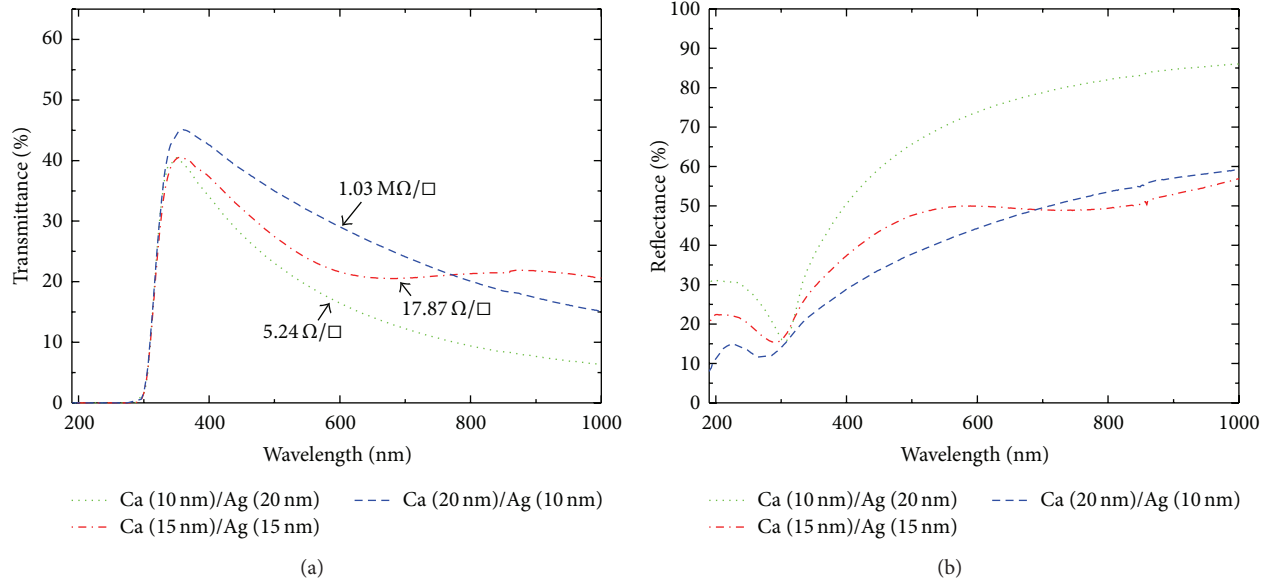


FIGURE 4: (a) The wavelength-dependent transmittance spectra with corresponding sheet resistances and (b) the wavelength-dependent reflectance spectra of Ca (10 nm)/Ag (20 nm), Ca (15 nm)/Ag (15 nm), and Ca (20 nm)/Ag (10 nm) electrodes deposited on glass substrates.

The sheet resistances of these three cathodes are also depicted in Figure 4(a). As shown in Figure 4(a), a large sheet resistance of  $1.03 \text{ M}\Omega/\square$  is obtained for Ca (20 nm)/Ag (10 nm) cathode. This may be caused by that the Ag layer is still not continuous here, in accordance with the previous conclusion that the percolation threshold of Ag in our case is approximately 11 nm. Meanwhile, the discontinuous Ag layer cannot effectively protect the Ca layer from oxygen and moisture so that Ca is oxidized, which also increase the sheet resistance. The poor conductivity of this cathode leads to a very low  $J_{\text{SC}}$  of  $0.31 \text{ mA}/\text{cm}^2$  (shown in Table 1).

As shown in Figure 4(a), although both Ca (10 nm)/Ag (20 nm) and Ca (15 nm)/Ag (15 nm) cathodes show good conductivity with a low sheet resistance, the transparency of Ca (15 nm)/Ag (15 nm) cathode is always better than that of Ca (10 nm)/Ag (20 nm) cathode in the visible and near infrared spectral range. Thus when illuminated from the cathode side, as shown in Table 1, a higher  $J_{\text{SC}}$  of  $1.90 \text{ mA}/\text{cm}^2$  and a higher PCE of 0.67% are obtained for OSCs with Ca (15 nm)/Ag (15 nm) cathode, compared with that of Ca (10 nm)/Ag (20 nm) cathode ( $J_{\text{SC}}$  of  $1.44 \text{ mA}/\text{cm}^2$  and PCE of 0.56%).

However, the situation becomes different when illuminated from the anode side. As shown in Figure 4(b), Ca (10 nm)/Ag (20 nm) cathode has a stronger reflectance than Ca (15 nm)/Ag (15 nm) cathode in the nearly entire spectral range discussed. Thus when illuminated from the anode side, more light is reflected from the Ca/Ag surface and arrives at the active layer a second time for OSCs based on Ca (10 nm)/Ag (20 nm) cathode. It leads to a higher  $J_{\text{SC}}$  of  $5.03 \text{ mA}/\text{cm}^2$  and a higher PCE of 2.01%, compared with that of Ca (15 nm)/Ag (15 nm) cathode ( $J_{\text{SC}}$  of  $4.70 \text{ mA}/\text{cm}^2$  and PCE of 1.79%).

Since good transparency and high PCE should be achieved simultaneously in the application of semitransparent OSCs, samples with the same stack as our devices but a larger area are fabricated. The wavelength-dependent transmittance spectra of corresponding OSCs with different thickness combination of Ca and Ag as the cathodes are shown in Figure 5. For comparison, the transmittance spectrum of the stack  $\text{MoO}_3$  (2 nm)/Ag (9 nm)/ $\text{MoO}_3$  (10 nm)/P3HT:PCBM (the device without the cathode) is also depicted in Figure 5. It is observed from Figure 5 that the spectral shapes of the transmittance curves are similar for four samples. Two minimums around 500 and 600 nm represent the absorption peak of P3HT:PCBM. The transparency of OSCs based on Ca (10 nm)/Ag (20 nm) cathode is the lowest nearly across the entire spectral range, with a small transparency peak of 16% at 365 nm. It is in agreement with the results shown in Figure 4. The best transparency is obtained for OSCs with Ca (15 nm)/Ag (15 nm) cathode, with a maximum of 32% at 690 nm. Meanwhile the performance of this device (PCE of 1.79% and 0.67% for illumination from the anode and cathode side, resp.) is comparable to that of similar ITO-based semitransparent OSCs (PCE of 1.59% and 0.75% for illumination from the anode and cathode side, resp.) [10, 11]. Thus ITO-free semitransparent OSCs based on Ca (15 nm)/Ag (15 nm) cathode are more preferred for the application.

Moreover, the stability has also been investigated for ITO-free semitransparent OSCs with Ca (15 nm)/Ag (15 nm) cathode. The unencapsulated OSCs were stored in the glove box and measured in air ambient conditions. The normalized PCE as a function of time is shown in Figure 6. As shown in Figure 6, PCE of the device remains 70% of the original efficiency after 262 h no matter the OSC is illuminated from the anode or cathode side. It is expected that the better stability could be obtained for our encapsulated ITO-free

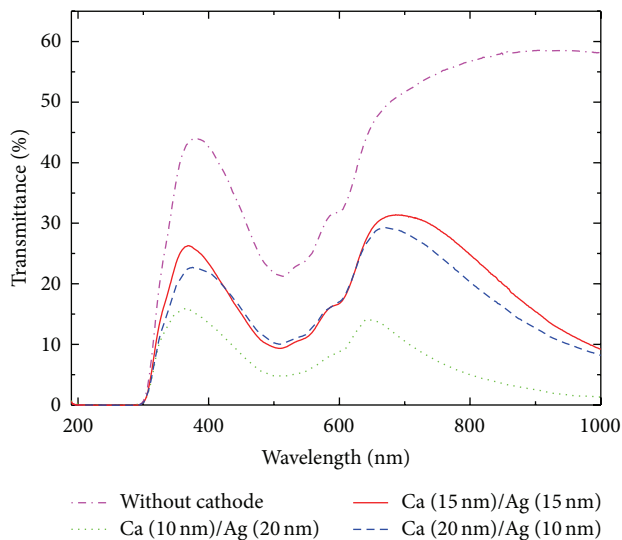


FIGURE 5: The wavelength-dependent transmittance spectra of ITO-free semitransparent OSCs with different thickness combination of Ca and Ag as the cathodes. For comparison, the transmittance spectrum of the stack  $\text{MoO}_3$  (2 nm)/Ag (9 nm)/ $\text{MoO}_3$  (10 nm)/P3HT:PCBM (the device without the cathode) is also depicted in Figure 5. Bottom illumination from the anode side is applied for measurement.

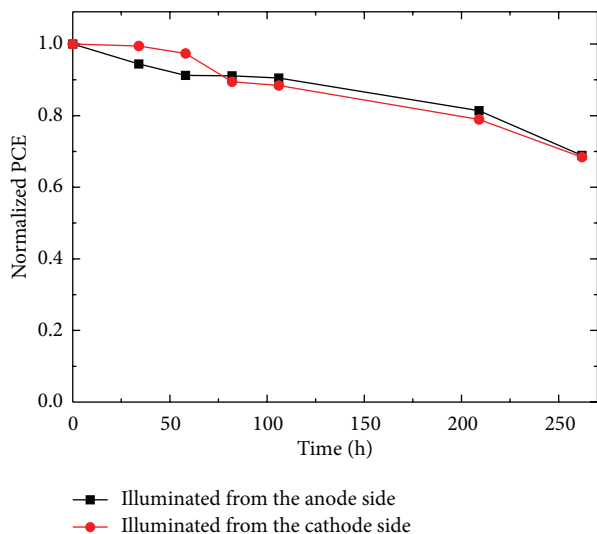


FIGURE 6: The variation of the normalized PCE with time.

semitransparent OSCs by avoiding oxidation and mechanical damage.

#### 4. Conclusions

In this paper, we have firstly demonstrated efficient ITO-free reference OSCs based on  $(\text{MoO}_3)/\text{Ag}$  anodes. The PCE of 2.71% is obtained for OSCs based on the optimal  $\text{MoO}_3$  (2 nm)/Ag (9 nm) anode (also the highest PCE among all the ITO-free reference OSCs), comparable to that of ITO-based reference OSCs (PCE of 2.85%). Then based on this

$\text{MoO}_3$  (2 nm)/Ag (9 nm) anode, ITO-free semitransparent OSCs with different thickness combination of Ca and Ag as the cathodes are fabricated. It combines the advantages of ITO-free OSCs and semitransparent OSCs simultaneously, providing a way for commercialization of OSCs. It is observed from our results that OSCs with Ca (15 nm)/Ag (15 nm) cathode have the optimal transparency. Meanwhile, the PCE of 1.79% (illuminated from the anode side) and 0.67% (illuminated from the cathode side) is obtained, comparable to that of similar ITO-based semitransparent OSCs (PCE of 1.59% and 0.75% for illumination from the anode and cathode side, resp.) [10, 11]. Although all the devices are only fabricated on glass substrates, our method and process can also be applied to flexible substrates. Meanwhile, the transparency and PCE of ITO-free semitransparent OSCs can be further improved by introducing a light couple layer. These results are instructive for further research of ITO-free semitransparent OSCs.

#### Conflict of Interests

The authors declare that there is no conflict of interests regarding the publication of this paper.

#### Acknowledgment

The authors gratefully acknowledge the support of NSFC (61106063).

#### References

- [1] C. J. Brabec, "Organic photovoltaics: technology and market," *Solar Energy Materials and Solar Cells*, vol. 83, no. 2-3, pp. 273–292, 2004.
- [2] P. Peumans, A. Yakimov, and S. R. Forrest, "Small molecular weight organic thin-film photodetectors and solar cells," *Journal of Applied Physics*, vol. 93, no. 7, pp. 3693–3723, 2003.
- [3] R. Søndergaard, M. Helgesen, M. Jørgensen, and F. C. Krebs, "Fabrication of polymer solar cells using aqueous processing for all layers including the metal back electrode," *Advanced Energy Materials*, vol. 1, no. 1, pp. 68–71, 2011.
- [4] F. C. Krebs, "Fabrication and processing of polymer solar cells: a review of printing and coating techniques," *Solar Energy Materials and Solar Cells*, vol. 93, no. 4, pp. 394–412, 2009.
- [5] H. F. Dam and F. C. Krebs, "Simple roll coater with variable coating and temperature control for printed polymer solar cells," *Solar Energy Materials and Solar Cells*, vol. 97, pp. 191–196, 2012.
- [6] M. A. Green, K. Emery, Y. Hishikawa, W. Warta, and E. D. Dunlop, "Solar cell efficiency tables (version 40)," *Progress in Photovoltaics: Research and Applications*, vol. 20, no. 5, pp. 606–614, 2012.
- [7] R. Schueppel, R. Timmreck, N. Allinger et al., "Controlled current matching in small molecule organic tandem solar cells using doped spacer layers," *Journal of Applied Physics*, vol. 107, no. 4, Article ID 044503, 2010.
- [8] D. W. Zhao, X. W. Sun, C. Y. Jiang, A. K. K. Kyaw, G. Q. Lo, and D. L. Kwong, "Efficient tandem organic solar cells with an Al/ $\text{MoO}_3$  intermediate layer," *Applied Physics Letters*, vol. 93, no. 8, Article ID 083305, 2008.

- [9] A. Hadipour, B. de Boer, and P. W. M. Blom, "Device operation of organic tandem solar cells," *Organic Electronics*, vol. 9, no. 5, pp. 617–624, 2008.
- [10] F. Li, S. Ruan, Y. Xu et al., "Semitransparent inverted polymer solar cells using  $\text{MoO}_3/\text{Ag}/\text{WO}_3$  as highly transparent anodes," *Solar Energy Materials and Solar Cells*, vol. 95, no. 3, pp. 877–880, 2011.
- [11] L. Shen, S. Ruan, W. Guo, F. Meng, and W. Chen, "Semitransparent inverted polymer solar cells using  $\text{MoO}_3/\text{Ag}/\text{V}_2\text{O}_5$  as transparent anodes," *Solar Energy Materials & Solar Cells*, vol. 97, pp. 59–63, 2012.
- [12] L. Shen, Y. Xu, F. Meng, F. Li, S. Ruan, and W. Chen, "Semitransparent polymer solar cells using  $\text{V}_2\text{O}_5/\text{Ag}/\text{V}_2\text{O}_5$  as transparent anodes," *Organic Electronics: Physics, Materials, Applications*, vol. 12, no. 7, pp. 1223–1226, 2011.
- [13] D. S. Hecht, L. Hu, and G. Irvin, "Emerging transparent electrodes based on thin films of carbon nanotubes, graphene, and metallic nanostructures," *Advanced Materials*, vol. 23, no. 13, pp. 1482–1513, 2011.
- [14] J. Lee, S. T. Connor, Y. Cui, and P. Peumans, "Solution-processed metal nanowire mesh transparent electrodes," *Nano Letters*, vol. 8, no. 2, pp. 689–692, 2008.
- [15] H. Chen, A. du Pasquier, G. Saraf, J. Zhong, and Y. Lu, "Dye-sensitized solar cells using ZnO nanotips and Ga-doped ZnO films," *Semiconductor Science and Technology*, vol. 23, no. 4, Article ID 045004, 2008.
- [16] H. Park, J. Kang, S. Na, D. Kim, and H. Kim, "Characteristics of indium-free GZO/Ag/GZO and AZO/Ag/AZO multilayer electrode grown by dual target DC sputtering at room temperature for low-cost organic photovoltaics," *Solar Energy Materials and Solar Cells*, vol. 93, no. 11, pp. 1994–2002, 2009.
- [17] N. Sun, G. Fang, P. Qin et al., "Bulk heterojunction solar cells with NiO hole transporting layer based on AZO anode," *Solar Energy Materials and Solar Cells*, vol. 94, no. 12, pp. 2328–2331, 2010.
- [18] Y. H. Kim, C. Sachse, M. L. MacHala, C. May, L. Müller-Meskamp, and K. Leo, "Highly conductive PEDOT:PSS electrode with optimized solvent and thermal post-treatment for ITO-free organic solar cells," *Advanced Functional Materials*, vol. 21, no. 6, pp. 1076–1081, 2011.
- [19] S. Choi, W. J. Potscavage Jr., and B. Kippelen, "ITO-free large-area organic solar cells," *Optics Express*, vol. 18, no. 19, pp. A458–A466, 2010.
- [20] F. Guo, X. Zhu, K. Forberich et al., "ITO-free and fully solution-processed semitransparent organic solar cells with high fill factors," *Advanced Energy Materials*, vol. 3, no. 8, pp. 1062–1067, 2013.
- [21] J. van de Lagemaat, T. M. Barnes, G. Rumbles et al., "Organic solar cells with carbon nanotubes replacing  $\text{In}_2\text{O}_3$ : Sn as the transparent electrode," *Applied Physics Letters*, vol. 88, no. 23, Article ID 233503, 2006.
- [22] D. Angmo and F. C. Krebs, "Flexible ITO-free polymer solar cells," *Journal of Applied Polymer Science*, vol. 129, no. 1, pp. 1–14, 2013.
- [23] L. Cattin, J. C. Bernède, and M. Morsli, "Toward indium-free optoelectronic devices: dielectric/metal/dielectric alternative transparent conductive electrode in organic photovoltaic cells," *Physica Status Solidi (A): Applications and Materials Science*, vol. 210, no. 6, pp. 1047–1061, 2013.
- [24] W. Cao, Y. Zheng, Z. Li, E. Wrzesniewski, W. T. Hammond, and J. Xue, "Flexible organic solar cells using an oxide/metal/oxide trilayer as transparent electrode," *Organic Electronics*, vol. 13, no. 11, pp. 2221–2228, 2012.
- [25] S. D. Yambem, A. Haldar, K. Liao, E. P. Dillon, A. R. Barron, and S. A. Curran, "Optimization of organic solar cells with thin film Au as anode," *Solar Energy Materials and Solar Cells*, vol. 95, no. 8, pp. 2424–2430, 2011.
- [26] S. D. Yambem, K. Liao, and S. A. Curran, "Flexible Ag electrode for use in organic photovoltaics," *Solar Energy Materials and Solar Cells*, vol. 95, no. 11, pp. 3060–3064, 2011.
- [27] S. Lim, D. Han, H. Kim, S. Lee, and S. Yoo, "Cu-based multilayer transparent electrodes: a low-cost alternative to ITO electrodes in organic solar cells," *Solar Energy Materials and Solar Cells*, vol. 101, pp. 170–175, 2012.
- [28] D. S. Ghosh, R. Betancur, T. L. Chen, V. Pruneri, and J. Martorell, "Semi-transparent metal electrode of CuNi as a replacement of an ITO in organic photovoltaic cells," *Solar Energy Materials and Solar Cells*, vol. 95, no. 4, pp. 1228–1231, 2011.
- [29] R. Sennett and G. Scott, "The structure of evaporated metal films and their optical properties," *Journal of the Optical Society of America*, vol. 40, pp. 203–210, 1950.
- [30] S. Kim, H. Ee, W. Choi et al., "Surface-plasmon-induced light absorption on a rough silver surface," *Applied Physics Letters*, vol. 98, no. 1, Article ID 011109, 2011.
- [31] S. Schubert, J. Meiss, L. Müller-Meskamp, and K. Leo, "Improvement of transparent metal top electrodes for organic solar cells by introducing a high surface energy seed layer," *Advanced Energy Materials*, vol. 3, no. 4, pp. 438–443, 2013.
- [32] S. Schubert, M. Hermenau, J. Meiss, L. Müller-Meskamp, and K. Leo, "Oxide sandwiched metal thin-film electrodes for long-term stable organic solar cells," *Advanced Functional Materials*, vol. 22, no. 23, pp. 4993–4999, 2012.
- [33] Z. Wang, C. Zhang, R. Gao et al., "Improvement of transparent silver thin film anodes for organic solar cells with a decreased percolation threshold of silver," *Solar Energy Materials and Solar Cells*, vol. 127, pp. 193–200, 2014.

## Research Article

# Block Textured a-Si:H Solar Cell

**Seung Jae Moon, Chang Min Keum, Ju-Yeon Kim, Jin Kuk Kim, and Byung Seong Bae**

*Department of Display Engineering, Hoseo University, Asan, Chungnam 336-795, Republic of Korea*

Correspondence should be addressed to Byung Seong Bae; [bsbae3@hanmail.net](mailto:bsbae3@hanmail.net)

Received 13 March 2014; Revised 5 May 2014; Accepted 26 May 2014; Published 23 June 2014

Academic Editor: Mohammad Yusri Hassan

Copyright © 2014 Seung Jae Moon et al. This is an open access article distributed under the Creative Commons Attribution License, which permits unrestricted use, distribution, and reproduction in any medium, provided the original work is properly cited.

A series of etching experiments on light trapping structure have been carried out by glass etching. The block structure provides long light traveling path and a constant distance between the cathode and anode electrodes regardless of the block height, which results in higher efficiency of the block textured solar cell. In terms of etching profile of the glass substrate, the addition of  $\text{NH}_4\text{F}$  resulted in the smooth and clean etching profile, and the steep slope of the block was obtained by optimizing the composition of etching solution. For a higher HF concentration, a more graded slope was obtained and the addition of  $\text{HNO}_3$  and  $\text{NH}_4\text{F}$  provided steep slope and clean etching profile. The effects of the block textured glass were verified by a comparison of the solar cell efficiency. For the textured solar cell, the surface was much rougher than that of the plain glass, which also contributes to the improvement of the efficiency. We accomplished block shaped light trapping structure for the first time by wet etching of the glass substrate, which enables the high efficiency thin film solar cell with the aid of the good step coverage deposition.

## 1. Introduction

The demand for renewable energy sources is increasing and the installation of photovoltaic (PV) systems on roofs or the facades of buildings in urban areas is expected to increase. According to the designed concept of esthetics and practicality, it is desirable for PV systems to blend in with the buildings and cityscapes [1]. To realize this, considerable efforts have been made to achieve the low cost of solar cells [2] and high conversion efficiency. Maximum stabilized efficiencies of more than 10% could be achieved for the best modules using the monolithic tandem interconnection of an hydrogenated amorphous silicon (a-Si:H) junction with microcrystalline silicon ( $\mu\text{c-Si:H}$ ) [3].

Texturing is one way of increasing the solar cell efficiency. Light scattering at textured interfaces is essential for the high efficiency of thin film solar cells [4, 5]. The a-Si:H solar cells considered in this paper are widely accepted thin-film solar cells because (a) silicon is abundant and nontoxic, (b) the process temperature is low, enabling module production on flexible and low cost substrates, (c) the technological capability for large-area deposition exists, such as plasma enhanced chemical vapor deposition (PECVD), and (d) the material requirements are low, 1 to 2  $\mu\text{m}$ , due to the high

absorption coefficient compared to crystalline silicon [6–9]. On the other hand, the efficiency of a-Si:H solar cells is approximately 10%, which is still lower than that of other solar cells, and texturing is one way of increasing the efficiency [10].

Reduction of the front surface reflectance, a good back surface reflector, and texturing are important for achieving the full benefits of optical absorption enhancement [11, 12]. In terms of texturing, one method involves etching the substrate. Surface texturing can reduce the light reflectance on the surface of cells quite efficiently and achieve enhanced light absorption inside the cells compared to flat surface cells [13, 14]. A low cost surface texturing method by wet etching using an alkaline solution is used widely for improving the short circuit current of the cells [15, 16]. To achieve the high efficiency, the transmitted light should be trapped in the solar cells to avoid escaping from the solar cell surfaces until it is absorbed [17]. Light trapping structures have been reported such as pyramid structure in crystalline silicon solar cell [16–20]. However, glass etching was not reported for the light trapping structure, and even the antireflection structure by glass etching was reported [21]. Therefore, we investigated etching characteristics of the glass for the block structure, which provides a long light traveling path. Block textured glass was prepared by wet etching a glass substrate

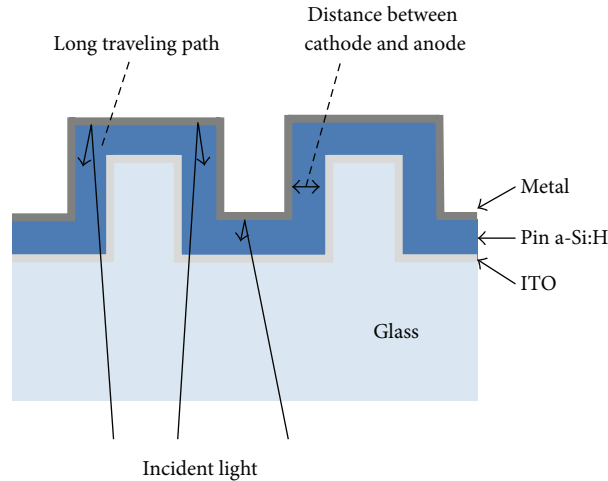


FIGURE 1: Suggested block textured thin film solar cell that provides long traveling path of the incident light while keeping the distance between the cathode and anode constant.

and a-Si:H solar cells were formed on the textured glass. The block structure as shown in Figure 1 provides a long light traveling path along the sidewall of the block while maintaining the distance between the cathode and anode invariable, regardless of the height of the block which is the traveling path of the light. Therefore, higher efficiency can be obtained using a block structure than that of a solar cell on the conventional plain glass. However, the way to form the block structure for the light trapping was not reported and we succeeded to accomplish a good shape of the block with wet etching. This light trap structure enhances efficiencies while keeping reducing layer thickness which contribute to make a very low cost technology [22, 23].

## 2. Experiment

For the efficient light trapping, the large height of the block such as 2 to 3  $\mu\text{m}$  is necessary. Large height of the block gives long light traveling path and improves light trapping effect. To obtain the block shape, the glass was etched using chemicals containing hydrofluoric acid (HF) and the etching condition was optimized.

The chemical composition and other etching conditions were varied to obtain the optimal block structure. The etching temperature was fixed at 40°C and the etching time was varied up to 200 s. The etching was carried out at different HF concentrations (10 wt.%, 20 wt.%). The chemicals used for etching were HF, HNO<sub>3</sub>, and NH<sub>4</sub>F, the compositions of which were optimized for the best block shape. Table 1 lists the etching rate under a range of etching conditions. The Cr was used as the masking material during glass etching [24]. In the case of the HF-only etching solution, the etching rate was high and the Cr mask was unable to endure the process [25, 26]. HNO<sub>3</sub>, H<sub>2</sub>SO<sub>4</sub>, and NH<sub>4</sub>F were tested to achieve a clean and high taper angle. Figure 2 shows the etching process by photolithography. Initially, a Cr layer was deposited after cleaning the glass. After Cr mask patterning by lithography, the glass substrate was etched to form a block structure. After

glass etching, the photoresist was removed. All experiments were carried out with a constant temperature bath. After etching, the surface of textured glass was examined by scanning electron microscopy (SEM) to observe the surface morphology and determine the etching rate.

After texturing the substrate, a-Si:H solar cell with the structure of ITO (indium tin oxide)/P-type a-Si:H/intrinsic a-Si:H/N-type a-Si:H/Al, was deposited. The silicon layers were deposited by PECVD and Al and ITO layers were deposited by sputtering. Initially, the ITO layer was deposited at a RF power of 50 W, process pressure of 2 mTorr, and 20 sccm of Ar gas. Subsequently, the p-i-n a-Si:H layers were deposited by PECVD at 250°C. The p-layer was prepared from a mixture of SiH<sub>4</sub>/H<sub>2</sub>/B<sub>2</sub>H<sub>6</sub> at a flow ratio of 150/120/60. The i-layer was prepared from a mixture of SiH<sub>4</sub>/H<sub>2</sub> at a flow ratio of 150/120. The n-layer was prepared from a mixture of SiH<sub>4</sub>/H<sub>2</sub>/PH<sub>3</sub> at a flow ratio of 150/120/30. An Al layer was deposited at a RF power of 125 W, process pressure of 5 mTorr, and 20 sccm of Ar gas. Table 2 lists the processing conditions of the a-Si:H solar cells.

## 3. Result and Discussion

In the suggested block textured solar cell, the shape of block texturing is important for achieving high conversion efficiency and the etching of the glass was investigated. After etching the glass, the shape was observed by scanning electron microscopy (SEM) for the various etching conditions as shown in Figure 3. HF is a typical glass etching solution; however, it was uncontrollable for high etching rate as it increased the concentration of HF and resulted in nonuniform etching surface profile. Therefore, other chemicals such as H<sub>2</sub>SO<sub>4</sub>, HNO<sub>3</sub>, and NH<sub>4</sub>F were investigated for better etching profile. In Figure 3, 1-1 and 1-2 show the etching results without NH<sub>4</sub>F, in which the etching surface was not uniform and as it increased the HF concentration etching rate increased as well as the surface roughness and nonuniformity. The effect of H<sub>2</sub>SO<sub>4</sub> is shown in 2-1 and 2-2. Addition of

TABLE 1: Etching rates according to the composition of the etching solution.

Number	Time (s)	Etchant (wt.%)				Etching rate ( $\mu\text{m/s}$ )
		HF (49%)	HNO <sub>3</sub>	H <sub>2</sub> SO <sub>4</sub>	NH <sub>4</sub> F	
1	60	20	15	—	—	0.05
2	60	20	15	—	15	0.04
3	60	10	—	15	—	0.03
4	60	10	—	15	15	0.02
5	60	10	15	—	—	0.01
6	60	10	15	—	15	0.03

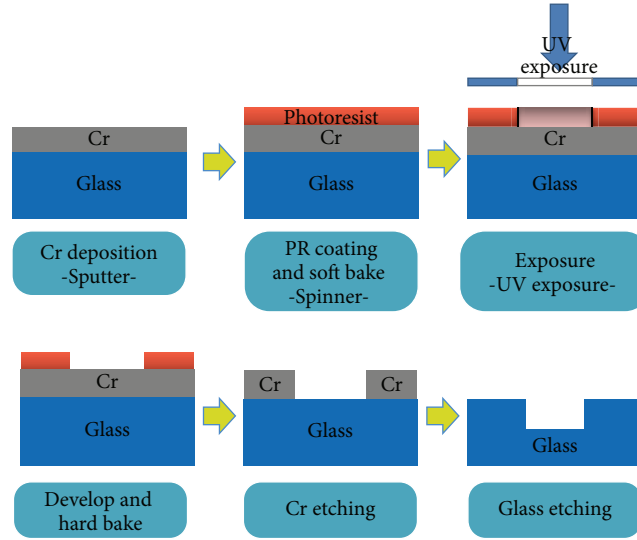


FIGURE 2: Texturing process by wet etching.

H<sub>2</sub>SO<sub>4</sub> increased the etching rate compared to the addition of HNO<sub>3</sub> and the etching surface was not much uniform. The addition of NH<sub>4</sub>F improved the nonuniformity of the etching surface; however, the surface was still not uniform. The clean etching was obtained at an etching solution with HF, HNO<sub>3</sub>, and NH<sub>4</sub>F, as shown in 3-1 and 3-2. Without NH<sub>4</sub>F, the etching profile was not clean, and the optimal condition was a solution containing 10 wt.% HF, 15 wt.% HNO<sub>3</sub>, and 15 wt.% NH<sub>4</sub>F under the etching temperature of 40°C.

Under these optimized etching conditions, experiments were conducted at various etching times. The SEM image of Figure 4(a) presents the etching profiles according to the etching times. With increasing etching time, the etched depth increased and isotropic etching was observed. In terms of the etching cross section, the upper part showed a stiff etching profile, whereas the lower part showed a slow etching profile. After an etching time of 200 s, 3.06  $\mu\text{m}$  height of the block was obtained, and the etching depth is shown in Figure 4(b).

At higher HF concentrations, a more graded slope was obtained, and the addition of HNO<sub>3</sub> and NH<sub>4</sub>F produced a steeper slope and a clean etching profile. After fine adjustment of the solution, an optimized block-textured surface of the glass was obtained as shown in Figure 5. An a-Si:H solar cell was formed on the block textured glass and compared with the solar cell on the conventional glass substrate. Among the

solar cells on the various slope block textured glass, the one with the steep slope did not operate well, which was attributed to a short between cathode and anode electrode due to the steep slope which results in thin layer of deposition material. However, the improved environment free of particles, any other contamination, and optimized PECVD conditions would provide high efficiency even with thin layer of the deposited material. Due to the short fail, the efficiency of the solar cell on the slow slope block textured glass was compared with that of the solar cell on the conventional plain glass. Figures 6(a) and 6(b) show SEM images of each type of solar cell, (a) is the solar cell on the conventional plain glass and (b) is the solar cell on the textured glass. The two types of solar cells were fabricated at the same time to be sure of the same characteristics of the solar cells. The efficiencies were measured under a solar simulator with AM 1.5 (1000 W/m<sup>2</sup>). Because the traveling paths of the incident light are different between those two samples, it is expected that the two samples will have different efficiencies. Figure 6(b) shows that the surface is much rougher for the block textured solar cells than that of conventional glass, which increases light scattering when the light is reflected at the metal electrode.

The thickness of the i-layer is a key parameter that can limit the performance of amorphous thin film solar cells because it determines the absorption of the incident light and

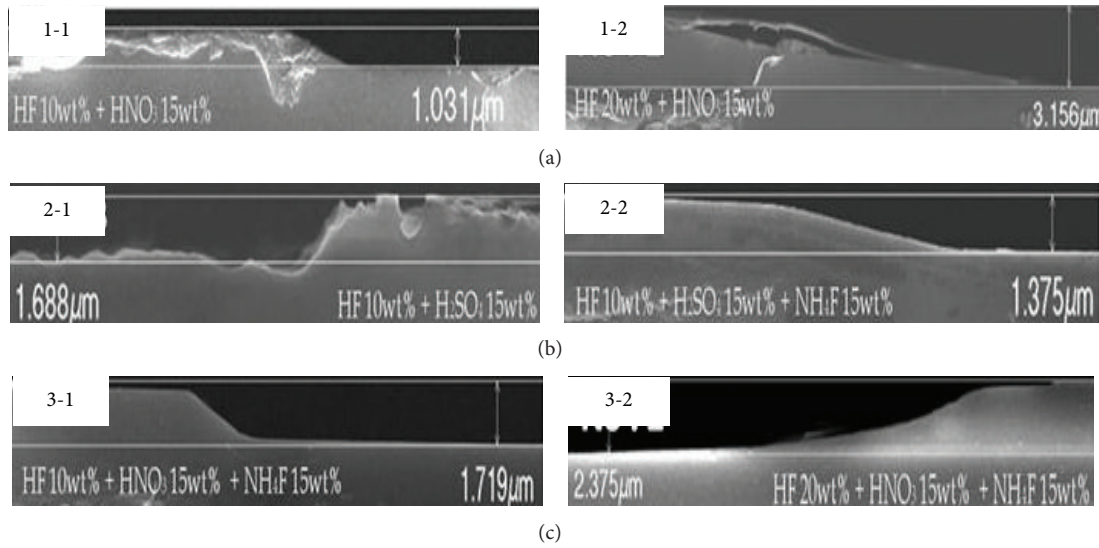


FIGURE 3: Etching profiles of the glass using different etching solutions; (a) etching results without  $\text{NH}_4\text{F}$ , (b) the effect of  $\text{H}_2\text{SO}_4$ , and (c) without  $\text{NH}_4\text{F}$ .

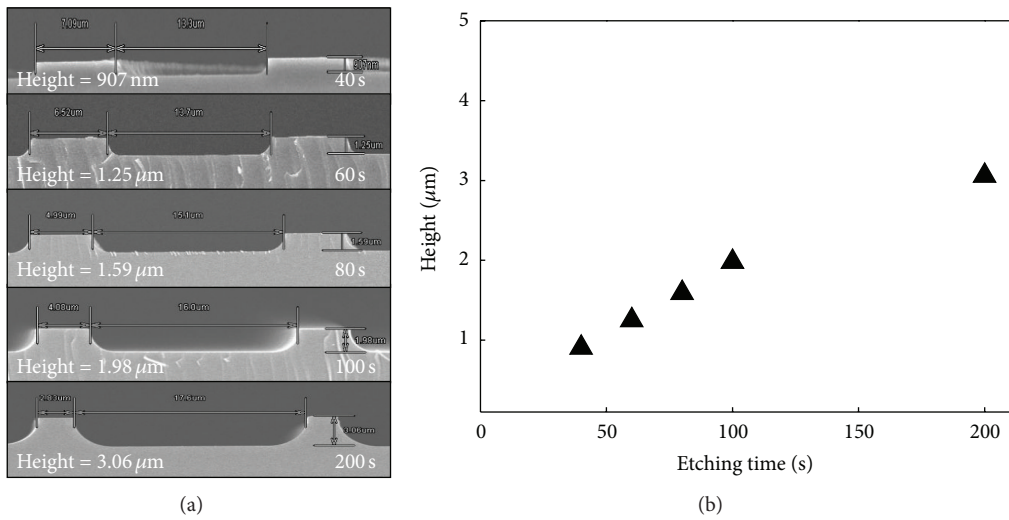


FIGURE 4: (a) SEM images of the etching profile according to the etching times and (b) the graph as a function of the etching time.

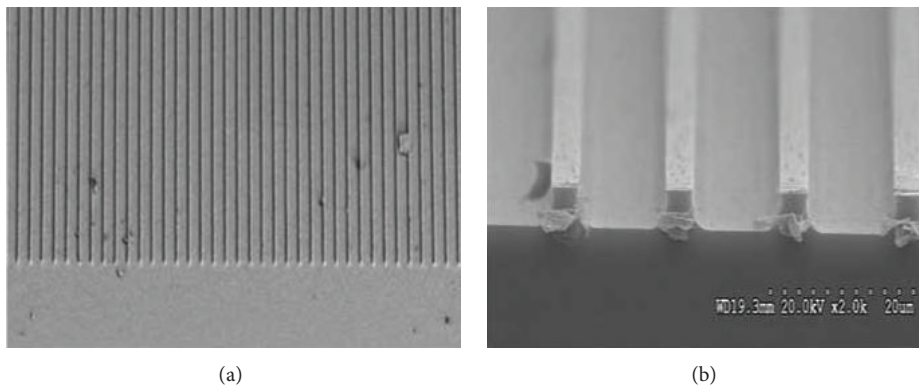


FIGURE 5: Block textured glass obtained under the optimized etching conditions.

TABLE 2: Process conditions of a-Si:H solar cell by PECVD.

Layer	Temperature (°C)	Electrode distance (mils)	Working pressure (Torr)	RF power (W)	Gas
N-type	250	1000	1.5	10	SiH <sub>4</sub> , H <sub>2</sub> , PH <sub>3</sub>
Intrinsic	250	1000	1.0	10	SiH <sub>4</sub> , H <sub>2</sub>
P-type	250	1000	1.5	10	SiH <sub>4</sub> , H <sub>2</sub> , B <sub>2</sub> H <sub>6</sub>

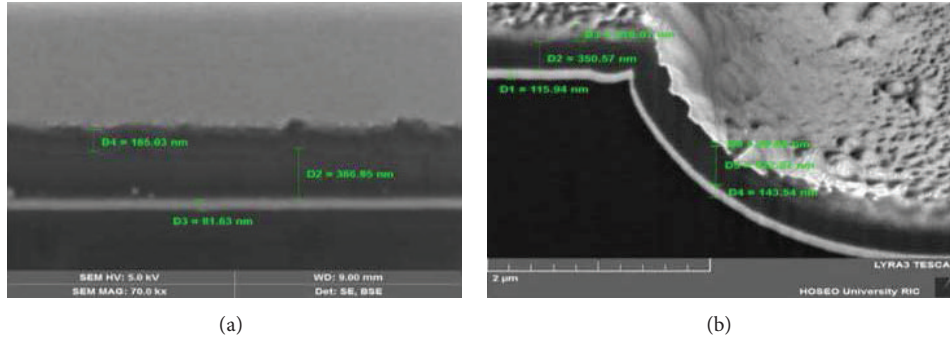
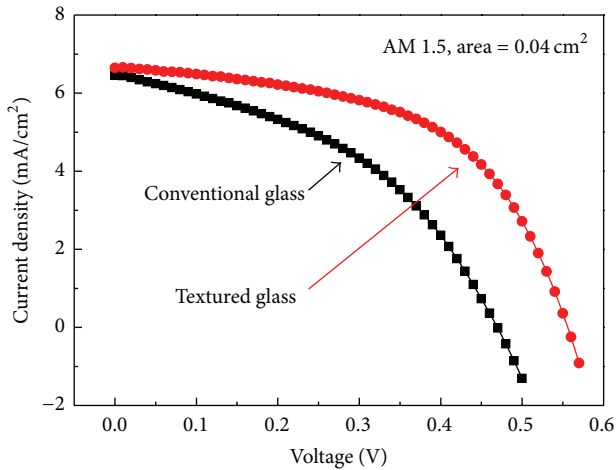


FIGURE 6: SEM images of a-Si:H solar cell on (a) conventional glass and (b) block textured glass.

TABLE 3: The comparison of the measured parameters with conventional plain glass substrate and block textured glass substrate.

	$V_{oc}$ (V)	$J_{sc}$ (mA/cm <sup>2</sup> )	F.F	Efficiency (%)
Conventional	0.47	6.45	0.43	1.30
Textured	0.54	6.64	0.54	2.00

FIGURE 7:  $J$ - $V$  curves of the fabricated solar cells.

the drift of the electrons and holes [27]. Since the increased thickness of the  $i$ -layer increases the recombination of the carriers, the efficiency decreases. On the other hand, in the suggested block textured structure, the recombination of the carriers can be minimized due to the short electrode distance with thin  $i$ -layer, even with the long light traveling path.

Figure 7 shows the  $J$ - $V$  characteristics of a-Si:H solar cells on conventional glass and textured glass. Although

the efficiencies of the solar cells were not high due to nonoptimized environment, a comparison between the two samples was possible because they were fabricated at the same time with the same conditions. The efficiency of the solar cell on the block textured glass was 1.5 times higher than that of the conventional one.

Block textured glass substrate showed higher efficiency than solar cell on the conventional plain glass; measured parameters were shown in Table 3. The short circuit current was not increased as much as the efficiency and can be attributed to the decrease of the short resistance between the cathode and anode due to the rough surface of the solar cell. The rough surface of the block textured solar cell also contributes to the higher conversion efficiency due to the increased light scattering at the back metal electrode. The increased open circuit voltage for the graded block structure was attributed to the decreased contact resistance which can reduce the voltage drop at the contact.

#### 4. Conclusion

To increase the efficiency, we suggested a block textured solar cell, which gives long traveling path of the incident light and maintains the distance between the cathode and anode electrodes invariable. The block structure was obtained by wet etching the glass substrate, and the condition was optimized to obtain a block shape. The addition of NH<sub>4</sub>F resulted in the smooth and clean etching profile, and the steep slope of the block was obtained by optimizing the etching solution. For a higher HF concentration, a more graded slope was obtained and the addition of HNO<sub>3</sub> and NH<sub>4</sub>F provided steep slope and clean etching profile. After depositing the a-Si:H solar cells on both substrates (conventional and block textured), the efficiencies of the solar cells were compared under the solar simulator with AM 1.5 (1000 W/m<sup>2</sup>). For the first time,

we developed the etching process for the block textured solar cell for high light trapping. The depth as high as  $3.06\ \mu\text{m}$  was achieved with good block shape by optimizing the etching condition. This suggested that block structure provides long light traveling path and low carrier recombination by short distance between cathode and anode.

## Conflict of Interests

The authors declare that there is no conflict of interests regarding the publication of this paper.

## References

- [1] A. V. Shah, R. Platz, and H. Keppner, "Thin-film silicon solar cells: a review and selected trends," *Solar Energy Materials and Solar Cells*, vol. 38, no. 1–4, pp. 501–520, 1995.
- [2] R. L. Mitchell, C. E. Witt, R. King, and D. Ruby, "PVMaT advances in the photovoltaic industry and the focus of future PV manufacturing R&D," in *Proceedings of the 29th IEEE Photovoltaic Specialists Conference*, vol. 29, pp. 1444–1447, May 2002.
- [3] M. Despeisse, C. Battaglia, M. Boccard et al., "Optimization of thin film silicon solar cells on highly textured substrates," *Physica Status Solidi (A)*, vol. 208, no. 8, pp. 1863–1868, 2011.
- [4] H. Sai and M. Kondo, "Effect of self-orderly textured back reflectors on light trapping in thin-film microcrystalline silicon solar cells," *Journal of Applied Physics*, vol. 105, no. 9, Article ID 094511, 2009.
- [5] K. L. Chopra, P. D. Paulson, and V. Dutta, "Thin-film solar cells: an overview," *Progress in Photovoltaics: Research and Applications*, vol. 12, no. 2-3, pp. 69–92, 2004.
- [6] D. V. Tsu, B. S. Chao, S. R. Ovshinsky, S. Guha, and J. Yang, "Effect of hydrogen dilution on the structure of amorphous silicon alloys," *Applied Physics Letters*, vol. 71, no. 10, pp. 1317–1319, 1997.
- [7] A. Shah, P. Torres, R. Tscharnner, N. Wyrsh, and H. Keppner, "Photovoltaic technology: the case for thin-film solar cells," *Science*, vol. 285, no. 5428, pp. 692–698, 1999.
- [8] I. Usman, A. Supu, S. Mursal, T. Winata, and M. Barmawi, "Application of a-Si:H in p-i-n solar cell by VHF-PECVD method," *Indonesian Journal of Physics*, vol. 15, no. 2, pp. 31–34, 2004.
- [9] Y. Ichikawa, T. Yoshida, T. Hama, H. Sakai, and K. Harashima, "Production technology for amorphous silicon-based flexible solar cells," *Solar Energy Materials and Solar Cells*, vol. 66, no. 1–4, pp. 107–115, 2001.
- [10] M. Moreno, D. Daineka, and P. Roca i Cabarrocas, "Plasma texturing for silicon solar cells: from pyramids to inverted pyramids-like structures," *Solar Energy Materials and Solar Cells*, vol. 94, no. 5, pp. 733–737, 2010.
- [11] Y. Inomata, K. Fukui, and K. Shirasawa, "Surface texturing of large area multicrystalline silicon solar cells using reactive ion etching method," *Solar Energy Materials and Solar Cells*, vol. 48, no. 1–4, pp. 237–242, 1997.
- [12] N. Sahraei, S. Venkataraj, P. Vayalakkara, and A. G. Aberle, "Optical absorption enhancement in amorphous silicon films and solar cell precursors using the Aluminum-induced glass texturing method," *International Journal of Photoenergy*, vol. 2014, Article ID 842891, 6 pages, 2014.
- [13] E. Yablonovitch, "Statistical ray optics," *Journal of the Optical Society of America*, vol. 72, no. 7, pp. 899–907, 1982.
- [14] H. W. Deckman, C. B. Roxlo, and E. Yablonovitch, "Maximum statistical increase of optical absorption in textured semiconductor films," *Optics Letters*, vol. 8, no. 9, pp. 491–493, 1983.
- [15] R. Watanabe, S. Abe, S. Haruyama, T. Suzuki, M. Onuma, and Y. Saito, "Evaluation of a new acid solution for texturization of multicrystalline silicon solar cells," *International Journal of Photoenergy*, vol. 2013, Article ID 951303, 6 pages, 2013.
- [16] Y. Fan, P. Han, P. Liang, Y. Xing, Z. Ye, and S. Hu, "Differences in etching characteristics of TMAH and KOH on preparing inverted pyramids for silicon solar cells," *Applied Surface Science*, vol. 264, pp. 761–766, 2013.
- [17] P. Campbell and M. A. Green, "Light trapping properties of pyramidally textured surfaces," *Journal of Applied Physics*, vol. 62, no. 1, pp. 243–249, 1987.
- [18] A. W. Smith and A. Rohatgi, "Ray tracing analysis of the inverted pyramid texturing geometry for high efficiency silicon solar cells," *Solar Energy Materials and Solar Cells*, vol. 29, no. 1, pp. 37–49, 1993.
- [19] A. W. Blakers, A. Wang, A. M. Milne, J. Zhao, and M. A. Green, "22.8% efficient silicon solar cell," *Applied Physics Letters*, vol. 55, no. 13, pp. 1363–1365, 1989.
- [20] J. Zhao, A. Wang, and M. A. Green, "24.5% efficiency silicon PERT cells on MCZ substrates and 24.7% efficiency PERL cells on FZ substrates," *Progress in Photovoltaics: Research and Applications*, vol. 7, no. 6, pp. 471–474, 1999.
- [21] Y. Du, M. Zhu, Y. Jin et al., "Broadband antireflective structures with hole for highly transparent glasses," *Optik*, vol. 124, no. 19, pp. 3799–3803, 2013.
- [22] J. Escarré, K. Söderström, M. Despeisse et al., "Geometric light trapping for high efficiency thin film silicon solar cells," *Solar Energy Materials and Solar Cells*, vol. 98, pp. 185–190, 2012.
- [23] T. Kratzla, A. Zindel, and R. Benz, "Oerlikon Solar's key performance drivers to grid parity," in *Proceedings of the European Photovoltaics Solar Energy Conference*, vol. 25, pp. 2807–2810, 2010.
- [24] C. Iliescu, F. E. H. Tay, and J. Miao, "Strategies in deep wet etching of Pyrex glass," *Sensors and Actuators A*, vol. 133, no. 2, pp. 395–400, 2007.
- [25] F. E. H. Tay, C. Iliescu, J. Jing, and J. Miao, "Defect-free wet etching through pyrex glass using Cr/Au mask," *Microsystem Technologies*, vol. 12, no. 10-11, pp. 935–939, 2006.
- [26] S. W. Youn and C. G. Kang, "Maskless pattern fabrication on Pyrex 7740 glass surface by using nano-scratch with HF wet etching," *Scripta Materialia*, vol. 52, no. 2, pp. 117–122, 2005.
- [27] P. Jelodarian and A. Kosarian, "Effect of p-layer and i-layer properties on the electrical behaviour of advanced a-Si:H/a-SiGe:H thin film solar cell from numerical modeling prospect," *International Journal of Photoenergy*, vol. 2012, Article ID 946024, 7 pages, 2012.

## Research Article

# Experimental Investigation on Thermoelectric Chiller Driven by Solar Cell

Yen-Lin Chen,<sup>1</sup> Zi-Jie Chien,<sup>2</sup> Wen-Shing Lee,<sup>2</sup> Ching-Song Jwo,<sup>2</sup> and Kun-Ching Cho<sup>3</sup>

<sup>1</sup> Department of Computer Science and Information Engineering, National Taipei University of Technology, Taipei 10608, Taiwan

<sup>2</sup> Department of Energy and Refrigerating Air-Conditioning Engineering, National Taipei University of Technology, Taipei 10608, Taiwan

<sup>3</sup> Department of Civil Engineering, Texas A&M University, College Station, TX 77843-3136, USA

Correspondence should be addressed to Kun-Ching Cho; tedjwo@gmail.com

Received 11 April 2014; Accepted 15 May 2014; Published 16 June 2014

Academic Editor: Chao-Rong Chen

Copyright © 2014 Yen-Lin Chen et al. This is an open access article distributed under the Creative Commons Attribution License, which permits unrestricted use, distribution, and reproduction in any medium, provided the original work is properly cited.

This paper presents experimental explorations on cooling performance of thermoelectric chillers being driven by solar cells, as well as comparison results to the performance being driven by fixed direct current. Solar energy is clear and limitless and can be collected by solar cells. We use solar cells to drive thermoelectric chillers, where the cold side is connected to the water tank. It is found that 250 mL of water can be cooled from 18.5°C to 13°C, where the corresponding coefficient of performance (COP) is changed between 0.55 and 1.05, when solar insolation is changed between 450 W/m<sup>2</sup> and 1000 W/m<sup>2</sup>. The experimental results demonstrate that the thermoelectric chiller driven by solar cell is feasible and effective for energy saving issues.

## 1. Introduction

Renewable energy resources become important energy sources over the world. People apply more renewable energy sources and technologies so as we can reduce the consumption of traditional fossil energy. Therefore, the carbon dioxide production can be significantly reduced, and global warming problem can also be slowed down [1]. Solar chillers could be accomplished by using one of the following refrigeration systems: vapor compression, adsorption refrigeration [2], and thermoelectric refrigeration systems. The first two systems require low and high pressure sides of working fluids in refrigeration cycles and are difficult to be developed into portable and lightweight solar devices used in outdoor environments. The thermoelectric refrigeration system can provide advantages of being small, lightweight, reliable, noiseless, portable, and of low cost in mass production [3]. In our studies, solar cells are used to drive the thermoelectric chillers.

Gaur and Tiwari found that the energy efficiency of solar cell is about 10% to 25% [4]. Based on the calculations of the solar cell modules made in laboratory, cadmium telluride

(CdTe) has shown that it can provide the minimum cost per unit electrical energy, whereas amorphous silicon (a-Si)/nanocrystalline silicon (nc-Si) can provide the minimum cost for unit electrical energy when commercial availability of solar modules is concerned. Copper indium gallium diselenide (CIGS) can achieve the lowest capitalized cost over all other solar cell technologies. Yang and Yin have presented a hybrid solar system that utilizes photovoltaic cells, thermoelectric modules, and hot water [5]. The hybrid solar system is superior to traditional PV systems with 30% higher output electric power.

Peltier effect and Seebeck effect were first discovered to present in metals as early as 1820s–1830s [6, 7]. Despite their low energy efficiency as compared to traditional devices, thermoelectric effects present distinct advantages such as compactness, precision, simplicity, and reliability. Applications of thermoelectric devices are very wide in many areas, including equipment used in military, aerospace, medical, industrial, consumer, and scientific institutions [8]. Solar-driven thermoelectric technologies have two types: the solar-driven thermoelectric refrigeration and the solar-driven thermoelectric power generation [9]. One important application

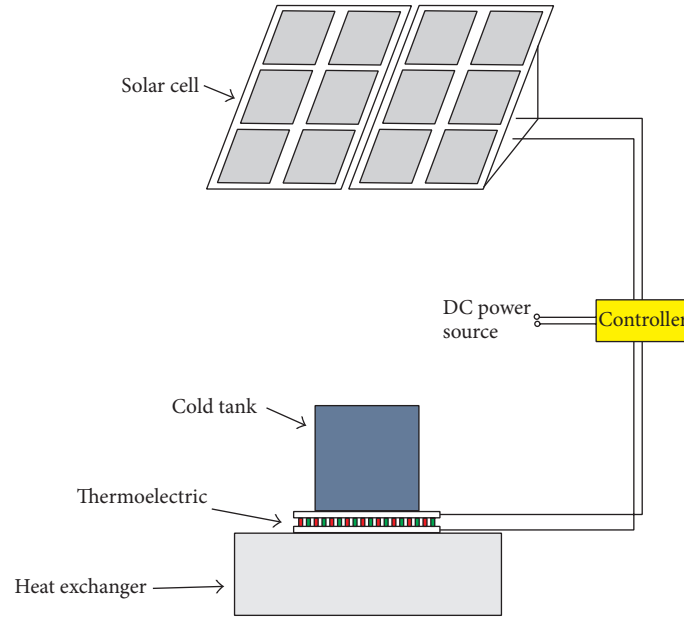


FIGURE 1: Solar thermoelectric chiller.

is thermoelectric generation with waste energy and renewable energy. Champier et al. incorporated wood stove with thermoelectric generator. In their system, the hot side of thermoelectric generator passes through hot air, whereas the cold side of thermoelectric generator is put under two liters of water tank. This system can produce up to 9.5 W as they used prototype of ten watts thermoelectric generator [10]. Meng et al. [11] presented a system that adopted the flushing water of blast furnace slag, and about 0.93 kW electrical energy can be produced per unit area when the temperature of flushing water starts at 100°C with a temperature drop of 1.5°C and the conversion efficiency is 2%. The cost recovery period of the equipment is about 8 years. Attia et al. [12] have reported an experimental power generation device that can produce electrical energy in milliwatts level by using standard bismuth telluride thermoelectric modules with a device size of about 10 cm<sup>3</sup>. Rezanian et al. [13] explored the effective pumping power for the cooling system at five temperature differences of the hot and cold sides of the thermoelectric generation device. Their experimental results demonstrated that there is a unique flow rate that gives maximum net power in the system at each temperature difference. Chávez Urbiola and Vorobiev [14] studied solar hybrid electric/thermal system using photovoltaic panels combined with a water/air-filled heat extracting unit and thermoelectric generators. Their experiment results showed that the hot side of thermoelectric generation at midday has a temperature of around 200°C and the cold side is approximately 50°C. This system generated 20 W of electrical energy and 200 W of thermal energy.

Another important application of thermoelectric is for cooling operations [15]. Dai et al. [3] conducted experimental investigation on thermoelectric refrigerator driven by solar cells. The results demonstrated that the unit could maintain the temperature in the refrigerator at 5–10°C and have a COP about 0.3. He et al. [16] conduct experiments on

thermoelectric cooling and heating system driven by solar power in a model room whose volume is 0.125 m<sup>3</sup> and performed the test in summer time. The resulting COP of their proposed thermoelectric device is of average 0.6. Zhou and Yu [17] present a generalized theoretical model for the optimization of a thermoelectric cooling system. Their analysis showed that the maximal COP and the maximal cooling capacity can be obtained when the finite thermal conductance is optimally allocated. Abdul-Wahab et al. [18] designed and built an affordable solar thermoelectric refrigerator. Their results indicated that the temperature of the refrigeration was reduced from 27°C to 5°C in approximately 44 minutes. The COP of their system was calculated and found to be about 0.16. Chang et al. [19] investigated the thermoelectric air-cooling module for electronic devices. The results demonstrated that their thermoelectric air-cooling module can provide better performance at a low heat loading condition.

This study develops the thermoelectric chiller driven by solar cell in daytime and direct current (DC) source in cloudy days or nighttime. The solar thermoelectric chiller is investigated in terms of COP and the temperature of thermoelectric through a specially designed test rig.

## 2. Configuration of the Solar Thermoelectric Chiller

Figure 1 is the schematics thermoelectric chiller driven by solar cell. The chiller mainly consists of the one solar cell, thermoelectric, controller, and water tank. The specifications of the proposed solar thermoelectric chiller are shown in Table 1. One solar cell can be commercially available. Solar insolation is 1000 W/m<sup>2</sup>; maximum of  $P_{\text{solar}}$  is 130 W. The maximum voltage of the solar cell is 17.6 V, the maximum

TABLE 1: Specifications of solar thermoelectric chiller.

Solar cell		Thermoelectric element	
At S	1000 W/m <sup>2</sup>	At T <sub>H</sub>	25°C
P <sub>solar,max</sub>	130 W	Q <sub>c,max</sub>	49 W
V <sub>solar,max</sub>	17.6 V	ΔT <sub>max</sub>	75°C
I <sub>solar,max</sub>	7.39 A	V <sub>tec,max</sub>	16.2 V
A	0.89 m <sup>2</sup>	I <sub>tec,max</sub>	5.3 A
η <sub>PV</sub>	13%	R <sub>tec</sub>	2.75 Ω
		α	0.0508 V/K
		K	0.38 WK <sup>-1</sup>
		Z	2.47 × 10 <sup>-3</sup> 1/K

current of the solar cell is 7.39 A, its area is 0.89 m<sup>2</sup>, and the corresponding energy efficiency of the solar cells η<sub>PV</sub> is 11%. We adopt a commercially available thermoelectric device; its size is 40 mm × 40 mm × 4.2 mm and the corresponding specifications are TEC-127-05 with 127 couples of *p-n* bismuth tin (BiSn) alloy thermoelement sandwiched between two thin ceramic plates. At the hot side, the temperature is 50°C. The maximal cooling production is 49 W. The maximum temperature difference between the hot and cold sides is 75°C. The maximum thermoelectric voltage is 16.2 V, and the maximum thermoelectric current is 5.3 A. The electrical resistance is 2.75 Ω. The function of the controller is switching power supply between solar cells and the DC power source. The water tank is filled with 250 mL of ambient temperature water.

The hot side of the thermoelectric system was connected to the heat exchanger to provide more cooling efficiency. The thermoelectric cooling process is performed when a fixed direct current is passed through one or more pairs of *n*-type to *p*-type junctions. As the differences of the current and temperature increase, Peltier cooling effect can be accordingly increased. However, main loss in Joule heat is also proportional to the square of the current and, therefore, eventually becomes the dominant factor. In the daytime, the thermoelectric chiller is driven by solar cells. In the nighttime, the thermoelectric chiller is driven by fixed direct current.

### 3. Experimental Study

*3.1. Theory Consideration.* Solar cell is used in driven thermoelectric chiller. The output electric power is calculated by the following equation [3]:

$$P_{\text{solar}} = SA\eta_{PV}, \quad (1)$$

where *S* is the solar insolation rate, *A* is the area of the solar cell to receive solar irradiation, and η<sub>PV</sub> is the efficiency of energy conversion from solar energy to electric power.

The heat absorption rate at the cold side, that is, the cooling capacity, can be obtained by

$$Q_c = \alpha IT_c - 0.5I^2 - K(T_h - T_c). \quad (2)$$

The input voltage of the thermoelectric is given by

$$V = \alpha (T_h - T_c) + IR. \quad (3)$$

The input electrical power of the thermoelectric is given by

$$P = \alpha I (T_h - T_c) + I^2 R. \quad (4)$$

The coefficient of performance of thermoelectric can be obtained by

$$\text{COP} = \frac{Q_c}{P}. \quad (5)$$

*3.2. Experiment Setup.* In order to quantitatively evaluate the cooling performance of a solar thermoelectric chiller, the following parameters should be considered: the solar cell power, the thermoelectric power consumption, the hot side and cold side temperatures of the thermoelectric system, and the coefficient of performance (COP). Figure 2 illustrates the schematic organization of our experimental system for determining cooling performance of the solar thermoelectric chiller.

All of the experiments used cooling 250 mL water in water tank, which was connected to the cold side of the thermoelectric system. The thermoelectric chiller was driven by a fixed 9.6 V direct current source and solar cells, respectively. According to (3), the voltage of thermoelectric is related to the Seebeck coefficient α, the temperature difference between hot and cold sides (T<sub>h</sub> - T<sub>c</sub>), the electric current of thermoelectric *I*, and the thermoelectric resistance *R*. The voltage of thermoelectric may change with respect to the changes of the above variables and approach to the fixed direct current. We investigate the cooling capacity of the solar thermoelectric chiller in 180 minutes. We used a power analyzer to measure the power consumption of the thermoelectric system. For data logging, we used a data logger and its associated software to grab the evaluation data. The *T*-type thermocouples were used for continuous measurement of hot side and cold side temperatures, ambient temperature, and water tank temperature. Type *T* (copper-constantan) thermocouples are suitable for measurements in the -200 to 350°C range and have a sensitivity of about 43 μV/°C. The pyranometer was used for continuous measurement of solar insolation. It is suitable for measurements in the 0 to 2000 W/m<sup>2</sup> range and has a sensitivity of about 0.1 W/m<sup>2</sup>.

Our research goal is to investigate solar thermoelectric chiller. We tested the solar thermoelectric chiller by two stages and proved feasibility.

(1) *First Stage Experiment.* Using DC source to drive the thermoelectric chiller, we measure the voltage, current, consuming power, the cold side and hot side temperatures, and cooling capacity and analyze the COP. We conduct the test experiments by duration of 180 minutes.

(2) *Second Stage Experiment.* Using the solar cell to drive thermoelectric chiller, we measure voltage, current, consuming power, the cold side and hot side temperatures, and cooling capacity and analyze the COP. We conduct the test experiments by duration of 180 minutes.

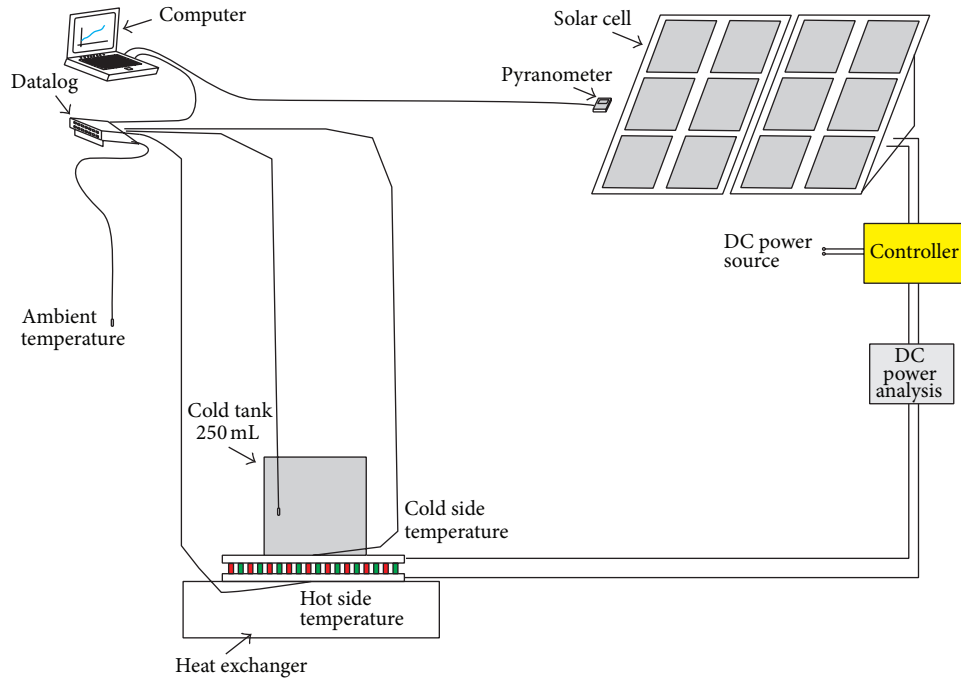


FIGURE 2: Experimental setup and measurement of solar thermoelectric cooler.

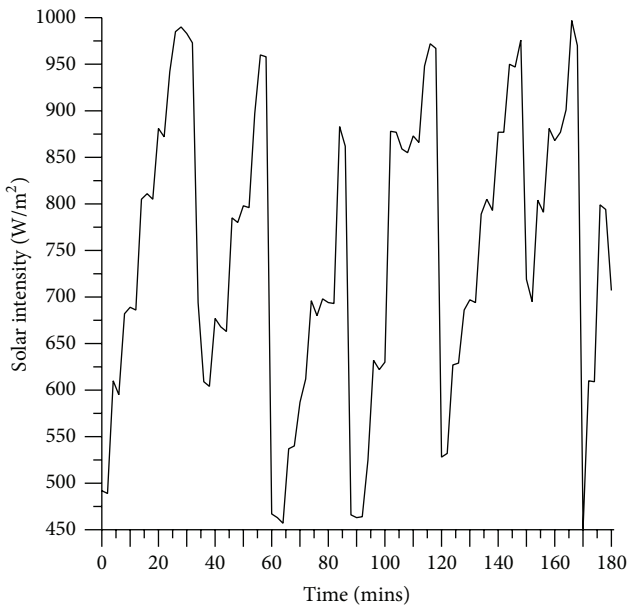
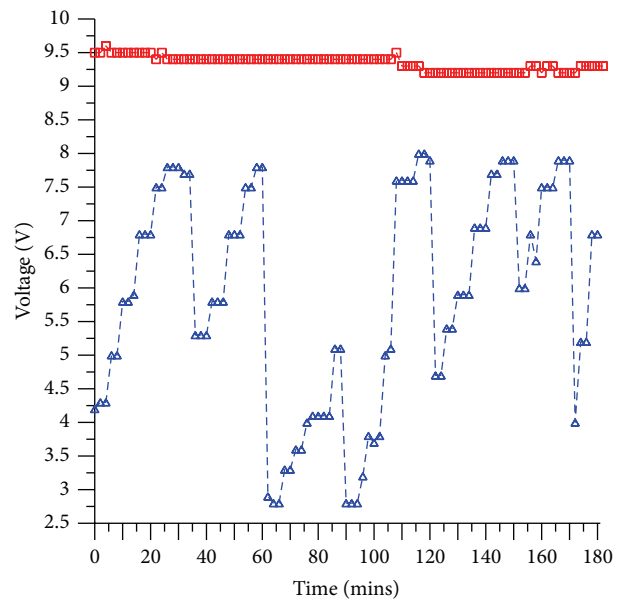


FIGURE 3: Light intensity distribution.



Energy source  
 -●- Driven by solar cell  
 -■- DC power source

FIGURE 4: The electric voltages of thermoelectric system driven by DC source and solar cells.

### 4. Results and Discussion

The proposed experiments used twelve halogens to simulate solar light. We adjust the voltage of halogen to change solar intensity. We adjust the light intensity from 450 W/m<sup>2</sup> to 1000 W/m<sup>2</sup> as shown in Figure 3. In Figure 4, the electric voltages of thermoelectric system are stable when the fixed direct current power is supplied to drive the thermoelectric

system, whereas the voltages of thermoelectric system are varied with respect to the variations of the solar insolation rates. According to Figures 3 and 4, the light intensity and the voltage of thermoelectric are positively correlated. When the lowest light intensity is about 450 W/m<sup>2</sup>, the voltage of

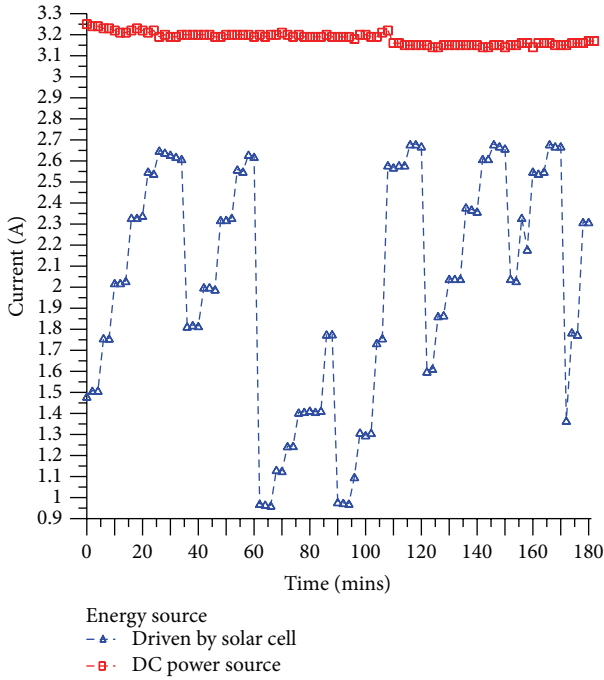


FIGURE 5: The electric currents of thermoelectric system driven by DC source and solar cells.

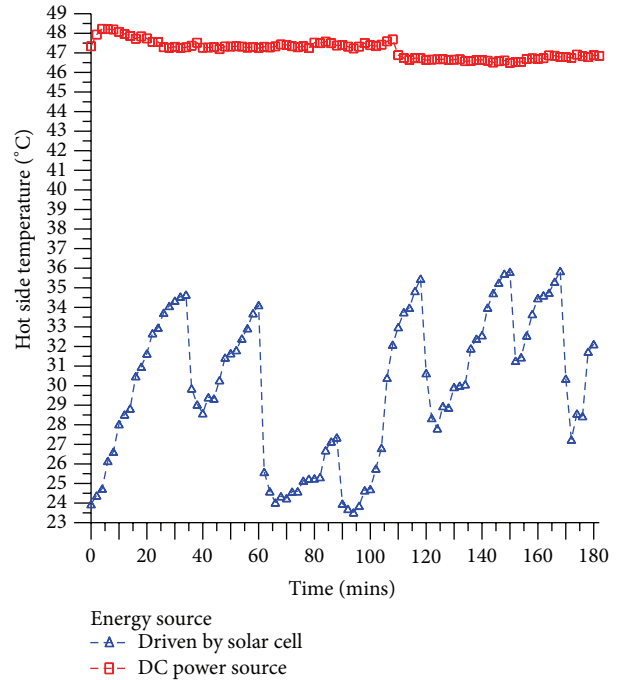


FIGURE 6: The hot side temperatures of the thermoelectric system by DC source and solar cells.

thermoelectric is about 2.7 V; when the highest light intensity is about  $1000 \text{ W/m}^2$ , the voltage of thermoelectric is about 8 V. In Figure 5, the electric currents of the thermoelectric system are stable when the fixed direct current power is supplied to drive the thermoelectric system, whereas the currents of the thermoelectric system are varied with respect to the variations of the solar insolation rates. In Figures 6 and 7, we used fixed direct current power to drive the thermoelectric system. The hot side temperature is maintained at about  $47^\circ\text{C}$ , and meanwhile the cold side temperature drops from  $0^\circ\text{C}$  to  $-3.5^\circ\text{C}$ . When we use the solar cell to drive the thermoelectric system, the hot side temperature and cold side temperature accordingly vary with respect to solar insolation rates. The highest hot side temperature is  $36^\circ\text{C}$ , and the least hot side temperature is  $23.5^\circ\text{C}$ , whereas the highest cold side temperature is  $6^\circ\text{C}$ , and the least hot side temperature is  $-3.5^\circ\text{C}$ .

Figures 8 and 9 show the cold tank temperatures and cooling capacities of the thermoelectric chiller driven by the fixed direct current power and the solar cells. For the thermoelectric chiller driven by the fixed direct current power, the cold tank temperature drops from  $20^\circ\text{C}$  to  $11^\circ\text{C}$ , and the cooling capacity is maintained at 12 W. For the thermoelectric chiller driven by the solar cell, the cold tank temperature drops rapidly from  $18.5^\circ\text{C}$  to  $14^\circ\text{C}$  when the cooling capacity changes from 10.5 W to 14 W and the average is cooling capacity 12.2 W. We can see that the cold tank temperature gently drops from  $14^\circ\text{C}$  to  $13^\circ\text{C}$  when cooling capacity changes from 5 W and 17.5 W; the average cooling capacity is 10.6 W in this range. As shown in Figures 10 and 11, when we use fixed direct current power to drive

TABLE 2: The average cooling capacity of the semiconductor of the system.

Result	Average					
	$S$ ( $\text{W/m}^2$ )	$V$ (V)	$I$ (A)	$P$ (W)	$Q_c$ (W)	COP
DC power source		9.4	3.2	34.3	11.9	0.35
Solar cell	747.9	5.9	2.0	16.7	11.2	0.74

the thermoelectric chiller, the input electric power of the thermoelectric chiller is maintained at about 35 W and the COP value is maintained at about 0.35. By comparison, when we adopt the solar cell to drive the thermoelectric chiller, the lowest value of the input electric power of the thermoelectric system is 5.5 W, while the highest value is 26 W, and the lowest COP is 0.55, while the highest COP is 1.05. We observe that the solar cell driven thermoelectric system can provide significantly better COP and needs lower input electric power consumption for the thermoelectric system. As shown in Table 2, the average cooling capacity of the solar driven system is 11.2 W, which is lower than the one of the system driven by fixed direct current of 11.9 W. By comparison, the average COP of the solar driven system is 0.74, which is better than the one driven by fixed direct current of 0.35. This is because the solar driven system is operated on an average of electric current of 2 A, which is a better operating point than that of the fixed direct current driven system.

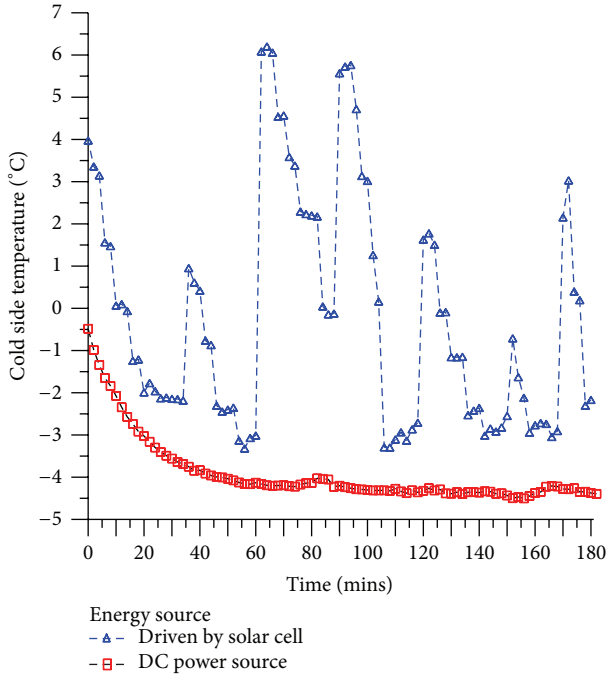


FIGURE 7: The cold side temperatures of the thermoelectric system by DC source and solar cells.

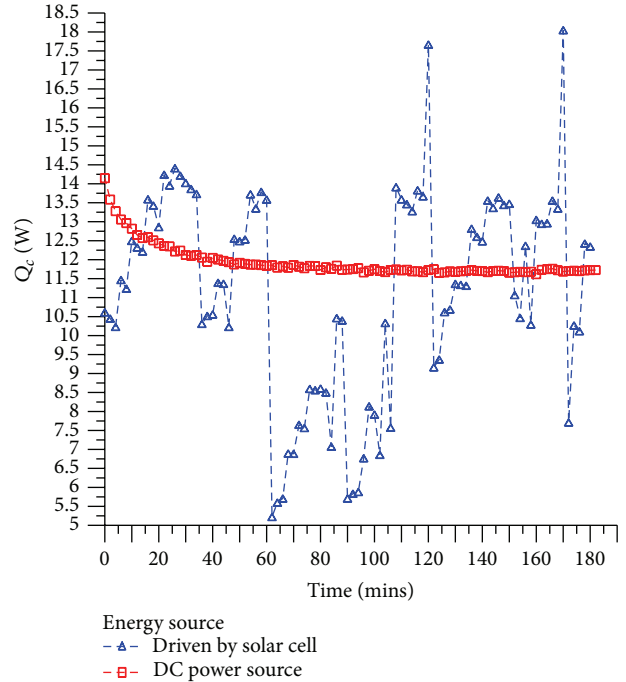


FIGURE 9: Cooling capacity of the thermoelectric system by DC source and solar cells.

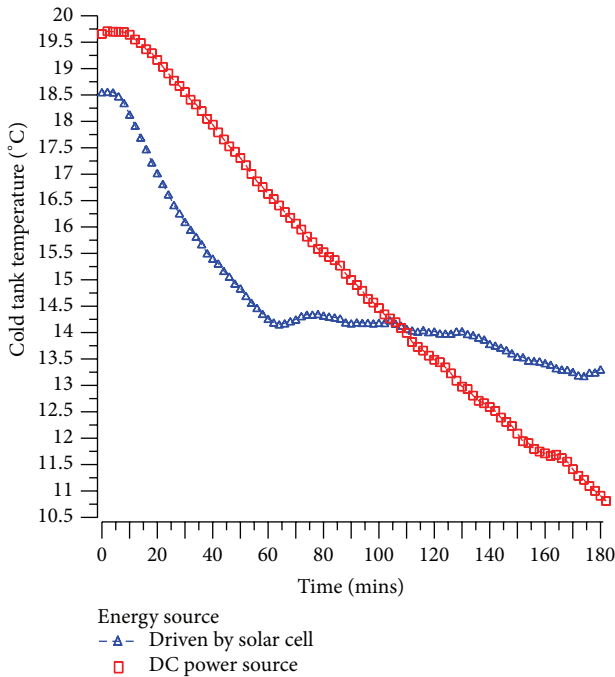


FIGURE 8: The cold tank temperatures of the thermoelectric system by DC source and solar cells.

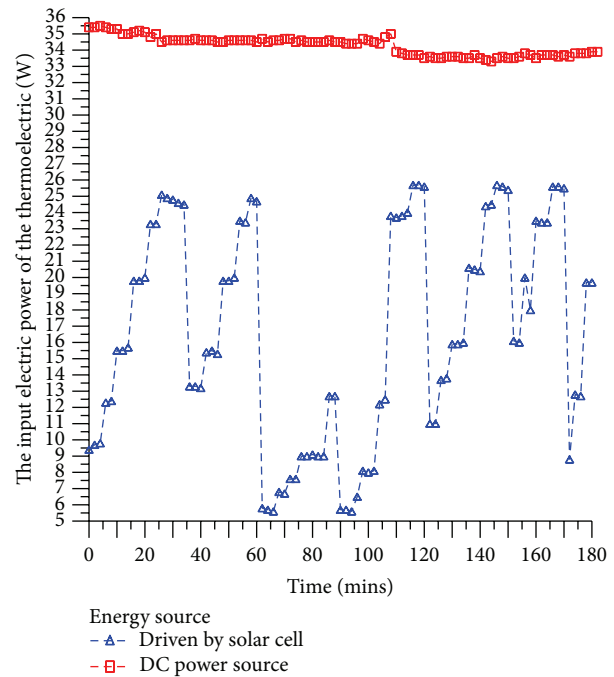


FIGURE 10: The input electric powers of the thermoelectric system by DC source and solar cells.

**5. Conclusions**

This study conducts experimental investigation on a thermoelectric chiller driven by solar cells. This experimental system has been tested, and the test results are presented. By comparing the experimental data of the thermoelectric

system driven by direct current source and by the solar cell, we found that the thermoelectric chiller driven by the direct current source provides the cooling capacity of 11.9 W, which is somewhat higher than the one driven by the solar cell (11.2 W). However, the COP obtained by the solar driven system is 0.74, which is significantly better than the one

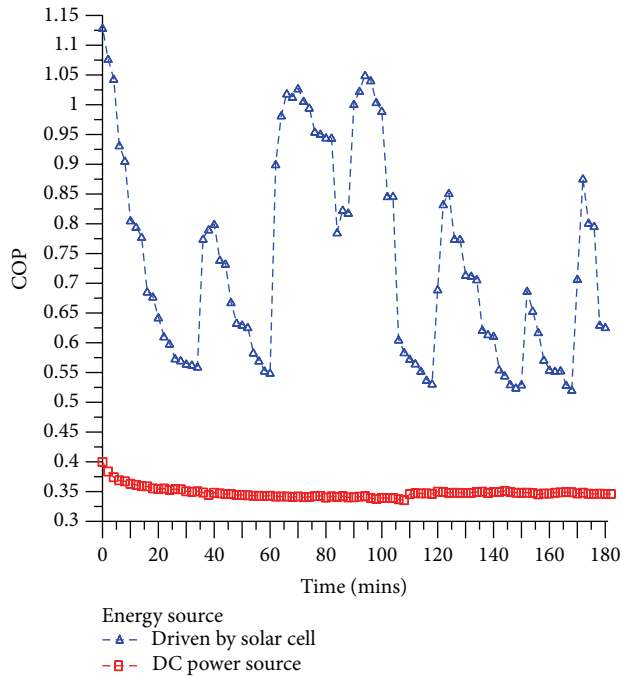


FIGURE 11: COPs of the thermoelectric chiller by DC source and solar cells.

driven by direct current of 0.35. Although the thermoelectric system driven by fixed direct current can provide stable cooling capacity, the thermoelectric chiller driven by the solar cell can provide significantly better COP, which ranges between 0.55 and 1.05, with an average of 0.74, than that driven by the fixed direct current. The experimental results also reveal that if the solar insolation rate can achieve  $450 \text{ W/m}^2$  to  $1000 \text{ W/m}^2$ , the solar thermoelectric chiller can provide feasible and effective performance.

## Nomenclature

$A$ :	Area of solar array, $\text{m}^2$
$I$ :	Electric current, A
$K$ :	Thermal conductance, $\text{WK}^{-1}$
$P_{\text{solar}}$ :	Output electric power of solar cell, W
$P$ :	Input electric power of the thermoelectric chiller, W
$Q_c$ :	Cooling capacity, W
$R$ :	Thermoelectric resistance, $\Omega$
$S$ :	Solar insolation,
$T_H$ :	Temperature of hot side, K, $^{\circ}\text{C}$
$T_C$ :	Temperature of cold side, K, $^{\circ}\text{C}$
$T_w$ :	Temperature of water in cold tank, K, $^{\circ}\text{C}$
$\Delta T_{\text{max}}$ :	Maximum temperature difference between hot and cold sides, K, $^{\circ}\text{C}$
$V$ :	Electric voltage, V
$Z$ :	Figure of merit, $1/\text{K}$
$\alpha$ :	Seebeck coefficient, $\text{V/K}$
$\eta_{\text{PV}}$ :	Energy efficiency of solar cells.

## Abbreviations

COP: Coefficient of performance  
 TEC: Thermoelectric cooler  
 DC: Direct current.

## Subscripts

solar: Solar cell  
 tec: Thermoelectric cooler  
 max: Maximum.

## Conflict of Interests

The authors declare that there is no conflict of interests regarding the publication of this paper.

## Acknowledgment

This project is financially sponsored by the National Science Council under Grants NSC-102-2219-E-027-006 and NSC-102-2622-E-027-027-CC2.

## References

- [1] D. Lalili, A. Mellit, N. Lourci, B. Medjahed, and C. Boubakir, "State feedback control and variable step size MPPT algorithm of three-level grid-connected photovoltaic inverter," *Solar Energy*, vol. 98, pp. 561–571, 2013.
- [2] Z.-J. Chien, H.-P. Cho, C.-S. Jwo, C.-C. Chien, S.-L. Chen, and Y.-L. Chen, "Experimental investigation on an absorption refrigerator driven by solar cells," *International Journal of Photoenergy*, vol. 2013, Article ID 490124, 6 pages, 2013.
- [3] Y. J. Dai, R. Z. Wang, and L. Ni, "Experimental investigation and analysis on a thermoelectric refrigerator driven by solar cells," *Solar Energy Materials & Solar Cells*, vol. 77, no. 4, pp. 377–391, 2003.
- [4] A. Gaur and G. N. Tiwari, "Performance of photovoltaic modules of different solar cells," *Journal of Solar Energy*, vol. 2013, Article ID 734581, 13 pages, 2013.
- [5] D. Yang and H. Yin, "Energy conversion efficiency of a novel hybrid solar system for photovoltaic, thermoelectric, and heat utilization," *IEEE Transactions on Energy Conversion*, vol. 26, no. 2, pp. 662–670, 2011.
- [6] S. B. Riffat and X. Ma, "Thermoelectrics: a review of present and potential applications," *Applied Thermal Engineering*, vol. 23, no. 8, pp. 913–935, 2003.
- [7] M. H. Elsheikh, D. A. Shnaeah, M. F. M. Sabri et al., "A review on thermoelectric renewable energy: principle parameters that affect their performance," *Renewable and Sustainable Energy Reviews*, vol. 30, pp. 337–355, 2014.
- [8] D. Mitrani, J. Salazar, A. Turó, M. J. García, and J. A. Chávez, "One-dimensional modeling of TE devices considering temperature-dependent parameters using SPICE," *Microelectronics Journal*, vol. 40, pp. 1398–1405, 2009.
- [9] H. Xi, L. Luo, and G. Fraisse, "Development and applications of solar-based thermoelectric technologies," *Renewable and Sustainable Energy Reviews*, vol. 11, no. 5, pp. 923–936, 2007.
- [10] D. Champier, J. P. Bédécarrats, T. Kousksou, M. Rivaletto, F. Strub, and P. Pignolet, "Study of a TE (thermoelectric) generator

incorporated in a multifunction wood stove,” *Energy*, vol. 36, no. 3, pp. 1518–1526, 2011.

- [11] F. Meng, L. Chen, F. Sun, and B. Yang, “Thermoelectric power generation driven by blast furnace slag flushing water,” *Energy*, vol. 66, pp. 965–972, 2014.
- [12] P. M. Attia, M. R. Lewis, C. C. Bomberger, and A. K. Prasad, “Experiment studies of thermoelectric power generation in dynamic temperature environments,” *Energy*, vol. 60, pp. 453–456, 2013.
- [13] A. Rezania, L. A. Rosendahl, and S. J. Andreasen, “Experimental investigation of thermoelectric power generation versus coolant pumping power in a microchannel heat sink,” *International Communications in Heat and Mass Transfer*, vol. 39, no. 8, pp. 1054–1058, 2012.
- [14] E. A. Chávez Urbiola and Y. Vorobiev, “Investigation of solar hybrid electric/thermal system with radiation concentrator and thermoelectric generator,” *International Journal of Photoenergy*, vol. 2013, Article ID 704087, 7 pages, 2013.
- [15] D. Zhao and G. Tan, “A review of thermoelectric cooling: materials, modeling and applications,” *Applied Thermal Engineering*, vol. 66, pp. 15–24, 2014.
- [16] W. He, J. Zhou, J. Hou, C. Chen, and J. Ji, “Theoretical and experimental investigation on a thermoelectric cooling and heating system driven by solar,” *Applied Energy*, vol. 107, pp. 89–97, 2013.
- [17] Y. Zhou and J. Yu, “Design optimization of thermoelectric cooling systems for applications in electronic devices,” *International Journal of Refrigeration*, vol. 35, no. 4, pp. 1139–1144, 2012.
- [18] S. A. Abdul-Wahab, A. Elkamel, A. M. Al-Damkhi et al., “Design and experimental investigation of portable solar thermoelectric refrigerator,” *Renewable Energy*, vol. 34, no. 1, pp. 30–34, 2009.
- [19] Y.-W. Chang, C.-C. Chang, M.-T. Ke, and S.-L. Chen, “Thermoelectric air-cooling module for electronic devices,” *Applied Thermal Engineering*, vol. 29, no. 13, pp. 2731–2737, 2009.

## Research Article

# Cost-Effectiveness Analysis of a PVGS on the Electrical Power Supply of a Small Island

**Cheng-Ting Hsu, Roman Korimara, and Tsun-Jen Cheng**

*Department of Electrical Engineering, Southern Taiwan University of Science and Technology, Tainan 710, Taiwan*

Correspondence should be addressed to Tsun-Jen Cheng; [chengtj@mail.stust.edu.tw](mailto:chengtj@mail.stust.edu.tw)

Received 6 April 2014; Accepted 21 May 2014; Published 12 June 2014

Academic Editor: Yen-Lin Chen

Copyright © 2014 Cheng-Ting Hsu et al. This is an open access article distributed under the Creative Commons Attribution License, which permits unrestricted use, distribution, and reproduction in any medium, provided the original work is properly cited.

This paper presents a feasibility study of a large simulated stadium-scale photovoltaic generation system (PVGS) on a small island. Both the PVGS contribution to the energy demand on the island and its financial analysis were analysed in this study. The maximum allowable PVGS installation capacity is obtained by executing load flow analysis without violating the voltage magnitude and voltage variation ratio limits. However, the estimated power generation of PVGS is applied to know its impact on the power system according to the hourly solar irradiation and temperature. After that, the cost-benefit analysis of payback years (PBY) and net present value (NPV) method is derived considering the cash flow from utilities annual fuel and loss saving, the operation and maintenance (O&M) cost, and the capital investment cost. The power network in Kiribati (PUB DNST) is selected for study in this paper. The simulation results are very valuable and can be applied to the other small islands for reducing the usage of fossil fuel and greenhouse gas emissions.

## 1. Introduction

With the abundant solar and wind energy in small island countries, over the last few years a number of influences have combined to lead to the increased interest in renewable distribution generation such as wind and solar. Environmental impact is a major factor in the consideration of this electrical power scheme, and there is generally accepted concern over greenhouse gases emission from thermal power plants. Reference [1] shows that developing various renewable energy resources is essential for achieving sustainable environment. In Kiribati priorities of the government in the energy sector are currently focused on locating additional finance for the expansion of rural electrification and on reducing cost of fuel imports. Due to the increasing cost of import fuel for the utility power generation causing saturation to the utility sector's overall operation cost, making it difficult for them to gain profit, the government of the day have no choice but to subsidize the utility sector annually to avoid power shutdown [2]. Fortunately, having the favorable position on the equator, the country has big advantage of developing application of

several types of renewable energy resources such as tidal energy, wind energy, and solar energy. With the population of only more than one hundred thousand in a wide total area of 811 km in Kiribati, a photovoltaic (PV) panel may be a good solution for fulfilling the energy requirement and protecting the environment. Thanks to World Bank that provided the finances, the first ever large photovoltaic plant with a total capacity of 500 kWp was installed in Kiribati [3].

For the engineering project of a large scale PVGS, the economic analysis should be performed to evaluate the profitability to ensure the investment cost can be recovered over the life cycle. The classical profitability analysis has been performed on PVGS in [4, 5]. A cost analysis of PV grid connection for several European countries is presented in [6]. It is concluded that the main factors affecting the PVGS deployment are the initial capital cost of the system, the feed-in tariff, and the capital cost subsidization rate. Reference [7] presented the economic aspects of a hybrid system with solar energy and wind energy production. Two economic indices of the NPV and the PBY are applied for the financial analysis for the PV system projects by considering the cash inflows

and the life-cycle expenses in [8, 9]. The parameters of NPV and payback period are used to determine the profitability of PV installation by including the reduction of pollutant emission [10].

Furthermore, the assumed electricity consumption of the station is much lower than the electric power generated by the PVGS. Accordingly, with the integration of the PVGS on the distribution system, the power flow of distribution system will be changed with the PV generation as well as the loading level of each bus. The power loss reduction that resulted from the power injection of the PVGS can be estimated by executing the distribution load flow analysis. The voltage variation of the practical distribution feeder due to PV generation is solved to determine the maximum PVGS penetration allowed without causing the violation of system operation constraints.

The paper is organized as follows. First, Section 2 presents the methodology of this research followed by the case study simulation results presented in Section 3. A brief introduction of PUB DNST network topology in a one-line diagram including its daily load demand is also shown in Section 3. Section 4 presents the financial analysis scheme followed by a conclusion in Section 5.

## 2. PVGS Feasibility Study Methodology

To evaluate the maximum installation capacity of PVGS without causing voltage violation, the load flow analysis is applied to solve the system voltage and power loss according to the hourly feeder loading and solar irradiation. After that, the cost-benefit analysis based on the NPV method from utility point of view is executed to know its effectiveness on energy saving. Figure 1 shows the flowchart of the proposed methodology. It is further described as the following steps.

Step 1 prepares the study system configuration and data for load flow analysis. The study network configuration should be identified for preparing a one-line diagram. By the way, the line segment attributes such as conductor size and length and distribution transformer capacity and impedance are also collected at the same time. It is also necessary to retrieve the hourly power generation and loading of the study system.

Step 2 is to find the maximum allowable installation capacity at the proposed installation site. It needs to execute 24-hour load flow analysis with and without considering the installation of PVGS. The output power of PVGS is assumed to be at its peak rating capacity during the load flow analysis. The simulation results for the voltage at all buses and power generation of each generation unit must be examined in order not to violate the limits. In this paper, all the buses voltage should be controlled within 0.95–1.05 p.u and the generator output power should be operated within 0.3–1.0 times of its rating capacity. In addition, the allowable voltage variation ratio (VVR) at all buses is limited within  $\pm 5\%$  to ensure power quality. And the VVR can be defined as

$$\text{VVR}_k (\%) = \frac{V_k^{\text{PVGS}} - V_k}{V_k} \times 100\%, \quad (1)$$

where  $V_k$  and  $V_k^{\text{PVGS}}$  are the voltage magnitude at bus  $k$  without and with PVGS, respectively.

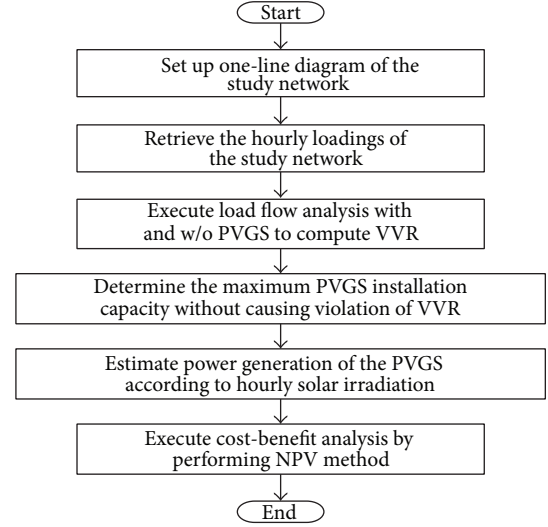


FIGURE 1: Flowchart of the proposed PVGS feasibility study methodology.

By executing the proposed methodology, the maximum PVGS installation is therefore obtained without violating the limits. By the way, the penetration level (PL) of renewable energy on the power system can be defined as

$$\text{PL} (\%) = \frac{\sum_i P_{PV}^i}{P_{\text{total}}} \times 100\%, \quad (2)$$

where  $P_{PV}^i$  is the rating capacity of the  $i$ th PVGS and  $P_{\text{total}}$  is the total power delivered to load.

Step 3 is used to estimate the power generation of PVGS. To make the analysis reasonable and able to be used in general case for varying solar irradiance condition, it is necessary to find out the mathematical model of the PVGS. In this paper, the PVGS model is obtained and verified by the actual system which has been installed at the Kaohsiung World Games Stadium in Taiwan [11]. The maximum power output of the PVGS is derived as (3), while the surface temperature ( $T_S$ ) of the PV panel is calculated as (4). Consider the following:

$$P_{\text{max}} = -1.15 \times 10^4 + 909G + 754T_S - 2GT_S \quad (\text{W}), \quad (3)$$

$$T_S = 0.903 + 0.0014G - 1.39 \times 10^{-7}G^2 \quad (^\circ\text{C}), \quad (4)$$

where  $G$  is the solar irradiance ( $\text{W}/\text{m}^2$ ). Therefore here in order to obtain the estimated power generation of PVGS, an hourly real solar irradiation was used. After that, the 24-hour load flow is performed again to know the actual effectiveness of PVGS on the power system.

Step 4 executes cost-benefit analysis. A financial analysis for the proposed PVGS based on the expected power generation is also investigated in this paper to ensure the feasibility of the system in not only the engineering aspect but also the economic aspect. This procedure can figure out whether or not the capital investment cost of the large scale PVGS can be fully recovered from the annual fuel and power loss saving over the system life cycle. The cost-benefit analysis

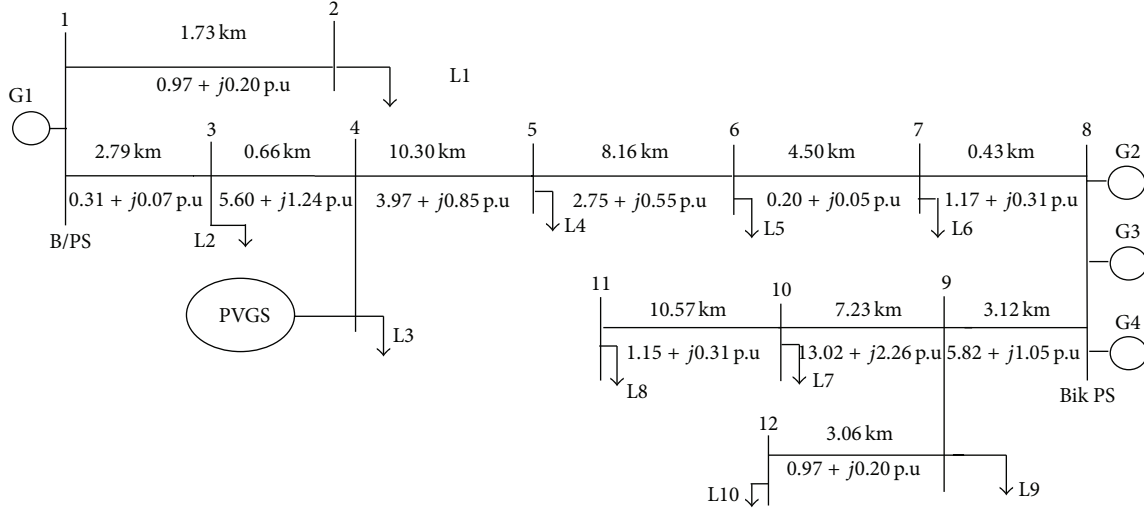


FIGURE 2: One-line diagram of the study of PUB DNST feeder.

adopts NPV and PBY method. The NPV of an investment is the sum of the present values of all cash flows such as capital investment and revenue generated over the life cycle. A project is considered to be financially feasible only if the corresponding NPV is positive. The NPV of the investment can be calculated by

$$\text{NPV} = -C_{\text{CI}} + \sum_{i=1}^n \text{PWF}^i * \text{CF}_i, \quad (5)$$

where  $C_{\text{CI}}$  is the capital investment cost of the PVGS and  $\text{PWF}^i$  and  $\text{CF}_i$  are the present worth factor and the net cash inflow for year  $i$ , respectively.  $\text{CF}_i$  can be further expressed as

$$\text{CF}_i = (C_{\text{APLS},i} + C_{\text{AFS},i}) * (1 - \text{dr})^i - C_{\text{O\&M},i}, \quad (6)$$

where  $C_{\text{APLS},i}$  and  $C_{\text{AFS},i}$  are the annual power loss saving cost and fuel saving cost at year  $i$ . And  $\text{dr}$  is the PVGS performance derating rate and the  $C_{\text{O\&M},i}$  is the annual operation and maintenance cost at year  $i$ , respectively.  $C_{\text{APLS},i}$  and  $C_{\text{AFS},i}$  can be further expressed as

$$C_{\text{APLS},i} = \text{CoE} * \left( \text{NSD}_{\text{yr}} * \sum_{h=1}^{24} (X_h^{\text{wpv}} - X_h^{\text{pv}}) + \text{NCD}_{\text{yr}} * \sum_{h=1}^{24} (X_h^{\text{wpv}} - X_h^{\text{pv}}) \right), \quad (7)$$

$$C_{\text{AFS},i} = \text{Gpc} * \left( \text{NSD}_{\text{yr}} * \sum_{h=1}^{24} (Y_h^{\text{wpv}} - Y_h^{\text{pv}}) + \text{NCD}_{\text{yr}} * \sum_{h=1}^{24} (Y_h^{\text{wpv}} - Y_h^{\text{pv}}) \right), \quad (8)$$

where  $X_h^{\text{wpv}}$ ,  $X_h^{\text{pv}}$ ,  $Y_h^{\text{wpv}}$ , and  $Y_h^{\text{pv}}$  are the PUB DNST's active power loss without PVGS, active power loss with PVGS, fuel consumed without PVGS, and fuel consumed with PVGS

for an hour  $h$ , respectively;  $\text{NSD}_{\text{yr}}$  and  $\text{NCD}_{\text{yr}}$  are the total number of sunny and cloudy for the year  $\text{yr}$ , respectively;  $\text{CoE}$  and  $\text{Gpc}$  are the cost of energy and the generator's production cost, respectively.

By the way, the PBY can be obtained by setting the value of NPV to be zero in (5).

### 3. Case Study: Electrical Power System Simulation

To determine how large the PV projects can be put into effect at the proposed installation site without violating the voltage limits, a large scale PVGS installed at PUB DNST in Kiribati was selected as a case study for computer simulation. Besides, a financial analysis is also performed in the last section of this paper to justify whether this PV project investment is viable or not.

Figure 2 shows the one-line diagram of the power system in Kiribati. The large scale PVGS is assumed to be installed at Bus 4. The existing network configuration can be described in more detail as follows. There is one diesel generator at Betio (Bus 1) with the available capacity of 1200 kW and three diesel generators at Bikenibeu (Bus 8) with the available capacities of 1350 kW each, which provide a base load at specific fuel consumption of 0.25 litre/kWh. The rating generators output voltage is 11 kV with an operating frequency of 50 Hz. Approximately 60 underground cables with various types are used in distributing 11 kV network around the island. There are 59 underground transformers in service, which are 11 kV/415 V step down transformers with rated capacity of 50, 100, 200, and 750 kVA.

Figure 3 shows typical daily load profile that was recorded on South Tarawa. It shows basically two insights: firstly, the peak load is 3.2 MW, which occurred at 11 hrs and 13 hrs; secondly, the off-peak load is 2 MW, which occurred from 5 hrs to 6 hrs. This figure also obviously shows that the high power consumption on the island occurs significantly during

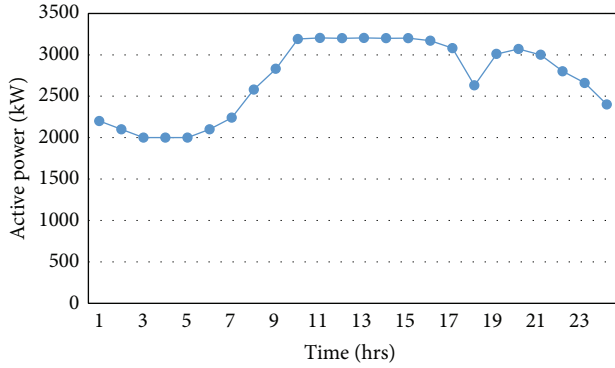


FIGURE 3: Typical daily load demand profile.

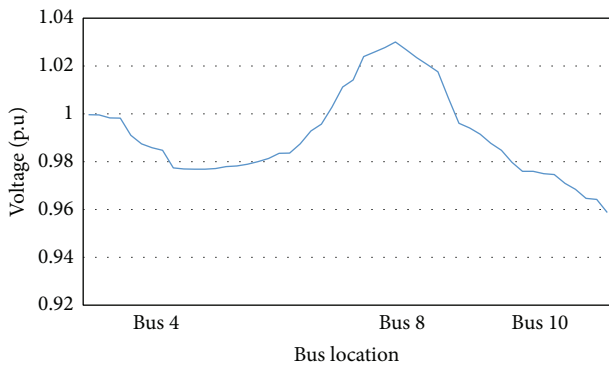


FIGURE 4: Voltage profile for utility sector without PVGS.

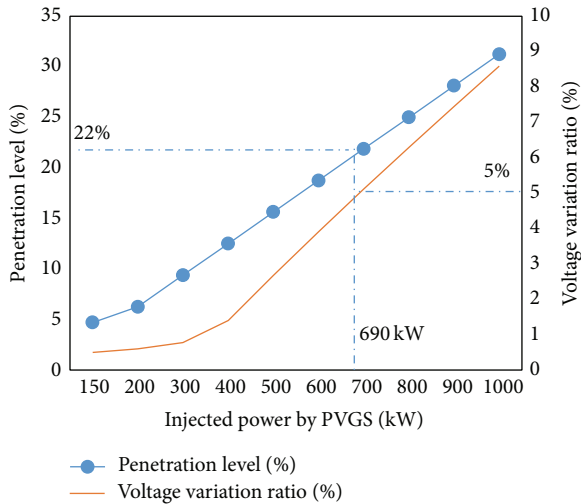


FIGURE 5: VVR and PL versus the injected power by PVGS.

working and business hours. In order to simplify the process of determining the annual load demand, it is assumed that all days throughout the year have the same load demands as shown in Figure 3. This assumption is based upon the fact that, in terms of the United Nation statistics, Kiribati is among the least developed countries in the world [12]. The profile

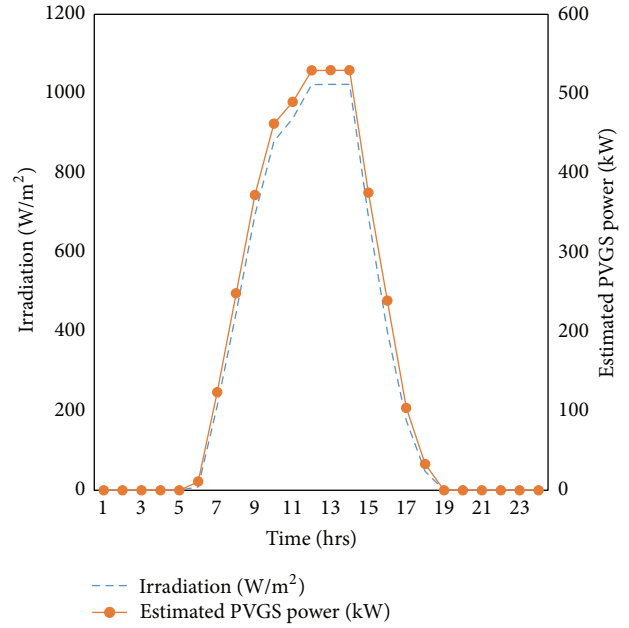


FIGURE 6: Daily solar irradiance and estimated PVGS power generation at sunny day.

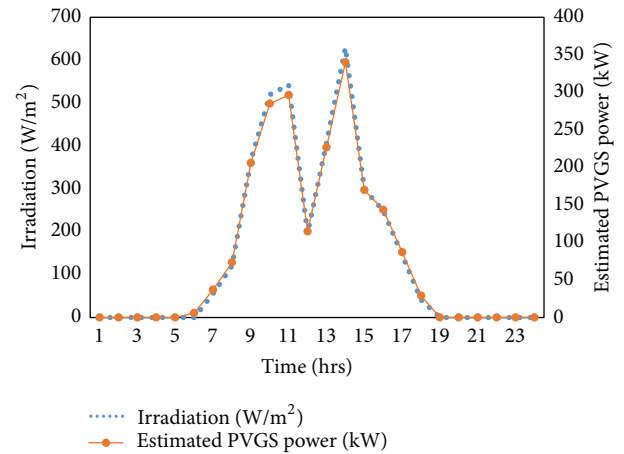


FIGURE 7: Daily solar irradiance and estimated PVGS power generation at cloudy day.

shows that the loading occurs during daytime, which implies that the power generation by the PV system can effectively offset Bus 4 feeder loading.

Based on the PUB DNST network topology and hourly loading, the load flow simulation results in Figure 4 show the voltage profile of the buses while regulating the voltage at G2-4 and G1 to 1.03 p.u. and 1.0 p.u., respectively. It is found that the voltages are varied between 0.956 p.u. and 1.03 p.u. in normal condition; these simulation results satisfy the voltage operation limits for providing well power quality to customers [1, 12].

Introducing the PVGS to the existing network may alter the voltage level at installation site (Bus 4) and nearby buses.

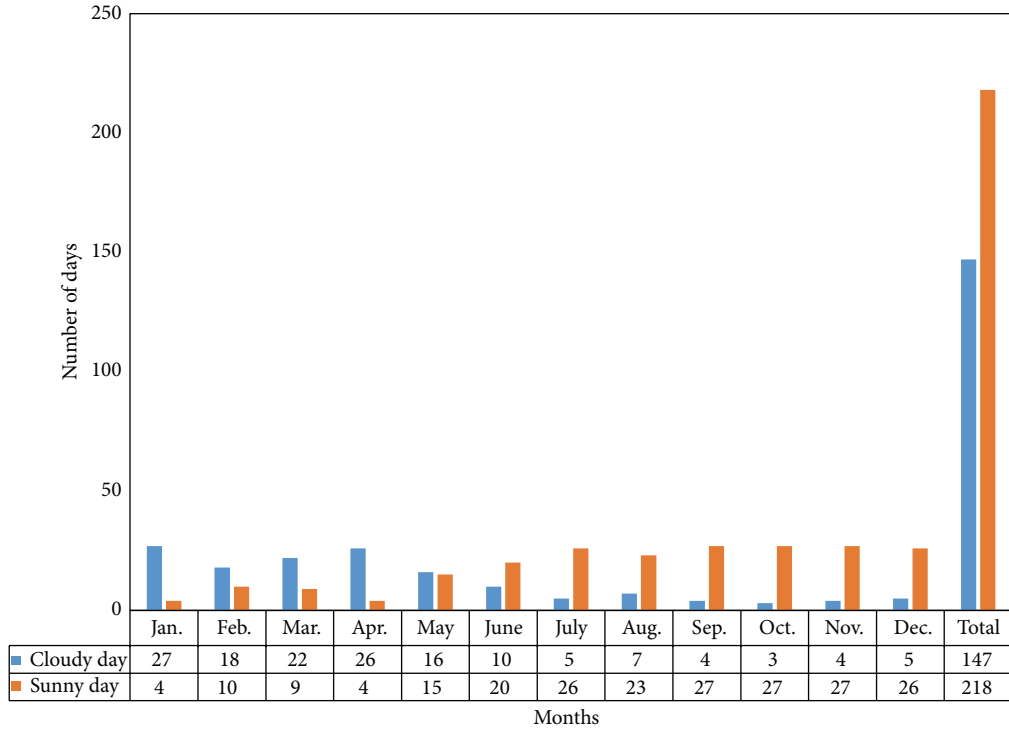


FIGURE 8: Monthly number of cloudy and sunny days for the year 2010.

In order to make sure the voltage level, at all buses, remains at required limits, the maximum allowed PVGS installation capacity will be taken into consideration. After applying the load flow analysis with different injected power of PVGS, it is found that the maximum allowable power at Bus 4 is 690 kW which corresponds to the penetration level of 22% as shown in Figure 5. This means that if PVGS installation capacity is larger than maximum allowable power, the penetration impact becomes more severe and may lead to overvoltage problem.

A sorting analysis of hourly weather data from Meteorology Office in Kiribati was performed to derive the sunny and cloudy duration curve of solar irradiation analysis. Figures 6 and 7 show recorded solar irradiation with simulated daily estimated PVGS generation for sunny and cloudy day, respectively. According to the weather information, a sunny day had sunshine duration of 13 hours in March 2010. With this solar irradiation condition, it is found that the estimated generation power for a 690 kWp PVGS is increased with the solar irradiation by applying the model at (3) and (4). The maximum power generation is 530 kW and occurs at 12 hrs. Also, a cloudy day has low solar irradiation and the maximum PV power generation is 340 kW at 14:30 pm. It is also found that the PV generation power fluctuates dramatically between 10:00 am and 14:00 pm due to the cloudy effect during the daytime period. A historical weather data provided by Meteorology Office in 2010 as presented in Figure 8 shows the monthly number of cloudy and sunny day, respectively. Besides, it also shows the total number of sunny and cloudy days in a year, respectively, that is, 218 (NSD<sub>2010</sub>) and 147

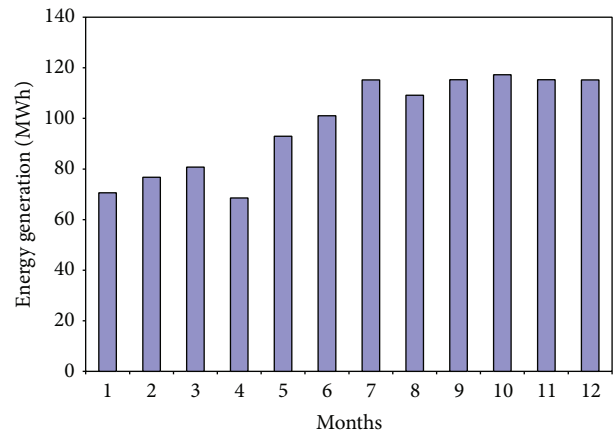


FIGURE 9: Annual energy generation from PVGS.

(NSD<sub>2010</sub>). In order to simplify the process of determining the annual PV power generation, it is assumed that all sunny days have the same sunny solar irradiation condition and all cloudy days have the same cloudy solar irradiation condition throughout the year. With this assumption a yearly PVGS contribution when the PVGS capacity of 690 kWp was installed at Bus 4 has been shown in Figure 9. A calculated result shows that, with the aforementioned PVGS capacity, an estimated total energy produced annually is 1178.14 MWh.

To perform 24-hour load flow simulation for proving the feasibility of the PVGS, existing network information and

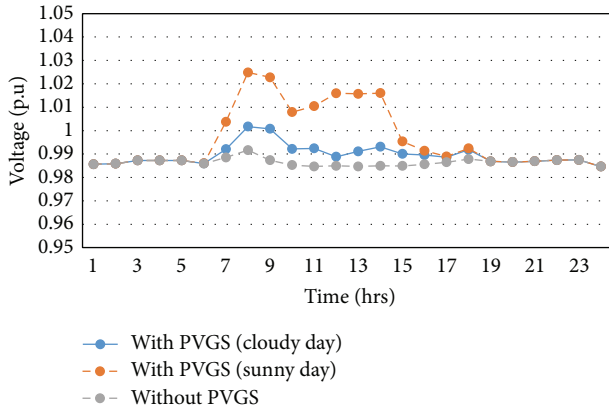


FIGURE 10: Voltage profile at Bus 4 with and without PVGS.

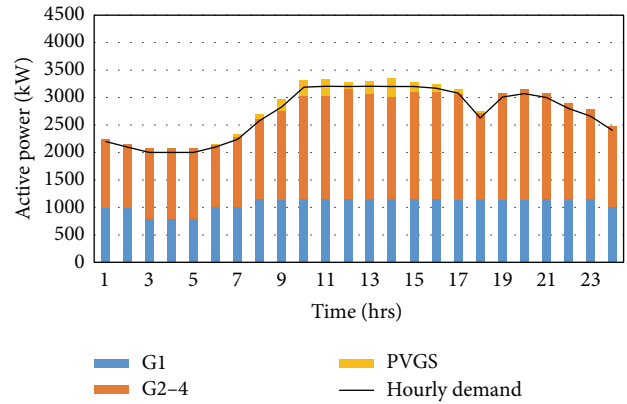


FIGURE 12: Hourly power generation and load demand for cloudy day.

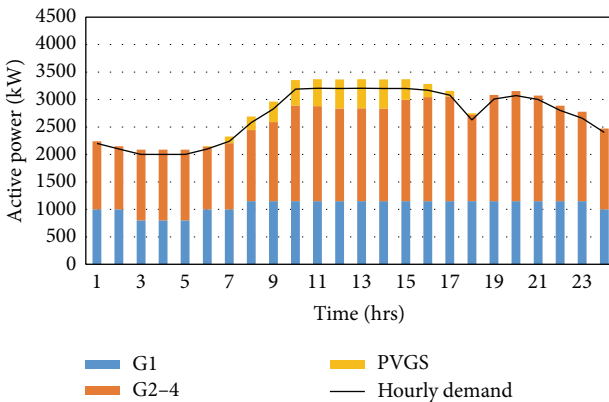


FIGURE 11: Hourly power generation and load demand for sunny day.

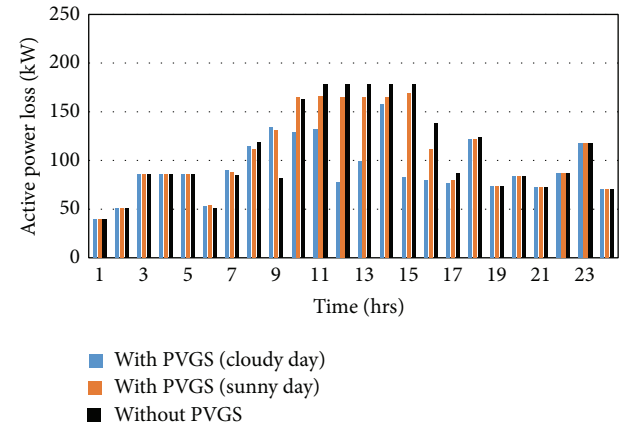


FIGURE 13: Hourly feeder losses with and without PVGS.

hourly estimated PVGS injected power are both included in the MatLab power program. Figure 10 shows hourly voltage profile at Bus 4 with and without considering the proposed 690 kWp PVGS. It is observed that the voltage fluctuation becomes larger due to PVGS power injection during daytime. For example, at 8:00 am the voltage level rises from 0.994 p.u to 1.025 p.u and the VVR is 3.12% for a sunny day. However, the voltage level and VVR of all buses are all within the acceptable range since the estimated PVGS power generation is less than the maximum installation capacity. Figures 11 and 12 show the hourly power generation and load demand for typical sunny day and cloudy day, respectively. Meanwhile, the corresponding hourly losses are shown in Figure 13. Without the PVGS, the highest loss of 178 kW occurs from 11:00 am to 15:00 pm and the lowest network loss of 39 kW occurs at 1:00 am, respectively. With the PVGS, the network loss fluctuated starting from 6:00 am to 18:00 pm and is reduced mostly due to the power injection of PVGS. In Kiribati, diesel generator usually consumes 0.25 litre of fuel at price of \$0.75/liter to produce 1 kWh. It means the production cost is 0.1875 c/kWh. Therefore the estimated hourly fuel consumption cost is as shown in Figure 14. It is also found

that the daily fuel cost is reduced from US\$4,630,180 to US\$167,246 for a sunny day and to US\$66,258 for a cloudy day if the proposed PVGS is installed.

#### 4. Case Study: Financial Analysis

This section executed the financial analysis of a large scale PV investment project in a small island. The purpose of this scenario is to analyze how much benefit that PUB DNST may take from installation of the proposed PVGS system. Thanks to the benefit of power loss reduction and fuel saving that resulted from PVGS contribution described in Section 3, the monthly trend of fuel cost with and without PVGS is presented in Figure 15. Calculated results by (8) show that fuel cost saving for 218 sunny days in the year 2010 is US\$167246, while for 147 cloudy days left the value is US\$66,258. Thus, annual fuel saving cost ( $C_{AFS}$ ) due to the PVGS is US\$233,505, while annual fuel cost without the PVGS is US\$4630180. Figure 16 shows the trend of network losses with and without PVGS system on PUB DNST. It is found that the annual network distribution loss has been reduced from 944 MW to 876 MW due to PVGS. Based on this, it may have an energy

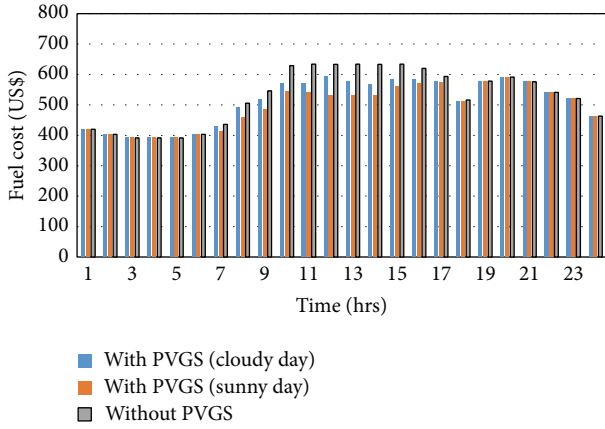


FIGURE 14: Hourly fuel cost with and without PVGS.

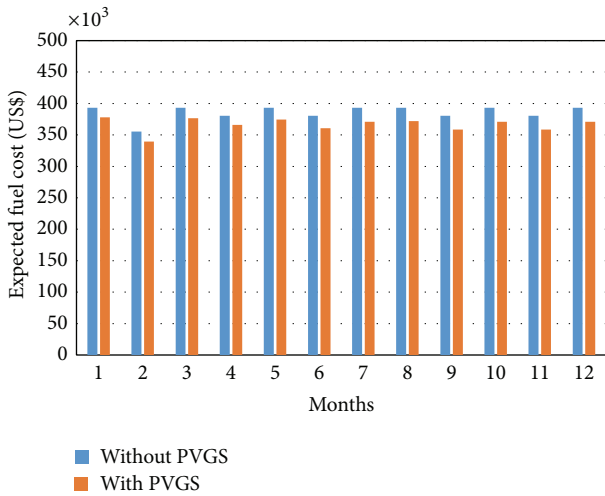


FIGURE 15: Monthly fuel cost with and without PVGS.

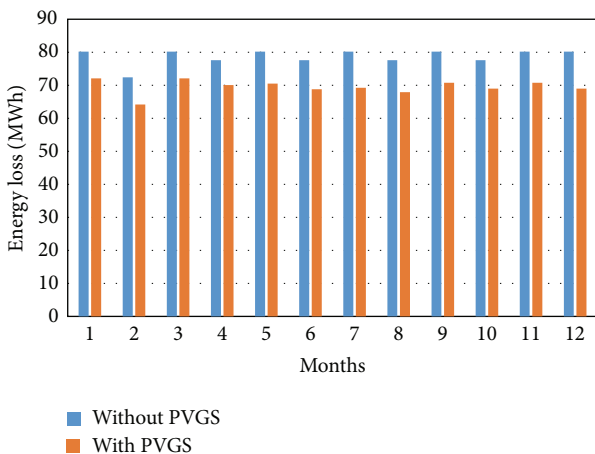


FIGURE 16: Monthly energy losses with and without PVGS.

TABLE 1: Parameters of the financial evaluation.

Items	Parameters
PWF	0.98039
Life cycle (year)	25
Annual O&M cost (\$)	16,172
PVGS's performance derating rate (%)	1.4
Capital investment cost (\$)	2,299,770
Annual power loss saving cost (\$)	26,800
Annual fuel saving cost (\$)	233,505

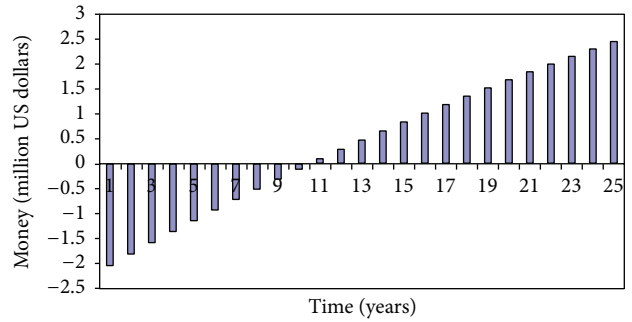


FIGURE 17: Net present value for installation capacity of 690 kWp PVGS.

loss saving of 67 MWh annually. Consequently, calculating result by (7) with the cost of energy (CoE) of 0.40 c/kWh in Kiribati, the energy loss saving cost is US\$26,800. Thus, due to the power injected by the PVGS to the power system, PUB may earn power loss saving cost ( $C_{APLS}$ ) of US\$26,800 annually.

Financial parameters used in this paper to calculate the estimated benefit from the PVGS are shown in Table 1. The present worth factor (PWF) is 0.98093 in the 25 years evaluation period. And the capital investment cost and annual O&M cost are US\$2,299,700 and US\$16172, respectively. Based on the saving derived due to the PVGS contribution, Table 1 shows the PVGS capital investment cost, which obviously is the present worth of spending for this year, that is, US\$2,299,700. With the aforementioned PVGS capital investment (or present worth spending) and the present worth of saving for the next 11 years, derived in Table 2, combined, the NPV is a positive value, that is, \$89,492. Thus the PVGS capital investment cost is more than justified by the continuing saving in losses and fuel consumption. Since the  $NPV = 0$ , then the evaluation is feasible. Here in Figure 17 it is shown that the PBV and the NPV over the entire PVGS lifetime are 11 years and \$2,466,424, respectively.

### 5. Conclusions

A large scale PV installation capacity has been analyzed both technically and economically on a small island distribution feeder to justify whether the PVGS investment is feasible or not from the utility sector's point of view. With the proposed

TABLE 2: Simulation results of NPV.

Year ( <i>i</i> )	PWF	$(1 - dr)^i$	Saving at present (\$)	Accumulated (\$)	NPV (\$)
1	0.98	0.98	239,345.55	239,345.55	-2,060,424.45
2	0.96	0.97	234,651.99	473,997.54	-1,825,772.46
3	0.94	0.95	230,050.46	704,048.00	-1,595,722.00
4	0.92	0.94	225,539.17	929,587.17	-1,370,182.83
5	0.91	0.93	221,116.35	1,150,703.52	-1,149,066.48
6	0.89	0.91	216,780.26	1,367,483.77	-932,286.23
7	0.87	0.90	212,529.20	1,580,012.97	-719,757.03
8	0.85	0.89	208,361.50	1,788,374.46	-511,395.54
9	0.84	0.88	204,275.53	1,992,649.99	-307,120.01
10	0.82	0.86	200,269.69	2,192,919.68	-106,850.32
11	0.80	0.85	196,342.40	2,389,262.08	89,492.08
12	0.79	0.84	192,492.12	2,581,754.20	281,984.20
13	0.77	0.83	188,717.35	2,770,471.55	470,701.55
14	0.76	0.82	185,016.60	2,955,488.15	655,718.15
15	0.74	0.80	181,388.43	3,136,876.58	837,106.58
16	0.73	0.79	177,831.40	3,314,707.99	1,014,937.99
17	0.71	0.78	174,344.13	3,489,052.11	1,189,282.11
18	0.70	0.77	170,925.24	3,659,977.35	1,360,207.35
19	0.69	0.76	167,573.40	3,827,550.75	1,527,780.75
20	0.67	0.75	164,287.28	3,991,838.03	1,692,068.03
21	0.66	0.74	161,065.61	4,152,903.64	1,853,133.64
22	0.65	0.73	157,907.11	4,310,810.75	2,011,040.75
23	0.63	0.72	154,810.55	4,465,621.30	2,165,851.30
24	0.62	0.71	151,774.72	4,617,396.02	2,317,626.02
25	0.61	0.70	148,798.42	4,766,194.44	2,466,424.44

installation site, it is found that maximum allowable power of the PVGS of 690 kWp may fit the voltage variation ratio limit of 5%. According to the hourly solar irradiation and temperature, the estimated power generation of PVGS is applied to execute the 24-hour load flow in a sunny day and cloudy day. It is found that the annual fuel saving of 311,333 litre and energy losses saving of 67 MWh are obtained due to the installation of PVGS. After that, a cost-benefit analysis is performed and it takes 11 years to recover the initial capital cost. In addition, the NPV over its entire life cycle is around \$2.47 million. This amount of NPV obtained in the 25-year period is sufficient enough to improve the utility sector in terms of cash flow injection to improve utility sector's annual internal operation cost or to allocate funding for the development of other essential renewable projects to achieve sustainable environment that in turn benefits the utility and the country as a whole.

### Conflict of Interests

The authors declare that there is no conflict of interests regarding the publication of this paper.

### Acknowledgment

This work is supported by the MOST of Taiwan (MOST 103-3113-E-214-002).

### References

- [1] C. H. Lin, W. L. Hsieh, C. S. Chen, C. T. Hsu, and T. T. Ku, "Optimization of photovoltaic penetration in distribution systems considering annual duration curve of solar irradiation," *IEEE Transactions on Power Systems*, vol. 27, no. 2, pp. 1090–1097, 2012.
- [2] "Kiribati Infrastructure Sector Review," <http://www.theprif.org/sites/theprif.org/files/Final%20Kiribati%20Infrastructure%20Sector%20Review.pdf>.
- [3] "Kiribati Climate Change," <http://www.climate.gov.ki/2013/03/26/new-solar-project-for-south-tarawa/>.
- [4] B. Chabot, "From costs to prices: economic analysis of photovoltaic energy and services," *Progress in Photovoltaics: Research and Applications*, vol. 6, no. 1, pp. 55–68, 1998.
- [5] G. Nofuentes, J. Armilera, and F. J. Muñoz, "Tools for the profitability analysis of grid-connected photovoltaic," *Progress in Photovoltaics: Research and Applications*, vol. 10, no. 8, pp. 555–570, 2002.
- [6] D. J. Swider, L. Beurskens, S. Davidson et al., "Conditions and costs for renewables electricity grid connection: examples in Europe," *Renewable Energy*, vol. 33, no. 8, pp. 1832–1842, 2008.
- [7] A. Roque, N. Fontes, J. Maia, C. Casimiro, and D. M. Sousa, "Economic aspects of a domestic micro-generation system," in *Proceedings of the 2009 6th International Conference on the European Energy Market (EEM '09)*, Leuven, Belgium, May 2009.

- [8] D. L. Talavera, G. Nofuentes, J. Aguilera, and M. Fuentes, "Tables for the estimation of the internal rate of return of photovoltaic grid-connected systems," *Renewable and Sustainable Energy Reviews*, vol. 11, no. 3, pp. 447–466, 2007.
- [9] G. Nofuentes, J. Aguilera, C. Rus, and R. L. Santiago, "A short assessment on the profitability of PV grid-connected systems using classical investment project analysis," in *Proceedings of the 3rd World Conference on Photovoltaic Energy Conversion*, pp. 2632–2635, Osaka, Japan, May 2003.
- [10] J. L. Bernal-Agustín and R. Dufo-López, "Economic and environmental analysis of grid connected photovoltaic systems in Spain," *Renewable Energy*, vol. 31, no. 8, pp. 1107–1128, 2006.
- [11] C. H. Lin, W. L. Hsieh, C. S. Chen, C. T. Hsu, T. T. Ku, and C. T. Tsai, "Financial analysis of a large-scale photovoltaic system and its impact on distribution feeders," *IEEE Transactions on Industry Applications*, vol. 47, no. 4, pp. 1884–1891, 2011.
- [12] "Least Developed Countries Factsheet," [https://www.un.org/en/development/desa/policy/cdp/ldc/profile/country\\_100.shtml](https://www.un.org/en/development/desa/policy/cdp/ldc/profile/country_100.shtml).

## Research Article

# The Effects of Annealing Parameters on the Crystallization and Morphology of Cu(In,Ga)Se<sub>2</sub> Absorber Layers Prepared by Annealing Stacked Metallic Precursors

Chia-Ho Huang<sup>1</sup> and Dong-Cherng Wen<sup>2</sup>

<sup>1</sup> Department of Mechanical Engineering, Lunghwa University of Science and Technology, Taoyuan 33306, Taiwan

<sup>2</sup> Department of Mechanical Engineering, China University of Science and Technology, Taipei 11581, Taiwan

Correspondence should be addressed to Chia-Ho Huang; [chhuang@mail.lhu.edu.tw](mailto:chhuang@mail.lhu.edu.tw)

Received 24 February 2014; Revised 7 May 2014; Accepted 7 May 2014; Published 11 June 2014

Academic Editor: Ho Chang

Copyright © 2014 C.-H. Huang and D.-C. Wen. This is an open access article distributed under the Creative Commons Attribution License, which permits unrestricted use, distribution, and reproduction in any medium, provided the original work is properly cited.

CIGS films are prepared by single-stage annealing of the solid Se-coated In/Cu-Ga bilayer precursor. The annealing processes were performed using various Ar pressures, heating rates, and soaking times. A higher Ar pressure is needed to fabricate highly crystalline CIGS films, as no extra Se-vapor source is supplied. As the heating rate increases, the surface morphologies of the CIGS films become looser and some cracks are observed. However, the influence of soaking time is insignificant and the selenization process only requires a short time when the precursors are selenized at a higher temperature with a lower heating rate and a higher Ar pressure. In this study, a dense chalcopyrite CIGS film with a thickness of about 1.5-1.6  $\mu\text{m}$ , with large grains ( $\sim 1.2 \mu\text{m}$ ) and no cracking or peeling is obtained after selenizing at a temperature of 550°C, an Ar pressure of 300 Torr, a heating rate of 60°C/min, and a soaking time of 20 min. By adequate design of the stacked precursor and controlling the annealing parameters, single-stage annealing of the solid Se-coated In/Cu-Ga bilayer precursor is simplified for the fabrication of a fully crystallized chalcopyrite CIGS absorber layers with good crystallization and large grains.

## 1. Introduction

Chalcopyrite Cu(In,Ga)Se<sub>2</sub> (CIGS) is a good absorber for high-efficiency thin film solar cells because of its favorable band gap and high-absorption coefficient for solar radiation [1]. Of the various ways of preparing CIGS absorber, postselenization of precursor layers is one of the leading methods [2, 3], with an efficiency of around 20% for high temperature annealing of vacuum-sputtered metals under selenium vapor (i.e., selenization) [4, 5]. In spite of such an excellent device performance, a complete understanding of the material produced is required, because the properties of films depend greatly on the process parameters and affect the quality of the resulting CIGS films. In particular, postselenization has an important effect on the structure and morphology of films. In order to reliably obtain the requisite film properties, it is essential to understand the effect of thermal annealing parameters on film properties.

Two selenization techniques, namely, conventional furnace annealing and rapid thermal processing, have been developed. In traditional annealing, Cu-Ga-In metallic precursors are selenized in selenium vapor, obtained from diethylselenide (DESe) or other organometallic precursors [6]. However, the low heating rate during selenization can cause Se to evaporate during the annealing process and can also cause the dewetting of Se. Furthermore, the use of toxic H<sub>2</sub>Se gas is limited in most cases. Although these problems can be avoided by rapid thermal annealing of the metallic precursors with Se pellets, instead of H<sub>2</sub>Se gas [7, 8], the incomplete reaction of the metallic precursors with Se often leaves an unreacted Cu-Ga metallic layer on the backside of the sample during the annealing, even after long annealing times [9]. A one-step sputtering process, using a single quaternary target, has been developed to simplify the fabrication process of CIGS absorber and to eliminate the waste of excess Se [10, 11]. The influence of working pressure

on the efficiency of CIGS based device was studied and the results show that the average efficiency of 6-7% is obtained at a wide working pressure range of 0.4–2.7 Pa by using KCN treatment and the best cell efficiency can reach 8% at the working pressure of 0.67 Pa [11]. However, it is still difficult to obtain high quality CIGS films by directly sputtering from a single CIGS target. Postselenization is necessarily used to improve device performance [12].

The feasibility of fabricating the chalcopyrite CIGS absorber layers by conducting the Se-coated single-layered precursor in a two-step postselenization process has been evaluated [13]. However, the impact of annealing parameters was not studied. In this paper, an alternative selenization process, applying a single-stage annealing of the solid Se-coated In/Cu-Ga bilayer precursors in a vacuum furnace, is proposed to produce single-phase chalcopyrite CIGS absorber. The effect of annealing parameters, such as inert gas pressure, heating rate, and soaking time, on the structure and morphology of the CIGS absorber formed after selenization in an Ar containing atmosphere is determined in this paper.

## 2. Experimental

CIGS absorber layers were grown on soda-lime glass (SLG) substrates, using a two-step process. The metallic precursor film deposition included DC-magnetron sputtering of the Cu-Ga and In layers at room temperature and thermal evaporation of Se. Preliminary deposition of the Cu-Ga and In layers shows that the thickness of each layer increased linearly with increasing deposition time; thus, the deposition rate of layers can be obtained by measuring the film thickness. The deposition parameters were optimized to obtain an absorber thickness of  $\sim 1.5 \mu\text{m}$ . The bottom layer of 350 nm thick Cu-Ga alloy film was deposited at a sputtering power of 100 W and Ar pressure of  $5.0 \times 10^{-3}$  Torr, from a Cu-Ga alloy target with 25 wt.% Ga, while In was deposited at a sputtering power of 40 W and Ar pressure of  $5.0 \times 10^{-3}$  Torr from an In target. The thickness of the In layer was adjusted by varying the deposition time to obtain precursor films with atomic compositions of  $\text{Cu}/(\text{In} + \text{Ga}) = 0.8\text{--}0.9$  and  $\text{Ga}/(\text{In} + \text{Ga}) = 0.1\text{--}0.3$ . As no extra Se-vapor source was used during the annealing process, the natural loss of Se during heating was compensated for by deposition of an excess of Se onto the precursor stack. A  $2 \mu\text{m}$  overstoichiometric Se layer was deposited at  $220^\circ\text{C}$  after preheating to  $150^\circ\text{C}$  for 10 min at a rate of  $20^\circ\text{C}/\text{s}$ . The substrate was rotated at 40 rpm, during deposition, to improve the film's uniformity.

The precursors were then selenized in an Ar atmosphere, using single-stage annealing at a constant temperature of  $550^\circ\text{C}$ . In order to determine the effect of annealing parameters, the annealing processes were performed using various Ar pressures and temperature profiles. Ar pressure from 1 Torr to 300 Torr was used, the heating rate was varied between  $60^\circ\text{C}/\text{min}$  and  $240^\circ\text{C}/\text{min}$ , and a soaking time at constant temperature from 20 min to 60 min was used. The cooling rate after selenization was about  $6^\circ\text{C}/\text{min}$ .

The surface morphologies of the films were analyzed using field emission scanning electron microscopy (SEM, JEOL, and JSM-6500F). The phases and crystal structure were

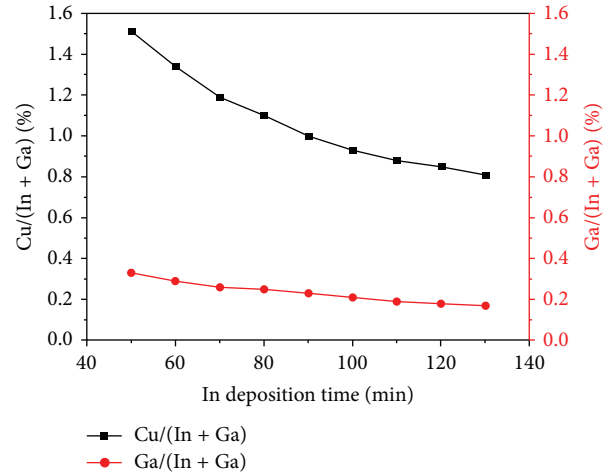


FIGURE 1: The atomic composition ratios of In/Cu-Ga precursors as a function of In deposition time.

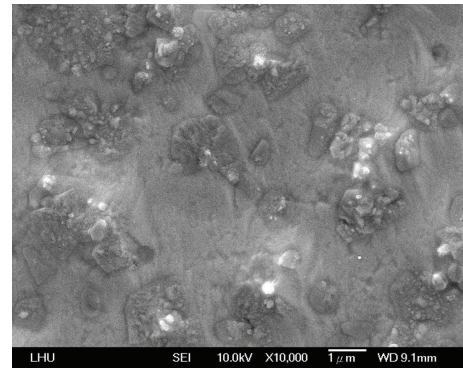


FIGURE 2: The surface morphology of the In/Cu-Ga precursor prepared with 120 min of In deposition time.

determined by X-ray diffraction (Rigaku-2000 X-ray diffractometer), using  $\text{Cu-K}\alpha$  radiation and an angle of incidence of  $1^\circ$ . The composition of the CIGS films was determined by energy dispersive X-ray fluorescence spectrometry (EDXRF, Solar metrology SMX).

## 3. Results and Discussion

**3.1. Analysis of the Precursors.** Firstly, the material properties of the as-deposited precursors are determined. The compositions of the In/Cu-Ga precursors with various In deposition time were analyzed by EDS and their atomic composition ratios are shown in Figure 1. When the In deposition time is 120 min, the precursor has the desired atomic composition of  $\text{Cu}/(\text{In} + \text{Ga}) = 0.85$  and  $\text{Ga}/(\text{In} + \text{Ga}) = 0.18$ , so this time was used for selenization. Figure 2 shows the surface morphologies of this standard precursor. Some large and discontinuous island-like grains are precipitated onto the flat surface. The EDS results show that the island-like grains are detected as In-rich alloys. However, the smoother background is detected to be Cu-rich alloys. The island-like grains are thought to be In hillocks, which form automatically,

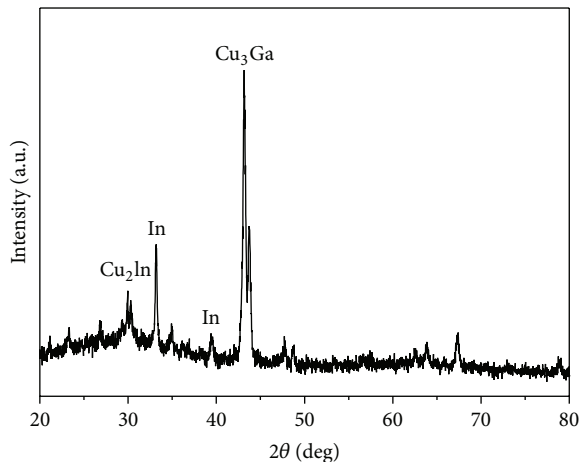


FIGURE 3: The XRD patterns of the In/Cu-Ga precursor produced using an In deposition time of 120 min. JCPDS:  $\text{Cu}_2\text{In}$  (00-026-0552),  $\text{Cu}_3\text{Ga}$  (00-044-1117), and In (03-065-9292).

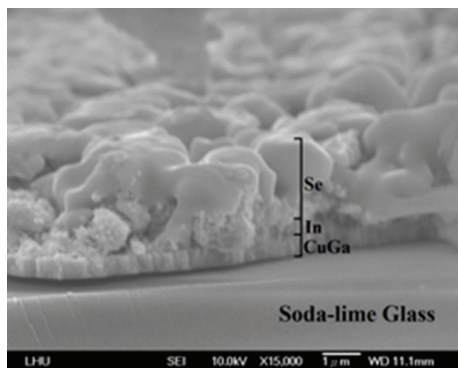


FIGURE 4: Cross-sectional SEM image of the solid Se-coated In/Cu-Ga precursor.

because of the high diffusion coefficient and low melting point of In [14]. Figure 3 shows the corresponding XRD pattern of the metallic precursor in Figure 2. As reported by Park et al. [15], a pure In peak and intermetallic  $\text{Cu}_2\text{In}$  and  $\text{Cu}_3\text{Ga}$ , as equilibrium phases at room temperature, are observed. The  $\text{Cu}_2\text{In}$  reflexes are of lower intensity than those for  $\text{Cu}_3\text{Ga}$ , which suggests that the latter phase is prominent. Figure 4 shows the cross-sectional SEM image of the solid Se-coated In/Cu-Ga precursor layer, deposited on the SLG substrates. Clearly, an expected 350 nm thick of Cu-Ga alloy film and 2  $\mu\text{m}$  of Se without peeling or cracking are observed. The Se layer evaporated onto the In/Cu-Ga layer yields a smooth surface and penetrates into and fully surrounds the In islands. The Se-coated In/Cu-Ga precursors were subsequently moved to the furnace, for selenization in an Ar containing atmosphere.

**3.2. The Effect of Ar Pressure.** As no extra Se-vapor source was supplied, the amount of Se that can react with In/Cu-Ga precursors, during annealing, is determined by the working pressure in the reaction chamber. There are two ways to

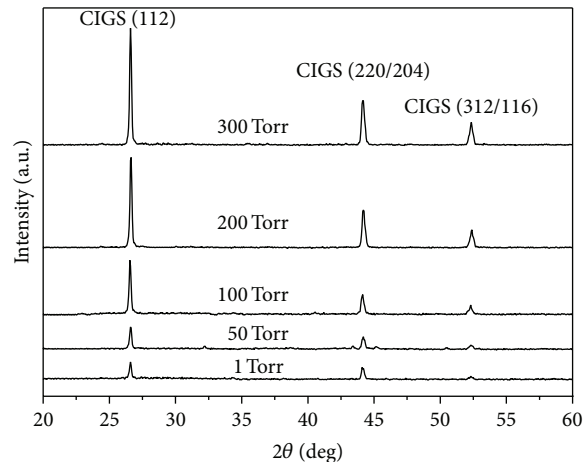


FIGURE 5: XRD patterns of the CIGS films, selenized using different Ar pressures.

control the working pressure. The first method uses the autogenous pressure, which is governed by the degree of evaporation of Se, and the second method uses an external control on the amount of internal pressure by pumping the inert gas into the chamber. The second method was used because of its simplicity.

Figure 5 shows the XRD patterns for the selenized CIGS films at different Ar pressures, from 1 to 300 Torr. For these runs, the heating rate during annealing was maintained at 90°C/min and the soaking time was 30 min. All of the CIGS films have the chalcopyrite phases, (112), (220)/(204), and (312)/(116), and diffraction peak (112) is the strongest. This shows that the CIGS films are polycrystalline and oriented along the (112) direction, parallel to the substrate. The XRD patterns do not show other complex peaks, which indicates that the single-stage annealing process may form acceptable chalcopyrite structures in CIGS thin films. This is likely, because the ramping rate for furnace annealing of these cases is far slower than for rapid thermal annealing processes; so, the time required to reach the desired temperature is sufficient for selenide compounds to form, ultimately developing CIGS [16].

Figure 5 also shows that the CIGS peaks increase as the Ar pressure increases, which may be attributed to the crystallization quality and grain growth. At lower Ar pressure, the working pressure is not sufficient to allow the Se to stay on the precursor layer. Se evaporates from the layer stack, instead of diffusing into it, so the layer goes from a weak CIGS peak, due to the Se deficiency, which indicates poor crystallinity or smaller grains in these cases. Increasing the Ar pressure decreases the evaporation of Se and improves the chemical reactivity of Se with the In/Cu-Ga precursors. As a result, the intensity of the CIGS peaks increases through the crystallinity improvement and the grain size increases. The change in the microstructure due to the increase in the Ar pressure is also confirmed by the SEM observations. In Figure 6, SEM images for three of the studied Ar pressures are shown for the lowest (1 Torr) and 100 Torr, and the highest Ar pressure (300 Torr).

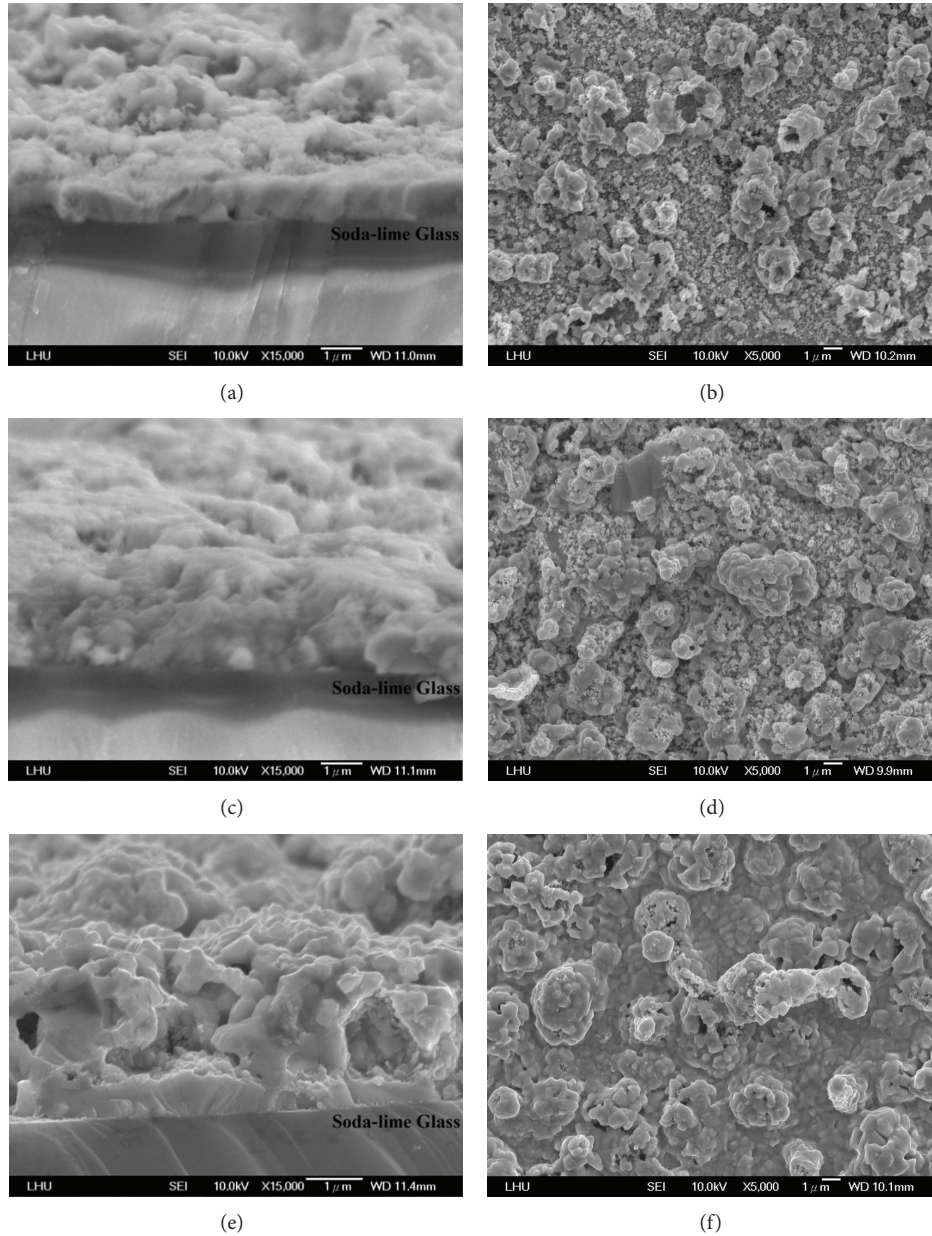


FIGURE 6: Cross-sectional and top-view SEM images of the CIGS films selenized at (a), (b) the lowest (1 Torr), (c) and (d) 100 Torr, and (e) and (f) the highest Ar pressure (300 Torr).

At the lowest Ar pressure, the thickness of the CIGS layer is thinner than that of the other samples and no obvious grains are seen. The low Ar pressure annealing process results in a marked loss of Se, due to vaporization, thereby significantly reducing the thickness of the CIGS layer. For an Ar pressure of 100 Torr, the thickness of the CIGS layer increases and the morphology of CIGS grains becomes more obvious. For the highest Ar pressure, some faceted surface and angled grain boundaries within the film are observed. The CIGS layer has a maximum thickness of about 1.5-1.6  $\mu\text{m}$  and the grains have a maximum diameter of  $\sim 1.2 \mu\text{m}$ , because more Se stays on the surface of the precursor layers and then reacts with the precursors to form CIGS. From these analyses, it is concluded

that the selenization process requires a higher Ar pressure to produce a better morphology and highly crystalline CIGS films, as no extra Se-vapor source is supplied.

**3.3. The Effect of Heating Rate.** Figure 7 shows the XRD patterns for the selenized CIGS films as a function of heating rate for a soaking time of 30 min and an Ar pressure that is fixed at 300 Torr. The CIGS peaks are smaller when the heating rate is increased. This means that increasing the heating rate for single-stage annealing of the solid Se-coated In/Cu-Ga precursors is detrimental to the crystallinity of the CIGS films. When the annealing temperature is ramped between the melting point of In ( $\sim 150^\circ\text{C}$ ) and Se ( $\sim 220^\circ\text{C}$ ), the Se

TABLE I: The elemental composition of CIGS films.

Soaking times (min)	Compositions (at %)				Ratios	
	Cu	In	Ga	Se	Cu/(In + Ga)	Ga/(In + Ga)
20	23.9	20.3	5.9	49.9	0.91	0.22
30	23.5	19.8	5.9	50.8	0.91	0.22
40	23.8	20.4	6.0	49.8	0.90	0.22
50	24.1	19.9	6.1	49.9	0.92	0.23
60	23.6	20.1	5.8	50.5	0.91	0.22

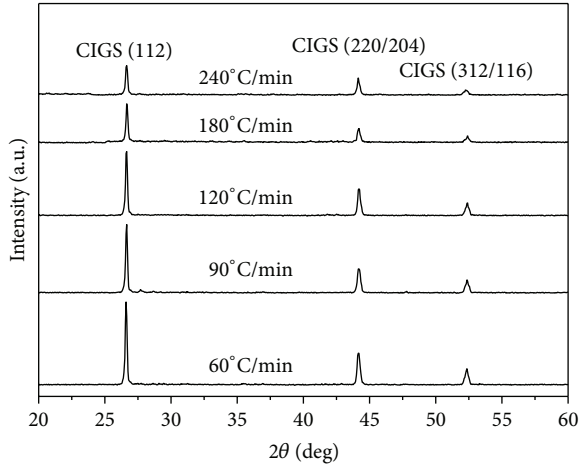


FIGURE 7: XRD patterns of the selenized CIGS films as a function of heating rate.

coating is fully incorporated into the surrounding In and diffuses into the Cu-Ga layer. This Se can react with the In and the intermetallic  $\text{Cu}_2\text{In}$  and  $\text{Cu}_3\text{Ga}$  of Cu-Ga precursor layer, subsequently converting itself into the metallic selenides,  $\text{In}_2\text{Se}_3$ ,  $\text{Cu}_2\text{Se}$ , and  $\text{Cu}_3\text{Se}_2$  [13, 17]. Increasing the annealing temperature to greater than  $330^\circ\text{C}$  [18] causes these metallic selenides to react to form the chalcopyrite phase by the following chemical reaction mechanism:  $\text{In}_2\text{Se}_3 + \text{Cu}_2\text{Se} \rightarrow 2\text{CuInSe}_2$  [19] and  $3\text{In}_2\text{Se}_3 + 2\text{Cu}_3\text{Se}_2 \rightarrow 6\text{CuInSe}_2 + \text{Se}(\text{g})$  [13].

The amount of diffused Se and metallic selenides depends on the time spent in the  $150\text{--}220^\circ\text{C}$  temperature range. This time interval is shorter if the heating rate is faster, so the intensity of the CIGS peaks is less and the crystallinity of CIGS films is poor. Figure 8 shows a comparison of cross-sectional and top-view SEM images of selenized CIGS layers produced using heating rates of  $60^\circ\text{C}/\text{min}$ ,  $120^\circ\text{C}/\text{min}$ , and  $240^\circ\text{C}/\text{min}$ . The faceted surface and angled grain boundaries of the CIGS structure become more obvious as the heating rate is reduced. The cross-sectional SEM images show that both the grain size and thickness of CIGS films increase with decreasing the heating rate. This observation is consistent with the results of XRD. However, as the heating rate increases, the surface morphologies of the CIGS films become looser and some cracks are observed, because the chalcopyrite structure does not completely form throughout

the entire depth of the precursor. A shorter period of time in the  $150\text{--}220^\circ\text{C}$  temperature range causes more Se to evaporate away from the layer stack. The lack of Se results in poor crystallinity of the CIGS layers.

**3.4. The Effect of Soaking Time.** Based on the above analyses, it is seen that a higher Ar pressure (300 Torr) and a lower heating rate ( $60^\circ\text{C}/\text{min}$ ) are beneficial to the formation of the chalcopyrite phase, so these two parameters are fixed and the influence of soaking time is studied. Figure 9 shows the XRD patterns for the CIGS films selenized at  $550^\circ\text{C}$ , for various soaking times. All of the films in this figure have the basic chalcopyrite and the difference in the peaks is insignificant. This means that the selenization process only requires a shorter time at a higher temperature. This is because the chalcopyrite structure completely forms when the precursor is annealed at  $550^\circ\text{C}$  for 20 min, which gives a stable structure. After the chalcopyrite structure forms, the growth of chalcopyrite grains in over prolonged soaking times is not apparent, so the difference between the peaks for the films soaked for longer soaking times and those for the 20 min sample is insignificant. Cross-sectional and top-view SEM images of 20 min selenized CIGS film are shown in Figure 10. As is seen, the grain characteristics and surface morphologies of this sample are similar to those for the 30 min sample shown in Figures 8(a) and 8(b), which confirms that a soaking time of 20 min is sufficient to form the chalcopyrite structure, when the precursors are selenized at an Ar pressure of 300 Torr, a heating rate of  $60^\circ\text{C}/\text{min}$ , and a temperature of  $550^\circ\text{C}$ .

The results show that the thickness of the annealed CIGS absorber layers increases with increasing the Ar pressure but decreases with increasing the heating rate. However, the influence of soaking time is insignificant when the Ar pressure and heating rate are fixed.

Table 1 lists the elemental compositions and atomic ratios of the CIGS films annealed at  $550^\circ\text{C}$  for different times. Compared with the as-deposited precursor, the  $\text{Cu}/(\text{In} + \text{Ga})$  ratios increase from 0.85 to 0.90–0.92 and the  $\text{Ga}/(\text{In} + \text{Ga})$  ratios increase from 0.18 to 0.22–0.23, because of the loss of In during selenization at high temperature. However, when the stable structure of the chalcopyrite phase is formed, after annealing at  $550^\circ\text{C}$  for 20 min, the difference in composition is insignificant for the samples annealed for a longer soaking time. The composition of all of the CIGS films remains almost constant. The detailed compositional uniformity of CIGS

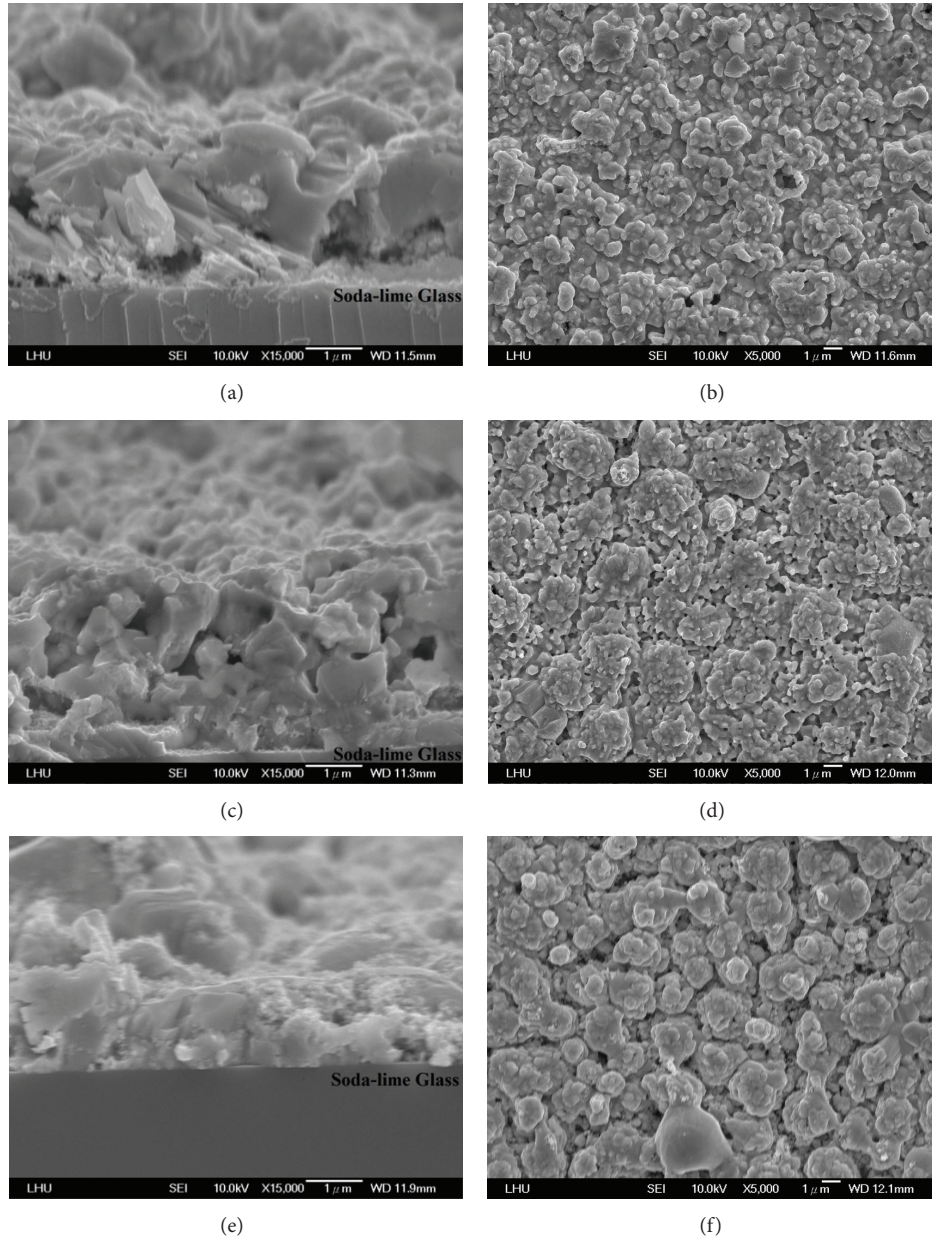


FIGURE 8: Cross-sectional and top-view SEM images of CIGS films made using (a), (b) the lowest (60°C/min), (c) and (d) 120°C/min, and (e) and (f) the highest heating rate (240°C/min).

films was also determined by X-ray fluorescence intensity measurements of the  $K_{\alpha 1,2}$  lines [20]. Figure 11 shows the depth profile of CIGS sample annealed at 550°C for 20 min. The high degree of detailed compositional uniformity with no evidence of phase segregation shows that the procedures used in this study are a successful way for the fabrication of single chalcopyrite structure CIGS film.

Finally, a heterojunction solar cell was fabricated and evaluated under simulated AM1.5 (100 mW/cm<sup>2</sup>) conditions at 25°C. In brief, the absorber film was immediately coated with a 50-nm-thick CdS buffer layer. The CdS layer was then covered with a 100 nm highly resistive intrinsic ZnO layer and then a highly doped n-type ZnO film with a typical thickness

of approximately 600 nm. The 2.5 μm Ni/Al front contact was deposited onto the ZnO using DC magnetron sputtering and there was no intentional heating of the substrate. A solar cell with 6.96% efficiency (open circuit voltage ( $V_{oc}$ ), 537 mV, a short circuit current ( $J_{sc}$ ) of 29.20 mA/cm<sup>2</sup>, and a fill factor (FF) of 47.55%) was produced. This efficiency approximates to the quality of the newly published results [11].

#### 4. Conclusions

A fully crystallized chalcopyrite CIGS absorber is fabricated by single-stage annealing of the solid Se-coated In/Cu-Ga

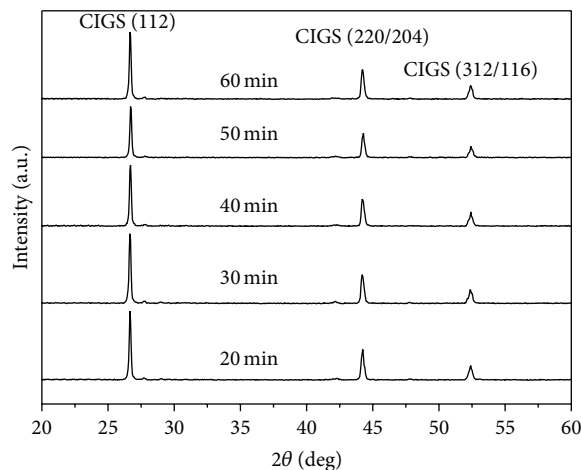


FIGURE 9: XRD patterns of the CIGS films selenized at 550°C for various soaking times.

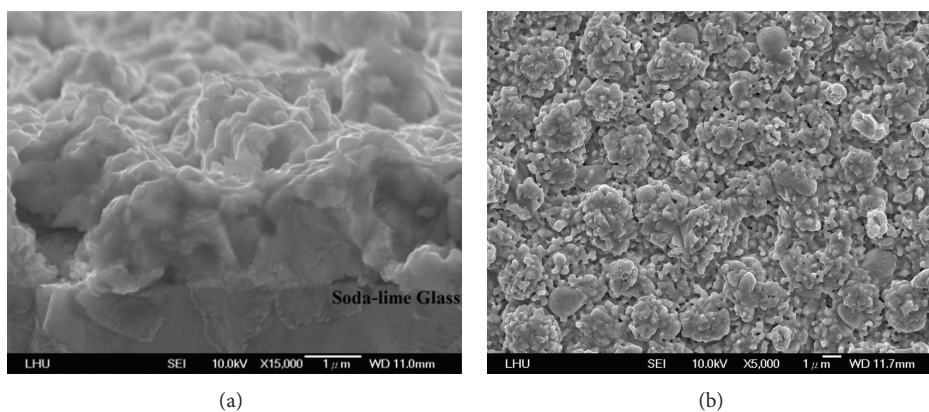


FIGURE 10: (a) Cross-sectional and (b) top-view SEM images of CIGS film selenized at 550°C for 20 min.

bilayer precursor, without an extra Se supply. The effect of the annealing parameters, including Ar pressure, heating rate, and soaking time, on the structure and morphology of the CIGS absorber is studied. The results show that the atomic composition of the precursors can be controlled by varying the thickness of the stacked layer. The selenization process requires a higher Ar pressure to produce a better morphology and highly crystalline CIGS films, as no extra Se-vapor source is supplied. The thickness of the CIGS films, after annealing, increases as the Ar pressure is increased. Increasing the heating rate is detrimental to the crystallinity of the CIGS films, because the amount of Se that can react with the metallic precursors depends on the time spent within the melting point range of In and Se. This time interval is shorter if the heating rate is faster. When a higher Ar pressure and a lower heating rate are used, the selenization process requires a shorter soaking time at a higher temperature. A dense CIGS film with a thickness of about 1.5-1.6  $\mu\text{m}$  with large grains ( $\sim 1.2 \mu\text{m}$ ) and no cracking or peeling phenomena is obtained at a selenizing temperature of 550°C, Ar pressure of 300 Torr, heating rate of 60°C/min, and soaking time of

20 min. This study demonstrates that by adequate design of the stacked precursor and by controlling the annealing parameters, single-stage annealing of the solid Se-coated In/Cu-Ga bilayer precursor is a simple way to fabricate fully crystallized chalcopyrite CIGS absorber layers with good crystallization and large grains.

### Highlights

- (1) The atomic composition of the precursors can be controlled by varying the thickness of the stacked layer.
- (2) Higher Ar pressure and a lower heating rate are used, and the annealing process requires a shorter soaking time at a higher temperature.
- (3) This study demonstrates that single-stage annealing of the solid Se-coated In/Cu-Ga bilayer precursor is a simple way to fabricate a fully crystallized chalcopyrite CIGS absorber layer with good crystallization and large grains.

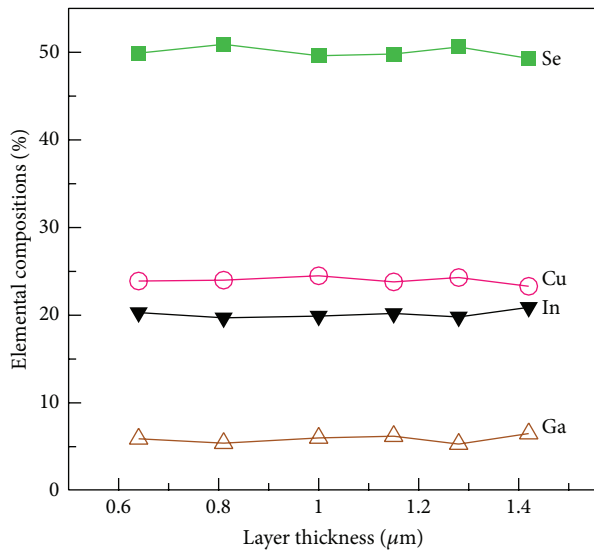


FIGURE 11: The XRF detailed compositional uniformity of Cu, In, Ga, and Se in the CIGS sample annealed at 550°C for 20 min.

## Conflict of Interests

The authors declare that there is no conflict of interests regarding the publication of this paper.

## References

- [1] H. Neumann, "Optical properties and electronic band structure of  $\text{CuInSe}_2$ ," *Solar Cells*, vol. 16, pp. 317–333, 1986.
- [2] R. W. Birkmire and E. Eser, "Polycrystalline thin film solar cells: present status and future potential," *Annual Review of Materials Science*, vol. 27, no. 1, pp. 625–653, 1997.
- [3] R. Caballero, C. Guillén, M. T. Gutiérrez, and C. A. Kaufmann, " $\text{CuIn}_{1-x}\text{Ga}_x\text{Se}_2$ -based thin-film solar cells by the selenization of sequentially evaporated metallic layers," *Progress in Photovoltaics: Research and Applications*, vol. 14, no. 2, pp. 145–153, 2006.
- [4] P. Jackson, D. Hariskos, E. Lotter et al., "New world record efficiency for  $\text{Cu}(\text{In,Ga})\text{Se}_2$  thin-film solar cells beyond 20%," *Progress in Photovoltaics: Research and Applications*, vol. 19, no. 7, pp. 894–897, 2011.
- [5] Y. Goushi, H. Hakuma, K. Tabuchi, S. Kijima, and K. Kushiya, "Fabrication of pentanary  $\text{Cu}(\text{In,Ga})(\text{Se,S})_2$  absorbers by selenization and sulfurization," *Solar Energy Materials and Solar Cells*, vol. 93, no. 8, pp. 1318–1320, 2009.
- [6] N. G. Dhere, S. S. Kulkarni, A. H. Jahagirdar, and A. A. Kadam, "Composition and morphology of partially selenized  $\text{CuIn}_{1-x}\text{Ga}_x\text{Se}_2$  thin films prepared using diethylselenide (DESe) as selenium source," *Journal of Physics and Chemistry of Solids*, vol. 66, no. 11, pp. 1876–1879, 2005.
- [7] X. Wang, S. S. Li, W. K. Kim et al., "Investigation of rapid thermal annealing on  $\text{Cu}(\text{In,Ga})\text{Se}_2$  films and solar cells," *Solar Energy Materials and Solar Cells*, vol. 90, no. 17, pp. 2855–2866, 2006.
- [8] S. Merdes, R. Mainz, H. Rodriguez-Alvarez et al., "Influence of precursor stacking on the absorber growth in  $\text{Cu}(\text{In,Ga})\text{S}_2$  based solar cells prepared by a rapid thermal process," *Thin Solid Films*, vol. 519, no. 21, pp. 7189–7192, 2011.
- [9] R. Mainz, R. Klenk, and M. C. Lux-Steiner, "Sulphurisation of gallium-containing thin-film precursors analysed in-situ," *Thin Solid Films*, vol. 515, no. 15, pp. 5934–5937, 2007.
- [10] Y. C. Lin, J. H. Ke, W. T. Yen, S. C. Liang, C. H. Wu, and C. T. Chiang, "Preparation and characterization of  $\text{Cu}(\text{In,Ga})(\text{Se,S})_2$  films without selenization by co-sputtering from  $\text{Cu}(\text{In,Ga})\text{Se}_2$  quaternary and  $\text{In}_2\text{S}_3$  targets," *Applied Surface Science*, vol. 257, no. 9, pp. 4278–4284, 2011.
- [11] C.-H. Chen, T.-Y. Lin, C.-H. Hsu, S.-Y. Wei, and C.-H. Lai, "Comprehensive characterization of Cu-rich  $\text{Cu}(\text{In,Ga})\text{Se}_2$  absorbers prepared by one-step sputtering process," *Thin Solid Films*, vol. 535, no. 1, pp. 122–126, 2013.
- [12] J. H. Shi, Z. Q. Li, D. W. Zhang, Q. Q. Liu, Z. Z. Sun, and S. M. Huang, "Fabrication of  $\text{Cu}(\text{In, Ga})\text{Se}_2$  thin films by sputtering from a single quaternary chalcogenide target," *Progress in Photovoltaics: Research and Applications*, vol. 19, no. 2, pp. 160–164, 2011.
- [13] G. S. Chen, J. C. Yang, Y. C. Chan, L. C. Yang, and W. Huang, "Another route to fabricate single-phase chalcogenides by post-selenization of Cu-In-Ga precursors sputter deposited from a single ternary target," *Solar Energy Materials and Solar Cells*, vol. 93, no. 8, pp. 1351–1355, 2009.
- [14] Z.-H. Li, E.-S. Cho, S. J. Kwon, and M. Dagenais, "Formation of  $\text{CuInSe}_2$  absorber by rapid thermal processing of electron-beam evaporated stacked elemental layers," *Journal of Materials Science: Materials in Electronics*, vol. 23, no. 4, pp. 964–971, 2012.
- [15] H. Park, S. C. Kim, S.-H. Lee et al., "Effect of precursor structure on  $\text{Cu}(\text{In,Ga})\text{Se}_2$  formation by reactive annealing," *Thin Solid Films*, vol. 519, no. 21, pp. 7245–7249, 2011.
- [16] H. K. Song, J. K. Jeong, H. J. Kim, S. K. Kim, and K. H. Yoon, "Fabrication of  $\text{CuIn}_{1-x}\text{Ga}_x\text{Se}_2$  thin film solar cells by sputtering and selenization process," *Thin Solid Films*, vol. 435, no. 1-2, pp. 186–192, 2003.
- [17] D. Bhattacharyya, I. Forbes, F. O. Adurodiya, and M. J. Carter, "Formation of  $\text{CuInSe}_2$  by the selenization of sputtered Cu/In layers," *Journal of Materials Science*, vol. 32, no. 7, pp. 1889–1894, 1997.
- [18] J. Koo, S. C. Kim, H. Park, and W. K. Kim, " $\text{Cu}(\text{In,Ga})\text{Se}_2$  thin film photovoltaic absorber formation by rapid thermal annealing of binary stacked precursors," *Thin Solid Films*, vol. 520, no. 5, pp. 1484–1488, 2011.
- [19] J. S. Park, Z. Dong, S. Kim, and J. H. Perepezko, "CuInSe<sub>2</sub> phase formation during  $\text{Cu}_2\text{Se}/\text{In}_2\text{Se}_3$  interdiffusion reaction," *Journal of Applied Physics*, vol. 87, no. 8, pp. 3683–3690, 2000.
- [20] C.-Y. Hsu, P.-C. Huang, Y.-Y. Chen, and D.-C. Wen, "Fabrication of a  $\text{Cu}(\text{In,Ga})\text{Se}_2$  thin film photovoltaic absorber by rapid thermal annealing of  $\text{CuGa}/\text{In}$  precursors coated with a Se layer," *International Journal of Photoenergy*, vol. 2013, Article ID 132105, 7 pages, 2013.

## Research Article

# Theoretical Insight into Organic Dyes Incorporating Triphenylamine-Based Donors and Binary $\pi$ -Conjugated Bridges for Dye-Sensitized Solar Cells

Shuxian Wei,<sup>1</sup> Xiaoqing Lu,<sup>1</sup> Xiaofan Shi,<sup>1</sup> Zhigang Deng,<sup>1</sup> Yang Shao,<sup>1</sup> Lianming Zhao,<sup>1</sup> Wenye Guo,<sup>1</sup> and Chi-Man Lawrence Wu<sup>2</sup>

<sup>1</sup> College of Science, China University of Petroleum, Qingdao, Shandong 266580, China

<sup>2</sup> Department of Physics and Materials Science, City University of Hong Kong, Kowloon, Hong Kong

Correspondence should be addressed to Xiaoqing Lu; [luxq@upc.edu.cn](mailto:luxq@upc.edu.cn) and Wenye Guo; [wgyuo@upc.edu.cn](mailto:wgyuo@upc.edu.cn)

Received 8 April 2014; Revised 11 May 2014; Accepted 19 May 2014; Published 11 June 2014

Academic Editor: Yen-Lin Chen

Copyright © 2014 Shuxian Wei et al. This is an open access article distributed under the Creative Commons Attribution License, which permits unrestricted use, distribution, and reproduction in any medium, provided the original work is properly cited.

The design of light-absorbent sensitizers with sustainable and environment-friendly material is one of the key issues for the future development of dye-sensitized solar cells (DSSCs). In this work, a series of organic sensitizers incorporating alkoxy-substituted triphenylamine (tpa) donors and binary  $\pi$ -conjugated bridges were investigated using density functional theory (DFT) and time-dependent DFT (TD-DFT). Molecular geometry, electronic structure, and optical absorption spectra are analyzed in the gas phase, chloroform, and dimethylformamide (DMF) solutions. Our results show that properly choosing the heteroaromatic atoms and/or adding one more alkoxy-substituted tpa group can finely adjust the molecular orbital energy. The solvent effect renders the HOMO-LUMO gaps of the tpa-based sensitizers decrease in the sequence of DMF solution < chloroform solution < gas phase. The absorption spectra are assigned to the ligand-to-ligand charge transfer (LLCT) characteristics via transitions mainly from tpa, 3,4-ethylenedioxythiophene (edot), and alkyl-substituted dithienosilole (dts) groups to edot, dts, and cyanoacrylic acid groups. The binary  $\pi$ -conjugated bridges play different roles in balancing the electron transfer and recombination for the different tpa-based sensitizers. The protonation/deprotonation effect has great effect on the HOMO-LUMO gaps and thus has great influence on the bands at the long wavelength region, but little influence on the bands at the short wavelength region.

## 1. Introduction

Dye-sensitized solar cells (DSSCs) are currently under active investigation for the solar energy utilization along with the growing worldwide demand for environmentally friendly energy sources [1–7]. The relative high performance, simple fabrication process, and low production costs render DSSCs as competitive alternative to conventional silicon devices. Usually, DSSCs are fabricated by sensitizers (dyes), photoanodes (mesoporous TiO<sub>2</sub> films), counterelectrodes, and electrolytes/hole transporters. So far, polypyridyl Ru(II)-based complexes are proven to be the most efficient sensitizers employed in DSSCs [8–11], such as the tetraprotonated Ru(4,4'-dicarboxy-2,2'-bipyridine)<sub>2</sub>(NCS)<sub>2</sub> complex (coded as N3) [8] and its doubly protonated analog (coded as N719)

[10]. Although highly efficient, with a high efficiency over 12.1% [12], Ru-based prototypes are facing the problem of costly synthesis and undesired environmental issues. Metal-free organic sensitizers, which are in good agreement with the trend of the future developments of DSSCs using environmentally friendly and inexpensive materials, show several advantageous features relative to Ru-based complexes: (1) diversity of organic molecular structures can ensure more diversity of sensitizers for DSSCs; (2) high molar extinction coefficients of organic sensitizers can render the use of thinner semiconductor to promote charge separation; (3) more flexibility of organic sensitizers can be beneficial for constructing semitransparent and/or multicolor solar cells. At present, the highest photon-to-electron energy conversion

efficiency has exceeded 13% for DSSCs using organic sensitizer [13].

From a theoretical point of view, a few criteria should be fulfilled for the design of ideal organic sensitizers: (1) the molecular orientation should facilitate intramolecular charge transfer, and spatial separation should maintain the photooxidized donor at a distance from the photoinjected electrons, diminishing the impact of back electron transfer processes; (2) the energy level of LUMO should be sufficiently high for efficient electron injection into the  $\text{TiO}_2$ , whereas the energy level of HOMO should be sufficiently low for efficient regeneration of the oxidized state; (3) the absorption band should extend from the whole visible region to near infrared range with strong absorption strength; (4) the stability should be good enough for about  $10^8$  turnover cycles of exposure to nature [14, 15]. Based on these requirements, the organic sensitizers are usually designed to be of electron donor-conjugated bridge-electron acceptor structure, called D- $\pi$ -A architecture, with  $\text{TiO}_2$  surface anchoring groups integrated into the acceptor moiety. Arylamines and alkylamines, due to strong electron donating abilities as well as efficient intramolecular charge transfer characteristics, are usually used as electron donors in the D- $\pi$ -A organic sensitizers [16–23]. Among them, DSSC using this metal-free organic sensitizer incorporating the lipophilic triphenylamine as electron donor and the hydrophilic cyanoacrylic acid as electron acceptor (coded as **C219**) has achieved an efficiency over 10% [24].

However, a detailed atomistic characterization of this sensitizer is still not clear enough. Such an atomistic characterization can not only provide information that complements the experimental work, but also help to understand the structural and the electronic properties for design of novel sensitizers with improved performances [25–28]. In this work, we present a theoretical characterization of **C219** and its derivatives 1–5. Molecular geometry, electronic structure, and spectral property of the sensitizers are investigated in the gas phase, chloroform, and dimethylformamide (DMF) solutions by means of the density functional theory (DFT) and time-dependent DFT (TD-DFT) calculations.

## 2. Computational Methods

All calculations on the tpa-based sensitizers were performed with DFT and TD-DFT in the Gaussian 09 program package [29]. The B3LYP exchange correlation functional in conjunction with the 6-31G(d) basis set, which has already been proved to be an optimal compromise between accuracy and computational cost for such large aromatic molecules [30], was employed in the geometrical optimizations without any symmetry constraints for the sensitizers considered in both gas phase and solutions. The solvent effects were evaluated using the nonequilibrium [31] implementation of the conductor-like polarizable continuum model (C-PCM) [32–34]. This approach provides results very close to those obtained by the original dielectric model for high dielectric constant solvents but is significantly more effective in geometry optimizations and less prone to the numerical errors

arising from the small part of the solute electron cloud lying outside the cavity [34]. TD-DFT calculations were used to investigate the optical properties of the sensitizers using the approximation of  $E_{0-0}$  with the lowest vertical excitation energy of the system at the ground state geometry, which can be accurately and efficiently calculated by TD-DFT [35]. The 50 lowest spin-allowed singlet-singlet transitions, up to an energy of at least  $\sim 4.0$  eV, were taken into account in the calculations of the adsorption spectra.

## 3. Results and Discussion

In the following sections, we start with the geometrical description of **C219** and its derivatives, followed by the discussion of electronic structures and molecular orbital energy levels and then the analysis of absorption spectra in the real environment of chloroform and DMF solutions, and finally the comparison of the relative light-harvesting efficiency (RLHE) of the tpa-based sensitizers.

**3.1. Geometrical Considerations.** The chemical structures of **C219** and its derivatives 1–5 are shown in Figure 1. **C219** is composed of three parts: (1) an alkoxy-substituted triphenylamine (tpa) as donor, (2) a cyanoacrylic acid as acceptor and anchoring group, and (3) a binary  $\pi$ -conjugated unit consisting of 3,4-ethylenedioxythiophene (edot) and alkyl-substituted dithienosilole (dts) as bridge [24]. For computational convenience, the  $\text{C}_6\text{H}_{13}^+$  and  $\text{C}_8\text{H}_{17}^+$  groups of the experimental **C219** sensitizer are replaced by methyl groups marked with blue dash-lined ellipses and red dash-lined circles, as shown in Figure 1. Considering that the electron transfer mainly takes place via the high  $\pi$ -electron conjugated tpa center to acceptor and/or bridge centers, the end-on substitutions of the  $\text{C}_6\text{H}_{13}^+$  and  $\text{C}_8\text{H}_{17}^+$  groups by methyl groups have slight influence on the spectral properties of the **C219** sensitizer.

In fact, these substitutions are checked in order not to result in appreciable changes in the electronic structures as well as the absorption spectra. The S atoms in the conjugated bridge of the prototype molecule **C219** are substituted by the same electron-rich heteroaromatic O and Se atoms in sensitizers 1 and 2. For sensitizers 3, 4, and 5, one more alkoxy-substituted tpa group is added to substitute the ethylenedioxy group in 1, **C219**, and 2. This structural design is based on two considerations: (1) the heteroaromatic atoms may adjust the molecular orbital energies appropriately and (2) one more alkoxy-substituted tpa group may not only enhance the electron-donating ability, but also effectively inhibit  $\text{I}_3^-$  from approaching the surface of  $\text{TiO}_2$  by forming a denser layer at the surface. In addition,  $\text{Na}^+$  is used to substitute for  $\text{H}^+$  on cyanoacrylic acid groups in order to evaluate the protonation/deprotonation effect, that is, 1', **C219'**, 2', 3', 4', and 5', as shown in Figure 1.

According to the experimental setup of **C219**, the solvents for calculations are chloroform (relative dielectric constant  $\text{EPS} = 4.71$ ) and DMF ( $\text{EPS} = 37.22$ ). The spectra recorded in different solvents are available, thus rendering it conceivable to investigate the solvent effects. For all the ground state

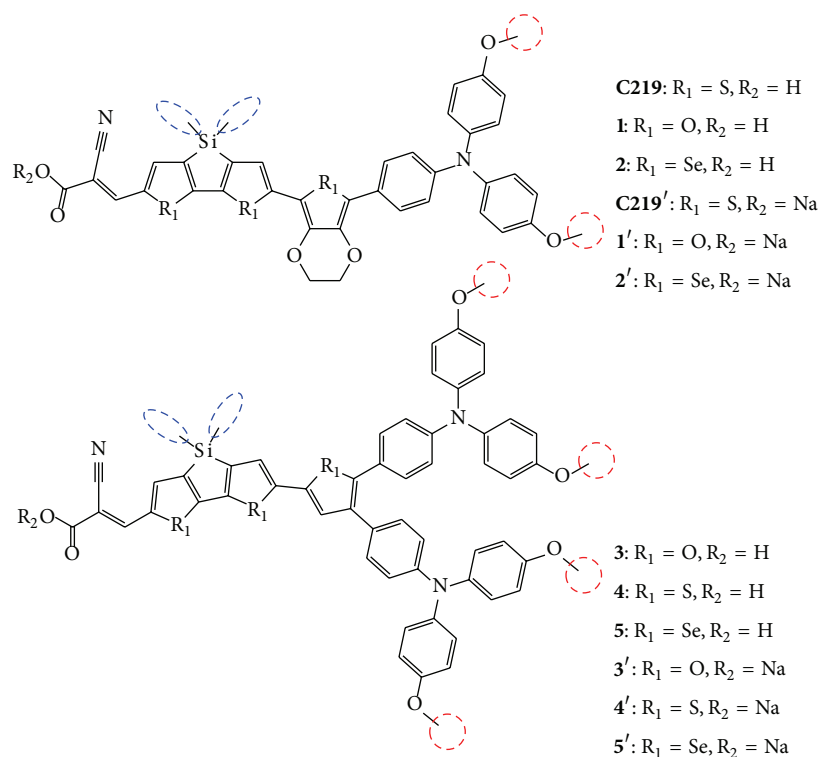


FIGURE 1: Schematic structures of the tpa-based sensitizers. The  $C_6H_{13}^+$  and  $C_8H_{17}^+$  groups in the tpa-based sensitizers are replaced by methyl groups marked with blue dash-lined ellipses and red dash-lined circles.

geometries, our results show that different solvents have no noticeable impact because of the difference of the solvent polarity.

**3.2. The Frontier Orbitals and Energy Levels.** The electronic excitation occurs mainly from the highest occupied molecular orbitals (HOMOs) to the lowest unoccupied molecular orbitals (LUMOs), and usually the HOMOs localize on the donor subunit and LUMOs on the acceptor subunit. The electronic structure analysis is thus essential to evaluate whether the molecular orbital contributions facilitate the efficient charge separation or not. Considering the similarity of their geometries, **C219** and **C219'** are chosen to exhibit the frontier molecular orbitals for **1**, **C219**, **2** and **1'**, **C219'**, **2'**, **4** and **4'** are used to show the frontier molecular orbitals for **3–5** and **3'–5'**, respectively. Figure 2 shows the selected frontier molecular orbitals of **C219**, **C219'**, **4** and **4'** calculated at the B3LYP/6-31G(d) level in chloroform solution. The first six frontier molecular orbital energies and the HOMO-LUMO gaps are depicted in Figure 3.

It is clear, seen from Figure 2, that the first three HOMOs (HOMO, HOMO-1, and HOMO-2) of **C219** are mainly composed of the  $\pi$  combinations of C and N on tpa, edot, and dts groups. Particularly, for the HOMO, considerable contribution is from the tpa ligand. This point is confirmed as one more tpa ligand is introduced in **4**, in which the first two HOMOs show almost entirely tpa-based characteristics.

The bridge involved or not in the HOMOs would be of great difference for the electron transfer. If the binary bridge of edot and dts is involved in the HOMOs, it would facilitate the direct transfer of electron from the donor to the acceptor subunit, but it is also easy to occur recombinations for the transferred electrons. Otherwise, it would prevent electron recombination effectively but is not beneficial for the electron transfer. The key point for the binary bridge is that spatial separation should balance the photooxidized donor at a distance from the photoinjected electrons, diminishing the impact of back electron transfer processes [24, 36–39]. In this sense, the binary bridge of edot and dts in **C219** plays a more positive role in promoting electron transfer but a more negative role in diminishing back electron transfer than that in **4** [24]. That is, the binary  $\pi$ -conjugated bridges play different roles in balancing the electron transfer and recombination for the different tpa-based sensitizers.

The first three LUMOs of **C219** are delocalized through the edot, dts, and cyanoacrylic acid groups, as shown in Figure 2. Sizeable contributions are from the cyanoacrylic acid group, which would facilitate the excited electrons injection into the semiconductors directly. The  $\pi^*$  orbitals from tpa ligand are almost not involved in the LUMOs. Considering that the LUMOs also include the spatial separation, it would be favorable for the electron recombination if the binary bridge of edot and dts is involved in the HOMOs. That is, **4** and **4'** are much better than **C219** and **C219'** for

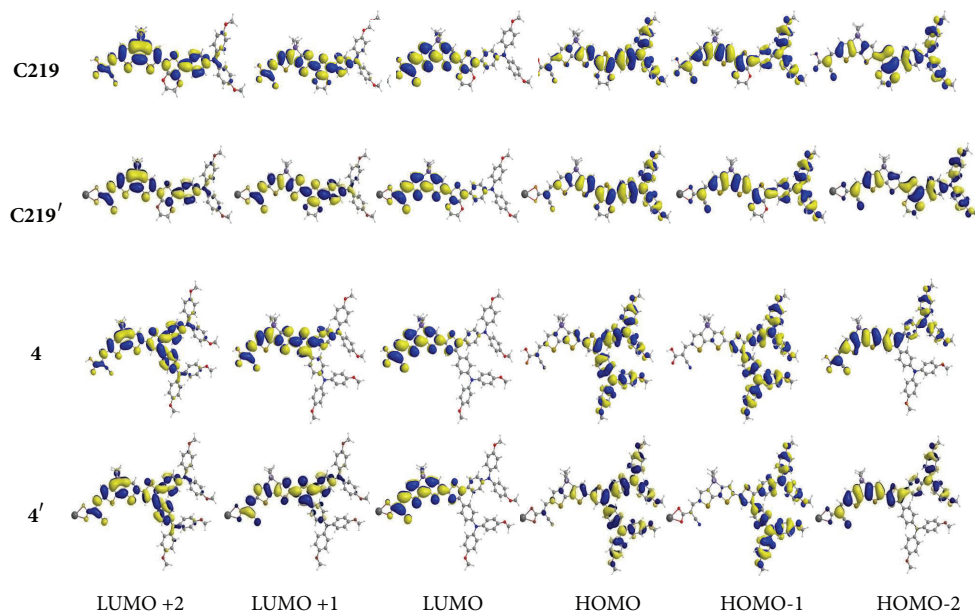


FIGURE 2: The frontier molecular orbitals of sensitizers **C219**, **C219'**, **4**, and **4'**. Isodensity contour = 0.02.

diminishing the impact of back electron transfer. Seen from Figure 2, substitutions of  $\text{Na}^+$  for  $\text{H}^+$  (**C219**, **4**  $\rightarrow$  **C219'**, **4'**) on cyanoacrylic acid groups have more effects on the LUMOs than the HOMOs, as mirrored by the alterations of the  $\text{Na}^+$ -associated cyanoacrylic acid orbital shapes. Substitutions of O and Se for S atom on the bridge alter the energy levels of the frontier molecular orbitals obviously. The energy levels of both HOMO and LUMO in the same framework are in the sequence of  $5 < 4 < 3$  and  $2 < \text{C219} < 1$  in the gas phase and solutions, as shown in Figure 3. This is due to the electron donating ability of the heteroatom involved,  $\text{Se} > \text{S} > \text{O}$ , which stabilizes the complexes by lowering their energy levels. Similar trend appears for the  $\text{Na}^+$ -substituted analogs.

As seen from Figure 3, the HOMO-LUMO gaps of the tpa-based sensitizers decrease in the sequence of DMF solution < chloroform solution < gas phase. For instance, the HOMO-LUMO gaps of **C219** are 1.92, 1.97, and 2.09 eV obtained in DMF, chloroform, and the gas phase, respectively. This trend is due to the interactions of the sensitizers and the surroundings with different relative dielectric constant. As the relative dielectric constant increases, that is, gas phase (EPS = 0.00) < chloroform solution (EPS = 4.71) < DMF solution (EPS = 37.22), the interaction between the tpa-based sensitizers and the surroundings increases, and thus intramolecular interactions become weak and their energy levels increase [40, 41]. The tpa-based sensitizers are less insensitive to the change of solvent, as mirrored by a 0.05 eV shift when going from chloroform solution to DMF solution, while more sensitive to the change when going from the gas phase to the solutions. Besides, substitutions of  $\text{Na}^+$  for  $\text{H}^+$  on cyanoacrylic acid groups have great effect on

the HOMO-LUMO gaps. As shown in Figure 3, the values increase by 0.28 and 0.31 eV when going from **C219** and **4** to **C219'** and **4'**, respectively. This is ascribed to the fact that these substitutions destabilize the LUMOs greater than the HOMOs and thus enlarge the HOMO-LUMO gaps, in good consistency with the alteration trend of the frontier molecular orbital distributions.

**3.3. Electronic Excitations and Absorption Spectra.** The absorption spectra of the tpa-based sensitizers are shown in Figure 4, in which  $\text{H}^+$ - and  $\text{Na}^+$ -contained sensitizers are depicted in Figures 4(a) and 4(b), respectively. Overall, the band line shapes obtained in the gas phase and solutions agree well with each other, but the spectra obtained in solutions are shifted toward the long wavelength region with respect to those obtained in the gas phase [42, 43]. Comparison of the results gained in two solutions shows that the spectra in DMF solution are slightly red-shifted with respect to those in chloroform solution. This trend is in good agreement with the sequence of the HOMO-LUMO gaps obtained in two solutions. As for the protonation/deprotonation effect, substitutions of  $\text{Na}^+$  for  $\text{H}^+$  render the spectra toward the short wavelength region, as shown in Figures 4(a) and 4(b). This trend agrees well with the enlarged HOMO-LUMO gaps of tpa-based sensitizers caused by these substitutions. In view of the real environment of DSSCs and the experimental setups, the results obtained in chloroform solution are used for the discussion of spectral properties as follows. Table 1 lists the selected excitation energies ( $E$ , nm), oscillator strength ( $f$ ), and relative orbital contributions to the optical transitions between 350 and 800 nm of the absorption spectra in chloroform solution.

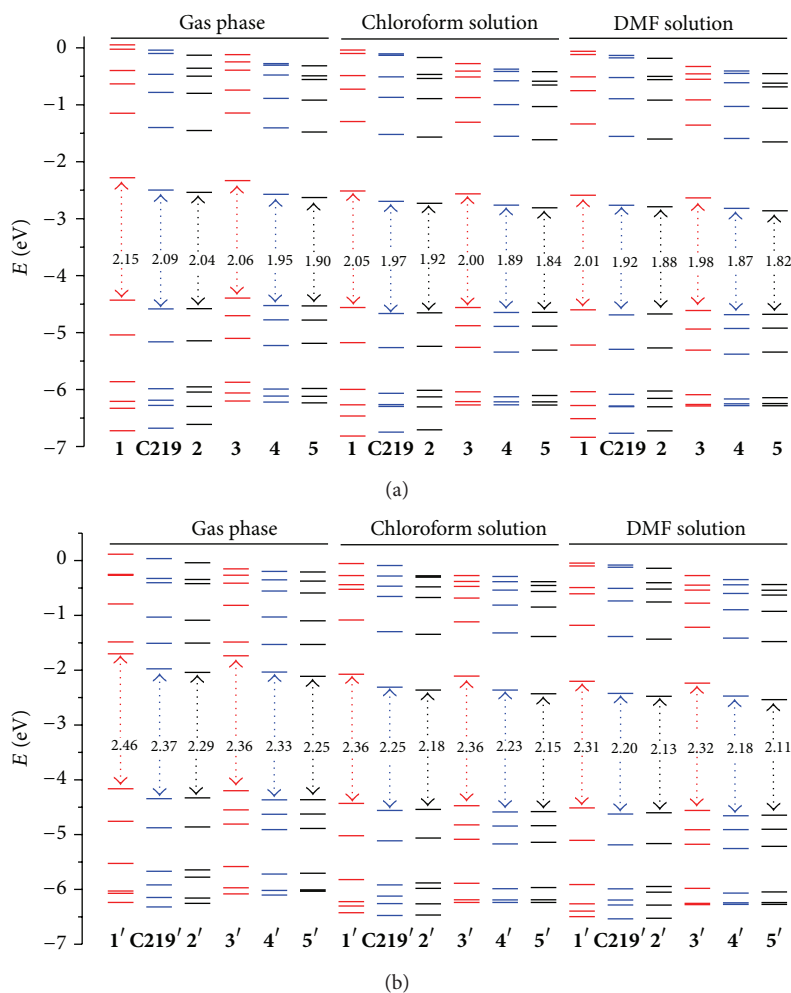


FIGURE 3: Energy levels and HOMO-LUMO gaps of the tpa-based sensitizers.

For **C219** in chloroform solution, four separated absorption bands are found to center at  $\sim 360$ ,  $\sim 439$ ,  $\sim 529$ , and  $\sim 714$  nm. At  $\sim 360$  nm, the band is composed of two peaks at 356.4 and 363.3 nm, originated from the starting orbitals of the HOMO/HOMO-1 combinations to the arriving orbitals of LUMO+1/LUMO+2 (see Table 1). Frontier orbital analysis shows that this band has the interligand and intraligand ligand-to-ligand charge transfer (LLCT) characteristics; that is, transitions occur from tpa, edot, and dts groups to edot, dts, and cyanoacrylic acid groups. Similarly, the bands at  $\sim 439$ ,  $\sim 529$ , and  $\sim 714$  nm also show interligand LLCT characteristics. It is quite different from the metal-centered complexes in previous investigations [25–28], in which spectra at the short wavelengths of the visible region show mainly the LLCT characteristic while those at the long wavelengths of the visible region show mixed characteristics of metal-to-ligand charge transfer (MLCT) and LLCT. For **C219**, there is an increasing trend of oscillator strength (which is regarded as the measure of the intensity of the absorption peaks [37, 44]) along with the shift of the absorption band toward the long wavelength region; that is, the stronger oscillator

strength appears in the band at the longer wavelength region. The lowest vertical excitation for **C219** occurs at 713.1 nm with the oscillator strength of 1.281, originated from the 100% HOMO  $\rightarrow$  LUMO transition. This transition occurs from tpa, edot, and dts groups to edot, dts, and cyanoacrylic acid groups, a mixed LLCT characteristic. Similar spectra and electronic excitation trends also appear for the O- and Se-substituted sensitizers **1** and **2**, as shown in Figure 4(a).

The spectra tend to shift toward the short wavelength region when substituting  $\text{Na}^+$  for  $\text{H}^+$ , as shown in Figure 4(b). For **C219'** in chloroform solution, four separated absorption bands are found to center at  $\sim 350$ ,  $\sim 424$ ,  $\sim 488$ , and  $\sim 630$  nm. Compared with the corresponding bands of **C219**, the substitution of  $\text{Na}^+$  for  $\text{H}^+$  has little effect on the bands at the short wavelength region ( $\sim 360$  and  $\sim 439$  nm versus  $\sim 350$  and  $\sim 424$  nm) but has great effect on the bands at the long wavelength region ( $\sim 529$  and  $\sim 714$  nm versus  $\sim 488$  and  $\sim 630$  nm). However, the increasing trend of oscillator strength in **1'**, **C219'** and **2'** is still the same as that in **C219** along with the absorption band toward the long

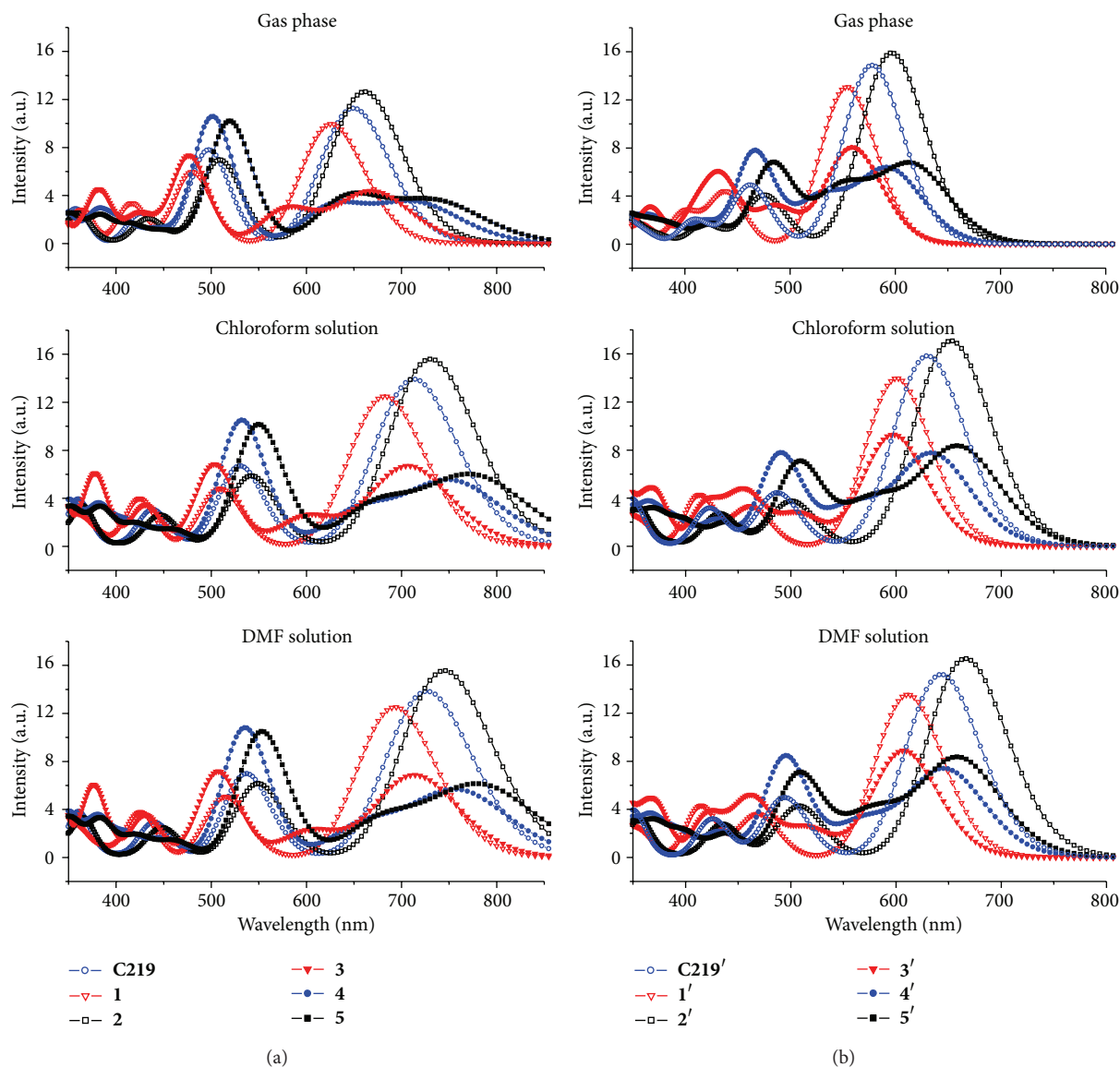


FIGURE 4: Simulated absorption spectra of  $H^+$ - (a) and  $Na^+$ - (b) contained tpa-based sensitizers.

wavelength region. The lowest vertical excitation for **C219'** occurs at 630.0 nm with the stronger oscillator strength of 1.456 than the corresponding value of **C219**. In the energy range investigated, the band calculated at  $\sim 630$  nm for **C219'** is in good agreement with the experimental result of 584 nm, more consistent than **C219** at  $\sim 714$  nm [24]. This means the spectra of the tpa-based organic sensitizers, as well as the energy levels and the HOMO-LUMO gaps, are sensitive to the protonation/deprotonation effect.

The introduction of one more alkoxy-substituted tpa group alters the spectra significantly, as shown in Figure 4. For **4** in chloroform solution, the oscillator strength of bands becomes weaker at the long wavelength region of 600–800 nm, while stronger at middle wavelength region of 500–600 nm than the corresponding values of **C219**.

With respect to oscillator strength, it will be affected by the electron-donating capability from  $\pi$ -conjugation and heteroaromatic groups in sensitizers [27, 44, 45]. Similar trends occur for the O- and Se-substituted sensitizers **3**, **5**, and their  $Na^+$ -substituted sensitizers **3'**, **4'**, and **5'**. For **4** at  $\sim 532$  nm, the band results from the 98% HOMO-2  $\rightarrow$  LUMO transition with the oscillator strength of 0.967 (see Table 1). This transition shows the interligand and intraligand LLCT characteristic from tpa, edot, dts, and even cyanoacrylic acid groups to edot, dts, and cyanoacrylic acid groups. The lowest vertical excitation for **4** occurs at 754.3 nm with the oscillator strength of 0.487, originated from the 100% HOMO  $\rightarrow$  LUMO transition. Obviously, this transition has interligand LLCT characteristic; that is, transition occurs from double tpa groups to edot, dts, and cyanoacrylic acid groups.

TABLE 1: Selected excitation energies ( $E$ , nm), oscillator strength ( $f$ ), and relative orbital contributions to the optical transitions between 350 and 800 nm of the absorption spectra of tpa-based sensitizers in chloroform solution<sup>a</sup>.

$E$	$f$	Composition	$E$	$f$	Composition
<b>C219</b>			<b>C219'</b>		
713.1	1.281	H - 0 → L + 0 (100%)	630.0	1.456	H - 0 → L + 0 (99%)
530.4	0.616	H - 1 → L + 0 (97%)	487.4	0.409	H - 1 → L + 0 (97%)
438.5	0.281	H - 0 → L + 1 (88%)	423.0	0.292	H - 0 → L + 1 (91%)
387.3	0.023	H - 3 → L + 0 (72%) H - 1 → L + 1 (14%)	354.5	0.085	H - 0 → L + 2 (67%) H - 1 → L + 1 (24%)
363.3	0.212	H - 0 → L + 2 (86%)	350.5	0.023	H - 0 → L + 3 (90%)
356.4	0.152	H - 1 → L + 1 (68%)			
<b>4</b>			<b>4'</b>		
754.3	0.487	H - 0 → L + 0 (100%)	635.1	0.699	H - 0 → L + 0 (99%)
658.2	0.286	H - 1 → L + 0 (99%)	559.7	0.314	H - 1 → L + 0 (98%)
532.3	0.967	H - 2 → L + 0 (98%)	490.5	0.713	H - 2 → L + 0 (97%)
450.5	0.137	H - 0 → L + 1 (94%)	429.5	0.201	H - 0 → L + 1 (93%)
412.3	0.170	H - 1 → L + 1 (79%) H - 3 → L + 0 (17%)	390.6	0.193	H - 1 → L + 1 (88%)
382.5	0.078	H - 4 → L + 0 (69%) H - 0 → L + 2 (25%)	366.4	0.267	H - 0 → L + 2 (81%)
381.9	0.211	H - 0 → L + 2 (62%) H - 4 → L + 0 (30%)	353.6	0.029	H - 0 → L + 3 (88%)
355.6	0.109	H - 2 → L + 1 (59%) H - 6 → L + 0 (24%)	350.9	0.076	H - 2 → L + 1 (70%)
352.2	0.029	H - 0 → L + 3 (88%)			
349.1	0.201	H - 1 → L + 2 (90%)			

<sup>a</sup>Only oscillator strength  $f > 0.02$  and orbital percentage  $> 10\%$  are reported, where H = HOMO and L = LUMO.

TABLE 2: The HOMO and LUMO energies, HOMO-LUMO gaps, lowest vertical excitation energies ( $E_A$ ), oscillator strengths ( $f$ ), and relative LHE (RLHE) for all sensitizers<sup>a</sup>.

Solutions	Sensitizers	LUMO	HOMO	HOMO-LUMO	$E_A$	$f$	RLHE
Chloroform	<b>1</b>	-2.51	-4.56	2.05	1.82	1.150	0.980
	<b>C219</b>	-2.70	-4.67	1.97	1.74	1.281	1.000
	<b>2</b>	-2.73	-4.65	1.92	1.70	1.435	1.016
	<b>3</b>	-2.56	-4.56	2.00	1.76	0.614	1.123
	<b>4</b>	-2.76	-4.65	1.89	1.65	0.487	1.000
DMF	<b>5</b>	-2.81	-4.64	1.84	1.60	0.524	1.040
	<b>1</b>	-2.59	-4.60	2.01	1.79	1.153	0.982
	<b>C219</b>	-2.76	-4.69	1.92	1.71	1.273	1.000
	<b>2</b>	-2.79	-4.67	1.88	1.67	1.431	1.017
	<b>3</b>	-2.64	-4.61	1.98	1.74	0.630	1.120
	<b>4</b>	-2.82	-4.69	1.87	1.63	0.500	1.000
	<b>5</b>	-2.86	-4.68	1.82	1.58	0.537	1.038

<sup>a</sup>All energies are in eV.

**3.4. Light-Harvesting Efficiency (LHE).** Light-harvesting efficiency (LHE), as a good indicator of the incident photon-to-electron conversion efficiency (IPCE), characterizes the ability of dyes in harvesting light. The LHE can be approximately expressed as [46]

$$\text{LHE} = 1 - 10^{-A} = 1 - 10^{-f}, \quad (1)$$

where  $A(f)$  is the absorption (oscillator strength) of the dye associated with the  $\lambda_{\max}$ , that is, the lowest vertical excitation energy ( $E_A$ ). Table 2 lists the HOMO and LUMO energies, HOMO-LUMO gaps, lowest vertical excitation energies ( $E_A$ ), oscillator strengths ( $f$ ), and relative LHE (RLHE) of all sensitizers calculated in chloroform and DMF solutions. According to the structural and spectral properties, the relative LHE (RLHE) is evaluated by comparing sensitizers

1, **C219** and **2** with **C219**, sensitizers **3**, **4**, and **5** with **4**. The influence of solutions on LHE is negligible, due to the little difference in  $E_A$  and  $f$  for sensitizers in different solutions, as shown in Table 2. For **1**, **C219** and **2** in chloroform solution, **2** owns the highest RLHE of 1.016, followed by **C219** with 1.000 and **1** of 0.980. This trend is in good agreement with the sequence of electron donating ability of heteroatoms involved,  $\text{Se} > \text{S} > \text{O}$ . For **3**, **4**, and **5** in chloroform solution, **3** shows the highest RLHE of 1.123, followed by **5** of 1.040 and **4** of 1.000. This indicates that the adjustment on the LHE via the heteroatoms would not be of much help after greatly enhancing the electron-donating group, such as another tpa donor involved.

#### 4. Conclusions

In this work, we have presented a theoretical investigation on organic sensitizers incorporating alkoxy-substituted triphenylamine donors and binary  $\pi$ -conjugated bridges based on DFT/TD-DFT calculations in the gas phase, chloroform, and DMF solutions. Our results show that properly choosing the heteroaromatic atoms and adding one more alkoxy-substituted tpa group can finely adjust the molecular orbital energies. Frontier orbital analysis shows that the three highest HOMOs are mainly composed of the  $\pi$  combinations on tpa, edot, and dts groups for **C219**-like sensitizers but only tpa group for **4**-like analogs. The three LUMOs are delocalized through the edot, dts, and cyanoacrylic acid groups for all tpa-based sensitizers. The HOMO-LUMO gaps of the tpa-based sensitizers decrease in the sequence of DMF solution < chloroform solution < gas phase, according well to the increase of relative dielectric constant of gas phase < chloroform solution < DMF solution. The spectra are assigned to the LLCT characteristics which are originated mainly from transitions of tpa, edot, and dts groups to edot, dts, and cyanoacrylic acid groups. The binary  $\pi$ -conjugated bridge plays a dual role in balancing the electron transfer and recombination for **C219**-like sensitizers but an active role in diminishing the impact of back electron transfer for **4**-like analogs. The protonation/deprotonation effect enlarges the HOMO-LUMO gaps and thus has great influence on the bands at the long wavelength region, but little influence on the bands at the short wavelength region.

#### Conflict of Interests

The authors declare that there is no conflict of interests regarding the publication of this paper.

#### Acknowledgments

This work was supported by NSFC (21303266), Shandong Province Natural Science Foundation (ZR2011EMZ002), Promotive Research Fund for Excellent Young and Middle-Aged Scientists of Shandong Province (BS2013CL031), PetroChina Innovation Foundation (2013D-5006-0406), and the Fundamental Research Funds for the Central Universities (13CX05004A, 13CX05020A, and 13CX02025A).

#### References

- [1] B. O'Regan and M. Grätzel, "A low-cost, high-efficiency solar cell based on dye-sensitized colloidal  $\text{TiO}_2$  films," *Nature*, vol. 353, no. 6346, pp. 737–740, 1991.
- [2] A. Hagfeldt and M. Grätzel, "Molecular photovoltaics," *Accounts of Chemical Research*, vol. 33, no. 5, pp. 269–277, 2000.
- [3] M. Grätzel, "Photoelectrochemical cells," *Nature*, vol. 414, no. 6861, pp. 338–344, 2001.
- [4] M. Grätzel, "Dye-sensitized solar cells," *Journal of Photochemistry and Photobiology C: Photochemistry Reviews*, vol. 4, no. 2, pp. 145–153, 2003.
- [5] M. Grätzel, "Applied physics: solar cells to dye for," *Nature*, vol. 421, no. 6923, pp. 586–587, 2003.
- [6] M. Grätzel, "Solar energy conversion by dye-sensitized photovoltaic cells," *Inorganic Chemistry*, vol. 44, no. 20, pp. 6841–6851, 2005.
- [7] L. M. Goncalves, V. de Zea Bermudez, H. A. Ribeiro, and A. M. Mendes, "Dye-sensitized solar cells: a safe bet for the future," *Energy & Environmental Science*, vol. 1, no. 6, pp. 655–667, 2008.
- [8] M. K. Nazeeruddin, A. Kay, I. Rodicio et al., "Conversion of light to electricity by *cis*- $\text{X}_2$ bis(2,2'-bipyridyl)-4,4'-dicarboxylate)ruthenium(II) charge-transfer sensitizers ( $\text{X} = \text{Cl}^-$ ,  $\text{Br}^-$ ,  $\text{I}^-$ ,  $\text{CN}^-$ , and  $\text{SCN}^-$ ) on nanocrystalline  $\text{TiO}_2$  electrodes," *Journal of the American Chemical Society*, vol. 115, no. 14, pp. 6382–6390, 1993.
- [9] P. Wang, S. M. Zakeeruddin, J. E. Moser et al., "Stable new sensitizer with improved light harvesting for nanocrystalline dye-sensitized solar cells," *Advanced Materials*, vol. 16, no. 20, pp. 1806–1811, 2004.
- [10] M. K. Nazeeruddin, F. de Angelis, S. Fantacci et al., "Combined experimental and DFT-TDDFT computational study of photoelectrochemical cell ruthenium sensitizers," *Journal of the American Chemical Society*, vol. 127, no. 48, pp. 16835–16847, 2005.
- [11] Y. Chiba, A. Islam, Y. Watanabe, R. Komiya, N. Koide, and L. Han, "Dye-sensitized solar cells with conversion efficiency of 11.1%," *Japanese Journal of Applied Physics*, vol. 45, no. 25, pp. 638–640, 2006.
- [12] Q. J. Yu, Y. H. Wang, Z. H. Yi et al., "High-efficiency dye-sensitized solar cells: the influence of lithium ions on exciton dissociation, charge recombination, and surface states," *ACS Nano*, vol. 4, no. 10, pp. 6032–6038, 2010.
- [13] S. Mathew, A. Yella, P. Gao et al., "Dye-sensitized solar cells with 13% efficiency achieved through the molecular engineering of porphyrin sensitizers," *Nature Chemistry*, vol. 6, no. 3, pp. 242–247, 2014.
- [14] M. Grätzel, "Conversion of sunlight to electric power by nanocrystalline dye-sensitized solar cells," *Journal of Photochemistry and Photobiology A: Chemistry*, vol. 164, no. 1–3, pp. 3–14, 2004.
- [15] N. Robertson, "Optimizing dyes for dye-sensitized solar cells," *Angewandte Chemie—International Edition*, vol. 45, no. 15, pp. 2338–2345, 2006.
- [16] T. Horiuchi, H. Miura, K. Sumioka, and S. Uchida, "High efficiency of dye-sensitized solar cells based on metal-free indoline dyes," *Journal of the American Chemical Society*, vol. 126, no. 39, pp. 12218–12219, 2004.
- [17] K. Hara, T. Sato, R. Katoh et al., "Novel conjugated organic dyes for efficient dye-sensitized solar cells," *Advanced Functional Materials*, vol. 15, no. 2, pp. 246–252, 2005.

- [18] D. P. Hagberg, T. Edvinsson, T. Marinado, G. Boschloo, A. Hagfeldt, and L. Sun, "A novel organic chromophore for dye-sensitized nanostructured solar cells," *Chemical Communications*, no. 21, pp. 2245–2247, 2006.
- [19] N. Koumura, Z.-S. Wang, S. Mori, M. Miyashita, E. Suzuki, and K. Hara, "Alkyl-functionalized organic dyes for efficient molecular photovoltaics," *Journal of the American Chemical Society*, vol. 128, no. 44, pp. 14256–14257, 2006.
- [20] S. Kim, J. K. Lee, S. O. Kang et al., "Molecular engineering of organic sensitizers for solar cell applications," *Journal of the American Chemical Society*, vol. 128, no. 51, pp. 16701–16707, 2006.
- [21] H. Choi, J. K. Lee, K. Song, S. O. Kang, and J. Ko, "Novel organic dyes containing bis-dimethylfluorenyl amino benzo[b]thiophene for highly efficient dye-sensitized solar cell," *Tetrahedron*, vol. 63, no. 15, pp. 3115–3121, 2007.
- [22] Z. J. Ning and H. Tian, "Triarylamine: a promising core unit for efficient photovoltaic materials," *Chemical Communications*, no. 37, pp. 5483–5495, 2009.
- [23] Z. J. Ning, Q. Zhang, H. C. Pei et al., "Photovoltage improvement for dye-sensitized solar cells via cone-shaped structural design," *The Journal of Physical Chemistry C*, vol. 113, no. 23, pp. 10307–10313, 2009.
- [24] W. D. Zeng, Y. M. Cao, Y. Bai et al., "Efficient dye-sensitized solar cells with an organic photosensitizer featuring orderly conjugated ethylenedioxythiophene and dithienosilole blocks," *Chemistry of Materials*, vol. 22, no. 5, pp. 1915–1925, 2010.
- [25] X. Q. Lu, S. X. Wei, C.-M. Lawrence Wu, W. Y. Guo, and L. M. Zhao, "Theoretical characterization of ruthenium complexes containing functionalized bithiophene ligands for dye-sensitized solar cells," *Journal of Organometallic Chemistry*, vol. 696, no. 8, pp. 1632–1639, 2011.
- [26] X. Q. Lu, C.-M. Lawrence Wu, S. X. Wei, and W. Y. Guo, "DFT/TD-DFT investigation of electronic structures and spectra properties of Cu-based dye sensitizers," *The Journal of Physical Chemistry A*, vol. 114, no. 2, pp. 1178–1184, 2010.
- [27] X. Q. Lu, S. X. Wei, C.-M. Lawrence Wu, S. R. Li, and W. Y. Guo, "Can polypyridyl Cu(I)-based complexes provide promising sensitizers for dye-sensitized solar cells? A theoretical insight into Cu(I) versus Ru(II) sensitizers," *The Journal of Physical Chemistry C*, vol. 115, no. 9, pp. 3753–3761, 2011.
- [28] X. Q. Lu, S. X. Wei, C.-M. Lawrence Wu et al., "Theoretical insight into the spectral characteristics of Fe(II)-based complexes for dye-sensitized solar cells-Part I: Polypyridyl ancillary ligands," *International Journal of Photoenergy*, vol. 2011, Article ID 316952, 11 pages, 2011.
- [29] M. J. Frisch, G. W. Trucks, H. B. Schlegel et al., *Gaussian 09, Revision A.1*, Gaussian, Wallingford, Conn, USA, 2009.
- [30] C. Angeli, M. Pastore, and R. Cimiraglia, "New perspectives in multireference perturbation theory: the n-electron valence state approach," *Theoretical Chemistry Accounts*, vol. 117, no. 5-6, pp. 743–754, 2007.
- [31] M. Cossi and V. Barone, "Time-dependent density functional theory for molecules in liquid solutions," *The Journal of Chemical Physics*, vol. 115, no. 10, pp. 4708–4717, 2001.
- [32] S. Miertš, E. Scrocco, and J. Tomasi, "Electrostatic interaction of a solute with a continuum. A direct utilization of AB initio molecular potentials for the prevision of solvent effects," *Chemical Physics*, vol. 55, no. 1, pp. 117–129, 1981.
- [33] M. Cossi, V. Barone, R. Cammi, and J. Tomasi, "Ab initio study of solvated molecules: a new implementation of the polarizable continuum model," *Chemical Physics Letters*, vol. 255, no. 4–6, pp. 327–335, 1996.
- [34] V. Barone and M. Cossi, "Quantum calculation of molecular energies and energy gradients in solution by a conductor solvent model," *The Journal of Physical Chemistry A*, vol. 102, no. 11, pp. 1995–2001, 1998.
- [35] F. D. Angelis, S. Fantacci, and A. Selloni, "Alignment of the dye's molecular levels with the TiO<sub>2</sub> band edges in dye-sensitized solar cells: a DFT-TDDFT study," *Nanotechnology*, vol. 19, no. 42, Article ID 424002, 2008.
- [36] J. Feng, Y. Jiao, W. Ma, M. K. Nazeeruddin, M. Grätzel, and S. Meng, "First principles design of dye molecules with ullazine donor for dye sensitized solar cells," *The Journal of Physical Chemistry C*, vol. 117, no. 8, pp. 3772–3778, 2013.
- [37] W. J. Fan, D. Z. Tan, and W.-Q. Deng, "Acene-modified triphenylamine dyes for dye-sensitized solar cells: a computational study," *ChemPhysChem*, vol. 13, no. 8, pp. 2051–2060, 2012.
- [38] K. P. Guo, K. Y. Yan, X. Q. Lu et al., "Dithiafulvenyl unit as a new donor for high-efficiency dye-sensitized solar cells: synthesis and demonstration of a family of metal-free organic sensitizers," *Organic Letters*, vol. 14, no. 9, pp. 2214–2217, 2012.
- [39] G. L. Zhang, H. Bala, Y. M. Cheng et al., "High efficiency and stable dye-sensitized solar cells with an organic chromophore featuring a binary  $\pi$ -conjugated spacer," *Chemical Communications*, no. 16, pp. 2198–2200, 2009.
- [40] M. Pastore, E. Mosconi, F. de Angelis, and M. Grätzel, "A computational investigation of organic dyes for dye-sensitized solar cells: benchmark, strategies, and open issues," *The Journal of Physical Chemistry C*, vol. 114, no. 15, pp. 7205–7212, 2010.
- [41] J. Preat, C. Michaux, D. Jacquemin, and E. A. Perpète, "Enhanced efficiency of organic dye-sensitized solar cells: triphenylamine derivatives," *The Journal of Physical Chemistry C*, vol. 113, no. 38, pp. 16821–16833, 2009.
- [42] J. Preat, C. Michaux, D. Jacquemin, and E. A. Perpète, "Enhanced efficiency of organic dye-sensitized solar cells: triphenylamine derivatives," *The Journal of Physical Chemistry C*, vol. 113, no. 38, pp. 16821–16833, 2009.
- [43] M. Pastore, E. Mosconi, F. de Angelis, and M. Grätzel, "A computational investigation of organic dyes for dye-sensitized solar cells: benchmark, strategies, and open issues," *The Journal of Physical Chemistry C*, vol. 114, no. 15, pp. 7205–7212, 2010.
- [44] N. Santhanamoorthi, C.-M. Lo, and J.-C. Jiang, "Molecular design of porphyrins for dye-sensitized solar cells: a DFT/TDDFT study," *The Journal of Physical Chemistry Letters*, vol. 4, no. 3, pp. 524–530, 2013.
- [45] C.-Y. Chen, M. Wang, J.-Y. Li et al., "Highly efficient light-harvesting ruthenium sensitizer for thin-film dye-sensitized solar cells," *ACS Nano*, vol. 3, no. 10, pp. 3103–3109, 2009.
- [46] H. S. Nalwa, *Handbook of Advanced Electronic and Photonic Materials and Devices: Conducting Polymers*, Academic Press, San Diego, Calif, USA, 2001.

## Research Article

# Fabrication of a Miniature Zinc Aluminum Oxide Nanowire Array Gas Sensor and Application for Environmental Monitoring

Chin-Guo Kuo,<sup>1</sup> Chi-Wu Huang,<sup>1</sup> Jung-Hsuan Chen,<sup>2</sup> and Yueh-Han Liu<sup>1</sup>

<sup>1</sup> Department of Industrial Education, National Taiwan Normal University, Taipei 10610, Taiwan

<sup>2</sup> Material and Chemical Research Laboratories, Industrial Technology Research Institute, Hsinchu 31040, Taiwan

Correspondence should be addressed to Jung-Hsuan Chen; [jhc2369@yahoo.com.tw](mailto:jhc2369@yahoo.com.tw)

Received 10 April 2014; Accepted 14 May 2014; Published 10 June 2014

Academic Editor: Ho Chang

Copyright © 2014 Chin-Guo Kuo et al. This is an open access article distributed under the Creative Commons Attribution License, which permits unrestricted use, distribution, and reproduction in any medium, provided the original work is properly cited.

A miniature n-type semiconductor gas sensor was fabricated successfully using zinc aluminum oxide nanowire array and applied to sense oxygen. The present study provided a novel method to produce zinc aluminum alloy nanowire 80 nm in diameter by the vacuum die casting technique and then obtain zinc aluminum oxide nanowire array using the thermal oxidation technique. The gas sensing properties were evaluated through the change of the sensitivity. The factors influencing the sensitivity of the gas sensor, such as the alloy composition, operating temperature, and oxygen concentration, were investigated further. Experimental results indicated that the maximum sensitivity could be acquired when the weight percentage of aluminum was 5% in zinc aluminum alloy at the operating temperature of 200°C.

## 1. Introduction

Oxygen gas monitors are widely used for employee and environmental safety. A rapid decrease of oxygen can make a very dangerous environment for employees and cause them to lose consciousness suddenly. Based on the fact mentioned, it is important to have an oxygen gas monitor for some special operating environments such as mines, pharmaceutical, semiconductor, and cryogenic supplier [1–4].

Metal oxide semiconductor sensors are most commonly utilized for the gas detection due to their low cost and flexibility in production [5, 6]. The detection principle of the conductive sensor is based on the change of the resistance of a semiconductor thin film upon the adsorption of gas molecules on the surface. The sensitivity of the thin film is strongly related to surface reaction. Some important factors influencing the surface reactions of gas sensors, such as chemical components, microstructures of sensing layers, temperature, and humidity, are investigated [7–10]. Among those factors, the main approaches for increasing the gas

sensitivity of the sensing materials are the size effects and doping by metal or other metal oxides [11–14].

Korotcenkov et al. [11] reported that the grain size effects in the sensor response of nanostructures SnO<sub>2</sub> and In<sub>2</sub>O<sub>3</sub> based thin film gas sensor and indicated the grain size can control almost all operating characteristics of solid state gas sensors such as sensor response, response times, recovery times, and stability and dependence on air humidity. However, the sensing mechanisms of the metal oxide gas sensors were too complicated to evaluate simply. The optimal grain size should be based on the detailed consideration of the parameters of sensors designed.

Chaudhari and his coworkers [14] reported the sensing characteristics of undoped and doped TiO<sub>2</sub> gas sensor and tried to improve the sensing properties of TiO<sub>2</sub> by addition of a small amount of various metal oxides, such as Al<sub>2</sub>O<sub>3</sub>. Their experimental results showed that TiO<sub>2</sub> sensor loaded with 5 wt.% Al<sub>2</sub>O<sub>3</sub> and 0.5 wt.% Pd would increase the sensitivity to H<sub>2</sub>S gas.

Since the gas sensing mechanism is a surface reaction, use of nanostructure materials is expected to improve gas

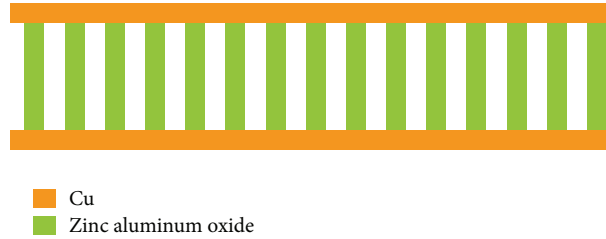


FIGURE 1: Schematic diagram of the prepared zinc aluminum oxide nanowire array gas sensor.

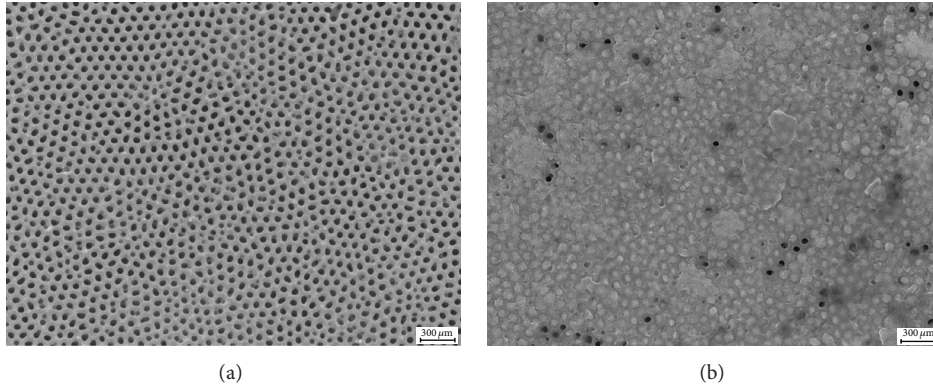


FIGURE 2: SEM images: (a) a porous alumina membrane with an ordering pore diameter of 80 nm and (b) zinc aluminum nanowire arrays fabricated in the alumina nanomold by the vacuum die casting process.

sensing characteristics. The present study combined both approaches mentioned above to fabricate a miniature metal oxide nanowire array sensor and apply it to the environmental monitor responding to oxygen. In addition, this study was also focused on changes of sensitivity of the gas sensor caused by factors such as chemical components, working temperature, and oxygen concentration.

## 2. Experimental Procedure

In this study, the metal oxide semiconductor gas sensor was carried out with a zinc aluminum oxide nanowire array incorporating a high surface area and aspect ratio.

Zinc aluminum oxide nanowires were fabricated using anodic aluminum oxide (AAO) as a template. The experimental procedure could be divided into four parts. First of all, an anodic alumina nanomold was obtained by etching a pure aluminum sheet with a purity of 99.7 wt.% in 0.3 M oxalic acid solution. Two steps of anode treatments were applied to obtain more uniform nanopores in this experiment. The first step of the anode treatment was carried out at a voltage 40 V and a temperature of 25°C for one hour. Afterward, removing alumina thin film from the surface of aluminum sheet was performed in the mixture of 6% phosphoric acid solution and 2% chromic acid solution at a temperature of 60°C. The second step of the anode treatment was carried out in the same process conditions indicated in the first step for 6 hours. Finally, aluminum substrate was removed using copper chloride solution and then the anodic alumina nanomold with a pore diameter of 80 nm could be obtained.

The second part of the procedure was the fabrication of zinc aluminum alloy by the vacuum melting method. The high purity of zinc and aluminum scraps were mixed and placed in a quartz glass tube. In order to prevent metal from oxidation during melting, the vacuum was extracted using a molecular turbo pump and kept at  $3 \times 10^{-6}$  torr. Then, the glass tube was placed in a furnace and the temperature was increased to 750°C for several minutes until all metal smelted and mixed well. After cooling, zinc aluminum alloy was obtained. More detailed process of the vacuum melting was described in our previous study [15, 16]. In this study, 3 zinc aluminum alloys with the different aluminum contents, 2%, 5%, and 10%, were prepared as listed in Table 1.

Furthermore, zinc aluminum alloy nanowire array was produced using the high vacuum die casting technique. A piece of zinc aluminum alloy and an alumina template were placed inside the chamber in which the vacuum pressure was maintained at  $10^{-6}$  torr. After the chamber was heated to 750°C, a hydraulic force was applied to the molten zinc aluminum alloy. During casting, the molten alloy was injected into the anodic alumina nanomold forming alloy nanowire array. The force required to introduce molten alloy into the nanomold is proportional to the surface tension of the melt. The surface tension of the molten zinc at 750°C is 719.7 dyne/cm and the surface tension of the molten aluminum at 750°C is 857.05 dyne/cm [17].

Therefore, the surface tension of the molten zinc aluminum alloy at 750°C can be calculated based on the alloy components. Additionally, the pressure for the molten metal injection into nanomold can be evaluated as follows [18]:

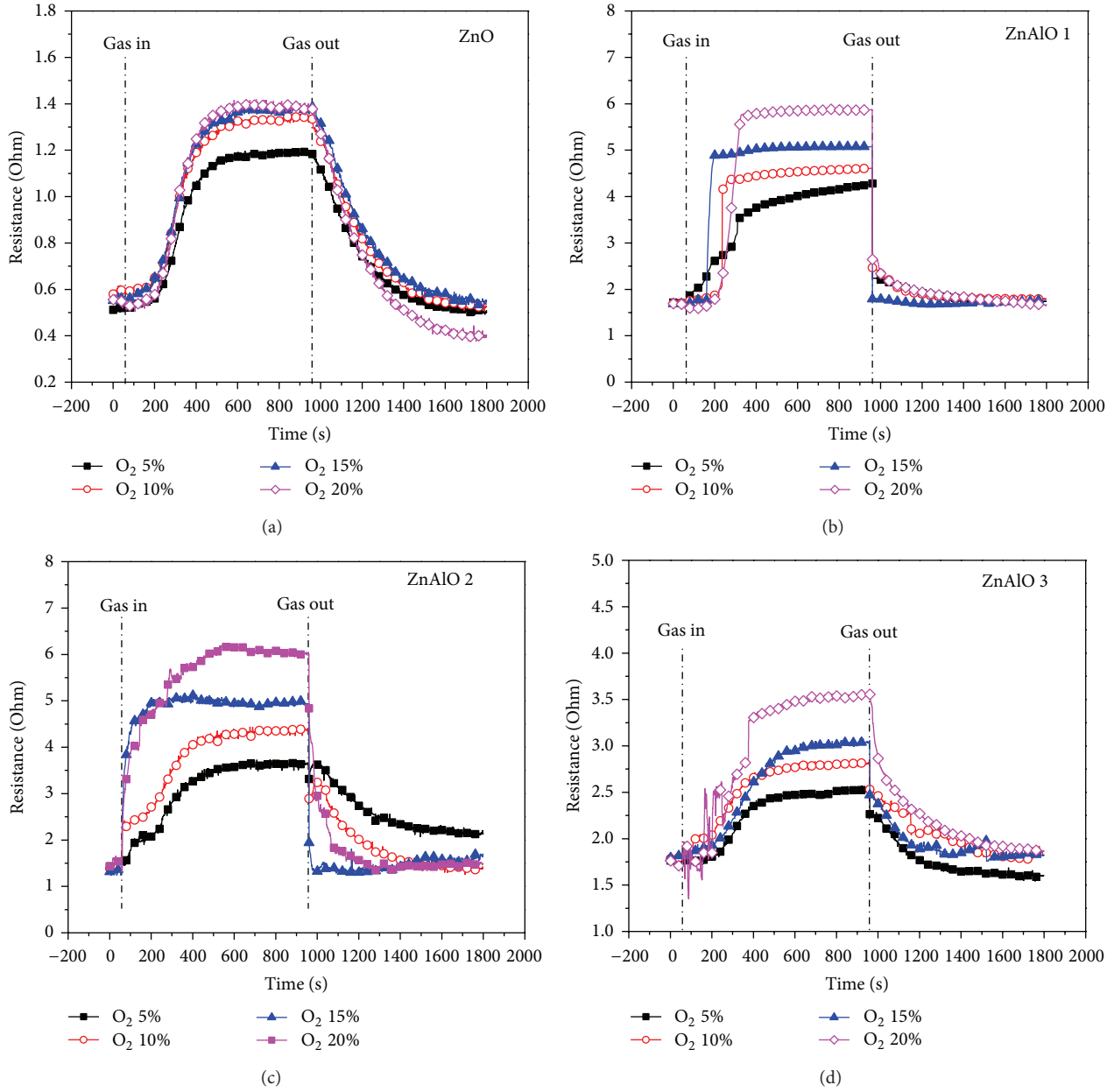


FIGURE 3: The effect of aluminum content on the resistance of zinc aluminum oxide gas sensor upon exposure to the various concentrations of oxygen at an operating temperature of 100°C.

TABLE 1: Al content, surface tension, and critical force to form nanowire of zinc-aluminum alloys prepared in this study.

Material	Aluminum content (wt.%)	Surface tension at 750°C (dyne/cm)	Critical force to form nanowire (dyne)	Alloy oxide
Zn-Al alloy1	2%	726.17	$3.01 \times 10^8$	ZnAlO 1
Zn-Al alloy2	5%	735.23	$2.96 \times 10^8$	ZnAlO 2
Zn-Al alloy3	10%	748.82	$2.92 \times 10^8$	ZnAlO 3

$P = F/A = -(2\gamma \cos \theta)/r$ , where  $F$  is the normal force,  $A$  is the area of the nanomold,  $r$  is the radius of the nanochannel,  $\gamma$  is the surface tension of the molten zinc aluminum alloy, and  $\theta$  is the contact angle between the melt and the porous alumina membrane. Therefore, the forces

required to inject the 3 molten zinc aluminum alloys into nanomolds are listed in Table 1. Solidification proceeded using a water cooling method at the bottom of the chamber. Zinc aluminum nanowire array was formed after cooling to room temperature. Finally, zinc aluminum oxide nanowire

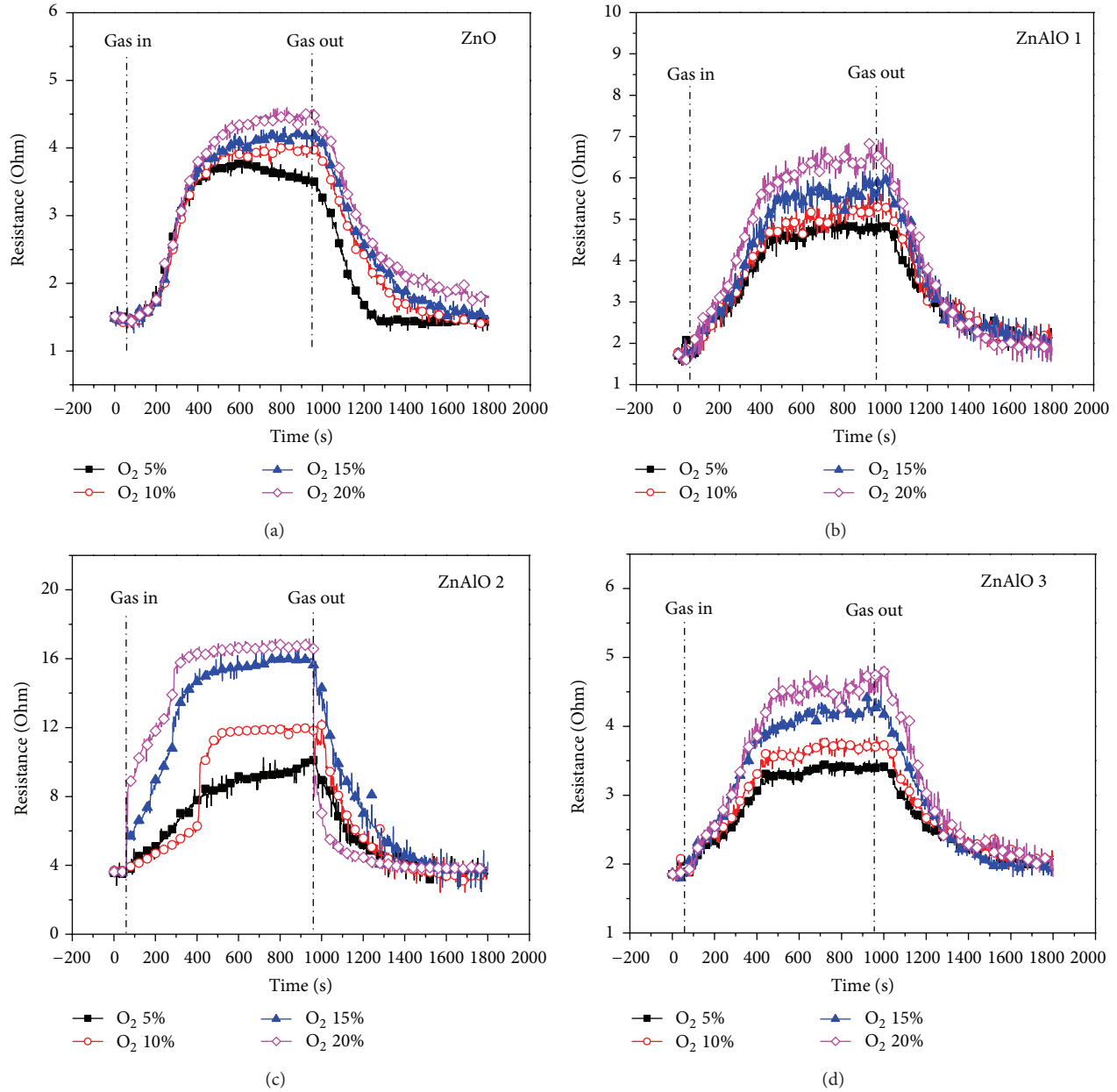


FIGURE 4: The effect of aluminum content on the resistance of zinc aluminum oxide gas sensor upon exposure to the various concentrations of oxygen at an operating temperature of 150°C.

TABLE 2: Element compositions of 3 zinc aluminum alloys prepared by the vacuum melting method.

Materials	Zn wt. %	Al wt. %
Zn-Al alloy1	97.96%	2.04%
Zn-Al alloy2	94.96%	5.04%
Zn-Al alloy3	89.71%	10.29%

array was fabricated through a thermal oxidation process. The nanowire array was put into an air furnace and a heat treatment at 250°C for 48 hours was applied to make all the

metal become metal oxide by reacting with oxygen and then zinc aluminum oxide nanowire array could be obtained.

Cu thin film was deposited at the top and bottom surface of zinc aluminum oxide nanowires array as the conductive layer of the gas sensor by vapor deposition technique. After that, aluminum oxide surrounding the nanowires was removed using sodium hydroxide solution. Figure 1 was the schematic diagram of zinc aluminum oxide nanowire array gas sensor produced in the present study.

The morphologies of the anodic alumina nanomold and zinc aluminum nanowire array were observed by scanning electron microscope. The gas sensing characteristics of zinc

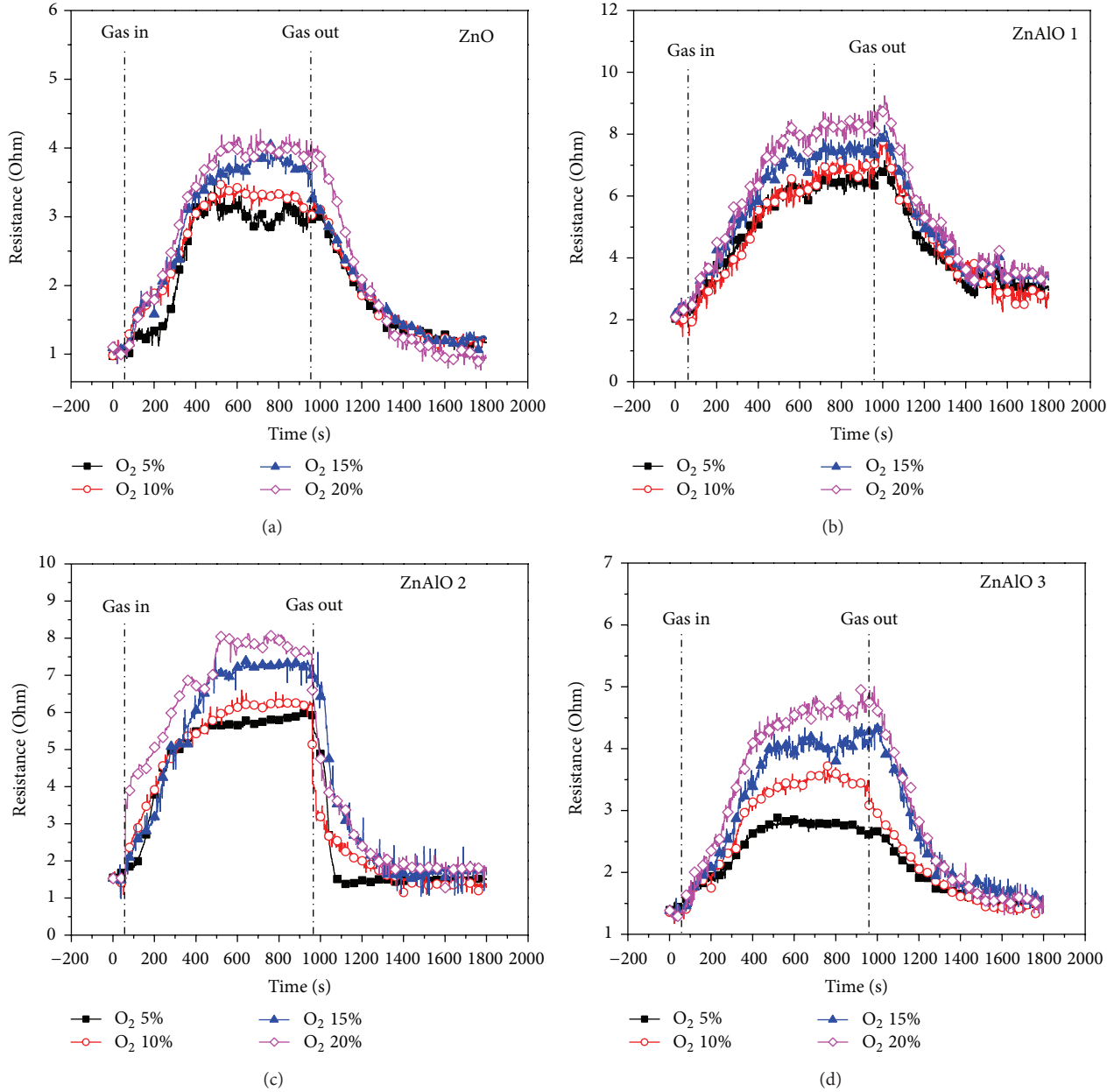


FIGURE 5: The effect of aluminum content on the resistance of zinc aluminum oxide gas sensor upon exposure to the various concentrations of oxygen at an operating temperature of 200°C.

aluminum oxide gas sensor were measured by the self-designed gas sensor test system.

### 3. Results and Discussion

An anodic alumina nanomold was produced by etching a pure aluminum sheet with a purity of 99.7 wt.% in 0.3 M oxalic acid solution for 6 hours. Figure 2(a) provided SEM image of the anodic aluminum nanomold with the pore diameter of 80 nm and an ordered and uniform array. The morphology of zinc aluminum nanowire array could be

observed in Figure 2(b). The composition of zinc aluminum alloy prepared by the vacuum melting method was detected by EDX analysis and presented in Table 2. The results were consistent with the design of the three zinc aluminum alloys.

Zinc oxide is a typical n-type semiconductor gas sensing material with direct band gap of about 3.37 eV at room temperature [19]. An n-type semiconductor material means that the majority of charge carriers are electrons, and an increase in conductivity occurs when the material interacts with a reducing gas. Conversely, reacting with an oxidizing gas would cause a decrease in conductivity. In this study, four nanowire array gas sensors (ZnO, ZnAlO 1, ZnAlO 2,

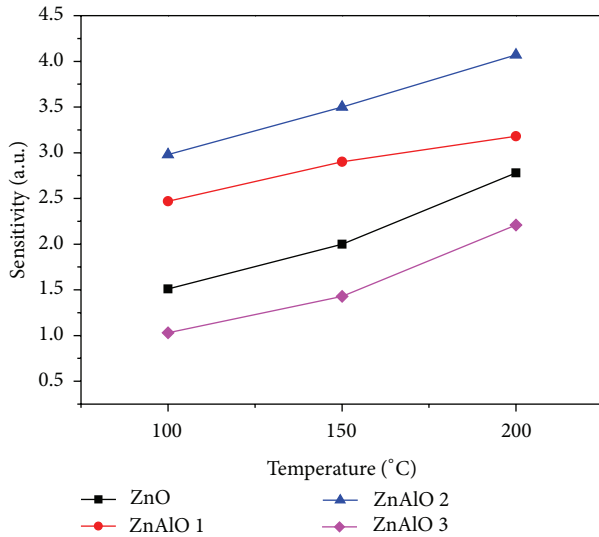


FIGURE 6: The operating temperature influence on the sensitivity of zinc aluminum oxide gas sensor upon exposure to oxygen 20 vol.%.

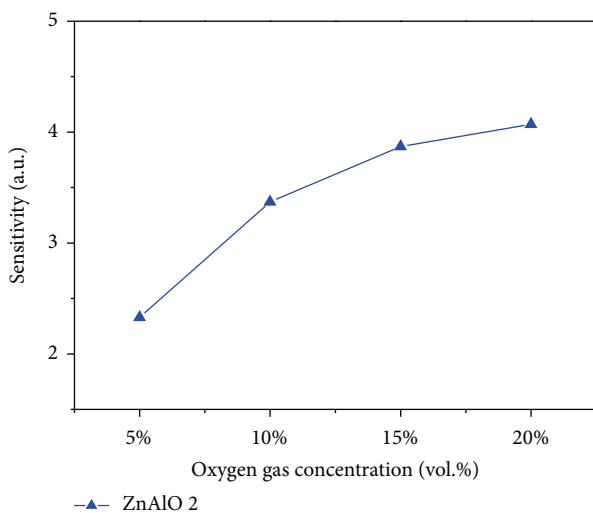


FIGURE 7: Oxygen concentration influence on the sensitivity of zinc aluminum oxide (ZnAlO 2) gas sensor at an operating temperature of 200°C.

and ZnAlO 3) were tested for the gas sensing properties and similar results were obtained as shown in Figures 3, 4, and 5. Figures 3–5 showed the time dependence of resistance of zinc aluminum oxide gas sensor on exposure to different concentrations of oxygen, 5%, 10%, 15%, and 20%. When oxygen was introduced into the measurement system, the resistance of zinc aluminum oxide gas sensor increased obviously. Based on the measurement results, zinc aluminum oxide nanowire array fabricated in this work had the same behavior as an n-type semiconductor. Besides, ZnAlO 2 had the better sensing properties, such as the change of the resistance after introduction of oxygen, the response time, and the recovery time, than other zinc aluminum oxide materials (ZnAlO 1 and ZnAlO 3) and zinc oxide.

Sensitivity ( $S$ ), an important parameter of gas sensors, can be defined as the ratio of the absolute difference between the stabilized resistances of gas sensors in the target gas and in the reference gas to the resistance in the reference gas, usually the dry air:  $S = |R_{\text{air}} - R_{\text{gas}}|/R_{\text{air}}$  [20].  $R_{\text{gas}}$  stands for the resistance of the gas sensor in the target gas and  $R_{\text{air}}$  means the resistance of the gas sensor in air. Sensitivities of four gas sensors on exposure to the same concentration of oxygen (20%) at various operating temperatures were shown in Figure 6. The results indicated that the sensitivity was highly correlated with the operating temperature and all gas sensors had the same tendency. The response of gas sensors to oxygen gas would be better at the higher operating temperature. It could also be seen that sensitivity of ZnAlO 2 gas sensor was significantly higher than those of the other three gas sensors. Furthermore, the effect of exposure to different concentrations of oxygen for ZnAlO 2 gas sensor was shown in Figure 7. The sensitivity of the gas sensor to oxygen increased with the concentration of oxygen.

#### 4. Conclusions

A miniature n-type semiconductor gas sensor provided in this study was performed with the zinc aluminum oxide nanowire array. Using the vacuum die casting and thermal oxidation technique, zinc aluminum oxide nanowire whose diameter was 80 nm could be fabricated; moreover, the order, uniform, and large area of nanowire array was very suitable for the device manufacture. The gas sensing properties responding to oxygen of the zinc aluminum oxide gas sensor were investigated. According to the results of the gas sensing characteristics measurement, zinc aluminum oxide nanowire array prepared from the zinc aluminum alloy consisting of 94.96 wt.% zinc and 5.04 wt.% aluminum had the optimum sensing properties. The sensitivity of the zinc aluminum oxide gas sensor increased with the operating temperature or the introduced oxygen concentration.

#### Conflict of Interests

The authors declare that there is no declare of interests regarding the publication of this paper.

#### Acknowledgments

The authors acknowledge the financial support of NSC 102-3113-S-003-008-G and NSC 102-3113-S-262-001.

#### References

- [1] G. Eranna, B. C. Joshi, D. P. Runthala, and R. P. Gupta, "Oxide materials for development of integrated gas sensors—a comprehensive review," *Critical Reviews in Solid State and Materials Sciences*, vol. 29, no. 3-4, pp. 111–188, 2004.
- [2] G. F. Fine, L. M. Cavanagh, A. Afonja, and R. Binions, "Metal oxide semi-conductor gas sensors in environmental monitoring," *Sensors*, vol. 10, no. 6, pp. 5469–5502, 2010.
- [3] N. Yamazoe, K. Suematsu, and K. Shimano, "Gas reception and signal transduction of neat tin oxide semiconductor sensor for

- response to oxygen," *Thin Solid Films*, vol. 548, pp. 695–702, 2013.
- [4] R. K. Meruva and M. E. Meyerhoff, "Catheter-Type sensor for potentiometric monitoring of oxygen, pH and carbon dioxide," *Biosensors and Bioelectronics*, vol. 13, no. 2, pp. 201–212, 1998.
- [5] K. Sadek and W. Moussa, "Studying the effect of deposition conditions on the performance and reliability of MEMS gas sensors," *Sensors*, vol. 7, no. 3, pp. 319–340, 2007.
- [6] S. Sharma and M. Madou, "Review article: a new approach to gas sensing with nanotechnology," *Philosophical Transactions of the Royal Society A*, vol. 370, no. 1967, pp. 2448–2473, 2012.
- [7] C. Wang, L. Yin, L. Zhang, D. Xiang, and R. Gao, "Metal oxide gas sensors: sensitivity and influencing factors," *Sensors*, vol. 10, no. 3, pp. 2088–2106, 2010.
- [8] G. Korotcenkova and B. K. Cho, "Instability of metal oxide-based conductometric gas sensors and approaches to stability improvement (short survey)," *Sensors and Actuators B*, vol. 156, no. 2, pp. 527–538, 2011.
- [9] A. Wisitsoraat, A. Tuantranont, E. Comini, G. Sberveglieri, and W. Wlodarski, "Characterization of n-type and p-type semiconductor gas sensors based on NiO<sub>x</sub> doped TiO<sub>2</sub> thin films," *Thin Solid Films*, vol. 517, no. 8, pp. 2775–2780, 2009.
- [10] X. Huang, F. Meng, Y. Sun, and J. Liu, "Study of factors influencing dynamic measurements using SnO<sub>2</sub> gas sensor," *Sensors and Materials*, vol. 17, no. 1, pp. 29–38, 2005.
- [11] G. Korotcenkov, S.-D. Han, B. K. Cho, and V. Brinzari, "Grain size effects in sensor response of nanostructured SnO<sub>2</sub>- and In<sub>2</sub>O<sub>3</sub>-based conductometric thin film gas sensor," *Critical Reviews in Solid State and Materials Sciences*, vol. 34, no. 1-2, pp. 1–17, 2009.
- [12] S. Aygün and D. Cann, "Hydrogen sensitivity of doped CuO/ZnO heterocontact sensors," *Sensors and Actuators B*, vol. 106, no. 2, pp. 837–842, 2005.
- [13] A. Rothschild and Y. Komem, "The effect of grain size on the sensitivity of nanocrystalline metal-oxide gas sensors," *Journal of Applied Physics*, vol. 95, no. 11 I, pp. 6374–6380, 2004.
- [14] G. N. Chaudhari, D. R. Bambole, A. B. Bodade, and P. R. Padole, "Characterization of nanosized TiO<sub>2</sub> based H<sub>2</sub>S gas sensor," *Journal of Materials Science*, vol. 41, no. 15, pp. 4860–4864, 2006.
- [15] C.-G. Kuo, H. Chang, L.-R. Hwang et al., "Fabrication of a Pb-Sn nanowire array gas sensor using a novel high vacuum die casting technique," *Electronic Materials Letters*, vol. 9, no. 4, pp. 481–484, 2013.
- [16] J.-H. Chen, S.-C. Lo, C.-G. Chao, and T.-F. Liu, "Microstructure and properties of Pb nanowires fabricated by casting," *Japanese Journal of Applied Physics*, vol. 47, no. 6, pp. 4815–4819, 2008.
- [17] I. S. Grigoriev and E. Z. Meilikhov, *Handbook of Physical Quantities*, CRC Press, Boca Raton, Fla, USA, 1997.
- [18] Z. Zhang, J. Y. Ying, and M. S. Dresselhaus, "Bismuth quantum-wire arrays fabricated by a vacuum melting and pressure injection process," *Journal of Materials Research*, vol. 13, no. 7, pp. 1745–1748, 1998.
- [19] S. K. Arya, S. Saha, J. E. Ramirez-Vick, V. Gupta, S. Bhansali, and S. P. Singh, "Recent advances in ZnO nanostructures and thin films for biosensor applications: review," *Analytica Chimica Acta*, vol. 737, pp. 1–21, 2012.
- [20] S. K. Gupta, A. Joshi, and K. Manmeet, "Development of gas sensors using ZnO nanostructures," *Journal of Chemical Sciences*, vol. 122, no. 1, pp. 57–62, 2010.

## Research Article

# Characterization of the Organic Thin Film Solar Cells with Active Layers of PTB7/PC<sub>71</sub>BM Prepared by Using Solvent Mixtures with Different Additives

Masakazu Ito,<sup>1</sup> Kumar Palanisamy,<sup>1</sup> Abhirami Kumar,<sup>1</sup> Vijay Srinivasan Murugesan,<sup>1</sup> Paik-Kyun Shin,<sup>2</sup> Norio Tsuda,<sup>1</sup> Jun Yamada,<sup>1</sup> and Shizuyasu Ochiai<sup>1</sup>

<sup>1</sup> Department of Electrical Engineering, Aichi Institute of Technology, Toyota, Aichi 470-0392, Japan

<sup>2</sup> Department of Electrical Engineering, Inha University, 100 Inha-ro, Nam-gu, Incheon 402-751, Republic of Korea

Correspondence should be addressed to Shizuyasu Ochiai; [ochiai@aitech.ac.jp](mailto:ochiai@aitech.ac.jp)

Received 11 April 2014; Revised 21 May 2014; Accepted 22 May 2014; Published 10 June 2014

Academic Editor: Mohammad Yusri Hassan

Copyright © 2014 Masakazu Ito et al. This is an open access article distributed under the Creative Commons Attribution License, which permits unrestricted use, distribution, and reproduction in any medium, provided the original work is properly cited.

Organic thin film solar cells (OTFSCs) were fabricated with blended active layers of poly[[4,8-bis((2-ethylhexyl)oxy)benzo[1,2-b:4,5-b']dithiophene-2,6-diyl][3-fluoro-2-[(2-ethylhexyl)carbonyl]thieno[3,4-b]thiophenediyl]] (PTB7)/[6,6]-phenyl-C<sub>71</sub>-butyric (PC<sub>71</sub>BM). The performances of active layers are prepared in chlorobenzene (CB) with different additives of 1-chloronaphthalene (CN) and 1,8-Diiodooctane (DIO) by a wet process with spin coating technique. The effects of different solvent additives on photovoltaic parameters such as fill factor, short circuit current density, and power conversion efficiency of active layers are reported. The absorption and surface morphology of the active layers are investigated using UV-visible spectroscopy and atomic force microscopy, respectively. The results indicate that structural and morphological changes were induced by the additives with solvent. The current density-voltage (*J-V*) characteristics of photovoltaic cells were measured under the illumination of simulated solar light with 100 mW/cm<sup>2</sup> (AM 1.5 G) by an Oriel 1000 W solar simulator. The OTFSCs of PTB7/PC<sub>71</sub>BM prepared with organic solvent additives of DIO+CN show more improved PCE of 4.96% by spin coating method.

## 1. Introduction

Recently, a great paradigm shift has occurred in the generation and consumption of energy. The so-called “clean” energy is consequently an utmost critical issue for all the nations and entire civilized societies. In the 34th G8 Toyako summit, it has been decided to cut the carbon emission up to 50% by the year 2050 [1], and realization of the “low-carbon-society” has been worked towards on global level. Moreover, the recent “Great East Japan Earthquake” has aroused a great attention to severe riskiness of nuclear power, so that recommencement of electricity generation by the nuclear power and construction of new nuclear power plant are rather reluctant. Consequently, a large scale electricity generation by new and renewable energy source has been raised as an urgent issue [2]. It has been reported [3] that electricity generation in Japan in November, 2012, was comprised of 2.7% from

nuclear power, 90.6% from fossil fuel, 6.2% from hydraulic power, and only 0.6% from new energy source, respectively, and the portion of renewable energy was still in the minute level of 10%. All of those kinds of situations have caused a critical status in Japan in terms of supply and demand of energy. Therefore, the Japanese government has devised a target in the general energy planning, aiming for elevating the proportion of “zero-emission-power source” up to 70% by the year 2030, so that introduction of the new and renewable energy source should be accelerated as fast as possible [4].

Solar light power generation could have a promising possibility for contributing to elevate the self-sufficiency of energy needs by domestic energy resource in Japan. It has been planned, therefore, that the mass of introduction for solar light power generation should be raised by ten times by the year 2020 and forty times by the year 2030. Additionally, an innovative solar light power generation is

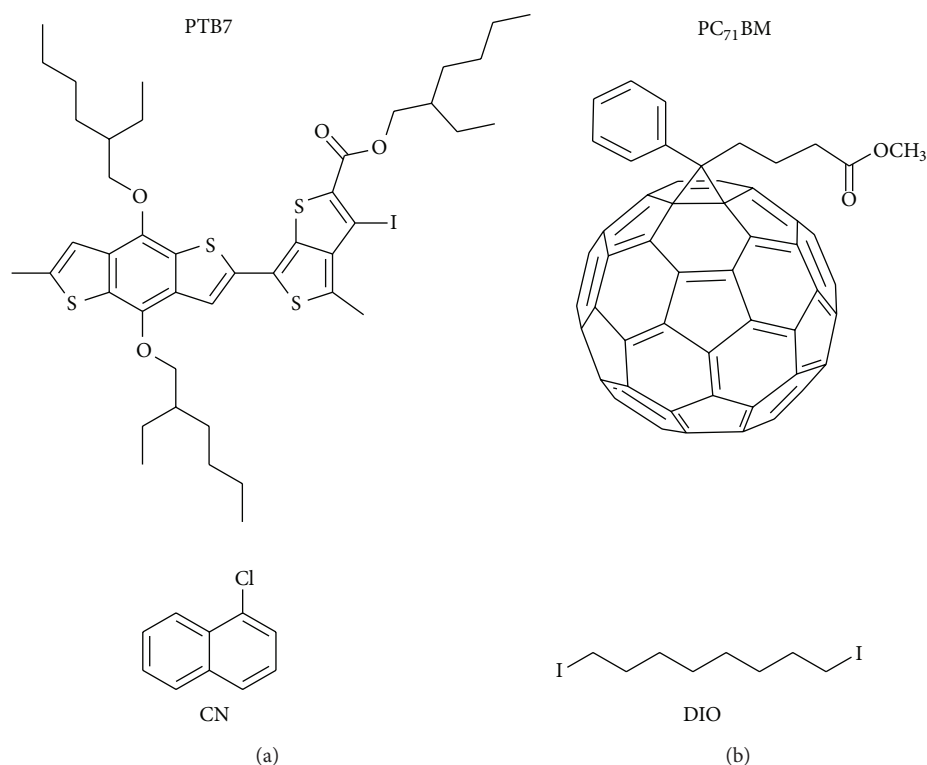


FIGURE 1: Molecular structures of PTB7, PC<sub>71</sub>BM, CN, and DIO.

aimed by establishing a sophisticated technology of solar cell through usage of new materials and device structure, so that power generation efficiency of over 40% and power generation cost of 7 Yen/kWh should be achieved after the year 2030 [5].

First-generation solar cells based on Si have demerits of high cost and limitation of installing location due to heavy weight. Second-generation solar cells based on inorganic compounds (amorphous/poly crystalline Si and CIGS) have been introduced in commercial market. Although second-generation solar cells show still relatively inferior power conversion efficiency, they are advantageous from a cost perspective. It is acutely expected for third-generation solar cells that they would have improved power conversion efficiency of over 40% and a merit of low cost comparable to those of the second-generation solar cells. Generally, organic thin film solar cells (OTFSCs) are acknowledged that they are lighter than any other counterparts and suitable for low-cost fabrication [6–9]. OTFSC materials have been focused towards the energy-consumption and environment friendly viewpoint. Recently, power conversion efficiency of the OTFSCs has been improved up to 10–11% [8–10]. Moreover, they could be formed to any shape due to flexible characteristic, so that they could be optimized for portable and/or wearable application [5]. Similar to the case of liquid crystal displays (LCDs) [11], light emitting diodes (LEDs), inorganic solar cells, and organic light emitting diodes (OLEDs) are based on similar materials and structures to those of OTFSCs. Recent rapid commercialization of the OLEDs is mainly concentrated on mobile display applications [12], but it is expected that

the market for OLEDs could be expanded in the near future to large-size TVs and lighting applications. The success of the OLEDs has motivated vigorous developments of OTFSCs based on devices and related materials [13].

In this present work, we report the performance of PTB7/PC<sub>71</sub>BM based OTFSCs prepared in chlorobenzene (CB) solvent with different additives. The active layers of PTB7/PC<sub>71</sub>BM were prepared by wet processes with spin coating technique. Organic solvent additives were varied to prepare the organic active layer, and the effect of the solvent additives was investigated in relation to surface topology of PTB7, PC<sub>71</sub>BM, and PTB7/PC<sub>71</sub>BM thin films. The performance of the resulting OTFSC devices and surface topology of the active layers were comparatively discussed.

## 2. Experimental Procedure

Active layers of organic thin film solar cell device were prepared using Poly[[4,8-bis[(2-ethylhexyl)oxy]benzo[1,2-b:4,5-b']dithiophene-2,6-diyl][3-fluoro-2-[(2-ethylhexyl)carbonyl]thieno[3,4-b]thiophenediyl]] (PTB7), as organic electron donor material, and [6,6]-Phenyl C<sub>71</sub> butyric acid methyl ester (PC<sub>71</sub>BM) used as electron acceptor material. Figure 1 shows the molecular structure of the PTB7, PC<sub>71</sub>BM, 1-chloronaphthalene (CN), and 1,8-Diiodooctane (DIO). PC<sub>71</sub>BM is an organic material chemically modified to be dissolved in an organic solvent. To enhance the hole transport characteristic, a thin film of

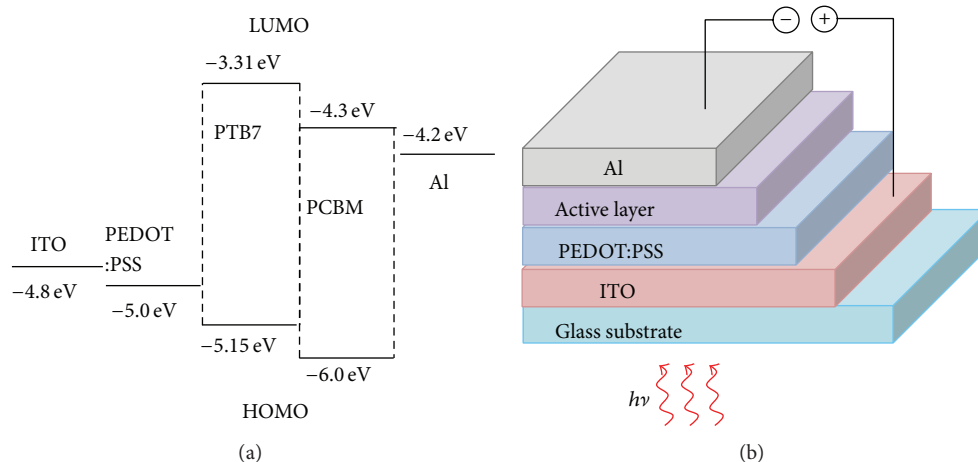


FIGURE 2: Schematics of the (a) energy band structure of the OTFSC with hole transfer layer of PEDOT:PSS and blended active layer of PTB7:PC<sub>71</sub>BM and (b) cross section view of OTFSC device.

poly(3,4-ethylenedioxythiophene):poly(styrenesulfonate) [PEDOT:PSS] was prepared by using a commercially available material of PH1000 (Heraeus Clevios), which serves as a hole transfer layer interfaced with the anode and electron donor layer of PTB7. While many organic materials could only be dissolved in organic solvents, PEDOT:PSS could be dissolved in water, and it could be easily used in wet process to prepare thin films. Moreover, PEDOT:PSS would serve for planarization of the unevenness on the ITO substrate surface as well as to enhance the interface characteristic of anode substrate and thin film.

As for the process to prepare the thin film components of OTFSC device, a spin coating technique was adopted for compatibility to large-area-sized device fabrication. Firstly, indium tin oxide (ITO) coated glass substrates were cleaned ultrasonically in a sequential step by using a neutral detergent, distilled water, acetone, and ethanol for 10 min, respectively. The cleaned substrates were exposed to UV in vacuum for 30 min, aiming for a hydrophilic state of the treated ITO substrates. Then hole transfer layer of PEDOT:PSS thin film was prepared on the substrate by spin coating technique: rotation speed of 5000 rpm and rotating time of 30 s. The PEDOT:PSS thin film was then annealed for 15 min at a temperature of 140°C. Composite organic active layers of PTB7:PC<sub>71</sub>BM with a relative ratio of 1:1.5 were deposited also by spin coating technique, where different organic solvents were used to prepare the precursor solutions: (1) 2 mL of pristine chlorobenzene (CB), (2) 2 mL of CB added with an additive of DIO (3 v%), (3) 2 mL of CB added with an additive of CN (3 v%), and (4) 2 mL of CB added with DIO (3 v%) and CN (3 v%). The PTB7:PC<sub>71</sub>BM (9 mg:13.5 mg) was dissolved in each organic solvent mixture and the spin coating process was carried out with a rotation speed of 800 rpm and rotation time of 60 s. The thickness of the active layer was ~86 nm, as measured using a Dektak II profilometer. Aluminum (Al) electrode (~100 nm) for the organic thin film solar cell device was then prepared by a thermal vacuum evaporation through a shadow mask in a high vacuum of

$1.3 \times 10^{-4}$  Pa and the effective area of the resulting device was 9 mm<sup>2</sup>.

The organic thin film solar cell device presented in this report is based on an electron donor layer of PTB7 with deep highest occupied molecular orbital (HOMO) level and low band gap interfaced with a fullerene derivative of PC<sub>71</sub>BM as a representative electron acceptor. Figure 2 shows a schematic of energy band diagram and device structure of the OTFSC. Performance of the OTFSC device was investigated by measuring the current density-voltage (*J-V*) characteristics in a solar simulator illuminated by a light source of Xn lamp combined with an air mass filter: 100 mW/cm<sup>2</sup>, AM 1.5. A shadow mask made of a thick black sheet was placed in front of the active device area in order to avoid the overestimation of the current density and power conversion efficiency. All measurements were carried out in air without any encapsulation.

As shown in Figure 2, PTB7 has the lowest unoccupied molecular orbital (LUMO) level of -3.31 eV and a HOMO level of -5.15 eV. It is generally acknowledged that P3HT has a LUMO level of -2.9 eV and HOMO level of -5.0 eV [14, 15]. It could be expected that PTB7 would reveal relatively narrow band gap and excellent light absorption characteristic. In addition, open circuit voltage of the OTFSC with PTB7:PC<sub>71</sub>BM would be similar to that of the OTFSC with P3HT:PCBM [16].

### 3. Results and Discussions

**3.1. Current Density- (*J*-) Voltage (*V*) Characteristics.** The current density-voltage (*J-V*) characteristics of OTFSC devices were measured under the illumination of simulated solar light with 100 mW/cm<sup>2</sup> (AM 1.5G) by an Oriel 1000 W solar simulator. *J-V* characteristics of the four different OTFSC devices based on blended active layer of PTB7:PC<sub>71</sub>BM are presented in Figure 3. Photovoltaic parameters of the four different OTFSC devices along with series resistance (*R<sub>s</sub>*)

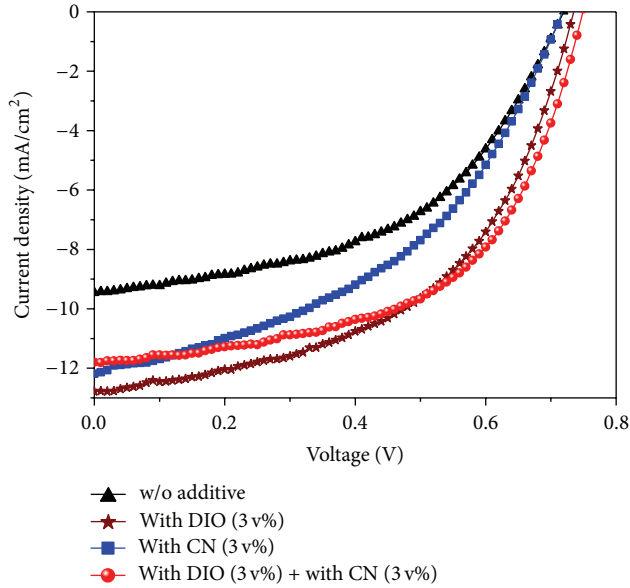


FIGURE 3:  $J$ - $V$  characteristics of the four different organic thin film solar cell devices based on blended active layer of PTB7:PC<sub>71</sub>BM prepared with different organic solvent mixture.

and shunt resistance ( $R_{sh}$ ) are given in Table 1: short circuit current density ( $J_{sc}$ ), open circuit voltage ( $V_{oc}$ ), fill factor (FF), and power conversion efficiency (PCE;  $\eta$ ).

The OTFSC of PTB7/PC<sub>71</sub>BM prepared with pristine organic solvent of CB reveals a PCE of 3.38%, which is distinctively lower than those of the OTFSC of PTB7/PC<sub>71</sub>BM prepared with organic solvent of CB with additives [6, 7, 17, 18]. On the other hand, the OTFSC of PTB7/PC<sub>71</sub>BM prepared with organic solvent of CB with additive of DIO (3 v%) shows high PCE of 4.89%. It may be attributed to the formation of interpenetrating network with better morphology by the addition of DIO, which decrease the series resistance and enhance the charge carrier transport properties, as well as increase of equivalent parallel resistance due to suppression of charge carrier recombination in the active layer. The OTFSC of PTB7/PC<sub>71</sub>BM prepared with organic solvent of CB with additive of CN (3 v%) shows a moderately improved PCE of 3.86% with low FF of 0.443. An additive of DIO with high boiling point (b.p.) of 169°C could influence the formation of nanoscale morphology of molecules, decrease of  $R_s$ , and increase of shunt resistance ( $R_{sh}$ ) due to suppression of hole-electron recombination. However, relatively higher b.p. of the CN (263°C) than that of the DIO might have resulted in a moderate formation of the nanomorphology of molecules. In the device prepared with CB+CN, the  $R_s$  is increased and  $R_{sh}$  is decreased. The decrease in  $R_{sh}$  is attributed to the leakage current induced by pinholes and traps in the active layer morphology and the increase in  $R_s$  is due to recombination loss. Therefore, FF of the device is reduced as consequences of both  $R_{sh}$  and  $R_s$ . The OTFSC of PTB7/PC<sub>71</sub>BM prepared with organic solvent additives of DIO+CN shows more improved PCE of 4.96%, which implies that the effect of the additive of DIO is dominant for enhancement of the device performance through better intermixing between PTB7 and PC<sub>71</sub>BM.

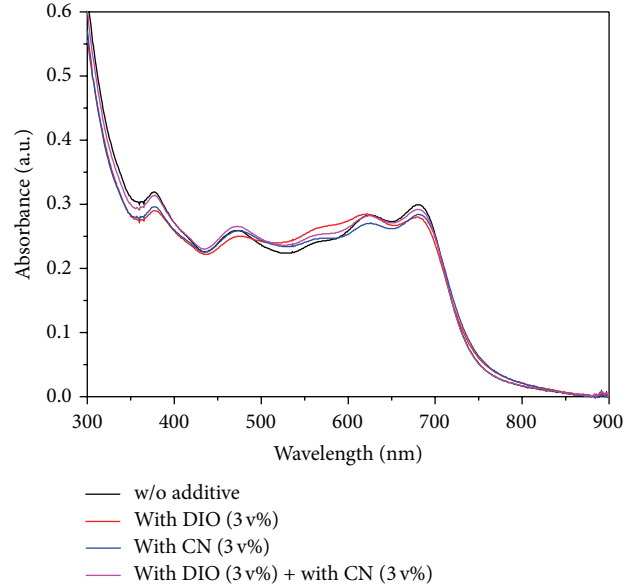


FIGURE 4: UV/Vis spectra of four different organic active layers of PTB7/PC<sub>71</sub>BM prepared with different organic solvent mixture.

The increase in FF (0.556) originates from the reduction in  $R_s$  by the additives of DIO+CN. Because of the smaller  $R_s$  and higher  $R_{sh}$ , the FF of the OTFSC prepared with DIO+CN additives was higher than that of the OTFSC prepared with DIO and OTFSC prepared with CN additives.

**3.2. Absorption and Atomic Force Microscopy Studies.** Absorption characteristic of four different organic active layers of PTB7/PC<sub>71</sub>BM was investigated by UV/Vis spectrophotometer and depicted in Figure 4. It can be seen that there is no shift of the absorption peak for the samples prepared with organic additives from that of the sample prepared with pristine CB. It indicates that the thin films prepared with additives have amorphous phase. Topology of the organic active layers was investigated by atomic force microscopy (AFM). The thin films of PTB7 were prepared by using the three varieties of organic solvent mixture: (1) PTB7 with pristine CB, (2) PTB7 with CB and DIO (3 v%), and (3) PTB7 with CB and CN (3 v%). Figure 5 shows the AFM images, and roughness parameters obtained from the AFM analysis are given in Table 2: peak-to-valley value and room-mean-square value. All the three samples show a minute formation of micrograins (Figure 5) and root-mean-square roughness of one-nanometer level. It indicates again that the thin films do not show any crystalline nature.

Effects of the organic solvent on the surface morphology of the PC<sub>71</sub>BM thin films were also investigated by AFM. Figure 6 shows the AFM images of the PC<sub>71</sub>BM thin films prepared by using pristine organic solvent of CB, CB with additive of DIO (3 v%), and CB with additive of CN (3 v%), respectively. Surface roughness parameters obtained from the AFM analysis are presented in Table 3: peak-to-valley value and root-mean-square value. All the PC<sub>71</sub>BM thin films (Table 3) reveal distinctively smaller parameters of surface

TABLE 1: Photovoltaic parameters of the four different organic thin film solar cell devices based on blended active layer of PTB7:PC<sub>71</sub>BM prepared with different organic solvent mixture.

PTB7:PC <sub>71</sub> BM in organic solvent mixture	$J_{sc}$ [mA/cm <sup>2</sup> ]	$V_{oc}$ [V]	FF	PCE( $\eta$ ) [%]	$R_s$ [ $\Omega$ ]	$R_{sh}$ [ $\Omega$ ]
CB without additive	9.46	0.72	0.496	3.38	167	3163
CB with DIO (3 v%)	12.78	0.74	0.516	4.89	74	3304
CB with CN (3 v%)	12.11	0.72	0.443	3.86	133	2256
CB with DIO (3 v%)+CN (3 v%)	11.90	0.75	0.556	4.96	63	5035

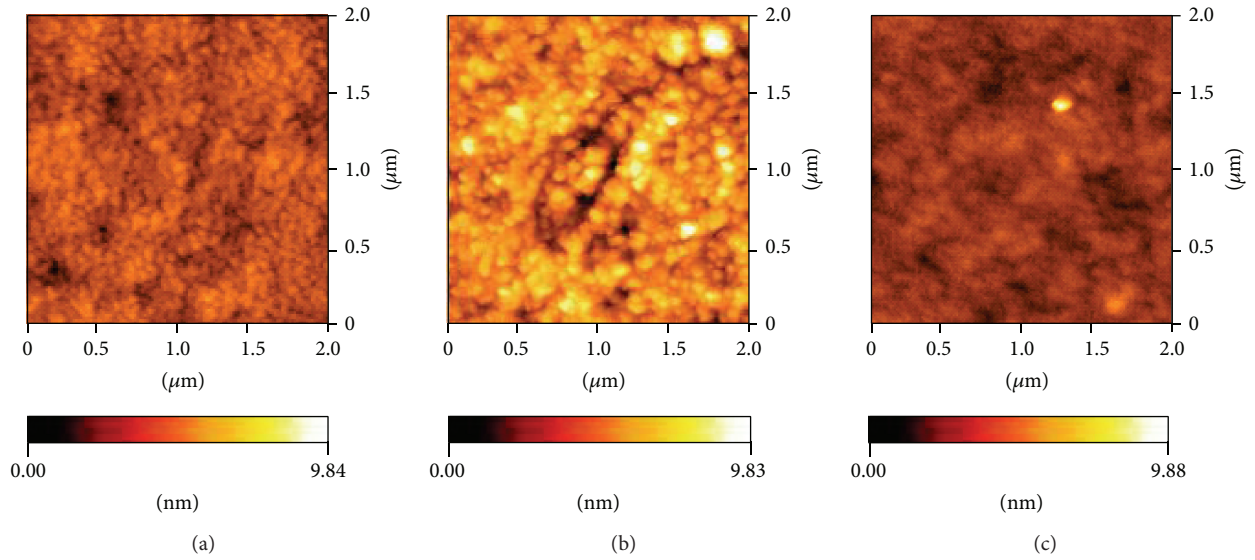


FIGURE 5: AFM images of the PTB7 thin films prepared with (a) pristine CB, (b) CB and additive of DIO (3 v%), and (c) CB and additive of CN (3 v%).

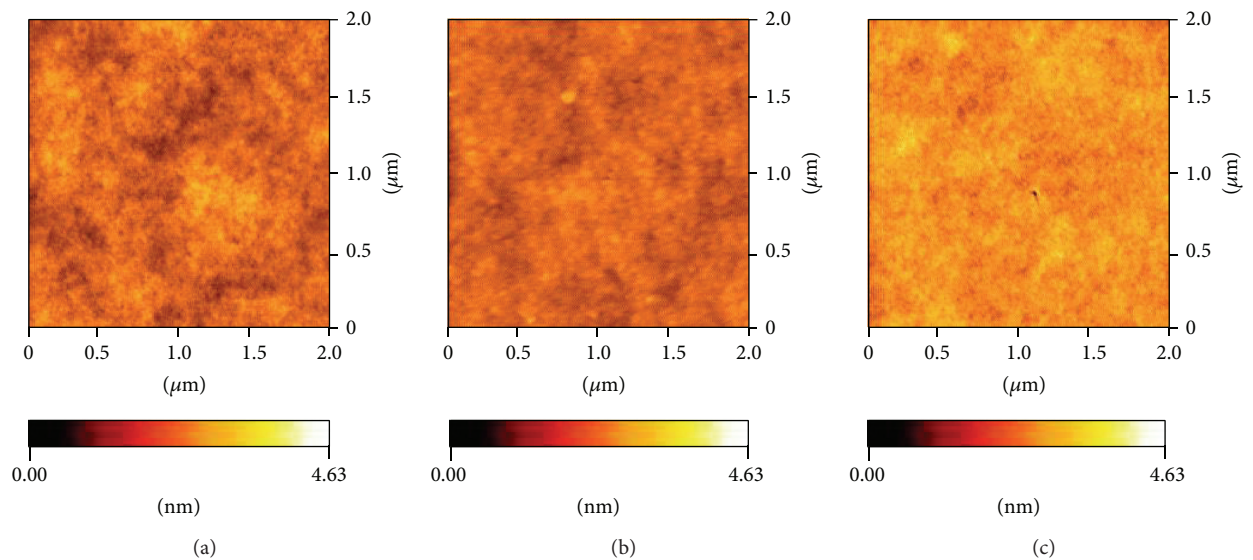


FIGURE 6: AFM images of the PC<sub>71</sub>BM thin films: (a) prepared with pristine CB, (b) prepared with CB and additive of DIO (3 v%), and (c) prepared with CB and additive of CN (3 v%).

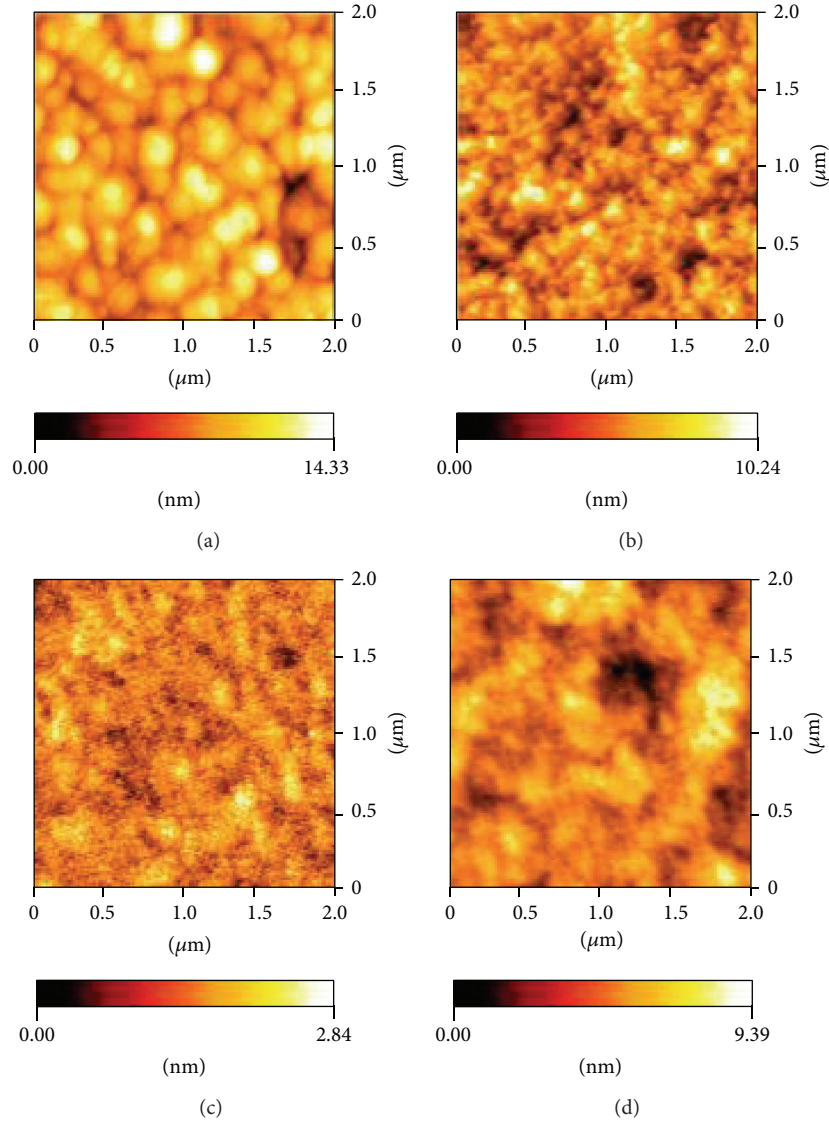


FIGURE 7: AFM images of the PTB7/PC<sub>71</sub>BM thin films: (a) prepared with pristine CB, (b) prepared with CB and DIO (3 v%), (c) prepared with CB and CN (3 v%), and (d) prepared with CB and DIO (3 v%)+CN (3 v%).

TABLE 2: Surface roughness parameters of the PTB7 thin films obtained from AFM analysis.

Layer	Peak-to-valley [nm]	Root-mean-square roughness [nm]
PTB7 with pristine CB	7.0	0.7
PTB7 with CB and DIO (3 v%)	12.7	1.5
PTB7 with CB and CN (3 v%)	9.3	0.6

roughness, which is quite different from the cases of PTB7 (Table 2). It can be observed (Figure 6) that PC<sub>71</sub>BM reveals excellent solubility in all the organic solvent mixtures of pristine CB, CB with additive of DIO (3 v%), and CB with additive of CN (3 v%) [19].

Finally, the effect of the organic solvent on the surface morphology of the resulting thin films of blended

TABLE 3: Surface roughness parameters of the PC<sub>71</sub>BM thin films obtained from AFM analysis.

Layer	Peak-to-valley [nm]	Root-mean-square roughness [nm]
PC <sub>71</sub> BM with pristine CB	3.4	0.4
PC <sub>71</sub> BM with CB and DIO (3 v%)	3.3	0.3
PC <sub>71</sub> BM with CB and CN (3 v%)	3.8	0.3

PTB7/PC<sub>71</sub>BM was investigated by AFM, which could play a decisive role in the performance of organic thin film solar cell. Figure 7 shows the surface topology of three different active layers of blended PTB7/PC<sub>71</sub>BM [14]. Surface roughness parameters of the PTB7:PC<sub>71</sub>BM prepared in CB

TABLE 4: Surface roughness parameters of the PTB7:PC<sub>71</sub>BM active layer obtained from AFM analysis.

Layer	Peak-to-valley [nm]	Root-mean-square roughness [nm]
PTB7:PC <sub>71</sub> BM with pristine CB	13.4	1.18
PTB7:PC <sub>71</sub> BM with CB and DIO (3 v%)	10.7	0.53
PTB7:PC <sub>71</sub> BM with CB and CN (3 v%)	11.8	0.72
PTB7:PC <sub>71</sub> BM with CB and DIO (3 v%) + CN (3 v%)	7.4	0.64

with different solvent additives are presented in Table 4. The PTB7/PC<sub>71</sub>BM thin film prepared by using pristine organic solvent of CB shows a large micrograin of 1  $\mu\text{m}$  (Figure 7(a)). It implies for the case that molecules of PTB7 and PC<sub>71</sub>BM might have insufficient mutual solubility during the thin film formation process, and a mutual interaction between the molecules might have an influence on such kind of thin film formation [20]. On the contrary, the PTB7/PC<sub>71</sub>BM thin film prepared with a mixture of CB and DIO (3 v%) reveals conspicuously smaller micrograins on the surface (Figure 7(b)). An interpenetrated blending through excellent percolation of micrograins might have been achieved for the molecules of PTB7 and PC<sub>71</sub>BM through the effect of organic solvent mixture of CB and DIO, which could be contributed to the distinctively enhanced PCE (4.89%) of the resulting OTFSC (Table 1) [6, 17]. The PTB7/PC<sub>71</sub>BM thin film prepared with a mixture of CB and CN (3 v%) (Figure 7(c)) shows smaller micrograins similar to the case of PTB7/PC<sub>71</sub>BM thin film prepared with a mixture of CB and DIO (3 v%) (Figure 7(b)), but it reveals an inferior connectivity between the micrograins. It might be a reason why the OTFSC prepared with a mixture of CB and CN (3 v%) reveals a moderate PCE of 3.86%, which is distinctively lower than that of the OTFSC with PTB7/PC<sub>71</sub>BM prepared with a mixture of CB and DIO, although it is rather higher than the OTFSC with PTB7/PC<sub>71</sub>BM prepared with pristine CB. The OTFSC of PTB7/PC<sub>71</sub>BM was prepared with organic solvent (CB) with additives of CN + DIO (3 v%), and the addition of DIO might have resulted in a moderate formation of the nanomorphology of molecules (Figure 7(d)), which implies that the PCE of the OTFSC further improved to 4.96%. The effect of the additive of DIO is dominant for enhancement of the device performance, so that it is similar to that of the OTFSC of PTB7/PC<sub>71</sub>BM prepared with organic solvent mixture of CB and DIO.

#### 4. Conclusions

The OTFSC devices were fabricated with blended active layers of PTB7/PC<sub>71</sub>BM with a relative ratio of 1:1.5. The active layers of PTB7/PC<sub>71</sub>BM were prepared by a spin coating process with four different kinds of organic solvents: (1) pristine CB, (2) CB with additive of DIO (3 v%), (3) CB with additive of CN (3 v%), and (4) CB with additives of DIO

(3 v%)+CN (3 v%). Solubility of the PTB7 and PC<sub>71</sub>BM in the organic solvent mixtures was investigated by surface topology of the resulting thin films through AFM images. PC<sub>71</sub>BM revealed excellent solubility in the organic solvent of pristine CB as well as in mixtures solvents of CB/DIO, CB/CN, and CB/DIO+CN. For the case of pristine CB, the resulting composite thin film of PTB7/PC<sub>71</sub>BM revealed relatively large micrograins of 1  $\mu\text{m}$  on the surface, which indicates an inferior mutual solubility and insufficient interpenetration of PTB7 and PC<sub>71</sub>BM in the organic solvent of CB. Conspicuously smaller micrograins of one-tenth level were observed for the PTB7/PC<sub>71</sub>BM thin film prepared with organic solvent mixture of CB and DIO (3 v%), which is possibly caused by improved percolation between PTB7 and PC<sub>71</sub>BM due to the effect of DIO. Consequently, PCE of 4.89% was achieved for the resulting OTFSC based on the interpenetrated active layer of PTB7/PC<sub>71</sub>BM prepared with organic solvent mixture of CB and DIO. Enhanced transport of charge carriers might have been achieved through formation of nanomorphology in the blended active layer of PTB7/PC<sub>71</sub>BM due to the effect of DIO added in organic solvent of CB. Although the PTB7/PC<sub>71</sub>BM prepared with organic solvent mixture of CB and CN (3 v%) showed improved nanomorphology compared to the sample prepared with pristine CB, sufficient connectivity of the micrograins might not be achieved, which could be resulted in suppression of charge-carrier transport. The moderate increase of PCE up to 3.86% might have been caused by the effect of organic solvent mixture of CB with CN. However, the OTFSC of PTB7/PC<sub>71</sub>BM prepared with organic solvent additives of DIO + CN shows formation of the intermixed nanomorphology, which implies that the PCE of the OTFSC further improved to 4.96% by spin coating method.

#### Conflict of Interests

The authors declare that there is no conflict of interests regarding the publication of this paper.

#### Authors' Contribution

Masakazu Ito and Palanisamy Kumar contributed equally to this work.

#### Acknowledgments

This research was partly supported by the MEXT-Supported Program for the Strategic Research Foundation at Private Universities (2010-2014) and the joint research between Aichi Institute of Technology and NDS.

#### References

- [1] Japan Ministry of Foreign Affairs (MOFA): 34th G8 Summit, overview, November 2008.
- [2] K. Koyama, "Latest IPCC report points to global warming and relevant human influence," *The Institute of Energy Economics Japan*, vol. 146, pp. 1–3, 2013.

- [3] H. Matsubara, "Tracking sustainable energy zones in japan: status of renewable energy supply in municipalities," *Japan for Sustainability, Newsletter*, no. 126, 2013.
- [4] A. Poh, A. Ling, S. Kokichi, and M. Masao, "The Japanese smart grid initiatives, investments, and collaborations (IJACSA)," *International Journal of Advanced Computer Science and Applications*, vol. 3, no. 7, pp. 1–11, 2012.
- [5] S. Koma, "Solar PV R & D roadmap and activities in Japan," in *Proceedings of the 6th NEDO-ADEME Workshop, New Energy and Industrial Technology Development Organization (NEDO '11)*, October 2011.
- [6] Y. Liang, Z. Xu, J. Xia et al., "For the bright future-bulk hetero-junction polymer solar cells with power conversion efficiency of 7.4%," *Advance Energy Material*, vol. 22, no. 20, pp. E135–E138, 2010.
- [7] C. Gu, Y. Chen, Z. Zhang et al., "Achieving high efficiency of PTB7-based polymer solar cells via integrated optimization of both anode and cathode interlayers," *Advance Energy Material*, 2014.
- [8] J. Youa, L. Doua, Z. Hongc, G. Li, and Y. Yanga, "Recent trends in polymer tandem solar cells research," *Progress in Polymer Science*, vol. 38, no. 12, pp. 1909–1928, 2013.
- [9] O. Adebajo, P. P. Maharjan, P. Adhikary, M. Wang, S. Yang, and Q. Qiao, "Triple junction polymer solar cells," *Energy & Environmental Science*, vol. 6, pp. 3150–3170, 2013.
- [10] R. Tagliaferro, D. Gentilini, S. Mastroianni et al., "Integrated tandem dye solar cells," *RSC Advances*, vol. 3, pp. 20273–20280, 2013.
- [11] M. V. Srinivasan, P. Kannan, and A. Roy, "Photo and electrically switchable behavior of azobenzene containing pendant bent-core liquid crystalline polymers," *Journal of Polymer Science A: Polymer Chemistry*, vol. 51, no. 4, pp. 936–946, 2013.
- [12] K. R. Sarma, "Recent advances in AM OLED technologies for application to aerospace and military systems," in *Head- and Helmet-Mounted Displays XVII; and Display Technologies and Applications for Defense, Security, and Avionics VI*, vol. 8383 of *Proceedings of SPIE*, p. 83830, Baltimore, Md, USA, 2012.
- [13] F. Zhu, "Semitransparent organic solar cells," *Frontiers of Optoelectronics*, vol. 7, no. 1, pp. 20–27, 2014.
- [14] V. Švrček, T. Yamanari, D. Mariotti, K. Matsubara, and M. Kondo, "Enhancement of hybrid solar cell performance by polythieno [3,4-b]thiophenebenzodithiophene and microplasma-induced surface engineering of silicon nanocrystals," *Applied Physics Letters*, vol. 100, no. 22, Article ID 223904, 2012.
- [15] U. R. Kortshagen, C.-Y. Liu, and Z. C. Holman, "Hybrid solar cells from P3HT and silicon nanocrystals," *Nano Letters*, vol. 9, no. 1, pp. 449–452, 2009.
- [16] B. Walker, A. B. Tamayo, X.-D. Dang et al., "Nanoscale phase separation and high photovoltaic efficiency in solution-processed, small-molecule bulk heterojunction solar cells," *Advanced Functional Materials*, vol. 19, no. 19, pp. 3063–3069, 2009.
- [17] P. Kumar, S. Kannappan, S. Ochiai, and P.-K. Shin, "High-performance organic solar cells based on a low-bandgap polythienothiophene-benzodithiophene polymer and fullerene composite prepared by using the airbrush spray-coating technique," *Journal of the Korean Physical Society*, vol. 62, no. 8, pp. 1169–1175, 2013.
- [18] S. Ochiai, S. Imamura, S. Kannappan, K. Palanisamy, and P.-K. Shin, "Characteristics and the effect of additives on the nanomorphology of PTB7/PC<sub>71</sub>BM composite films," *Current Applied Physics*, vol. 13, pp. S58–S63, 2013.
- [19] Z. He, C. Zhong, S. Su, M. Xu, H. Wu, and Y. Cao, "Enhanced power-conversion efficiency in polymer solar cells using an inverted device structure," *Nature Photonics*, vol. 6, no. 9, pp. 591–595, 2012.
- [20] W. A. Hamed, R. Yahya, A. L. Bola, and H. N. M. E. Mahmud, "Recent approaches to controlling the nanoscale morphology of polymer-based bulk-heterojunction solar cell," *Energies*, vol. 6, no. 11, pp. 5847–5868, 2013.

## Review Article

# Competing in the Global LED Industry: The Case of Taiwan

**Yu-Shan Su**

*Department of Industrial Education, National Taiwan Normal University, No. 162, He-Ping E. Road, Taipei 106, Taiwan*

Correspondence should be addressed to Yu-Shan Su; [yssu@ntnu.edu.tw](mailto:yssu@ntnu.edu.tw)

Received 2 April 2014; Revised 19 May 2014; Accepted 19 May 2014; Published 5 June 2014

Academic Editor: Ho Chang

Copyright © 2014 Yu-Shan Su. This is an open access article distributed under the Creative Commons Attribution License, which permits unrestricted use, distribution, and reproduction in any medium, provided the original work is properly cited.

Light-emitting diode (LED) is a very essential application for energy-savings nowadays. The revenue of the Taiwan LED components industry is ranked top one in the world, followed by that of Japan and South Korea. Based on the advantage of their electronics industry, Taiwanese LED companies create a unique model to compete with the international firms. Large international LED companies achieve economies of scale by vertically integrating their operations. Taiwanese LED companies specialize and achieve an optimal efficiency by vertically disintegrating across the upstream, midstream, and downstream sectors in the value chains. Taiwanese LED companies create economies of scale and economies of scope through a complete industrial value chain.

## 1. Introduction

Energy-savings are getting more and more important in recent years, since both global warming and energy reduction are getting more and more serious. Light-emitting diode (LED) is a very essential application for energy-savings nowadays. Asia is the major of the global production base for the LED industry and home to the four countries with the highest LED revenue, namely, Taiwan, Japan, South Korea, and China. In 2010, Asia accounted for 81.3% of the global market share. The revenue of global high-power LEDs reached US\$10.1 billion in 2012, with an annual growth rate of 13.4%. The high-power LED market share of Taiwanese, Japanese, South Korean, and Chinese firms, when combined, amounts to 61.3% of the global total, leading the global LED industry [1].

The revenue of Taiwanese LED components industry reached US\$4,673 million in 2011, which accounts for approximately 30% of the global total, ranking first in the world. In 2010 and 2011, not only the revenue of Taiwanese LED components industry was the highest in the world but also Taiwanese LED industry has become the leader of the global LED industry. Developed for four decades, Taiwanese firms play an important role in the global LED industry. And Taiwanese LED industry has established a complete

industrial value chain. The upstream and midstream revenue was approximately US\$1,800 million and the downstream revenue was approximately US\$2,800 million 2011 [2].

Japanese firms have been the global leaders of the LED industry with its high-level technologies and capabilities for a significant length of time. In the past, Japanese firms claimed over half of the global market share. Global market share of Japanese firms declined to 41.5% in 2010 because of strong Taiwanese firms and aggressive Korean and Chinese firms. The fast-growing South Korean firms secured a market share of 10% in 2010. In 2002, Korean companies of Samsung LED and LG Innotek have aggressively expanded their LED industries and pioneered the market of liquid crystal displays (LCD) televisions with LED backlighting. The market share of Chinese firms was 5% in 2010 and continues to grow [2].

There are numerous advantages of LEDs, such as their compact size, long lifespan, high luminous efficiency, durability, power-saving abilities, and pollution-free characteristics. Many governments worldwide have focused on the LED industry in recent years. In the future, LEDs will be used primarily for lighting purposes, such as the lighting management systems of the high-efficiency light source and the intelligent lighting systems. In Taiwan, more than 800 LED-related firms exist, with an employment population of over 20,000. By 2015, the revenue of the Taiwanese LED industry

is estimated to exceed US\$18,000 million, transforming LEDs from tiny electronic components into a leading industry that attracts worldwide attention.

This paper focuses on the LED components industry and analyzes the trends and developments of the LED industry in Taiwan and in the globe. The positioning and competitive advantage of Taiwanese firms in the global LED industry is also analyzed.

## 2. Analysis of Global LED Industry

*2.1. Scope of LED Industry.* Composed of semiconductor materials, LEDs combine semiconductor electrons and electron holes to emit photons that can be made into light-emitting components. The LED industry comprises the following two parts (see Figure 1): (1) the components industry, which includes epitaxies, grains, packaging, and modules, and (2) the application industry, which includes light bulbs and alternative light sources. This study focuses on the LED component industry.

The value chain of LED industry included (1) single chips and epitaxial wafer (Epi-wafer) in the upstream sector, (2) grain in the midstream sector, and (3) package and module in the downstream sector (see Figure 2).

- (1) Upstream sector of Epi-wafer: where the primary products include single chip and epitaxial wafer. Wafer is formed by cutting monocrystalline silicon stick into single wafer substrates and growing material compounds on substrates using Metal Organic Chemical Vapor Deposition (MOCVD) method.
- (2) Midstream sector of grain process: where the primary products are grain. Epitaxial wafer diffusion and metal evaporation are performed as required, followed by wafer masking, etching, and heat treatment to create grain electrodes. Finally, the grain is cut, tested, and inspected to complete the midstream production of grain.
- (3) Downstream sector of package and module: various LED components are formed through a series of processes, including die bonding, wiring, wax sealing, and baking.

*2.2. History of Global LED Industry.* During the initial stage of the developments, LEDs only emitted infrared or red light with the addition of GaAs. As material sciences advanced, energy released as light was applied to produce various diodes capable of generating lights of varying colors. LEDs possess a number of advantages, such as low power consumption, durable components, radiation-free characteristics, and a compact size. As the luminous efficiency gradually improves, LEDs have become an ideal substitute for traditional lighting systems. The history of LED development is provided below (see Table 1).

In 1907, Henry Joseph Round of Radio Corporation of America first found that light-emitting components have the characteristics of a rectifier. The first components were named light-emitting diodes, abbreviated as LEDs, and published

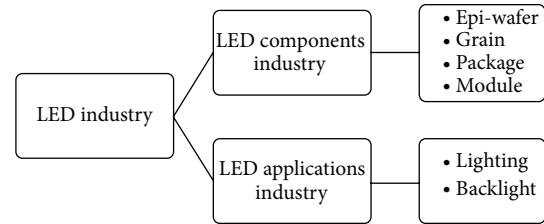


FIGURE 1: Scope of the LED industry. Source: this study.

in the journal [3]. In 1955, Rubin Braunstein of Radio Corporation of America identified the infrared radiation effects of GaAs and other semiconductor alloys for the first time. In 1962, Nick Holonyak Jr. of General Electric Company in United States developed the first light-emitting diode that could emit visible red light suitable for practical use. In 1992, Shuji Nakamura of Nichia Corporation in Japan developed the first GaN diodes. In 1995, Shuji Nakamura of Nichia Corporation successfully fabricated green- and blue-light GaN LEDs. In 1996, Shuji Nakamura proposed fabricating white-light LEDs using blue-light InGaN LEDs to excite fluorescent substances. In 1998, Nichia Corporation launched the first white LED product. In 2012, the Cree Company in United States introduced a luminous efficiency of 254 lm/W, establishing a new record of aluminous efficiency [4].

*2.3. Analysis of Global LED Value Chain.* The global LED market grew substantially recently. The market share of Taiwanese, Japanese, South Korean, and Chinese firms combined accounted for 81.3% of the global total in 2010 and over 80% in 2011. The primary LED producers have been based in Asia in the world. In the future, the primary arena of the global LED industry will continue to base in Asia. And Taiwanese, Japanese, and South Korean firms will be the dominant players. The global LED value chain is analyzed below (see Figure 2).

As the established renewable energy industry drives the industrial developments of the LED industry, international giants like Philips, Sony, Hitachi, and Samsung are moving aggressively into the LED market [5]. Most large companies from Europe, the United States, Japan, and South Korea are vertically integrated companies that comprise upstream, midstream, and downstream segments. A number of global lighting conglomerates (such as Phillips Company in Netherlands and Sharp Corporation in Japan) are vertically integrated companies supplying a large variety of LED components and appliance products. Top ten global LED suppliers are listed in the following table (see Table 2) [6].

In Taiwan, labors were divided across three sectors during the initial stage, that is, upstream, midstream, and downstream sections. Subsequently, this was transformed into a two-sector model, comprising an (1) up-midstream sector of Epi-wafer and grain process and (2) downstream sector of package, with the (1) up-midstream sector of Epi-wafer and grain process including the firms of Epistar, Huga, FormosaEpiraxy, Techcore and (2) the downstream sector of package including the firms of Everlight, Lite-on, and

TABLE 1: The history of global LED industry.

Year	Events
1907	Henry Joseph Round, who worked in Radio Corporation of America, found the first LED of SiC and published it in a journal.
1955	Rubin Braunstein, who worked in Radio Corporation of America, identified the emitted infrared radiation of GaAs and other semiconductor alloys for the first time.
1962	The first LED that could emit visible red light suitable for practical use was developed by Nick Holonyak, who worked in General Electric Company.
1992	Shuji Nakamura of Japanese Nichia Corporation developed the first GaN diodes.
1994	Shuji Nakamura of Japanese Nichia Corporation developed fabricated green- and blue-light GaN LEDs.
1996	Shuji Nakamura of Japanese Nichia Corporation developed fabricating white-light LEDs using blue-light InGaN LEDs to excite fluorescent substances.
1998	Japanese Nichia Corporation launched the first white LED product.
2002	The 5 W of LED appeared in the market, and the luminous efficiency was approximately 18 to 22 lm/w.
2009	Japanese Nichia Corporation introduced a new luminous efficiency record of 249 lm/w.
2010	The revenue of Taiwanese LED components industry reached US\$4,554 million and ranked top 1 in the world
2011	The revenue of Taiwanese LED components reached US\$4,673 million and ranked top 1 in the world.
2012	U.S. Cree Company introduced a new luminous efficiency record of 254 lm/W.

Source: this study.

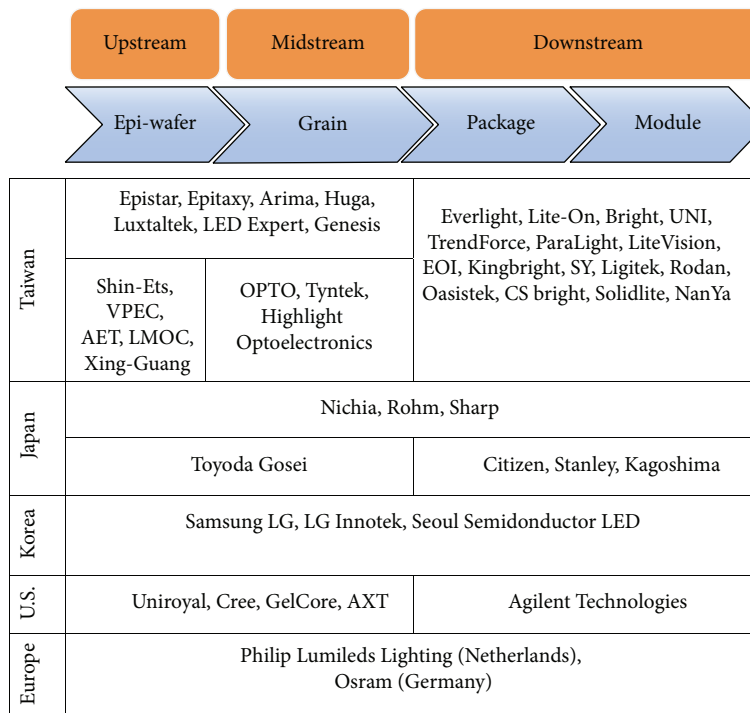


FIGURE 2: Value chain of global LED industry. Source: this study.

Kingbright. Also, Everlight Electronics Corporation is among the top-ten LED suppliers in the world (see Table 2) [6].

In Japan, the technological capabilities of Japanese high-power LEDs lead the global LED component industry. Nichia Corporation and Toyoda Gosei Company are the leading holders of LED patents globally. Facing low-priced competition from Taiwanese and South Korean suppliers in recent years, the market share of Japanese firms slipped to approximately 30% in 2011, behind that of Taiwan, and ranked second in the world. In Japan, many LED firms are

vertically integrated (such as Nichia, Rohm, and Sharp), with upstream suppliers including Toyoda Gosei Company and downstream suppliers including the firms of Citizen, Stanley, and Kagoshima.

In South Korea, electronics firms have gained a rapidly expanding market share in recent years because of their brand advantages. The market share of Korean firms Samsung LED, LG Innotek, and Seoul Semiconductor LED grew rapidly to 26% in 2011, assuming the position of the third largest supplier in the world. With the support of the South Korean

TABLE 2: Top 10 global LED components suppliers in 2013.

Rank	Supplier	Country	Revenue (unit: million USD)
1	Nichia Corporation	Japan	2058
2	Samsung LED	Korea	1390
3	Osram Company	Germany	1189
4	LG Innotek	Korea	933
5	Seoul Semiconductor LED	Korea	921
6	Cree Company	USA	895
7	Philips Lumileds Lighting Company	Netherlands	821
8	Toyota-Gosei Company	Japan	538
9	Sharp Corporation	Japan	486
10	Everlight Electronics Corporation	Taiwan	448

Source: Strategies Unlimited (2014) [5].

government, major companies such as Samsung and LG have adopted vertically integrated operations.

In United States and Europe, because of the economic downturn and sluggish global market, the market share of the U.S. and European firms, which had previously secured the high-end segment of the LED industry, comprised approximately 20% of the global market share in 2011. In the United States, up- and midstream integrated suppliers include Uniroyal, Cree, GelCor, AXT and downstream suppliers include Agilent Technologies Company. In Europe, Philip Lumileds Lighting Company of Netherlands and Osram Company of Germany are vertically integrated suppliers.

In China, the Chinese government provides subsidies to domestic firms for production equipment, land, leasing, and taxation, as well as market opportunities to foster the rapid developments of numerous Chinese LED suppliers. The revenue of the Chinese LED components industry has reached a growth rate of 24% in 2012 [6].

**2.4. Revenue Scale of Global LED Industry.** In 2011, the revenue of the global LED components industry (including Epi-wafer, grain, and package and module) reached US\$16,600 million (see Table 3 and Figure 3) [1, 2]. Taiwanese, Japanese, and South Korean firms have become the main players of the global LED component industry, with their combined revenue accounting for 73% of the world total. In 2010, the global LED component market experienced a 6.5% recession for the first time. Driven by the rapid merging of the suppliers and a proliferating lighting market, the price of LED components remained stable in 2012, and the global components market rebounded to the 2011 level. As the performance of LEDs improves, and the energy-saving policies of the governments implement and industrial economies of scale achieve, the LED market will continue to grow in the future. The revenue is estimated to increase to approximately US\$41.5 billion by

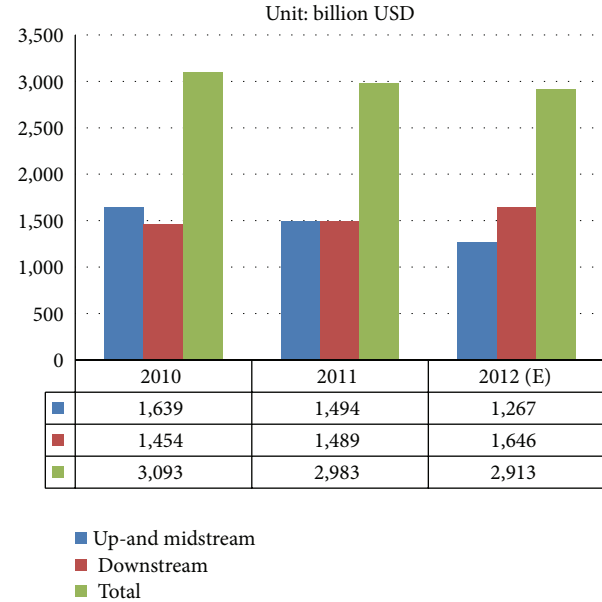


FIGURE 3: 2012 revenue of global LED industry. Source: Topology Research Institute (2012) [1]. Up- and midstream: Epi-wafer and grain. Downstream: package and module.

2016, with the rate of growth reaching 46% between 2010 and 2016 [7].

**2.5. The Relations between International Companies and Taiwanese Companies.** Coopetition behavior between LED manufactures is explored by patent analysis. For example, Nichia has the advantages in the field of LED components, while Osram has the advantages in the field of phosphor [8]. There are existing cooperative opportunities for the LED manufactures because their technological capabilities are partially complementary. Since numerous LED patents are set to expire in 2012, cross-licensing will increase the strategic development of patent networks and create opportunities for late comers. Technological licensing is the only gateway into LED markets. For example, Taiwanese Epistar Corporation and Korean firms Samsung LED, LG Innotek, and Seoul Semiconductor LED obtained technological authorization from five of the main global LED suppliers first. The relations between international LED companies and Taiwanese LED companies are shown in the following table (see Table 4).

### 3. Trends of Global LED Technologies and Markets

**3.1. Trends of Global LED Technologies.** There are four directions for the trends of the global LED technologies.

*(1) Enhancing Luminous Efficiency.* Currently, the average luminous efficiency of high-end products is 150 lm/W [4]. In 2012, Japanese Toyoda Gosei Company mass produced and sold 170 lm/W LED packaging components, exceeding other companies. According to the goals set by the U.S. DOE, the luminous efficiency of white-light LED components will

TABLE 3: Rank of revenue of global LED components industry (by country).

Year	2009			2010			2011			2012 (E)		
Rank	Country	Revenue (unit: billion USD)	%	Country	Revenue (unit: billion USD)	%	Country	Revenue (unit: billion USD)	%	Country	Revenue (unit: billion USD)	%
1	Japan	2,746	28%	Taiwan	4,554	28%	Taiwan	4,673	27%	Japan	4,860	28%
2	Taiwan	2,719	28%	Japan	4,089	26%	Japan	4,33	26%	Taiwan	4,594	26%
3	Korea	1,377	14%	Korea	3,185	20%	Korea	3,323	20%	Korea	3,477	20%
4	Europe	1,127	12%	Europe	1,737	11%	Europe	1,686	10%	China	1,610	9%
5	U.S.	926	9%	U.S.	1,337	8%	China	1,465	9%	Europe	1,598	9%
6	China	838	9%	China	1,182	7%	U.S.	1,367	8%	U.S.	1,364	8%

Source: adapted from PIDA (2012) [2].

TABLE 4: Relations between international LED companies and Taiwan LED companies.

International company	Country	U.S. patents	Relations with Taiwanese companies
Philips Lumileds Lighting Company	Netherlands	4127	(i) Epistar Corporation is licensed by the technology of AlInGaP light-emitting diode from Philips Company. (ii) Epistar Corporation entered HV LED supply chain of Philips Company successfully.
Osram Company	Germany	643	(i) Everlight Corporation is authorized by Osram Company with white and colorful technologies. (ii) Epistar Corporation allied with Deltato Company to develop HV LED grain to get mass orders from Osram Company.
Cree Company	United States	567	Taiwanese firms, for example, Epistar Corporation, Epitaxy Company, and Genesis Technology Company, have the pricing advantage, while Cree Company with strong LED lighting performed decline in 2011.
Nichia Corporation	Japan	477	(i) OPTO Company gained orders of cutting grain from Nichia Corporation. (ii) Everlight Corporation succeeded in the sue with Nichia Corporation.
Toyoda Gosei Company	Japan	347	(i) Epistar Corporation cross-licensed with Toyoda Gosei Company to access LEDs on III-V semiconductor technology patents in 2010. (ii) Epistar Corporation and Toyoda Gosei Company formed joint venture named TE OPTO Corporation.

Source: this study.

reach 200 lm/W by 2014, and prices will decline to approximately US\$2/klm. And we expect that the technological progress achieved by companies worldwide will soon surpass this goal.

(2) *Extending LED Lifespan.* Currently, a LED component can operate for 40,000 to 50,000 hours in its lifetime [4]. For special occasions, where the replacement of the light source is difficult (e.g., the ceilings of factories and airports that are extremely far from the ground), long-life LED light sources are required. The LED components of Toyoda Gosei Company can operate for up to 60,000 hours. Compared with traditional incandescent bulbs, LEDs are far more energy-efficient, long-lasting (100,000 hr compared with 1000 hr), and environmentally friendly [5]. Thus, they are suitable for use in special circumstances and can satisfy the demands of the global market.

(3) *Developing High-Voltage (HV) LEDs.* Currently, most single LED chips are based on a low voltage of 3 V, but voltage in the mains ranges between 100 V and 220 V [4]. Thus, reducing

the voltage from the mains will lead to a significant loss of power. Taiwanese Epistar Corporation began developing HV LEDs in the early stage, followed by latecomers Cree Company (in the United States) and Seoul Semiconductor LED (in Korea). HV LEDs possess the advantages of a compact size and the ability to be customized into various forms for integration. Thus, they have the potential for large-scale deployment in the lighting market over the next 2 to 5 years.

(4) *Enhancing the Acceptability of Solar-Powered LED Lighting Technology.* LED lanterns powered by batteries, which are charged by grid electricity or small solar panels, have emerged as a cost-competitive alternatives to kerosene and other fuel-based lighting technologies. Solar-powered LED lighting technologies have a niche in rural areas that are off-grid and have no available electricity for the most part [9–13]. Solar-powered LED lights are increasing popularly, because the lower retail price of these lights can make them more affordable to lower-income households. Solar-powered LED lights offer off-grid energy service for rural areas or

developing countries like Malawi, Zambia, and Cambodia, and so forth.

For the developments of future technologies, solar-powered LED lighting technologies [9–13] can offer the off-grid energy services for the rural area and for the poor, while white LED based PV lighting systems [14] and organic LED lighting technologies [15, 16] can continue to be explored in the area of energy saving lighting technologies. Besides, power management and intelligent control [17–19], thermal analysis and optimization [20, 21], cooling [22], and reliability issue [23] are also important for LED technology developments. Particularly, solar power, fuel cells, and LEDs combine to light the way towards green economy [24].

**3.2. Trends of Global LED Market.** The global high-power LED market reached US\$12.5 billion in 2011, 9.8% higher than that in 2010 [6]. Specifically, the lighting sector grew from US\$1.2 billion to US\$1.8 billion, with a growth rate of 44%. According to the market forecasts for the next five years, the market demands for lighting will increase, whereas the market demand for backlight lighting is expected to decline. The use of OLED will increase substantially because of smart phones.

In 2012, the annual revenue for high-power LEDs reached US\$10.1 billion globally (see Figure 4), with a growth rate of 13.4%. The market share of Taiwanese, Japanese, and South Korean firms combined amounted to 61.3% in 2012, and the global LED industry is dominated by Asia [3, 25]. In 2012, the growth of LED products in China was primarily concentrated on low-power LEDs, with a growth rate of 30%. Among the high-power LED application categories, in 2012, large-scale displays using LED backlighting accounted for 34.1%, followed by lighting applications, which accounted for 16.7%. These figures are estimated to reach 28.7% and 33.4% in 2014, respectively [25].

Currently, because energy-efficient light bulbs are still used extensively, the rate of penetration for LED bulbs was only 5.4% in 2012, that is, 1.05 billion bulbs, indicating a significant potential for market growth in the future. The penetration rate of the global LED lighting market is expected to increase from 11.3% in 2012 to 25.8% in 2014, with the revenue growing from US\$16.5 billion in 2012 to US\$41.9 billion in 2014. Promotional policies and preferential implementations have been introduced in countries worldwide to boost their developments of the LED lighting market. In the general lighting market, LEDs are anticipated to comprise 50% of the market share in Japan, 30% in South Korea, and 20% in China by 2015 [4].

In the rapidly growing LED light bulb market, new products developed in 2012 will replace the standard 60 W incandescent bulbs. Currently, an LED bulb equivalent to 60 W, with a brightness of 800 lm, prices up to US\$40. The selling price, which can be accepted by most consumers, varies between the different regions: (1) in the Japanese market, the selling price is US\$25; (2) in the European and the U.S. market, the selling price is approximately US\$15; and (3) in the newly emerging markets, the selling price is approximately US\$7.

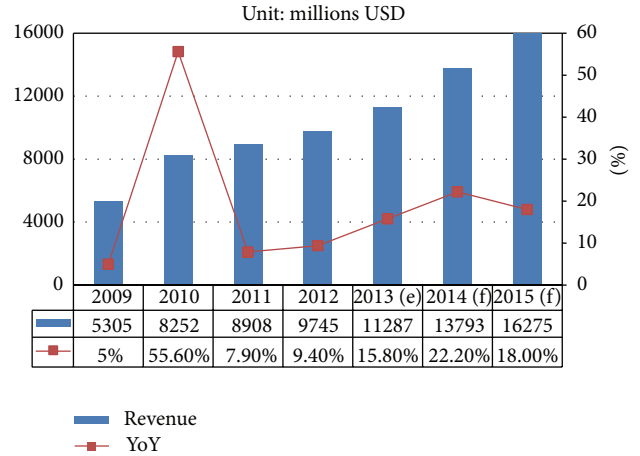


FIGURE 4: 2009–2015 prediction of global high-power LED market. Source: DIGITIMES (2013) [4].

## 4. Analysis of Taiwan LED Industry

**4.1. History of Taiwan LED Industry.** Taiwanese LED industry has been developed for 40 years (see Table 5). Because of the relatively few obstacles and capital requirements for packaging technology, the downstream package and module sector were first built up by Taiwanese firms in the 1970s. In the 1980s, industrial value chain of Taiwan was extended to include the midstream sector of grains process. In the 1990s, through technological diffusion and investments from U.S. overseas Taiwanese scholars, Taiwanese LED industry reached the developments of upstream sectors of the epitaxial process. In 2001, because of its technological accomplishments and expansion into the South Korean market, Taiwanese LED industry not only successfully branched into the GaN LED market, but also took the leadership of the global LED industry. The history of the industrial developments is as follows.

In 1972, Texas Instruments Incorporation established the first packaging plant in Taiwan. In 1975, Lite-On Technology Corporation established a LED packaging production line and became a pioneer among downstream packaging firms. From 1983, upstream technologies were focused by Taiwanese firms after the Optotech Corporation and Tyntek Corporation were set up and the downstream packaging industry was experiencing substantial growth. In 1996, the Taiwan Industrial Technology Research Institute collaborated with downstream packaging firms to establish a joint venture named Epistar Corporation, which focused on upstream LED processes. After the investments of the MOCVD research and technology transfer provided by several downstream suppliers of Epistar Corporation, a complete LED industrial value chain has been established in Taiwan. In 2005, Epistar Corporation merged with Epitech Corporation and High-link Technology Corporation. In 2007, Epistar Corporation merged with United Epitaxy Company. In 2009, the Taiwanese government initiated a program called “rising sun” to promote the green energy industry. At that time, the LED and solar photovoltaic industries were considered “the

TABLE 5: The history of Taiwan LED industry.

Year	Events
1972	The first packaging plant in Taiwan was set up by the Texas Instruments Incorporation.
1975	Lite-On Technology Corporation set up a LED packaging production line and become a pioneer among downstream packaging firms.
1983	After the Optotech Corporation and Tyntek Corporation were set up, not only the downstream packaging sector grew substantially but also upstream technologies were focused by Taiwanese LED firms.
1996	ITRI collaborated with Epitech Corporation to establish a joint venture named Epistar Corporation, which focused on upstream LED process.
2005	Epistar Corporation merged with Epitech Corporation.
2009	LED and solar photovoltaic industries are promoted by a “rising sun” program proposed by Taiwanese government.
2010	The revenue of Taiwanese LED components reached US\$4,554 million and ranked top 1 in the world.
2011	The revenue of Taiwanese LED components reached US\$4,673 million dollars and ranked top 1 in the world.
2012	The “entire Taiwan LED street lighting program” was implemented by Taiwanese government to further stimulate rapid growth in LED industry.

Source: this study.

two rising industries” and shortlisted as key programs for development. The revenue of the LED components industry in Taiwan reached US\$4,554 million in 2010, the highest in the world. In 2011, the revenue of LED components industry in Taiwan reached US\$4,673 million, the highest in the world. In 2012, the “entire Taiwan LED street lighting program” was implemented to further stimulate rapid growth of the LED industry.

*4.2. Analysis of Taiwan LED Value Chain.* Depending on the manufacturing processes, the LED industry can be divided into three sectors, that is, (1) the upstream epitaxial wafer sector, (2) the midstream grain sector, and (3) the downstream package and module sector. Unlike large-scale international manufacturers that adopt vertical integration, Taiwanese companies adopt a division of labor across upstream, midstream, and downstream sectors to form professional cooperation. Because of the low entry barriers of the LED downstream package and module sector, Taiwanese firms penetrated the market from the downstream package and module sector in the early stage and maintained a continual growth after extending to the upstream and midstream sectors. Since the mass production of GaN-based LEDs in Taiwan, to reduce internal costs and increase revenue, the division of labor in the industry was transformed from the formerly trisegmented pattern (covering upstream, midstream, and downstream segments) into a bisegmented pattern (including up-midstream sector of Epi-wafer and grain process and the downstream sector of package and module) (see Figure 5).

Major up- and midmidstream suppliers include Epistar, Huga, FormosaEpitaxy, and Techcore, in which Epistar Corporation is the largest red-light LED suppliers in the world. Downstream suppliers include Everlight, Lite-On, and Kingbright. Also, there are vertically integrated suppliers in Taiwan, such as Lextar Electronics Corporation and Taiwan Semiconductor Manufacturing Company.

For the revenue of the up- and midstream Epi-wafer and grain production, Taiwanese firms ranked top 1 in the world. For the revenue of the downstream package and module production, Taiwanese firms ranked the third in the world, behind only Japan and South Korea. Taiwanese LED packaging products can generally be categorized as SMD LED, Infrared components, and LED displays. The focus of the future market is expected to shift from LED displays to LED lighting, since the growth of the liquid crystal displays (LCD) sales have been sluggish over the past several years.

*4.3. Clusters of Taiwan LED Industry.* Three science parks are major industrial clusters in Taiwan, namely, Hsinchu Science Park, Central Taiwan Science Park, and Southern Taiwan Science Park (see Figure 6) [2]. These science parks converge into the clusters of the semiconductor and optoelectronic industries, forming a complete industrial value chain ranging from the upstream material and design to the downstream packaging and peripheral devices. Based on the sound foundation in its semiconductor industry, Taiwanese firms enjoy a competitive advantage regarding their talents and technologies in the LED and optoelectronic industry, which built up the highest density of LED epitaxial machinery in the world. Due to being supported by the upstream supply of materials in the semiconductor and optoelectronics industries, Taiwanese firms can effectively reduce the costs and cycle of the developments, thereby playing a significant role in the global LED value chain.

In the Hsinchu Science Park, most suppliers belong to the LED up- and midstream sector of the wafers and grains. Also, there are vertically integrated LED suppliers, which integrated downstream sector of packaging and modeling. In the Central and Southern Taiwan Science Parks, most suppliers belong to the LED up- and midstream sector of the wafer and grain industries.

*4.4. Revenue Scale of Taiwan LED Industry.* The revenue of Taiwanese LED components industry is ranked the first



FIGURE 5: Value chain of Taiwanese LED industry. Source: this study.

in the world (see Figure 7) [2]. The revenue of the global LED industry was US\$16,600 million in 2011, with a slight growth of 2.6% compared to the US\$16,100 million in 2010. The revenue of Taiwanese LED production reached US\$4,673

million in 2011. The revenue of Taiwanese downstream sector of packaging and module reached US\$2,877 million in 2011, whereas the revenue of the upstream and midstream sectors of the epitaxial wafer and grain reached US\$1,796 million.

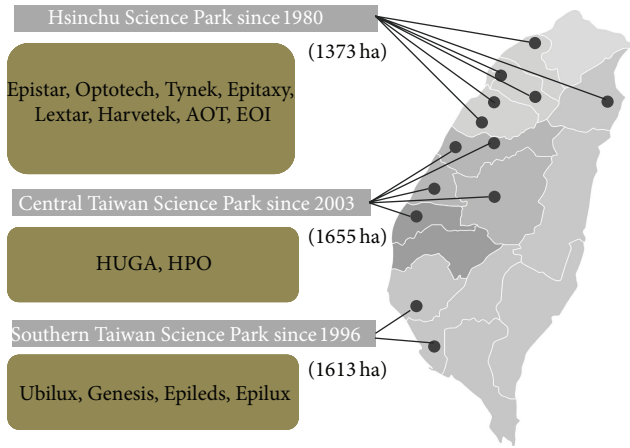


FIGURE 6: LED firms in Taiwan Science Parks. Source: PIDA (2012) [2].

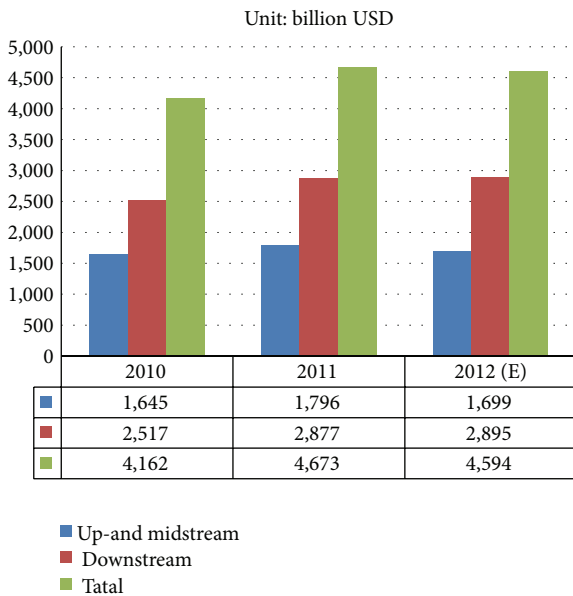


FIGURE 7: Revenue of Taiwanese LED industry. Source: PIDA (2012) [2]. Up- and midstream: Epi-wafer and grain. Downstream: package and module.

In 2012, the global revenue of LED components industry will reach US\$17,503 million and that of Taiwan will be US\$4,594 million by estimation [2].

The revenue of the Taiwanese LED components industry reached \$4,673 million in 2011, which accounts for approximately 30% of the global total, making the Taiwanese LED industry a global leader. Analyzing the three main science parks in Taiwan, the LED revenue for the Hsinchu Science Park was the highest at US\$1,367 million, of which the revenue of the up- and midstream Epi-wafer and grain sector declined by nearly 10.9%, and the revenue of the downstream package and module sector increased by 1.5%. The LED revenue for the Southern Taiwan Science Park was approximately US\$497 million, growing slightly at a rate of

4.7%. The LED revenue for the Central Taiwan Science Park, which was established after the other two parks, was US\$12 million [2].

4.5. *SWOT Analysis of Taiwan LED Industry.* SWOT analysis of Taiwanese LED industry is made in this study (see Table 6).

(1) *Strength.* In 2011, LED revenue in Taiwan was ranked the first place in the world. Known as a kingdom of electronics, a complete value chain was built up in the semiconductor industry in Taiwan. Based on the electronics industry, LED industry can be developed rapidly in Taiwan. Taiwanese firms have invested in its LED industry for 40 years and developed a complete industrial value chain with numerous firms actively involving in upstream, midstream, and downstream segments. Furthermore, because of experienced technologies and managements, Taiwanese firms can provide customized services according to customers' needs. The Taiwanese government has provided significant support to promote the "two rising stars of optoelectronics" policy (the LED and solar photovoltaic industries) because the development of this industry is among those that should be prioritized.

(2) *Weakness.* Unlike the brand establishment by other large-scale international firms from Japan, Korea, Europe, and the United States, Taiwanese firms follow the original equipment manufacturer (OEM) mode. Taiwanese production is primarily export-oriented, and R&D inputs are relatively limited. Most of the key technologies in Taiwan are restricted by patents held by large-scale international companies in the U.S. and Japan; thus, patent infringement occasionally occurs. Large international firms practice cross-licensing and cooperative development, whereas Taiwanese suppliers rely on the agreements of unilateral authorization from large international companies to obtain key technologies for mass production and sales.

(3) *Opportunity.* Because governments worldwide have implemented energy-saving policies, the LED industry has developed rapidly in recent years. Improvements in LED performance can be employed extensively in numerous fields with high added value, such as the global adoption of LED backlight displays, landscape lighting, and energy-saving road lighting. Taiwanese LED products are sold at lower prices than those produced in Europe, the United States, and Japan; therefore, they are more competitive in the global LED market.

(4) *Threat.* Taiwanese suppliers are primarily OEM oriented; thus, their capabilities for the high-end products are relatively weak. Taiwanese enterprises focus more on reducing the costs of manufacturing. In the future, R&D capability should be improved in Taiwan. In recent years, panel manufacturers from South Korea (e.g., LG Electronics and Samsung Electronics) and China are developing rapidly, becoming strong competitors of Taiwanese firms. In addition, traditional lighting products are also competitive products for LED lighting products because of their improved performance and reduced price.

TABLE 6: SWOT analysis of Taiwan LED industry.

Strength	Weakness
(1) Rank Top 1 for LED revenue in 2010, 2011. (2) Advantage of Taiwanese electronics industry. (3) A complete value chain of Taiwanese semiconductor industry was built up. (4) A complete value chain of Taiwanese LED industry was built up. (5) Taiwanese firms have experience in technologies and managements. (6) Taiwanese firms can provide customized service. (7) The LED has been supported by the Taiwanese government.	(1) Taiwanese firms follow the OEM mode. (2) Taiwanese firms are Weak in establishing branding. (3) R&D inputs are relatively limited by Taiwanese firms. (4) Taiwanese firms focus more on cost down in manufacturing. (5) Key technologies are restricted by patents held by international companies. (6) Taiwanese production is mostly exported. (7) Taiwanese suppliers rely on unilateral authorization from international companies to obtain key technologies.
Opportunity	Threat
(1) Governments worldwide have implemented energy-saving policies. (2) Improvements in LED performance can be employed in many fields, for example, energy-saving lighting. (3) Taiwanese LED products have lower price in the global LED market. (4) Emerging markets are increasing.	(1) Taiwanese suppliers are primarily OEM oriented. (2) Capabilities for high-end products are relatively weak. (3) Korean and Chinese Panel manufacturers are developing rapidly, becoming strong competitors of Taiwanese firms. (4) Traditional lighting products are competitive products for LED lighting products.

Source: this study.

## 5. Conclusion

Taiwanese firms play an important role in the global LED components industry. The advantages of its electronics industry and the industrial clusters have enabled Taiwanese firms to expand the LED industry rapidly. A complete value chain was established in Taiwanese LED industry, with the vertical disintegration across upstream, midstream, and downstream segments. Up- and midstream suppliers specialize in the production of the LED wafers and grains, and downstream suppliers specialize in the production of the LED packaging and module. Taiwanese LED firms at various sections of the value chain have unique specialties and efficient operations to achieve the economies of scope. A number of firms with significantly financial support achieve the economies of scale by vertically integrating their operations. Taiwanese LED suppliers have an important role in the global LED value chain because of their comprehensive division of labor and excellent manufacturing capacities.

## Conflict of Interests

The author declares that there is no conflict of interests regarding the publication of this paper.

## Acknowledgment

The author particularly thank Taiwan National Science Council for financial support (Grants NSC 101-3113-S-003-014- and NSC 100-3113-S-003-014-). The author owes special thanks to the research teams who collected the data for this paper.

## References

- [1] Topology Research Institute, *2011-2012 Forecast of Global LED Revenue*, Topology Research Institute, Taipei, Taiwan, 2012.
- [2] Photonics Industry & Technology Development Association, *The 2012 Yearbook of LED Market, Industrial Applications, and Standard Developments*, Photonics Industry & Technology Development Association, Taipei, Taiwan, 2012.
- [3] H. J. Round, "A note on carborundum," *Electrical World*, vol. 49, p. 309, 1907.
- [4] DIGITIMS, *2009-2015 Prediction of Global High-Power LED Market*, DIGITIMS, Taipei, Taiwan, 2014.
- [5] J. A. Mathews, "Latecomer strategies for catching-up: the cases of renewable energies and the LED programme," *Technological Learning, Innovation and Development*, vol. 1, no. 1, pp. 34-42, 2007.
- [6] Strategies Unlimited, *The Worldwide Market for LEDs Market Review and Forecast*, Strategies Unlimited, Silicon Valley, NC, USA, 2014.
- [7] Photonics Industry & Technology Development Association, *2011-2012 Global Photonics Markets and Taiwan Photonics Industry*, Photonics Industry & Technology Development Association, Taipei, Taiwan, 2012.
- [8] Y. Chen and B. Chen, "Utilizing patent analysis to explore the cooperative competition relationship of the two LED companies: Nichia and Osram," *Technological Forecasting and Social Change*, vol. 78, no. 2, pp. 294-302, 2011.
- [9] R. Pode, "Solution to enhance the acceptability of solar-powered LED lighting technology," *Renewable and Sustainable Energy Reviews*, vol. 14, no. 3, pp. 1096-1103, 2010.
- [10] E. Adkins, S. Eapen, F. Kaluwile, G. Nair, and V. Modi, "Off-grid energy services for the poor: introducing LED lighting in the Millennium Villages Project in Malawi," *Energy Policy*, vol. 38, no. 2, pp. 1087-1097, 2010.
- [11] K. Kornbluth, B. Pon, and P. Erickson, "An investigation of the cost and performance of a solar-powered LED light designed as an alternative to candles in Zambia: a project case study," *Renewable and Sustainable Energy Reviews*, vol. 16, no. 9, pp. 6737-6745, 2012.
- [12] B. Huang, C. Chen, P. Hsu, W. Tseng, and M. Wu, "Direct battery-driven solar LED lighting using constant-power control," *Solar Energy*, vol. 86, no. 11, pp. 3250-3259, 2012.

- [13] B. J. Huang, M. S. Wu, P. C. Hsu, J. W. Chen, and K. Y. Chen, "Development of high-performance solar LED lighting system," *Energy Conversion and Management*, vol. 51, no. 8, pp. 1669–1675, 2010.
- [14] O. S. Sastry, V. K. Devi, P. C. Pant, G. Prasad, R. Kumar, and B. Bandyopadhyay, "Development of white LED based PV lighting systems," *Solar Energy Materials and Solar Cells*, vol. 94, no. 9, pp. 1430–1433, 2010.
- [15] N. T. Kalyani and S. J. Dhoble, "Organic light emitting diodes: energy saving lighting technology—a review," *Renewable and Sustainable Energy Reviews*, vol. 16, no. 5, pp. 2696–2723, 2012.
- [16] Y. Kajikawa and Y. Takeda, "Citation network analysis of organic LEDs," *Technological Forecasting and Social Change*, vol. 76, no. 8, pp. 1115–1123, 2009.
- [17] O. Krejcar and R. Frischer, "Smart intelligent control of current source for high power LED diodes," *Microelectronics Journal*, vol. 44, no. 4, pp. 307–314, 2013.
- [18] B. Huang, C. Chen, C. Ong, B. Du, and P. Hsu, "Development of constant-power driving control for light-emitting-diode (LED) luminaire," *Applied Thermal Engineering*, vol. 50, no. 1, pp. 645–651, 2013.
- [19] X. Lee, C. Lin, Y. Chang, H. Chen, and C. Sun, "Power management of direct-view LED backlight for liquid crystal display," *Optics and Laser Technology*, vol. 46, no. 1, pp. 142–144, 2013.
- [20] T. Cheng, X. Luo, S. Huang, and S. Liu, "Thermal analysis and optimization of multiple LED packaging based on a general analytical solution," *International Journal of Thermal Sciences*, vol. 49, no. 1, pp. 196–201, 2010.
- [21] J. Wang, R. Wang, T. Chang, and D. Hwang, "Development of 30Watt high-power LEDs vapor chamber-based plate," *International Journal of Heat and Mass Transfer*, vol. 53, no. 19-20, pp. 3990–4001, 2010.
- [22] I. Y. Chen, M. Guo, K. Yang, and C. Wang, "Enhanced cooling for LED lighting using ionic wind," *International Journal of Heat and Mass Transfer*, vol. 57, no. 1, pp. 285–291, 2013.
- [23] M. Chang, D. Das, P. V. Varde, and M. Pecht, "Light emitting diodes reliability review," *Microelectronics Reliability*, vol. 52, no. 5, pp. 762–782, 2012.
- [24] S. Dow, "Fuel cells and LEDs combine to light the way towards the green economy," *Fuel Cells Bulletin*, vol. 2011, no. 8, pp. 12–14, 2011.
- [25] LEDinside, *Analysis of 2013 LED Lighting*, LEDinside, Taipei, Taiwan, 2014.

## Research Article

# Prepared and Characteristics of ZnO:YAG/Silicon Nanostructure Diodes Prepared by Ultrasonic Spraying

Chih-Hung Hsu, Lung-Chien Chen, and Jia-Ren Wu

*Department of Electro-Optical Engineering, National Taipei University of Technology, No. 1, Section 3, Chung-Hsiao E. Road, Taipei 106, Taiwan*

Correspondence should be addressed to Lung-Chien Chen; ocean@ntut.edu.tw

Received 5 February 2014; Revised 2 May 2014; Accepted 3 May 2014; Published 26 May 2014

Academic Editor: Chao-Rong Chen

Copyright © 2014 Chih-Hung Hsu et al. This is an open access article distributed under the Creative Commons Attribution License, which permits unrestricted use, distribution, and reproduction in any medium, provided the original work is properly cited.

This work presents a novel white light source. An yttrium aluminum garnet (YAG) phosphor incorporated zinc oxide (ZnO) (ZnO:YAG) film is deposited on a silicon substrate by ultrasonic spray pyrolysis to form a nanostructure diode. A nanoflower consisting of a hexagonal nanopetal is formed on the surfaces of the silicon substrate. A white broad band at the room temperature photoluminescence ranging from 420 to 650 nm for the ZnO:YAG/silicon nanostructure diode was observed. The white broad band consists of the emissions of defect level transition of the ZnO film and the  $^3D_4$  level to the  $^7F_6$  and  $^7F_5$  level transitions of  $Ce^{3+}$  ions.

## 1. Introduction

Solid state lighting is the next generation light source, owing to its potential luminescence efficiency. The white light source of the solid state lighting consists of multiple emissions in visible. For example, GaN-based white light-emitting diode (LED) is the most widely used solid state light source, which included a blue LED chip and a yellow phosphor coating. The advantages of the GaN-based LED white light source are long lifetime, high energy efficiency, small size, ability to produce color light directly without filtering, and integration with other semiconductor electronic elements [1–6]. However, the disadvantages of the GaN-based LED white light source are high manufacturing cost and low yield rate due to the expensive growth technology and source materials of metal-organic chemical vapor deposition and the Ga-N bonding mechanism, respectively.

Therefore, it is imperative to develop a novel and low-cost white light device for light source. ZnO is commonly used as a material for optical device applications in the UV range owing to its wide direct band gap (3.37 eV) [7–10]. Several articles about n-ZnO/p-GaN heterostructure LED were reported [11–13]. However, that is a UV range structure, and no optical characteristics were demonstrated.

In this work, an yttrium aluminum garnet (YAG) phosphor incorporated ZnO film is deposited on silicon substrate by ultrasonic spray pyrolysis to form a ZnO:YAG/silicon nanostructure diode. Additionally, the crystallinity of YAG phosphor incorporated into ZnO films is studied using X-ray diffraction (XRD) analysis. The optoelectronic characteristics of the ZnO:YAG/Si nanostructure diode are also studied.

## 2. Experimental Details

ZnO incorporated yttrium aluminum garnet (YAG) phosphor film was deposited by ultrasonic spray pyrolysis on p-type silicon substrates at atmospheric pressure in nitrogen ( $N_2$ ) gas, at a flow rate of 100 sccm for 20–60 min. The ZnO incorporated YAG phosphor film (YAG phosphor at 0, 1, 5, and 10 at wt%) (phosphor: NYAG4156, INTEMATIX, US) was produced by spraying aqueous solutions. Zinc acetate, ammonium acetate, and YAG phosphor were mixed in D.I. water to prepare the precursor solution. The solutions were stirred at room temperature for 1h and then moved into a commercial ultrasonic nebulizer which makes the solutions be aerosol which contains TAG phosphor. The aerosol was transported to the substrate by high purity nitrogen gas and the substrate was kept at 500°C. The YAG phosphor

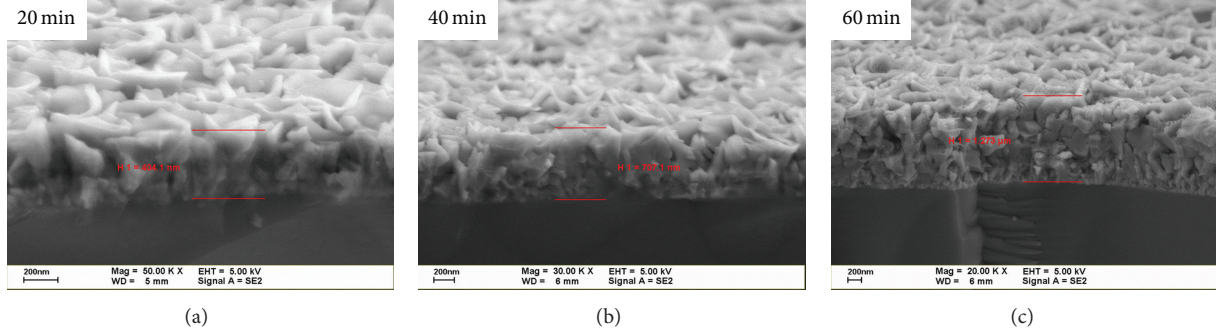


FIGURE 1: FESEM micrographs of the ZnO:YAG films (YAG phosphor at 5 wt%) with various deposition times: (a) 20 min, (b) 40 min, and (c) 60 min.

was incorporated in the film when the deposition of ZnO occurs. Single crystalline boron-doped p-type silicon with resistivity of  $10 \Omega\text{-cm}$  was used as the substrate, which was etched with HCl for 5 min before deposition. An aerosol of the precursor solution was then generated using a commercial ultrasonic nebulizer. Ag/Ni electrodes were formed by evaporation onto both the surfaces of the ZnO:YAG layer and the silicon substrate, to complete the nanostructure diodes. Next, the morphology of film was studied by field emission scanning electron microscope (FESEM). The crystallinity was investigated by X-ray diffraction (XRD) using a rotating anode Rigaku X-ray diffractometer with  $\text{Cu-K}\alpha_1$  radiation at a wavelength of  $1.54 \text{ \AA}$ , where the radiation was generated at 45 kV and 40 mA. Additionally, photoluminescence (PL) was measured at room temperature (RT). The excitation source for photoluminescence was a frequency-quadrupled Nd:YAG laser, which emitted 266 nm, 6 ns pulses at a 5 Hz repetition rate. The current-voltage ( $I$ - $V$ ) characteristics were measured using a Keithley 2420 programmable SourceMeter. Hall measurement was employed to study the electrical properties of the ZnO films with different concentrations of incorporated YAG which were deposited on glass substrate.

### 3. Results and Discussion

Figure 1 shows the FESEM micrographs of the ZnO:YAG (YAG phosphor at 5 wt%) films with various deposition times. The micrographs indicate that nanoflower consists of hexagonal nanopetal on the surface of the films, as shown in Figure 1. The nanoflower sizes were approximately 400 nm and the size of nanoflower almost has no changes with deposition time increasing. The average deposition rate is about 20 nm/min. The origin of the hexagonal nanoflower may contribute to decomposition and random nucleation of solution precursor leading to the formation of three-dimensional ZnO nuclei [7, 14, 15]. As the growth proceeds, the growth direction is longitudinal. However, as the growth process is terminated, the three-dimensional growth becomes two-dimensional growth owing to the reduction of the source and the aggregation of the residue precursor, subsequently leading to formation of the hexagonal nanopetal on the surface of the substrate [14, 15].

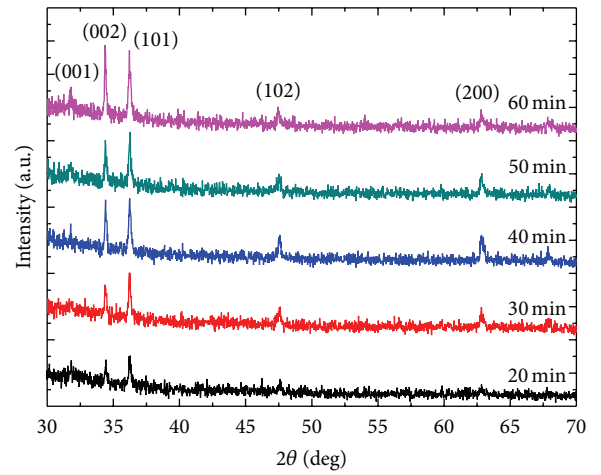


FIGURE 2: X-ray diffraction patterns of the ZnO:YAG films with various deposition times.

Figure 2 shows a typical X-ray diffraction (XRD) pattern of ZnO film incorporated YAG phosphor deposited on a sapphire substrate prepared by the ultrasonic spraying pyrolysis method. Three dominant diffraction peaks, that is, ZnO (100) ( $2\theta = 31.79^\circ$ ), ZnO (002) ( $2\theta = 34.37^\circ$ ), and ZnO (101) ( $2\theta = 36.21^\circ$ ), are observed in the range from 30 to  $45^\circ$ . The film demonstrates a polycrystalline structure. The sample deposited for 20 min has the maximum ZnO (101) diffraction peak height. As the deposition time increase exceeds 40 min, the intensity in ZnO (002) diffraction peaks becomes higher than the intensity in ZnO (101) diffraction peaks. This may contribute to the fact that the grain with orientation of (002) is dominant. In order to attain the detailed structure information, the grain size  $G$  along with the  $c$ -axis was calculated according to Scherrer's equation [16]:

$$G = \frac{0.9\lambda}{\beta \cos \theta}, \quad (1)$$

where  $G$ ,  $\lambda$ ,  $\beta$ , and  $\theta$  denote the grain size, the X-ray wavelength, the full width at half maximum (FWHM) in radians, and the Bragg angle of (002) or (101) peak, respectively. The grain sizes for the samples deposited with 20, 30, 40,

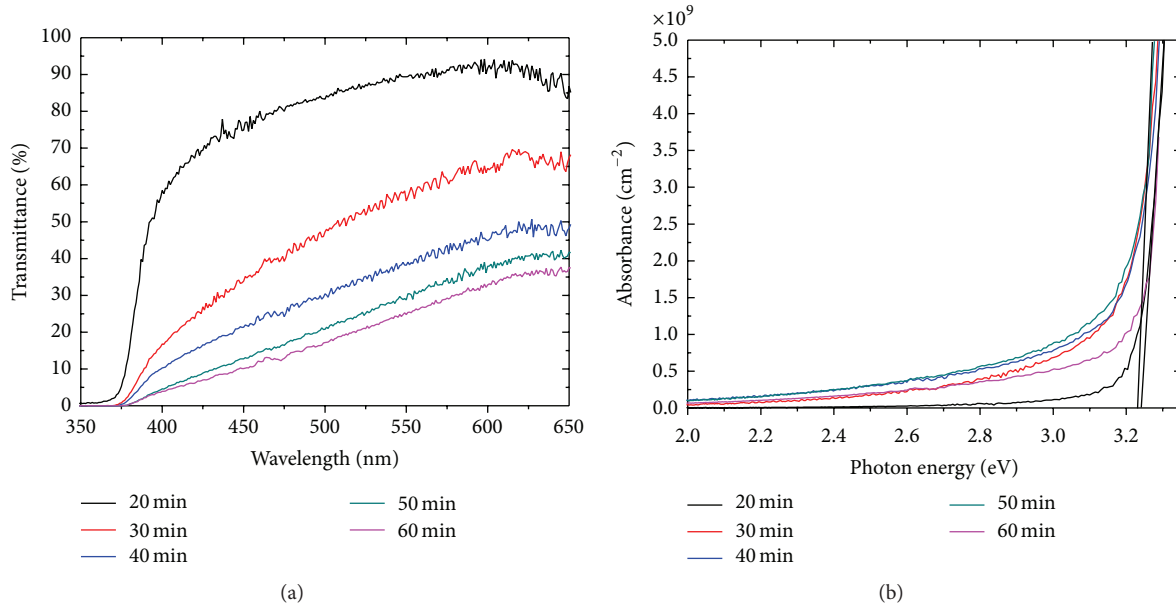


FIGURE 3: (a) Transmittance spectra of the ZnO:YAG films deposited for various times. (b) Relationship between the square of the absorbance and photon energy for the ZnO:YAG films.

50, and 60 min are 25.97, 32.14, 36.13, 39.78, and 46.18 nm, respectively. Therefore, the crystallinity of the samples with longer deposition time is better.

Figure 3(a) plots the transmittance spectra of the YAG incorporated ZnO films deposited for various times, and Figure 3(b) shows the results of the absorption measurements for the YAG incorporated ZnO films. It can be seen from Figures 3(a) and 3(b) that, as the deposition time increases, the transmittance decreases due to the thickness of the YAG incorporated ZnO increasing, and the absorbance edge keep almost in 3.15 eV. Typically, the band gap of ZnO film is around 3.37 eV corresponding to the absorption edge at 370 nm [14]. The red shift may be attributed to the defects in the YAG incorporated ZnO film [8, 17].

Figure 4 presents the room temperature (RT) PL spectra of the ZnO:YAG (YAG phosphor at 5 wt%) deposited for 60 min. The inset shows the photoexcited luminescent photographs. According to Figure 4, the RT PL spectrum of the YAG incorporated ZnO reveals one peak, denoted as peak A, that is, at  $\sim 3.27$  eV (382 nm), and a broad band included four weak peaks, denoted as peaks B, C, and D at 2.71 eV (456 nm), 2.56 eV (484 nm), and 2.28 eV (544 nm), respectively. Peak A has the shortest wavelength and, therefore, is interpreted as being associated with free-exciton (FE) or band-to-band (B-B) recombination in the ZnO. Additionally, its position is reasonably close to that of the band gap of ZnO at RT, which is  $\sim 3.285$  eV (377.5 nm) [8–10, 15, 17, 18]. Peak B may be attributed to the band-to-deep level transition in the ZnO film. Peaks C and D may correspond to the  $^5D_4$  level to the  $^7F_6$  and  $^7F_5$  level transitions of  $Ce^{3+}$  ions, respectively [19–21]. The color of photoluminescence is nearly white, as shown in Figure 5. The white light may contribute to the wide emission band ranging from 420 to 650 nm. Figure 5 shows

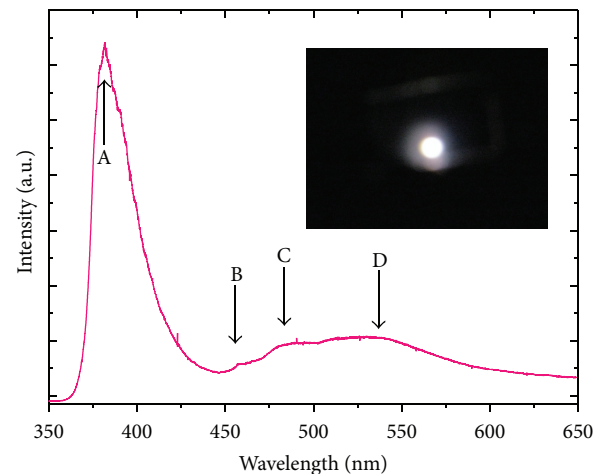


FIGURE 4: RT PL spectra of ZnO:YAG phosphor (YAG phosphor at 5 wt%) on silicon substrate. The inset shows the photoexcited luminescent photographs.

the PL spectra of the ZnO:YAG thin films with different incorporated concentration at the RT. The intensity of all the peaks increases when the incorporated concentration increases. The chromaticity coordinates of the ZnO:YAG films at 1, 5, and 10 wt% on Si substrate are presented in the CIE chromaticity diagram, as shown in Figure 6. With the increasing incorporated concentration of YAG, the chromaticity coordinates move in white light area from  $x = 0.2786$ ,  $y = 0.3417$  (CCT = 7958) for the sample at 1 wt% to  $x = 0.2476$ ,  $y = 0.3665$  (CCT = 9328) for the sample at 10 wt%. Therefore, the ZnO:YAG film on Si substrate is suitable for solid state lighting because it has a stable white

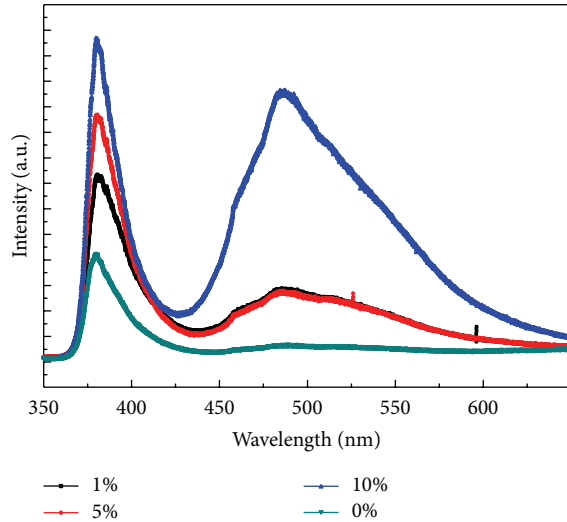


FIGURE 5: PL spectra of the ZnO thin films with different concentrations of incorporated YAG at room temperature.

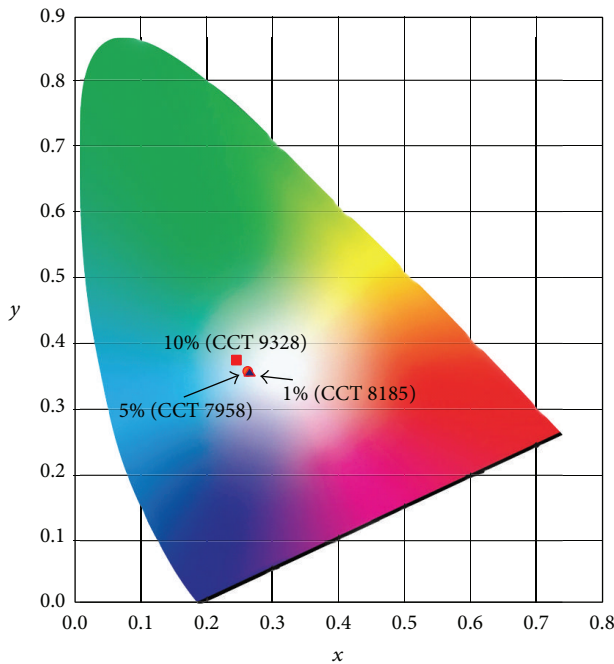


FIGURE 6: Chromaticity coordinates of the ZnO:YAG films at 1, 5, and 10 wt% on Si substrate.

light color when the incorporated concentration is in the range of 1–5 wt%.

Figure 7 shows the resistivity and the mobility as a function of the different concentrations for phosphor doped ZnO. In undoped ZnO thin films, the resistivity and the mobility were  $33 \Omega\text{-cm}$  and  $1.7 \text{ cm}^2/\text{V}\cdot\text{s}$ , respectively. When phosphor doped ZnO at 1 wt %, the resistivity increases, phosphor doped concentration up to 5 and 10 wt %, and then it increases again. On the contrary, the mobility decreases with increasing the doped concentration. The changes in

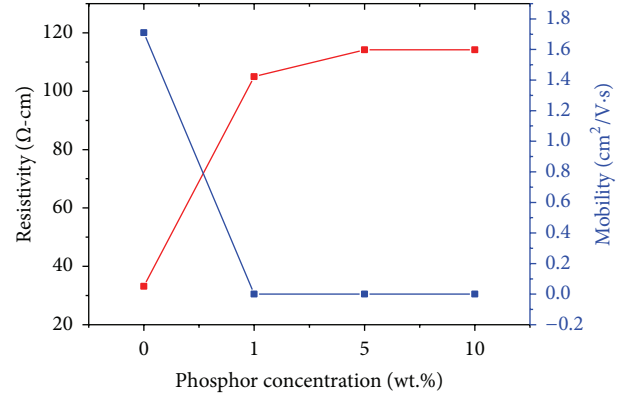


FIGURE 7: Resistivity and mobility of the ZnO thin films with different concentrations of incorporated YAG deposited on glass substrate.

electrical properties of ZnO film for the defects increase caused by the doping of the phosphor.

Figure 8(a) plots typical  $I$ - $V$  characteristics of the YAG phosphor incorporated ZnO/silicon heterostructure diodes at room temperature. The inset presents the cross-section of the completed structure. Figure 8(b) plots the current-voltage ( $I$ - $V$ ) of the Ni/Ag/ZnO:YAG and Ni/Ag/p-Si pad-to-pad structures, to check for ohmic characteristics and to optimize the performance of the devices. The diode has a turn-on forward bias of  $\sim 5$  V. The forward bias is high because the ohmic contact condition is not optimized yet. Diode  $I$ - $V$  characteristics can be expressed by the Shockley equation:

$$I = I_0 \left[ \exp \left( \frac{qV}{nKT} \right) - 1 \right], \quad (2)$$

where  $I_0$  is the saturation current density and  $n$  is the ideality factor. Equation (2) gives an ideality factor  $n$  and saturation current  $I_0$  of 1.56 and 1.89 nA, respectively, indicating that when a diffusion current flows in the reverse direction, the reverse leakage current prior to breakdown is around  $10^{-5}$  A. The breakdown voltage is soft and as high as around  $-5$  V.

## 4. Conclusions

In summary, an yttrium aluminum garnet (YAG) phosphor incorporated zinc oxide (ZnO) (ZnO:YAG) film has deposited on a silicon substrate by ultrasonic spray pyrolysis. A nanoflower consisting of a hexagonal nanopetal is formed on the surfaces of the silicon substrate, and the sizes of the nanoflower are approximately 400 nm. The ZnO:YAG/silicon nanostructure diode has a turn-on forward bias of  $\sim 5$  V. The reverse leakage current prior to breakdown is around  $10^{-5}$  A. The breakdown voltage is soft and as high as around  $-5$  V. A white broad band at room temperature photoluminescence ranging from 420 to 650 nm was observed. The white broad band consists of the emissions of defect level transition of the ZnO film and the  $^5D_4$  level to the  $^7F_6$  and  $^7F_5$  level transitions of  $\text{Ce}^{3+}$  ions.

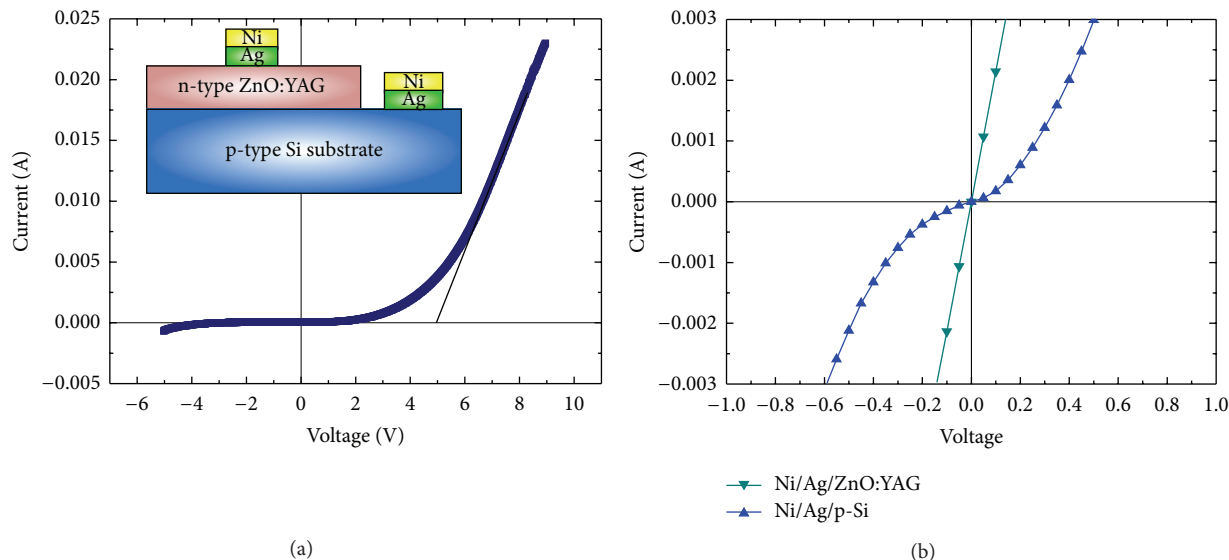


FIGURE 8: (a) Typical current-voltage characteristics of ZnO:YAG/silicon nanostructure diode. The inset shows the cross-section of the completed structure of the ZnO:YAG/silicon nanostructure diode. (b) The current-voltage ( $I$ - $V$ ) characteristics of Ni/Ag/ZnO:YAG and Ni/Ag/p-Si junctions, respectively.

## Conflict of Interests

The authors declare that there is no conflict of interests regarding the publication of this paper.

## Acknowledgment

Financial support of this work was provided by the National Science Council of the Republic of China under Contract no. NSC 101-2221-E-027-054.

## References

- [1] Y. C. Shen, J. J. Wierer, M. R. Krames et al., "Optical cavity effects in InGaN/GaN quantum-well-heterostructure flip-chip light-emitting diodes," *Applied Physics Letters*, vol. 82, no. 14, pp. 2221–2223, 2003.
- [2] T. Mukai, M. Yamada, and S. Nakamura, "Characteristics of InGaN-based UV/blue/green/amber/red light-emitting diodes," *Japanese Journal of Applied Physics, Part 1: Regular Papers and Short Notes and Review Papers*, vol. 38, no. 7 B, pp. 3976–3981, 1999.
- [3] L.-C. Chen and Y.-L. Huang, "High reliability GaN-based light-emitting diodes with photo-enhanced wet etching," *Solid-State Electronics*, vol. 48, no. 7, pp. 1239–1242, 2004.
- [4] L.-C. Chen, J.-B. Huang, P.-J. Cheng, and L.-S. Hong, "InGaN blue light-emitting diodes with ZnO nucleation layers prepared by the sol-gel method," *Semiconductor Science and Technology*, vol. 22, no. 10, pp. 1178–1182, 2007.
- [5] L.-C. Chen and Y.-M. Ho, "Ag and zinc oxide-doped indium oxide ohmic contacts to p-type GaN for flip-chip LED applications," *Journal of Physics D: Applied Physics*, vol. 40, no. 21, pp. 6514–6517, 2007.
- [6] L.-C. Chen, C.-H. Tien, and C.-S. Mu, "Effects of spin-polarized injection and photoionization of MnZnO film on GaN-based lightemitting diodes," *Optics Express*, vol. 18, no. 3, pp. 2302–2308, 2010.
- [7] S. C. Su, Y. M. Lu, Z. Z. Zhang et al., "The optical properties of ZnO/ZnMgO single quantum well grown by P-MBE," *Applied Surface Science*, vol. 254, no. 22, pp. 7303–7305, 2008.
- [8] X. H. Wang, B. Yao, D. Z. Shen et al., "Optical properties of p-type ZnO doped by lithium and nitrogen," *Solid State Communications*, vol. 141, no. 11, pp. 600–604, 2007.
- [9] X. H. Zhang, S. J. Chua, A. M. Yong et al., "Exciton radiative lifetime in ZnO nanorods fabricated by vapor phase transport method," *Applied Physics Letters*, vol. 90, no. 1, Article ID 013107, 2007.
- [10] Y. Danhara, T. Hirai, Y. Harada, and N. Ohno, "Exciton luminescence of ZnO fine particles," *Physica Status Solidi (C) Current Topics in Solid State Physics*, vol. 3, no. 10, pp. 3565–3568, 2006.
- [11] W. C. Li, H. L. Tsai, H. C. Chen et al., "Structural investigation of n-ZnO/p-GaN ultraviolet light-emitting diodes grown by atomic layer deposition," *Functional Materials Letters*, vol. 4, no. 3, pp. 221–224, 2011.
- [12] S. K. Jha, O. Kutsay, I. Bello, and S. T. Lee, "ZnO nanorod based low turn-on voltage LEDs with wide electroluminescence spectra," *Journal of Luminescence*, vol. 133, pp. 222–225, 2013.
- [13] H.-Y. Shih, S.-H. Cheng, J.-K. Lian, T.-Y. Lin, and Y.-F. Chen, "Light-emitting devices with tunable color from ZnO nanorods grown on InGaN/GaN multiple quantum wells," *Optics Express*, vol. 20, no. 6, pp. A270–A277, 2012.
- [14] H.-W. Sun, G.-Y. Kim, Y.-S. Jung, W.-K. Choi, and D. Byun, "Growth and properties of ZnO nanoblade and nanoflower prepared by ultrasonic pyrolysis," *Journal of Applied Physics*, vol. 97, no. 4, Article ID 044305, 2005.
- [15] L.-C. Chen and C.-C. Huang, "Optoelectronic characteristics of YAG phosphor-incorporated ZnO films deposited by ultrasonic spray pyrolysis," *Nanoscale Research Letters*, vol. 7, article 627, 2012.

- [16] C. H. Hsu, L. C. Chen, and X. Zhang, "Effect of the Cu source on optical properties of CuZnO films deposited by ultrasonic spraying," *Materials*, vol. 7, pp. 1261–1270, 2014.
- [17] X.-Y. Li, H.-J. Li, Z.-J. Wang et al., "Effect of substrate temperature on the structural and optical properties of ZnO and Al-doped ZnO thin films prepared by dc magnetron sputtering," *Optics Communications*, vol. 282, no. 2, pp. 247–252, 2009.
- [18] J.-H. Lim, C.-K. Kong, K.-K. Kim, I.-K. Park, D.-K. Hwang, and S.-J. Park, "UV electroluminescence emission from ZnO light-emitting diodes grown by high-temperature radiofrequency sputtering," *Advanced Materials*, vol. 18, no. 20, pp. 2720–2724, 2006.
- [19] G. Phaomei, R. S. Ningthoujam, W. R. Singh et al., "Luminescence switching behavior through redox reaction in  $\text{Ce}^{3+}$  co-doped  $\text{LaPO}_4:\text{Tb}^{3+}$  nanorods: re-dispersible and polymer film," *Dalton Transactions*, vol. 40, no. 43, pp. 11571–11580, 2011.
- [20] Y. Zhang, L. Li, X. Zhang, and Q. Xi, "Temperature effects on photoluminescence of  $\text{YAG}:\text{Ce}^{3+}$  phosphor and performance in white light-emitting diodes," *Journal of Rare Earths*, vol. 26, no. 3, pp. 446–449, 2008.
- [21] A. Lakshmanan, R. S. Kumar, V. Sivakumar, P. C. Thomas, and M. T. Jose, "Synthesis, photoluminescence and thermal quenching of  $\text{YAG}:\text{Ce}$  phosphor for white light emitting diodes," *Indian Journal of Pure and Applied Physics*, vol. 49, no. 5, pp. 303–307, 2011.

## Research Article

# Performance Evaluation of a Small Scale Modular Solar Trigeneration System

**Handong Wang**

*M. & E. School of Shenzhen Polytechnic, Shenzhen, Guangdong 518055, China*

Correspondence should be addressed to Handong Wang; [zlwhtd@szpt.edu.cn](mailto:zlwhtd@szpt.edu.cn)

Received 5 April 2014; Accepted 7 May 2014; Published 25 May 2014

Academic Editor: Mohammad Yusri Hassan

Copyright © 2014 Handong Wang. This is an open access article distributed under the Creative Commons Attribution License, which permits unrestricted use, distribution, and reproduction in any medium, provided the original work is properly cited.

In order to improve the efficiency of solar thermal power (STP) system, a novel modular system combining cooling, heating, and power generation (CCHP) is proposed and introduced in this work. This modular CCHP system can simultaneously provide 10 kW electricity,  $-15\sim 5^{\circ}\text{C}$  coolant, and  $60^{\circ}\text{C}$  hot water to meet the requirements of cooling, heating, and electricity in a general family or other fields. The flow chart and working process of the modular system are introduced, based on which the energy and exergy efficiencies at the CCHP and STP operation modes are primarily evaluated and discussed. The results show that when the output electricity is constant, the overall efficiencies of energy and exergy of the system operating at the CCHP mode are 9.37 times and 2.62 times as big as those of the system operating at the STP mode, respectively. Thus, the modular solar thermal CCHP system can improve the energy and exergy efficiencies. Furthermore, calculation shows that both the overall energy and exergy efficiencies decrease with increase of inlet vapor temperature at given inlet vapor pressure, but both the efficiencies increase with increase of inlet vapor pressure at given inlet temperature.

## 1. Introduction

Solar thermal power (STP) systems produce electricity (power) in much the same way as conventional power stations. The difference is that STP systems obtain energy by concentrating solar radiation and converting it to high temperature steam or gas to drive a turbine or engine. In STP systems, the incoming radiation is tracked by mirror fields which concentrate the energy towards collectors or absorbers. Then, the received solar radiation is transferred thermally to the working medium. The heated fluid operates as in conventional power stations directly (if steam or air is used as a medium) or indirectly through a heat exchanging steam generator on the turbine unit which then drives the generator (i.e., a turbine or engine). In STP systems, the collected and transferred thermal energy can be stored with special thermal tanks which can continuously supply high temperature working medium to drive the generator for several hours after sunset. Compared to photovoltaic (PV) power systems, the characteristics of electricity generated by STP systems are almost the same as those of electricity generated by traditional power stations. Thus, the output

electricity can be supplied to a power net without inverters which are necessary in PV power systems. As it can avoid environment pollution problems caused by fossil fuel power systems, the STP technology is considered as one of the greenest technologies in power fields.

There are many researches about STP systems. Among them, Pons and Clark proposed a system based on dish solar collectors and Stirling engines [1]. Goswami presented a study on solar thermal power. In his work, a relatively recent cycle has been proposed in which thermal energy is used to produce work and to generate a subambient temperature stream that is suitable for cooling applications [2]. You and Hu studied a medium-temperature solar thermal power system and its efficiency optimization; they declared that the optimum saturation temperature in the boiler was about  $201^{\circ}\text{C}$  and the thermal efficiency and the exergetic efficiency of the system were 17.9% and 25.12%, respectively [3].

Lu and Goswami investigated the optimization of a novel combined power-refrigeration thermodynamic cycle and cooling thermodynamic cycle for low temperature heat sources [4]. Tamm et al. published the theoretical and

experimental results of a novel combined power and cooling thermodynamic cycle for low temperature heat sources in [5, 6], respectively. Vijayaraghavan and Goswami presented a research on organic working fluids for a combined power and cooling cycle and found that, under optimum conditions, thermodynamic efficiencies achievable with organic fluid mixtures were lower than those obtained with ammonia-water mixtures, but the refrigeration temperatures achievable using organic fluid mixtures were higher than those using ammonia-water mixtures [7]. Kane et al. also presented a small hybrid solar power system [8].

There are also many researches on STP systems based on ammonia-water power cycle. For example, Xu and Goswami investigated the thermodynamic property of ammonia-water mixtures for power cycle applications [9]. Analysis of a new thermodynamic cycle for combined power and cooling using low and mid temperature solar collectors is studied by Goswami and Xu [10] and by Xu et al. [11]. Ammonia-based combined power-refrigeration cycle at low refrigeration temperatures is analyzed by Lu and Goswami [12]. A novel ammonia-water cycle for power and refrigeration cogeneration is presented by Zhang et al. [13]. Abdel-Rehim also investigated an ammonia-water-based power-refrigeration system with parabolic trough solar collectors [14].

In recent years, Mayere and Riffat proposed a micro-combined heating-power system with output capacity less than 10 kW for domestic power generation. They declared that the systems could utilize about 75% of solar energy to provide electric and thermal energy directly to end-users, and the microsystems had relatively the same efficiencies compared to large scale systems which were said to be matured technologies [15]. Borello et al. investigated the matching of an advanced small scale combined heat and power (CHP) Rankine cycle plant with end-user (i.e., a hotel) thermal and electric load [16].

As we know, most of researches on CCHP systems are mainly about the system with combustion power generator, but few are about solar thermal CCHP systems. Among few references about the solar thermal CCHP system, Su et al. proposed and discussed a distributed energy system for cooling-heating-power cogeneration for a single building [17]. In their work, solar energy is used as the only heat source to drive a closed Brayton cycle to generate power. The waste heat dissipated by the turbine is utilized by a recovery refrigeration cycle to provide cooling or is directly transferred by heat exchangers for heating. When the system is further combined with a fuel cell system, the whole system can provide cooling-heating power continuously in day and night. In fact, the system proposed in [17] is just a cooling-power or heating-power cogeneration system which cannot supply cooling, heating, and power simultaneously.

References review indicates that most of STP plants are large systems which need huge areas to install mirror fields. In order to investigate the feasibility and efficiency of small scale systems, a micromodular solar thermal CCHP system is proposed and introduced in this work. This microsolar thermal CCHP system can meet the requirements of families, farms, islands, and other places lack of electricity. In this work, the flow chart and working process of the modular solar

thermal CCHP system are firstly introduced. And, then, the performances at typical conditions are primarily evaluated and discussed.

## 2. Description and Working Process of the Modular CCHP System

In order to meet the demands of power, cooling, and heating in general families or small farms, the function of the modular solar thermal CCHP system is given as follows: supplying 10 kW electricity,  $-15\sim 5^{\circ}\text{C}$  coolant, and  $60^{\circ}\text{C}$  hot water. This part mainly presents the conceptual design and working process of the modular solar thermal CCHP system. At present, each module is designed to regularly generate 10 kW electricity. It mainly consists of solar collectors and absorbers, thermal energy storage tanks, a vapor generator (heat exchanger or boiler), a power generator, an absorption refrigerator, a water heater, and a cooling unit, as shown in Figure 1. In this CCHP system, the power generation is based on the principle of Rankine cycle. This is different from the system presented in [17] which was based on the closed Brayton cycle.

The modular CCHP system can be divided into two parts. The first part is called solar thermal unit (STU) which includes the solar collectors, thermal storage tanks, heat exchanger (vapor generator or boiler), and the first fluid pump. The second part is called power and end-users (PEU) which consists of the heat exchanger, power generator, DAR (diffusion absorption refrigerator), water heater, cooling unit, and the second fluid pump. In the first part (STU), the first fluid flows through the solar collectors and absorbers and becomes high-temperature fluid which releases heat to the second fluid in the heat exchanger and is subsequently pumped to the solar collector to begin the next circulation. When solar energy is sufficient, the first fluid can be pumped into the thermal energy storage tanks and the excess thermal energy can be stored for continuously generating power, cooling, and heating after sunset.

In the second part (PEU), the second fluid becomes vapor (or steam) after being heated by the first fluid in the heat exchanger. Then, the vapor drives the power generator to produce electricity. The exhausted vapor from the power generator subsequently enters into the absorption refrigerator to produce cooling and supply low temperature coolant to users. The second fluid leaving from the absorption refrigerator may still be a mixture of vapor and hot water, and its temperature is still high enough to produce hot water in the water heater by exchanging heat with the external circulating water. If necessary, the second fluid leaving the water heater enters into the cooling unit to be condensed thoroughly. Finally, the second fluid liquid is pumped back to the heat exchanger (vapor generator) to begin the next circulation. Of course, if the second fluid completely becomes hot water when it leaves the water heater, the cooling unit can be shut off to save energy. This is also one of the advantages of the modular solar thermal CCHP system. Thus, the first part and the second part can be integrated into one system by the heat exchanger (i.e., vapor generator or boiler).

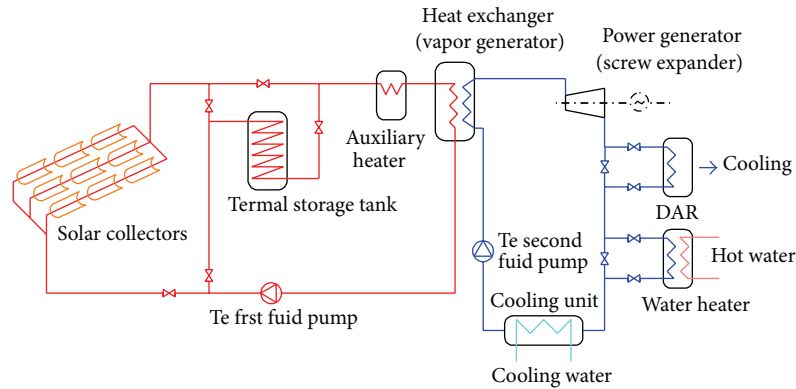


FIGURE 1: Conceptual flow chart of the modular solar thermal CCHP system.

At present, parabolic trough or dish reflectors with heat absorbers are chosen to be the solar collectors and absorbers in which thermal oil is chosen as the first fluid. The designed temperature of the first fluid is 150~250°C. The second fluid can be water or other organic substances with low-boiling temperatures based on the available temperature of the first fluid. The heat exchanger is used to generate vapor and it can be a shell-tube or a plate-type heat exchanger. The thermal storage tanks are used to store excess thermal energy for generating power after sunset. One kind of phase-change materials is chosen as the thermal-store medium in the thermal storage tanks. It can reduce the occupied area of the tanks. An auxiliary heater is equipped to reheat the first fluid if necessary. The auxiliary heater can be a natural gas or an oil driven heater.

The power generator is the key equipment of the system. It is difficult to find a suitable microvapor turbine as the output electricity is less than 10 kW in each CCHP module. But fortunately, we have noticed that there is a manufacturer who can provide one kind of microscrew engine with output power of 10 kW. Furthermore, the driving medium of screw engines can be vapor or mixture of vapor and water. Thus, a 10 kW microscrew engine is chosen to be the power generator in the modular solar thermal CCHP system.

Water heater is mainly a heat exchanger used to heat the external circulating water. A plate type heat exchanger can be used as water heater in the modular CCHP system.

Of course, pumps are necessary to drive the fluids in the modular solar thermal CCHP system. The main pumps include a first fluid pump, a second fluid pump, a coolant pump and solution pumps in the absorption refrigerator, a hot water pump in the water heater, and a cooling water pump in the cooling unit.

If the refrigerator should meet the requirements of freezing/chilling food and air conditioning, the temperature of coolant should be lower than 0°C. Thus, general LiBr-H<sub>2</sub>O absorption refrigerators with the evaporating temperature above 0°C cannot be used at this field though its efficiency is relatively higher. A novel diffusion-absorption refrigerator (DAR) proposed by the author is used to supply low temperature coolant in the modular solar thermal CCHP system. The diagram of flow chart of the novel DAR is shown in

Figure 2. Experimental researches have shown that this novel DAR can be driven by 72~96°C hot water to provide -13~5°C coolant [18]. Because the temperature of the second fluid leaving from the power generator is higher than 96°C, -15~5°C coolant is feasibly obtained in the modular CCHP system. Furthermore, as the DAR has unitary pressure in the whole system, the pumps in the novel DAR are just used to overcome the flowing resistance of the fluids. Thus, the pumps in the novel DAR consume less electricity than the pumps used in other absorption refrigerators.

The novel DAR consists of a generator, a condenser, an adiabatic spray evaporator and an evaporator heat exchanger, an adiabatic spray absorber and a solution cooler, a solution heat exchanger, a reservoir, and circulation pumps, in which the generator, condenser, evaporator heat exchanger, solution cooler, and solution heat exchanger are plate heat exchangers. The working fluid is the triple fluid of LiNO<sub>3</sub>-NH<sub>3</sub>-He, in which LiNO<sub>3</sub>, NH<sub>3</sub>, and He (helium) are used as absorbent, refrigerant, and diffusion gas, respectively. The principle or working process of the DAR shown in Figure 2 can be described as follows.

At first, the hot water or vapor enters into the generator and heats the strong solution (high concentration of ammonia). When the strong solution temperature reaches its saturate point, ammonia vapor escapes and separates from solution. Vapor is condensed by cooling water in the condenser and liquid ammonia subsequently enters the spray evaporator in which diffusion and evaporation take place and some liquid ammonia evaporates to cool down the remaining liquid ammonia. Then the remaining liquid ammonia with low temperature is pumped into the evaporator heat exchanger to exchange heat with the coolant and subsequently goes back to the evaporator to take part in the next diffusion-evaporation process. And the evaporated ammonia vapor in the evaporator mixes with the diffusion gas Helium and then flows into the spray absorber by one of the gas pipes. At the same time, the weak solution separated from the generator flows through the solution heat exchanger and is cooled down by the strong solution pumped out from reservoir. The precooled weak solution is then pumped through the solution cooler and subcooled by cooling water and subsequently sprayed into the spray absorber. In spray

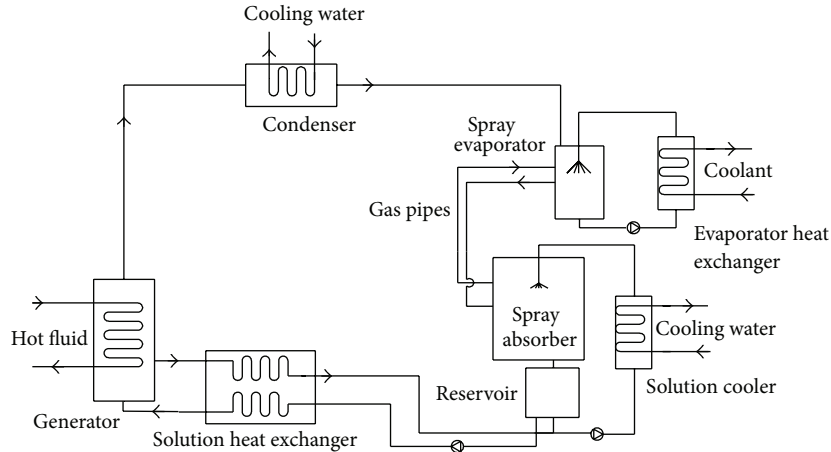


FIGURE 2: Diagram of flow chart of the novel DAR.

absorber, the falling weak solution absorbs ammonia vapor from gas mixture ( $\text{NH}_3$  and He) and becomes strong solution at the outlet of absorber, while the gas mixture with less ammonia, because of its smaller density, rises and enters into the evaporator by the other gas pipe to take part in the next diffusion-absorption process. The strong solution then leaves absorber and enters into the reservoir and is consequently pumped into the generator after getting preheated by the high temperature weak solution in the solution heat exchanger. It can be seen that there are two circulations in the operation. One is the solution circulation in the circuit consisting of the generator, vapor-solution separator, solution heat exchanger, solution cooler, spray absorber, and reservoir. The other is the gas circulation in the circuit mainly consisting of the spray absorber and evaporator.

DAR has advantages such as single-pressure, having no need of throttling valve, little noise, easy maintenance, and long service life. The equipped low power consumption pumps not only increase the amount of solution circulation and make it possible to enlarge refrigeration capacity, but also avoid the strict limitation of relative position of each part. Moreover, the use of an adiabatic spray absorber and plate heat exchangers makes it more compact. It should be mentioned that the circulation pumps in this DAR are just used to overcome the flow resistance. This is different to the ones used in other absorption refrigeration systems in which the pumps should provide higher pressure to build high pressure region. So the input power of each pump in Figure 2 is very small, which can obviously reduce electricity consumption.

The operation modes of the modular CCHP system shown in Figure 1 are very flexible and it can be easily changed from one to another as follows:

- (a) combined cooling, heating, and power generation (CCHP);
- (b) combined cooling and power generation (CCP);
- (c) combined heating and power generation (CHP);
- (d) combined cooling and heating (CCH);

- (e) power generation (this mode is equivalent to a general STP system);
- (f) cooling;
- (g) heating.

In each operation mode, the thermal energy storage can be determined to operate or shut off according to the collected solar energy. This modular system can simultaneously provide 10 kW electricity,  $-15\sim 5^\circ\text{C}$  coolant, and  $60^\circ\text{C}$  hot water to meet the requirements of cooling, heating, and power consumption in a general family or other fields. It also can be assembled to be a bigger system by connecting several modules together to meet the requirements of different fields.

Based on this work, we are designing and constructing a prototype of this modular trigeneration system in our campus. Further theoretical and experimental researches will be conducted in the future.

### 3. Performance Evaluation and Discussion

As mentioned above, the second fluid in Figure 1 may be water or an organic working fluid, but water ( $\text{H}_2\text{O}$ ) was chosen as the second fluid (i.e., the power cycle medium) to evaluate the performance of the solar thermal CCHP system. The reason is that this is a trigeneration system, and the DAR should be driven by heat source with temperature higher than  $96^\circ\text{C}$  to obtain  $-15^\circ\text{C}$  coolant. If an organic working fluid is chosen as the second fluid, the temperature of the second fluid at outlet of the power generator will be too low to drive the DAR to obtain  $-15^\circ\text{C}$  coolant. For example, if the second fluid is R245fa and its temperature at inlet of the power generator is  $150^\circ\text{C}$ , the temperature at outlet of the power generator is just about  $83^\circ\text{C}$  when the expansion ratio of the power generator is given as 4. Though this outlet temperature ( $83^\circ\text{C}$ ) can start the DAR, it is not high enough to drive the DAR to obtain  $-15^\circ\text{C}$  coolant. Thus, water was chosen as the second fluid to meet the trigeneration requirement. In other words, if the required coolant temperature is above  $0^\circ\text{C}$ , an organic working fluid such as R245fa may be an ideal candidate of the second fluid.

TABLE 1: Parameters of the second fluid at the inlet/outlet of each part.

State point	Pressure (MPa)	Temperature ( $^{\circ}\text{C}$ )	Medium and dryness
1	0.6	160	Overheated vapor, $x^* = 1$
2	0.15	111.35	Wet vapor, $x = 0.9482$
2a	0.15	111.35	Wet vapor, $x = 0.5$
4	0.15	111.35	Saturated water, $x = 0$
5	0.6	111.42	Subcooled water, $x = 0$
6	0.6	158.83	Saturated water, $x = 0$

\*  $x$  stands for the dryness of vapor.

TABLE 2: Input power of each pump.

Input power (kW)	Pumps in DAR			Cooling water pump	Hot water pump	The second fluid pump	The first fluid pump
	Absorber pump	Solution pump	Evaporator pump				
	0.37	0.09	0.09	1.1	0.09	2.2	2.2

In addition, attentions were mainly paid to the comparison of CCHP and STP modes. In other words, only the operation modes of A (i.e., CCHP mode) and E (i.e., STP mode) mentioned above are considered in the next evaluation to compare the efficiencies of CCHP and STP systems. It also should be mentioned that the effect of thermal storage and auxiliary heater is not taken into account at this work when evaluating the performance of the solar thermal CCHP system.

**3.1. Assumptions and Calculation Methodology.** Before evaluating the performance, some assumptions are given as follows.

- (1) The total output electricity is given as 10 kW. The expansion ratio, expansion efficiency, and the work-to-electric efficiency of the power generator are 4.0, 0.75, and 1.0, respectively.
- (2) The thermal energy collected by solar collectors is adequate for power generation. The input energy of the system is calculated by the input energy of vapor flowing through the power generator.
- (3) The efficiencies of the novel DAR and the heat exchanger in water heater are 0.3 and 0.8, respectively.
- (4) The flow resistance of the second fluid is neglected.
- (5) The efficiency of each pump is given as 0.75.

The power cycle of the second fluid (water) in the temperature-entropy ( $T$ - $s$ ) diagram is shown in Figure 3. The parameters of the second fluid at the inlet/outlet of each part are given in Table 1. The rated input power of each pump is given in Table 2.

When the system operates in mode E (i.e., power generation or STP mode), the vapor leaving the power generator is still assumed to be wet vapor. The parameters in this mode are shown in Table 1. The STP cycle consists of the cycle 1-2-4-5-6-7-1 as shown in Figure 3. In the cycle, 2-4 is a cooling process and the cooling unit in Figure 1 should

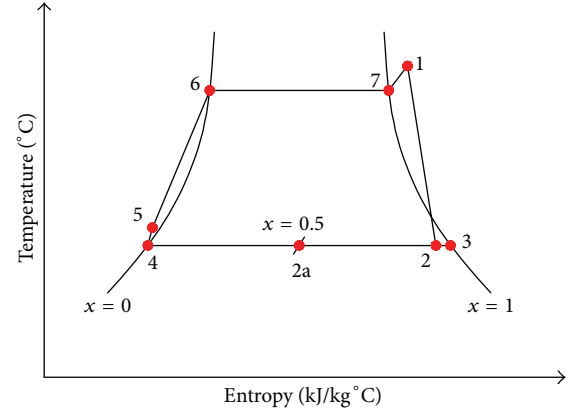


FIGURE 3: Power cycle of the second fluid (water).

operate to condense the exhausted vapor leaving from the power generator in the STP mode. Thus, the condensed saturated water can be reused and circulated in the second part (PEU) of the system.

In Figure 3, the total input thermal energy of the system can be determined by

$$Q_{v,in} = m_s (h_1 - h_5), \quad (1)$$

where  $Q_{v,in}$  is the total input thermal energy of the system, kW;  $m_s$  is the mass flow rate of the second fluid (steam or water), kg/s; and  $h_1$  and  $h_5$  are the specific enthalpies of state points of 1 and 5, respectively, kJ/(kg $^{\circ}\text{C}$ ).

The power output of the system  $N_{PG}$  can be calculated by

$$N_{PG} = m_s (h_1 - h_2). \quad (2)$$

If the thermal energy of processes of 2-2a and 2a-4 in Figure 3 are used to drive the DAR and the water heater,

respectively, the cooling capacity of the DAR and heating capacity of the water heater can be calculated by, respectively,

$$\begin{aligned} Q_C &= m_s (h_2 - h_{2a}) \eta_{\text{DAR}}, \\ Q_{\text{HW}} &= m_s (h_{2a} - h_4) \eta_{\text{WH}}, \end{aligned} \quad (3)$$

where  $Q_C$  is the cooling capacity of the refrigerator, kW, and  $Q_{\text{HW}}$  is the heating capacity of the water heater, kW.  $\eta_{\text{DAR}}$  and  $\eta_{\text{WH}}$  are the efficiencies of DAR and water heater, respectively.

The overall energy efficiency (i.e., the first law efficiency) of the CCHP system is determined by

$$\eta_s = \frac{N_{\text{PG}} + Q_C + Q_{\text{HW}} - \sum N_{p,i}}{Q_{v,\text{in}}}, \quad (4)$$

where  $\eta_s$  is the overall energy efficiency of the solar thermal CCHP system and  $\sum N_{p,i}$  is the total input power of pumps, kW. The input power of the second fluid pump ( $N_{p,\text{sec}}$ ) depends on the vapor flow rate and it can be calculated as

$$N_{p,\text{sec}} = \frac{1000m_s (p_5 - p_4)}{\rho_4}, \quad (5)$$

where  $p_4$  and  $p_5$  are the inlet pressure and outlet pressure of the second fluid pump (as shown in Figure 3), MPa, and  $\rho_4$  is the density of the second fluid at the inlet of the pump,  $\text{kg/m}^3$ .

Each input power of the other pumps is calculated based on its rated input power as shown in Table 2.

The overall exergy efficiency (i.e., the second law efficiency) of the solar thermal CCHP system is determined by

$$\eta_{\text{ex}} = \frac{N_{\text{PG}} + E_C + E_{\text{HW}} - \sum N_{p,i}}{E_{v,\text{in}}}, \quad (6)$$

where  $\eta_{\text{ex}}$  is the overall exergy efficiency of the solar thermal CCHP system;  $E_C$  is the exergy of cooling capacity of the refrigerator, kW;  $E_{\text{HW}}$  is the exergy of heating capacity of the water heater, kW;  $E_{v,\text{in}}$  is the exergy of input thermal energy of the system, kW; and  $\sum N_{p,i}$  is the total exergy of input power of pumps, kW.

Thus, the  $E_C$ ,  $E_{\text{HW}}$ , and  $E_{v,\text{in}}$  in (6) can be calculated as, respectively,

$$E_C = Q_C \left( \frac{T_0 + 273.15}{T_e + 273.15} - 1 \right), \quad (7)$$

$$E_{\text{HW}} = Q_{\text{HW}} \left( 1 - \frac{T_0 + 273.15}{T_{\text{HW}} + 273.15} \right), \quad (8)$$

$$E_{v,\text{in}} = Q_{v,\text{in}} \left( 1 - \frac{T_0 + 273.15}{T_{\text{hs}} + 273.15} \right), \quad (9)$$

where  $T_0$ ,  $T_e$ ,  $T_{\text{HW}}$ , and  $T_{\text{hs}}$  are the average temperatures of environment, evaporator, hot water, and hot fluid in the heat exchanger (vapor generator), respectively. In this case study, the  $T_0$ ,  $T_e$ , and  $T_{\text{HW}}$  are given as 25°C, -10°C, and 111.35°C, respectively. The averaged  $T_{\text{hs}}$  is given to be 10°C higher than the temperature of vapor at outlet of the vapor generator; that is,  $T_{\text{hs}} = T_1 + 10$ .

## 3.2. Results and Discussion

### 3.2.1. Performance Comparison of CCHP and STP Modes.

Based on the above conditions, primary calculation shows that when the system operates in the mode of E (i.e., equivalent STP mode) and generates 10 kW electricity, the necessary input vapor energy is 126.42 kW. Under the conditions shown in Tables 1 and 2, the energy and exergy utilization profiles for operation modes A and E are shown in Figures 4 and 5, respectively.

The pumps operating in the mode E consume energy of 2.235 kW so that the net output electricity is 7.765 kW. Thus, the overall energy efficiency of the system ( $\eta_s$ ) in the mode E is only 6.14%. Moreover, tremendous thermal energy should be released by cooling water to condense the exhausted vapor of the power generator. In this case, the thermal energy released by cooling water is 92.09% of the input energy. The energy consumption of cooling water pump and the released thermal energy seriously deteriorate the overall energy efficiency of solar energy utilization. In this STP mode, the overall exergy efficiency of the system is 18.77% which is less than the results of [3]. In [3], the exergy efficiency was 25.12% but the saturation temperature in the boiler was about 201°C which is higher than that in this work (namely, 160°C).

When the system operates in the mode A (CCHP mode) and the working conditions are as shown in Table 1, the cooling unit can be shut off because of the subsequent utilization of refrigerator and water heater. Calculation shows that in the CCHP mode the system can produce 10 kW electricity, 16.51 kW cooling, and 49.13 kW heating, and the overall energy efficiency of the system reaches 57.56% which is 9.37 times as big as that of mode E (STP mode). In the CCHP mode, the pumps consume 2.875 kW and the net output electricity is 7.125 kW. Though the net output electricity of the CCHP mode is less than that of the STP mode, the extra recovered cooling and heating promote obviously the overall efficiency of the CCHP mode. The gained heating capacity in water heater can heat city water from 20°C to 60°C with flow rate of 1.05 m<sup>3</sup>/h. In the CCHP mode, the overall exergy efficiency is 49.21% which is 2.62 times as big as that of the STP mode. It is obvious that the CCHP mode can significantly improve the performance of the solar thermal CCHP system.

Figures 4 and 5 show that when the system operates in mode E (STP mode), the losses of energy and exergy are 92.09% and 75.82%, respectively. But when it operates in mode A (CCHP mode), the losses of energy and exergy are only 40.17% and 43.84%, respectively. So the CCHP operation mode can significantly improve the energy utilization efficiency.

In addition, if the coolant temperature is above 0°C, for example, just meeting the requirement of air conditioning, the DAR can be replaced by a high efficiency LiBr-H<sub>2</sub>O absorption refrigerator. Thus, the overall efficiency of the system can be promoted greatly. For example, if the coefficient of performance (COP) of LiBr-H<sub>2</sub>O absorption refrigerator is given as 1.0 with 5°C evaporator temperature and the total

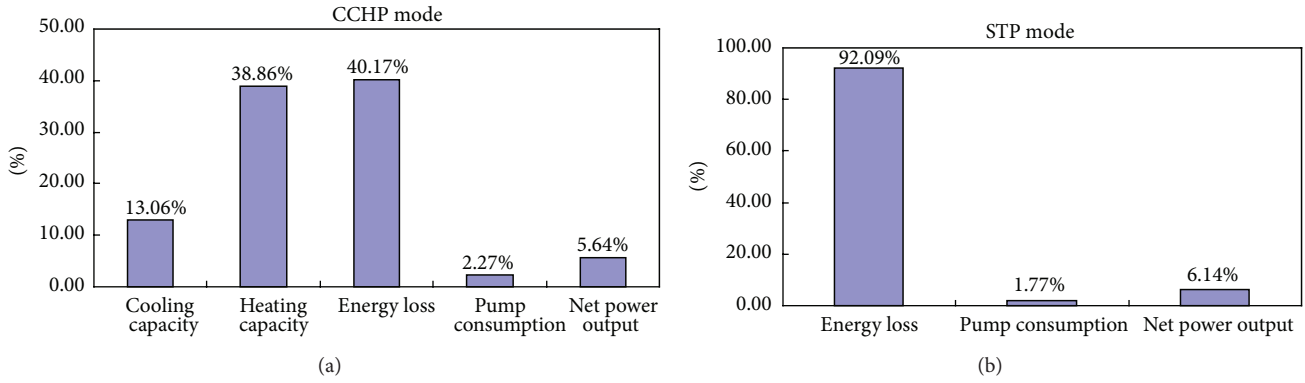


FIGURE 4: Energy utilization profiles of operation modes A (CCHP) and E (STP).

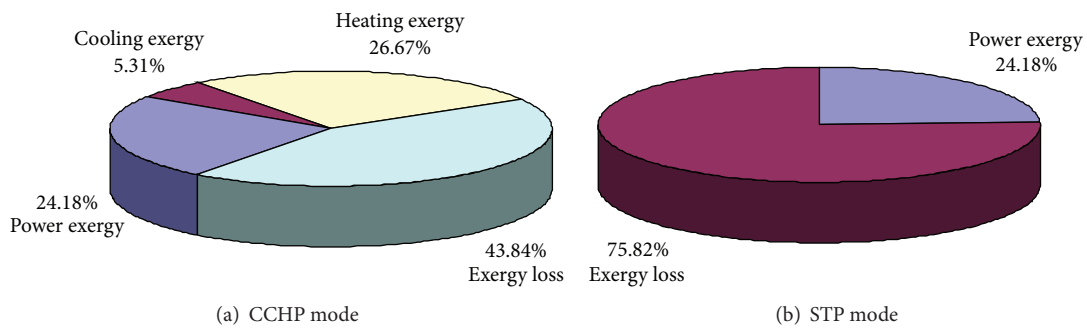


FIGURE 5: Exergy utilization profiles of operation modes A and E.

input power of the additional solution pumps is 5 kW, the overall energy efficiency and exergy efficiency of the CCHP system can reach 84.59% and 53.47%, respectively. It sounds more attractive.

3.2.2. *Influence of Inlet Vapor Parameters.* Calculations show that when the total output electricity is given as 10 kW and the expansion ratio of the screw expander (power generator) is 4.0, the efficiencies of the STP or CCHP mode vary with the inlet pressure and temperature of vapor entering the power generator, as shown in Figure 6.

Figures 6(a) and 6(b) illustrate that when the inlet vapor temperature ( $T_{in}$ ) is constant, all the energy and exergy efficiencies of the CCHP and STP mode increase with inlet vapor pressure increasing. But it is not very obvious for the STP mode or the overall energy efficiency of the CCHP mode. The overall exergy efficiency of CCHP mode increases rapidly with inlet vapor pressure increasing. It means that higher inlet vapor pressure can improve the efficiencies of the CCHP and STP modes, especially the exergy efficiency of the CCHP mode.

Figure 6(c) shows that the exergy efficiency of STP mode decreases obviously with the inlet vapor temperature when the inlet vapor pressure is constant though the energy efficiency of STP mode slightly increases with the inlet vapor temperature increasing. The reason is that the input heat capacity (i.e., input energy) decreases about 11.37%, while the

input exergy increases 32.39% when the inlet temperature varies from 160°C to 300°C. Figure 6(d) shows that the higher the inlet vapor temperature, the smaller the overall energy and exergy efficiencies of CCHP mode if the inlet vapor pressure is constant. Figures 6(c) and 6(d) illustrate that the exergy efficiencies of both CCHP and STP modes cannot benefit from a higher inlet vapor temperature at given conditions. Calculations also indicate that it is suitable to keep the inlet vapor temperature the same as the saturate temperature at given inlet vapor pressure. Though this may cause the status of end-expansion to be in the wet vapor region, it is also acceptable because the screw expander can operate with wet vapor without any problem.

Figure 6 indicates that the CCHP system can benefit from higher inlet vapor pressure, but not the higher inlet vapor temperature. It also means that in this solar thermal CCHP system, the temperature of the first fluid in solar collectors should not be much higher than the corresponding saturate temperature of the inlet vapor of the screw expander. The detailed effect and optimum parameters need to be investigated in future theoretical and experimental researches.

#### 4. Conclusions

The above analyses indicate that the proposed micromodular solar thermal CCHP system is feasible and it can significantly improve the energy and exergy efficiencies of solar thermal

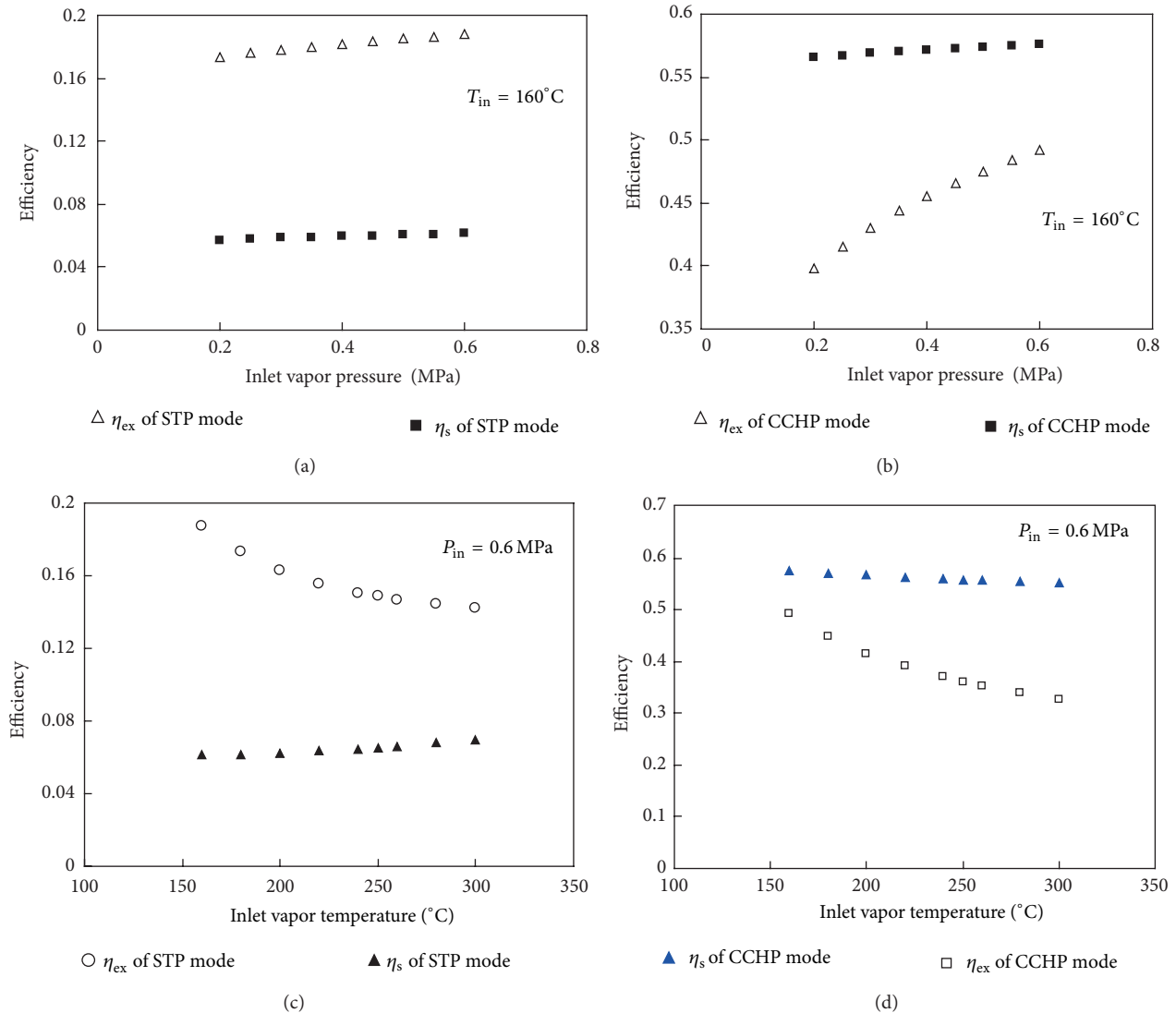


FIGURE 6: The effects of inlet vapor parameters on the overall efficiencies of energy and exergy.

power systems. It has seven optional operation modes. This makes its operation more flexible. It also can be assembled to be a large system by connecting several modules to meet the requirements of different fields.

Primary calculations show that overall energy and exergy efficiencies of the CCHP operation mode are obviously higher than that of the STP mode when the output electricity is given as a constant. In order to obtain the highest overall performance, a high efficient absorption refrigerator and water heater should be equipped to the modular CCHP system.

Analyses show that the performance of CCHP system is affected by the pressure and temperature of vapor at inlet of the power generator. When the inlet vapor pressure is constant, higher inlet vapor temperature deteriorates both the energy and exergy efficiencies of the CCHP system. On the other hand, higher inlet vapor pressure can improve both the energy and exergy efficiencies of the CCHP system. Thus, if it is available, the inlet vapor pressure should be as

high as possible. In this work, the inlet vapor temperature and pressure are mainly determined on the basis of the cost of solar collectors, the available screw expander, and its characteristics when the output electricity is given as 10 kW. Thus, the inlet vapor temperature and pressure of the vapor entering the screw expander are given as 160 $^{\circ}\text{C}$  and 0.6 MPa, respectively. Though the lower inlet vapor pressure may cause lower efficiency of the CCHP system, it can reduce the initial investment.

Anyway, this work makes it possible to efficiently utilize solar thermal power in microdistributed energy systems though only the CCHP and STP operation modes are primarily analyzed and compared. Further research such as optimum design, effect of the solar radiation, characteristics of solar collectors and absorbers, and detailed simulation and experiments will be conducted to investigate the performance characteristics of the CCHP at all operation modes, especially when there are not so many demands for electricity, hot water, or cooling capacity in the next researches. In addition,

the effect of the thermal storage and the auxiliary heater on the system performance also needs investigation. Fortunately, we are designing an experimental system as a prototype to investigate this CCHP system with the financial support of Shenzhen government. Some theoretical and experimental researches will be carried out soon.

### Conflict of Interests

The author declares that there is no conflict of interests regarding the publication of this paper.

### Acknowledgment

The author is grateful to Shenzhen Science and Technology Innovation Committee for supporting this research (no. JCYJ20130331150226792).

### References

- [1] R. L. Pons and T. B. Clark, "A dish-stirling solar-thermal power system," *International Journal of Ambient Energy*, vol. 1, no. 3, pp. 133–148, 1980.
- [2] D. Y. Goswami, "Solar thermal power: status of technologies and opportunities for research," in *Proceedings of the 2nd ASME-ISHMT Heat and Mass Transfer Conference*, pp. 57–60, Tata McGraw-Hill, New Delhi, India, 1995.
- [3] Y. You and E. J. Hu, "A medium-temperature solar thermal power system and its efficiency optimisation," *Applied Thermal Engineering*, vol. 22, no. 4, pp. 357–364, 2002.
- [4] S. Lu and D. Y. Goswami, "Optimization of a novel combined power/refrigeration thermodynamic cycle," *Journal of Solar Energy Engineering*, vol. 125, no. 2, pp. 212–217, 2003.
- [5] G. Tamm, D. Y. Goswami, S. Lu, and A. A. Hasan, "Novel combined power and cooling thermodynamic cycle for low temperature heat sources, Part I: theoretical investigation," *Journal of Solar Energy Engineering*, vol. 125, no. 2, pp. 218–222, 2003.
- [6] G. Tamm and D. Y. Goswami, "Novel combined power and cooling thermodynamic cycle for low temperature heat sources, part II: experimental investigation," *Journal of Solar Energy Engineering*, vol. 125, no. 2, pp. 223–229, 2003.
- [7] S. Vijayaraghavan and D. Y. Goswami, "Organic working fluids for a combined power and cooling cycle," *Journal of Energy Resources Technology*, vol. 127, no. 2, pp. 125–130, 2005.
- [8] M. Kane, D. Larrain, D. Favrat, and Y. Allani, "Small hybrid solar power system," *Energy*, vol. 28, no. 14, pp. 1427–1443, 2003.
- [9] F. Xu and D. Y. Goswami, "Thermodynamic properties of ammonia-water mixtures for power-cycle applications," *Energy*, vol. 24, no. 6, pp. 525–536, 1999.
- [10] D. Y. Goswami and F. Xu, "Analysis of a new thermodynamic cycle for combined power and cooling using low and mid temperature solar collectors," *Journal of Solar Energy Engineering*, vol. 121, no. 2, pp. 91–97, 1999.
- [11] F. Xu, D. Y. Goswami, and S. S. Bhagwat, "A combined power/cooling cycle," *Energy*, vol. 25, no. 3, pp. 233–246, 2000.
- [12] S. Lu and D. Y. Goswami, "Theoretical analysis of ammonia-based combined power/refrigeration cycle at low refrigeration temperatures," in *Proceedings of the Solar Engineering 2002*, pp. 117–125, American Society of Mechanical Engineers, Reno, Nev, USA, June 2002.
- [13] N. Zhang, R. Cai, and N. Lior, "A novel ammonia-water cycle for power and refrigeration cogeneration," in *Proceedings of the ASME International Mechanical Engineering Congress and Exposition (IMECE '04)*, pp. 183–196, ASME, Anaheim, Calif, USA, 2004.
- [14] Z. S. Abdel-Rehim, "A new system to produce cooling and power using solar thermal energy," *Energy Sources A: Recovery, Utilization and Environmental Effects*, vol. 33, no. 17, pp. 1636–1650, 2011.
- [15] A. Mayere and S. Riffat, "A novel solar driven micro-CHP system: a state of the art review," *Journal of Energy and Power Engineering*, vol. 4, no. 11, pp. 30–35, 2010.
- [16] D. Borello, A. Corsini, F. Rispoli, and E. Tortora, "A co-powered biomass and concentrated solar power rankine cycle concept for small size combined heat and power generation," *Energies*, vol. 6, no. 3, pp. 1478–1496, 2013.
- [17] Y. X. Su, Z. D. Fei, and X. X. Yang, "Investigation on the distributed energy system for cooling-heating-power combined cycle driven by solar energy," *Energy Engineering*, vol. 5, pp. 24–27, 2004.
- [18] H. D. Wang, "Experimental study on LiNO<sub>3</sub>-NH<sub>3</sub> diffusion-absorption refrigeration system," *Key Engineering Materials*, vol. 474–476, pp. 2335–2340, 2011.

## Research Article

# Improved Performance for Dye-Sensitized Solar Cells Using a Compact TiO<sub>2</sub> Layer Grown by Sputtering

Hung-Chih Chang,<sup>1</sup> Ming-Jenq Twu,<sup>2</sup> Chun-Yao Hsu,<sup>3</sup> Ray-Quen Hsu,<sup>1</sup> and Chin-Guo Kuo<sup>4</sup>

<sup>1</sup> Department of Mechanical Engineering, National Chiao Tung University, 1001 Ta Hsueh Road, Hsinchu 30010, Taiwan

<sup>2</sup> Department of Mechatronic Engineering, National Taiwan Normal University, 162 Heping East Road, Section 1, Taipei 10610, Taiwan

<sup>3</sup> Department of Mechanical Engineering, Lunghwa University of Science and Technology, No. 300, Section 1, Wanshou Road, Guishan, Taoyuan 33306, Taiwan

<sup>4</sup> Department of Industrial Education, National Taiwan Normal University, 162 Heping East Road, Section 1, Taipei 10610, Taiwan

Correspondence should be addressed to Chin-Guo Kuo; [chinguo7@yahoo.com.tw](mailto:chinguo7@yahoo.com.tw)

Received 22 March 2014; Accepted 5 April 2014; Published 22 May 2014

Academic Editor: Ho Chang

Copyright © 2014 Hung-Chih Chang et al. This is an open access article distributed under the Creative Commons Attribution License, which permits unrestricted use, distribution, and reproduction in any medium, provided the original work is properly cited.

This work determines the effect of compact TiO<sub>2</sub> layers that are deposited onto fluorine-doped tin oxide (FTO), to improve the performance of dye-sensitized solar cells (DSSC). A series of compact TiO<sub>2</sub> layers are prepared using radio frequency (rf) reactive magnetron sputtering. The films are characterized using X-ray diffraction (XRD), atomic force microscopy (AFM), scanning electron microscopy (SEM), and UV-Vis spectroscopy. The results show that when the Ar/O<sub>2</sub>/N<sub>2</sub> flow rates are 36:18:9, the photo-induced decomposition of methylene blue and photo-induced hydrophilicity are enhanced. After annealing at 450°C in an atmosphere ambient for 30 min, the compact TiO<sub>2</sub> layers exhibit higher optical transmittance. The XRD patterns for the TiO<sub>2</sub> films for FTO/glass show a good crystalline structure and anatase (101) diffraction peaks, which demonstrate a higher crystallinity than the ITO/glass films. As a result of this increase in the short circuit photocurrent density, the open-circuit photovoltage, and the fill factor, the DSSC with the FTO/glass and Pt counter electrode demonstrates a solar conversion efficiency of 7.65%.

## 1. Introduction

Photocatalytic TiO<sub>2</sub> materials are widely used in antipollution applications, deodorization, dust-proofing, and for high-performance dye-sensitized solar cells (DSSC) because of their unique physical, chemical, and optical properties, their lack of toxicity, and low cost [1]. The energy gap for titanium dioxide for photocatalysts is about 3.2 eV, so ultraviolet excitation causes electrons to jump to the conduction band to form electron-hole pairs. The holes formed in the catalyst are used to degrade organic materials or undesired pollutants for antipollution, deodorization, and antibacterial uses [2, 3]. Because N-doped TiO<sub>2</sub> (TiO<sub>2</sub>:N) powders or thin films have better photocatalytic properties than undoped TiO<sub>2</sub> films [4], some studies have added nitrogen gas during the growth of TiO<sub>2</sub> films, to increase the photocatalytic activity of TiO<sub>2</sub> in the visible-light region [5, 6]. Using N-doped TiO<sub>2</sub> results

in significant improvements in the visible light response and photocatalytic degradation [7].

Since the first report of a DSSC by O'Regan and Grätzel, in 1991 [8], they have been intensively studied as a potential replacement for standard solar cells because of their relatively high efficiency and low cost [9], compared with p-n junction photovoltaic devices [10, 11]. A typical DSSC consists of dye molecules that act as sensitizers, a porous TiO<sub>2</sub> layer, a fluorine-doped tin oxide (FTO) substrate, an electrolyte charge carrier, and a platinized FTO substrate as a so-called counter electrode or cathode. The structure, morphology and crystalline phases of TiO<sub>2</sub> play an important role in the performance of DSSC's. The nano-sized porous structure TiO<sub>2</sub> layer is widely used as an electrode in DSSC, to allow a high density of dye molecules to be embedded onto the TiO<sub>2</sub> surface and enhance the photo absorption process [12]. However, the porous structure of the TiO<sub>2</sub> layer

TABLE 1: The deposition conditions for TiO<sub>2</sub>.

Substrate	nonalkali glass 25 × 25 × 1 mm <sup>3</sup>			
Target	Ti (99.99% purity)			
Gas	Ar, O <sub>2</sub> , N <sub>2</sub> (99.99% purity)			
Base pressure	5.0 × 10 <sup>-6</sup> torr			
Spin speed of the substrate	10 rpm			
Substrate-to-target distance	80 mm			
rf power	100 W			
Sputtering pressure	10 mtorr			
Substrate temperature	300°C			
Sample	Ar flow rate (mL/min)	O <sub>2</sub> flow rate (mL/min)	N <sub>2</sub> flow rate (mL/min)	Ar : O <sub>2</sub> : N <sub>2</sub>
Number 1	35	35	0	1 : 1 : 0
Number 2	48	24	0	2 : 1 : 0
Number 3	54	18	0	3 : 1 : 0
Number 4	20	20	20	1 : 1 : 1
Number 5	29	29	14	1 : 1 : 0.5
Number 6	25	25	8	1 : 1 : 0.33
Number 7	27	14	14	2 : 1 : 1
Number 8	36	18	9	2 : 1 : 0.5
Number 9	36	18	6	2 : 1 : 0.33
Number 10	45	14	14	3 : 1 : 1
Number 11	45	15	7	3 : 1 : 0.5
Number 12	41	14	4	3 : 1 : 0.33

can cause an electrical short between the liquid electrolyte and the FTO substrate, which leads to a decrease in cell efficiency. A potential means of preventing recombination is the application of a compact metal-oxide film between the nano-sized porous TiO<sub>2</sub> layer and the FTO substrate. Of these metal oxides, TiO<sub>2</sub> is the most effective electrolyte blocker and has been extensively studied [13, 14]. This compact layer improves the adhesion of the porous TiO<sub>2</sub> to the FTO substrate and provides a larger TiO<sub>2</sub>/FTO contact area and more effective electron transfer from the porous TiO<sub>2</sub> to the FTO by preventing the electron recombination process [15]. A compact TiO<sub>2</sub> layer is prepared using many growth techniques, such as sputtering, chemical vapor deposition, spin-coating, or spray pyrolysis. In particular, the compact TiO<sub>2</sub> layer produced by sputtering deposition is simple and inexpensive and is widely used in DSSC studies [16, 17].

This study determines the carrier blocking effect of a compact TiO<sub>2</sub> layer that is deposited onto a FTO substrate, using radio frequency (rf) reactive magnetron sputtering, with a Ti metal target, Ar as the plasma gas and O<sub>2</sub> and N<sub>2</sub> as the reactive gases. The effect of the Ar/O<sub>2</sub>/N<sub>2</sub> flow ratios on the structure, surface morphology, photocatalytic activity, and DSSC conversion efficiency of TiO<sub>2</sub> thin films is studied. The nano-sized porous TiO<sub>2</sub> layer is coated using the sol-gel process and calcination at 450°C and 500°C. The working electrode is a dye-sensitized TiO<sub>2</sub> film that is immobilized on a fluorine-doped tin oxide (FTO) substrate. The Pt and carbon counter electrode are coated onto FTO/glass substrates.

## 2. Experiments

Compact TiO<sub>2</sub> layers were coated onto FTO/glass substrates (nonalkali glass, 25 × 25 × 1 mm<sup>3</sup>) by rf reactive magnetron sputtering from a high purity Ti target in an Ar/O<sub>2</sub>/N<sub>2</sub> atmosphere, using a constant sputtering pressure (10 mtorr), rf power (100 W), substrate temperature (300°C) and distance between the substrate and the target (80 mm), and variable flow rates for argon, oxygen, and nitrogen. All of the samples were deposited by rotating the substrate (10 rpm), to ensure good surface morphology. Before deposition, the system was evacuated to a pressure of less than 5.0 × 10<sup>-6</sup> torr. The detailed deposition conditions are listed in Table 1. The substrates were cleaned, in acetone, using ultrasound, rinsed with deionized water, and dried in nitrogen. Samples 1–3 (TiO<sub>2</sub>) were deposited in an Ar/O<sub>2</sub> atmosphere, without nitrogen gas. Samples 4–12 (TiO<sub>2-x</sub>N<sub>x</sub>) were deposited in an Ar/O<sub>2</sub>/N<sub>2</sub> atmosphere and nitrogen gas was added in different fractions. The TiO<sub>2</sub> films were characterized by their deposition rates, hydrophilic properties, photocatalytic behavior, and morphology.

The porous TiO<sub>2</sub> film was coated onto the compact TiO<sub>2</sub>/FTO/glass using a mixture of P-25 with the TiO<sub>2</sub> sol-gel component studied in [18, 19]. The TiO<sub>2</sub> sol-gel was mixed with 0.3 g of commercially available Degussa P-25, to avoid any cracking of the film. The gels were predried for 20 min at 50°C and then sintered in a furnace at 450°C and 500°C (heating rate 10°C/min) for 30 min in air ambient, to produce the bare TiO<sub>2</sub> electrode used in this work to fabricate the

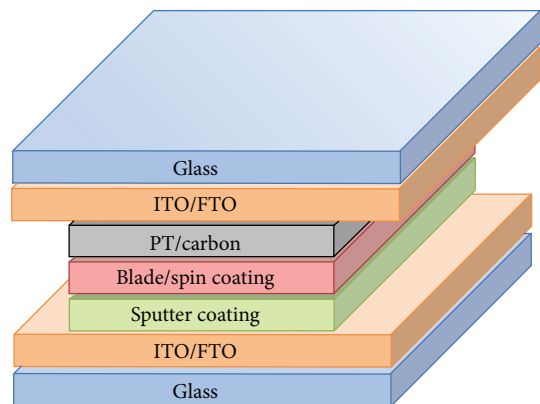


FIGURE 1: The structure of an assembled DSSC with a sputtered compact  $\text{TiO}_2$  layer/FTO/glass and other layers.

DSSC. The porous  $\text{TiO}_2$  films were immersed into the dye (N 719) complex, for 24 h at room temperature [20, 21].

The Pt and carbon counter electrode was coated onto FTO/glass substrates using DC sputtering with pure Ar gas and a DC power of 30 W. The dye-adsorbed  $\text{TiO}_2$  working electrode and the counter electrode were assembled into a sandwich-type cell and sealed with a hot-melt sealant. Figure 1 shows a schematic diagram of a DSSC with a sputtered compact  $\text{TiO}_2$  layer/FTO/glass. Dense  $\text{TiO}_2$  passivating layers were used to prevent any leakage to the liquid electrolyte by electron transfer.

The photo-induced hydrophilicity was evaluated using contact angle measurements to pure water, which were performed at room temperature in an ambient atmosphere, using a contact angle meter (FACE CA-VP150) with an experimental error of less than  $1^\circ$ . The photocatalytic behavior of the  $\text{TiO}_2$  coatings was assessed using a combination of ultraviolet irradiation and absorption measurements. The  $\text{TiO}_2$  was placed in  $10 \mu\text{M}$  methylene blue (MB) aqueous solution and irradiated for 4 hours, using  $1.5 \text{ mW}/\text{cm}^2$  UV lights. The observed photodecomposition of the aqueous solution is seen in the UV-Vis spectrum (measured using a UVP UVL-225D with a wavelength range of 300–800 nm) as a decrease in the maximum absorbance as the irradiation increases. The film thickness and crystal structure were, respectively, measured using  $\alpha$ -step (surface profiler system, Dektat) and XRD (Rigaku-2000). The morphology and the roughness were determined using SEM (JEOL JSM-6500F) and AFM (SPA 400).

The power used to test the prepared DSSC was a 150 W Xe lamp, which simulates sunlight (AM 1.5). Before the test, the distance between the light source and the sample was adjusted to allow a light source density of  $100 \text{ mW}/\text{cm}^2$ . The cell performance parameters, including the short-circuit current density ( $J_{\text{sc}}$ ), the open-circuit voltage ( $V_{\text{oc}}$ ), the fill factor (FF), and the photoelectronic conversion efficiency ( $\eta$  (%)) =  $J_{\text{sc}} \times V_{\text{oc}} \times \text{FF} / \text{total incident energy} \times 100$ ), were measured and calculated using the  $J$ - $V$  characteristics of DSSC's.

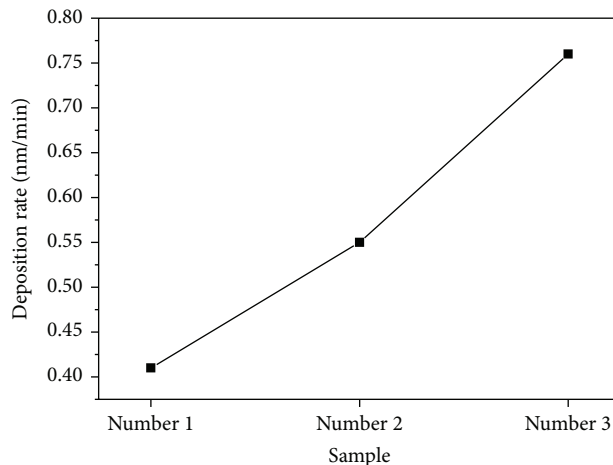


FIGURE 2: The  $\text{TiO}_2$  deposition rate for samples number 1, number 2, and number 3 (without nitrogen addition).

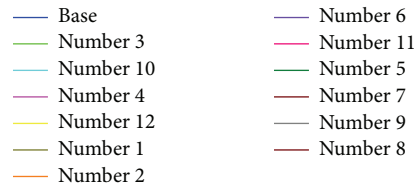
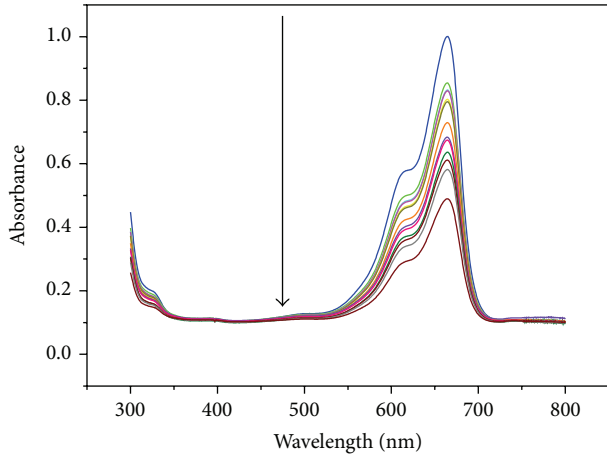
TABLE 2: The deposition rate and roughness value for the  $\text{TiO}_2$  films.

Samples	Deposition rate (nm/min)	Roughness, Ra (nm)
Number 1	0.41	0.32
Number 2	0.55	0.33
Number 3	0.76	0.44
Number 4	0.86	0.35
Number 5	0.65	0.47
Number 6	0.73	0.77
Number 7	0.79	2.77
Number 8	0.89	1.21
Number 9	0.75	2.25
Number 10	0.68	4.12
Number 11	0.71	3.95
Number 12	0.82	2.89

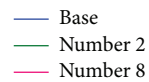
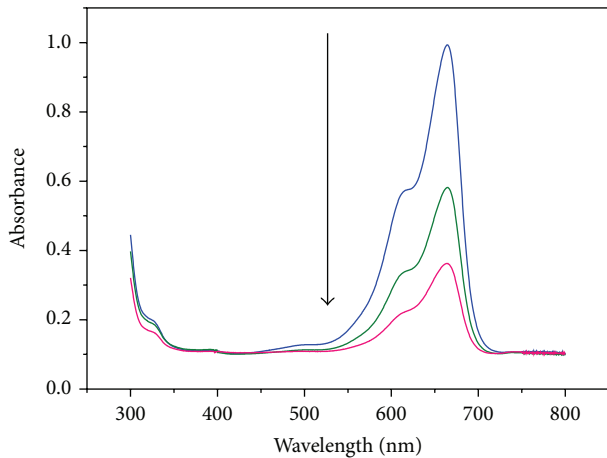
### 3. Results and Discussion

#### 3.1. Characteristics of $\text{TiO}_2$ Obtained by rf Reactive Sputtering.

The  $\text{TiO}_2$  photocatalytic thin films deposited on glass substrates demonstrate very good adherence. No cracking or peel off is observed after deposition. Figure 2 shows the deposition rates for samples number 1, number 2, number and 3. These three samples (where nitrogen was added) were deposited using  $\text{O}_2$  flow-rate ratios from 35 to 18 mL/min (see Table 1). The deposition rate increases as the  $\text{O}_2$  partial pressure decreases. Greater oxygen flow increases the probability of collision with  $\text{Ar}^+$  ions and decreases the energy of the  $\text{Ar}^+$  ions that bombard the Ti surface. Increasing the  $\text{O}_2$  flow rate also results in a significant decrease in the sputtering voltage [22]. Therefore, the dissociation gas is reduced, along with the plasma density and the deposition rate. Table 2 shows the deposition rates and roughness values for all samples. For nitrogen-doped samples, the roughness is increased when the Ar flow fraction is increased.



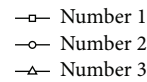
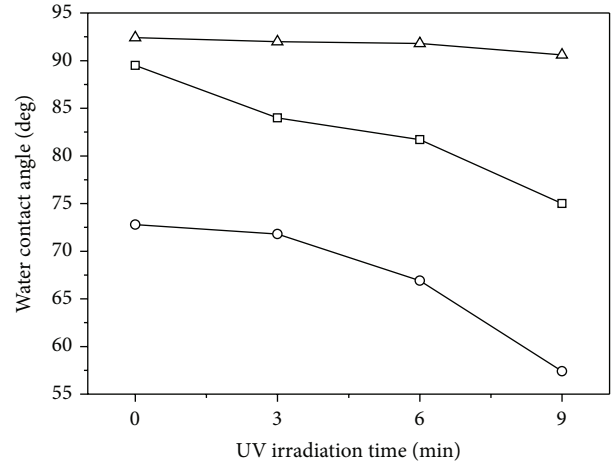
(a)



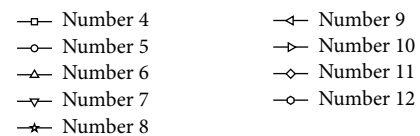
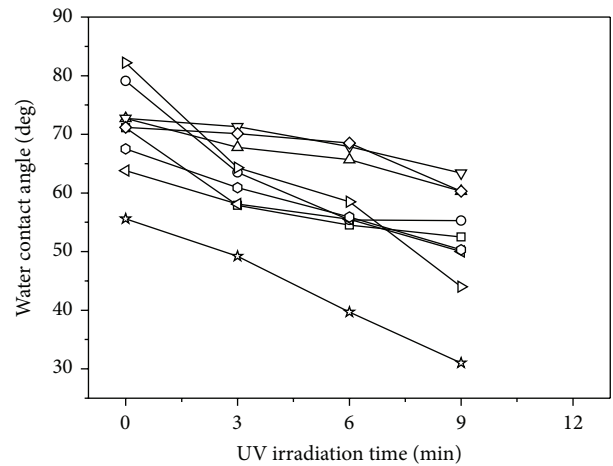
(b)

FIGURE 3: The absorption spectrum for MB aqueous solution ( $10 \mu\text{M}$ ,  $\text{pH} = 7.0$ ), after UV irradiation for 4 h: (a) samples 1–12 and (b) samples number 2 and number 8.

Figure 3(a) shows the absorption spectrum for MB under UV irradiation for 4 h, for films deposited under various coating conditions. If no nitrogen is added during the deposition process, the best degradation of MB is demonstrated by sample number 2, with a MB absorbance of 0.74. When nitrogen is added during the deposition process, the best absorbance of MB is 0.54, for sample number 8. The deposition parameters for sample number 8 are a rf power of 100 W, a deposition pressure of 10 mtorr, an  $\text{Ar}/\text{O}_2/\text{N}_2$  flow rate of 36/18/9 mL/min, and substrate temperature of



(a)



(b)

FIGURE 4: The change in the water contact angle after UV irradiation: (a) without nitrogen addition and (b) with nitrogen addition.

$300^\circ\text{C}$ . Figure 3(b) shows the absorption spectrum of MB under visible light irradiation for 4 h for the deposited film samples number 2 and number 8. This result shows that  $\text{TiO}_{2-x}\text{N}_x$  exhibits photocatalytic characteristics and the MB degradation of  $\text{TiO}_{2-x}\text{N}_x$  film is better than that of  $\text{TiO}_2$  film.

Figures 4(a) and 4(b) show the change in the water contact angle after UV irradiation for 9 min, without and with the addition of nitrogen, respectively. Figure 4(a) shows that the contact angles for the  $\text{TiO}_2$  films decrease by  $1^\circ$ ,  $14^\circ$ , and  $13^\circ$ , for samples number 1, number 2 and, number 3, respectively, after UV irradiation for 9 min. Figure 4(b) shows that the average contact angle for  $\text{TiO}_{2-x}\text{N}_x$  film deposited

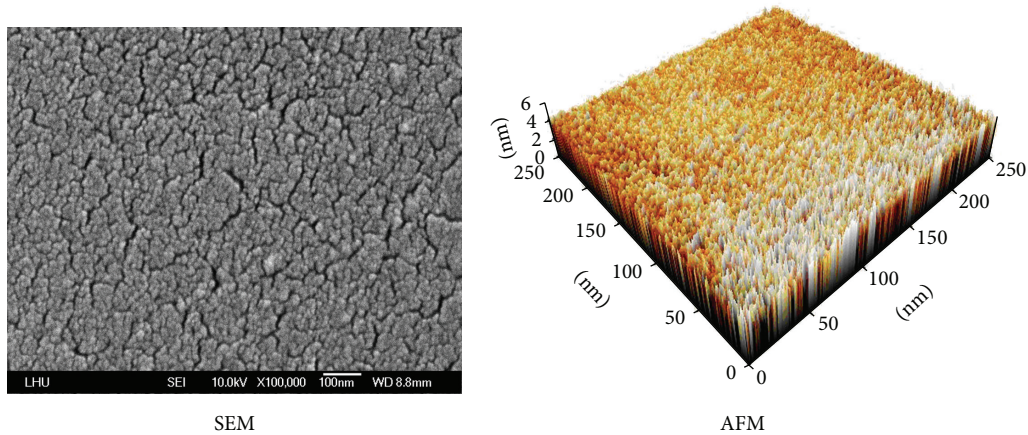


FIGURE 5: The SEM and AFM images for sample number 2.

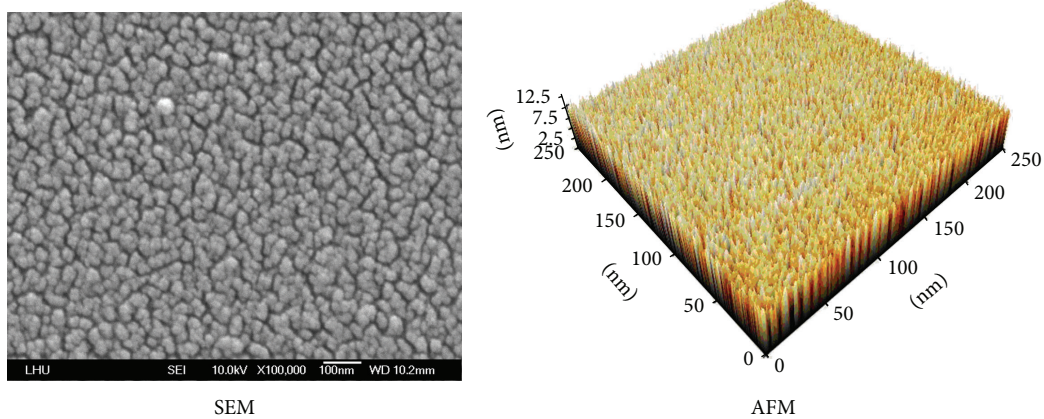


FIGURE 6: The SEM and AFM images for sample number 8.

with the addition of nitrogen is  $20^\circ$  less after UV irradiation. This result shows that the photo-induced hydrophilicity of  $\text{TiO}_{2-x}\text{N}_x$  film is better than that of  $\text{TiO}_2$  film.

The best degradation occurs for samples number 2 and number 8, without and with nitrogen addition, respectively, as determined by AFM and SEM. Figures 5 and 6 show the morphology of samples number 2 and number 8, respectively. The columnar structures of the two films are identified using AFM. The respective roughness ( $R_a$ ) values for samples number 2 and number 8 are 0.33 nm and 1.21 nm (see Table 2). The atomic number ratio for the surface and the volume is an important parameter for photocatalytic properties. A higher ratio results in greater photocatalytic activity. When the roughness value decreases, the photocatalytic activity decreases, because there is less surface area. In contrast, when the roughness is greater, the photocatalytic activity is greater, because there is a larger surface area.

**3.2. DSSC Characterization.** Figure 7 shows the transmittance spectra as a function of wavelengths in the visible range for compact  $\text{TiO}_2$  layers. After annealing at  $450^\circ\text{C}$  in

an atmosphere ambient for 30 min, the compact  $\text{TiO}_2$  layers demonstrate higher optical transmittance. However, when the annealing temperature is  $500^\circ\text{C}$ , the optical transmittance decreases slightly.

SEM analysis was used to determine the morphology of the  $\text{TiO}_2$  porous layer produced using the sol-gel method onto the compact  $\text{TiO}_2$  layers (sputtered with  $\text{Ar}/\text{O}_2/\text{N}_2$  flow rates of 36:18:9; sample number 8)/FTO substrate, as shown in Figure 8. The samples were annealed at  $450^\circ\text{C}$  in an atmosphere ambient for 30 min. After sputtering the compact  $\text{TiO}_2$  layers are dense and evenly coated to prevent charge recombination, which adheres to the electrode surface strongly (Figure 8(a)). The SEM images show the porous  $\text{TiO}_2$  film over the sputtered compact layer that is produced using sol-gel with spin coating has proper density and the crystallite size (Figure 8(b)), which gives a more efficient DSSC. The cross-section of the films was observed by SEM. Figure 9(a) corresponds to Figure 8(b) and Figure 9(b) corresponds to Figure 8(c). These results confirm a sponge-like structure for the  $\text{TiO}_2$  layer, which is a prerequisite for a highly efficient DSSC. Figure 10 shows the XRD patterns

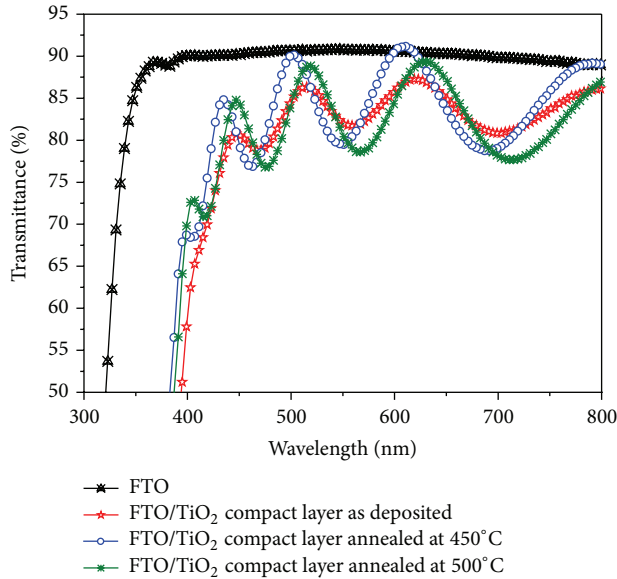


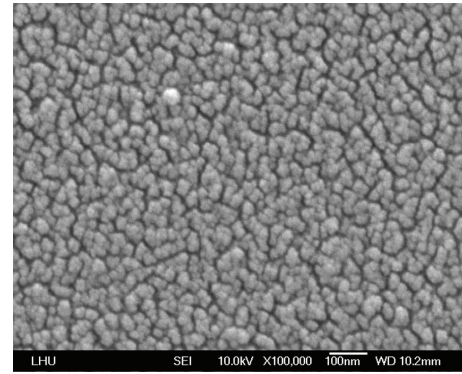
FIGURE 7: The optical transmittance spectra for a compact TiO<sub>2</sub> layer/FTO/glass.

for the TiO<sub>2</sub> films. FTO/glass shows a good crystalline structure and anatase (101) diffraction peaks that have a higher crystallinity than the ITO/glass films.

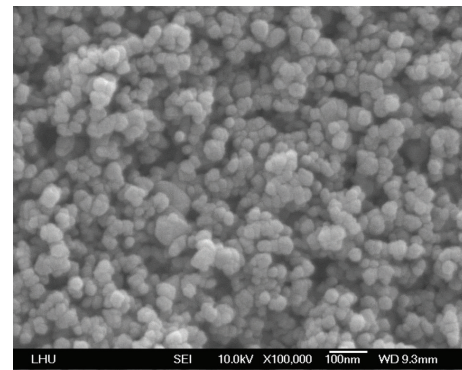
In order to compare the performance of a DSSC fabricated on the FTO/glass substrate and the ITO/glass substrate, using Pt counter electrodes and carbon counter electrodes [23], a conventional DSSC was prepared, as shown in Figure 11. Figure 11 shows the photocurrent-voltage (*J-V*) characterization of the DSSC with a sputtered compact TiO<sub>2</sub> layer, under AM 1.5 solar irradiation with a density of 100 mW/cm<sup>2</sup>. The performance parameters are summarized in Table 3. The short circuit photocurrent density (*J<sub>sc</sub>*), the open-circuit photovoltage (*V<sub>oc</sub>*), and the fill factor for the FTO/glass substrate using Pt counter electrodes are greater than those for the other samples. With ITO/glass, using the carbon counter electrodes, conversion efficiency decreases to 1.51%, from 4.98%, for Pt counter electrodes. This increase in the *J<sub>sc</sub>*, the *V<sub>oc</sub>*, and the fill factor means that the DSSC with the FTO/glass and a Pt counter electrode has a solar conversion efficiency of 7.65%, compared with 4.98% for the cell prepared using ITO/glass.

#### 4. Conclusions

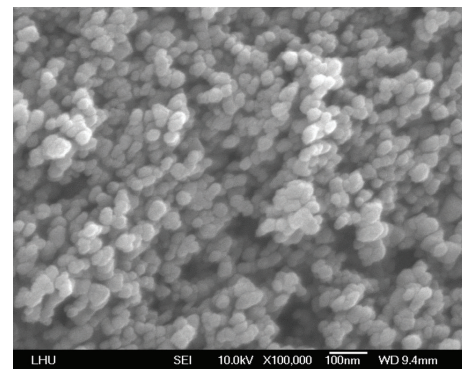
This study successfully deposits TiO<sub>2</sub> and TiO<sub>2-x</sub>N<sub>x</sub> onto ITO/glass and FTO/glass substrates. The flow rates for Ar (plasma gas), O<sub>2</sub>, and N<sub>2</sub> (reactive gases) are varied, but the rf power, the deposition pressure, and the substrate temperature are fixed. The results show that the photo-induced hydrophilicity of TiO<sub>2-x</sub>N<sub>x</sub> film is better than that of TiO<sub>2</sub> film. The best absorbance of methylene blue (MB) is 0.54, for sample number 8 (the Ar/O<sub>2</sub>/N<sub>2</sub> flow rates are 36:18:9), after UV irradiation for 4 h. This result shows



(a)



(b)



(c)

FIGURE 8: The SEM images of (a) sputtered TiO<sub>2</sub> compact layer on FTO/glass (sample number 8), (b) porous TiO<sub>2</sub> on TiO<sub>2</sub> compact layers/FTO/glass, produced using the sol-gel with spin coating method and (c) porous TiO<sub>2</sub> on compact TiO<sub>2</sub> layers/FTO/glass, produced using the sol-gel with blade coating method.

that MB degradation for TiO<sub>2-x</sub>N<sub>x</sub> film is better than that for TiO<sub>2</sub> film. After annealing, the compact TiO<sub>2</sub> layers exhibit higher optical transmittance. The TiO<sub>2</sub> porous layer on the TiO<sub>2</sub> compact layers/FTO substrate produced using the sol-gel method exhibits a sponge-like structure, which is a prerequisite for a highly efficient DSSC. For ITO/glass with carbon counter electrodes, the conversion efficiency decreases to 1.51%, from 4.98% for Pt counter electrodes. The short circuit photocurrent density (*J<sub>sc</sub>*), the open-circuit

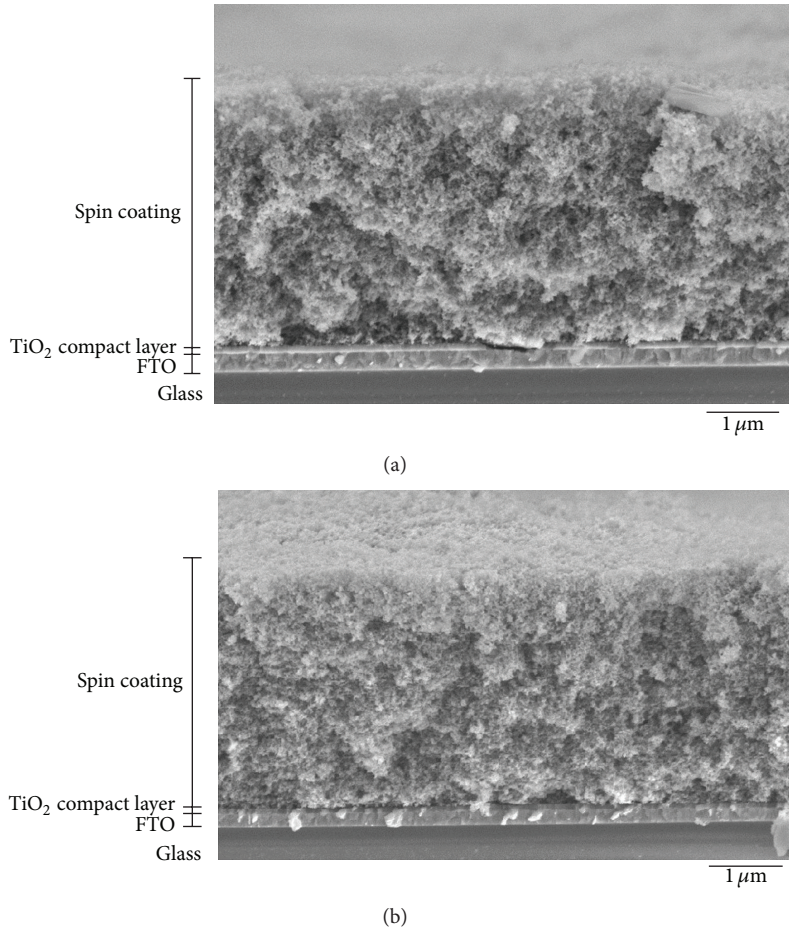


FIGURE 9: The SEM cross-sectional image (a) corresponding to Figure 8(b) and (b) corresponding to Figure 8(c).

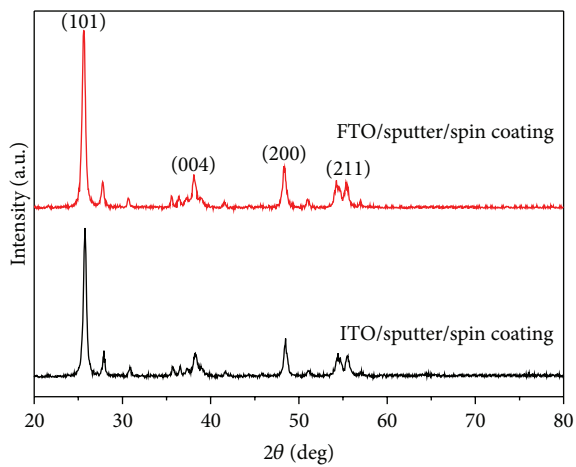


FIGURE 10: The XRD patterns for the TiO<sub>2</sub> films, annealed at 450°C.

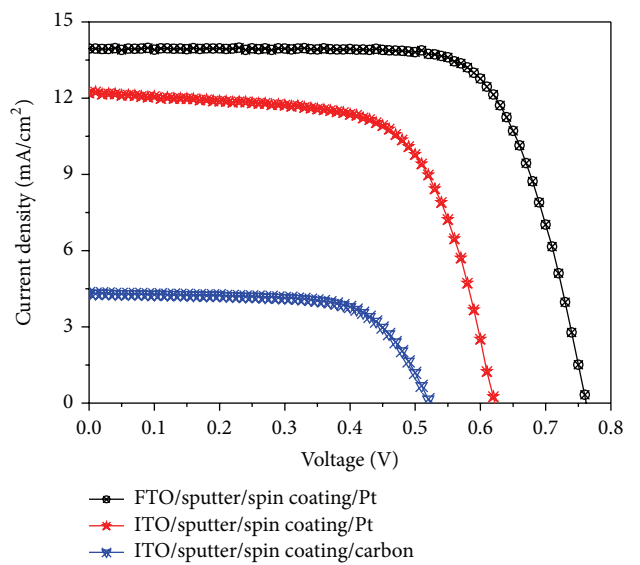


FIGURE 11: Current-voltage plots for the DSSC with a sputtered compact TiO<sub>2</sub> layer, using carbon and Pt counter electrodes and FTO and ITO/glass, under AM 1.5 solar irradiation with a density of 100 mW/cm<sup>2</sup> (TiO<sub>2</sub> annealed at 450°C).

photovoltage ( $V_{oc}$ ), and the fill factor for the FTO/glass substrate with Pt counter electrodes are greater than those of the other samples.

TABLE 3: Photovoltaic performance of DSSCs with sputtered compact TiO<sub>2</sub> layer, with carbon and Pt counter electrodes, using FTO and ITO/glass.

	$V_{oc}$ (V)	$J_{sc}$ (mA/cm <sup>2</sup> )	Fill factor	Efficiency $\eta$ (%)
FTO/sputter/spin coating/Pt	0.762	13.95	0.720	7.65
ITO/sputter/spin coating/Pt	0.622	12.38	0.647	4.98
ITO/sputter/spin coating/carbon	0.522	4.33	0.668	1.51

## Conflict of Interests

The authors declare that there is no conflict of interests regarding the publication of this paper.

## References

- [1] M. Hamadani, A. Gravand, and V. Jabbari, "High performance dye-sensitized solar cells (DSSCs) achieved via electrophoretic technique by optimizing of photoelectrode properties," *Materials Science in Semiconductor Processing*, vol. 16, pp. 1352–1359, 2013.
- [2] H. Choi, E. Stathatos, and D. D. Dionysiou, "Photocatalytic TiO<sub>2</sub> films and membranes for the development of efficient wastewater treatment and reuse systems," *Desalination*, vol. 202, no. 1–3, pp. 199–206, 2007.
- [3] D. Y. Chen, C. C. Tsao, and C. Y. Hsu, "Photocatalytic TiO<sub>2</sub> thin films deposited on flexible substrates by radio frequency (RF) reactive magnetron sputtering," *Current Applied Physics*, vol. 12, no. 1, pp. 179–183, 2012.
- [4] H. Irie, Y. Watanabe, and K. Hashimoto, "Nitrogen-concentration dependence on photocatalytic activity of TiO<sub>2</sub>-xNx powders," *Journal of Physical Chemistry B*, vol. 107, no. 23, pp. 5483–5486, 2003.
- [5] Y. Nakano, T. Morikawa, T. Ohwaki, and Y. Taga, "Origin of visible-light sensitivity in N-doped TiO<sub>2</sub> films," *Chemical Physics*, vol. 339, no. 1–3, pp. 20–26, 2007.
- [6] C.-G. Kuo and B.-J. Sheen, "Seaweed chlorophyll on the light-electron efficiency of DSSC," *Journal of the Chinese Chemical Society*, vol. 58, no. 2, pp. 186–190, 2011.
- [7] Y.-L. Kuo, T.-L. Su, F.-C. Kung, and T.-J. Wu, "A study of parameter setting and characterization of visible-light driven nitrogen-modified commercial TiO<sub>2</sub> photocatalysts," *Journal of Hazardous Materials*, vol. 190, no. 1–3, pp. 938–944, 2011.
- [8] B. O'Regan and M. Grätzel, "A low-cost, high-efficiency solar cell based on dye-sensitized colloidal TiO<sub>2</sub> films," *Nature*, vol. 353, no. 6346, pp. 737–740, 1991.
- [9] K. R. Bae, C. H. Ko, Y. Park et al., "Structure control of nanocrystalline TiO<sub>2</sub> for the dye-sensitized solar cell application," *Current Applied Physics*, vol. 10, no. 3, pp. S406–S409, 2010.
- [10] P.-C. Huang, C.-H. Huang, M.-Y. Lin, C.-Y. Chou, C.-Y. Hsu, and C.-G. Kuo, "The effect of sputtering parameters on the film properties of molybdenum back contact for CIGS solar cells," *International Journal of Photoenergy*, vol. 2013, Article ID 390824, 8 pages, 2013.
- [11] J. H. Qi, Y. Li, T. T. Duong, H. J. Choi, and S. G. Yoon, "Dye-sensitized solar cell based on AZO/Ag/AZO multilayer transparent conductive oxide film," *Journal of Alloys and Compounds*, vol. 556, pp. 121–126, 2013.
- [12] Y.-S. Jin, K.-H. Kim, W.-J. Kim, K.-U. Jang, and H.-W. Choi, "The effect of RF-sputtered TiO<sub>2</sub> passivating layer on the performance of dye sensitized solar cells," *Ceramics International*, vol. 38, no. 1, pp. S505–S509, 2012.
- [13] C. G. Kuo, C. Y. Hsu, S. S. Wang, and D. C. Wen, "Photocatalytic characteristics of TiO<sub>2</sub> films deposited by magnetron sputtering on polycarbonate at room temperature," *Applied Surface Science*, vol. 258, pp. 6952–6957, 2012.
- [14] H.-J. Kim, J.-D. Jeon, D. Y. Kim, J.-J. Lee, and S.-Y. Kwak, "Improved performance of dye-sensitized solar cells with compact TiO<sub>2</sub> blocking layer prepared using low-temperature reactive ICP-assisted DC magnetron sputtering," *Journal of Industrial and Engineering Chemistry*, 2012.
- [15] H. Chang, T. L. Chen, K. D. Huang, S. H. Chien, and K. C. Hung, "Fabrication of highly efficient flexible dye-sensitized solar cells," *Journal of Alloys and Compounds*, vol. 504, no. 1, pp. S435–S438, 2010.
- [16] H. Seo, M.-K. Son, J.-K. Kim, I. Shin, K. Prabakar, and H.-J. Kim, "Method for fabricating the compact layer in dye-sensitized solar cells by titanium sputter deposition and acid-treatments," *Solar Energy Materials and Solar Cells*, vol. 95, no. 1, pp. 340–343, 2011.
- [17] C. G. Kuo, C. F. Yang, L. R. Hwang, and J. S. Huang, "Effects of titanium oxide nanotube arrays with different lengths on the characteristics of dye-sensitized solar cells," *International Journal of Photoenergy*, vol. 2013, Article ID 650973, 6 pages, 2013.
- [18] Y. M. Sung, "Deposition of TiO<sub>2</sub> blocking layers of photovoltaic cell using RF magnetron sputtering technology," *Energy Procedia*, vol. 34, pp. 582–588, 2013.
- [19] M. H. Abdullah and M. Rusop, "RF sputtered tri-functional antireflective TiO<sub>2</sub> (arc-TiO<sub>2</sub>) compact layer for performance enhancement in dye-sensitized solar cell," *Ceramics International*, vol. 38S, pp. S505–S509, 2012.
- [20] L. Zhang, Y. Zhu, Y. He, W. Li, and H. Sun, "Preparation and performances of mesoporous TiO<sub>2</sub> film photocatalyst supported on stainless steel," *Applied Catalysis B: Environmental*, vol. 40, no. 4, pp. 287–292, 2003.
- [21] Y. Chen, E. Stathatos, and D. D. Dionysiou, "Sol-gel modified TiO<sub>2</sub> powder films for high performance dye-sensitized solar cells," *Journal of Photochemistry and Photobiology A: Chemistry*, vol. 203, no. 2–3, pp. 192–198, 2009.
- [22] H. Tomaszewski, H. Poelman, D. Depla et al., "TiO<sub>2</sub> films prepared by DC magnetron sputtering from ceramic targets," *Vacuum*, vol. 68, no. 1, pp. 31–38, 2002.
- [23] C. G. Kuo, C. F. Yang, M. J. Kao et al., "An analysis and research on the transmission ratio of dye sensitized solar cell photoelectrodes by using different etching process," *International Journal of Photoenergy*, vol. 2013, Article ID 151973, 8 pages, 2013.

## Research Article

# The Photocatalytic Activity and Compact Layer Characteristics of TiO<sub>2</sub> Films Prepared Using Radio Frequency Magnetron Sputtering

H. C. Chang,<sup>1</sup> H. H. Huang,<sup>2</sup> C. Y. Wu,<sup>2</sup> R. Q. Hsu,<sup>1</sup> and C. Y. Hsu<sup>2</sup>

<sup>1</sup> Department of Mechanical Engineering, National Chiao Tung University, 1001 University Road, Hsinchu 30010, Taiwan

<sup>2</sup> Department of Mechanical Engineering, Lunghwa University of Science and Technology, No. 300, Sec. 1, Wanshou Road, Guishan, Taoyuan 33306, Taiwan

Correspondence should be addressed to C. Y. Hsu; [cyhsu@mail.lhu.edu.tw](mailto:cyhsu@mail.lhu.edu.tw)

Received 7 March 2014; Revised 18 April 2014; Accepted 18 April 2014; Published 22 May 2014

Academic Editor: Ho Chang

Copyright © 2014 H. C. Chang et al. This is an open access article distributed under the Creative Commons Attribution License, which permits unrestricted use, distribution, and reproduction in any medium, provided the original work is properly cited.

TiO<sub>2</sub> compact layers are used in dye-sensitized solar cells (DSSCs) to prevent charge recombination between the electrolyte and the transparent conductive substrate (indium tin oxide, ITO; fluorine-doped tin oxide, FTO). Thin TiO<sub>2</sub> compact layers are deposited onto ITO/glass by means of radio frequency (rf) magnetron sputtering, using deposition parameters that ensure greater photocatalytic activity and increased DSSC conversion efficiency. The photoinduced decomposition of methylene blue (MB) and the photoinduced hydrophilicity of the TiO<sub>2</sub> thin films are also investigated. The photocatalytic performance characteristics for the deposition of TiO<sub>2</sub> films are improved by using the Grey-Taguchi method. The average transmittance in the visible region exceeds 85% for all samples. The XRD patterns of the TiO<sub>2</sub> films, for sol-gel with spin coating of porous TiO<sub>2</sub>/TiO<sub>2</sub> compact/ITO/glass, show a good crystalline structure. In contrast, without the TiO<sub>2</sub> compact layer (only porous TiO<sub>2</sub>), the peak intensity of the anatase (101) plane in the XRD patterns for the TiO<sub>2</sub> film has a lower value, which demonstrates inferior crystalline quality. With a TiO<sub>2</sub> compact layer to prevent charge recombination, a higher short-circuit current density is obtained. The DSSC with the FTO/glass and Pt counter electrode demonstrates the energy conversion efficiency increased.

## 1. Introduction

Dye-sensitized solar cells (DSSCs) have been extensively studied as a promising alternative to conventional solar cells that use a p-n junction because of their reasonable conversion efficiency, low cost, environmentally friendly components, use of a flexible cell design, and simple fabrication process, when compared to silicon solar cells [1]. DSSCs are the next-generation solar cells [2]. If low cost and highly efficient DSSCs can be developed, it will be an important new direction for the development of solar cells. A typical DSSC consists of dye molecules that act as sensitizers, a nanoporous metal oxide film (TiO<sub>2</sub> semiconductor material), a transparent conducting oxide (indium tin oxide, ITO), an electrolyte charge carrier, and a counter electrode (Pt or carbon) [3]. The dye and metal oxide, which are used for the sensitizer and

the electrode, respectively, are important to the photoelectric conversion efficiency of DSSCs [4].

TiO<sub>2</sub> is one of the most popular photocatalytic materials, so it has many commercial applications, such as antibacterial applications, waste purification, self-cleaning, and sensors [5]. It is also used for photoelectrodes and in high performance DSSC applications because it has an adequate photore-sponse and effective electron transport [6]. A high incident photon to current conversion efficiency is expected for TiO<sub>2</sub> films that have a better phase structure and crystallinity and a higher specific surface area [7]. The control of the TiO<sub>2</sub> nanostructures is very important for the photovoltaic performance of a DSSC [8]. In order to improve the conversion efficiency of DSSCs, several studies have focused on the structural design, material development, photovoltaic characterization, and analysis of the mechanism of TiO<sub>2</sub>

TABLE 1: The factor and level settings for sputter deposition of TiO<sub>2</sub> compact layers.

Substrate	Soda-lime glass, 20 × 20 × 1 mm <sup>3</sup>			
Target	TiO <sub>2</sub> (99.99% purity)			
Gas	Ar and O <sub>2</sub> (99.99% purity)			
Base pressure	5.0 × 10 <sup>-6</sup> torr			
Substrate-to-target distance	80 mm			
Substrate temperature	Room temperature			
Substrate rotate vertical axis	10 rpm			
Symbol	Control factor	Level 1	Level 2	Level 3
A	rf power (W)	100	130	160
B	Sputtering pressure (mtorr)	3	5	7
C	O <sub>2</sub> /(Ar + O <sub>2</sub> ) (%)	10	30	50
D	Deposition time (hr)	2	3	4

nanoparticles [9]. Mesoporous TiO<sub>2</sub> is widely used as an electrode in DSSCs to produce a high surface area for the adsorption of a greater density of dye molecules, which produces a significant increase in the photocurrent [10]. However, the highly porous structure of the TiO<sub>2</sub> layer can cause an electrical shortage and recombination of the charge/electrons, which interferes with the unidirectional electron transport that takes place at the TiO<sub>2</sub> layer/dye molecule and ITO/TiO<sub>2</sub> layer interfaces [11]. This leakage by electronic back transfer leads to a decrease in cell efficiency. To avoid this problem, the primary method used to prevent recombination is the use of a TiO<sub>2</sub> compact layer (blocking layer) between the ITO and the porous TiO<sub>2</sub> layer [11]. This compact layer can be prepared using many growth techniques, such as sputter deposition, dip-coating, chemical vapor deposition, and spray pyrolysis.

This study determines the optical, structural, and surface properties of a TiO<sub>2</sub> compact layer that is grown by radio frequency (rf) magnetron sputtering on the ITO electrodes, as a function of the deposition parameters that ensure higher photocatalytic activity and greater DSSC conversion efficiency. The nanoporous TiO<sub>2</sub> upper layer is coated using the sol-gel process and calcination at 450°C. Moreover, the working electrode which is made of a dye-sensitized TiO<sub>2</sub> film that is immobilized onto a fluorine-doped tin oxide (FTO) substrate is also investigated.

The Taguchi method is a powerful tool for the design of high quality systems, which can be used to design low cost products, with improved quality [12]. To optimize the deposition process for TiO<sub>2</sub> photocatalytic films, a statistical analysis of the signal-to-noise ratio (*S/N*) is performed, using an analysis of variance (ANOVA). The optimal deposition parameters are obtained by analyzing the results for various experimental permutations [13, 14]. Table 1 shows the effect on the quality of the TiO<sub>2</sub> photocatalytic films of four deposition parameters at three levels: the rf power, the sputtering pressure, the Ar-O<sub>2</sub> ratio, and the deposition time. An L<sub>9</sub> (3<sup>4</sup>, with four columns and nine rows) orthogonal array is used.

## 2. Experimental

The TiO<sub>2</sub> photocatalytic thin films (compact layer) were coated onto ITO/glass substrates (and FTO/glass), using rf magnetron sputtering. The reactive and sputtering gases were O<sub>2</sub> (purity: 99.99%) and Ar (purity: 99.99%), respectively. The commercially available, hot pressed, and sintered ceramic target TiO<sub>2</sub> had a diameter of 50.8 mm and 99.99% purity (Elecmat, USA).

Prior to coating, the target was presputtered for 15 min, in order to remove any contamination, and the substrates were ultrasonically cleaned and degreased in acetone, rinsed in deionised water, and subsequently dried with nitrogen gas. A vacuum, of base pressure 5.0 × 10<sup>-6</sup> Torr, was applied before deposition. The distance between the substrate and the target (80 mm) and the rotational speed of the substrate (10 rpm) were constant. By adjusting the experimental permutations, this study determined the effect of each deposition parameter on the deposition rate for TiO<sub>2</sub>/ITO/glass, the methylene blue (MB) absorbance, the contact angle to a pure water droplet, the surface morphology, and the crystal structure.

The porous TiO<sub>2</sub> film (p-TiO<sub>2</sub>) was coated onto the TiO<sub>2</sub> compact/ITO/glass (and TiO<sub>2</sub> compact/FTO/glass) using a mixture of TiO<sub>2</sub> powders (P-25, particle size: <25 nm, 99.7%) with the TiO<sub>2</sub> sol-gel component studied in [15]. The TiO<sub>2</sub> sol-gel was mixed with 0.3 g of commercially available Degussa P-25, to avoid any cracking of the film. The TiO<sub>2</sub> sol-gel was produced using spin coating and blade coating. The gels were predried for 15 min at 50°C and then sintered in a box furnace at 450°C (heating rate 10°C/min) for 30 min in air ambient, to produce the bare TiO<sub>2</sub> electrode used in this work to fabricate the DSSC. The porous TiO<sub>2</sub> films were immersed into the dye solution (0.4 mM N719 dye solution, Solaronix, Switzerland, Di-tetrabutylammonium cis-bis(isothiocyanato)bis(2, 2'-bipyridyl-4,4'-dicarboxylato)-ruthenium(II); chemical formula C<sub>58</sub>H<sub>86</sub>N<sub>8</sub>O<sub>8</sub>RuS<sub>2</sub>; Mol Wt: 1188.55) complex for 24 h at room temperature.

TABLE 2: The experimental results and the  $S/N$  ratios for the deposition rate, the contact angle, and the MB absorbance for the  $\text{TiO}_2$  compact layer coatings (the experiments were repeated twice).

Exp.	Factors				Deposition rate ( $\text{\AA}/\text{min}$ )		$S/N$ (dB)	Water contact angle (degree)		$S/N$ (dB)	MB absorbance		$S/N$ (dB)
	A	B	C	D	T1	T2		T1	T2		T1	T2	
1	1	1	1	1	3.35	3.00	9.9953	90.73	91.30	-39.182	1.328	1.332	-2.4770
2	1	2	2	2	2.73	3.04	9.1653	92.13	91.87	-39.275	1.327	1.325	-2.4508
3	1	3	3	3	2.19	2.23	6.8868	73.91	75.40	-37.461	1.296	1.293	-2.2420
4	2	1	2	3	4.85	4.97	13.8197	89.75	90.28	-39.086	1.198	1.187	-1.5292
5	2	2	3	1	4.35	3.95	12.3307	91.01	92.71	-39.262	1.284	1.283	-2.1679
6	2	3	1	2	4.84	4.76	13.6239	93.57	94.68	-39.474	1.205	1.200	-1.6017
7	3	1	3	2	6.38	6.11	15.9046	71.70	72.30	-37.146	1.287	1.284	-2.1814
8	3	2	1	3	7.48	7.25	17.3403	95.35	94.81	-39.561	1.077	1.074	-0.6322
9	3	3	2	1	4.73	4.82	13.5783	63.79	62.39	-35.999	1.031	1.030	-0.2609

Note: A = rf power (W), B = process pressure (Pa), C =  $\text{O}_2/(\text{Ar} + \text{O}_2)$  flow rate ratio (%), and D = deposition time (hr).

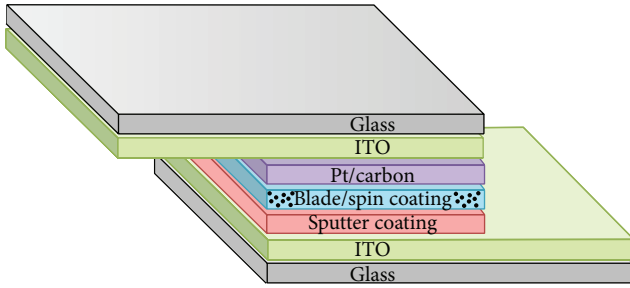


FIGURE 1: A schematic diagram of a DSSC with an rf-sputtered  $\text{TiO}_2$  compact layer/ITO/glass on the ITO electrode.

The Pt counter electrode was coated onto ITO/glass (and FTO/glass) substrates using DC sputtering with pure Ar gas and a DC power of 30 W. The dye-adsorbed  $\text{TiO}_2$  working electrode and the counter electrode were assembled into a sandwich-type cell and sealed with a hot-melt sealant. Figure 1 shows a schematic diagram of a DSSC with an rf-sputtered  $\text{TiO}_2$  compact layer/ITO/glass on the ITO electrode. In order to prevent the leakage by electron transfer to the liquid electrolyte, dense  $\text{TiO}_2$  passivating layers were used.

The phase identification of the particles produced using various deposition parameters was performed by X-ray diffraction (Rigaku-2000 spectrometer), using  $\text{Cu-K}\alpha$  radiation (40 kV, 30 mA, and  $\lambda = 0.1541$  nm). The photoinduced hydrophilicity of the  $\text{TiO}_2$  thin films was evaluated by measurement of the contact angle to pure water, using a contact angle meter (FACE CAVP150) that is accurate to less than  $1^\circ$ . A black light (UVP UVL-225D) lamp with a principal wavelength of 365 nm ( $1.5 \text{ mW}/\text{cm}^2$  at the film surface) was the UV light source. The decomposition of MB aqueous solution ( $10 \mu\text{M}$ ) was photocatalyzed. An UV-Vis-NIR spectrometer (Jasco V-670) was used to measure the absorption spectra of the MB solution as a function of the UV irradiation time. The film thickness was measured, using

a surface profilometer ( $\alpha$ -step, AMBIOS XP-1). The surface morphology was analyzed using a field emission scanning electron microscope (FESEM, JEOL JSM-6500F). The crystal structure of the films was characterized by X-ray diffraction (Rigaku-2000 spectrometer), using  $\text{Cu-K}\alpha$  radiation (40 kV, 30 mA, and  $\lambda = 0.1541$  nm), with a grazing incidence angle of  $1^\circ$ . The scanning rate was  $5^\circ/\text{min}$ .

The power used to test the prepared DSSC was a 150 W Xe lamp, which simulates sunlight (AM 1.5). Before the test, the distance between the light source and the sample was adjusted to allow a light source density of  $100 \text{ mW}/\text{cm}^2$ . The cell performance parameters, including the short-circuit current density ( $J_{\text{sc}}$ ), the open-circuit voltage ( $V_{\text{oc}}$ ), the fill factor (FF), and the photoelectric conversion efficiency ( $\eta(\%) = J_{\text{sc}} \times V_{\text{oc}} \times \text{FF}/\text{total incident energy} \times 100$ ), were measured and calculated using the  $J$ - $V$  characteristics of DSSC.

### 3. Results and Discussion

**3.1. The Photocatalytic Activity of the  $\text{TiO}_2$  Compact Films.** The  $\text{TiO}_2$  compact films were deposited onto ITO soda-lime glass substrates. The optimization of the parameter settings involved comparing the signal-noise ( $S/N$ ) ratios, using the Taguchi method. In order to optimize the  $\text{TiO}_2$  compact films deposition parameters, the water contact angle and the MB absorbance had the smaller the better characteristics and the deposition rate had the larger the better characteristics. The respective  $S/N$  ratios for the smaller the better characteristic and the larger the better characteristic are expressed as follows (Taguchi et al. [13]):

$$\left(\frac{S}{N}\right)_S = -10 \log \frac{1}{n} \sum_{i=1}^n y_i^2 \quad (1)$$

$$\left(\frac{S}{N}\right)_L = -10 \log \frac{1}{n} \sum_{i=1}^n \frac{1}{y_i^2},$$

where  $n$  is the number of iterations for the experiment and  $y_i$  is the  $i$ th average value of the characteristic measured.

TABLE 3: The ANOVA results for the deposition rate, the water contact angle, and the MB absorbance.

Factor	Degree of freedom	Sum of square	Variance	Contribution ( $P$ %)
Deposition rate ( $\text{\AA}/\text{min}$ )				
A	2	74.4166	37.2083	84.45
B	2	6.1132	3.0566	6.93
C	2	6.1644	3.0822	7.00
D	2	1.4211	0.7106	1.62
Total	8	88.1153		100
Water contact angle (degree)				
A	2	4.4559	2.22793	33.68
B	2	4.4483	2.22417	33.62
C	2	3.7790	1.88950	28.56
D	2	0.5472	0.27359	4.14
Total	8	13.2304		100
MB absorbance				
A	2	2.80223	1.40111	54.36
B	2	0.72560	0.36280	14.07
C	2	1.03120	0.51560	20.00
D	2	0.59634	0.29817	11.57
Total	8	5.15538		100

Using (1), the  $S/N$  ratio values were computed for deposition rate, water contact angle, and MB absorbance in the  $\text{TiO}_2$  compact layers coatings, as shown in Table 2. The hydrophilicity of the  $\text{TiO}_2$  films was determined by measuring the water contact angle. The change in the water contact angle is shown as a function of UV irradiation time for the  $\text{TiO}_2$  films deposited with parameter sets in the orthogonal arrays (Table 2). When the  $\text{TiO}_2$  film surface is irradiated by UV light for 12 min, the water contact angles of all of the films begin to decrease (less than  $63^\circ$ , sample number 9), which indicates that the film surface becomes more hydrophilic. The absorption spectra for the MB aqueous solution degraded by  $\text{TiO}_2$  photocatalytic film after 240 min UV irradiation are shown for the orthogonal array settings (Table 2). The  $\text{TiO}_2$  films deposited using the parameter sets in the orthogonal arrays from number 1 to number 9 show MB absorbance between 1.33 and 1.03.

An analysis of variance (ANOVA) was used to determine the effect of a change in the process parameters on the process response. Table 3 shows the ANOVA results for the deposition rate, the water contact angle, and the MB absorbance. Table 3 shows that the variables that most significantly affect the deposition rate, the water contact angle, and the MB absorbance are the rf power ( $P = 84.45\%$ ,  $33.68\%$ , and  $54.36\%$ ), the sputtering pressure ( $P = 6.93\%$ ,  $33.62\%$ , and  $14.07\%$ ), and the argon-oxygen ratio ( $P = 7.00\%$ ,  $28.56\%$ , and  $20.00\%$ ).

Grey relational analysis (GRA) provides an efficient solution to difficult problems that involve multiple performance characteristics that are uncertain, have multiple inputs, and

TABLE 4: The Grey relational grade and its ranking for the  $\text{TiO}_2$  compact layer coatings.

Exp.	Grey relational grade	Rank
1	0.3595	8
2	0.3526	9
3	0.4252	6
4	0.4551	4
5	0.3914	7
6	0.4356	5
7	0.5698	3
8	0.7007	2
9	0.8329	1

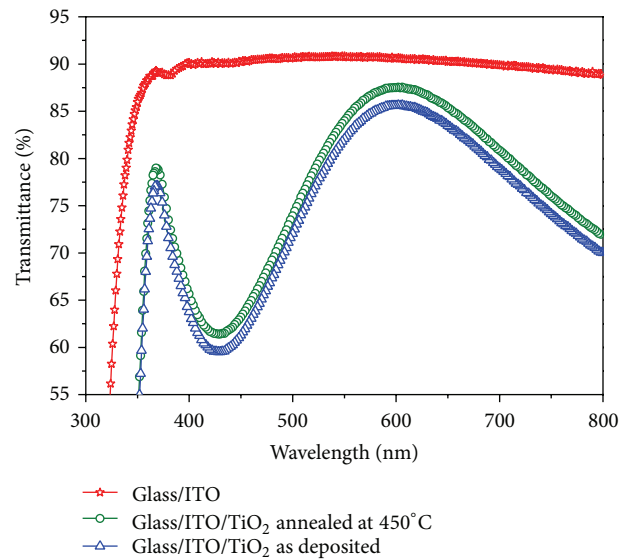


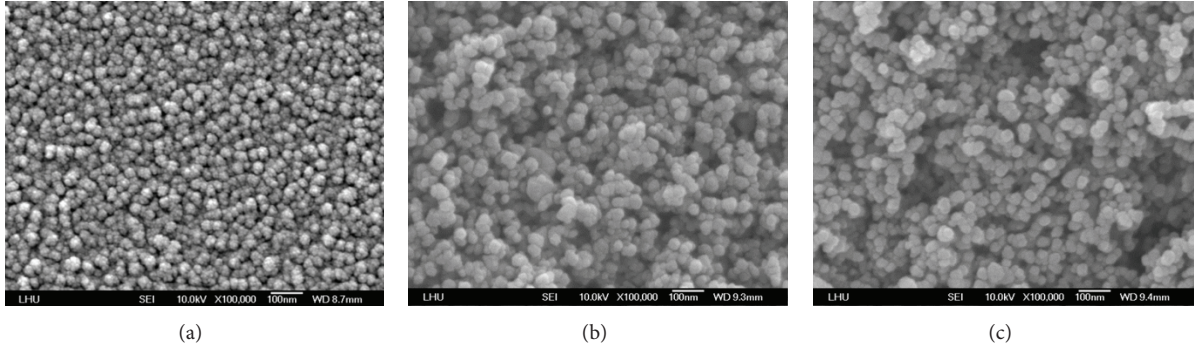
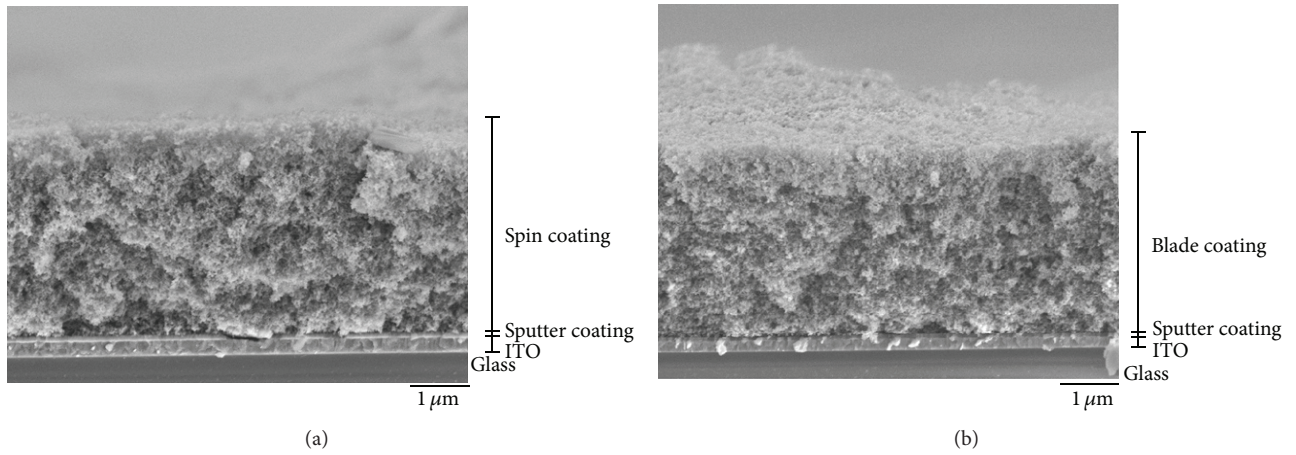
FIGURE 2: The optical transmittance spectra for  $\text{TiO}_2$  compact layer/ITO/glass.

generate discrete data. The objective of this study is to optimize the deposition parameters for the  $\text{TiO}_2$  compact films using GRA, which is used extensively in various industries [16].

The optimum combination does not yield suitable process parameters with a single performance characteristic (Taguchi method) for the  $\text{TiO}_2$  compact films coated. In order to optimize the deposition parameters, the deposition rate, the contact angle, and the MB absorbance, multiple performance characteristics (grey relational analysis) must be analyzed. The calculated grey relational grade is taken as the inspected value in the Taguchi method. Table 4 shows the grey relational grade and its ranking for the  $\text{TiO}_2$  compact layer coatings. A comparison of the experimental results for the orthogonal array ( $A_3B_3C_2D_1$ ) and the photocatalytic activity optimal parameter set ( $A_3B_3C_2D_3$ ) for  $\text{TiO}_2$  film deposition is shown in Table 5. The multiple performance characteristics for the deposition of  $\text{TiO}_2$  thin films are greatly improved

TABLE 5: The confirmation test results for the multiple performance characteristics, using the initial and the optimal process parameters.

Level	Initial process parameters	Optimal process parameters	Improvement rate (%)
	$A_3B_3C_2D_1$	$A_3B_3C_2D_3$	
Deposition rate ( $\text{\AA}/\text{min}$ )	4.775	5.48	12.87
Contact angle (degree)	63.09	53.47	15.25
MB absorbance	1.0305	0.865	16.06

FIGURE 3: (a) The SEM images for sputtered  $\text{TiO}_2$  compact layer on ITO/glass, (b) the SEM images for porous  $\text{TiO}_2$  onto  $\text{TiO}_2$  compact/ITO/glass, produced using the sol-gel with spin coating method, and (c) the SEM images for porous  $\text{TiO}_2$  onto  $\text{TiO}_2$  compact/ITO/glass, produced using the sol-gel with blade coating method.FIGURE 4: The SEM cross-sectional image of  $\text{TiO}_2$  (a) corresponding to Figure 3(b) and (b) corresponding to Figure 3(c).TABLE 6: The performance of a DSSC prepared using a photoelectrode with and without a  $\text{TiO}_2$  compact layer, using carbon and Pt counter electrodes, and using ITO/glass and FTO/glass.

	$V_{oc}$ (V)	$J_{sc}$ ( $\text{mA}/\text{cm}^2$ )	Fill factor	Efficiency $\eta$ (%)
ITO/sputter/spin coating/carbon	0.54	4.38	0.676	1.59
ITO/sputter/blade coating/carbon	0.53	4.08	0.666	1.44
ITO/spin coating/carbon	0.52	3.18	0.639	1.05
ITO/blade coating/carbon	0.52	3.07	0.572	0.90
ITO/sputter/spin coating/Pt	0.51	12.86	0.678	4.46
ITO/sputter/blade coating/Pt	0.49	10.73	0.675	3.51
ITO/spin coating/Pt	0.58	6.02	0.644	2.24
ITO/blade coating/Pt	0.61	5.10	0.649	2.01
FTO/sputter/spin coating/Pt	0.70	17.22	0.641	7.73
FTO/sputter/blade coating/Pt	0.77	12.79	0.750	7.36
FTO/spin coating/Pt	0.79	12.39	0.692	6.79
FTO/blade coating/Pt	0.79	10.80	0.771	6.53

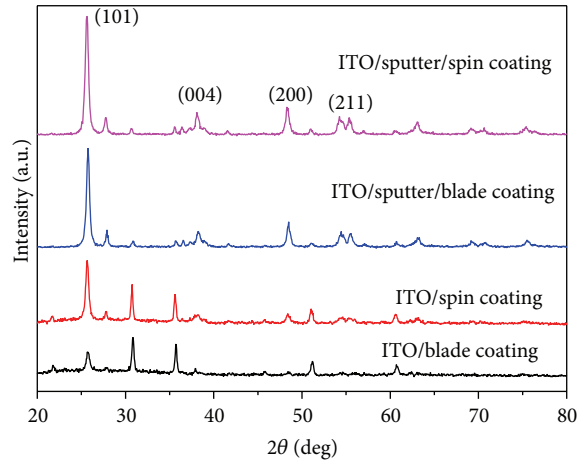


FIGURE 5: The XRD patterns for the  $\text{TiO}_2$  films after being annealed at  $450^\circ\text{C}$ .

by using the Grey-Taguchi method. The improvement in the deposition rate is 12.87%, that in the water contact angle is 15.25%, and that in the MB absorbance is 16.06%.

The transmittance spectra are shown as a function of wavelengths in the range between 300 and 800 nm for  $\text{TiO}_2$  compact layers in Figure 2. The average transmittance in the visible region exceeds 85% for all samples, but transmission in the UV-near visible region decreases abruptly. After annealing treatment, the optical transmittance of the film is increased.

**3.2. DSSC Conversion Efficiency.** SEM analysis was used to determine the morphology of the sputtered  $\text{TiO}_2$  compact layers (with photocatalytic activity optimal parameters,  $A_3B_3C_2D_3$ ) on the ITO substrate and the thick  $\text{TiO}_2$  porous layer produced using the sol-gel method, as shown in Figure 3. The uniform and smooth surfaces of the sputtered compact accumulation film are well covered by spherical particles, which are densely coated with a small grain size (Figure 3(a),  $\text{TiO}_2$  compact/ITO/glass). This is necessary to prevent charge recombination between the ITO and the porous  $\text{TiO}_2$  layer [17, 18]. The SEM images show the porous  $\text{TiO}_2$  film over the sputtered compact layer, produced using the sol-gel with spin coating method (Figure 3(b), porous  $\text{TiO}_2/\text{TiO}_2$  compact/ITO/glass) and the sol-gel with blade coating method (Figure 3(c), porous  $\text{TiO}_2/\text{TiO}_2$  compact/ITO/glass). The porous  $\text{TiO}_2$  film structure is not dense and the crystallite size of the  $\text{TiO}_2$  is increased. DSSC efficiency is improved by producing a  $\text{TiO}_2$  electrode with a large surface area and optimum pore structure [19, 20].

The cross-section of the  $\text{TiO}_2$  films was observed by SEM. Figure 4(a) corresponds to Figure 3(b) and Figure 4(b) corresponds to Figure 3(c). The  $\text{TiO}_2$  compact/ITO films produced using the photocatalytic activity optimal deposition conditions ( $A_3B_3C_2D_3$ ) are highly compacted and homogeneous and adhere perfectly to the glass substrate. These results

confirm a spongelike structure for the  $\text{TiO}_2$  layer (Figure 4), which is a prerequisite for a highly efficient DSSC [21]. The characteristics of the  $\text{TiO}_2$  materials depend significantly upon the surface morphology, the crystal structure, and the crystallization.

Figure 5 shows that the XRD patterns of the  $\text{TiO}_2$  films, produced using the sol-gel with spin coating of porous  $\text{TiO}_2/\text{TiO}_2$  compact/ITO/glass, show a good crystalline structure and anatase (101) diffraction peaks that demonstrate a higher crystallinity than the other films. In contrast, without the  $\text{TiO}_2$  compact layer (only porous  $\text{TiO}_2$ ), the peak intensity of the anatase (101) plane in the XRD patterns for the  $\text{TiO}_2$  film has a lower value, which demonstrates inferior crystalline quality.

Good performance for the counter electrode requires a low internal resistance and raw material cost. The best material for the counter electrode is Pt, which shows excellent electrochemical activity for  $\text{I}_3^-$  reduction at film thicknesses of 2~10 nm [22, 23]. Figure 6 shows the photo current-voltage ( $I$ - $V$ ) characteristics for the DSSC under AM1.5 solar irradiation with  $100\text{ mW}/\text{cm}^2$  illumination, with and without the  $\text{TiO}_2$  compact layer. Figure 6(a) shows a carbon counter electrode and ITO/glass, Figure 6(b) shows a Pt counter electrode and ITO/glass, and Figure 6(c) shows a Pt counter electrode and FTO/glass [24]. The corresponding cell parameters are summarized in Table 6, which shows the performance of the DSSC. With a  $\text{TiO}_2$  compact layer to prevent charge recombination, a higher  $J_{\text{sc}}$  is obtained. The energy conversion efficiency ( $\eta$ ) increases if a Pt counter electrode is used instead of a carbon counter electrode.

For the purposes of comparison, the energy conversion efficiency for the DSSC film deposited on FTO glass is also given. FTO substrates have good optoelectronic performance and higher energy conversion efficiency than ITO substrates. Table 6 shows that a FTO/sputter/spin coating/PT setup increases the conversion efficiency of the DSSC, with  $V_{\text{oc}} = 0.70\text{ V}$ ,  $J_{\text{sc}} = 17.22\text{ mA}/\text{cm}^2$ , a fill factor = 0.641, and an energy conversion efficiency as high as 7.73%.

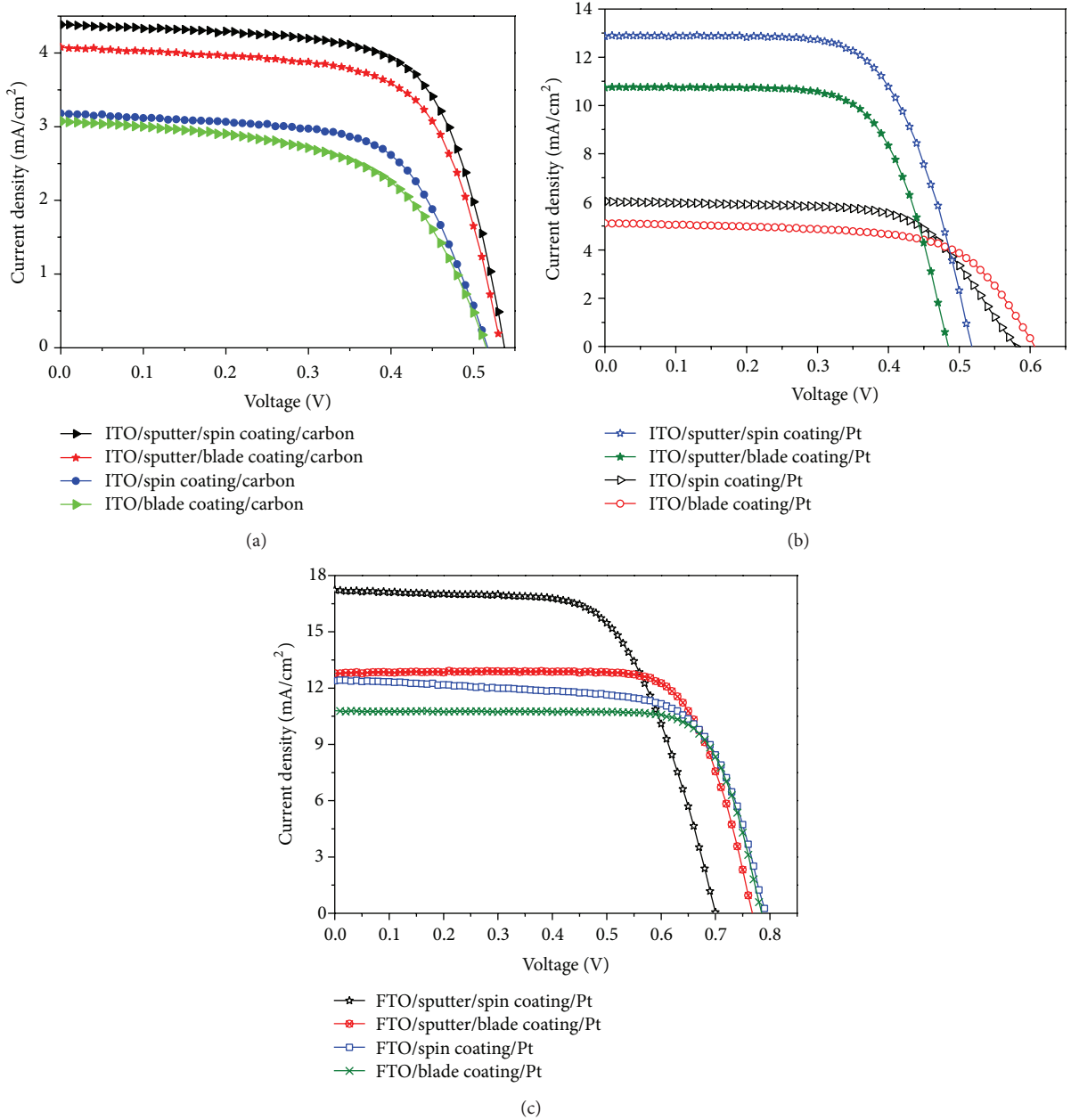


FIGURE 6: The *I-V* characteristics for DSSCs fabricated with and without a TiO<sub>2</sub> compact layer, (a) using a carbon counter electrode and ITO/glass, (b) using a Pt counter electrode and ITO/glass, and (c) using a Pt counter electrode and FTO/glass, under AM 1.5 solar irradiation with a density of 100 mW/cm<sup>2</sup>.

### 4. Conclusion

TiO<sub>2</sub> films (compact layer) are coated onto ITO/glass substrates (and FTO/glass), using rf magnetron sputtering. The reactive and sputtering gases are O<sub>2</sub> and Ar, respectively. The multiple performance characteristics for the deposited TiO<sub>2</sub> compact films' photocatalytic activity are greatly improved by using the Grey-Taguchi method. The improvement in the deposition rate is 12.87%, that in the water contact angle is 15.25%, and that in the MB absorbance is 16.06%. The porous

TiO<sub>2</sub> film that covers the sputtered compact layer produced by the sol-gel method has a structure which is not dense and a crystallite size that is increased. The XRD patterns for TiO<sub>2</sub> films produced using sol-gel with spin coating of porous TiO<sub>2</sub>/TiO<sub>2</sub> compact/ITO/glass result in a good crystalline structure and the anatase (101) diffraction peaks demonstrate a higher degree of crystallinity. The energy conversion efficiency ( $\eta$ ) for a Pt counter electrode is greater than that for a carbon counter electrode. The experimental results show that FTO/sputter/spin coating/PT setup increases

the conversion efficiency of the DSSC, with  $V_{oc} = 0.70$  V,  $J_{sc} = 17.22$  mA/cm<sup>2</sup>, the fill factor = 0.641, and an energy conversion efficiency as high as 7.73%.

### Conflict of Interests

The authors declare that there is no conflict of interests regarding the publication of this paper.

### Acknowledgments

The authors gratefully acknowledge the support of the Kung Chi Technology Co., Ltd., the Ministry of Education of Taiwan, through Grant nos. 102G-88-022 and 102 M-88-021, and the Chung-Shan Institute of Science & Technology (Armaments Bureau).

### References

- [1] Y.-S. Jin, K.-H. Kim, W.-J. Kim, K.-U. Jang, and H.-W. Choi, "The effect of RF-sputtered TiO<sub>2</sub> passivating layer on the performance of dye sensitized solar cells," *Ceramics International*, vol. 38, no. 1, pp. S505–S509, 2012.
- [2] K. Nithyanandam and R. Pitchumani, "Analysis and design of dye-sensitized solar cell," *Solar Energy*, vol. 86, no. 1, pp. 351–368, 2012.
- [3] H. Chang, T. L. Chen, K. D. Huang, S. H. Chien, and K. C. Hung, "Fabrication of highly efficient flexible dye-sensitized solar cells," *Journal of Alloys and Compounds*, vol. 504, no. 1, pp. S435–S438, 2010.
- [4] K. R. Bae, C. H. Ko, Y. Park et al., "Structure control of nanocrystalline TiO<sub>2</sub> for the dye-sensitized solar cell application," *Current Applied Physics*, vol. 10, no. 3, pp. S406–S409, 2010.
- [5] C. G. Kuo, C. Y. Hsu, S. S. Wang, and D. C. Wen, "Photocatalytic characteristics of TiO<sub>2</sub> films deposited by magnetron sputtering on polycarbonate at room temperature," *Applied Surface Science*, vol. 258, pp. 6952–6957, 2012.
- [6] C.-T. Wang and C.-F. Yen, "Titania nanocomposite thin films with enhanced photovoltaic efficiency: effects of Ti-alkoxide sol and compact layer," *Surface and Coatings Technology*, vol. 206, no. 8-9, pp. 2622–2627, 2012.
- [7] M. C. Kao, H. Z. Chen, and S. L. Young, "Dye-sensitized solar cells with TiO<sub>2</sub> nanocrystalline films prepared by conventional and rapid thermal annealing processes," *Thin Solid Films*, vol. 519, no. 10, pp. 3268–3271, 2011.
- [8] S. Yuan, Y. Li, Q. Zhang, and H. Wang, "Anatase TiO<sub>2</sub> sol as a low reactive precursor to form the photoanodes with compact films of dye-sensitized solar cells," *Electrochimica Acta*, vol. 79, pp. 182–188, 2012.
- [9] J. Yu, Q. Li, and Z. Shu, "Dye-sensitized solar cells based on double-layered TiO<sub>2</sub> composite films and enhanced photovoltaic performance," *Electrochimica Acta*, vol. 56, no. 18, pp. 6293–6298, 2011.
- [10] L. Meng, T. Ren, and C. Li, "The control of the diameter of the nanorods prepared by dc reactive magnetron sputtering and the applications for DSSC," *Applied Surface Science*, vol. 256, no. 11, pp. 3676–3682, 2010.
- [11] H. J. Kim, J. D. Jeon, D. Y. Kim, J. J. Lee, and S. Y. Kwak, "Improved performance of dye-sensitized solar cells with compact TiO<sub>2</sub> blocking layer prepared using low-temperature reactive ICP-assisted DC magnetron sputtering," *Journal of Industrial and Engineering Chemistry*, vol. 18, pp. 1807–1812, 2012.
- [12] C.-C. Chen, C.-C. Tsao, Y.-C. Lin, and C.-Y. Hsu, "Optimization of the sputtering process parameters of GZO films using the Grey-Taguchi method," *Ceramics International*, vol. 36, no. 3, pp. 979–988, 2010.
- [13] G. Taguchi, E. A. Elsayed, and T. Hsaing, *Quality Engineering in Production Systems*, McGraw-Hill, New York, NY, USA, 1989.
- [14] P. C. Huang, C. H. Huang, M. Y. Lin, C. Y. Chou, C. Y. Hsu, and C. G. Kuo, "The effect of sputtering parameters on the film properties of molybdenum back contact for CIGS solar cells," *International Journal of Photoenergy*, vol. 2013, Article ID 390824, 8 pages, 2013.
- [15] L. Zhang, Y. Zhu, Y. He, W. Li, and H. Sun, "Preparation and performances of mesoporous TiO<sub>2</sub> film photocatalyst supported on stainless steel," *Applied Catalysis B: Environmental*, vol. 40, no. 4, pp. 287–292, 2003.
- [16] J. L. Deng, *The Essential Method of Grey Systems*, HUST Press, Wuhan, China, 1992.
- [17] S. Vijayalakshmy and B. Subramanian, "Enhanced performance of dye-sensitized solar cells with TiO<sub>2</sub> blocking layers and Pt counter electrodes prepared by physical vapor deposition (PVD)," *Electrochimica Acta*, vol. 116, pp. 334–342, 2014.
- [18] C. G. Kuo, C. F. Yang, L. R. Hwang, and J. S. Huang, "Effects of titanium oxide nanotube arrays with different lengths on the characteristics of dye-sensitized solar cells," *International Journal of Photoenergy*, vol. 2013, Article ID 650973, 6 pages, 2013.
- [19] K. H. Ko, Y. C. Lee, and Y. J. Jung, "Enhanced efficiency of dye-sensitized TiO<sub>2</sub> solar cells (DSSC) by doping of metal ions," *Journal of Colloid and Interface Science*, vol. 283, no. 2, pp. 482–487, 2005.
- [20] C. G. Kuo, C. F. Yang, M. J. Kao et al., "An analysis and research on the transmission ratio of dye sensitized solar cell photoelectrodes by using different etching process," *International Journal of Photoenergy*, vol. 2013, Article ID 151973, 8 pages, 2013.
- [21] M. Hocevar, U. O. Krasovec, M. Bokalic et al., "Sol-gel based TiO<sub>2</sub> paste applied in screen-printed dye-sensitized solar cells and modules," *Journal of Industrial and Engineering Chemistry*, vol. 19, pp. 1464–1469, 2013.
- [22] C. H. Yoon, R. V. R. Vittal, J. Lee, W.-S. Chae, and K.-J. Kim, "Enhanced performance of a dye-sensitized solar cell with an electrodeposited-platinum counter electrode," *Electrochimica Acta*, vol. 53, no. 6, pp. 2890–2896, 2008.
- [23] H. Chang, C. H. Chen, M. J. Kao, S. H. Chien, and C. Y. Chou, "Photoelectrode thin film of dye-sensitized solar cell fabricated by anodizing method and spin coating and electrochemical impedance properties of DSSC," *Applied Surface Science*, vol. 275, pp. 252–257, 2013.
- [24] M. H. Abdullah and M. Rusop, "Multifunctional graded index TiO<sub>2</sub> compact layer for performance enhancement in dye sensitized solar cell," *Applied Surface Science*, vol. 284, pp. 278–284, 2013.

## Research Article

# Analyzing Thermal Module Developments and Trends in High-Power LED

**Jung-Chang Wang**

*Department of Marine Engineering, National Taiwan Ocean University (NTOU), No. 2 Pei-Ning Road, Keelung 20224, Taiwan*

Correspondence should be addressed to Jung-Chang Wang; [jcwang@ntou.edu.tw](mailto:jcwang@ntou.edu.tw)

Received 27 February 2014; Revised 8 April 2014; Accepted 11 April 2014; Published 18 May 2014

Academic Editor: Ching-Song Jwo

Copyright © 2014 Jung-Chang Wang. This is an open access article distributed under the Creative Commons Attribution License, which permits unrestricted use, distribution, and reproduction in any medium, provided the original work is properly cited.

The solid-state light emitting diode (SSLED) has been verified as consumer-electronic products and attracts attention to indoor and outdoor lighting lamp, which has a great benefit in saving energy and environmental protection. However, LED junction temperature will influence the luminous efficiency, spectral color, life cycle, and stability. This study utilizes thermal performance experiments with the illumination-analysis method and window program (vapour chamber thermal module, VCTM V1.0) to investigate and analyze the high-power LED (Hi-LED) lighting thermal module, in order to achieve the best solution of the fin parameters under the natural convection. The computing core of the VCTM program employs the theoretical thermal resistance analytical approach with iterative convergence stated in this study to obtain a numerical solution. Results showed that the best geometry of thermal module is 4.4 mm fin thickness, 9.4 mm fin pitch, and 37 mm fin height with the LED junction temperature of 58.8°C. And the experimental thermal resistances are in good agreement with the theoretical thermal resistances; calculating error between measured data and simulation results is no more than ±7%. Thus, the Hi-LED illumination lamp has high life cycle and reliability.

## 1. Introduction

High-power light-emitting diodes (Hi-LEDs) of the solid-state semiconductor devices are emerging and growing rapidly in the globe nowadays. They are employed by indoor and outdoor lighting lamps with white Hi-LEDs appearance, which has many particular advantages involving small size, light weight, long lifetime, quick time response, antivibration, low power consumption, and energy saving issues [1]. Although Hi-LED lighting lamps with less carbon emission are renewable and clean for our living environment and their response time is very short resulting from solid-state direct driving of low voltage, the thermal management and control (TM&C) is needed urgently to resolve the problems of luminous efficiency (lm/W) and light costs (NTD/lm) for Hi-LEDs lighting lamps. Single Hi-LED with 1 mm<sup>2</sup> area usually has above 100 W/cm<sup>2</sup> heat flux. This serious thermal concentration results in a hot-spot phenomenon, and how to control thermal energy is still a major issue to deal with during device packing and application of Hi-LEDs [2–4]. The heat dissipation problems of Hi-LED include three parts

including chip heat dissipation, encapsulation, and system level. LEDs are mounted on metal printed circuit board (MPCB) to enable good dissipation of heat generated from the LEDs. Currently, LED based plates may be divided into several kinds [5–8]. Their responsibility is to conduct heat capacity to the exterior surroundings through the thermal module. The junction temperature ( $T_j$ ) of LED immediately influences luminous efficiency and quality. This is because the light intensity of LEDs and lifetime of the P-N composition plane  $T_j$  change in inverse proportion, so it is an important thermal management problem to reduce the  $T_j$  surpassing 60°C [9]. Higher junction temperature reduces the luminous flux output and brightness and also affects the wave length of photons, changing LED illumination color and lowering its lifetime. It quickly transfers the heat generated by the LED chip to an external heat sink, and through the based plate and cooling module to dissipate heat to the surroundings, can increase the intensity of illumination and LED lifetime.

Eisermann et al. [10] used insulating high-intensity light-emitting diodes aluminum substrates to be attached to a conductor deposited on the dielectric with low-cost systems.

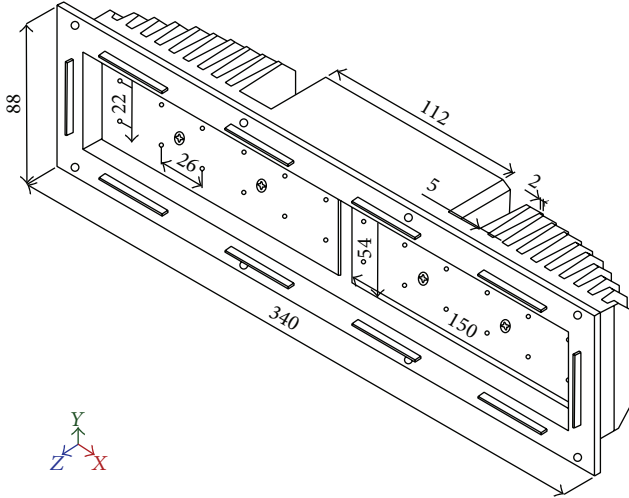


FIGURE 1: LED illumination lamp.

Arik et al. [11, 12] pointed that the heat flux raises over  $80 \text{ W/cm}^2$  with the steady increase in LED power consumption resulting in a hot-spot phenomenon problem. In addition, the high spreading resistance is caused by the heat sink, which has a larger area than the chip. The hot-spot effect and high spreading resistance result in a higher junction temperature for the LED, which should be kept under  $120^\circ\text{C}$ . The reliability and lighting life of LEDs are dependent on junction temperature in normal operating temperature. Wang et al. [13] applied a vapor chamber in a 30 Watt high-power LEDs vapor chamber-based plate and utilized the Windows program VCTM V1.0 to calculate the thermal performance of a LEDs vapor chamber-based plate thermal module. Because of the high thermal performance of the vapour chamber (thermal conductivity above  $800 \text{ W/mK}$ ), which solves the hot-spot problem of Hi-LEDs, the proposal method can spread the heat of the LEDs rapidly to the vapour chamber and conduct it to the thermal module [14–16].

The LED illumination lamp configuration utilized in this paper is shown in Figure 1. There are twelve LED chips ( $2 \times 6$  matrixes) of white color on single aluminum metal core printed circuit board (Al-MCPCB). The dimensions of single LED chip and Al-MCPCB are  $1 \times 1 \text{ mm}^2$  and  $150 \times 54 \times 2 \text{ mm}^3$ , respectively. One LED lighting module has two Al-MCPCBs with twenty-four LED chips. The overall dimensions and material of the present heat sink are  $340 \times 88 \times 50 \text{ mm}^3$  and die-casting aluminum. There are twenty taper fins ( $2 \times 5 \text{ mm}^2$ ) to dissipate heat capacity from Hi-LEDs into surroundings. Ten fins heights are 12, 18, 22, 26, 30, 32, 34, 35, 36, and 37 mm successively and place center symmetry with pitch of 9 mm. And the weight of the whole heat sink is about 1.92 kg. The paper utilized the thermal performance illumination experiments and numerical analysis to test and design the thermal module of LED lighting lamp, especially, in order to obtain these better parameters including lower LED junction temperature, fin geometries, lighter weight of heat sink, and LED vapour chamber-based plate through thermal resistance analysis and VCTM V1.0 [13].

## 2. Analysis Methodology

**2.1. Thermal Performance Experiment and Procedure.** Figure 2 reveals the experimental apparatus and thermal resistance network of one Hi-LED lighting module. The experimental methods stated in this paper are mainly aimed at testing the thermal performance of the one LED lighting module supplied by Macroblock Corp. in Taiwan. Digital power supply of ADC50-10 with a maximum voltage and ample of 50 and 10, respectively, is directly connected to Hi-LEDs heat source and supplies the direct current (D.C.) for four kinds of input powers involving 16, 20, 24, and 30 W. Another input power is alternative current (A.C.) with 110 volts to the one Hi-LED lighting module. The measurement error of the digital power supply is  $\pm(0.5\% + 2\text{digits})$ . All measured temperature points are sixteen T-type thermocouples composed of the materials of copper and nickel as shown in Figure 3. A thermocouple named CH14 is attached on the surface of the LED chip to measure the maximum temperature ( $T_L$ ). CH15 measures the side temperature ( $T_S$ ) near the LED chip. Four thermocouples (CH1 to CH4) are attached on the front surface of Al-MCPCB to measure its temperature. And  $T_M$  is the mean temperature of them.  $T_F$  is the average temperature of CH5 to CH8 that are measuring the skin temperatures of fins. CH9 measures the temperature of power adapter belonging to Hi-LED light module. CH10 to CH13 are the reference temperatures in order to compare numerical temperatures. Lastly, a thermocouple is placed on the back side of the Hi-LED lighting module to measure the ambient temperature ( $T_a$ ). These thermocouples are connected to the data recorder of GL-800APS, which has 40 measuring channels and the recording time is 0.1 ms, to record their values, and the measurement error is  $\pm 1\%$ . Thermocouple of type T has a maximum measuring range from  $-200^\circ\text{C}$  to  $+350^\circ\text{C}$  and an error range of  $\pm 0.5^\circ\text{C}$ . When the temperatures and illumination of LED are in a steady state and their recording curves appear as a horizontal line, one experimental team stops. Every team spends about one hour. There are three inclined angles of  $0^\circ$  (horizontality),  $-90^\circ$  (verticality), and  $90^\circ$  (antigravity) to experiment as shown in Figure 4 in the present study.

Equation (1) defined the thermal resistances, which are generally employed to assess the thermal performances of a thermal module and also an important parameter in thermal module design. The larger the total thermal resistance is, the poorer the thermal performance of thermal modules is and the higher the junction temperature of Hi-LEDs heat source is. Consider

$$R_t = \frac{\Delta T}{Q_{\text{in}}} = R_L + R_M + R_{\text{HS}} + R_a. \quad (1)$$

In (1),  $R_t$  is the total thermal resistance ( $^\circ\text{C/W}$ ),  $\Delta T$  is the temperature difference ( $^\circ\text{C}$ ), and  $Q_{\text{in}}$  is the input power of Hi-LEDs (W). And  $R_t$  is defined as the temperature difference (the junction temperature of LED  $T_L$  minus the ambient temperature  $T_a$ ) divided by the total heat transfer rate  $Q_{\text{in}}$ . The  $R_L$  is the LED thermal resistance, defined as the effective temperature difference at the LED ( $T_L$  minus the side temperature near the LED chip  $T_S$ ) divided by  $Q_{\text{in}}$ . The  $R_M$  is the Al-MCPCB thermal resistance, defined as

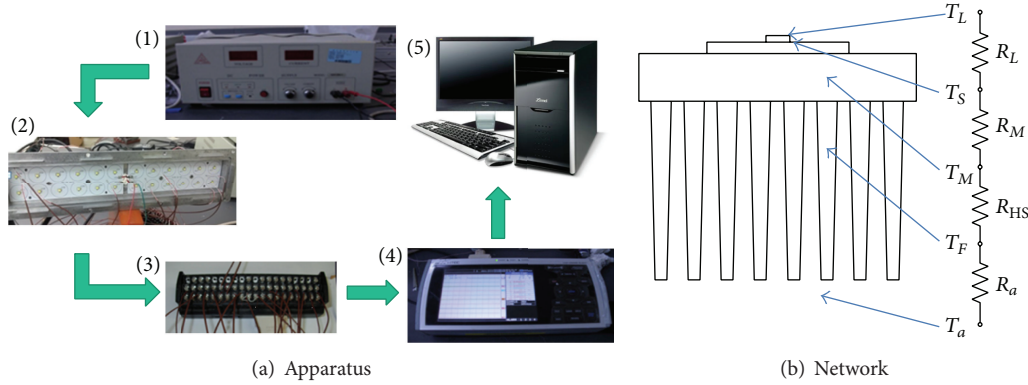


FIGURE 2: Experimental apparatus and thermal resistance network.

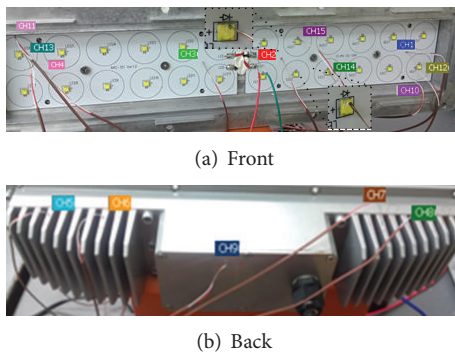


FIGURE 3: Measuring positions.

the temperature difference ( $T_S$  minus the average temperature of the Al-MCPCB  $T_M$ ) divided by  $Q_{in}$ . The  $R_{HS}$  is the heat sink thermal resistance, defined as the temperature difference ( $T_M$  minus the average temperature of the fins  $T_F$ ) divided by  $Q_{in}$ . The  $R_a$  is the convection resistance, defined as the temperature difference ( $T_F$  minus  $T_a$ ) divided by  $Q_{in}$ . Moreover, the thermal resistances belong to derived variable and include temperature and heat transfer rate, which are measured with experimental instruments. Certain error should exist between the data measured during experiment. The concept of propagation of error is introduced to calculate experimental error and fundamental functional relations for propagation of error [13]. An experimental error is represented with a relative error and the maximum relative error of thermal resistances defined is within  $\pm 10\%$  except the  $R_{HS}$ .

**2.2. Numerical Analysis.** One of the major purposes of this study is to design the best thermal performance of thermal module of Hi-LED illumination lamp. Nowadays, in the LED lighting industry, conventional thermal modules of Hi-LED lamp are designed and adjusted by the engineers' experience. Consequently, manufacturing more experimental testing activities may ameliorate the thermal performance of Hi-LED lighting thermal module. However, expenses of testing samples once more and waiting time for samples preparation do not achieve the cost-efficiency for the rapid

development-period market of LED lighting industry. In view of this point, employing numerical analysis is a theme in the present study. The temperature and flow fields of LED lighting model can be simulated and predicted via finite volume method (FVM) based on a 3D numerical approach belonging to computational fluid dynamics (CFD), in which fluid mechanics, discrete mathematics, numerical methods, and computer technologies are integrated by computer-aided design (CAD) and engineering (CAE). Icepak commercial electronic heat transfer analysis software developed by American Fluent Inc. is adopted in this paper. The entire analytical model can be set up and simulated through the file conversion skill between CAD/CFD. The numerical analysis can be divided into three parts involving preprocessing, numerical solving, and postprocessing. With respect to preprocessing, above all, a 3-dimensional (3D) geometrical model of LED light module is drawn and established through 3D CAD software. Moreover, some slight influence characteristics will be neglected so as to decrease the computation grid elements and simulation time when establishing 3D geometrical model. Although we comprehend the mechanism of free convection well, the complexities of fluid motion make it very difficult to acquire simple analytical relations for heat transfer through solving the governing equations of motion and energy. Another reason is that the natural convection heat transfer coefficient depends on the geometry of the surface as well as its orientation, variation of temperature on the surface, and the thermophysical properties of the fluid. Figure 5 exhibits the grid elements and boundary conditions. The top, bottom, and sides of the computer system cabinet are specified as open boundary conditions and the wall thickness of the enclosure is considered to be negligible.

The differential governing equation of a steady state thermal analysis of LED lighting module is shown as (2). More detailed derivations of the heat conduction equation can be found in [17]. Consider

$$\nabla \cdot (k \nabla \cdot T) = q_{in}, \quad (2)$$

where  $k$  is the thermal conductivity of three-dimensional model of the LED lighting system and  $q_{in}$  is the LEDs input heat flux. The governing equations are solved by means of

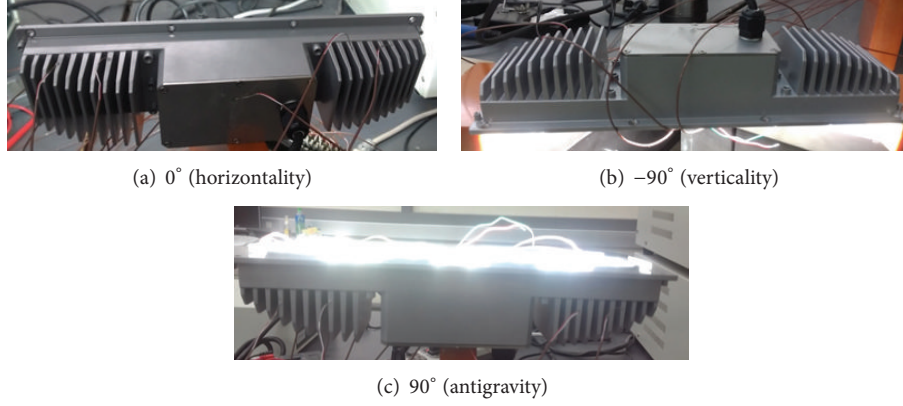


FIGURE 4: Three inclined angles.

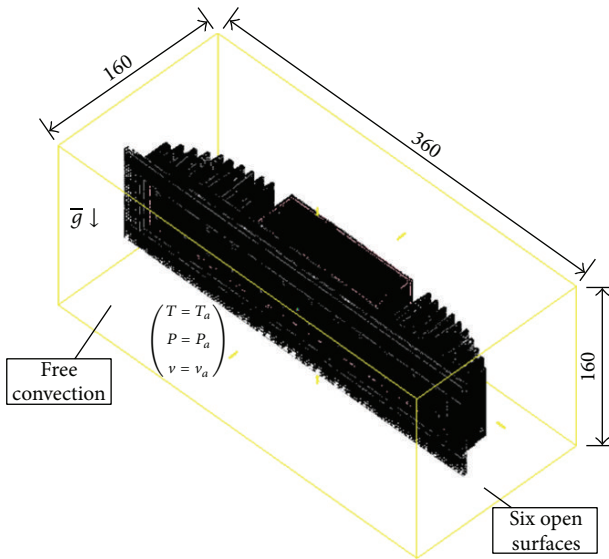


FIGURE 5: Mesh and boundary conditions.

the commercial software ANSYS Icepak v13.0.1 in which a finite volume scheme is used to discretize the governing equations. In conducting solid regions of LEDs lighting module, ANSYS Icepak solves a simple conduction equation that includes the heat flux due to conduction and volumetric heat sources within the solid as shown in (3). Equation (3) is solved simultaneously with the energy transport equation. Consider

$$\frac{\partial(\rho h)}{\partial t} = \nabla \cdot (k \nabla \cdot T) + S_h, \quad (3)$$

where  $\rho$  is density,  $h$  is sensible enthalpy  $h = \int_{T_{ref}}^T C_p dT$ , where  $T_{ref}$  is 298.15 K,  $k$  is conductivity,  $T$  is temperature, and  $S_h$  is the volumetric heat source.

In the flow regions to yield a fully coupled conduction/convection heat transfer prediction can be written through

$$\frac{\partial(\rho h)}{\partial t} + \nabla \cdot (\rho h \bar{v}) = \nabla \cdot ((k + k_t) \nabla \cdot T) + S_h, \quad (4)$$

where  $\bar{v}$  is fluid velocity,  $k_t$  is the conductivity due to turbulent transport ( $k_t = 0$  in this problem), and the source term  $S_h$  includes any volumetric heat sources you have defined. The mass and momentum conservation equations can be written, respectively, as

$$\frac{\partial \rho}{\partial t} + \nabla \cdot (\rho \cdot \bar{v}) = 0 \quad (5)$$

$$\frac{\partial(\rho \cdot \bar{v})}{\partial t} + (\rho \bar{v} \bar{v}) = -\nabla p + \nabla \cdot (\bar{\bar{\tau}}) + \rho \bar{g} + \bar{F}, \quad (6)$$

where  $p$  is the static pressure,  $\bar{\bar{\tau}}$  is the stress tensor ( $= \mu[(\nabla \bar{v} + \nabla \bar{v}^T) - 2/3 \nabla \cdot \bar{v} I]$ ,  $\mu$  is the molecular viscosity,  $I$  is the unit tensor, and the second term on the right-hand side is the effect of volume dilation.),  $\rho \bar{g}$  is the gravitational body force, and  $\bar{F}$  contains other source terms that may arise from resistances, sources, and so forth. The abovementioned governing equations are solved by Icepak code which is a commercial software program of fully 3D steady/unsteady and turbulent/laminar flows application in electronic heat transfer industry [17]. The finite volume method is applied to transfer the partial differential equations to algebraic relations. Then the implicit algorithm is used to solve the obtained algebraic equations. In order to solve the Navier-Stokes and continuity equations the SIMPLE method supplying the pressure-velocity coupling is used.

In the simulation system, two base plates are employed to evaluate the thermal performance of the Hi-LED lighting module. One is the original base plate of Al-MCPCB, and the other is the LED vapour chamber-based plate [13]. A vapor chamber made of C1100 oxygen-free copper is applied in the present paper. Its porosity of the capillary structure in the interior of cavity is under 0.5, and the maximum fill-up amount is under  $15 \text{ mm}^3$ . Pure water containing low oxygen content less than 10 ppb is enclosed as the working fluid and filled up in the interior of the vapour chamber. Its advantages are embodied in its thermal-physics properties such as extremely high latent heat and thermal conductivity and low viscosity, as well as its nontoxicity and incombustibility. The relational theorem and thermal performance of vapour chamber based on the systematic dimensional analysis of

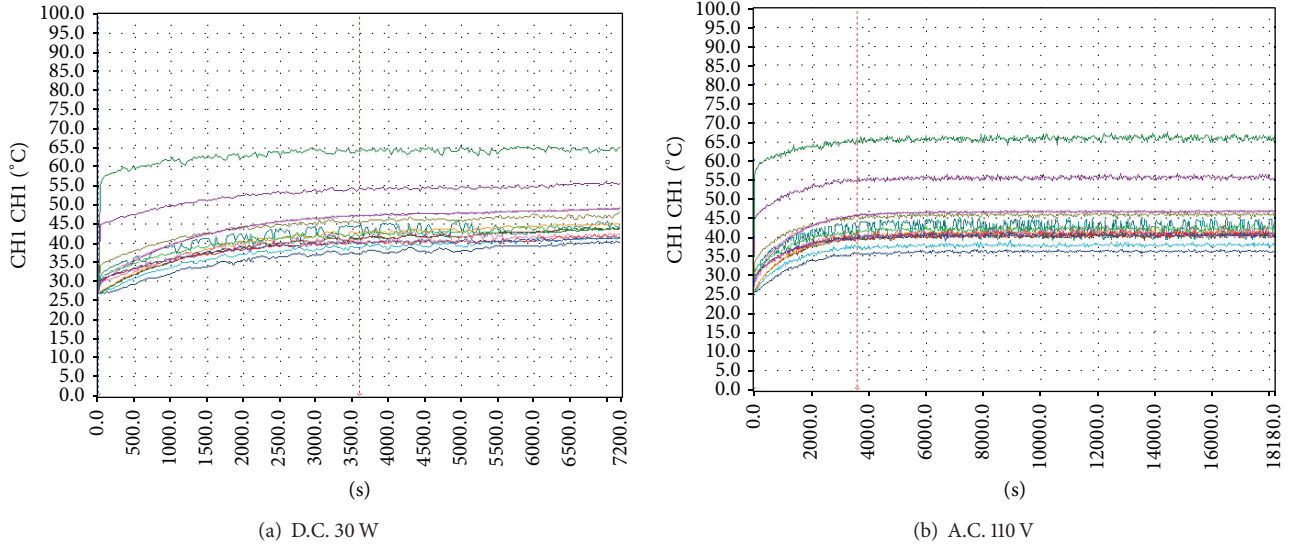


FIGURE 6: Temperatures with time.

the [F.L.T. $\theta$ .] in Buckingham  $\Pi$  Theorem derive empirical formula of the effective thermal conductivity as [13, 18]. In order to avoid repetition, they are not shown in this study. According to Wang's empirical equation (7), in [18], the equivalent thermal conductivity of the vapor chamber depends on its dimensions and heat flux.  $L_{V.C.}$  is the length of the vapor chamber,  $W_{V.C.}$  is width,  $t_{V.C.}$  is thickness, and  $q_{in}$  is the heat flux of LED heat source. Consider

$$K_{eff} = 46.1 \cdot (L_{V.C.} \cdot W_{V.C.})^{0.5} \cdot (t_{V.C.})^{0.24} \cdot (q_{in})^{0.28}. \quad (7)$$

Finally, input the boundary conditions and thermophysical properties, in which the ambient temperature  $T_a$  is set to 25°C (changed with experimental surroundings); a constant external static pressure boundary condition is applied for the six open surfaces, free convection, the grid pattern is structural one and the entire simulation analysis type is steady state, and ANSYS Icepak solves the Navier-Stokes equations for transport of mass, momentum, and energy when it calculates laminar flow with heat transfer. The thermal conductivity of Al-MCPCB assumes 24 W/mk [5]. All conditions of the simulation LED lighting models containing LED heater, heat sink, fins, and housing are the same except the base plates. In order to validate the reliability and accuracy of the present experimental results, the boundary conditions, properties of material, and input parameters are all tallied with these experimental conditions. For the entire Hi-LED lighting module, about  $2.9 \times 10^5$  grid elements are used, iterations are about 500, and it will take about 20 hours to simulate each scenario using one CPU calculation. Then, the problems are solved after the solution convergence with the minimum reduction in normalized residuals for each variable including continuity, momentum, and energy at less than criterions of  $1.0 \times 10^{-3}$  for each case. A mesh sensitivity study is performed by changing the number of grid cells to validate the accuracy of the numerical simulations. When the total number of grid points used for the computations increases

from  $2.9 \times 10^5$  to  $5.2 \times 10^5$ , the change of the maximum CPU temperature is within 1%. There is little to be gained by increasing the mesh number as this will require more computation resources and time. Therefore the grid  $2.9 \times 10^5$  is sufficient for the present simulation. The comparisons of these temperatures and thermal resistances between the experimental results and the computational results of Icepak will be made. Furthermore, obtaining the velocity distributions, temperatures from the simulation results and the simulation thermal resistances are calculated through (1). The present analysis is possible to reduce much cost of manufacture and rapid design Hi-LED lighting thermal modules or improve the thermal performance of existing LED lighting system within a short period.

### 3. Results and Discussions

Figure 6 reveals the experimental results of D.C. 30 W and A.C. 110 V (A.C. 30 W) at incline angle of 0°. All temperatures are almost stable after one hour. The  $T_L$  of CH14 are about 65°C and 66°C, respectively, for D.C. 30 W and A.C. 110 V. Figure 7 shows the numerical results of temperature and velocity under input power of A.C. 30 W at incline angle of 0°. The maximum temperature is 62.6°C and velocity is 0.26 m/s. In the presence of a temperature gradient, forced convection heat transfer will occur. However, we consider situations for which there is no forced velocity by a fan or a pump in the present study, yet convection currents exist within fluid, which are referred to as nature or free convection. The free convection flow velocities are generally much smaller than those associated with forced convection. And the free convection fluid motion is due to buoyancy forces resulting from gravitational field and temperature gradient within fluid. The Grashof number (Gr) plays the same role in free convection that the Reynolds number (Re) plays in forced convection. For a vertical flat plate situation, the turbulent

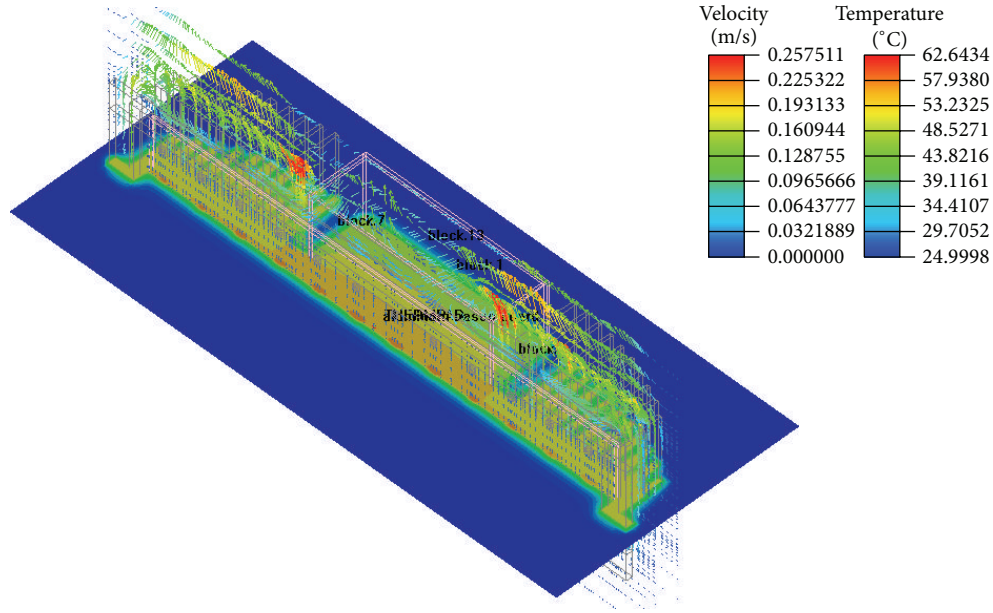


FIGURE 7: Icepak simulation results.

TABLE 1: Comparisons between experimental and numerical temperatures of D.C. 30 W ( $T_a = 25.7^\circ\text{C}$ ).

CH	1	2	3	4	5	6	7	8	9	10	11	12	13	14	15
Measured data ( $^\circ\text{C}$ )	40	39.5	41.9	41.8	39.2	40.3	39.8	39.9	35.9	45.6	45.5	45.5	45.4	<b>64.7</b>	54.8
Simulation result ( $^\circ\text{C}$ )	39	41.1	41.1	41.8	39.9	39.2	40.5	40.5	41.1	X	X	44.8	46.4	<b>65.2</b>	56.3
Error (%)	-2.5	4	-1.9	0	1.7	2.7	1.7	1.5	14.4	X	X	-1.5	2.2	<b>0.7</b>	2.7

TABLE 2: Comparisons between experimental and numerical thermal resistances of D.C. 30 W.

	$R_L$	$R_M$	$R_{HS}$	$R_a$	$R_t$
Measured data ( $^\circ\text{C}/\text{W}$ )	0.33	0.47	0.03	0.47	1.30
Simulation result ( $^\circ\text{C}/\text{W}$ )	0.30	0.52	0.02	0.48	1.32
Error (%)	9.1	-10.6	33.3	-2.1	-1.5

flow may happen when Rayleigh number ( $Ra$ ) is larger than the value of  $1.0 \times 10^9$ . The ratio value of  $Ra$  to  $Gr$  is named by the Prandtl number ( $Pr$ ). We evaluate these dimensionless numbers that the maximum  $Re$  is about  $1.0 \times 10^3$ , the  $Pr$  is 0.71, and the approximate  $Ra$  is  $1.9 \times 10^7$  in the present study. Therefore, the approximate  $Gr$  is  $2.7 \times 10^7$ . The Richardson number ( $Ri$ ) of " $Gr/Re^2$ " is about 27 to verify the present study is free convection assumption. Consequently, with the exception of some simple cases, heat transfer relations in free convection are based on experimental studies.

Tables 1 and 2 show all experimental and simulation temperatures and thermal resistances at input power of D.C. 30 W incline angle of  $0^\circ$ . The errors are within 4% between experimental and simulation temperature except

CH9. And their total thermal resistances are all 1.29 W/mk. The simulation results are in agreement with experimental results. The present CFD model is proper for simulating the LED lighting module. Tables 3 and 4 exhibit all experimental and simulation temperatures and thermal resistances at input power of A.C. 30 W incline angle of  $0^\circ$ . The errors are within 7% between experimental and simulation temperature except CH9. And their total thermal resistances are, respectively, 1.31 W/mk and 1.26 W/mk. The differences between the calculated fin temperatures and the experimental data are slight based on Tables 1 and 3, which can verify the reliability and accuracy of the results obtained. Furthermore, as it can be observed from these tables, the accuracy of the present work in comparisons is good. All experimental temperatures with times are shown in Table 5 under three input powers, 16 W, 20 W, and 24 W, and three incline angles. For D.C. 16 W, they reach stability at almost 20 minutes. The maximum temperatures are  $51^\circ\text{C}$  for  $0^\circ$  and  $90^\circ$  and  $52.3^\circ\text{C}$  for  $-90^\circ$ . For D.C. 20 W, they reach stability at almost 30 minutes. The maximum temperatures are  $55^\circ\text{C}$  for  $0^\circ$  and  $90^\circ$  and  $56.1^\circ\text{C}$  for  $-90^\circ$ . For D.C. 24 W, they reach stability at almost 40 minutes. The maximum temperatures are  $59^\circ\text{C}$  for  $0^\circ$  and  $90^\circ$  and  $60.3^\circ\text{C}$  for  $-90^\circ$ . These temperatures of  $-90^\circ$  are all higher than those of  $0^\circ$  and  $90^\circ$  resulting from these structures of fins, which impeded lifting flows at  $-90^\circ$  inclination. And

TABLE 3: Comparisons between experimental and numerical temperatures of A.C. 30 W ( $T_a = 25.5^\circ\text{C}$ ).

CH	1	2	3	4	5	6	7	8	9	10	11	12	13	14	15
Measured data ( $^\circ\text{C}$ )	41.0	41.8	41.4	41.3	39.9	39.9	42.3	41.6	37.4	46.9	46.8	45.4	45.6	<b>64.4</b>	54.1
Simulation result ( $^\circ\text{C}$ )	39.9	39.8	40.0	40.6	38.7	39.3	39.3	39.9	44.8	X	X	44.2	42.9	<b>62.6</b>	53.8
Error (%)	-2.6	-4.7	-3.3	-1.6	-3	-1.5	-7	-4	14.4	X	X	-2.6	-5.9	<b>-2.4</b>	-0.5

TABLE 4: Comparisons between experimental and numerical thermal resistances of A.C. 30 W.

	$R_L$	$R_M$	$R_{HS}$	$R_a$	$R_t$
Measured data ( $^\circ\text{C}/\text{W}$ )	0.34	0.42	0.02	0.51	1.29
Simulation result ( $^\circ\text{C}/\text{W}$ )	0.29	0.46	0.03	0.46	1.24
Error (%)	14.7	-9.5	-33.3	9.8	3.9

the thermal streams considered thus far had a principle body dimension aligned primarily with the direction of action of the gravity force [17]. The resultant flow patterns were parallel to its surface. For other inclinations, the principal body dimension is nearly perpendicular to the gravity vector and hence to the direction of action of the buoyance force especially for  $90^\circ$  inclination.

Experimental study of the final goal is to improve and optimize the thermal module of fin section and lower LED junction temperature. The present original thermal module has the highest fin of 37 mm. Thus, 37 mm fin height as a standard modifies the fin geometry and improves the required optimum fin pitch of 8.4 mm and the best fin thickness of 5.4 mm, but the fear have error, so there is calculated in the optimal spacing of the thickness reduction with the addition of 1 mm as shown in Table 6. Table 6 displays the modified fin computed from the original fin to optimize spacing and thickness. In summary, we select  $(5.4 \pm 1, 8.4 \pm 1)$  employed into numerical analysis in order to compare the thermal performances between them. Therefore, there are nine fin designs including (4.4, 7.4), (4.4, 8.4), (4.4, 9.4), (5.4, 7.4), (5.4, 8.4), (5.4, 9.4), (6.4, 7.4), (6.4, 8.4), and (6.4, 9.4) to consider the optimum LED thermal module. The best result pitch is the 9.4 mm and the optimum thickness is the 4.4 mm. The modified fin count is 14. Figure 8 reveals that the modified thermal module with about 1.43 kg reduced the weight of 490 g. The optimum pitch and thickness in order, first set the ambient temperature is  $25^\circ\text{C}$ , will find that the original LED temperature drop of  $2.9^\circ\text{C}$ , if the original Al-MCPCB to heat spreader plate (Vapour Chamber, V.C.) [17], which fins did not improve when the LED temperature  $59.1^\circ\text{C}$ , the temperature of the fin improved  $55.2^\circ\text{C}$ , the temperature difference at  $4.1^\circ\text{C}$  as shown in Table 7. The reason is that the interior working fluid of the V.C. does not burn out after the operating temperature scope, taking along the quantity of heat flow through the working fluid vaporization. This causes the V.C. to dissipate in a two-dimensional direction, making thermal spreading effect better than that of the Al-MCPCB.

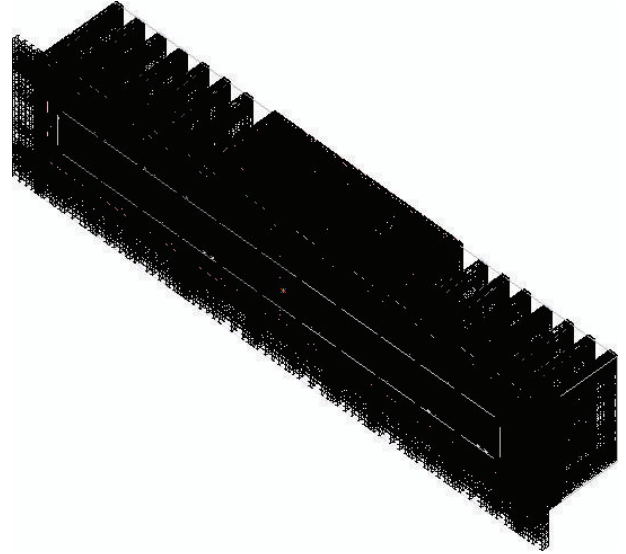


FIGURE 8: Modified fins.

Hence, the LED vapor chamber-based plate quickly dissipates the heat flow from LED heat sources to the exterior cooling module resulting from the interior two-phase flow.

#### 4. Conclusion

For centuries, all mankind have applied light generated by thermal radiation on many lighting things; now rapid progress of semiconductor and solid-state cold light technologies in recent decades make mankind forward to green environmental protection and energy-saving lighting world in the 21st century. The present paper describes thermal performance experiments to investigate and design the Hi-LED lighting thermal module and achieve the optimization of the fin parameters under the natural convection. Results show that the thermal performance of the vapour chamber is better than that of Al-MCPCB, proving that it can effectively reduce the LED junction temperature. And comparing numerical results with the experimental values, the calculating error is no more than  $\pm 7\%$  based on some specified conditions in this study. The thermal performance of the Hi-LED lighting module with modified fins and V.C. is better than that of the original LED lighting module above  $6.5^\circ\text{C}$ . We establish the relations between experimental and numerical studies in the present paper. The numerical results are in good agreement with the experimental results in the present study.

TABLE 5: Experimental temperatures.

Time (min.)	CH1	CH2	CH3	CH4	CH5	CH6	CH7	CH8	CH9	CH10	CH11	CH12	CH13	CH14	CH15
16 W <sub>90</sub> ° ( $T_a = 27.4^\circ\text{C}$ )															
0	27.4	27.3	27.3	27.4	27.3	27.4	27.4	27.4	27.4	27.4	27.3	27.4	27.4	<b>27.4</b>	27.4
0.5	28.7	28.7	28.9	28.9	27.4	27.5	27.5	27.5	27.4	28.1	28.3	30.6	29.4	<b>41.7</b>	34.9
1	29.9	30.1	30.6	31.1	27.6	28.1	28.2	28.1	27.9	29.9	30.1	33	31.8	<b>46</b>	37.9
5	31.2	31.1	31	31.5	28.7	28.9	29	29	27.9	30.7	31.1	33.2	32.2	<b>46.6</b>	38.4
10	32	32.3	32.3	33	29.8	30.1	30	30.2	28.8	32.4	32.7	34.3	33.6	<b>47.4</b>	39.2
20	33.1	32.6	33.2	33.6	31.1	31.9	31.5	31.6	30.1	34.6	35	35.8	33.9	<b>47.4</b>	39
30	34.7	34	34.8	35.3	32.2	32.8	33	33.4	31.3	36.1	36.6	37.5	36.2	<b>48.5</b>	40.2
40	35.3	35.3	36.1	36.8	33.3	34	33.6	34.1	32.2	37.5	38	38.2	37.6	<b>49.5</b>	41.3
50	35.5	36.7	36.1	37.3	34.3	35.1	34.6	35.1	33.2	38.7	39	39.4	37.9	<b>50</b>	41.9
60	36.2	36.3	35.4	36.8	35.6	35.2	35.1	36.2	33.7	39.3	39.4	39.3	38.3	<b>51.3</b>	42.9
16 W <sub>0</sub> ° ( $T_a = 28.5^\circ\text{C}$ )															
0	28.4	28.6	28.5	28.6	28.5	28.6	28.6	28.6	28.4	28.6	28.6	28.5	28.5	<b>28.4</b>	28.4
0.5	29.7	29.7	30	30.1	28.7	29.1	29	29.2	28.4	30	30.4	32	30.6	<b>43.5</b>	36.6
1	30.4	30.9	31.3	31.3	28.9	29.4	29.4	29.4	28.5	30.5	30.9	32.8	31.4	<b>47.1</b>	39.2
2	30.5	30.6	31.2	31.5	29.1	29.9	29.7	29.8	28.7	30.9	31.5	33.2	31.5	<b>46.4</b>	38.6
3	30.8	31.1	31.8	31.9	29.2	30.2	30.1	30.2	28.6	31.3	31.7	33.2	32	<b>47.1</b>	39
5	31.3	31.6	32.4	32.3	30.1	30.9	30.7	30.7	28.9	32	32.5	33.8	32.2	<b>48.2</b>	40
10	32.1	31.7	32.1	32.9	30.8	32	31.6	31.9	29.5	33.3	33.7	34.7	33.1	<b>47.3</b>	39
20	33.5	33.7	33.8	34.1	32.6	33.9	33.6	33.8	30.9	35.1	35.6	35.7	34.2	<b>48.7</b>	40.7
30	33.6	34.5	35	34.8	33.7	35	34.8	35.1	31.9	36.2	36.8	36.2	35	<b>50.1</b>	41.9
40	34.7	34.6	35.1	36	34.2	35.8	35.3	35.6	32.1	37	37.5	36.7	35.9	<b>47.9</b>	40.4
50	35	35.4	35.2	35.7	34.8	36.3	35.9	36.2	32.8	37.5	38.1	37.4	36.2	<b>49.3</b>	41.2
60	34.6	35.8	35.9	36.2	34.8	36.5	36.1	36.4	32.6	37.9	38.4	37.2	36.4	<b>51.3</b>	42.7
16 W <sub>-90</sub> ° ( $T_a = 28.3^\circ\text{C}$ )															
0	28.2	28.2	28.2	28.2	28.2	28.4	28.3	28.3	28.4	28.4	28.3	28.2	28.2	<b>28.2</b>	28.2
0.5	30.1	30.1	30.3	30	28.3	28.5	28.4	28.4	28.6	29.5	29.9	32	30.6	<b>46.4</b>	39.1
1	30.1	30.3	30.4	30.5	28.3	28.5	28.4	28.4	28.4	29.8	30	32.1	30.9	<b>46</b>	38.2
2	30.5	30.4	30.7	30.8	28.4	28.7	28.6	28.6	28.6	30.4	30.6	32.7	31.3	<b>46.5</b>	39
3	31.2	31	31.3	31.4	29.2	29.5	29.1	29.1	28.9	30.8	31.3	33.3	31.9	<b>47.3</b>	39.4
5	32.2	31.9	31.9	32	29.5	29.9	29.3	29.6	29.2	31.5	32	34.1	32.4	<b>48.1</b>	40.5
10	33.7	33.2	33.1	33.1	30.8	31.1	30.4	30.7	30.4	33.2	33.7	35.4	33.7	<b>49.3</b>	41.8
20	34.5	34.4	34	34.4	31.5	32.4	31.6	31.9	32.7	35.5	35.7	37.4	34.9	<b>50</b>	41.7
30	36.5	36	35.8	35.7	32.9	33.6	32.7	33.3	34	37.1	37.4	38.9	36.3	<b>51.7</b>	44
40	37.7	36.8	36.3	36	33.4	34.6	33.5	33.7	35	38.2	38.1	39.9	36.5	<b>52.1</b>	44.3
50	38.5	37.8	36.6	37	34.5	35.3	33.7	34.5	36.2	39.1	39.1	40.4	37.6	<b>53.1</b>	45.4
60	39.3	38.5	38.1	38.1	34.8	35.6	34.4	35.3	36.5	39.7	40	41.3	38.5	<b>53.7</b>	46.5
20 W <sub>90</sub> ° ( $T_a = 26.9^\circ\text{C}$ )															
0	26.9	27	27	27	26.8	26.8	26.8	26.8	26.8	27	27	27	27	<b>26.9</b>	26.8
0.5	28.8	29	29.6	29.4	26.4	26.7	26.6	26.6	26.6	28.5	28.7	32.1	30.2	<b>46.4</b>	39.5
1	29.4	29.5	30.2	30	26.7	26.9	26.8	26.7	26.8	29.1	29.5	32.3	30.9	<b>48.1</b>	40.5
10	32.2	32.4	33.2	33	29.3	30.1	29.3	29.3	28.7	33.2	33.6	35.8	34.4	<b>51.2</b>	43.2
20	34.4	35	34.8	34.7	30.5	32	31.6	31.8	30.5	36.1	36.7	38.1	35.6	<b>53.6</b>	45.7
30	36.2	35.9	36.1	36.8	31	32.3	31.9	32.4	32	38	38.3	39.4	37.5	<b>53.8</b>	46.6
40	36	36.6	37.1	37.6	31.3	32.9	32.8	32.4	32.5	39.2	39.3	39.6	38.8	<b>54.8</b>	47
50	36.3	37.5	36.4	37.5	33.4	35.3	35.1	35.4	33.2	39.9	40.1	40.2	37.4	<b>54.8</b>	46.1
60	37.5	37.8	38.4	38	33.3	34.4	33.5	33.2	33.3	40.4	40.6	41.1	39.5	<b>54.9</b>	47.2

TABLE 5: Continued.

Time (min.)	CH1	CH2	CH3	CH4	CH5	CH6	CH7	CH8	CH9	CH10	CH11	CH12	CH13	CH14	CH15
20 W <sub>0</sub> ° ( $T_a = 28.0^\circ\text{C}$ )															
0	28.1	28	28	28.1	28.1	28.1	28.1	28.1	27.9	28.1	28.1	28.1	28.1	<b>28.1</b>	28.1
0.5	30.4	30.2	30.8	30.9	28.1	28.6	28.6	28.6	28	29.9	30.3	33	31.3	<b>48.7</b>	40
1	30.8	30.7	31.7	31.5	28.2	28.9	28.8	28.8	28.2	30.3	30.9	33.6	31.8	<b>50.7</b>	41.4
2	31.1	30.7	31.5	31.4	28.8	29.4	29.2	29.3	27.9	30.8	31.3	33.8	31.8	<b>50.6</b>	40.6
3	31.4	31.3	32.5	32.3	29.3	30	29.9	29.9	28.1	31.4	31.8	34.1	32.3	<b>50.8</b>	41.4
5	31.9	32.3	33.2	33	30	30.9	30.8	30.8	28.8	32.3	33.1	34.8	33.1	<b>52.2</b>	42.4
10	33.1	33.1	34.2	33.9	31.1	32.2	31.5	32.3	29.7	34.2	34.6	36.2	34.2	<b>52.3</b>	42.8
20	34.3	35.3	35.1	35.6	33.7	35.1	34.9	35	31.5	36.6	37.2	37.3	35.6	<b>53.7</b>	43.5
30	35	35.9	36.5	37	34.8	36.5	36.5	36.5	32.6	38.3	38.8	38.2	36.8	<b>55.2</b>	45.1
40	35.9	37	36.5	36.9	36.1	37.6	37.3	37.6	33.7	39.2	40	39	37.2	<b>55.5</b>	45.5
50	35.9	36.7	37.1	38.2	36.2	38.1	37.8	38.2	33.9	39.9	40.5	39.3	38.1	<b>54.9</b>	46.7
60	35.9	38.1	37.7	38.5	36.8	38.7	38.5	38.7	34.3	40.4	41.1	39.4	38.6	<b>56.1</b>	46.3
20 W <sub>-90</sub> ° ( $T_a = 26.5^\circ\text{C}$ )															
0	26.4	26.5	26.5	26.6	26.5	26.6	26.5	26.6	27.4	27.4	27.4	26.6	26.6	<b>26.5</b>	26.5
0.5	28.4	28.6	28.5	28.6	26.5	26.8	26.6	26.7	27.2	28.3	28.7	30.8	29.4	<b>45.8</b>	38.3
1	29.4	29.5	29.5	29.6	26.7	27.1	26.8	26.9	27.3	28.9	29.5	31.9	30.3	<b>48.1</b>	39.7
2	29.5	29.5	29.3	29.8	26.9	27.6	27.5	27.5	27.3	29.5	30.1	32.3	30.7	<b>48.1</b>	39.2
3	29.9	30.2	29.9	30.3	27.2	27.7	27.5	27.6	27.5	30.1	30.5	33	31	<b>49.5</b>	40
5	30.8	31	30.9	31	27.8	28.4	28.2	28.5	27.9	31.1	31.4	33.8	31.9	<b>49.8</b>	41
10	32	32	31.5	32.3	28.8	29.5	29.1	29.2	29.9	33	33.6	35.6	32.9	<b>50.8</b>	41.7
20	34.6	34.8	34.2	34.9	31.2	32.1	31.5	31.6	32.3	35.9	36.3	38.1	35.5	<b>53.1</b>	44.1
30	34.6	35.3	34.8	35.1	31.1	32.3	31.8	31.8	33.9	37.6	37.6	38.9	35.6	<b>53.6</b>	44
40	34.8	36.3	35.6	36.2	31.7	33.1	32.5	33.2	35	38.6	38.8	39.7	36.8	<b>54.4</b>	44.7
50	36.4	37.2	36.2	36.9	31.9	33.7	33.1	33.8	35.8	39.4	39.5	40.7	37.3	<b>55.1</b>	45.3
60	36.3	37.1	36.3	36.5	32.1	33.6	32.7	33	36.5	39.8	40	41.3	36.8	<b>54.9</b>	45.1
24 W <sub>90</sub> ° ( $T_a = 26.5^\circ\text{C}$ )															
0	26.4	26.4	26.5	26.4	26.4	26.4	26.4	26.4	26.4	26.6	26.6	26.5	26.5	<b>26.6</b>	26.5
0.5	31.6	31.6	31.8	31.8	29.1	29.4	29.2	29.2	29.2	31	31.3	34.7	32.8	<b>52.6</b>	41.5
1	32.1	31.9	32.1	32.2	29.1	29.6	29.6	29.6	29.2	31.7	31.9	35.3	33.5	<b>53.6</b>	42.4
10	35	36.1	36	36.5	32.4	33.3	33.1	33.6	31.5	36.6	37.2	39.1	37.4	<b>55.3</b>	45
20	36.1	36.7	37.2	37.8	35.6	36.6	36.3	36.5	34	39.9	40.3	41.5	38.8	<b>56.8</b>	45.8
30	38.6	37.8	38.3	38.5	35.5	36.7	36.7	37.8	36.1	42.1	42.7	43.6	40.8	<b>56.4</b>	46.3
40	38.8	37.8	38.5	38.4	37.5	38.5	37.3	38.9	37.3	43.5	44	45.3	42.7	<b>59.8</b>	48.5
50	38.9	38.8	39.3	38.5	37.2	38.7	38.1	39.7	38.3	44.6	45.2	45.3	42.1	<b>59.2</b>	50
60	38.9	39.8	40.3	38.7	37.5	38.9	39.4	40.6	38.9	45.1	45.8	44.6	43.6	<b>59.4</b>	50.6
24 W <sub>0</sub> ° ( $T_a = 28.4^\circ\text{C}$ )															
0	28.4	28.4	28.4	28.4	28.4	28.5	28.5	28.5	28.5	28.5	28.5	28.5	28.5	<b>28.5</b>	28.5
0.5	30.6	30.5	31.1	30.9	28.4	28.6	28.6	28.5	28.3	29.8	30	34.1	31.8	<b>52.6</b>	43.1
1	31.6	31.4	32.6	32.3	28.6	29	28.9	28.8	28.6	30.7	31.3	34.9	32.9	<b>55.1</b>	44.3
2	31.9	31.7	32.7	32.6	28.9	29.5	29.2	29.3	28.3	31.4	31.8	35.6	33.2	<b>55</b>	43.7
3	32.3	32.3	33.3	33.3	29.5	30.1	30	30	28.5	32	32.5	35.7	33.5	<b>55.3</b>	44.1
5	32.9	32.6	33.9	33.7	30.1	30.9	30.9	30.8	28.8	32.7	33.2	36.4	34.2	<b>56.2</b>	45.2
10	34.6	34.5	35.5	35.4	32.3	33.8	33.6	33.7	30.7	35.6	36.3	38.1	35.8	<b>56.9</b>	46.1
20	36.7	36.7	37	38	35.6	37	36.5	36.7	32.6	38.9	39.6	40.3	38.7	<b>59.3</b>	48.5
30	36.9	38.3	38.2	39	37.1	38.7	38.4	38.6	34	40.8	41.3	40.9	39.3	<b>59.9</b>	49.3
40	37.2	39.2	39.3	40.2	38	39.9	39.4	39.7	34.8	41.8	42.4	41	40.4	<b>60.1</b>	47.9

TABLE 5: Continued.

Time (min.)	CH1	CH2	CH3	CH4	CH5	CH6	CH7	CH8	CH9	CH10	CH11	CH12	CH13	CH14	CH15
50	37.5	39.8	39.5	40.7	38.6	40.7	40.6	40.5	35.6	42.7	43.3	41.4	40.6	<b>61.3</b>	48.6
60	37.9	39.2	38.9	40	38.7	40.9	40.1	40.7	35.8	43.1	44	41.9	41.3	<b>59.7</b>	50.5
24 W <sub>-90°</sub> ( $T_a = 28.2^\circ\text{C}$ )															
0	28.1	28.3	28.2	28.3	28.1	28.3	28.1	28.3	28.3	28.3	28.3	28.3	28.1	<b>28.1</b>	28.1
0.5	30.6	31.1	30.8	30.7	28	28.5	27.9	28.4	28.7	30.7	31.1	33.5	31.3	<b>52</b>	43.1
1	31.5	31.4	31.7	32	28.5	29.1	28.3	28.6	29	31.4	31.9	34.5	32.1	<b>53.5</b>	43.9
2	31.5	31.8	31.8	32.2	28.5	29.1	28.4	28.3	28.8	32.1	32.6	34.5	32.2	<b>52.4</b>	42.4
3	31.8	32.3	31.8	32.4	28.9	29.8	29.4	29.8	29	32.7	33.2	34.9	33.3	<b>52.8</b>	43.8
5	33.2	33.4	32.9	33.7	29.5	30.8	29.6	29.8	29.7	33.8	34.1	36.9	33.7	<b>55.2</b>	45.3
10	34.7	35	35.2	35.1	30.8	32.3	31.1	32.3	31.1	36	36.4	38.7	35.4	<b>56.4</b>	46.6
20	36.8	37	36.2	37.2	32.3	34.4	32.3	33.2	34.4	39.1	39.6	41.1	37.1	<b>57.6</b>	47.5
30	38.2	38.4	37.8	38.4	33.1	35	33.1	34.1	36.3	40.9	41.3	42.6	38.1	<b>58.6</b>	48.6
40	39.3	39.6	39.4	39.7	33.7	36.1	34.2	35	36.9	42.2	42.4	44	39.2	<b>59.5</b>	50
50	38.9	39.8	38.9	40.4	33.8	36.2	34.4	35.9	38.3	42.9	43.4	43.8	40.3	<b>59.4</b>	48.9
60	39.7	40.5	39.8	40.3	34.2	36.8	34.6	36.6	37.9	43.4	43.8	44.8	40.2	<b>60.3</b>	50.8

TABLE 6: Optimization fin geometry (3 × 3).

S (mm)	t (mm)		
	4.4	5.4	6.4
7.4	N = 7 LED temperature 60°C	N = 7 LED temperature 59.8°C	N = 7 LED temperature 59.7°C
8.4	N = 7 LED temperature 59.45°C	N = 7 LED temperature 59.2°C	N = 7 LED temperature 59.8°C
9.4	N = 7 <b>LED temperature 59.1°C</b>	N = 7 LED temperature 59.4°C	N = 7 LED temperature 60.4°C

TABLE 7: Comparisons between original design and modified design.

	CH										
	1	2	3	4	7	8	9	12	13	14	15
Original fins (°C)	39.2	38.2	38.2	39.1	37.9	37.9	43	42.2	42.2	<b>61.7</b>	53.2
Optimal fins (°C)	37.5	37.8	37.8	38.6	36.8	36.7	42.5	41.6	42.5	<b>58.8</b>	51.1
Original fins with V.C. (°C)	42.1	41.2	41.2	42.3	41	40.7	45.8	44.9	44.9	<b>59.1</b>	53.1
<b>Optimal fins with V.C. (°C)</b>	37.6	37.8	37.8	38.8	36.8	36.7	42.7	41.7	42.4	<b>55.2</b>	49.7

## Nomenclature

$A$ : Area,  $\text{m}^2$

$H$ : Height, m

$L$ : Length, m

$R$ : Thermal resistance,  $^\circ\text{C}/\text{W}$

$T$ : Temperature,  $^\circ\text{C}$

$W$ : Width, m

$g$ : Gravitational acceleration,  $\text{m}/\text{s}^2$

$h$ : Heat transfer coefficient,  $\text{W}/\text{m}^2\text{ }^\circ\text{C}$

$k$ : Thermal conductivity,  $\text{W}/\text{m }^\circ\text{C}$

$t$ : Thickness, m

$q_{\text{in}}$ : Heat transfer rate, W

Gr: Grashof number, dimensionless

Pr: Prandtl number, dimensionless

Ra: Rayleigh number, dimensionless

Re: Reynolds number, dimensionless

Ri: Richardson number, dimensionless.

## Subscripts

$a$ : Ambient

fin: Fin

V.C.: Vapour chamber.

## Conflict of Interests

The author declares that there is no conflict of interests regarding the publication of this paper.

## Acknowledgments

The author is particularly grateful to Macroblock, Inc., and ARC Solid-State Lighting Corporation, for providing research funding for this study as well as samples of LED lamps. And the author also would like to thank all colleagues and students who contributed to this study.

## References

- [1] G. B. Stringfellow and M. George Craford, *High Brightness Light Emitting Diodes: Semiconductors and Semimetals*, vol. 48, chapter 2, Academic Press, San Diego, Calif, USA, 1997.
- [2] J. C. Wang, "Investigation on application of LED to energy-saving lamp," *Combustion Quarterly* 4, vol. 18, no. 1, pp. 3–11, 2009.
- [3] J. H. Choi and M. W. Shin, "Thermal investigation of LED lighting module," *Microelectronics Reliability*, vol. 52, no. 5, pp. 830–835, 2012.
- [4] C.-J. Weng, "Advanced thermal enhancement and management of LED packages," *International Communications in Heat and Mass Transfer*, vol. 36, no. 3, pp. 245–248, 2009.
- [5] J. C. Wang, "Thermal investigations on LED vapor chamber-based plates," *International Communications in Heat and Mass Transfer*, vol. 38, no. 9, pp. 1206–1212, 2011.
- [6] A. Christensen and S. Graham, "Thermal effects in packaging high power light emitting diode arrays," *Applied Thermal Engineering*, vol. 29, no. 2-3, pp. 364–371, 2009.
- [7] M. Ha and S. Graham, "Development of a thermal resistance model for chip-on-board packaging of high power LED arrays," *Microelectronics Reliability*, vol. 52, no. 5, pp. 836–844, 2012.
- [8] J. C. Wang, "Thermoelectric transformation and illuminative performance analysis of a novel LED-MGVC device," *International Communications in Heat and Mass Transfer*, vol. 48, pp. 80–85, 2013.
- [9] J. C. Wang and C. L. Huang, "Vapor chamber in high power LEDs," in *Proceedings of the 5th International Microsystems, Packaging, Assembly and Circuits Technology Conference (IMPACT '10)*, pp. 1–4, Taipei, Taiwan, 2010.
- [10] E. Eisermann, K. Höll, W. Smetana, W. Tusler, M. Unger, and J. Whitmarsh, "Comparison of low cost, insulated aluminium substrates used as integrated heat sinks with conventional technology," *Microelectronics International*, vol. 26, no. 2, pp. 3–9, 2009.
- [11] M. Arik, J. Petroski, and S. Weaver, "Thermal challenges in the future generation solid state lighting applications: light emitting diodes," in *Proceedings of the 8th Intersociety Conference on Thermal and Thermomechanical phenomena in Electronic Systems*, pp. 113–120, San Diego, Calif, USA, June 2002.
- [12] M. Arik, C. Becker, S. Weaver, and J. Petroski, "Thermal management of LEDs: package to system," in *Proceedings of the 3rd International Conference on Solid State Lighting*, vol. 5187, pp. 64–75, August 2003.
- [13] J. C. Wang, R. T. Wang, T. L. Chang, and D. S. Hwang, "Development of 30 Watt high-power LEDs vapor chamber-based plate," *International Journal of Heat and Mass Transfer*, vol. 53, no. 19-20, pp. 3990–4001, 2010.
- [14] H. S. Huang, Y. C. Chiang, C. K. Huang, and S. L. Chen, "Experimental investigation of vapor chamber module applied to high-power light-emitting diodes," *Experimental Heat Transfer*, vol. 22, no. 1, pp. 26–38, 2009.
- [15] J. C. Wang, "Thermal module design and analysis of a 230 W LED illumination lamp under three incline angles," *Microelectronics Journal*, vol. 45, no. 4, pp. 416–423, 2014.
- [16] J. C. Hsieh, H. J. Huang, and S. C. Shen, "Experimental study of micro rectangular groove structure covered with multi mesh layers on performance of flat plate heat pipe for LED lighting module," *Microelectronics Reliability*, vol. 52, pp. 1071–1079, 2012.
- [17] J. C. Wang and S. L. Chen, "Air cooling module applications to consumer-electronic products," *InTech*, chapter 14, pp. 339–366, 2011.
- [18] J. C. Wang and R. T. Wang, "A novel formula for effective thermal conductivity of vapor chamber," *Experimental Techniques*, vol. 35, no. 5, pp. 35–40, 2011.

## Research Article

# Investigation of Elastic Energy on Single Crystal GaN Nanobeams with Different Span

Shang-Chao Hung,<sup>1</sup> Cheng-Fu Yang,<sup>2</sup> and Yi-Cheng Hsu<sup>3</sup>

<sup>1</sup> Department of Information Technology & Communication, Shih Chien University, Kaohsiung Campus, Kaohsiung 845, Taiwan

<sup>2</sup> Department of Chemical and Materials Engineering, National University of Kaohsiung, Kaohsiung 811, Taiwan

<sup>3</sup> Department of Biomechatronics Engineering, National Pingtung University of Science and Technology, Pingtung 912, Taiwan

Correspondence should be addressed to Shang-Chao Hung; [schung99@gmail.com](mailto:schung99@gmail.com)

Received 15 March 2014; Accepted 15 April 2014; Published 12 May 2014

Academic Editor: Ho Chang

Copyright © 2014 Shang-Chao Hung et al. This is an open access article distributed under the Creative Commons Attribution License, which permits unrestricted use, distribution, and reproduction in any medium, provided the original work is properly cited.

This research presents a novel technique which can more efficiently fabricate different spans of nanobeams on the same substrate. It requires less time to prepare specimen and further shortens the process of aligning, clamping, and testing. Also, we probe into the elastic deformation properties of clamped freestanding GaN nanobeams with different spans. In the bending process, displacement,  $D$ , corresponding to load,  $P$  is strongly dependent on the span of nanobeam at the same penetration depth and a distinct linearity is observed. Young's moduli  $E$  of the GaN in this study are calculated as  $171.3 \text{ GPa} \pm 5.4\%$  and  $264.2 \text{ GPa} \pm 4.7\%$  by strain energy methods, respectively, for the longer and shorter spans of nanobeams, serving as a simple supporting beam of elastic material under small deformation. The result shows that, even under small deformation, the rigidity enhancement helps the shorter nanobeam store more elastic energy.

## 1. Introduction

Since the conversion of mechanical energy into electric one has been realized as a nanogenerator for the recycle energy issue, Nitride-based one-dimensional nanomaterials have attracted much attention [1, 2]. Among them, the materials AlN, InN, and GaN are usually fabricated by bottom-up growing techniques and the top-down growing methods also involve in some GaN-based nanogenerator fabrication [3]. This means that nanogenerator can be realized by semiconductor processing techniques. In nanogenerator experiment in which the kinetic energy is transferred into the elastic one, it is interesting to note that the output current is significantly dependent on the bended nanorods with different aspect ratio whereas the magnitudes of the deflecting kinetic energy are equal [3]. Furthermore, the deflecting direction is perpendicular to the axial direction ( $c$ -plane of GaN film) of nanorods which were stretched on the outer surface and were compressed on the inner surface [4], which consequently creates the rigidity. The shorter aspect ratio will produce more rigidity than that in longer one at

the same displacement. This means that the shorter a nanorod is, the more energy is needed to bend a nanorod. Therefore, considering its elastic behavior, the shorter nanorod can store more energy. The mechanical characterization of one-dimensional nanostructure with different aspect ratio has proven itself a fertile ground for further research. However, their sizes and configurations, which cannot be precisely tested by conventional measures, have posed great challenges to the mechanical characterization of nanostructures. To acquire better measurement, axial loading for uniaxial compression is adopted in experiments concerning mechanical behavior about one-dimensional GaN nanomaterials [5, 6]. In this method, the advanced group III nitride semiconductor nanotube fabrication technology makes intricate manipulations unnecessary. Besides, precise alignment of an individual nanotube is still a challenging task. Various novel methods have been developed to overcome the aligning problem, such as microelectromechanical system (MEMS) test [7–9], micro/nanoindentation tests [10–13], tensile tests [14], and bending tests [15–17], each of which has its contribution and advantages. Unfortunately, aligning, clamping, and testing of

individual nanowire between two fixed ends still demand great specimen preparation time.

To offer a better solution, this report presents a novel, more efficient technique which can fabricate different spans of nanobeams on a homogeneous substrate. It requires less time to prepare specimen and shortens the process of aligning, clamping, and testing of individual nanobeam between two fixed ends. In this study, nanobeams, fabricated by focused ion beam (FIB, FEI Nova-200 NanoLab Compatible) with different spans, are clamped in between two homogeneous fixed ends as simple supporting beams. They are subjected to tension or compression loads in an *in situ* transmission electron microscopy. These bending tests of nanobeams install a conical tip inside the transmission electron microscopy (TEM) chamber, improving the visibility for alignment, load, and displacement. In addition to testing the elastic energy of nanobeams, we also conduct experiments for the linear relationship of stress and strain with different spans.

## 2. Experiment

Firstly, a slice of GaN with a feature size  $\sim 250$  nm in width,  $10 \mu\text{m}$  in length, and  $3 \mu\text{m}$  in depth was peeled from single crystal GaN film by FIB (FEI Nova-200 NanoLab Compatible) at 5 keV. The single crystal GaN film was grown as prior study showed in a standard process by metal organic chemical vapor deposition (MOCVD) on sapphire (0 0 0 1) [3]. Secondly, this single crystal GaN slice was then postpatterned and machined by FIB again with a tilted angle of  $30^\circ$  to generate a uniform set of suspended bridge structures of different lengths.

After fabrication, the geometric parameters of each nanobeam on the GaN substrate were measured from scanning electron microscope (SEM) observations. The length ranges are  $\sim 1.5$  and  $\sim 2.0 \mu\text{m}$ , while the width is  $z = \sim 250 \mu\text{m}$ . The thickness of the GaN nanobeams was examined by TEM cross-section observation to be  $y = \sim 50\text{--}195$  nm while the as-deposited thickness ( $y$ -direction) was average 125 nm and formed a hexagonal columnar grain structure in  $c$ -axis.

The fabrication process and cross-sectional structures of GaN nanobeams are depicted in Figure 1. The right part of Figure 1 reveals the transverse geometry of the fabricated nanobeam. The trapezoid shape is formed by the FIB machining of the GaN substrate. Surface morphologies and cross-sectional views of these two GaN nanobeam samples were then examined by SEM and TEM.

Figures 2(a) and 2(b) are the tilted top view SEM images, showing the fabricated nanobeam samples with different length. The nanobeam length,  $L$ , is defined as the suspending distance between two tops of supporting leg with column-like ends. Therefore, the  $2 \mu\text{m}$  and  $1.5 \mu\text{m}$  lengths of nanobeams are with aspect ratios of  $\sim 10$  and  $\sim 7$ , respectively. *In situ* TEM was then performed to observe and evaluate the mechanical behavior of the GaN nanobeams with different aspect ratio. After the vertical alignment was completed, the displacement between the specimen and conical tip was measured by using a TEM with the loading device installed, given that TEM can precisely locate interfaces and sharply measure

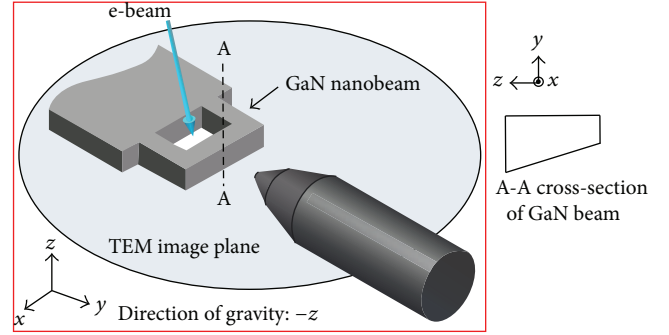


FIGURE 1: A schematic illustration showing a single crystal GaN nanobeam machined by FIB and a nanomechanical test and loading direction of a nanobeam in TEM. The right part is a cross-section view of GaN nanobeam with a cross-section area of  $0.03125 \mu\text{m}^2$  after machining by FIB.

the displacement and contact point of the loading tip. All observations are conducted in an accelerating voltage of 15 kV under vacuum ( $1.5 \times 10^{-5}$  Pa). When the *in situ* experiment is being exercised, the loading rate of  $10 \text{ nms}^{-1}$  is applied continuously to load the tested specimen and then unloaded at the same rate while a preset maximum load displacement of 200 nm was reached.

## 3. Result and Discussion

Figures 3(a) and 3(b) show the loading-unloading characteristics of the nanoindentation test, targeting these two different spans of single crystal GaN nanobeams with an aspect ratio of  $\sim 10$  (i.e., sample I) and an aspect ratio of  $\sim 7$  (i.e., sample II), operating in *in situ* TEM at room temperature, respectively, whereas the (a)-(b)-(c)/(c)-(d)-(e) symbols denote the experimental loading/unloading data, respectively.

It is found that the maximum loading forces on sample I and sample II in penetration indentation depth of  $\sim 200$  nm (point (c) of the loading curve) were  $\sim 30 \mu\text{N}$  and  $\sim 172 \mu\text{N}$ , respectively. However, the eventual slope changes transpire in point (b) of Figures 3(a) and 3(b) when the loads get beyond  $\sim 8 \mu\text{N}$  and  $\sim 20 \mu\text{N}$ , while the maximum linear deflections are 90 nm and 80 nm in sample I and sample II, respectively. The linear elastic behavior of both nanobeam specimens became nonlinear when the loading force was continually increased beyond the point (b) in Figures 3(a) and 3(b). The sudden increase of slope suggests the existence of more complex elastic and plastic behaviors, particularly on the shorter span of GaN nanobeam system (sample II). In the shorter one (sample II), the slope was found to increase dramatically from  $\sim 20 \mu\text{N}$  to  $\sim 172 \mu\text{N}$  while the penetration depth is increasing from 80 nm to 200 nm as shown on point (b) to point (c) in Figure 3(b). Clearly, shorter specimen, namely, sample II, needs more load and work than longer ones to be pressed to the same depth of the pressed sample I. In indentation test, longer GaN nanobeam specimen shows more linear elasticity than shorter ones as shown in the contrast of sample I and sample II.

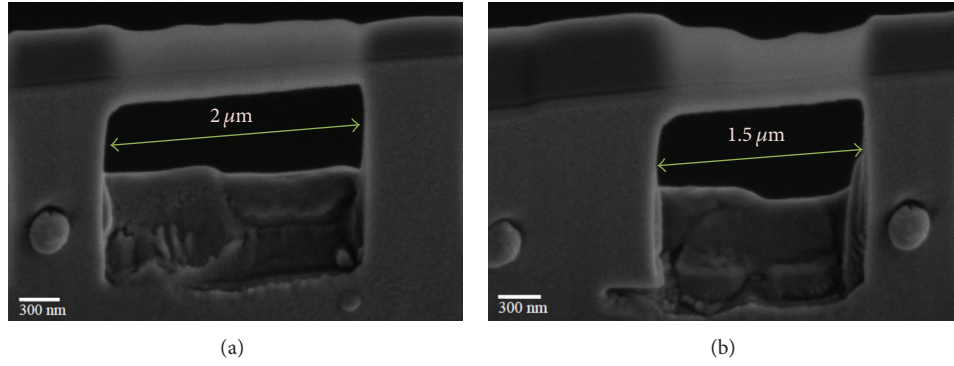


FIGURE 2: Tilted 45° top-view FESEM images of nanobeams with 2.0  $\mu\text{m}$  (a) and 1.5  $\mu\text{m}$  (b) in length and 250 nm in width after being machined by FIB.

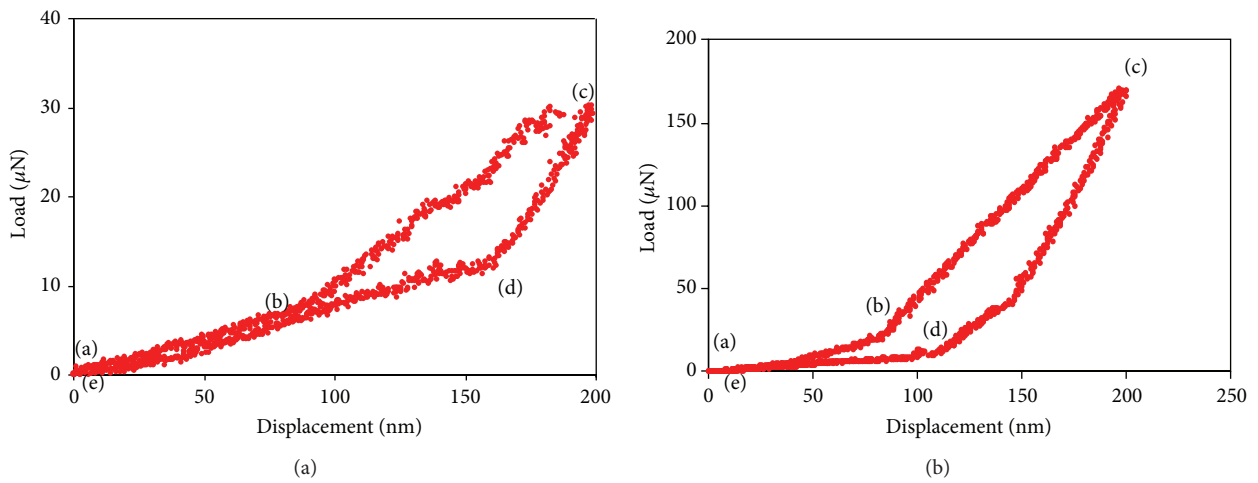


FIGURE 3: Experimentally observed loading and unloading behavior by indenting on the center of the span of 2.0  $\mu\text{m}$  (a) and 1.5  $\mu\text{m}$  (b) of GaN nanobeams with equal indentation depth using a conical indenter in TEM.

More interestingly, both unloading curves return approximately to the original position. The perfect retreats of the loading and unloading curves indicate that the elastic energy can be stored and released in both of the indentation tests of the freestanding nanobeam systems without considering the aspect ratio.

As we know, axial tensile force is also introduced when the nanobeam systems are displaced at the center section in this study. Therefore, the enhancement of nanobeam rigidity and nonlinearity in force versus displacement variation is transpired [18]. Furthermore, assuming the prestretch was produced when the film was being grown by MOCVD, in a nanobeam fabrication can be neglected in the same specimen, the load-deflection behaviors in a given indentation test will be affected by four factors [19]: geometrical nonlinearity introduced by kinematic effects, plastic deformation, increasing contact area during indentation, and rate dependent material effect. Fortunately, limiting displacements in the bending test can minimize the influence of these four factors.

Given the elastic behavior shown in the experimental data, when at low displacement, the loading force of both nanobeams increased linearly with the displacement. This

means that both GaN nanobeam systems exhibited linear elastic characteristics, when they were operated in low displacement. Under large deformation, the theoretical bases of the nanobeam test obey the classical beam theory with concern in substrate deformation [20].

Under small deformation (line (a)-(b) in Figures 3(a) and 3(b)), the deflection,  $D$ , is linearly proportional to the lateral load,  $P$ . Therefore, we define the slope,  $k$ . On the other hand, for small deformation of unloading curves (line (d)-(e) in Figures 3(a) and 3(b)), the data of the recovery also exhibit a linear relationship between unload and deflection. We define the slope,  $j$ . It is found that the slope  $j$  is almost the same as the slope  $k$  in Figure 3(a), further suggesting a good linear elastic behavior observed in higher aspect ratio of GaN nanobeam system, compared to that in lower aspect ratio of GaN nanobeam system.

For a given nanobeam sample with available values of sample length and thickness, the linear relationship between stress and strain in simple tension or compression can be expressed by the equation  $P = kD$ , in which  $D$ ,  $P$ , and  $k$  are displacement, correspondence to load, and a constant of proportionality, respectively. The equation is commonly

TABLE 1: The experimentally measured data and calculating results of GaN nanobeam systems with different span.

Systems	Span	Deflection displacement	Loading force	Moment of inertia $I$ on $z$ -axis	Young's modulus $E$
Sample I	2 $\mu\text{m}$	90 nm	$8.01 \pm 0.23 \mu\text{N}$	$8.64 \times 10^{-5} \mu\text{m}^4$	$171.3 \text{ GPa} \pm 5.4\%$
Sample II	1.5 $\mu\text{m}$	80 nm	$20.32 \pm 0.43 \mu\text{N}$	$6.65 \times 10^{-5} \mu\text{m}^4$	$264.2 \text{ GPa} \pm 4.7\%$

known as Hook's law, a rule only applied to ordinary tension and compression. Young's modulus is then obtained by measuring the nanobeam displacement as a function of the applied load.

For a two-end fixed beam used here, Young's modulus cannot be determined from merely a slope of deflection versus load. We have to also consider linear elastic beam bending theory. The possibility of linear elastic deformation is discussed below. We assume that the GaN nanobeam systems are simple supporting beam systems, subjected to a vertical loading  $P$  ( $y$ -direction). The linear force  $P$  is proportional to  $y$  and its value is  $P_0$  when  $y = y_0$ . Then  $P = (P_0/y_0)ydy$ , and the work is

$$W = \int_0^{y_0} \left( \frac{P_0}{y_0} \right) y dy \frac{P_0 y_0}{2}. \quad (1)$$

When an elastic material is deformed, this work can be stored in the form of potential energy. In this case, potential energy is strain energy  $U$  which can be expressed by the equation

$$U = \frac{P^2 L^3}{96EI} = W = \frac{P_0 y_0}{2}. \quad (2)$$

The displacement is

$$y_0 = \frac{PL^3}{48EI}, \quad (3)$$

where  $I$ ,  $E$ , and  $L$  are the moment of inertia, Young's modulus, and span of the clamped portion of the beam, respectively. The moments of inertia on  $z$ -axis of nanobeam systems are calculated as  $I = 8.64 \times 10^{-5} \mu\text{m}^4$  and  $6.65 \times 10^{-5} \mu\text{m}^4$  for the lengths of 2.0  $\mu\text{m}$  (sample I) and 1.5  $\mu\text{m}$  (sample II), respectively. The beam's deflections at the point where  $P$  is applied are 90 nm and 80 nm.

The force is assumed to change linearly as a function of bending displacement when the experiment was conducted on the curve of point (a) to point (b) in Figures 3(a) and 3(b). The average loading forces on deflection displacement of 90 nm and 80 nm are obtained as  $8.01 \pm 0.23 \mu\text{N}$  and  $20.32 \pm 0.43 \mu\text{N}$ , respectively. Therefore, we can estimate Young's modulus  $E$  from formula (3) by equating the work done to the strain energy in the nanobeam. Young's modulus  $E$  in this study is calculated as  $171.3 \text{ GPa} \pm 5.4\%$  and  $264.2 \text{ GPa} \pm 4.8\%$  for the longer nanobeam system (sample I) and shorter nanobeam system (sample II), respectively. Table 1 depicts the data and calculating results of GaN nanobeam systems with different spans. It is found that the enhancement of nanobeam rigidity, a byproduct of axial tensile force, is strongly dependent on the span of nanobeam even under small deformation. Notably, the axial direction of a deflected

nanobeam in this experiment is not on  $c$ -axis of GaN film examined in nanogenerator studies but is perpendicular to the  $c$ -axis of nanobeam.

A series of *in situ* TEM images of sample I, as shown in Figure 4, presents the elastic-plastic behavior described by the data of Figure 3(a). Figure 4(a) shows the nanobeam before the deflecting experiment. When the tip gradually loads downward to the nanobeam at the beginning of the nanoindentation, the conical tip can easily bend the clamped GaN nanobeam because it is freestanding, with no barrier to restrict the bending process.

When a certain bending indentation depth has been achieved, as shown on point (b) in Figure 3(a) corresponding to Figure 4(b), a dramatic slope change occurs. Such change later brings about rigidity when the loading exceeds the linear elastic of the nanobeam. At this moment, the property of the nanomechanical action starts to change: the linear beam-like behavior is now turned into a nonlinear one.

The maximum loading force deforming the nanobeam by the conical tip on point (c) in Figure 3(a) is given in Figure 4(c). Here, the relative location between conical tip and nanobeam can be easily targeted. This image shows that the loading force is not a perfectly concentrated load, suggesting the transition from single point bending indentation of a beam to surface stretching indentation. Moreover, the locations which are not contacted by the conical tip possess good elastic recovery.

Another dramatic slope switch can be found in Figure 4(d) corresponding to point (d) in Figure 3(a). Figure 4(e) corresponding to point (e) in Figure 3(a) shows the finished view of the deflected nanobeam, as expected, in which the nanobeam recovered perfectly to the original location as shown in Figure 4(a).

## 4. Conclusions

This research investigates a novel technique which can fabricate different span of nanobeams on a substrate and it does not require significant amounts of specimen preparation time for aligning, clamping, and testing of individual nanobeam between two fixed ends. In this study, nanobeams fabricated by focused ion beam with different spans are clamped in between two homogeneous fixed ends as simple supporting beams, subjected to load in an *in situ* TEM. These *in situ* TEM analyses provide details of bending to stretching-induced mechanical deformation.

It is found that a more conspicuous linear elastic behavior is observed in indentation test of longer GaN nanobeam specimen (sample I). Young's moduli have also been studied by strain energy method with presuming GaN nanobeams as simply supported beam systems of elastic material. The slopes of the  $L$ - $D$  curves standing for the linear relationship between

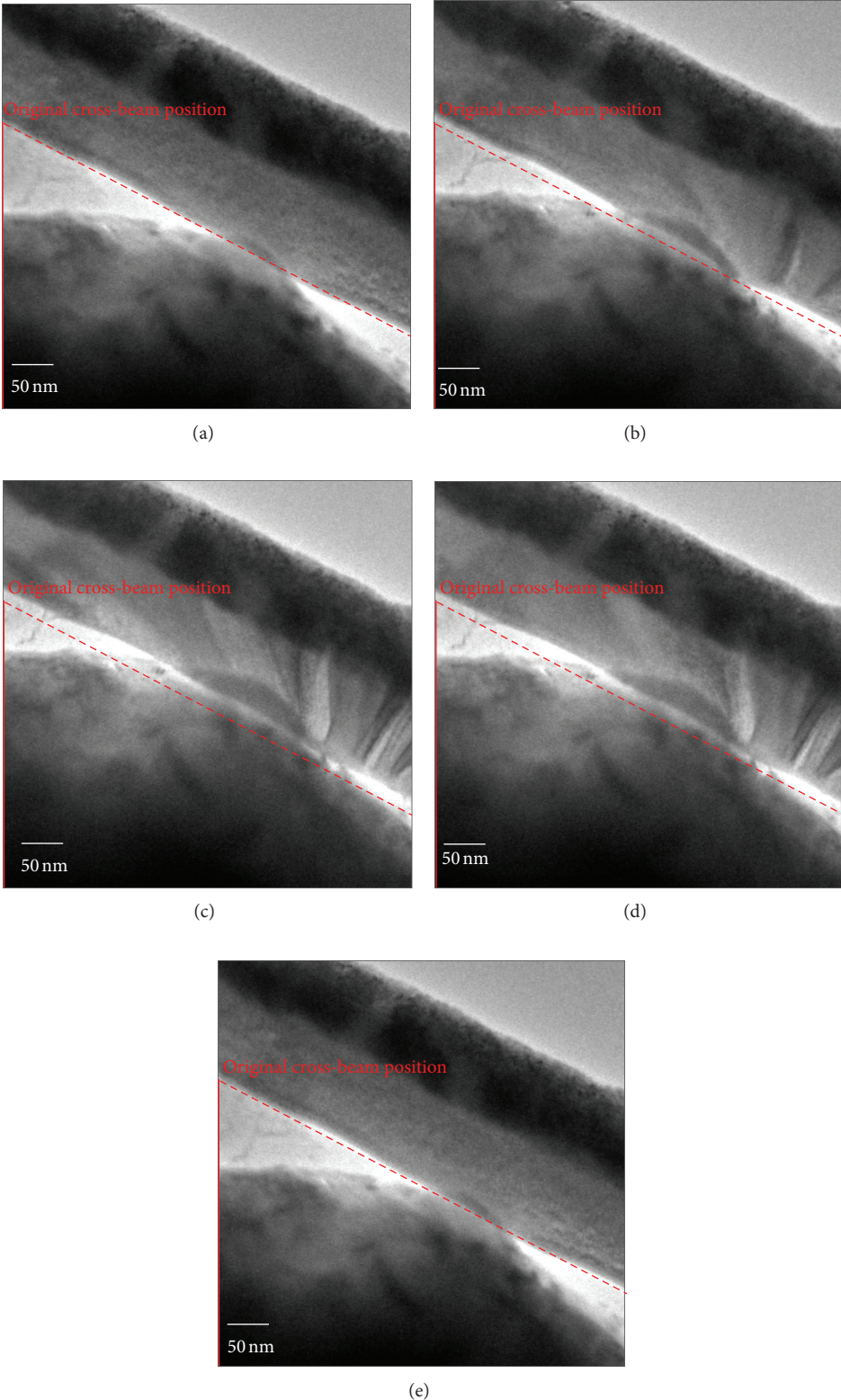


FIGURE 4: A sequence of images extracted from a video recording of sample I, corresponding to the indentation experiment performed in point (a) to point (e) of Figure 3(a), showing the deformation stages: (a) the GaN nanobeam before loading, (b) at the end of linear loading, (c) the bended nanobeam at peak load, (d) during unloading at the end of nonlinear or plastic deformation, and (e) nearly no residual deformation after full separation.

stress and strain at the initial phase of tests prove that the enhancement of nanobeam rigidity is strongly dependent on the span of nanobeam even under small deformation.

### Conflict of Interests

The authors declare that there is no conflict of interests regarding the publication of this paper.

### Acknowledgments

This work was supported by the National Science Council of Taiwan under Contract nos. NSC 99-2221-E-158-009, NSC 100-2221-E-158-002, and NSC 102-2221-E-020-016 and the Shih Chien University Kaohsiung Campus (USC-102-05-05017 and USC-102-08-01006). The authors' thanks also go to the Chemical and Materials Engineering Department of National University of Kaohsiung, Center for Micro/Nano Science and Technology of National Sun Yat-Sen University for the equipment support, and Dr. Shang Chao Hung for technical support.

### References

- [1] W. S. Su, Y. F. Chen, C. L. Hsiaoand, and L. W. Tu, "Generation of electricity in GaN nanorods induced by piezoelectric effect," *Applied Physics Letters*, vol. 90, no. 6, Article ID 063110, 2007.
- [2] X. Wang, J. Song, F. Zhang, C. He, Z. Hu, and Z. Wang, "Electricity generation based on one-dimensional group-III nitride nanomaterials," *Advanced Materials*, vol. 22, pp. 2155–2160, 2010.
- [3] S.-C. Hung, "Generation of piezoelectricity by deflecting nanorods vertically on GaN template," *Journal of the Electrochemical Society*, vol. 158, no. 12, pp. H1265–H1269, 2011.
- [4] Z. L. Wang and J. Song, "Piezoelectric nanogenerators based on zinc oxide nanowire arrays," *Science*, vol. 312, no. 5771, pp. 243–246, 2006.
- [5] S.-C. Hung, Y.-K. Su, T.-H. Fang, and S.-J. Chang, "Shell buckling behavior investigation of individual gallium nitride hollow nanocolumn," *Applied Physics A*, vol. 84, no. 4, pp. 439–443, 2006.
- [6] S.-C. Hung, Y.-K. Su, T.-H. Fang, S.-J. Chang, and L.-W. Ji, "Buckling instabilities in GaN nanotubes under uniaxial compression," *Nanotechnology*, vol. 16, no. 10, pp. 2203–2208, 2005.
- [7] M. Naraghi, I. Chasiotis, H. Kahn, Y. Wen, and Y. Dzenis, "Novel method for mechanical characterization of polymeric nanofibers," *Review of Scientific Instruments*, vol. 78, no. 8, Article ID 085108, 2007.
- [8] M. Naraghi, T. Ozkan, I. Chasiotis, S. S. Hazra, and M. P. de Boer, "MEMS platform for on-chip nanomechanical experiments with strong and highly ductile nanofibers," *Journal of Micromechanics and Microengineering*, vol. 20, no. 12, Article ID 125022, 2010.
- [9] Y. Zhu and H. D. Espinosa, "An electromechanical material testing system for in situ electron microscopy and applications," *Proceedings of the National Academy of Sciences of the United States of America*, vol. 102, no. 41, pp. 14503–14508, 2005.
- [10] S. M. Han, R. Saha, and W. D. Nix, "Determining hardness of thin films in elastically mismatched film-on-substrate systems using nanoindentation," *Acta Materialia*, vol. 54, no. 6, pp. 1571–1581, 2006.
- [11] G. M. Pharr and W. C. Oliver, "Measurement of thin film mechanical properties using nanoindentation," *MRS Bulletin*, vol. 17, pp. 28–33, 1992.
- [12] F. Yang and J. C. M. Li, "Adhesion of a rigid punch to an incompressible elastic film," *Langmuir*, vol. 17, no. 21, pp. 6524–6529, 2001.
- [13] T.-Y. Zhang, L.-Q. Chen, and R. Fu, "Measurements of residual stresses in thin films deposited on silicon wafers by indentation fracture," *Acta Materialia*, vol. 47, no. 14, pp. 3869–3878, 1999.
- [14] H. D. Espinosa, B. C. Prorok, and M. Fischer, "A methodology for determining mechanical properties of freestanding thin films and MEMS materials," *Journal of the Mechanics and Physics of Solids*, vol. 51, no. 1, pp. 47–67, 2003.
- [15] J. Schweitz, "Mechanical characterization of thin films by micromechanical techniques," *MRS Bulletin*, vol. 17, pp. 34–45, 1992.
- [16] M. J. Kobrinsky, E. R. Deutsch, and S. D. Senturia, "Effect of support compliance and residual stress on the shape of doubly supported surface-micromachined beams," *Journal of Microelectromechanical Systems*, vol. 9, no. 3, pp. 361–369, 2000.
- [17] T.-Y. Zhang, Y.-J. Su, C.-F. Qian, M.-H. Zhao, and L.-Q. Chen, "Microbridge testing of silicon nitride thin films deposited on silicon wafers," *Acta Materialia*, vol. 48, no. 11, pp. 2843–2857, 2000.
- [18] A. Heidelberg, L. T. Ngo, B. Wu et al., "A generalized description of the elastic properties of nanowires," *Nano Letters*, vol. 6, no. 6, pp. 1101–1106, 2006.
- [19] K. C. Maner, M. R. Begley, and W. C. Oliver, "Nanomechanical testing of circular freestanding polymer films with sub-micron thickness," *Acta Materialia*, vol. 52, no. 19, pp. 5451–5460, 2004.
- [20] S. P. Timoshenko and S. Woinowsky-Krieger, *Theory of Plates and Shells*, McGraw-Hill, New York, NY, USA, 1959.

## Research Article

# Fabrication of a Zinc Aluminum Oxide Nanowire Array Photoelectrode for a Solar Cell Using a High Vacuum Die Casting Technique

Chin-Guo Kuo,<sup>1</sup> Jung-Hsuan Chen,<sup>2</sup> and Yueh-Han Liu<sup>1</sup>

<sup>1</sup> Department of Industrial Education, National Taiwan Normal University, Taipei 10610, Taiwan

<sup>2</sup> Material and Chemical Research Laboratories, Industrial Technology Research Institute, Hsinchu 31040, Taiwan

Correspondence should be addressed to Jung-Hsuan Chen; [jhc2369@yahoo.com.tw](mailto:jhc2369@yahoo.com.tw)

Received 7 March 2014; Accepted 14 April 2014; Published 6 May 2014

Academic Editor: Chao-Rong Chen

Copyright © 2014 Chin-Guo Kuo et al. This is an open access article distributed under the Creative Commons Attribution License, which permits unrestricted use, distribution, and reproduction in any medium, provided the original work is properly cited.

Zinc aluminum alloy nanowire was fabricated by the vacuum die casting. Zinc aluminum alloy was melted, injected into nanomold under a hydraulic pressure, and solidified as nanowire shape. Nanomold was prepared by etching aluminum sheet with a purity of 99.7 wt.% in oxalic acid solution. A nanochannel within nanomold had a pore diameter of 80 nm and a thickness of 40  $\mu\text{m}$ . Microstructure and characteristic analysis of the alumina nanomold and zinc-aluminum nanowire were performed by scanning electron microscope, X-ray diffraction analysis, and energy dispersive X-ray spectroscopy. Zinc aluminum oxide nanowire array was produced using the thermal oxidation method and designed for the photoelectrode application.

## 1. Introduction

Fossil fuels have the finite resources that will eventually dwindle and make too environmental damages to retrieve. As time goes on, they will become too expensive to utilize. Therefore, the development of the renewable energy, such as solar energy and wind, are necessary immediately.

Solar energy conversion is a highly attractive topic for clean and renewable power for the future. Dye sensitized solar cell (DSSC) is a type of Solar cell and has a significant potential to be a low cost alternative to conventional photovoltaic device. Various metal oxide nanostructures such as  $\text{TiO}_2$ ,  $\text{ZnO}$ ,  $\text{Fe}_2\text{O}_3$ ,  $\text{ZrO}_2$ ,  $\text{Nb}_2\text{O}_5$ ,  $\text{Al}_2\text{O}_3$ , and  $\text{CeO}_2$  have been successfully employed as photoelectrodes in SCs [1–11]. Among the above metal oxide nanostructures,  $\text{ZnO}$  draws much attraction for its particular properties.  $\text{ZnO}$  is a direct wide bandgap semiconductor ( $E_g = 3.4 \text{ eV}$ ) with large exciton binding energy ( $\sim 60 \text{ meV}$ ). The efficiency of a DSSC is strongly dependent on the charge recombination at the interface. The injected electron can be recaptured by the dye before diffusing into the bulk causing the losses of efficiency. The interfacial recombinations can be retarded by coating a thin layer of a second insulator, such as  $\text{Al}_2\text{O}_3$

[12]. Similar results are also demonstrated by Palomares et al. [13]. Palomares and his coworkers state that the conformal growth of an overlayer of  $\text{Al}_2\text{O}_3$  on a nanocrystalline  $\text{TiO}_2$  film would result in a 4-fold retardation of interfacial charge recombination and a 30% improvement in photovoltaic device efficiency.

Therefore, it is supposed that zinc aluminum oxide nanowire would have better efficiency than zinc oxide nanowire and be a promising candidate for highly efficient SCs. Until now, few literatures mentioned the fabrication or synthesis of zinc aluminum oxide nanowire. The purpose of the research reported here was to propose a novel method to fabricate zinc aluminum oxide nanowire and apply the nanowires in the photoelectrode for DSSCs. Most important benefits of this method are the composition of nanowire could be controlled precisely and it is also easy to adjust the component.

## 2. Experimental Procedure

In this study, zinc aluminum oxide nanowires were fabricated using anodic aluminum oxide (AAO) as a template. The experimental procedure could divide into four parts. First of

all, an anodic alumina nanomold was obtained by etching a pure aluminum sheet with a purity of 99.7 wt.% in 0.3 M oxalic acid solution. Two steps of anode treatments were applied to obtain more uniform nanopores in this experiment. The first step of the anode treatment was carried out at a voltage 40 V and a temperature of 25°C for one hour. Afterward removing alumina thin film from the surface of aluminum sheet was performed in the mixture of 6% phosphoric acid solution and 2% chromic acid solution at a temperature of 60°C. The second step of the anode treatment was carried out in the same process conditions indicated in the first step for 6 hours. Finally, aluminum substrate was removed using copper chloride solution and then the anodic alumina nanomold with a pore diameter of 80 nm could be obtained. Since the alumina membrane has an excellent chemical stability and could maintain its porous structure under the high temperature and pressure conditions, it is a very suitable mold [14, 15].

The second part of the procedure was the fabrication of zinc-aluminum alloy by the vacuum melting method. The high purity of zinc and aluminum scraps were mixed and placed in a quartz glass tube. In order to prevent metal from oxidation during melting, the vacuum was extracted using a molecular turbo pump and kept at  $3 \times 10^{-6}$  torr. Then, the glass tube was placed in a furnace and the temperature was increased to 750°C for several minutes until all metal is smelted and mixed well. After cooling, zinc-aluminum alloy was obtained. More detailed process of the vacuum melting was described in our previous study [16, 17].

Furthermore, zinc-aluminum alloy nanowire array was produced using the high vacuum die casting technique. A piece of zinc-aluminum alloy and an alumina template were placed inside the chamber in which the vacuum pressure was maintained at  $10^{-6}$  torr. After the chamber was heated to 750°C, a hydraulic force was applied to the molten zinc-aluminum alloy. During casting, the molten alloy was injected into the anodic alumina nanomold forming alloy nanowire array. The force required to introduce molten alloy into the nanomold is proportional to the surface tension of the melt. The surface tension of the molten zinc at 750°C is 719.7 dyne/cm and the surface tension of the molten aluminum at 750°C is 857.05 dyne/cm [18]. Therefore, the surface tension of the molten zinc-aluminum alloy at 750°C is 748.82 dyne/cm by calculation. Additionally, the pressure for the molten metal injection into nanomold can be evaluated as [19]  $P = F/A = -(2\gamma \cos \theta)/r$ , where  $F$  is the normal force,  $A$  is the area of the nanomold,  $r$  is the radius of the nanochannel,  $\gamma$  is the surface tension of the molten zinc-aluminum alloy, and  $\theta$  is the contact angle between the melt and the porous alumina membrane. The surface tension of the molten zinc-aluminum is 748.82 dyne/cm and the contact angle is 104.85°. Therefore, the force required to inject the molten alloy into nanomold is  $3.01 \times 10^8$  dyne. Solidification proceeded using a water cooling method at the bottom of the chamber. The zinc-aluminum nanowire array was formed after cooling to room temperature.

Finally, zinc aluminum oxide nanowire array was fabricated through a thermal oxidation process. The fabrication

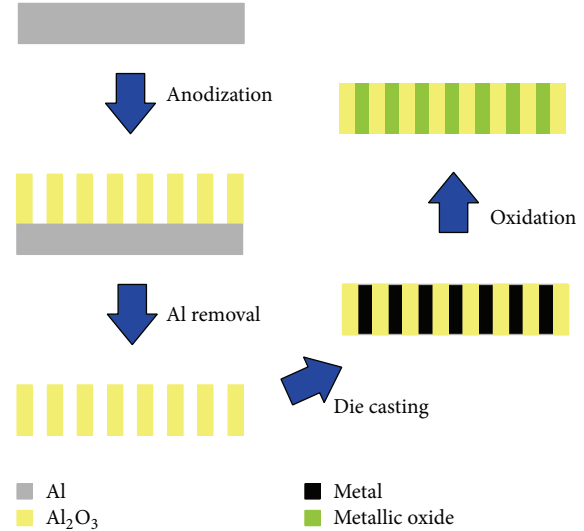


FIGURE 1: Schematic diagram of the zinc aluminum oxide nanowire array fabricated in this work.

procedure of zinc aluminum oxide nanowire array is illustrated in Figure 1. The nanowire array was put into an air furnace and applied a heat treatment at 250°C for 24 hours. After that, the aluminum oxide surrounding the nanowire was removed using sodium hydroxide solution and then zinc aluminum oxide nanowire array could be obtained.

The morphologies and the dimensions of the anodic alumina nanomold and the zinc aluminum nanowire array were observed by scanning electron microscope (SEM). The composition and crystallinity of the zinc-aluminum alloy nanowires were detected by X-ray diffraction (XRD) spectrum and energy dispersive spectroscopy (EDS). Differential scanning calorimeter (DSC) was used to measure the thermal characteristics of zinc-aluminum alloy.

### 3. Results and Discussion

In this study, porous alumina nanomold was produced using the anodization method with a two-step process in oxalic acid solution. The porous alumina nanomold was formed on aluminum with the equilibrium of oxide dissolution at the interface of the alumina/electrolyte and oxide grown at the metal/alumina interface [18]. Figures 2(a) and 2(b) are the morphologies of the anodic alumina membrane prepared in 0.3 M oxalic acid solution for 6 hours. SEM images of the porous alumina membrane reveal that the nanopores with a diameter of 80 nm and a thickness 40  $\mu$ m are ordered and uniform arrays.

When metal smelts under a high temperature or the temperature higher than its melting point, metallic vapor volatilizes and causes the loss of the composition. In our study, zinc has a larger vapor pressure ( $\sim 2 \times 10^4$  Pa) at the temperature of 750°C than aluminum ( $\sim 10^{-4}$  Pa) [20], and the loss of zinc would be more serious than aluminum. Therefore, it is necessary to compensate for the consumption of zinc to maintain the final composition of the prepared alloy

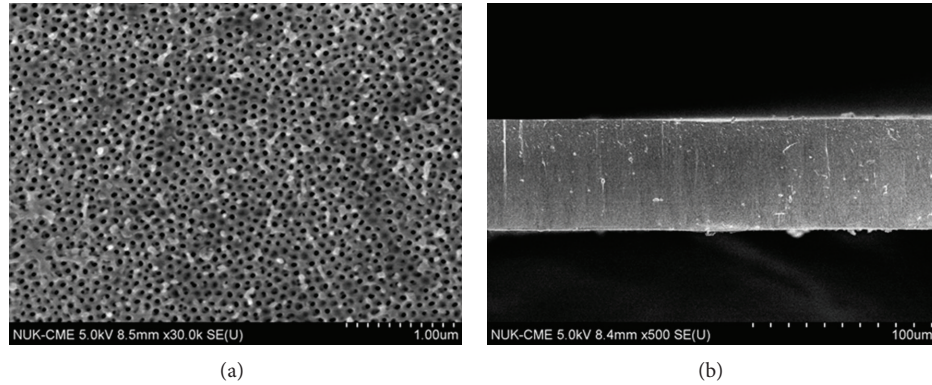


FIGURE 2: SEM images: (a) a porous alumina membrane with an ordering pore diameter of 80 nm and (b) the thickness of the porous alumina membrane was measured as 40  $\mu\text{m}$  from the cross-section image.

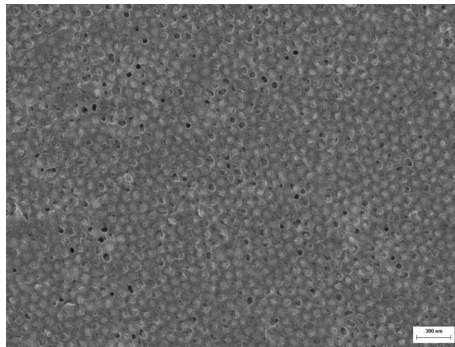


FIGURE 3: SEM images of zinc aluminum alloy nanowire arrays. Zinc aluminum nanowire array was fabricated in the alumina nanomold by the vacuum die casting process.

with the desired proportion. By the aid of the thermodynamic calculation, 90 wt.% zinc-10 wt.% aluminum alloy could be produced precisely.

Using vacuum die casting technique, the molten zinc-aluminum alloy was introduced into the alumina nanomold and then forming zinc-aluminum alloy nanowire array. Figure 3 shows that the zinc-aluminum nanowires with the diameter of 80 nm exhibit the uniform distribution and have the high filling ratio. EDS results display that the percentage of zinc is 89.71 wt.%, whereas the percentage of aluminum is 10.29 wt.%. In addition, the result of XRD analysis of zinc aluminum nanowires is shown in Figure 4. The diffraction pattern proves the crystal structure and identifies the composition of alloy as theoretical composition. Figure 5 shows that the melting temperature of the zinc-aluminum alloy is 418.03°C obtained by DSC measurement. The melting point of the alloy is consistent with that indicated in the zinc aluminum binary alloy phase diagram [21].

Au thin film was deposited at the top surface of zinc aluminum oxide nanowires array as the conductive layer of the photoelectrode by vapor deposition technique. After that, the fabrication of the nanowire array photoelectrode was completed. Figure 6 is the schematic diagram of the nanowire array photoelectrode produced in the present study. For this

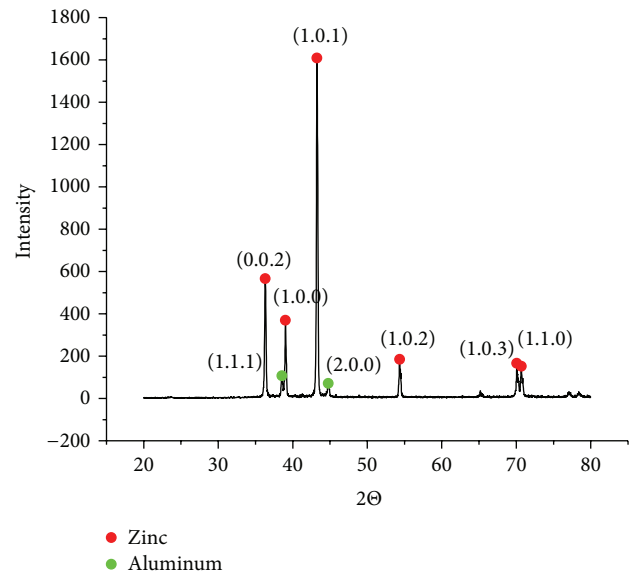


FIGURE 4: X-ray diffraction profiles of zinc-aluminum alloy composed of 90 wt.% zinc and 10 wt.% aluminum.

kind of photoelectrode, an ordered topology would increase the rate of electron transport and a nanowire electrode may improve the quantum efficiency of DSSCs depending on achieving the higher dye loadings through an increase in surface area. Therefore, the high aspect ratio zinc aluminum oxide photoelectrode designs for nanostructured semiconductor photoelectrodes in photoelectrochemical cells would be expected to enhance the attainable solar energy conversion efficiencies.

#### 4. Conclusions

The present study provided a novel method to produce zinc-aluminum alloy nanowire with 80 nm in diameter and 40  $\mu\text{m}$  in length. The vacuum die casting applied a hydraulic pressure to inject the molten zinc-aluminum into the anodic alumina nanomold and then obtained zinc-aluminum alloy

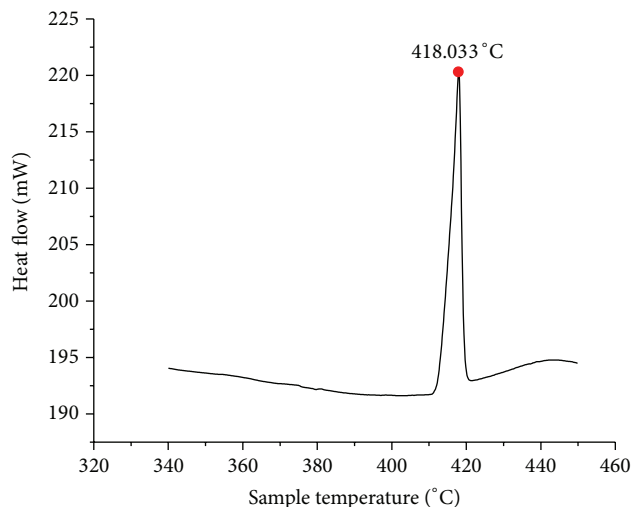


FIGURE 5: DSC thermographs of zinc-aluminum alloy composed of 90 wt.% zinc and 10 wt.% aluminum.

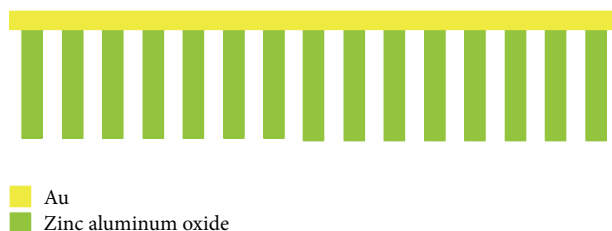


FIGURE 6: Schematic diagram of the prepared zinc aluminum oxide nanowire array photoelectrode.

nanowire after solidification. XRD and DSC results showed that zinc-aluminum alloy prepared in this work was a hypereutectic structure in which the weight percentage of zinc was 89.71% and the weight percentage of aluminum was 10.29%. Using thermal oxidation technique, zinc aluminum oxide nanowire array was fabricated successfully. The order, uniform, and a large area of nanowire array were more suitable for device manufacture or other applications. In this study, zinc aluminum oxide nanowire array was applied as the photoelectrode of DSSCs.

## Conflict of Interests

The authors declare that there is no conflict of interests regarding the publication of this paper.

## Acknowledgments

The authors acknowledge the financial support of NSC 102-3113-S-003-008-G and NSC 102-3113-S-262-001.

## References

[1] N. O. V. Plank, M. E. Welland, J. L. MacManus-Driscoll, and L. Schmidt-Mende, "The backing layer dependence of open circuit

voltage in ZnO/polymer composite solar cells," *Thin Solid Films*, vol. 516, no. 20, pp. 7218–7222, 2008.

- [2] M. Q. Lv, D. J. Zheng, M. D. Ye et al., "Densely aligned rutile TiO<sub>2</sub> nanorod arrays with high surface area for efficient dye-sensitized solar cells," *Nanoscale*, vol. 4, pp. 5872–5879, 2012.
- [3] J. E. Boercker, J. B. Schmidt, and E. S. Aydil, "Transport limited growth of zinc oxide nanowires," *Crystal Growth and Design*, vol. 9, no. 6, pp. 2783–2789, 2009.
- [4] M. Cavas, P. K. Gupta, A. A. Al-Ghamdi, Z. H. Gafer, F. El-Tantawy, and F. Yakuphanoglu, "Preparation and characterization of dye sensitized solar cell based on nanostructured Fe<sub>2</sub>O<sub>3</sub>," *Materials Letters*, vol. 105, pp. 106–109, 2013.
- [5] P. Ramasamy, D. H. Lim, J. S. Kim, and J. W. Kim, "A general approach for synthesis of functional metal oxide nanotubes and their application in dye-sensitized solar cells," *RSC Advances*, vol. 4, pp. 2858–2864, 2014.
- [6] M. Kovendhan, D. P. Joseph, P. Manimuthu et al., "Spray deposited Nb<sub>2</sub>O<sub>5</sub> thin film electrodes for fabrication of dye sensitized solar cells," *Transactions of the Indian Institute of Metals*, vol. 64, no. 1-2, pp. 185–188, 2011.
- [7] N. Jeon and D. W. Kim, "Dye-sensitized solar cells assembled with composite gel polymer electrolytes containing nanosized Al<sub>2</sub>O<sub>3</sub> particles," *Journal of Nanoscience and Nanotechnology*, vol. 13, pp. 7955–7958, 2013.
- [8] H. Yu, Y. Bai, X. Zong, F. Q. Tang, G. Q. M. Lu, and L. Z. Wang, "Cubic CeO<sub>2</sub> nanoparticles as mirror-like scattering layers for efficient light harvesting in dye-sensitized solar cells," *Chemical Communications*, vol. 48, pp. 7386–7388, 2012.
- [9] H. Chang, K.-C. Cho, C.-G. Kuo et al., "Application of a Schottky barrier to dye-sensitized solar cells (DSSCs) with multilayer thin films of photoelectrodes," *Journal of Alloys and Compounds*, vol. 509, no. 1, pp. S486–S489, 2011.
- [10] M. J. Kao, H. Chang, C. G. Kuo, K. D. Huang, and Y. L. Chen, "Fabrication and characterization of photoelectrode thin films with different morphologies of TiO<sub>2</sub> nanoparticles for dye-sensitized solar cells," *Journal of Nanoscience and Nanotechnology*, vol. 11, pp. 7459–7462, 2011.
- [11] M. J. Kao, H. Chang, K. C. Cho, C. G. Kuo, S. H. Chien, and S. S. Liang, "Analysis of the electron transport properties in dye-sensitized solar cells using highly ordered TiO<sub>2</sub> nanotubes and TiO<sub>2</sub> nanoparticles," *Journal of Nanoscience and Nanotechnology*, vol. 12, pp. 3515–3519, 2012.
- [12] M. Law, L. E. Greene, A. Radenovic, T. Kuykendall, J. Liphardt, and P. Yang, "ZnO-Al<sub>2</sub>O<sub>3</sub> and ZnO-TiO<sub>2</sub> core-shell nanowire dye-sensitized solar cells," *Journal of Physical Chemistry B*, vol. 110, no. 45, pp. 22652–22663, 2006.
- [13] E. Palomares, J. N. Clifford, S. A. Haque, T. Lutz, and J. R. Durrant, "Slow charge recombination in dye-sensitized solar cells (DSSC) using Al<sub>2</sub>O<sub>3</sub> coated nanoporous TiO<sub>2</sub> films," *Chemical Communications*, no. 14, pp. 1464–1465, 2002.
- [14] S. Shingubara, "Fabrication of nanomaterials using porous alumina templates," *Journal of Nanoparticle Research*, vol. 5, no. 1-2, pp. 17–30, 2003.
- [15] Y. T. Pang, G. W. Meng, L. D. Zhang et al., "Arrays of ordered Pb nanowires and their optical properties for laminated polarizers," *Advanced Functional Materials*, vol. 12, pp. 719–722, 2002.
- [16] C. G. Kuo, H. Chang, L. R. Hwang et al., "Fabrication of a Pb-Sn nanowire array gas sensor using a novel high vacuum die casting technique," *Electronic Materials Letters*, no. 9, pp. 481–484, 2013.
- [17] J.-H. Chen, S.-C. Lo, C.-G. Chao, and T.-F. Liu, "Microstructure and properties of Pb nanowires fabricated by casting," *Japanese Journal of Applied Physics*, vol. 47, no. 6, pp. 4815–4819, 2008.

- [18] I. S. Grigoriev and E. Z. Meilikhov, *Handbook of Physical Quantities*, CRC Press, Boca Raton, Fla, USA, 1997.
- [19] Z. Zhang, J. Y. Ying, and M. S. Dresselhaus, "Bismuth quantum-wire arrays fabricated by a vacuum melting and pressure injection process," *Journal of Materials Research*, vol. 13, no. 7, pp. 1745–1748, 1998.
- [20] O. Jessensky, F. Müller, and U. Gösele, "Self-organized formation of hexagonal pore arrays in anodic alumina," *Applied Physics Letters*, vol. 72, no. 10, pp. 1173–1175, 1998.
- [21] W. R. Osório, C. M. Freire, and A. Garcia, "The effect of the dendritic microstructure on the corrosion resistance of Zn-Al alloys," *Journal of Alloys and Compounds*, vol. 397, no. 1-2, pp. 179–191, 2005.

## Research Article

# Effects of Hydrogen Plasma on the Electrical Properties of F-Doped ZnO Thin Films and p-i-n $\alpha$ -Si:H Thin Film Solar Cells

Fang-Hsing Wang,<sup>1</sup> Shang-Chao Hung,<sup>2</sup> Cheng-Fu Yang,<sup>3</sup> and Yen-Hsien Lee<sup>1</sup>

<sup>1</sup> Department of Electrical Engineering and Graduate Institute of Optoelectronic Engineering, National Chung Hsing University, Taichung 40227, Taiwan

<sup>2</sup> Department of Electrical Information Technology and Communications, Shih Chien University, Kaohsiung Campus, Kaohsiung 84550, Taiwan

<sup>3</sup> Department of Chemical and Materials Engineering, National University of Kaohsiung, Kaohsiung 81147, Taiwan

Correspondence should be addressed to Cheng-Fu Yang; [cfyang@nuk.edu.tw](mailto:cfyang@nuk.edu.tw)

Received 10 March 2014; Accepted 11 April 2014; Published 4 May 2014

Academic Editor: Yen-Lin Chen

Copyright © 2014 Fang-Hsing Wang et al. This is an open access article distributed under the Creative Commons Attribution License, which permits unrestricted use, distribution, and reproduction in any medium, provided the original work is properly cited.

1.5 wt% zinc fluoride ( $\text{ZnF}_2$ ) was mixed with zinc oxide powder to form the F-doped ZnO (FZO) composition. At first, the FZO thin films were deposited at room temperature and  $5 \times 10^{-3}$  Torr in pure Ar under different deposition power. Hall measurements of the as-deposited FZO thin films were investigated, and then the electrical properties were used to find the deposition power causing the FZO thin films with minimum resistance. The FZO thin films with minimum resistance were further treated by  $\text{H}_2$  plasma and then found their variations in the electrical properties by Hall measurements. Hydrochloric (HCl) acid solutions with different concentrations (0.1%, 0.2%, and 0.5%) were used to etch the surfaces of the FZO thin films. Finally, the as-deposited, HCl-etched as-deposited, and HCl-etched  $\text{H}_2$ -plasma-treated FZO thin films were used as transparent electrodes to fabricate the p-i-n  $\alpha$ -Si:H thin film solar cells and their characteristics were compared in this study. We would show that using  $\text{H}_2$ -plasma-treated and HCl-etched FZO thin films as transparent electrodes would improve the efficiency of the fabricated thin film solar cells.

## 1. Introduction

ZnO is a nontoxic, abundant, and inexpensive material; in addition, impurity-doped ZnO can have electrical and optical properties comparable to the expensive indium tin oxide (ITO) currently used commercially. For that, impurity-doped ZnO is a possible candidate for transparent conducting oxides (TCOs) for potential applications as a transparent electrode in flat panel displays (FPDs) and photovoltaic solar cells [1]. TCO thin films have been widely used in the applications of solar cells, flat panel displays, and more optoelectronic products. TCO thin films show a good combination of electrical conductivity at ambient temperature and optical transparency in a visible region [2]. Some especially interesting properties of ZnO-based thin films are their low cost, ready availability, and high chemical stability. ZnO is a II-VI n-type semiconductor with a wide band gap of approximately 3.3 eV at room temperature. Group III donor elements, such as B [3], Al [4], and Ga [5], are added to

improve the electrical properties of ZnO thin films. Fluorine, the ionic radius (0.136 nm) of which is similar to that of oxygen (0.132 nm), may be an adequate anion doping candidate due to lower lattice distortion compared with Al, Ga, and In, but comparatively few studies on fluorine-doped ZnO (F-doped ZnO) can be found in the past researches [6, 7].

In this study, 1.5 wt% zinc fluoride ( $\text{ZnF}_2$ ) was mixed with zinc oxide powder to fabricate the F-doped ZnO (FZO) ceramic target for sputtering process [8]. In the past, Al-doped ZnO (AZO) thin films were deposited on glass substrate by RF magnetron sputtering by changing the substrate temperature from room temperature (RT) to 300°C [4]. From this literature, we would know that hydrogen ( $\text{H}_2$ ) has large effect on the ZnO-based TCO thin films. When  $\text{H}_2$  was used as deposition atmosphere during the deposition process [4] or used as plasma treatment [9, 10] after the deposition process, the ZnO-based TCO thin films will enhance their carrier concentration and improve their resistivity. In the

past, we also found that the  $H_2$ -plasma treatment on the deposited AZO thin films has large influence on their physical (transparency ratio and grain size) and electrical (energy gap and resistivity) properties [11]. For that, the plasma enhanced chemical vapor deposition (PECVD)  $H_2$  was treated on the as-deposited FZO thin films (abbreviated as plasma-treated FZO thin films). The effects of  $H_2$  plasma on the properties of FZO thin films were compared by observing the carrier concentration, carrier mobility, and resistivity. The FZO thin films under differently treated parameters were also used as the transparent electrodes of the  $\alpha$ -Si thin film solar cells. The current-voltage characteristics of the fabricated  $\alpha$ -Si thin film solar cells were measured to determine the effects of treated parameters of the FZO thin films on the characteristics of the fabricated  $\alpha$ -Si solar cells.

## 2. Experimental

1.5 wt% zinc fluoride ( $ZnF_2$ ) (99.995%) was mixed with zinc oxide powder (99.999%) to form the F-doped ZnO (abbreviated as FZO) composition. After being dried and ground, the FZO powder was calcined at  $600^\circ C$  for 1 h, then ground again, and mixed with polyvinyl alcohol (PVA) as binder. The mixed powders were uniaxially pressed into pellets of 5 mm thickness and 54 mm diameter using a steel die. After debinding, the FZO pellet was sintered at  $1060^\circ C$  for 3 h. Glass substrates (Corning 1737) with an area of  $3.3 \times 3.3 \text{ cm}^2$  were cleaned ultrasonically with isopropyl alcohol (IPA) and deionized (DI) water and then dried under a blown nitrogen gas. The base pressure of the sputtering chamber was below  $5 \times 10^{-6}$  Torr and the working pressure was maintained at  $5 \times 10^{-3}$  Torr in pure Ar (99.995%) ambient (abbreviated as-deposited FZO thin films). FZO thin films with a thickness of about  $650 \text{ nm} \pm 10\%$  were deposited by RF magnetron sputtering on glass substrates at room temperature (RT) by controlling deposition time to find the deposition parameters at which FZO thin films had optimally electrical characteristics. At the first, the FZO thin films were deposited by changing RF power from 50 W to 150 W at RT. Thicknesses of the FZO thin films were measured using a SEMF-10 ellipsometer and confirmed by field emission scanning electron microscopy (FESEM). The crystalline structure of the FZO thin films was identified by X-ray diffraction (XRD), while the thin films' Hall-effect coefficients were determined by a Bio-Rad Hall set-up. The optical transmission spectrum was recorded using a Hitachi U-3300 UV-Vis spectrophotometer in the 300–800 nm wavelength range. The as-deposited FZO thin films with optimally electrical characteristics were treated by the plasma enhanced chemical vapor deposition (PECVD) hydrogen ( $H_2$ ) (abbreviated as plasma-treated FZO thin films). The working pressure was maintained at 1 Torr under the 300 sccm  $H_2$  flow rate. The plasma power was changed from 0 W (without  $H_2$  plasma treatment) to 100 W, and the plasma-treated temperature and time were  $200^\circ C$  and 60 min.

After that, the thicknesses of the as-deposited and plasma-treated FZO thin films were extended to 1000 nm  $\pm 10\%$ , and then their surfaces were etched by wet etching performed in diluted HCl solution with concentrations of 0.1%, 0.2%, and 0.5% in  $H_2O$  to acquire the textured FZO thin

films. The thickness of the etched FZO thin films was around 650 nm, which was obtained by controlling the etched time. Also, the surface texture of the etched FZO thin films was observed by FESEM. The etched as-deposited and plasma-treated FZO thin films were used as substrates to fabricate the superstrate p-i-n  $\alpha$ -Si:H thin film solar cells. Thin film solar cells were fabricated using a single-chamber plasma-enhanced chemical vapor deposition unit at  $200^\circ C$ , with a working pressure of  $700 \times 10^{-3}$  Torr and a deposition power of 20 W. The p-type  $\alpha$ -Si thin films (thickness was about 20 nm) were deposited by controlling the gas flowing rates for  $H_2 = 100 \text{ sccm}$ ,  $SiH_4 = 20 \text{ sccm}$ ,  $CH_4 = 10 \text{ sccm}$ , and  $B_2H_6 = 40 \text{ sccm}$ . The i-type  $\alpha$ -Si thin films (400 nm) were deposited by using  $H_2 = 100 \text{ sccm}$  and  $SiH_4 = 10 \text{ sccm}$ , and the p-type  $\alpha$ -Si (50 nm) thin films were deposited by using  $H_2 = 100 \text{ sccm}$ ,  $SiH_4 = 20 \text{ sccm}$ , and  $PH_3 = 20 \text{ sccm}$ , respectively. The current-voltage characteristic of the fabricated solar cells was measured under an illumination intensity of  $300 \text{ mW/cm}^2$  and an AM 1.5 G spectrum.

## 3. Results and Discussion

An increase in orientation during crystalline growth is possible according to the model of Van der Drift, which is often referred to as "survival of the fastest" model. Even the grain sizes are not really formed, this model is based on different growth rates of the crystal planes. At first, the thin films start growing in random crystal orientation at the initial layer, they grow fastest in the plane parallel to the substrate and then grow at the cost of the others [12]. This "survival of the fastest" model implies a related increase in crystal orientation, which is called figure of merit in a growth of thin films, but the model cannot explain an increase in grain sizes with increasing thin films' thickness [13]. Figure 1 shows that even different deposition powers were used, all FZO thin films exhibited a strong (002) peak at  $2\theta = 34.24^\circ$  and a weak (004) peak, which indicate that the c-axis is predominantly oriented parallel to the substrate normal. The results in Figure 1 prove that the deposited FZO thin films have the figure of merit in c-axis orientation. The absence of additional peaks in the XRD patterns excludes the possibility of any extra phases and/or large-size precipitates in the FZO thin films. The diffraction intensity of the (002) peak increased as the deposition power increased from 50 W to 150 W.

The results of the carrier mobility, carrier concentration, and resistivity shown Figure 2 indicate that the electrical properties of the FZO thin films were dependent on deposition power. When plasma molecules are deposited on a glass substrate, many defects result and inhibit electron movement. As different deposition powers are used during the deposition process, two factors are believed to cause an increase in the carrier mobility of the FZO thin films. First, higher deposition power provides more energy and thus enhances the motion of plasma molecules, which will improve the crystallization and grain size growth of the FZO thin films, and also the defects in the thin films will be decreased. Second, as deposition power is raised, the defects in the FZO thin films decrease, and that will cause the decrease in the inhibiting of the barriers electron transportation

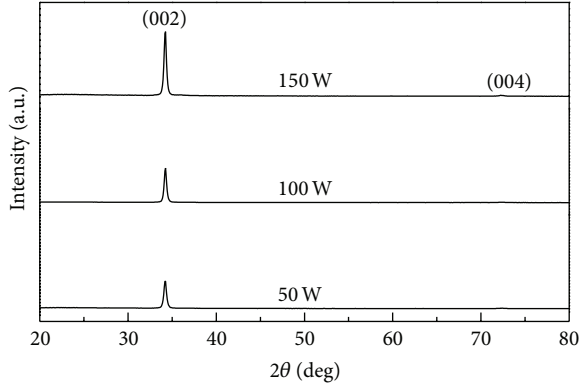


FIGURE 1: X-ray diffraction (XRD) patterns of the FZO thin films as a function of deposition power.

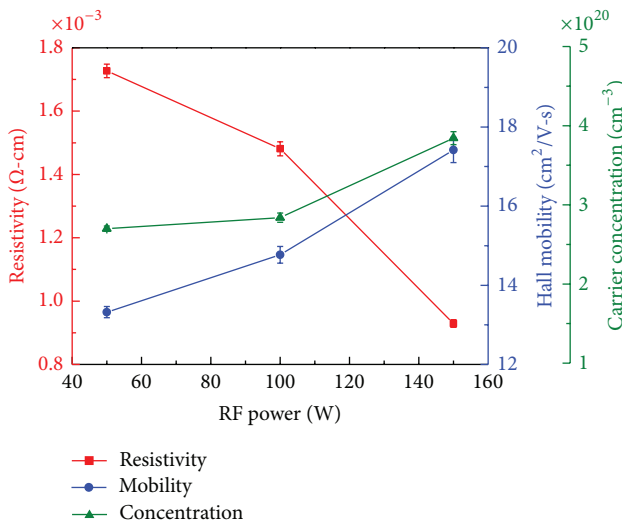


FIGURE 2: Carrier mobility, carrier concentration, and resistivity of the FZO thin films as a function of deposition power.

[14]. The results in Figure 1 suggest that this condition will dominate the characteristics of the deposited FZO thin films. As Figure 2 shows, both the carrier concentration and carrier mobility of the FZO thin films linearly increased with deposition power and reached the maximum concentration and carrier mobility at 150 W. The resistivity of the TCO thin films is proportional to the reciprocal of the product of carrier concentration  $N$  and mobility  $\mu$ :

$$\rho = \frac{1}{Ne\mu}. \quad (1)$$

Both the carrier concentration and the carrier mobility contribute to the conductivity. The resistivity decreased from  $1.72 \times 10^{-3} \Omega\text{-cm}$  to  $9.29 \times 10^{-4} \Omega\text{-cm}$  as the deposition power increased from 50 W to 150 W. The minimum resistivity of the FZO thin films at deposition power of 150 W is mainly caused by the carrier concentration and mobility being at their maximum.

Because of the maximum mobility and carrier concentration and the minimum resistivity, the 150 W-deposited FZO thin films are used for further treatment by  $H_2$  plasma.

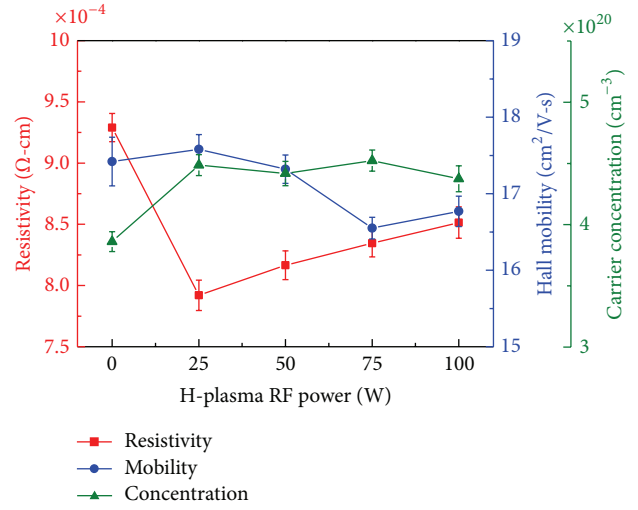


FIGURE 3: Carrier mobility, carrier concentration, and resistivity of the FZO thin films as a function of  $H_2$ -plasma-treated power.

Figure 3 shows the carrier mobility, carrier concentration, and resistivity of the FZO thin films as a function of  $H_2$  plasma power. The mobility slightly increased as plasma power of  $H_2$  increased from 0 W (without  $H_2$  plasma treatment) to 25 W and then it decreased as plasma power was further increased. The carrier concentration first increased as plasma power of  $H_2$  increased from 0 W (without  $H_2$  plasma) to 25 W and then it reached a saturation value as plasma power was further increased. However, resistivity is really improved as plasma process is used because the carrier concentration is increased as  $H_2$  plasma is used. 25 W-plasma-treated FZO thin films have the minimum resistivity of  $7.92 \times 10^{-4} \Omega\text{-cm}$  because the mobility and carrier concentration have their maximum. As the plasma power is higher than 25 W, the mobility of the FZO thin films decreases because their surfaces are destroyed by  $H_2$  plasma.

Rough interfaces are usually introduced into solar cells by using substrates with textured surface [15]. It is well known that the front TCO thin films with textured surface can scatter more light at the TCO/ $\alpha$ -Si:H(p) interface and haze ratio is strongly influenced by the surface morphologies of TCO thin films or/and glass substrates. Therefore, the surface structures of glass substrate and TCO thin films play a vital role to improve the performance of thin film solar cells. A suitable textured surface is very important to increase the haze ratio and scatter an incident light, particularly the long wavelength light (red and near-infrared), to extend the effective path length within the active silicon layer and subsequent light trapping inside the absorber material of the solar cell [15]. In this study, diluted HCl etching of the as-deposited and plasma-treated FZO thin films has been carried out at room temperature to develop the textured surfaces for enhancing the efficiency of solar cells. FZO thin films deposited at 150 W, room temperature, and  $5 \times 10^{-3}$  Torr with thickness of 1000 nm were used as the etching samples. Figure 4 shows the etching rate of the FZO thin films as a function of concentration of HCl solution; the etched time was dependent on the concentration of HCl solution. As the

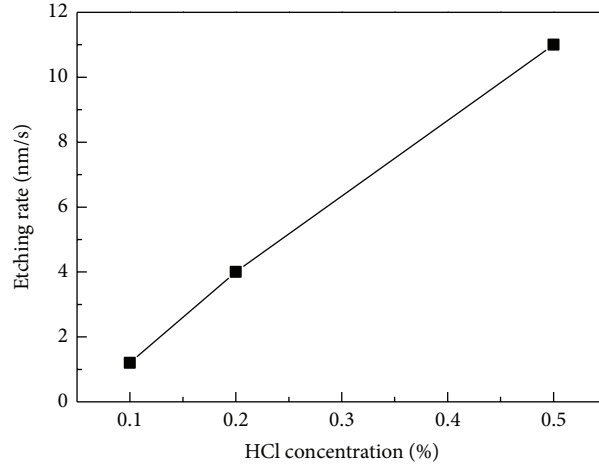


FIGURE 4: Etching rate of the FZO thin films as a function of HCl solution concentration.

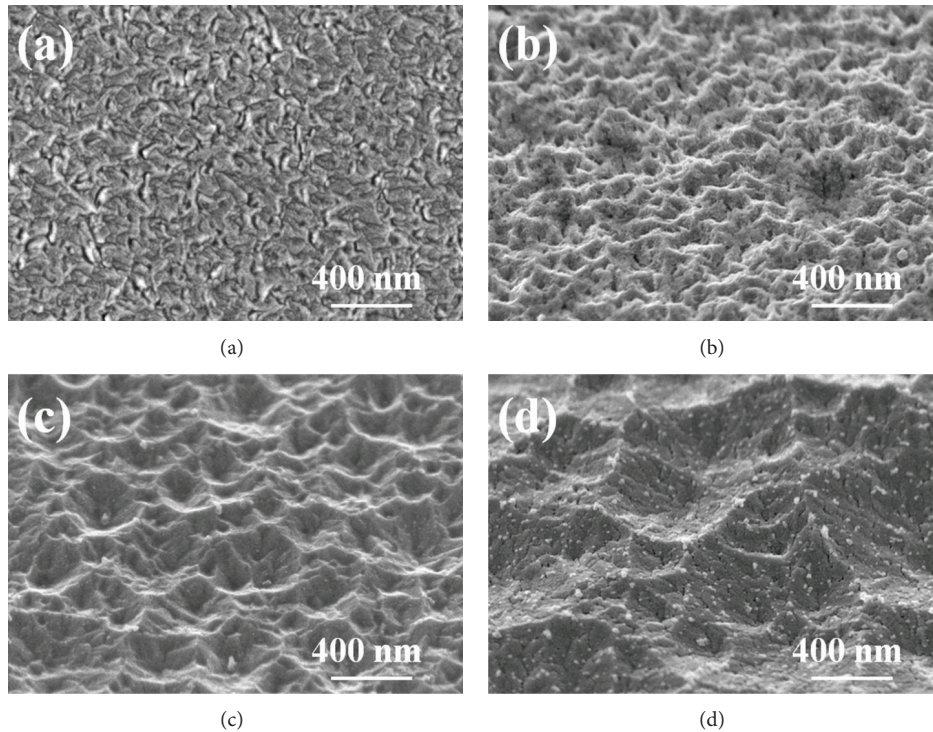


FIGURE 5: Surface morphology of the FZO thin films (a) as-deposited and etched at different HCl concentrations (b) 0.1%, (c) 0.2%, and (d) 0.5%, respectively.

concentration of HCl solution increased from 0.1% to 0.5%, the etched rate linearly increased from 1.2 nm/s to 11 nm/s, and the thickness of the etched FZO thin films was controlled at around 650 nm.

Figure 5 shows the surface morphology of the etched FZO thin films, and also the etched time was dependent on the concentration of HCl solution. Compared with the results shown in Figure 5, the surface roughness increased significantly after HCl etching. The etching process causes the thin films' surfaces to develop a crater-like cave and the size of cave increases with increasing HCl concentration. Figures 6(a) and 6(b) depict the total and diffused transmittance of the textured FZO thin films for various concentrations of

HCl solution. The average total transmittance of as-deposited FZO thin film substrates was 82.8%, whereas the textured FZO thin films showed that the average total transmittance decreased with increasing concentration of HCl solution in the visible (400~800 nm) wavelength region. The average total transmittances of 81.1%, 79.2%, and 78.8% were shown by the textured FZO thin films with various concentrations of HCl solution, including 0.1%, 0.2%, and 0.5%, respectively. In general, the diffused transmittance is related to the surface structure and roughness of the textured FZO thin films. The average diffused transmittance of the as-deposited FZO thin films was around 1.7%, whereas it varied from 0.7% to 4.0% in the visible wavelength region. As the concentrations

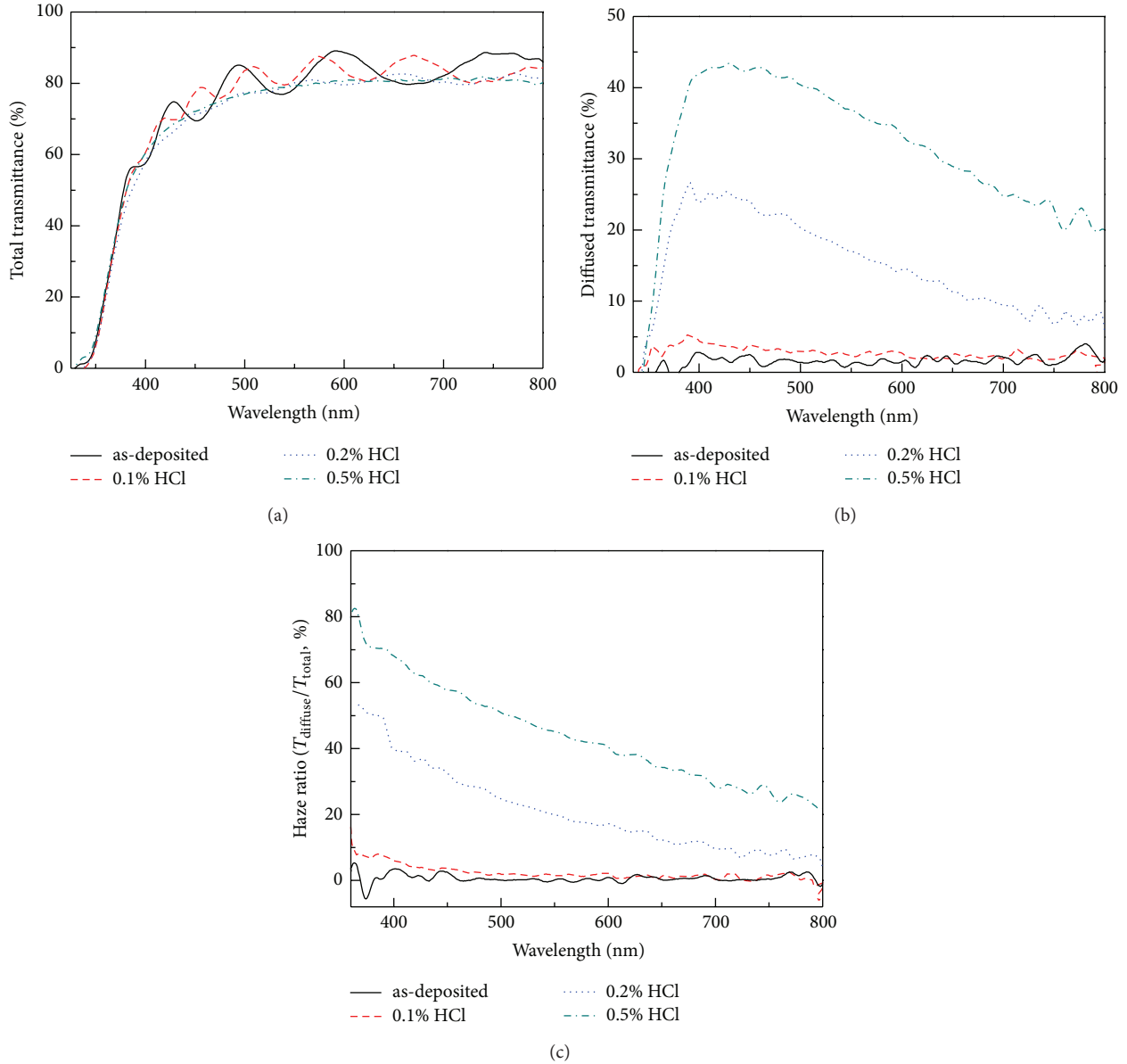


FIGURE 6: The optical characteristics: (a) total transmittance, (b) diffused transmittance, and (c) haze ratio of the HCl etched FZO substrates.

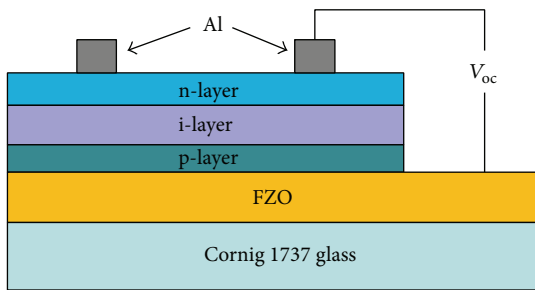


FIGURE 7: Structure configuration of the hydrogenated amorphous silicon thin film solar cells.

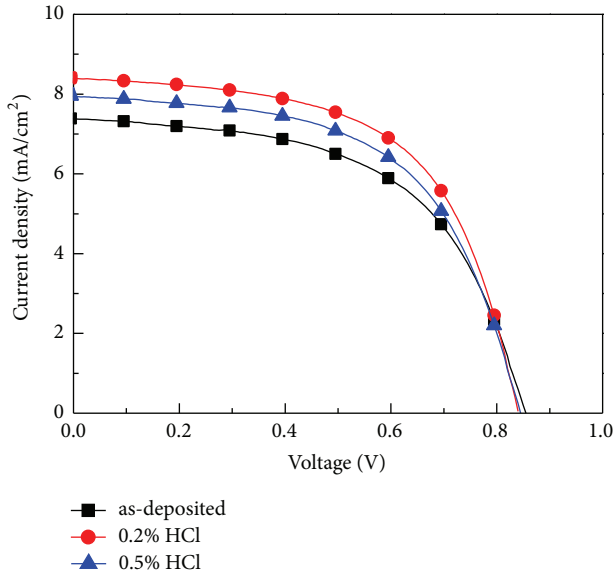
of HCl solution were 0.1 mol %, 0.2 mol %, and 0.5%, the average diffused transmittances were 2.6%, 15.0%, and 32.8%, whereas, in the visible wavelength region, they varied from

1.3% to 4.1%, from 1.3% to 25.3%, and from 20.0% to 43.4%, respectively. As the concentrations of HCl solution were 0.1 mol%, 0.2 mol%, and 0.5%, the maximum diffused transmittances were 5.4% (at 390 nm wavelength), 26.7% (at 390 nm wavelength), and 43.4% (at 430 nm wavelength), respectively. Figure 6(c) shows the haze ratio of the textured FZO thin films with various concentrations of HCl solution. The ratio of diffused to total transmittance is known as haze ratio. The average haze ratio of the textured FZO thin films in visible wavelength region was varied from 0.65%, 1.74%, 18.4%, and 41.2% as the HCl solution concentrations were 0.1 mol%, 0.2 mol%, and 0.5%, respectively.

A p-i-n structure is usually used for  $\alpha$ -Si thin film solar cells, as opposed to an n-i-p structure. This is because the mobility of electrons in  $\alpha$ -Si:H is roughly 1 or 2 orders of magnitude larger than that of holes, and thus the collection

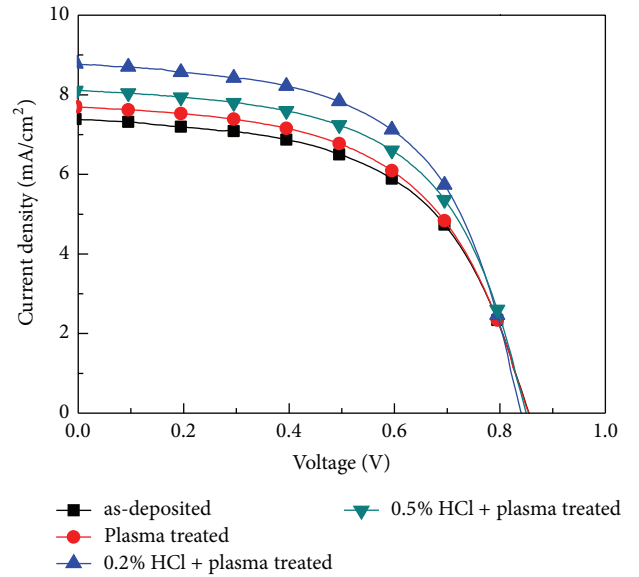
TABLE 1:  $V_{oc}$  value,  $J_{sc}$  value, and F.F. value of the fabricated amorphous silicon thin film solar cells.

FZO parameters	Abbreviated	$V_{oc}$ (V)	$J_{sc}$ (mA/cm <sup>2</sup> )	F.F.	Efficiency (%)
as-deposited	A-FZO	0.855	7.380	0.558	3.52
0.2% HCl	A2-FZO	0.843	8.394	0.585	4.14
0.5% HCl	A5-FZO	0.846	7.942	0.570	3.83
plasma treated	P-A-FZO	0.854	7.692	0.552	3.63
0.2% HCl + plasma treated	P-A2-FZO	0.840	8.764	0.578	4.26
0.5% HCl + plasma treated	P-A5-FZO	0.850	8.109	0.574	3.95

FIGURE 8: Current-voltage characteristics of the p-i-n  $\alpha$ -Si:H thin film solar cells under illumination.

rate of electrons moving from the n- to p-type contact is better than holes moving from p- to n-type contact. For that, the superstrate p-i-n hydrogenated  $\alpha$ -Si thin film solar cells were fabricated using a single-chamber PECVD unit at 200°C, and the structures of the designed solar cells are shown in Figure 7; no antireflective coatings were deposited on the cells. Although there are several reports related to the etching of glass substrates to improve the efficiency of the  $\alpha$ -Si thin film solar cells, texturing of patterned FZO thin films for high haze ratio in thin film solar cells is focused. At the first, as the as-deposited and etched as-deposited FZO thin film substrates are used, the values of open-circuit voltage ( $V_{oc}$ ), short-circuit current density ( $J_{sc}$ ), fill factor (F.F.), and efficiency ( $\eta$ ) are measured for the devices fabricated on those substrates.

Table 1 shows the measured current-voltage characteristics of the solar cells (substrate size  $3.3 \times 3.3$  cm<sup>2</sup>) under illumination as a function of differently treated processes. The abbreviated names of the FZO thin films under different processes are also shown in Table 1. Figure 8 shows that as the A-FZO, A2-FZO, and A5-FZO were used to fabricate the thin film silicon solar cells, the  $V_{oc}$  values of the solar cells were 0.855 V, 0.843 V, and 0.846 V; the  $J_{sc}$  values were 7.380 mA/cm<sup>2</sup>, 8.394 mA/cm<sup>2</sup>, and 7.942 mA/cm<sup>2</sup>; the F.F. values were 0.558, 0.585, and 0.570; and the efficiencies were

FIGURE 9: Current-voltage characteristics of the p-i-n  $\alpha$ -Si:H thin film solar cells under illumination.

$3.52 \pm 0.17$ ,  $4.14 \pm 0.13$ , and  $3.83 \pm 0.15$ , respectively. Those results suggest that the surface texture (or the haze ratio) of the FZO thin films is the key parameter to improve the performance of the  $\alpha$ -Si:H thin film solar cells.

Figure 9 shows that as the P-A-FZO, P-A2-FZO, and P-A5-FZO were used to fabricate the thin film silicon solar cells, the  $V_{oc}$  values of the solar cells were 0.854 V, 0.840 V, and 0.850 V; the  $J_{sc}$  values were 7.692 mA/cm<sup>2</sup>, 8.764 mA/cm<sup>2</sup>, and 8.109 mA/cm<sup>2</sup>; the F.F. values were 0.552, 0.578, and 0.574; and the efficiencies were  $3.63 \pm 0.15$ ,  $4.26 \pm 0.11$ , and  $3.95 \pm 0.13$ , respectively. As Figure 9 shows, the  $V_{oc}$  value and F.F. value had no changes, the  $J_{sc}$  value increased, and the efficiency increased as the H<sub>2</sub> plasma was used to treat the nonetched and etched FZO thin films. Those measured results of the fabricated  $\alpha$ -Si thin film solar cells are also compared in Table 1. The greater efficiencies in etched FZO substrates are mainly ascribable that as the haze ratio increases, the absorption of light increases, and then the short-circuit current density increases.

#### 4. Conclusions

In this study, resistivity is really improved as H<sub>2</sub>-plasma process was used because the carrier concentration was increased

and 25 W plasma-treated FZO thin films have the minimum resistivity of  $7.92 \times 10^{-4} \Omega\text{-cm}$ . The average haze ratio of the etched as-deposited FZO thin films increased from 0.65% to 41.2% as the concentration of HCl solution increased from 0.0% (nonetched) to 0.5%. As the as-deposited FZO thin films in the fabricated  $\alpha\text{-Si:H}$  thin film solar cells were changed to the 0.2 HCl-etched FZO ones, the  $J_{sc}$  values were improved from  $7.380 \text{ mA/cm}^2$  to  $8.394 \text{ mA/cm}^2$ , the F.F. values were improved from 0.558 to 0.585, and the efficiencies were improved from  $3.52 \pm 0.17$  to  $4.14 \pm 0.13$ , respectively. When the 0.2 HCl-etched  $\text{H}_2$ -plasma-treated FZO thin films were used as the electrodes, the fabricated solar cells had the optimal characteristics of  $J_{sc}$  value of  $8.764 \text{ mA/cm}^2$ , F.F. value of 0.578, and efficiency of  $4.26 \pm 0.11$ , respectively. For the FZO thin films, the haze ratio increased with increasing concentration of HCl solution and the carrier concentration increased as  $\text{H}_2$  plasma was used. That would effectively enhance light trapping and increase the electrons inside the absorber material of solar cells and then improve the efficiency of the fabricated thin film solar cells.

### Conflict of Interests

The authors declare that there is no conflict of interests regarding the publication of this paper.

### Acknowledgments

The authors acknowledge financial supports of NSC 101-2221-E-005-065, NSC 102-2622-E-390-002-CC3, and NSC 102-2221-E-390-027.

### References

- [1] Ü. Özgür, Y. I. Alivov, C. Liu et al., "A comprehensive review of ZnO materials and devices," *Journal of Applied Physics*, vol. 98, no. 4, Article ID 041301, 103 pages, 2005.
- [2] T. Minami, "Substitution of transparent conducting oxide thin films for indium tin oxide transparent electrode applications," *Thin Solid Films*, vol. 516, no. 7, pp. 1314–1321, 2008.
- [3] B. N. Pawar, G. Cai, D. Ham et al., "Preparation of transparent and conducting boron-doped ZnO electrode for its application in dye-sensitized solar cells," *Solar Energy Materials and Solar Cells*, vol. 93, no. 4, pp. 524–527, 2009.
- [4] C. C. Huang, F. H. Wang, and C. F. Yang, "Effects of deposition temperature and hydrogen flow rate on the properties of the Al-doped ZnO thin films and amorphous silicon thin-film solar cells," *Applied Physics A*, vol. 112, no. 4, pp. 877–883, 2013.
- [5] F. H. Wang, C. C. Huang, C. F. Yang, and H. T. Tzeng, "Optical and electrical properties of the different magnetron sputter power  $300^\circ\text{C}$  deposited  $\text{Ga}_2\text{O}_3\text{-ZnO}$  thin films and applications in p-i-n  $\alpha\text{-Si:H}$  thin-film solar cells," *International Journal of Photoenergy*, vol. 2013, Article ID 270389, 7 pages, 2013.
- [6] L. Cao, L. Zhu, J. Jiang, R. Zhao, Z. Ye, and B. Zhao, "Highly transparent and conducting fluorine-doped ZnO thin films prepared by pulsed laser deposition," *Solar Energy Materials and Solar Cells*, vol. 95, no. 3, pp. 894–898, 2011.
- [7] H. S. Yoon, K. S. Lee, T. S. Lee et al., "Properties of fluorine doped ZnO thin films deposited by magnetron sputtering," *Solar Energy Materials and Solar Cells*, vol. 92, no. 11, pp. 1366–1372, 2008.
- [8] F. H. Wang, C. F. Yang, and Y. H. Lee, "Deposition of F-doped ZnO transparent thin films using  $\text{ZnF}_2$ -doped ZnO target under different sputtering substrate temperatures," *Nanoscale Research Letters*, vol. 9, no. 1, article 97, 2014.
- [9] R. Das, T. Jana, and S. Ray, "Degradation studies of transparent conducting oxide: a substrate for microcrystalline silicon thin film solar cells," *Solar Energy Materials and Solar Cells*, vol. 86, no. 2, pp. 207–216, 2005.
- [10] N. Ohashi, Y. Wang, T. Ishigaki et al., "Lowered stimulated emission threshold of zinc oxide by hydrogen doping with pulsed argon-hydrogen plasma," *Journal of Crystal Growth*, vol. 306, no. 2, pp. 316–320, 2007.
- [11] F. H. Wang, C. F. Yang, J. C. Liou, and I. C. Chen, "Effects of hydrogen on the optical and electrical characteristics of the sputter-deposited  $\text{Al}_2\text{O}_3$ -doped ZnO thin films," *Journal of Nanomaterials*, vol. 2014, Article ID 857614, 7 pages, 2014.
- [12] F. C. M. van de Pol, F. R. Blom, and T. J. A. Popma, "R.F. planar magnetron sputtered ZnO films I: structural properties," *Thin Solid Films*, vol. 204, no. 2, pp. 349–364, 1991.
- [13] A. van der Drift, "Evolutionary selection, a principle governing growth orientation in vapour-deposited layers," *Philips Research Reports*, vol. 22, pp. 267–288, 1967.
- [14] Y. Igasaki and H. Saito, "Substrate temperature dependence of electrical properties of ZnO:Al epitaxial films on sapphire (12 $\bar{1}$ 0)," *Journal of Applied Physics*, vol. 69, no. 4, pp. 2190–2195, 1991.
- [15] F. Wang, H. Chang, C. Tseng, C. Huang, and H. Liu, "Influence of hydrogen plasma treatment on Al-doped ZnO thin films for amorphous silicon thin film solar cells," *Current Applied Physics*, vol. 11, supplement 1, pp. S12–S16, 2011.

## Research Article

# Enhanced Particle Swarm Optimization-Based Feeder Reconfiguration Considering Uncertain Large Photovoltaic Powers and Demands

Ying-Yi Hong,<sup>1</sup> Faa-Jeng Lin,<sup>2</sup> and Fu-Yuan Hsu<sup>1</sup>

<sup>1</sup> Department of Electrical Engineering, Chung Yuan Christian University, Chungli City 320, Taiwan

<sup>2</sup> Department of Electrical Engineering, National Central University, Chungli City 320, Taiwan

Correspondence should be addressed to Ying-Yi Hong; [yyh10632@yahoo.com.tw](mailto:yyl0632@yahoo.com.tw)

Received 19 February 2014; Accepted 8 April 2014; Published 30 April 2014

Academic Editor: Ching-Song Jwo

Copyright © 2014 Ying-Yi Hong et al. This is an open access article distributed under the Creative Commons Attribution License, which permits unrestricted use, distribution, and reproduction in any medium, provided the original work is properly cited.

The Kyoto protocol recommended that industrialized countries limit their green gas emissions in 2012 to 5.2% below 1990 levels. Photovoltaic (PV) arrays provide clear and sustainable renewable energy to electric power systems. Solar PV arrays can be installed in distribution systems of rural and urban areas, as opposed to wind-turbine generators, which cause noise in surrounding environments. However, a large PV array (several MW) may incur several operation problems, for example, low power quality and reverse power. This work presents a novel method to reconfigure the distribution feeders in order to prevent the injection of reverse power into a substation connected to the transmission level. Moreover, a two-stage algorithm is developed, in which the uncertain bus loads and PV powers are clustered by fuzzy-c-means to gain representative scenarios; optimal reconfiguration is then achieved by a novel mean-variance-based particle swarm optimization. The system loss is minimized while the operational constraints, including reverse power and voltage variation, are satisfied due to the optimal feeder reconfiguration. Simulation results obtained from a 70-bus distribution system with 4 large PV arrays validate the proposed method.

## 1. Introduction

The Kyoto protocol mandated that industrialized countries should reduce their greenhouse gas emissions in 2012 to 5.2% below their 1990 levels [1]. The Copenhagen Accord later called for the mitigation of global emissions in order to restrict rises in global temperatures to a maximum of 2°C [2]. To attain a low carbon environment, utilizing renewable energy is essential to provide electric power in power systems. Of all renewable energies, wind-turbine generators (WTG), and solar photovoltaic (PV) can provide the cleanest energy to consumers. Although a single unit size of WTG is generally much larger than that of a PV array, the former requires additional effort in terms of installation and maintenance. WTG is also limited by its produced noise, possibly damaging the ecosystem by altering the migration patterns of birds or other animals. However, solar PV arrays can provide noise-free energy,

which may be installed in rural fields and rooftops of houses in urban areas. Solar PV has been widely studied in a power system, including solar power prediction [3], capacity sizing [4], and maximum power point tracking [5, 6]. These works focus only on solar PV modules without addressing system operation problems, which the penetration of solar PV energies in a distribution system causes (e.g., reverse power and high voltages at downstream customers).

Designed as interconnected networks, electric distribution networks are operated in a radial structure. The feeder configuration problem attempts to find a radial operating structure that optimizes network performance while satisfying operation constraints. In practice, distribution system operators may tend to reduce the system real-power loss and enhance voltage quality under normal conditions [7–12]. Jeon and Kim integrated tabu search with the simulated annealing algorithm to minimize system losses in [7]. The tabu search

attempts to determine a solution using the greatest-descent-like algorithm which could not ensure any convergence property [7]. Lin et al. presented a refined genetic algorithm (RGA) to mitigate system losses [8]. Traditional crossover and mutation strategies were adjusted through a competition mechanism in RGA. Morton and Mareels presented a brute-force solution to determine the status of each switch in order to minimize system loss in a radial distribution system [9]. The graph theory, which guarantees a global optimum yet requires an exhaustive search, was used in [9]. Wu and Tsai presented an approach based on particle swarm optimization (PSO) with an integer code to determine the switch operation schemes, which minimizes the system loss via the feeder reconfiguration in a distribution system [10]. Amanulla et al. presented a binary PSO-based algorithm to find the optimal statuses of the switches in order to maximize the reliability and minimize the real-power loss in a power system [11]. Hong and Ho proposed a Prufer-number-based genetic algorithm to reconfigure a network to ensure that the voltage drops caused by faults in voltage-sensitive areas are feasible [12]. Kavousi-Fard and Niknam proposed a self-adaptive modification method based on the clonal selection algorithm to reduce the cost of active power losses of the network and the customer interruption costs through the feeder reconfiguration [13]. Kavousi-Fard and Akbari-Zadeh used the shuffled frog leaping algorithm to reconfigure the network by considering three reliability indices and total system losses [14]. Kavousi-Fard et al. used a firefly algorithm to investigate the multiobjective probabilistic distribution feeder reconfiguration problem considering reliability [15].

The widely-installed renewable energy resources in the power system have issued new concerns regarding the feeder reconfiguration. Niknam et al. proposed a probabilistic method considering the uncertainty regarding the active and reactive load forecast errors as well as the wind-turbine output power variations concurrently to study the feeder reconfiguration. Self-adaptive modified teacher learning optimization algorithm was proposed to solve the multiobjective probabilistic problem [16]. Niknam et al. assessed the distribution feeder reconfiguration strategy, solved by a self-adaptive bat algorithm, and examined the effect of renewable energy sources on the reliability of the power system [17]. Niknam et al. proposed a two-stage approach: the roulette wheel mechanism in conjunction with the Weibull/Gaussian probability distribution functions of wind and demands were implemented to produce deterministic equivalents (scenarios); the feeder reconfiguration problem was then solved by the adaptive modified particle swarm optimization [18]. Su et al. presented a binary PSO-based method aiming at enhancing feeder configuration and reactive power control to accommodate more distributed generation resources [19]. Malekpour et al. presented an adaptive PSO algorithm to determine the optimal feeder reconfiguration while considering the uncertainty caused from the wind power generation and load demand [20]. The point estimate method was used to calculate the stochastic power flow [20]. Niknam et al. presented a honey bee mating optimization algorithm to investigate the distribution feeder reconfiguration problem

while considering the effect of renewable energy sources on a system performance index [21].

Above literature survey reveals that system loss is a generally accepted performance index in the feeder reconfiguration problem. However, the above studies have the following limitations, which should be addressed in the modern smart grid:

- (1) renewable generation resources. Although they were not considered in conventional feeder reconfiguration problems [3–15], they should be considered in modern smart distribution systems;
- (2) uncertainty in renewable energies. Although uncertainty should be addressed in this area, owing to their intermittent characteristics, Kavousi-Fard and Niknam disregarded this essential factor [13, 21]. Although the uncertainty factor in renewable energies was considered in [16, 20], the point estimate method sampling two extra unsymmetrical operating points is considered to be less accurate than the Monte-Carlo simulation method [16, 20];
- (3) coordination between VAR controllers and switches. To regulate the voltage profile in the distribution system, the statuses of all switches should incorporate with VAR controllers (inverters of distributed generation resources); however, most studies have ignored this factor [2–21];
- (4) searching optimal statuses of switches: In contrast to genetic algorithms, tabu search, and other metaheuristic algorithms [3–9, 12–17, 21], PSO can search for the optimal solution efficiently. In addition to the encoding technique [10, 11, 18–20], the search approach should also be improved to make the PSO algorithm more reliable and robust.

Therefore, this work presents a novel method based on the mean-variance concept of particles (i.e., possible solutions) in PSO to determine the optimal status of each switch in the distribution system. Uncertainties in the power generation from solar PV arrays and demands are clustered to become scenarios with different weighting factors. Restated, uncertainties in the problem are transformed into scenarios. The inverters of solar PV arrays are then fully utilized to coordinate with the switches to regulate the voltage profile in order to minimize the system losses using the interior-point algorithm. More specifically, rather than stochastic power flow studies, the regulated voltages of solar PV arrays in each scenario are adjusted by the interior-point-based optimal power flow with fixed switches determined by the enhanced PSO algorithm.

The rest of this paper is organized as follows. Section 2 introduces the assumptions in the studied problem and presents the mathematical formulation of the problem. Section 3 then describes the proposed method based on fuzzy-c-means and enhanced PSO algorithm. Section 4 summarizes the simulation results. Conclusions are finally drawn in Section 5, along with recommendations for future research.

## 2. Assumptions and Problem Formulation

**2.1. Assumptions.** The following assumptions are made for the problem to avoid high voltages at the downstream customers and prevent the reverse power injected into the transmission level at the swing buses (substations).

- (a) The status of each tie switch is determined one day ahead by the preventive control using forecasted PV powers and demands with uncertainties. The voltages of inverter-based solar PV arrays are evaluated as supplemental results to support the preventive control. These inverter-controlled voltages should be recomputed in the real-time corrective control. For the preventive control, the scenarios are predetermined based on the empirical experience. No control action for the tie switch is needed once the scenarios occur. That is, a predetermined network configuration is used for many scenarios. Thus, preventive control is highly applicable to uncertainty caused from the wind powers and demands.
- (b) The inverter in either a rural field or an urban area at a bus can be considered as an aggregated one. Restated, hundreds of inverters of the solar PV arrays at a bus are operated with the same setting automatically or according to the commands of operators. Thus, a bus with large solar PV arrays is considered a voltage-controlled bus rather than a constant PQ bus.
- (c) The control center of a distribution system can communicate with the inverters through wire or wireless communication media in the demand management system (DMS) or SCADA. This assumption is applicable owing to the requirement of advanced ICT architecture in the smart distribution system.
- (d) The DC voltage of a solar PV array is boosted to a higher DC voltage, which is generally supported by a capacitor. This higher DC voltage is then modulated to a nominal AC voltage via an inverter. To achieve the voltage regulation and prevent the injection of reverse power into the transmission level (swing buses), the DC bus between the boost converter and inverter must be supported by an energy storage; the inverter must be bidirectional as well. Alternatively, a capacitor is still used for the conventionally adopted inverter, and an additional inductor is used for an appended rectifier in parallel. When the PV arrays produce (absorb) the reactive power into (from) the power system, the corresponding bus operates with a lagging (leading) power factor.

**2.2. Problem Formulation.** As described in Section 1, an operator has many performance indices available to determine the switch statuses. Assume that the operator attempts to minimize the real-power losses and satisfy all operational constraints. In particular, no reverse power is injected into the transmission levels. Further, assume that more than one substation (between the transmission and distribution systems) acts as swing buses in the studied problem. According to

the above four assumptions, the studied problem can be formulated as follows:

$$\text{Min } f(\tilde{V}, \tilde{\theta}, \tilde{P}, \tilde{Q}, x) \quad (1)$$

s.t.

$$PM(\tilde{V}, \tilde{\theta}, \tilde{P}, \tilde{Q}, x) = 0, \quad (2)$$

$$QM(\tilde{V}, \tilde{\theta}, \tilde{P}, \tilde{Q}, x) = 0, \quad (3)$$

$$V_n^{\min} \leq \tilde{V}_n \leq V_n^{\max}, \quad n = 1, \dots, N, \quad (4)$$

$$I_\ell^{\min} \leq \tilde{I}_\ell \leq I_\ell^{\max}, \quad \ell = 1, \dots, L, \quad (5)$$

$$\tilde{P}_{sw}^j \geq 0, \quad j = 1, 2, \dots, NS, \quad (6)$$

$$|\tilde{PF}_{pv}| \geq PF^{\min}, \quad pv = 1, 2, \dots, NP. \quad (7)$$

The symbols are defined as follows:

$f(\tilde{V}, \tilde{\theta}, \tilde{P}, \tilde{Q}, x)$ : stochastic real-power loss in the system

$PM(\tilde{V}, \tilde{\theta}, \tilde{P}, \tilde{Q}, x)$ : vector of the stochastic real-power balance equations

$QM(\tilde{V}, \tilde{\theta}, \tilde{P}, \tilde{Q}, x)$ : vector of the stochastic reactive power balance equations

$\tilde{V}$ : vector of stochastic voltage magnitudes at all buses

$\tilde{\theta}$ : vector of stochastic phase angles at all buses

$\tilde{P}$ : vector of stochastic real-power injections at all buses

$\tilde{Q}$ : vector of stochastic reactive power injections at all buses

$x$ : vector of statuses of all switches (1 or 0)

$\tilde{V}_n$ : stochastic voltage magnitude at bus  $n$ ,  $n = 1, \dots, N$

$\tilde{I}_\ell$ : stochastic line flow at line  $\ell$ ,  $\ell = 1, \dots, L$

$\tilde{P}_{sw}^j$ : total stochastic power injected into substation  $j$ ,  $j = 1, 2, \dots, NS$

$\tilde{PF}_{pv}$ : stochastic power factor at the  $pv$ th photovoltaic array,  $pv = 1, 2, \dots, NP$

$N$ : number of system buses

$L$ : number of system lines

$NS$ : number of substations (swing buses)

$NP$ : number of voltage controlled buses with solar PV arrays.

The values of components in  $x$  must ensure that the structure of distribution system is radial, and no islands occur in the system.

TABLE 1: Installed capacities of PV arrays and parameters of the Weibull distributions.

Bus	Installed capacities (kW)	Scale parameter ( $\kappa$ )	Shape parameter ( $\gamma$ )
13	750	0.35	2
26	3000	0.35	2
44	500	0.35	2
61	4500	0.35	2

### 3. Proposed Method

The mathematical formulation shown in (1)–(7) incorporated with the radial and nonislanding constraints is a stochastic mixed binary programming problem. This problem has difficulty in treating stochastic equality constraints in (2) and (3) and stochastic inequality constraints in (4)–(7). Thus, by using the fuzzy-c-means (FCM), the proposed method identifies the best representative scenarios with no random variables. This work presents a novel mean-variance-based PSO algorithm to determine the statuses of switches for all scenarios. Once the status of each switch is given, the nonstochastic representative scenarios can be solved using traditional robust nonlinear programming referred to herein as interior-point algorithm. By using the “fmincon” developed in MATLAB software, this work implements the interior-point algorithm. A detailed description of “fmincon” can be found in [22], which will be neglected herein.

*3.1. Fuzzy-c-Means to Identify Representative Scenarios.* Both PV power generations and demands are random variables with different stochastic distributions. Theoretically, the Monte-Carlo simulation can obtain an accurate solution in case the number of sampled PV power generations and demands from their stochastic distributions is sufficiently large. However, the Monte-Carlo simulation requires a very long CPU time. If these sampled PV power generations and demands can be clustered, then the center of each cluster can serve as a representative scenario. FCM attempts to identify the representative scenarios obtained from all random variables with their individual stochastic distributions. Restated, the scenarios with real values are generated according to the stochastic distributions of all random variables (PV power generations and demands). The data sets in these scenarios are clustered using FCM. Namely, the center vector in each cluster refers to the representative scenario, and the sum of membership values in each cluster indicates the corresponding weighting factor for this representative scenario.

Bezdek et al. defined  $J(U, V)$  as an objective function in the FCM algorithm [23] as follows:

$$J(U, V) = \sum_{i=1}^M \sum_{c=1}^C (\mu_{ci})^m \|X_i - V_c\|^2, \quad 1 \leq m < \infty, \quad (8)$$

where  $C$  signifies the clustering number, which is determined in Section 3.2, and is fixed for in FCM. Additionally,  $M$

denotes the number of data sets generated from the Monte-Carlo simulation herein;  $V_c$  refers to the vector of the center in the  $c$ th cluster;  $X_i$  denotes the  $i$ th data vector for clustering; the membership function value  $\mu_{ci}$  serves as a weighting factor between  $V_c$  and  $X_i$ . After the minimum of  $J(U, V)$  is gained, the  $M$  data vectors are partitioned into  $C$  clusters. Let symbols  $h$  and  $\varepsilon$  represent the iterative index and convergence tolerance, respectively. Bezdek developed the following four algorithmic steps to attain the optimum.

*Step 1.* Initialize a matrix of membership functions as follows:

$$U^{(h)} = [\mu_{ci}^{(h)}] \in R^{C \times M}, \quad (9)$$

where initial  $h$  equals 0.

*Step 2.* Let  $h = h + 1$ . Compute the center of the  $c$ th cluster as follows:

$$V_c = \frac{\sum_{i=1}^M (\mu_{ci}^{(h)})^m X_i}{\sum_{i=1}^M (\mu_{ci}^{(h)})^m} \quad 1 \leq c \leq C, \quad 1 \leq i \leq M. \quad (10)$$

*Step 3.* Update  $\mu_{ci}^{(h)}$  for all  $X_i$ ,  $i = 1, \dots, M$ .

Consider

$$\mu_{ci}^{(h)} = \frac{1}{\sum_{j=1}^C [\|X_i - V_c\| / \|X_i - V_j\|]^{2/(m-1)}}. \quad (11)$$

*Step 4.* If  $\|U^{(h)} - U^{(h-1)}\| < \varepsilon$ , stop; otherwise, go to Step 2.

*3.2. Optimal Number of Clusters.* Yang and Wu proposed a partition separation (PS) validity index, in which a normalized partition coefficient is aggregated with an exponential separation measure for each cluster [24].

The PS validity index for cluster  $c$  is defined as follows:

$$PS(c) = \sum_{i=1}^M \frac{\mu_{ci}^2}{\mu_{ci}^{\max}} - \exp\left(-\frac{\min_{c \neq k} \{\|V_c - V_k\|^2\}}{\beta_T}\right), \quad (12)$$

where  $\mu_{ci}^{\max} = \max_{1 \leq c \leq C} \{\sum_{i=1}^M \mu_{ci}^2\}$ ,  $\beta_T = (\sum_{c=1}^C \|V_c - \bar{V}\|^2)/C$ , and  $\bar{V}$  denotes the mean of all  $V_c$ s.

The PS validity index for  $C$  clusters is defined as follows:

$$PS(C) = \sum_{c=1}^C PS(c). \quad (13)$$

A large  $PS(C)$  refers to a situation in which cluster  $c$  is compact inside and far away from other  $(C - 1)$  clusters. Consequently, the optimal number  $C^*$  (i.e.,  $C$  defined in Section 3.1) of clusters can be obtained as follows:

$$C^* = \max_{2 \leq C \leq \sqrt{M}} PS(C). \quad (14)$$

*3.3. Mean-Variance-Based PSO Algorithm to Determine  $x$ .* As an evolutionary optimization method, PSO minimizes an objective function (performance index) by imitating

TABLE 2: PS validity indices for different numbers of clusters.

C	2	3	4	5	6	7	8	9	10
PS	1.687	2.245	2.434	2.283	2.232	1.875	3.039	0.886	2.388

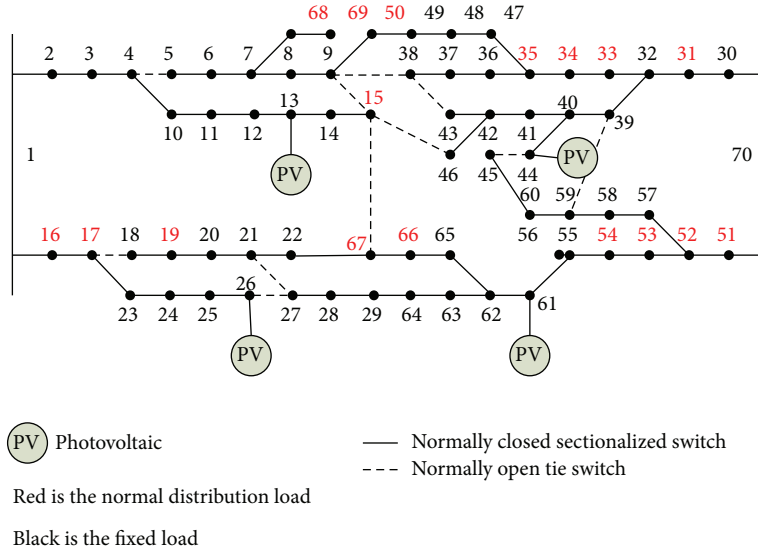


FIGURE 1: One-line diagram for the 70-bus distribution system.

the behavior of schooling fish or flocking birds [25, 26]. PSO comprises a population of particles (individuals) that represent possible solutions moving in a  $\psi$ -dimensional search space. The iterative temporary solution and updated value of a particle  $p$  are called the position and velocity, respectively. Let vectors  $x_p$  and  $\Delta x_p$  be the  $\psi$ -dimensional position and velocity of particle  $p$ ,  $p = 1, 2, \dots, P$  (i.e., number of population size), respectively.

The proposed method is based on the mean of the particles and standard deviation (squared root of variance) of the distances between any two particles in the  $t$ th iterations. The updated value of a particle  $p$  at iteration  $t$  is expressed as follows:

$$\begin{aligned} \Delta x_p^{t+1} = & w^t \Delta x_p^t + a^t r_1^t (p_{\text{best}}^t - x_p^t) \\ & + b^t r_2^t (g_{\text{best}}^t - x_p^t) + c^t r_3^t (g_{\text{best}}^t - \bar{x}_p^t), \end{aligned} \quad (15)$$

where the inertia weight  $w^t$  is decreased linearly from 0.5 to 0.3 because a large  $w^t$  is used for global searches, whereas local searches require a small  $w^t$ . The symbols  $r_1, r_2,$  and  $r_3$  are random numbers within  $[0, 1]$ . Additionally,  $p_{\text{best}}^t$  and  $g_{\text{best}}^t$  are the best position of a particle in the iteration  $t$  and the best known position up to present, respectively. The learning factors  $a$  and  $b$  should meet  $a + b \leq 4$  [25, 26] and are defined as

$$a^t = b^t = 1 + \frac{1}{(1 + \exp(f(g_{\text{best}}^1)/f(g_{\text{best}}^t)))}. \quad (16)$$

Since the last term on the right hand side of (15) is appended, compared to the original PSO,  $c^t = 4 - a^t - b^t$ . Also,  $\bar{x}_p^t$  is a  $\psi$ -dimensional vector of the mean values of all particles. The last term introduced in (15) is used to coordinate the global and local searches.

Let  $\sigma^t$  be the standard deviation of all distances among particles in the  $t$ th iteration. If all distances follow a Gaussian distribution, then  $\bar{x}_p^t \pm 3\sigma^t$  covers 99.7% of all particles. Let  $\eta^t = 3 - 2c^t$ . Because  $c^t$  in (15) decreases to zero, the values of  $\eta^t$  are increased to 3. This work recommends that the particles outside the distance of  $\bar{x}_p^t \pm \eta^t \sigma^t$  in iteration  $t$  should be discarded. These discarded particles are substituted by  $g_{\text{best}}^t$ . Restated, if  $x_p^t$  is inside the  $\bar{x}_p^t \pm \eta^t \sigma^t$ , then

$$x_p^{t+1} = x_p^t + \Delta x_p^t. \quad (17)$$

If  $x_p^t$  is outside  $\bar{x}_p^t \pm \eta^t \sigma^t$ , then

$$x_p^{t+1} = g_{\text{best}}^t + \Delta x_p^t. \quad (18)$$

In this work,  $x_p^{t+1}$  denotes the vector of statuses of all switches. All elements of  $x_p^{t+1}$  are bounded to 0 or 1 through the sigmoid function. Because the number of switches with "closed" statuses is fixed (say  $\xi$ ) for a distribution system to ensure a radial structure, the largest  $\xi$  elements in  $x$  are rounded to 1 and the remaining elements are reset to 0.



TABLE 4: Optimal results before feeder reconfiguration.

Scenario	1	2	3	4	5	6	7	8
Voltage magnitude (p.u.)								
$V_1$	1.041	1.043	1.039	1.045	1.026	1.047	0.974	1.019
$V_{13}$	1.021	1.034	1.015	1.021	1.006	1.020	0.950	0.991
$V_{26}$	1.050	1.050	1.050	1.050	1.050	1.050	0.984	1.050
$V_{44}$	1.015	1.010	1.008	1.012	1.006	1.009	1.024	1.014
$V_{61}$	1.049	1.000	0.980	0.974	1.050	1.035	1.009	1.014
$V_{70}$	1.050	1.050	1.050	1.050	1.047	1.050	1.050	1.050
Reactive power (kVAr)								
$Q_{13}$	109.684	185.963	81.792	82.203	111.297	54.847	0.002	56.510
$Q_{26}$	207.808	209.497	206.809	206.289	209.705	204.487	-361.796	207.732
$Q_{44}$	130.072	56.783	33.835	87.807	49.377	55.037	502.178	105.918
$Q_{61}$	941.614	545.250	392.784	345.034	819.679	832.136	954.342	657.163
Real power at swing bus (kW)								
$P_1$	361.171	304.607	375.732	473.122	91.277	557.162	-95.092	50.501
$P_{70}$	1953.526	2640.701	2912.282	2902.069	1877.819	2241.501	2800.633	2410.641
Total load (kW)	4286.679	4276.304	4285.446	4281.481	4280.026	4281.264	4278.722	4279.626
Loss (kW)	117.429	148.208	182.827	184.226	135.961	129.235	193.034	153.292
Aggregating loss = 157.874 kW								

TABLE 5: Optimal results after the feeder reconfiguration using the proposed method.

Scenario	1	2	3	4	5	6	7	8
Voltage magnitude (p.u.)								
$V_1$	1.050	1.050	1.050	1.050	1.046	1.050	1.037	1.040
$V_{13}$	1.013	1.024	1.008	1.009	1.009	1.004	1.004	0.994
$V_{26}$	1.036	1.032	1.038	1.030	1.050	1.026	1.050	1.050
$V_{44}$	0.994	1.014	1.012	1.016	0.978	0.998	1.015	1.014
$V_{61}$	1.050	1.047	1.029	1.023	1.050	1.050	1.030	1.050
$V_{70}$	1.025	1.050	1.050	1.050	1.016	1.035	1.050	1.046
Reactive power (kVAr)								
$Q_{13}$	109.686	185.963	81.792	82.204	111.298	54.847	145.300	56.510
$Q_{26}$	358.888	321.407	376.783	302.842	415.400	266.856	419.470	411.446
$Q_{44}$	130.073	56.783	33.835	87.807	49.378	55.037	76.380	105.918
$Q_{61}$	541.639	545.250	392.784	345.034	532.708	530.894	404.858	532.886
Real power at swing bus (kW)								
$P_1$	1209.57	1149.71	1223.55	1324.58	928.005	1415.21	702.954	885.934
$P_{70}$	1081.67	1726.06	1974.25	1959.51	1016.86	1356.16	1893.88	1508.39
Loss (kW)	93.979	78.674	92.627	93.126	111.735	101.945	84.322	86.471
Aggregating loss = 92.875 kW								

After the status of each switch is determined using the mean-variance-based PSO, the topology of a distribution system is fixed. Additionally, the uncertainties in wind powers and demands are modeled by many scenarios with real numbers obtained by FCM. Thus, each scenario becomes a traditional nonlinear “optimal power flow” (OPF) problem, which adjusts the inverter-controlled voltages to minimize the weighting real-power losses and meets the operational constraints, including the reverse power. The weighting factor

of the objective function for each scenario  $c$  is evaluated by  $\sum_i \mu_{ci}$  where the  $i$ th data set belongs to the  $c$ th cluster. In this work, the optimal power flow problem is solved using the interior-point algorithm developed in MATLAB software.

#### 4. Simulation Results

A case study involving a 70-bus distribution system is used as an example [27], as shown in Figure 1, to show the simulation

TABLE 6: Optimal results after feeder reconfiguration using chaos-based PSO and GA.

Scenario	1	2	3	4	5	6	7	8
Voltage magnitude (p.u.)								
$V_1$	1.050	1.050	1.050	1.050	1.046	1.050	1.037	1.040
$V_{13}$	1.019	1.030	1.015	1.015	1.015	1.011	1.011	1.000
$V_{26}$	1.036	1.032	1.038	1.030	1.050	1.026	1.050	1.050
$V_{44}$	0.992	1.011	1.009	1.014	0.976	0.995	1.013	1.011
$V_{61}$	1.050	1.047	1.029	1.023	1.050	1.050	1.030	1.050
$V_{70}$	1.026	1.050	1.050	1.050	1.017	1.035	1.050	1.046
Reactive power (kVAr)								
$Q_{13}$	109.686	185.963	81.792	82.204	111.298	54.847	145.300	56.510
$Q_{26}$	358.889	321.407	376.783	302.842	418.678	266.856	422.320	415.772
$Q_{44}$	130.073	56.783	33.835	87.807	49.378	55.037	76.380	105.918
$Q_{61}$	536.509	545.250	392.784	345.034	526.576	525.289	404.859	528.011
Real power at swing bus (kW)								
$P_1$	1145.56	1087.05	1159.05	1260.09	864.00	1350.20	639.51	820.838
$P_{70}$	1146.37	1791.07	2039.45	2024.28	1082.32	1421.35	1958.74	1573.05
Loss (kW)	94.658	81.017	93.310	93.400	113.189	102.117	85.737	86.035
Aggregating loss = 93.738 kW								

results obtained by the proposed method. Buses 1 and 70 are two substations (the swing buses). The solid lines denote the normally closed sectionalized switches, and the dot lines are normally open tie switches. Totally, the statuses of 79 switches must be determined in this work by the proposed mean-variance-based PSO.

Four large solar PV arrays are installed at buses 13, 26, 44, and 61. Characteristics of the solar PV arrays are the Weibull distributions; that is,  $\text{pdf}(P_g) = (\kappa/\gamma)(P_g/\gamma)^{\kappa-1} \exp(-(P_g/\gamma)^\kappa)$ , where  $P_g$  denotes the PV generation. Table 1 lists the installed capacities of all PV arrays and their parameters of the Weibull distributions.

In this system, the loads at 17 buses are modeled by the Gaussian distributions. They are buses 15–17, 19, 31, 33–35, 50–54, and 66–69. The mean and standard deviation of each stochastic load are 0.8 p.u. and 5% (based on its original MVA), respectively. The loads at other buses are fixed.

Three hundred sets of PV generations and loads are randomly produced using the parameters of the Weibull and Gaussian distributions, respectively; that is,  $M = 300$ , in this work. Next, by using FCM, these 300 sets of data are clustered together by considering different  $C$ . Theoretically, the maximum number of clusters is  $\sqrt{300}$  ( $\cong 17$ , see (14)). However, the computational burden in a PC is considered here; let the maximum number of clusters be 10. The total CPU time ( $C = 2, 3, \dots, 10$ ) to cluster these sampled PV generations and loads is 1.38 s, which was estimated by a PC with Intel Core i5 2.50 GHz and 8 GB RAM. Table 2 lists the PS validity indices for  $C = 2, 3, \dots, 10$ . This table reveals that the optimal clustering number is 8 (i.e.,  $C^* = 8$  in (14)) because its corresponding PS validity value (3.039) is the largest.

The 8 representative scenarios obtained by FCM were examined first by running OPF. The voltage profile and reactive powers were adjusted using 4 inverter-based solar PV

at buses 13, 26, 44, and 61. Table 3 lists the 17 load buses with their representative real- and reactive-power loads (p.u.) in the 8 representative scenarios. The 4 solar PV arrays generate real power only initially with the unity power factor. This table also shows the weighting factor obtained by FCM for each scenario.

First, the interior-point-based OPF was used to regulate the voltage profile and minimize the system losses individually for these 8 scenarios. Table 4 summarizes the optimal results before the feeder reconfiguration. This table reveals that a reverse power  $-95.092$  kW was injected into bus 1 in scenario 7. There is also reverse reactive power ( $-361.796$  kVAr) at bus 26. The other scenarios had no reverse power at buses 1 and 70.

By using the proposed method, the statuses of 79 switches were determined using the mean-variance-based PSO; the voltage profile was also regulated using the interior-point-based OPF. The population size was 10, and the inertia was decreased linearly from 0.5 to 0.3 in 100 iterations in the proposed PSO algorithm. Table 5 lists the optimal solutions obtained by the proposed method. The injection powers  $-95.092$  (bus 1) and  $2,800.633$  kW (bus 70) before feeder reconfiguration were changed to  $702.954$  (bus 1) and  $1,893.876$  kW (bus 70) after feeder reconfiguration in scenario 7, respectively. The system losses were also reduced from  $157.874$  to  $92.875$  kW. The proposed method required  $11,835.41$  CPU seconds to attain the optimal solution. Figure 2 shows the optimal feeder reconfiguration using the proposed method.

Table 6 shows the optimal solutions gained by using chaos-based PSO and GA. The results gained by chaos-based PSO and GA are the same. The numerical parameters used in the chaos-based PSO are the same as those in the proposed method. The crossover and mutation rates in GA are

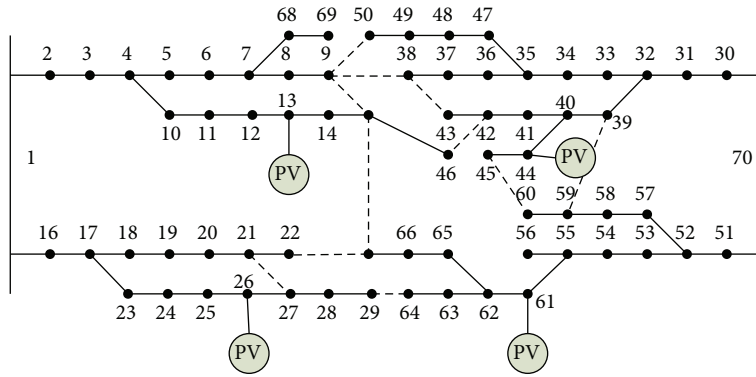


FIGURE 2: Optimal feeder reconfiguration using the proposed method.

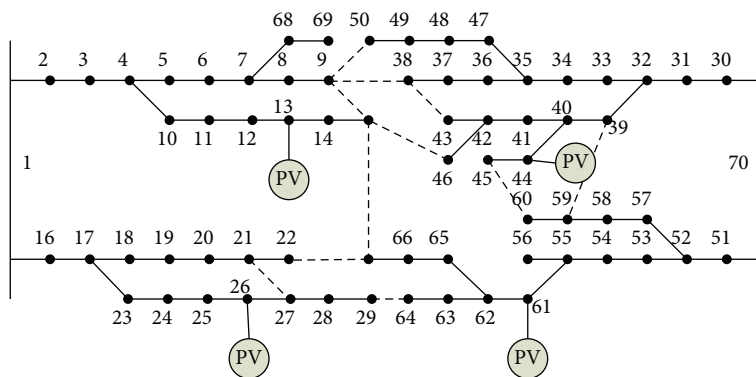


FIGURE 3: Optimal feeder reconfiguration obtained by chaos-based PSO and GA.

0.8 and 1/790, respectively. The merits of the proposed method are as follows. (a) The CPU times required by chaos-based PSO (15,224.55 s) and GA (18,508.64 s) are much longer than that (11,835.41 s) required in the proposed method. (b) The aggregating loss attained by the proposed method is 92.875 kW, which is smaller than 93.738 kW obtained by both chaos-based PSO and GA. Figure 3 illustrates the optimal feeder reconfiguration obtained by the chaos-based PSO and GA algorithms.

## 5. Conclusions

This work presents a novel method that incorporates FCM, partition separation validity index, mean-variance-based PSO, and interior-point-based optimal power flow to conduct feeder reconfiguration in order to prevent the reverse power caused by uncertain solar PV arrays from injecting into the transmission level. The novelties are as follows: (a) the uncertainty in the PV powers and demands is modeled by multiple scenarios gained by FCM in order to avoid probabilistic calculations; (b) the novel mean-variance-based PSO implements an adaptive elite strategy that replaces the particles far away from  $g_{best}^t$  with  $g_{best}^t$ . The number of replacement decreases according to the standard deviation of distances among particles. Simulation results demonstrate that the proposed method is faster than the chaos-based PSO method. Furthermore, the proposed method can solve the problem

with the reverse power and high voltage at the customers' side while minimizing the system loss.

## Conflict of Interests

The authors declare that there is no conflict of interests regarding the publication of this paper.

## Acknowledgments

The authors would like to thank the National Science Council of the Republic of China, Taiwan, for financially supporting this research under Contract no. NSC103-3113-P-008-001. Ted Knoy is appreciated for his editorial assistance.

## References

- [1] "Kyoto Protocol to the United Nations—framework convention on climate change," December 1997.
- [2] The Copenhagen Accord, "United Nations Climate Change Conference," December 2009.
- [3] V. L. Brano, G. Ciulla, and M. D. Falco, "Artificial neural networks to predict the power output of a PV panel," *International Journal of Photoenergy*, vol. 2014, Article ID 193083, 12 pages, 2014.

- [4] M. Engin, "Sizing and simulation of PV-wind hybrid power system," *International Journal of Photoenergy*, vol. 2013, Article ID 217526, 10 pages, 2013.
- [5] K. H. Chao, L. Y. Chang, and H. C. Liu, "Maximum power point tracking method based on modified particle swarm optimization for photovoltaic systems," *International Journal of Photoenergy*, vol. 2013, Article ID 583163, 6 pages, 2013.
- [6] H. Mahamudul, M. Saad, and M. I. Henk, "Photovoltaic system modeling with fuzzy logic based maximum power point tracking algorithm," *International Journal of Photoenergy*, vol. 2013, Article ID 762946, 10 pages, 2013.
- [7] Y. J. Jeon and J. C. Kim, "Network reconfiguration in radial distribution system using simulated annealing and tabu search," in *IEEE PES Winter Meeting*, pp. 23–27, January 2000.
- [8] W.-M. Lin, F.-S. Cheng, and M.-T. Tsay, "Distribution feeder reconfiguration with refined genetic algorithm," *IEE Proceedings: Generation, Transmission and Distribution*, vol. 147, no. 6, pp. 349–354, 2000.
- [9] A. B. Morton and I. M. Y. Mareels, "An efficient brute-force solution to the network reconfiguration problem," *IEEE Transactions on Power Delivery*, vol. 15, no. 3, pp. 996–1000, 2000.
- [10] W.-C. Wu and M.-S. Tsai, "Application of enhanced integer coded particle swarm optimization for distribution system feeder reconfiguration," *IEEE Transactions on Power Systems*, vol. 26, no. 3, pp. 1591–1599, 2011.
- [11] B. Amanulla, S. Chakrabarti, and S. N. Singh, "Reconfiguration of power distribution systems considering reliability and power loss," *IEEE Transactions on Power Delivery*, vol. 27, no. 2, pp. 918–926, 2012.
- [12] Y.-Y. Hong and S.-Y. Ho, "Determination of network configuration considering multiobjective in distribution systems using genetic algorithms," *IEEE Transactions on Power Systems*, vol. 20, no. 2, pp. 1062–1069, 2005.
- [13] A. Kavousi-Fard and T. Niknam, "Optimal distribution feeder reconfiguration for reliability improvement considering uncertainty," to appear in *IEEE Transactions on Power Delivery*.
- [14] A. Kavousi-Fard and M. R. Akbari-Zadeh, "Reliability enhancement using optimal distribution feeder reconfiguration," *Neurocomputing*, vol. 106, pp. 1–11, 2013.
- [15] A. Kavousi-Fard, T. Niknam, and A. Bazia, "A novel multi-objective self-adaptive modified firefly algorithm for optimal operation management of stochastic DFR strategy," *International Transactions on Electrical Energy Systems*, 2014.
- [16] T. Niknam, A. Kavousi Fard, and A. Baziar, "Multi-objective stochastic distribution feeder reconfiguration problem considering hydrogen and thermal energy production by fuel cell power plants," *Energy*, vol. 55, pp. 680–691, 2014.
- [17] T. Niknam, A. Kavousi Fard, and A. Baziar, "Multi-objective stochastic distribution feeder reconfiguration problem considering hydrogen and thermal energy production by fuel cell power plants," *Energy*, vol. 64, pp. 342–354, 2014.
- [18] T. Niknam, A. Kavousifard, and J. Aghaei, "Scenario-based multiobjective distribution feeder reconfiguration considering wind power using adaptive modified PSO," *IET Renewable*, vol. 6, no. 4, pp. 236–247, 2012.
- [19] S.-Y. Su, C.-N. Lu, R.-F. Chang, and G. Gutiérrez-Alcaraz, "Distributed generation interconnection planning: a wind power case study," *IEEE Transactions on Smart Grid*, vol. 2, no. 1, pp. 169–177, 2011.
- [20] A. R. Malekpour, T. Niknam, A. Pahwa, and A. Kavousi-Fard, "Multi-objective stochastic distribution feeder reconfiguration in systems with wind power generators and fuel cells using the point estimate method," *IEEE Transactions on Power Systems*, vol. 28, no. 2, pp. 1483–1492, 2013.
- [21] T. Niknam, A. K. Fard, and A. Seifi, "Distribution feeder reconfiguration considering fuel cell/wind/photovoltaic power plants," *Renewable Energy*, vol. 37, no. 1, pp. 213–225, 2012.
- [22] *Optimization Toolbox-Fmincon, MATLAB, the MathWorks*, 2009.
- [23] J. C. Bezdek, R. Ehrlich, and W. Full, "FCM: the fuzzy c-means clustering algorithm," *Computers and Geosciences*, vol. 10, no. 2–3, pp. 191–203, 1984.
- [24] M.-S. Yang and K.-L. Wu, "A new validity index for fuzzy clustering," in *Proceedings of the 10th IEEE International Conference on Fuzzy Systems*, pp. 89–92, Melbourne, Australia, December 2001.
- [25] J. Kennedy and R. Eberhart, *Swarm Intelligence*, Morgan Kaufmann Publishers, Elsevier, San Francisco, Calif, USA, 2001.
- [26] R. Eberhart and J. Kennedy, "New optimizer using particle swarm theory," in *Proceedings of the 6th International Symposium on Micro Machine and Human Science*, pp. 39–43, October 1995.
- [27] A. R. Malekpour and T. Niknam, "A probabilistic multi-objective daily Volt/Var control at distribution networks including renewable energy sources," *Energy*, vol. 36, no. 5, pp. 3477–3488, 2011.

## Research Article

# Building Professional Competencies Indices in the Solar Energy Industry for the Engineering Education Curriculum

Chin-Guo Kuo<sup>1</sup> and Chi-Cheng Chang<sup>2</sup>

<sup>1</sup> Department of Industrial Education, National Taiwan Normal University, No. 162, Section 1, Ho-Ping East Road, Taipei 106, Taiwan

<sup>2</sup> Department of Information Management, Lunghwa University of Science and Technology, No. 300, Section 1, Wanshou Road, Guishan, Taoyuan County 333, Taiwan

Correspondence should be addressed to Chi-Cheng Chang; [chig@mail.lhu.edu.tw](mailto:chig@mail.lhu.edu.tw)

Received 21 March 2014; Accepted 16 April 2014; Published 29 April 2014

Academic Editor: Ho Chang

Copyright © 2014 C.-G. Kuo and C.-C. Chang. This is an open access article distributed under the Creative Commons Attribution License, which permits unrestricted use, distribution, and reproduction in any medium, provided the original work is properly cited.

This study aims to develop professional competency indices and their subindices as needed by the solar energy industry, to establish a basis for development of the engineering education curriculum. The methodologies adopted by the study are literature analysis, expert advisories, and focus groups. The study focuses on the establishment of competency indices by experts at stock market-listed companies and then confirms these competencies with focus groups. The study found that the competencies required by the solar industry consist of knowledge, skills, and attitudes in the areas of materials development and applications, photovoltaic technology, cell manufacturing technology, biotechnology, chemical technology, power generation and electricity, process development and improvement, data collection and analysis, industry regulation, green energy beliefs, and working attitudes and values. The results of this study can be used as the basis for the cultivation, selection, and employment of industry professionals.

## 1. Introduction

Green energy is an important industrial sector in this era of international competition. This energy sector includes (1) the main industries of solar photovoltaic and LED lighting and (2) the general potential industries of wind power, biofuels, hydrogen and fuel cells, energy information and communication, and electric vehicles among others [1]. The solar energy industry is one of the most important “green energy” industries. The output value of Taiwan’s solar industry as a whole is expected to exceed 15 billion NTD in 2015, with the silicon solar cell module accounting for much of it, at the same time as it ranks number 4 in the world [1]. The maintenance of international competitiveness and sustainable development in the industry in the future will mainly depend on the quality of the industry’s human resources. How to provide the professional competencies needed by the industry and to further develop curricula to nurture talent are the core priorities of engineering education.

Research into the solar industry in the past has focused primarily on several different but related areas, including

business strategy, scientific knowledge and technology, tools and software applications, processes, and optimisation development. For example, in the area of business strategy, Chang and Kuo [2] studied two sets of dynamic business competencies needed in the industry; in the technical area, there was a study of Kuo et al. [3]. In professional competencies and solar energy competency standards and applications, O’net [4] established 51 industrial competency standards. Although there are not many studies focusing on how to teach energy technologies in engineering education, there is still energy education research related to ecology by Acikgoz [5] and the literature of solar energy education investigated by Dalitz et al. [6]. In summary, solar industry engineer training studies mainly take competence-based and resource-based perspectives. Competence-based approaches can help build the core competencies of solar business professionals, so that enterprises can develop their core competencies with market segmentation. In terms of business strategy, resource-based approaches regard the professional talents of solar industry engineers as one of an enterprise’s core resources, on the basis of which maximum benefit may be

generated from the competitive market for the organisation, through the domination and appropriate allocation of resources.

In recent years, the solar industry has had to adapt to an ultracompetitive environment. An enterprise's competitive advantage derived from resource strength is quickly eroded as a result of its competitors' technological innovations [7, 8]. Moreover, the operations of international companies in the solar industry generally focus on the vertical integration of the supply chain, while Taiwan's manufacturers mostly focus on specialised manufacturing [9, 10]. In view of the rapid changes in the technical content of a business's technologies, and since Taiwan's advantages are in manufacturing, one of the biggest problems of engineering education is how to keep up with the changes in the professional competencies required by the industry and how to plan and design the curricula needed to foster the talent required for industrial development. Therefore, to establish a basis for the solution of this problem, this study aims to establish professional competency indices and their subindices for the solar energy industry. The research may contribute, firstly, as a basis for the planning and designing of the curriculum for the training of engineers in higher education and, secondly, in the industrial sector, as an important reference for enterprises needing to select, train, and utilise their human resources or to cultivate management's successors.

## 2. Theoretical Background

The solar industry requires highly talented professionals. Competence-based and resource-based theories have been regarded as two important approaches to supporting the competency and developing the talent of professionals working in the solar industry. Only if workers have the appropriate competencies can they perform their tasks satisfactorily, making competency extremely important [11, 12]. "Competency," here, can be defined as a prerequisite for a particular occupation, or a set of performance standards, as well as the ability to complete the work/task [13]. In competence-based theory, I-O psychologists generally take the competency model formed by KSAOs (Knowledge, Skill, Ability, Others) as a suitable way to describe the critical capabilities required for performing a particular job [14]. Therefore, "Competency" can also be regarded as the set of capabilities that you should have when engaging in a particular task [15]. This competency can be further subdivided into general competency, management competency, professional competency, and core competency [16]. With the professional competency expected by the employer establishing a baseline, the techniques and skills exhibited by technical personnel allow prediction of their job performance [17, 18].

The resource-based approach regards professional talent as a rare, unique, irreplaceable but intangible asset of the solar industry, on the basis of which the competitive advantage of the enterprise can be created [19]. In other words, the resource-based approach considers the unique resources

within the enterprise as the fundamental source of competitive advantage of solar industry enterprises but with the talent of the individual engineers working there forming the core of this unique resource [2]. When an individual possesses the professional competencies required for performing his job, he owns the resources value desired by the enterprise, allowing him to be hired from the labour market. Therefore, following Sandberg and Pinnington [13], this study defines professional competencies as a set of capabilities possessed by university graduates allowing them to successfully perform the task when engaged in professional missions in the field of solar energy.

## 3. Dimensions of Professional Competency

In their study of solar company executives, Chang and Kuo [2] pointed out that solar executives should have a common core of dynamic competencies listed as follows: environmental sensing competencies, learning absorption competency, social networking competencies, and coordination and integration competencies. In addition, particular dynamic competencies required will include competency in discerning market growth momentum, competency in mastering market timing, and competency in changing or creating customer demand. Meanwhile, from the route of structuralism, the various dimensions of professional competency, as seen by the engineering education certification standards of ABET [20], include the important core competencies of problem solving, innovation, and information competency. The problem of competency gaps that these different approaches throw up was explored by Abdullah et al. [21] with their advocating of the idea of soft and hard skills, the former including ICT skills, personal qualities, thinking skills, interpersonal skills, management skills, and communication skills. Cilliers [22] regarded that these soft skills should also include "ability to produce reports," while the hard skills should include "practical usage of software tools," "circuit construction," "operating and troubleshooting systems and equipment," "process, control, and installation," and "quality and reliability testing". On the other hand, in "Solar Energy Systems Engineers", O'net [4] lists the titles of this job, ten major tasks of engagement required by the job, and data collected for each competency application including tools and technology, interests, work values, wages, and employment trends.

In summary, based on the 51 competency standards in O'net [4] and the work of Cilliers [22], Kuo and Sheen [23], Abdullah et al. [21], and others, this study drafted 11 professional competencies (with their subcompetencies) as follows: materials development and application competency, photovoltaic technology competency, cell manufacturing technology competency, biotechnology competency, chemical technology competency, power generation and power competency, process development and improvement competency, data collection and analysis competency, regulation competency, green energy beliefs competency, and work attitudes and values competency.

TABLE 1: The expert sampling list of Taiwan's solar enterprises.

Distribution	Business item	The number of manufacturers	%	The size of sample collected (%)
Upstream	Silicon materials, silicon wafer materials	17	13.93	8 (47.06%)
Midstream	Solar cell	15	12.30	16 (34.04%)
	Solar cell module	18	14.73	
	Thin film solar cell module	9	7.38	
	Dye-sensitized solar cell	3	2.46	
	Concentrating solar cell module	2	1.64	
	Downstream		58	
	Solar PV system	39	31.98	
	Solar PV power converter	10	8.20	
	Solar PV access/supplier	9	7.38	
Total		122	100	45 (100%)

## 4. Methodology

*4.1. Literature Analysis.* The aim is through literature analysis to obtain the professional competencies and subcompetencies that should be possessed by working solar engineers, as a basis for expert advisories and expert focus group discussion.

*4.2. Expert Advisory.* As they show the point of view of the enterprises employing engineers, the aim of the expert advisory is to establish the professional competency dimensions and to obtain the professional competencies required of working engineers, as expressed by company representatives. Samples were ten Taiwan solar companies listed on the stock market, two upstream in the solar raw materials industry, five midstream in the solar manufacturing industry, and three downstream in the solar module and integration industry, with subjects interviewed coming from middle and upper-level management.

*4.3. Focus Group Method.* The aim is to edit the draft subcompetencies developed for each professional competency dimension. The composition of expert groups is shown in Table 1. In terms of sampling, of the total existing 122 Taiwan solar manufacturers, representatives from the upstream solar raw materials industry (e.g., pure metals, iron and titanium alloys and other metal materials, and silicon chip production); the midstream solar manufacturing industry (e.g., amorphous silicon thin film solar cells and modules; monocrystalline and polycrystalline silicon solar cells and modules; silicon solar cells and modules; polysilicon solar cells and modules; and silicon thin film solar cells), and the downstream solar module and integration industry (e.g., small-scale solar power systems, solar electric power converters, and solar power systems) were gathered. In three focus group meetings, industrial and academic experts were jointly invited to discuss the draft, with the invited industrial experts coming from manufacturers with a scale of more than 30 employees, and totalling 45 experts as working-level

heads. From academia, nine scholars within the field were also invited to participate in the discussion.

## 5. Results and Discussion

This study found that solar industry professional competency is composed of 11 professional dimensions, with each professional competency composed of several subdimensions, as shown in Table 2. In the application of research methods in response to a need to establish the professional competencies required in an industry, the DACUM (Develop A Curriculum) method is usually used, with the experts using brainstorming techniques to obtain the needed professional skill directory/listing [24]. On the other hand, in the Delphi method, the experts' anonymous input is used to seek advisory consistency between the professional competency and its subcompetencies [25]. In the V-tech method, the enterprise survey emphasises a large sample within a single industry to get a list of general professional competencies needed for engagement in the specific professional career [26]. This study adopted the expert advisory method, emphasising qualitative expert interviews through close contact with benchmark solar companies listed on the stock market. Together with the focus group method, through discussions with solar industry experts, the professional competencies and their subcompetencies in the solar industry were thus confirmed. Therefore, the research method adopted by this study can essentially be regarded as an application of the DACUM method.

In terms of subcompetencies, the professional engineers sought in the solar job market not only necessarily possess technical knowledge and hard skills but also need soft skills. The talent to develop materials and processes that satisfy market demand is composed of soft and hard skills [27, 28]. Each competency dimension and subdimension obtained by this study are composed of three fields, namely, knowledge, skill, and attitude. Moreover, all the important soft skills are also fully covered in the study, at the same time as both the

TABLE 2: The solar professional competency dimensions and connotations.

Dimension	Competency connotation
(1) Materials development and application competency	<ol style="list-style-type: none"> <li>(1) Understand the materials development process</li> <li>(2) Understand the solar cell principle</li> <li>(3) Understand solar light-absorbing material type and characteristic differences</li> <li>(4) Understand polymer characteristics and energy development</li> <li>(5) Understand the polymer application technology</li> </ol>
(2) Photovoltaic technology competency	<ol style="list-style-type: none"> <li>(1) Understand the principles of solid state physics</li> <li>(2) Understand the characteristics of semiconductor materials</li> <li>(3) Understand core photovoltaic technology</li> <li>(4) Understand the main problems of the solar industry</li> <li>(5) For solar industry issues, be able to propose solutions</li> </ol>
(3) Cell manufacturing technology competency	<ol style="list-style-type: none"> <li>(1) Understand solar cell material type and characteristic differences</li> <li>(2) Analyse the application relationship between cell type and energy</li> <li>(3) Understand the industry's process and packaging technology</li> <li>(4) Understand the technology of cell manufacturing</li> </ol>
(4) Biotechnology competency	<ol style="list-style-type: none"> <li>(1) Have integrated the interdisciplinary knowledge of the solar industry</li> <li>(2) Understand the concepts of energy and renewable energy</li> <li>(3) Understand the application of relevant energy and renewable energy knowledge</li> <li>(4) Be able to apply relevant knowledge of energy and renewable energy</li> <li>(5) Understand the relations between solar panel power generation and the environment</li> </ol>
(5) Chemical technology competency	<ol style="list-style-type: none"> <li>(1) Understand the principles of chemistry, physical chemistry, analytical chemistry, and organic chemistry</li> <li>(2) Understand interdisciplinary engineering-related processes</li> <li>(3) Have constructed an energy integration platform</li> <li>(4) Understand materials analysis techniques</li> <li>(5) Understand physical and chemical technologies</li> </ol>
(6) Power generation and power competency	<ol style="list-style-type: none"> <li>(1) Understand monitor principles</li> <li>(2) Understand solar panel principles</li> <li>(3) Understand the principles and structure of solar power generation</li> <li>(4) Understand the relevant principles of solid state physics</li> <li>(5) Understand thin film technology</li> </ol>
(7) Process development and improvement competency	<ol style="list-style-type: none"> <li>(1) Understand the key technology of packaging materials</li> <li>(2) Understand the relevant principles of process development</li> <li>(3) Be able to apply relevant knowledge to improve processes</li> <li>(4) Have skills in assembly technology of solar products</li> <li>(5) Possess knowledge of industrial safety and health principles</li> </ol>
(8) Data collection and analysis competency	<ol style="list-style-type: none"> <li>(1) Understand the principles of industrial safety</li> <li>(2) Understand the principles of environmental pollution prevention and control</li> <li>(3) Be able to explain solar cell and energy efficiency and carbon reduction relationships</li> <li>(4) Know how to collect and analyse data on demand</li> <li>(5) Understand the represented significance of data</li> </ol>
(9) Regulation competency	<ol style="list-style-type: none"> <li>(1) Understand relevant solar power policies</li> <li>(2) Understand relevant renewable energy policies</li> <li>(3) Understand the renewable energy incentives</li> </ol>
(10) Green energy belief competency	<ol style="list-style-type: none"> <li>(1) Be engaged in enhancing self-skills, professional knowledge</li> <li>(2) Identify with green beliefs</li> <li>(3) Possess the desire to implement environmental protection, sustainable management, and development measures</li> <li>(4) Identify with solar power industry professional advancement, enabling promotion of green energy industry development</li> </ol>
(11) Work attitudes and values	<ol style="list-style-type: none"> <li>(1) Have a sense of mission and a passion for work</li> <li>(2) Have positive work values</li> <li>(3) Exhibit a positive professionalism</li> <li>(4) Have a sense of integrity and business ethics</li> <li>(5) Embody the spirit of innovation and research</li> </ol>

mental model and system concepts are adopted [29], in line with the requirement to foster professional talent.

## 6. Conclusions

Although international competition in green energy is fierce, fuelled by a demand for human technology that will achieve global ecological sustainability, the industry still attracts universal attention. Since talent is the force that drives industrial development, this study selected the industry, and solar energy in particular, as the topic of research. The study is grounded in competence-based and resource-based theories, regarding solar energy professionals to be the important human resource of enterprises, and understanding they need to possess various basic competencies to perform their job duties. Therefore, this study selected benchmarking enterprises that are listed on the stock market from the upstream, midstream, and downstream sectors of the Taiwanese solar energy industry as the source of its expert advisories for its professional competency dimensions, coupled with focus group meetings to establish professional solar industry sub-competencies. In summary, this study found 11 professional competencies, with subcompetencies, which can be regarded as professional standards required by university graduates to become working professional engineers.

In terms of practical applications, the results of this study can be used as selection criteria for enterprises in the field of solar energy for the further development of their staff or as professional-level assessment criteria for recruitment and promotion. In the area of university education, the results of this study can be also used as a basis for planning and designing curricula for programs in renewable and sustainable energy. In the future, the implementation of such curricula is expected to nurture the talent appropriate to the needs of the solar industry, benefitting the industry by closing the gap between those needs and the present competencies of university graduates. Therefore, this study specially demonstrates the contributions to engineering education associated with a concentration on the solar industry's training needs, at the same time as it benefits the industry's own selection and employment need.

As for research restrictions, the study only focuses on professional competencies common to all solar enterprises and does not focus on professional competencies required by specific enterprises upstream, midstream, or downstream. This study also did not explore the subcompetencies of a single solar expertise, that of process design, software and hardware technologies, and tools applications. We invite interested researchers to carry out further studies.

## Conflict of Interests

The authors declare that there is no conflict of interests regarding the publication of this paper.

## Acknowledgments

The authors acknowledge the financial support of NSC 102-3113-S-003-008-G and NSC 102-3113-S-262-001.

## References

- [1] MOEAEC, "Green energy industry information net," 2014, <http://www.taiwangreenenergy.org.tw/>.
- [2] C. C. Chang and C. G. Kuo, "Exploring dynamic capabilities of executives of solar product manufacturers," *African Journal of Business Management*, vol. 7, no. 40, pp. 4188–4198, 2013.
- [3] C. G. Kuo, C. F. Yang, M. J. Kao et al., "An analysis and research on the transmission ratio of dye sensitized solar cell photoelectrodes by using different etching process," *International Journal of Photoenergy*, vol. 2013, Article ID 151973, 8 pages, 2013.
- [4] O'net, "17-2199.11—Solar Energy Systems Engineers," 2014, <http://www.onetonline.org/link/summary/17-2199.11>.
- [5] C. Acikgoz, "Renewable energy education in Turkey," *Renewable Energy*, vol. 36, no. 2, pp. 608–611, 2011.
- [6] R. Dalitz, P. Toner, and T. Turpin, *VET and the Diffusion and Implementation of Innovation in the Mining, Solar Energy and Computer Games Sectors*, Department of Education, Employment and Workplace Relations, Australian Government, 2011.
- [7] H.-Y. Liu and C.-W. Hsu, "Antecedents and consequences of corporate diversification: a dynamic capabilities perspective," *Management Decision*, vol. 49, no. 9, pp. 1510–1534, 2011.
- [8] C. C. Chang, "An IPA-embedded model for evaluating creativity curricula," *Innovations in Education and Teaching International*, vol. 51, no. 1, pp. 59–71, 2014.
- [9] MIC, "Outlook for the Global Emerging Solar Photovoltaic Market, 2011 Recap and 2012 Forecast," Market Intelligence & Consulting Institute, 2014, [http://mic.iii.org.tw/english/store/en\\_3\\_mic\\_store\\_1.2.1.1.asp?doc\\_sqno=9010](http://mic.iii.org.tw/english/store/en_3_mic_store_1.2.1.1.asp?doc_sqno=9010).
- [10] C. G. Kuo, C. F. Yang, L. R. Hwang, and J. S. Huang, "Effects of titanium oxide nanotube arrays with different lengths on the characteristics of dye-sensitized solar cells," *International Journal of Photoenergy*, vol. 2013, Article ID 650973, 6 pages, 2013.
- [11] Z. Lim, C. Anderson, and S. McGrath, "Professional skills development in a resource-poor setting: the case of pharmacy in Malawi," *International Journal of Educational Development*, vol. 32, no. 5, pp. 654–664, 2012.
- [12] C. C. Chang, "Improving employment services management using IPA technique," *Expert Systems with Applications*, vol. 40, no. 17, pp. 6948–6954, 2013.
- [13] J. Sandberg and A. H. Pinnington, "Professional competence as ways of being: an existential ontological perspective," *Journal of Management Studies*, vol. 46, no. 7, pp. 1138–1170, 2009.
- [14] F. J. Landy and J. M. Conte, *Work in the 21st Century*, McGraw-Hill, New York, NY, USA, 2004.
- [15] C. C. Chang, "Exploring IT entrepreneurs' dynamic capabilities using Q-technique," *Industrial Management & Data Systems*, vol. 112, no. 8, pp. 1201–1216, 2012.
- [16] D. Hellriegel, S. E. Jackson, and J. W. Slocum, *Management: A Competency Based Approach*, Winter Ventures, Hanover, Pa, USA, 1998.
- [17] S. J. Hysong, "The role of technical skill in perceptions of managerial performance," *Journal of Management Development*, vol. 27, no. 3, pp. 275–290, 2008.
- [18] C. C. Chang, "Building an approach to evaluate capabilities development," *Pensee Journal*, vol. 76, no. 1, pp. 167–179, 2014.
- [19] J. B. Barney, "Firm resources and sustained competitive advantage," *Journal of Management*, vol. 17, no. 1, pp. 99–120, 2000.
- [20] ABET, "Criteria for accrediting engineering programs 2012-2013," 2013, <http://www.abet.org/DisplayTemplates/DocsHandbook.aspx?id=3143>.

- [21] A. G. K. Abdullah, S. H. Keat, M. H. Abdullah, and M. Purba, "Mismatch between higher education and employment in Malaysian electronic industry: an analysis of the acquired and required competencies," *International Journal of Engineering Education*, vol. 28, no. 5, pp. 1232–1242, 2012.
- [22] C. B. Cilliers, "Student perception of academic writing skills activities in a traditional programming course," *Computers & Education*, vol. 58, no. 4, pp. 1028–1041, 2012.
- [23] C.-G. Kuo and B.-J. Sheen, "Seaweed chlorophyll on the light-electron efficiency of DSSC," *Journal of the Chinese Chemical Society*, vol. 58, no. 2, pp. 186–190, 2011.
- [24] O. Gazman, "Industry-based skills standards for building operators—a business case," *Strategic Planning for Energy and the Environment*, vol. 32, no. 3, pp. 25–38, 2013.
- [25] R. L. Jacobs and M. J. Bu-Rahmah, "Developing employee expertise through structured on-the-job training (S-OJT): an introduction to this training approach and the KNPC experience," *Industrial and Commercial Training*, vol. 44, no. 2, pp. 75–84, 2012.
- [26] C. Dede, "Emerging influences of information technology on school curriculum," *Journal of Curriculum Studies*, vol. 32, no. 2, pp. 281–303, 2000.
- [27] H. Baytiyeh, "Disparity between college preparation and career demands for graduating engineers," *Journal of Engineering Education*, vol. 28, no. 5, pp. 1221–1231, 2012.
- [28] P. C. Huang, C. H. Huang, M. Y. Lin, C. Y. Chou, C. Y. Hsu, and C. G. Kuo, "The effect of sputtering parameters on the film properties of molybdenum back contact for CIGS solar cells," *International Journal of Photoenergy*, vol. 2013, Article ID 390824, 8 pages, 2013.
- [29] C. Capelo and J. F. Dias, "A feedback learning and mental models perspective on strategic decision making," *Educational Technology Research and Development*, vol. 57, no. 5, pp. 629–644, 2009.

## Research Article

# Growth of Anodic Aluminum Oxide Templates and the Application in Fabrication of the BiSbTe-Based Thermoelectric Nanowires

Chin-Guo Kuo,<sup>1</sup> Yuan-Tai Hsieh,<sup>2</sup> Cheng-Fu Yang,<sup>3</sup> Ching-Ho Huang,<sup>4</sup> and Chia-Ying Yen<sup>1</sup>

<sup>1</sup> Department of Industrial Education, National Taiwan Normal University, Taipei 106, Taiwan

<sup>2</sup> Department of Electronic Engineering, Southern Taiwan University, Tainan 710, Taiwan

<sup>3</sup> Department of Chemical and Materials Engineering, National University of Kaohsiung, Kaohsiung 811, Taiwan

<sup>4</sup> Taipei Municipal Nangang Vocational High School, Taipei 115, Taiwan

Correspondence should be addressed to Cheng-Fu Yang; [cfyang@nuk.edu.tw](mailto:cfyang@nuk.edu.tw)

Received 13 January 2014; Revised 13 March 2014; Accepted 13 March 2014; Published 9 April 2014

Academic Editor: Ho Chang

Copyright © 2014 Chin-Guo Kuo et al. This is an open access article distributed under the Creative Commons Attribution License, which permits unrestricted use, distribution, and reproduction in any medium, provided the original work is properly cited.

A two-step electrochemical anodization was used to form the anodic aluminum oxide (AAO) thin films with nanotube arrays of self-organized honeycomb structure. Al foil was anodized in 10% sulfuric acid ( $H_2SO_4$ ) and 3% oxalic acid ( $H_2C_2O_4$ ) at 25°C at constant voltage of 40 V for 60 min for two times. Ethylene glycol ( $C_2H_6O_2$ ) was used as a solution and 0.3 M potassium iodide (KI) was used to improve the solution's conductivity. Different electrolyte concentrations of  $Bi(NO_3)_3 \cdot 5H_2O$ ,  $SbCl_3$ , and  $TeCl_4$  were added into  $KI-C_2H_6O_2$  solution and the cyclic voltammetry experiment was used to find the reduced voltages of  $Bi^{3+}$ ,  $Sb^{3+}$ , and  $Te^{4+}$  ions. The potentiostatic deposition and pulse electrodeposition (PED) processes were used to deposit the  $(Bi,Sb)_{2-x}Te_{3+x}$ -based materials. Field-emission scanning electron microscope and energy dispersive spectrometers were used to analyze the compositions of the deposited  $(Bi,Sb)_{2-x}Te_{3+x}$ -based materials. After finding the optimal deposition parameter of the PED process the AAO nanotube arrays were used as the templates to deposit the  $(Bi,Sb)_{2-x}Te_{3+x}$ -based thermoelectric nanowires.

## 1. Introduction

Thermoelectric energy conversion has attracted much interest as a possible application for environmentally friendly electric-power generators and highly reliable, accurate temperature controllable refrigerators used as electronic devices because it is one of the simplest technologies applicable to energy conversion [1–4]. The efficiency of thermoelectricity is governed by a basic property of thermoelectric material, and the figure of merit of a thermoelectric material is defined by

$$ZT = \frac{S^2 T \delta}{(\kappa_e + \kappa_l)}, \quad (1)$$

where  $T$  is the absolute temperature. As (1) shows, optimally thermoelectric materials will have high electrical conductivity ( $\delta$ ), low thermal conductivity (the electron thermal

conductivity  $\kappa_e$  and the lattice thermal conductivity  $\kappa_l$ ), and high thermoelectric power ( $S$ , Seebeck coefficient). For a material to be good in thermoelectric application, it must have a high thermoelectric figure of merit  $ZT$ . Much of the recent work on thermoelectric materials has focused on the ability of heterostructures and quantum confinement to increase efficiency over bulk materials [5–7].

So far, the thermoelectric materials used in applications have all been in bulk (3D) and thin film (2D) forms. However, Hicks and Dresselhaus had pointed out that low-dimensional materials have better efficiency than bulk ones due to low-dimensional effects on both charge carriers and lattice waves [8]. However, since the 1960s only slow progress has been made in enhancing  $ZT$  [9], either in  $(Bi,Sb)_{2-x}Te_{3+x}$ -based alloys or in other thermoelectric material. The validity of attaining higher  $ZT$  value in low-dimensional systems has been experimentally demonstrated on  $Bi_2Te_3/Sb_2Te_3$  superlattices [10] and on  $PbTe/PbSeTe$

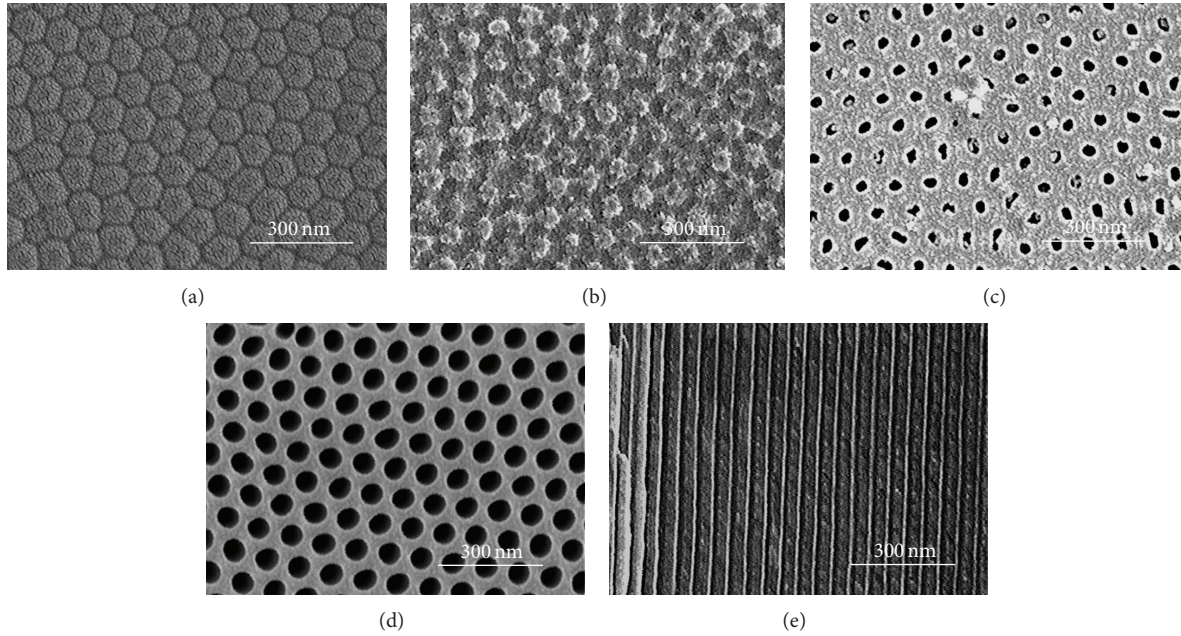


FIGURE 1: 3 wt%-KOH was used to remove the barrier layer as a function of etched time: (a) 0 min, (b) 3 min, (c) 6 min, and (d) 7.5 min, respectively, and (e) side view of nanotubes.

quantum dots [11] with  $ZT \sim 2.4$  and 1.6, respectively, at 300 K. Therefore, nanowires are potentially structured to get good thermoelectrical systems for application. In the past, electrochemical deposition was a useful method to deposit the thin films in different morphologies, including thin films and nanowires [12]. Various techniques, including chemical vapor deposition [10], molecular beam epitaxy [13], vapor-liquid-solid growth process [14], and hydrothermal process [15], have been applied to synthesize thin film-, nanowire-, or nanotube-structured thermoelectric materials. Compared to those methods, electrodeposition is one of the most cost-effective techniques to fabricate the nanostructured materials [16]. Bismuth telluride- ( $\text{Bi}_2\text{Te}_3$ -) [17] and  $(\text{Bi,Sb})_2\text{Te}_3$ -based alloys [18] are very attractive thermoelectric (TE) materials due to their high energy conversion efficiency at ambient temperature for achieving power generation without requiring any driving parts or cooling systems in electronic devices. In this study, we tried to investigate a new method for fabrication of the  $(\text{Bi,Sb})_{2-x}\text{Te}_{3+x}$ -based thermoelectric materials with one-dimension (1D) structure. Anodic aluminum oxide (AAO) thin films with the nanotube structure were used as template to fabricate the  $(\text{Bi,Sb})_{2-x}\text{Te}_{3+x}$ -based nanowires. At first, ethylene glycol ( $\text{C}_2\text{H}_6\text{O}_2$ ) was used as the solution and 0.3 M potassium iodide (KI) was added to improve the conductivity of the solution. Electrolyte formulas with different concentrations of  $\text{Bi}(\text{NO}_3)_3 \cdot 5\text{H}_2\text{O}$ ,  $\text{SbCl}_3$ , and  $\text{TeCl}_4$  were used to find the effects of ionic concentrations on the composition fluctuation of the reduced  $(\text{Bi,Sb})_{2-x}\text{Te}_{3+x}$ -based materials by using the potentiostatic deposition process. Finally, the ethylene glycol solution contains 0.015 M  $\text{Bi}(\text{NO}_3)_3 \cdot 5\text{H}_2\text{O}$ , 0.005 M  $\text{SbCl}_3$ , and 0.0075 M  $\text{TeCl}_4$  and was used to deposit  $(\text{Bi,Sb})_{2-x}\text{Te}_{3+x}$ -based nanowires in AAO

templates by means of the pulse electrodeposition (PED) process.

## 2. Experimental Details

For the AAO templates, annealed high-purity (99.99%) aluminum foil was electropolished in a mixture of  $\text{HClO}_4$  (25% in volume ratio) and  $\text{C}_2\text{H}_5\text{OH}$  (75%) until the root-mean-square surface roughness of a typical  $10 \mu\text{m} \times 10 \mu\text{m}$  area was 1 nm. In this study a two-step electrochemical anodization was used to form the AAO template [19]. For the first anodization process, the foil was anodized in 10% sulfuric acid ( $\text{H}_2\text{SO}_4$ ) and 3% oxalic acid ( $\text{H}_2\text{C}_2\text{O}_4$ ) at  $25^\circ\text{C}$  at constant voltage of 40 V for 5 h, for that the AAO substrates with nanotube arrays of self-organized honeycomb structure were obtained. Then the semifinished AAO templates were produced and subsequently the thick oxide was stripped away by immersing the AAO samples in a mixture containing 2 wt% chromic acid and 6 wt% phosphoric acid at  $60^\circ\text{C}$ . The second anodization process, which was similar to the first stage, was carried out until the remaining Al sample was completely anodized, and the finished AAO templates were thus fabricated [20]. Nevertheless, we further widened the pores of AAO templates by using a 5 wt% phosphoric acid solution at  $25^\circ\text{C}$  for 30 min. The cylindrical nanotubes penetrated the entire thickness of the AAO templates. As Figure 1(a) shows, the hole diameter of each pore was approximately 70 nm and the pitch between one neighboring pores, as Figure 1(b) shows, was about 100 nm. In order to deposit the  $(\text{Bi,Sb})_{2-x}\text{Te}_{3+x}$ -based nanowires the barrier layer between the AAO nanotubes and Al plate should be removed.

The 3 wt%-KOH was used as the etched electrolyte solution; Figures 1(a)–1(d) show the effect of the KOH-etched time; 75 min was enough to remove barrier layer. For that, the cylindrical nanotubes penetrated the entire thickness of the AAO templates; as Figure 1(e) shows, the hole diameter of each tube was approximately 60~65 nm and the hole wall of each tube was around 35~40 nm.

In the conventional direct current (DC) plating, only one parameter of current density ( $I$ ) can be varied. But in pulse electrodeposition (PED) process three independent variables, including (a) on time ( $T_{on}$ ), (b) off time ( $T_{off}$ ), and (c) peak current density (IP), can be used as the independent variables. For that, the PED process was used to deposit the  $(\text{Bi, Sb})_{2-x}\text{Te}_{3+x}$ -based thermoelectric nanomaterials and nanowires. In pulse current (PC), the duty cycle corresponding to the percentage of total time of a cycle is given by [21]

$$\text{Duty cycle} = \frac{T_{on}}{(T_{off} + T_{on})} = T_{on}f, \quad (2)$$

where  $f$  is frequency, defined as the reciprocal of the cycle time. That is,

$$\text{Frequency } (f) = \frac{1}{(T_{off} + T_{on})} = \frac{1}{T}. \quad (3)$$

PC will deposit metal at the same rate as the provided DC average pulse current density equals the latter. The average current density (IA), in pulse plating, is defined as

$$\text{IA} = \text{peak current (IP)} \times \text{duty cycle}. \quad (4)$$

The successfully practical applications of the nanostructured thermoelectric devices must investigate a cost-effective and high throughput fabrication process. At first, potentiostatic deposition process was used as the deposition process, ethylene glycol ( $\text{C}_2\text{H}_6\text{O}_2$ ) was used as a solution, and 0.3 M potassium iodide (KI) was added to improve the conductivity of the solution.  $\text{Bi}(\text{NO}_3)_3 \cdot 5\text{H}_2\text{O}$ ,  $\text{SbCl}_3$ , and  $\text{TeCl}_4$  were used as the electrolyte sources. The effect of electrolyte concentrations on the compositions of the deposited  $(\text{Bi, Sb})_{2-x}\text{Te}_{3+x}$ -based materials was investigated. Next, the duration of  $T_{off}$  ( $T_{on}$  was set at 0.2 s) and the reduced voltage during the duration of  $T_{on}$  were changed to find the optimal deposition parameters to get the  $(\text{Bi, Sb})_{2-x}\text{Te}_{3+x}$ -based materials with  $(\text{Bi} + \text{Sb})/\text{Te}$  atomic ratio close to 2/3. Finally, deposition of  $(\text{Bi, Sb})_{2-x}\text{Te}_{3+x}$ -based nanowires in AAO templates was investigated by means of pulse deposition process by using the ethylene glycol solution containing 0.015 M  $\text{Bi}(\text{NO}_3)_3 \cdot 5\text{H}_2\text{O}$ , 0.005 M  $\text{SbCl}_3$ , 0.0075 M  $\text{TeCl}_4$ , and 0.3 M KI. The field-emission scanning electron microscope (FESEM) and energy dispersive spectrometers (EDS) were used to observe the morphology and analyze the composition of the deposited  $(\text{Bi, Sb})_{2-x}\text{Te}_{3+x}$  materials and nanowires.

### 3. Results and Discussion

At first, we used the cyclic voltammetry experiment to find the optimally reduced voltages of  $\text{Bi}^{3+}$ ,  $\text{Sb}^{3+}$ , or  $\text{Te}^{4+}$  ions, respectively. The working electrode potential was linearly

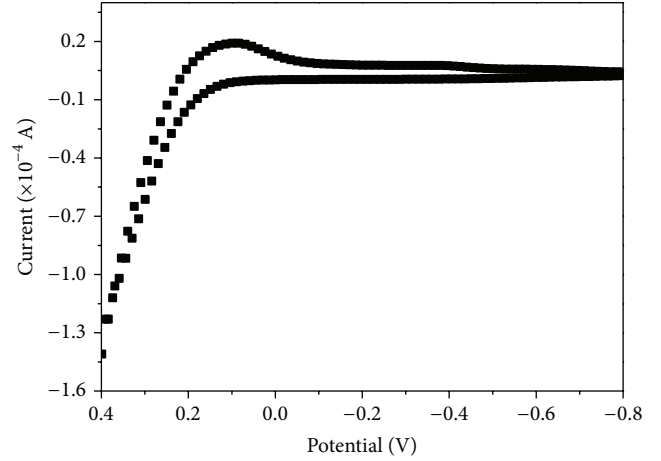


FIGURE 2: Cyclic voltammetry curve of the 0.3 M KI in ethylene glycol.

ramped versus time like linear sweep voltammetry, and the experiment's scan rate was 10 mV/sec and the scan range is 0.4 V to  $-0.7$  V. If only pure ethylene glycol ( $\text{C}_2\text{H}_6\text{O}_2$ ) was used as analyte, the current peak for the reduced and oxidized reactions was not observed (not shown here). If only 0.3 M KI was added into  $\text{C}_2\text{H}_6\text{O}_2$  as electrolyte, the current peak for the reduced and oxidized reactions was not observed in the range of 0.20 V to  $-0.70$  V (not shown here). As the voltage was in the range of 0.20 V to 0.40 V, the oxidized current increased, as Figure 2 shows. Those results prove that the ethylene glycol is used as the solvent, KI can be added to improve the conductivity, and they will not influence the results of the cyclic voltammetry deposition. And next, 0.01 M  $\text{Bi}(\text{NO}_3)_3 \cdot 5\text{H}_2\text{O}$ , 0.01 M  $\text{SbCl}_3$ , and 0.01 M  $\text{TeCl}_4$  each alone was added and pure ethylene glycol was used as analyte. The reduced reactions found that starting reduction voltages of  $\text{Bi}^{3+}$ ,  $\text{Sb}^{3+}$ , and  $\text{Te}^{4+}$  ions were  $-0.23$  V,  $-0.23$  V, and 0.20 V, respectively (not shown here). The results of the cyclic voltammetry curves suggest that  $\text{Te}^{4+}$  will be the first ions being reduced into metal.

If 0.01 M  $\text{Bi}(\text{NO}_3)_3 \cdot 5\text{H}_2\text{O}$  and 0.01 M  $\text{TeCl}_4$  were coadded in pure ethylene glycol, the cyclic voltammetry curve was as shown in Figure 3; if 0.01 M  $\text{Bi}(\text{NO}_3)_3 \cdot 5\text{H}_2\text{O}$ , 0.01 M  $\text{SbCl}_3$ , and 0.01 M  $\text{TeCl}_4$  were all added in pure ethylene glycol, the cyclic voltammetry curve was as shown in Figure 4. The first reduced reaction in Figures 3 and 4 started at around 0.2 V. From the results of using 0.01 M  $\text{Bi}(\text{NO}_3)_3 \cdot 5\text{H}_2\text{O}$ , 0.01 M  $\text{SbCl}_3$ , and 0.01 M  $\text{TeCl}_4$  each alone we can confirm that is the reduction process of the  $\text{Te}^{4+}$  ions. Those results suggest that, as large negative voltage was used as the reduced voltage, the deposited compositions are composed of Bi, Sb, and Te. The reduction of  $\text{Bi}^{3+}$ ,  $\text{Sb}^{3+}$ , and  $\text{Te}^{4+}$  ions is not unique; they cannot be reduced alone by electrodeposition but can be reduced when codeposited with other elements, defined as induced codeposition. As ethylene glycol is used as analyte, the induced codeposition process, which is found in using water as analyte, will not happen. The large difference in the

TABLE 1: Effects of deposition voltage on the composition of the  $(\text{Bi,Sb})_{2-x}\text{Te}_{3+x}$ -based materials; the deposition time was 60 min. Electrolyte formula was (a) 0.03 M  $\text{Bi}(\text{NO}_3)_3 \cdot 5\text{H}_2\text{O}$  and 0.04 M  $\text{TeCl}_4$  (b) 0.01 M  $\text{Bi}(\text{NO}_3)_3 \cdot 5\text{H}_2\text{O}$ , 0.01 M  $\text{SbCl}_3$ , and 0.01 M  $\text{TeCl}_4$ , respectively.

Compositions	0.03 M $\text{Bi}(\text{NO}_3)_3 \cdot 5\text{H}_2\text{O}$ and 0.04 M $\text{TeCl}_4$		0.01 M $\text{Bi}(\text{NO}_3)_3 \cdot 5\text{H}_2\text{O}$ , 0.01 M $\text{SbCl}_3$ , and 0.01 M $\text{TeCl}_4$		
	Te	Bi	Sb	Te	Bi
0.0 V			0	94.5	5.5
-0.2 V	61.855	38.15	5.32	89.22	5.54
-0.3 V	63.48	36.52	37.35	44.05	18.61
-0.4 V	56.94	43.07	36.23	44.01	19.78
-0.5 V	64.1	35.9	41.42	33.72	24.86
-0.6 V	70.23	29.77	45.15	44.75	10.11

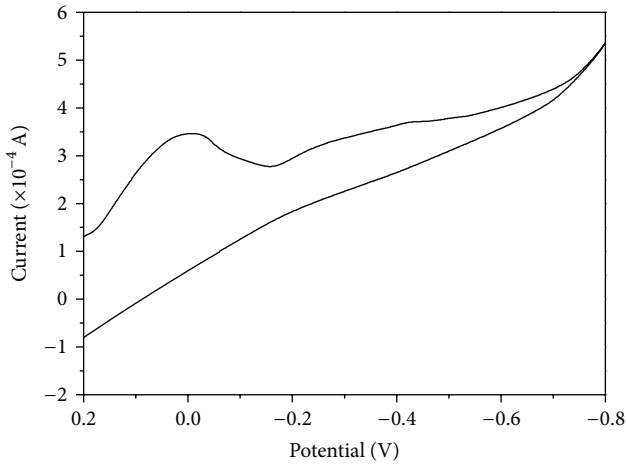


FIGURE 3: Cyclic voltammetry curve of 0.3 M KI, 0.01 M  $\text{Bi}^{3+}$ , and 0.01 M  $\text{Te}^{4+}$  in ethylene glycol.

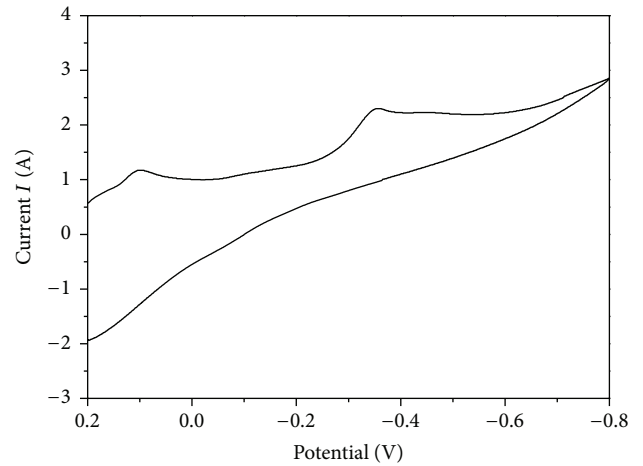


FIGURE 4: Cyclic voltammetry curve of 0.3 M KI, 0.01 M  $\text{Bi}^{3+}$ , 0.01 M  $\text{Sb}^{3+}$ , and 0.01 M  $\text{Te}^{4+}$  in ethylene glycol.

reduced voltages of  $\text{Bi}^{3+}$ ,  $\text{Sb}^{3+}$ , and  $\text{Te}^{4+}$  ions will cause this result.

When more than two different ions exist in the analyte and the cyclic voltammetry process under different reduced voltage is used, the obtained metallic compounds have different compositions. For that, the potentiostatic deposition process was used to deposit the  $(\text{Bi,Sb})_{2-x}\text{Te}_{3+x}$ -based materials. FESEM observation on the surface morphology and EDS analyses on the composition of the deposited  $(\text{Bi,Sb})_{2-x}\text{Te}_{3+x}$ -based materials were used to find the relationships between the deposition voltage and the deposition compositions. Table 1 shows the effects of different deposition voltage and different electrolyte formula on the composition of the deposited  $(\text{Bi,Sb})_{2-x}\text{Te}_{3+x}$ -based materials, and deposition time is 60 min.

At first, 0.03 M  $\text{Bi}(\text{NO}_3)_3 \cdot 5\text{H}_2\text{O}$  and 0.04 M  $\text{TeCl}_4$  were used as the electrolyte formulas to find the variation in the composition of the deposited  $\text{Bi}_{2-x}\text{Te}_{3+x}$ -based materials. The results in Table 1 show that, as reduced voltage was changed from -0.2 V to -0.6 V, the Bi/Te ratio first increased, reached a maximum value at -0.4 V, and then decreased with further increasing of reduced voltage. However, as the voltage was in the range of -0.2 V to -0.5 V, the composition of the deposited  $\text{Bi}_{2-x}\text{Te}_{3+x}$ -based materials was close to Bi/Te = 2/3

( $\text{Bi}_2\text{Te}_3$ ). When the electrolyte formula of 0.01 M  $\text{Bi}(\text{NO}_3)_3 \cdot 5\text{H}_2\text{O}$ , 0.01 M  $\text{SbCl}_3$ , and 0.01 M  $\text{TeCl}_4$  was used, as Table 1 shows, as the voltage was 0.0 V to -0.2 V, the main element was Te. The  $(\text{Bi,Sb})_{2-x}\text{Te}_{3+x}$  composition was obtained as the voltage was in the range of -0.30 V to -0.60 V.

The results in Table 1 reveal that the electrolyte formula and the deposition voltage are the two important parameters to influence the composition of the deposited  $(\text{Bi,Sb})_{2-x}\text{Te}_{3+x}$ -based materials. Table 1 also shows that, as the reduced voltage is changed from 0.00 V to -0.50 V, the concentrations of Bi and Sb increase; two reasons are believed to cause this result. First, the reduced reactions of  $\text{Bi}^{3+}$ ,  $\text{Sb}^{3+}$ , and  $\text{Te}^{4+}$  start at -0.23 V, -0.23 V, and 0.20 V. For that, as 0.00 V to -0.20 V is used, the main element in the deposited materials is Te. As the voltage is equal to and smaller than -0.30 V, the driving forces of reduction for Bi and Sb increase and the concentrations of Bi and Sb in the deposited materials increase. Second, the driving force for mass transfer is typical difference in chemical potential, though other thermodynamic gradients may couple with the flow of mass and drive it as well. As the voltage value is more negative (means the applied voltage is larger than the needed reduction voltage), the mass transfer effect will influence the composition of the deposited  $(\text{Bi,Sb})_{2-x}\text{Te}_{3+x}$

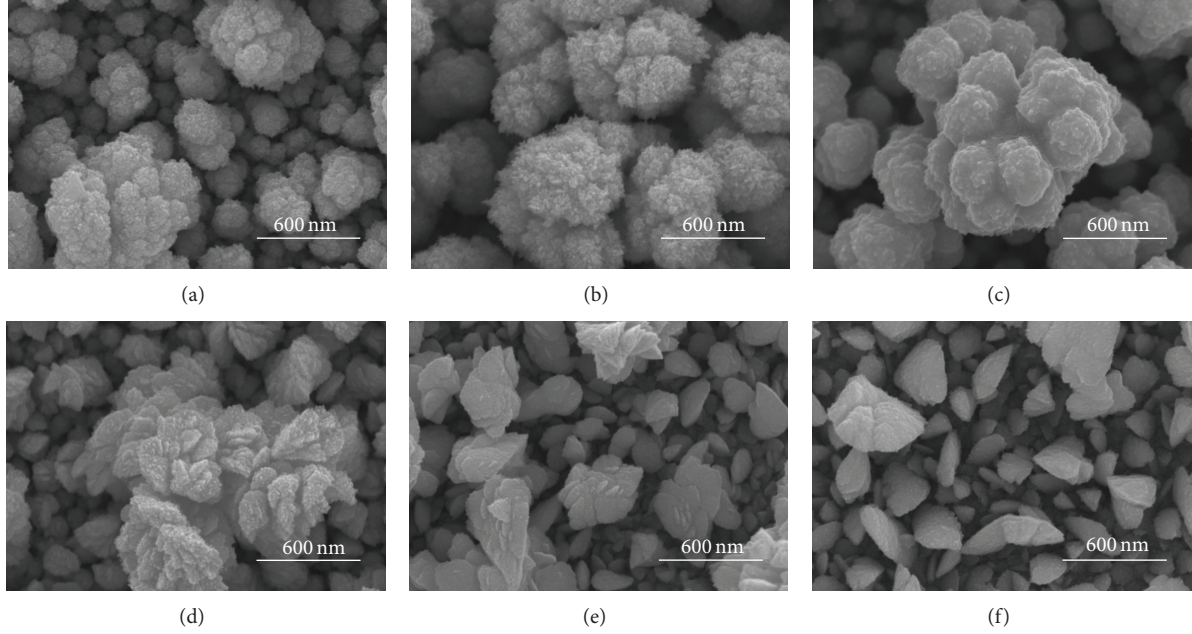


FIGURE 5: SEM micrographs of the electrolyte formula  $0.015 \text{ M Bi(NO}_3)_3 \cdot 5\text{H}_2\text{O}$ ,  $0.005 \text{ M SbCl}_3$ , and  $0.0075 \text{ M TeCl}_4$ ; pulse voltage was set at  $-0.4 \text{ V}$ ,  $T_{\text{on}}$  was set at  $0.2 \text{ s}$ , and  $T_{\text{off}}$  was changed: (a)  $T_{\text{off}} = 0.1 \text{ s}$ , (b)  $T_{\text{off}} = 0.4 \text{ s}$ , (c)  $T_{\text{off}} = 1 \text{ s}$ , (d)  $T_{\text{off}} = 1.6 \text{ s}$ , (e)  $T_{\text{off}} = 2 \text{ s}$ , and (f)  $T_{\text{off}} = 4 \text{ s}$ .

TABLE 2: Effects of pulse deposition parameters on the composition of the  $(\text{Bi,Sb})_{2-x}\text{Te}_{3+x}$  materials; (a) the bias voltage was set at  $-0.4 \text{ V}$ ,  $T_{\text{on}}$  was set at  $0.2 \text{ s}$ , and  $T_{\text{off}}$  was changed from  $0.1 \text{ s}$  to  $4 \text{ s}$ . (b)  $T_{\text{on}}$  and  $T_{\text{off}}$  were set at  $0.2 \text{ s}$  and  $1 \text{ s}$ , and the pulse voltage was changed.

Different $T_{\text{off}}$	Pulse (voltage = $-0.4 \text{ V}$ , $T_{\text{on}} = 0.2 \text{ s}$ )			Different voltage (V)	Pulse ( $T_{\text{on}} = 0.2 \text{ s}$ , $T_{\text{off}} = 1 \text{ s}$ )		
	Sb	Te	Bi		Sb	Te	Bi
$T_{\text{off}} = 0.1 \text{ s}$	7.09	31.29	61.63	$0.0 \text{ V}$	—	—	—
$T_{\text{off}} = 0.4 \text{ s}$	7.71	41.05	51.25	$-0.2 \text{ V}$	—	—	—
$T_{\text{off}} = 1 \text{ s}$	12.02	69.43	18.54	$-0.3 \text{ V}$	27.16	66.60	5.59
$T_{\text{off}} = 1.6 \text{ s}$	7.22	79.62	13.16	$-0.4 \text{ V}$	32.88	56.95	10.17
$T_{\text{off}} = 2 \text{ s}$	5.77	84.06	10.17	$-0.5 \text{ V}$	24.38	56.13	19.49
$T_{\text{off}} = 4 \text{ s}$	6.24	86.30	7.46	$-0.6 \text{ V}$	25.36	51.31	23.33

materials. The results in Table 1 also suggest that, as the concentrations of  $\text{Bi}^{3+}$ ,  $\text{Sb}^{3+}$ , and  $\text{Te}^{4+}$  ions are close to each other, a Te-rich composition will be obtained in the deposited  $(\text{Bi,Sb})_{2-x}\text{Te}_{3+x}$  materials.

When larger negative voltage is used as bias in the potentiostatic deposition process, the electrolyte concentrations (or ion diffusion effect) will influence the composition of the deposited  $(\text{Bi,Sb})_{2-x}\text{Te}_{3+x}$ -based materials. If we control the diffusion rates of ions ( $\text{Bi}^{3+}$ ,  $\text{Sb}^{3+}$ , and  $\text{Te}^{4+}$ ), we can regulate the composition of the deposited  $(\text{Bi,Sb})_{2-x}\text{Te}_{3+x}$ -based materials. For that, the pulse deposition process is used to deposit  $(\text{Bi,Sb})_{2-x}\text{Te}_{3+x}$ -based materials by using the electrolyte formula of  $0.015 \text{ M Bi(NO}_3)_3 \cdot 5\text{H}_2\text{O}$ ,  $0.005 \text{ M SbCl}_3$ , and  $0.0075 \text{ M TeCl}_4$ . The bias voltage was set at  $-0.40 \text{ V}$ , the duration of off time ( $T_{\text{off}}$ ) was changed from  $0.1 \text{ s}$  to  $4 \text{ s}$ , and the bias on time ( $T_{\text{on}}$ ) was set at  $0.2 \text{ s}$ . Table 2 first compares the results of the EDS analysis as a function of duration of  $T_{\text{off}}$ . As the duration of  $T_{\text{off}}$  was  $0.2 \text{ s}$ , the  $(\text{Bi} + \text{Sb})/\text{Te}$  atomic ratio was larger than  $2/3$  ( $2/3$  means close to  $(\text{Bi,Sb})_2\text{Te}_3$ ); as the duration of  $T_{\text{off}}$  was in the range of

$0.4 \text{ s} \sim 1 \text{ s}$ , the  $(\text{Bi} + \text{Sb})/\text{Te}$  atomic ratio was close to  $2/3$ ; as the duration of  $T_{\text{off}}$  was longer than  $1 \text{ s}$ , the Te atomic ratio was larger than  $70\%$ .

Table 2 also compares the variation in the composition of the deposited  $(\text{Bi,Sb})_{2-x}\text{Te}_{3+x}$ -based materials as the reduced voltage during the  $T_{\text{on}}$  state was changed, where  $T_{\text{on}}$  and  $T_{\text{off}}$  were set at  $0.2 \text{ s}$  and  $1 \text{ s}$  and the pulse voltage was changed from  $-0.3 \text{ V}$  to  $-0.6 \text{ V}$ . Also,  $0.015 \text{ M Bi(NO}_3)_3 \cdot 5\text{H}_2\text{O}$ ,  $0.005 \text{ M SbCl}_3$ , and  $0.0075 \text{ M TeCl}_4$  were used as the electrolyte formula. As Table 2 shows, as the reduced voltage was in the range of  $-0.3 \text{ V}$  to  $-0.6 \text{ V}$ , the atomic ratio of  $(\text{Bi} + \text{Sb})/\text{Te}$  was close to  $2/3$ . As the reduced voltage was in the range of  $-0.4 \text{ V}$  to  $-0.6 \text{ V}$ , the deposited  $(\text{Bi,Sb})_{2-x}\text{Te}_{3+x}$ -based materials revealed the p-typed thermoelectric property, because the Te atomic ratio was smaller than  $60\%$ . Those results prove that, as the mass transfer effect of  $\text{Te}^{4+}$  is controlled, the more  $\text{Bi}^{3+}$  and  $\text{Sb}^{3+}$  ions will be reduced into Bi and Sb and the composition of the deposited  $(\text{Bi,Sb})_{2-x}\text{Te}_{3+x}$ -based materials will be close to p-typed  $(\text{Bi,Sb})_2\text{Te}_3$ . Undoubtedly, the pulse deposition process can

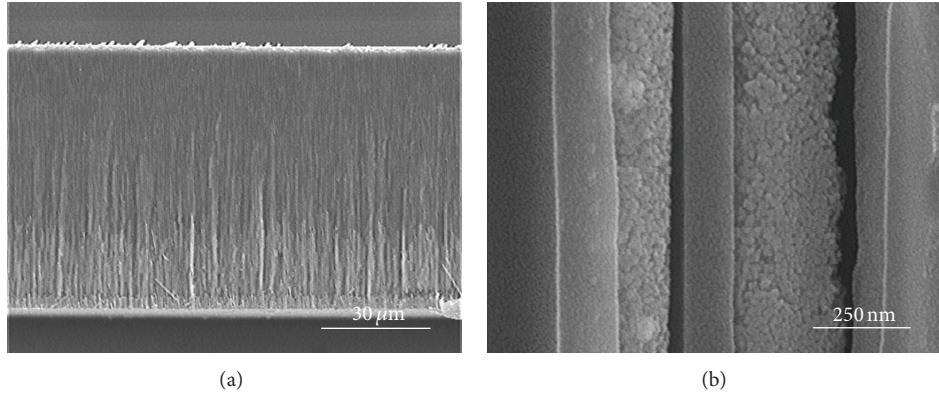


FIGURE 6: SEM micrographs of the  $(\text{Bi, Sb})_{2-x}\text{Te}_{3+x}$ -based nanowires; the bias voltage was set at  $-0.4\text{ V}$ ,  $T_{\text{on}}/T_{\text{off}}$  was  $0.2\text{ s}/0.6\text{ s}$ , and the electrolyte formula was  $0.015\text{ M Bi}(\text{NO}_3)_3 \cdot 5\text{H}_2\text{O}$ ,  $0.005\text{ M SbCl}_3$ , and  $0.0075\text{ M TeCl}_4$ . (a) Side view with smaller ratio and (b) side view with larger ratio.

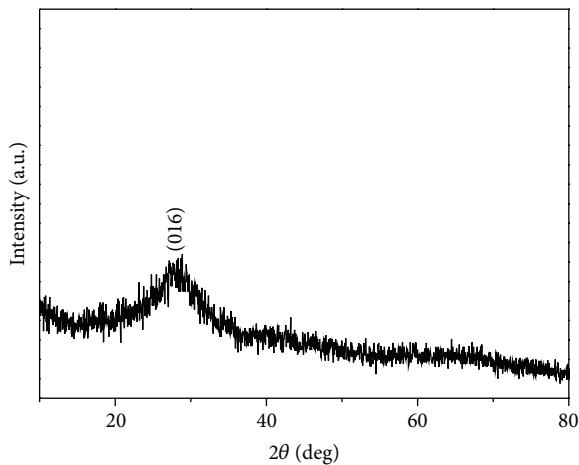


FIGURE 7: XRD pattern of the  $(\text{Bi, Sb})_{2-x}\text{Te}_{3+x}$ -based nanowire.

control the composition of the deposited  $(\text{Bi, Sb})_{2-x}\text{Te}_{3+x}$ -based materials.

Figure 5 shows the SEM micrographs of the electrolyte formula  $0.015\text{ M Bi}(\text{NO}_3)_3 \cdot 5\text{H}_2\text{O}$ ,  $0.005\text{ M SbCl}_3$ , and  $0.0075\text{ M TeCl}_4$  as a function of  $T_{\text{off}}$  ( $0.1\text{ s} \sim 4\text{ s}$ ); the reduced voltage was set at  $-0.4\text{ V}$  and  $T_{\text{on}}$  was set at  $0.2\text{ s}$ . As  $T_{\text{off}}$  was in the range of  $0.1\text{ s} \sim 1\text{ s}$ , as Figures 5(a)–5(c) show, the deposited  $(\text{Bi, Sb})_{2-x}\text{Te}_{3+x}$ -based materials revealed a structure of nanoscale particles, which were aggregated together; as longer  $T_{\text{off}}$  was used, as Figures 5(d)–5(f) show for  $T_{\text{off}}$  in the range of  $1.6\text{ s} \sim 4\text{ s}$ , the deposited materials changed from nanoscale-aggregated particles to disk-typed particles. From the EDS analysis shown in Table 2, more Te in the deposited  $(\text{Bi, Sb})_{2-x}\text{Te}_{3+x}$ -based materials is the reason to cause the variation in the morphology. Compared with the results in Table 2 and Figure 5, as  $T_{\text{on}}$  is set at  $0.2\text{ s}$ ,  $T_{\text{off}}$  equal to or longer than  $1\text{ s}$  is not suitable to deposit the  $(\text{Bi, Sb})_{2-x}\text{Te}_{3+x}$ -based nanowires, because the main composition is Te and the pulse deposition process leads to large disk-typed particles.

Finally, the electrolyte formula of  $0.015\text{ M Bi}(\text{NO}_3)_3 \cdot 5\text{H}_2\text{O}$ ,  $0.005\text{ M SbCl}_3$ , and  $0.0075\text{ M TeCl}_4$  in the pulse

deposition process was used to deposit the  $(\text{Bi, Sb})_{2-x}\text{Te}_{3+x}$ -based nanowires. The AAO template used to deposit the  $(\text{Bi, Sb})_{2-x}\text{Te}_{3+x}$ -based nanowires had the diameter of  $120 \sim 270\text{ nm}$ , as the deposited nanowires show in Figure 6. As the reduced voltage was  $-0.4\text{ V}$ , the  $T_{\text{on}}/T_{\text{off}}$  was  $0.2\text{ s}/0.6\text{ s}$ , and the cycle time was  $10^5$ ; the  $(\text{Bi, Sb})_{2-x}\text{Te}_{3+x}$ -based nanowires were successfully grown in AAO templates. The SEM picture for that the nanowires is shown in Figure 6(a), they had the length of  $25 \sim 40\text{ }\mu\text{m}$ . The diameter of nanowires was dependent on that of AAO template, which was in the range of  $120 \sim 270\text{ nm}$  as Figure 6(b) shows, and the atomic ratio for Bi:Sb:Te is  $4.12:32.05:63.83$ . XRD pattern of  $(\text{Bi, Sb})_{2-x}\text{Te}_{3+x}$ -based nanowires is shown in Figure 7; the amorphous phase and (016) peak were observed. This result suggests that, as the AAO template and pulse deposition process are used to deposit the  $(\text{Bi, Sb})_{2-x}\text{Te}_{3+x}$ -based nanowires, the  $(\text{Bi, Sb})_{2-x}\text{Te}_{3+x}$  phase can be formed. Figure 8 shows the EDS analysis of the  $(\text{Bi, Sb})_{2-x}\text{Te}_{3+x}$ -based nanowires; the photos show that the detective intensity of Te is higher than those of Bi and Sb, which match the results shown in Table 2.

## 4. Conclusions

When pulse deposition process was used, the  $T_{\text{on}}/T_{\text{off}}$  ratio and the reduced voltage would influence the composition of the  $(\text{Bi, Sb})_{2-x}\text{Te}_{3+x}$ -based materials. As the duration of  $T_{\text{off}}$  was in the range of  $0.4\text{ s} \sim 1\text{ s}$ , the  $(\text{Bi} + \text{Sb})/\text{Te}$  atomic ratio was close to  $2/3$ ; as the duration of  $T_{\text{off}}$  was longer than  $1\text{ s}$ , the Te atomic ratio was larger than  $70\%$ . As  $T_{\text{on}}$  and  $T_{\text{off}}$  were set at  $0.2\text{ s}$  and  $1\text{ s}$ , and the pulse voltage was changed from  $-0.4\text{ V}$  to  $-0.6\text{ V}$ , the deposited  $(\text{Bi, Sb})_{2-x}\text{Te}_{3+x}$ -based materials revealed the p-typed thermoelectric property, because the Te atomic ratio was smaller than  $60\%$ . As the reduced voltage was  $-0.4\text{ V}$  and the  $T_{\text{on}}/T_{\text{off}}$  was  $0.2\text{ s}/0.6\text{ s}$ , the  $(\text{Bi, Sb})_{2-x}\text{Te}_{3+x}$ -based nanowires were successfully grown in AAO templates. The nanowires had the length of  $25 \sim 40\text{ }\mu\text{m}$  and the diameter of  $120 \sim 270\text{ nm}$ , and the atomic ratio for Bi:Sb:Te was  $4.12:32.05:63.83$ .

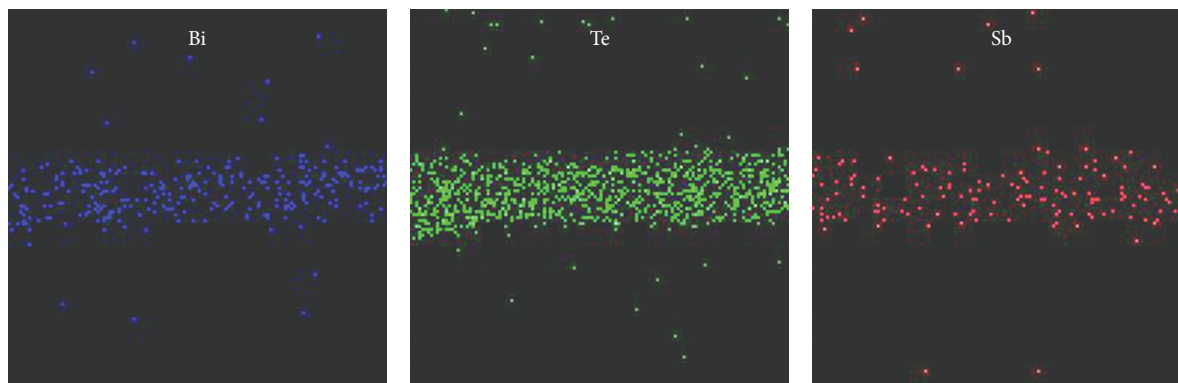


FIGURE 8: EDS analysis of the  $(\text{Bi, Sb})_{2-x}\text{Te}_{3+x}$ -based nanowire.

### Conflict of Interests

The authors declare that there is no conflict of interests regarding the publication of this paper.

### Acknowledgments

The authors acknowledge the financial support of NSC 102-3113-S-003-008-G, NSC 102-3113-S-262-001, NSC 102-2221-E-218-036, and NSC 102-2221-E-390-027.

### References

- [1] G. Mahan, B. Sales, and J. Sharp, "Thermoelectric materials: new approaches to an old problem," *Physics Today*, vol. 50, no. 3, pp. 42–47, 1997.
- [2] J. Y. Hwang, H. Mun, J. Y. Cho et al., "Electronic and thermal transport properties of complex structured Cu-Bi-Se thermoelectric compound with low lattice thermal conductivity," *Journal of Nanomaterials*, vol. 2013, Article ID 502150, 7 pages, 2013.
- [3] A. I. Boukai, Y. Bunimovich, J. Tahir-Kheli, J. Yu, W. A. Goddard III, and J. R. Heath, "Silicon nanowires as efficient thermoelectric materials," *Nature*, vol. 451, no. 7175, pp. 168–171, 2008.
- [4] K. F. Hsu, S. Loo, F. Guo et al., "Cubic  $\text{AgPb}_m\text{SbTe}_{2+m}$ : bulk thermoelectric materials with high figure of merit," *Science*, vol. 303, no. 5659, pp. 818–821, 2004.
- [5] K. Kadel, L. Kumari, W. Z. Li, J. Y. Huang, and P. P. Provencio, "Synthesis and thermoelectric properties of  $\text{Bi}_2\text{Se}_3$  nanostructures," *Nanoscale Research Letters*, vol. 6, no. 1, article 57, 2011.
- [6] D. M. T. Kuo and Y. C. Chang, "Effects of interdot hopping and Coulomb blockade on the thermoelectric properties of serially coupled quantum dots," *Nanoscale Research Letters*, vol. 7, article 257, 2012.
- [7] P. Slobodian, P. Riha, R. Olejnik, M. Kovar, and P. Svoboda, "Thermoelectric properties of carbon nanotube and nanofiber based ethylene-octene copolymer composites for thermoelectric devices," *Journal of Nanomaterials*, vol. 2013, Article ID 792875, 7 pages, 2013.
- [8] L. D. Hicks and M. S. Dresselhaus, "Effect of quantum-well structures on the thermoelectric figure of merit," *Physical Review B*, vol. 47, no. 19, pp. 12727–12731, 1993.
- [9] Z. Fan, J. Zheng, H. Q. Wang, and J. C. Zheng, "Enhanced thermoelectric performance in three-dimensional superlattice of topological insulator thin films," *Nanoscale Research Letters*, vol. 7, article 570, 2012.
- [10] R. Venkatasubramanian, E. Siivola, T. Colpitts, and B. O'Quinn, "Thin-film thermoelectric devices with high room-temperature figures of merit," *Nature*, vol. 413, no. 6856, pp. 597–602, 2001.
- [11] T. C. Harman, P. J. Taylor, M. P. Walsh, and B. E. LaForge, "Quantum dot superlattice thermoelectric materials and devices," *Science*, vol. 297, no. 5590, pp. 2229–2232, 2002.
- [12] Y. Jia, D. Yang, B. Luo, S. Liu, M. O. Tade, and L. Zhi, "One-pot synthesis of Bi-Ni nanowire and nanocable arrays by coelectrodeposition approach," *Nanoscale Research Letters*, vol. 7, article 130, 2012.
- [13] T. C. Harman, P. J. Taylor, D. L. Spears, and M. P. Walsh, "Thermoelectric quantum-dot superlattices with high ZT," *Journal of Electronic Materials*, vol. 29, no. 1, pp. L1–L2, 2000.
- [14] D. Li, Y. Wu, R. Fan, P. Yang, and A. Majumdar, "Thermal conductivity of Si/SiGe superlattice nanowires," *Applied Physics Letters*, vol. 83, no. 15, pp. 3186–3188, 2003.
- [15] Y. Li, J. Wang, Z. Deng et al., "Bismuth nanotubes: a rational low-temperature synthetic route," *Journal of the American Chemical Society*, vol. 123, no. 40, pp. 9904–9905, 2001.
- [16] F. Xiao, C. Hangarter, B. Yoo, Y. Rheem, K. Lee, and N. V. Myung, "Recent progress in electrodeposition of thermoelectric thin films and nanostructures," *Electrochimica Acta*, vol. 53, no. 28, pp. 8103–8117, 2008.
- [17] R. J. Mehta, Y. Zhang, C. Karthik et al., "A new class of doped nanobulk high-figure-of-merit thermoelectrics by scalable bottom-up assembly," *Nature Materials*, vol. 11, no. 3, pp. 233–240, 2012.
- [18] K. T. Kim and G. H. Ha, "Fabrication and enhanced thermoelectric properties of alumina nanoparticle-dispersed  $\text{Bi}_{0.5}\text{Sb}_{1.5}\text{Te}_3$  matrix composites," *Journal of Nanomaterials*, vol. 2013, Article ID 821657, 6 pages, 2013.
- [19] H. Masuda and K. Fukuda, "Ordered metal nanohole arrays made by a two-step replication of honeycomb structures of anodic alumina," *Science*, vol. 268, no. 5216, pp. 1466–1468, 1995.
- [20] T. Fang, T. H. Wang, S. Kang, and C. Chuang, "Indentation deformation of mesoporous anodic aluminum oxide," *Current Applied Physics*, vol. 9, no. 4, pp. 880–883, 2009.
- [21] M. S. Chandrasekar and M. Pushpavanam, "Pulse and pulse reverse plating-Conceptual, advantages and applications," *Electrochimica Acta*, vol. 53, no. 8, pp. 3313–3322, 2008.